Understanding Complex Systems

Springer : COMPLEXITY

Aneta Stefanovska
Peter V. E. McClintock *Editors*

Physics of Biological Oscillators

New Insights into Non-Equilibrium and Non-Autonomous Systems

Springer

Springer Complexity

Springer Complexity is an interdisciplinary program publishing the best research and academic-level teaching on both fundamental and applied aspects of complex systems—cutting across all traditional disciplines of the natural and life sciences, engineering, economics, medicine, neuroscience, social and computer science.

Complex Systems are systems that comprise many interacting parts with the ability to generate a new quality of macroscopic collective behavior the manifestations of which are the spontaneous formation of distinctive temporal, spatial or functional structures. Models of such systems can be successfully mapped onto quite diverse "real-life" situations like the climate, the coherent emission of light from lasers, chemical reaction-diffusion systems, biological cellular networks, the dynamics of stock markets and of the internet, earthquake statistics and prediction, freeway traffic, the human brain, or the formation of opinions in social systems, to name just some of the popular applications.

Although their scope and methodologies overlap somewhat, one can distinguish the following main concepts and tools: self-organization, nonlinear dynamics, synergetics, turbulence, dynamical systems, catastrophes, instabilities, stochastic processes, chaos, graphs and networks, cellular automata, adaptive systems, genetic algorithms and computational intelligence.

The three major book publication platforms of the Springer Complexity program are the monograph series "Understanding Complex Systems" focusing on the various applications of complexity, the "Springer Series in Synergetics", which is devoted to the quantitative theoretical and methodological foundations, and the "Springer Briefs in Complexity" which are concise and topical working reports, case studies, surveys, essays and lecture notes of relevance to the field. In addition to the books in these two core series, the program also incorporates individual titles ranging from textbooks to major reference works.

Indexed by SCOPUS, INSPEC, zbMATH, SCImago.

Series Editors

Understanding Complex Systems

Founding Editor: S. Kelso

More information about this series at http://www.springer.com/series/5394

Aneta Stefanovska · Peter V. E. McClintock
Editors

Physics of Biological Oscillators

New Insights into Non-Equilibrium and Non-Autonomous Systems

Springer

Editors
Aneta Stefanovska
Department of Physics
Lancaster University
Lancaster, UK

Peter V. E. McClintock
Department of Physics
Lancaster University
Lancaster, UK

ISSN 1860-0832 ISSN 1860-0840 (electronic)
Understanding Complex Systems
ISBN 978-3-030-59804-4 ISBN 978-3-030-59805-1 (eBook)
https://doi.org/10.1007/978-3-030-59805-1

This Springer imprint is published by the registered company Springer Nature Switzerland AG
The registered company address is: Gewerbestrasse 11, 6330 Cham, Switzerland

Foreword by Alex A. R. Webb

An oscillation is the repetitive variation in time of some measure, or between two or more different states. Oscillations occur not only in mechanical systems, but also in other kinds of dynamical system. To the non-specialist it might be a surprise that biological systems can arrange into networks that form robust oscillating dynamical systems, but this is a frequent property of biological networks. By biological oscillators we mean any system with repeated cycles of activity or abundance of a biological component (e.g., metabolite or protein). Biological oscillators include community behaviors, such as seen in ecological studies; however in this book the focus is on oscillations in cellular or physiological activities within a single organism.

Broadly, biological oscillators can be divided into three categories. First, there are those that oscillate for a short period before damping and arise from a perturbation to the system, such as metabolic and homeostatic control mechanisms, including the oscillatory dynamics in glycolysis. The second category of biological oscillators involves stimulus-induced oscillatory behaviors including oscillatory dynamics of signal relays within and between cells, oscillations of blood flow and oscillations in firing of neurons in the brain. Lastly there are the self-sustaining endogenous rhythms including the heart pacemaker, breathing and blood flow in mammals, circadian oscillations, cell division cycles and developmental clocks. These distinctions between the different types of biological oscillations are arbitrary and the boundaries are blurred because all have some self-sustaining properties, and all can have nonautonomous properties affected by other signals. These are some of the complex issues discussed in the pages of this book.

Another level of complexity is introduced by the hierarchy of interactions between oscillators. In both single- and multi-cellular organisms, oscillators often can occur within a single cell, however, interactions between cells can reinforce, amplify and make the oscillations more robust, such as found in the oscillations between the neurons of the suprachiasmatic nucleus of the circadian pacemaker of mammalian brains. In the mammalian circadian pacemaker, the oscillatory dynamics are generated by transcriptional feedback loops of gene expression,

protein synthesis and protein degradation in the individual cells, and are reinforced by electrical coupling between the cells, resulting in a very robust multicellular circadian oscillator.

Physics has developed powerful conceptual and mathematical tools to understand the behavior of physical oscillators, such as pendula. Remarkably, the analogies from the physical world have proven to be useful in describing, modeling and understanding the behaviors and dynamics of biological oscillators. Physics offers much to the biologist, providing formal descriptions of systems that are too complex to be understood intuitively, and predictive power, which is required to turn discovery into application. Whilst useful, there are challenges in applying concepts from the physical world to biological oscillators. Physical descriptions of oscillators are often applied to designed mechanical or electronic systems in which the components and connections are known and well understood. Often, in studying biological oscillators, the number of components, the nature of the components, the network of interactions between the components and the mechanisms by which these interactions occur are either assumed, or known for only a few of the components that make up the oscillator.

Biological oscillators can be formed by very simple systems comprising only two components, but are often formed of very complex networks that can be nearly fully connected and therefore have a high degree of feedback. For example, the mutual gene regulatory networks that are part of the 24-hour circadian oscillator of plant cells involve mutual regulation between at least 30 genes in a nearly fully connected network. This means it is often difficult to obtain a model of the interactions in the network in which one can have full confidence. The nature of the oscillatory dynamics in biological systems can be complex, involving many changes in state, abundance and location of the components. In the plant circadian oscillator as an example, feedback between components can occur through protein-DNA interactions regulating the expression of component parts, phosphorylation to affect protein activity, ubiquitination to affect protein stability and translocation between the cytoplasm and nucleus to regulate accessibility of transcriptional regulators to DNA.

One of the most challenging features of biological oscillators, compared to those designed by humans, is that at different times in the oscillatory cycle, the network of regulatory connections in the oscillator can change. For example, in the circadian oscillators that drive 24 hour rhythms in plants and humans, the proteins that form the regulatory network vary greatly in their abundance over the cycle because of oscillations in protein translation and breakdown, which are the basis of the oscillatory dynamics. Thus, theoretical and mathematical descriptions of biological oscillators must describe not only the dynamics and properties of the oscillator, but also how those change through the oscillatory cycle. This is a particular challenge when considering non-autonomous oscillators that respond to external inputs, which probably represents most biological oscillators, because regulation by an external signal can be affected by the state and availability of a component in the oscillator, meaning that regulatory inputs are subject themselves to feedback control from the oscillator.

It is these similarities and differences between physical and biological oscillators which resulted in the Physics of Biological Oscillators (POBO) conference at Chicheley Hall, UK in 2018, a meeting held in celebration of the 60th birthday of Aneta Stefanovska who has contributed so much to the development of the subject. This book captures the discussions and presentations during three wonderful days of exciting science, in which experts in different disciplines grappled with the immense intellectual challenges of finding the best ways to describe, analyze, model and understand the properties, functions, behaviors and uses of biological oscillators. The chapters summarizing the presentations by researchers across the different disciplines give an insight into the different biological systems being investigated and the variety of Physics approaches being used. It was exhilarating to spend three days in the company of researchers from different disciplines trying to bridge the gaps between the experts in different fields to understand these fundamental biological behaviors. This seems an even more amazing experience looking back through the lens of the COVID-19 pandemic which hit during the final stages of production of this book. I hope you enjoy the invigorating intellectual stimulation contained within these chapters as much as I have.

August 2020

Alex A. R. Webb
Department of Plant Sciences
University of Cambridge
Cambridge, UK

Preface

This book derives mainly from a Research Workshop *Physics of Biological Oscillators: New Insights into Non-Equilibrium and Non-Autonomous Systems*[1] held in Chicheley Hall (27–30 November 2018): see photograph. It was a highly interdisciplinary event that brought together some of the best international experts working on the vexed problem of how best to treat the non-autonomous oscillatory systems that crop up so often in biology. They included life scientists who investigate and measure the oscillations and the physicists, chemists, mathematicians, information theorists, and engineers seeking to understand their fundamental nature and origins and to devise useful applications of this knowledge. Thus, although their work lies in seemingly very different scientific areas—ranging from mathematics to the experimental recording and analysis of real data—they were all addressing in one way or another the problem of time-variability in oscillatory systems. They gave presentations about how to measure, analyze, model, and understand such data as well as considering applications to medicine, both actual and potential. Nearly all of the experts, assembled from 19 countries, kindly agreed to write up their presentations for publication thereby providing the basis for the book.

Lancaster, UK

Aneta Stefanovska
Peter V. E. McClintock

[1] www.physicsoflife.org.uk/physics-of-biological-oscillators.html.

Participants in the POBO Research Workshop *Physics of Biological Oscillators: New Insights into Non-Equilibrium and Non-Autonomous Systems*, outside the front door of Chicheley Hall, Buckinghamshire, UK, where the event took place. Photograph by M. G. Rosenblum (University of Potsdam)

Acknowledgements

As editors we would like to thank the huge number of individuals and organizations that made this book possible. First and foremost, of course, we thank the authors who wrote the individual chapters, and then amended them, striving to make them, not only scientifically accurate, but also understandable across the interdisciplinary divide. We are much indebted to all the anonymous reviewers, who went through the chapter manuscripts in detail and offered thoughtful advice on how they might be improved. We are grateful to Marion McClintock for her helpful comments and suggestions on the text. We thank all the participants in our *POBO* research workshop whose presentations in Chicheley Hall have given rise to the book, as well as the several organizations that supported the event, including: the Engineering and Physical Sciences Research Council (EPSRC) Network on Emergence and Physics Far From Equilibrium; the EPSRC Physics of Life Network (PoLNet); the EPSRC Physical Sciences Programme; the Institute of Physics; the International Union of Pure and Applied Physics (IUPAP); and Lancaster Helium Ltd. We are especially grateful to Dr. Karis Baker who runs PoLNeT for her continuing encouragement and support.

August 2020

Aneta Stefanovska
Peter V. E. McClintock

Contents

Contributors

Christian Aalkjær Department of Biomedical Sciences, University of Copenhagen, Copenhagen, Denmark;
Institute of Biomedicine, University of Aarhus, Aarhus, Denmark

Yunus A. Abdulhameed Department of Physics, Lancaster University, Lancaster, UK;
Now at Department of Mathematics, University of Texas at San Antonio, San Antonio, TX, USA

Takashi Amemiya Graduate School of Environment and Information Sciences, Yokohama National University (YNU), Hodogaya-ku, Yokohama, Kanagawa, Japan

Ronny P. Bartsch Department of Physics, Bar-Ilan-University, Ramat Gan, Israel

Alona Ben-Tal School of Natural and Computational Sciences, Massey University, North Shore, Auckland, New Zealand

Martin Bier Department of Physics, East Carolina University, Greenville, North Carolina, USA

Nikolai K. Chemeris Institute of Cell Biophysics, Russian Academy of Sciences, Pushchino, Russian Federation

Andrew J. Chipperfield Bioengineering Science Group, Faculty of Engineering and the Environment, University of Southampton, Highfield, Southampton, UK

Geraldine F. Clough Human Development & Health, Faculty of Medicine, Southampton General Hospital, University of Southampton, Southampton, UK

Antonio Colantuoni Department of Clinical Medicine and Surgery, Federico II University Medical School, Naples, Italy

Andreas Daffertshofer Faculty of Behavioural and Movement Sciences, Amsterdam Movement Sciences & Institute for Brain and Behaviour Amsterdam, Vrije Universiteit Amsterdam, Amsterdam, The Netherlands

Ingo Fietze Interdisziplinäres Schlafmedizinisches Zentrum, Charitecentrum Für Pneumologie CC12, Charité – Universitätsmedizin Berlin, Berlin, Germany

Pedro L. Gambús Department of Anesthesia, Hospital Clinic de Barcelona, Barcelona, Spain;
Biomedical Engineering, Universidad de Barcelona, Barcelona, Spain

Erik Gengel Institute for Physics and Astronomy, Universit of Potsdam, Potsdam, Germany;
Friedrich-Ebert Stiftung, Bonn, Germany

Martin Glos Interdisziplinäres Schlafmedizinisches Zentrum, Charitecentrum Für Pneumologie CC12, Charité – Universitätsmedizin Berlin, Berlin, Germany

Abdulrazaq G. Habib Department of Medicine, Bayero University, Kano, Nigeria

Jens Christian Brings Jacobsen Department of Biomedical Sciences, University of Copenhagen, Copenhagen, Denmark

Peter E. Kloeden Mathematische Institut, Universität Tübingen, Tübingen, Germany

Ivana Kovacic Faculty of Technical Sciences, Centre of Excellence for Vibro-Acoustic Systems and Signal Processing, University of Novi Sad, Novi Sad, Serbia

Gennady V. Krasnikov Tula State Lev Tolstoy Pedagogical University, Tula, Russian Federation

Jan Krämer Kardiovaskuläre Physik, Arbeitsgruppe Nichtlineare Dynamik, Fachbereich Physik, Humboldt-Universität Berlin, Berlin, Germany

Dominga Lapi Department of Clinical Medicine and Surgery, Federico II University Medical School, Naples, Italy

Klaus Lehnertz Department of Epileptology and Helmholtz Institute for Radiation and Nuclear Physics and Interdisciplinary Centre for Complex Systems, University of Bonn, Bonn, Germany

David Lloyd School of Biosciences, and of Engineering, Cardiff University, Cardiff, Wales, UK

Maxime Lucas Turing Center for Living Systems, CNRS, Aix-Marseille University, Marseille, France

Anita Lunding PhyLife, Institute of Biochemistry and Molecular Biology, University of Southern Denmark, Odense M, Denmark

Yaopeng Ma Department of Physics, Bar-Ilan-University, Ramat Gan, Israel

Robert S. MacKay Mathematics Institute and Centre for Complexity Science, University of Warwick, Coventry, UK

Pablo Martínez-Vázquez Deutsches Primaten Zentrum (DPZ), Goettingen, Germany

Peter V. E. McClintock Department of Physics, Lancaster University, Lancaster, UK

Kazuyuki Nakamura School of Interdisciplinary Mathematical Sciences, Meiji University, Nakano-ku, Tokyo, Japan;
JST, PRESTO, Kawaguchi, Saitama, Japan

Hiroya Nakao Department of Systems and Control Engineering, Tokyo Institute of Technology, Tokyo, Japan

Satoshi Nakata Graduate School of Integrated Sciences for Life, Hiroshima University, Higashi-Hiroshima, Japan

Julian M. I. Newman Department of Mathematics, University of Exeter, Exeter, UK

Lars Folke Olsen PhyLife, Institute of Biochemistry and Molecular Biology, University of Southern Denmark, Odense M, Denmark

Thomas Penzel Interdisziplinäres Schlafmedizinisches Zentrum, Charitecentrum Für Pneumologie CC12, Charité – Universitätsmedizin Berlin, Berlin, Germany;
Saratov State University, Saratov, Russia

Bastian Pietras Institute of Mathematics, Technische Universität Berlin & Bernstein Center for Computational Neuroscience, Berlin, Germany

Arkady Pikovsky Institute for Physics and Astronomy, Universit of Potsdam, Potsdam, Germany;
Higher School of Economics, Nizhny Novgorod, Russia;
Department of Control Theory, Institute of Information Technologies, Mathematics and Mechanics, Lobachevsky University Nizhny Novgorod, Nizhny Novgorod, Russia

Dragi Radomirovic Faculty of Agriculture, University of Novi Sad, Novi Sad, Serbia

Johan Raeder Department of Anaesthesia, University of Oslo and Senior Consultant, Oslo University Hospital, Oslo, Norway

Kenichi Shibata Graduate School of Environment and Information Sciences, Yokohama National University (YNU), Hodogaya-ku, Yokohama, Kanagawa, Japan

Angela Shore Institute of Biomedical and Clinical Science, University of Exeter Medical School, Exeter, UK

Tomislav Stankovski Faculty of Medicine, Ss. Cyril and Methodius University in Skopje, Skopje, North Macedonia;
Department of Physics, Lancaster University, Lancaster, UK

Aneta Stefanovska Department of Physics, Lancaster University, Lancaster, UK

Arina V. Tankanag Institute of Cell Biophysics, Russian Academy of Sciences, Pushchino, Russian Federation

Marjola Thanaj Bioengineering Science Group, Faculty of Engineering and the Environment, University of Southampton, Highfield, Southampton, UK

Clare Thorn Institute of Biomedical and Clinical Science, University of Exeter Medical School, Exeter, UK

Constantino Tsallis Centro Brasileiro de Pesquisas Fisicas and National Institute of Science and Technology for Complex Systems, Rio de Janeiro - RJ, Brazil

Vesna Vuksanović Health Data Research UK and Swansea University Medical School, Swansea, Wales, UK;
Aberdeen Biomedical Imaging Centre, Institute for Medical Sciences University of Aberdeen, Aberdeen, Scotland, UK

Masatoshi Watanabe Graduate School of Medicine, Mie University, Tsu, Mie, Japan

Erik Weber Jensen R&D of Quantium Medical/Fresenius Kabi. Barcelona & Automatic Control and Informaic (ESAII) Department, Centre for Biomedical Research (CREB) UPC-Barcelonatech, Barcelona, Spain

Niels Wessel Kardiovaskuläre Physik, Arbeitsgruppe Nichtlineare Dynamik, Fachbereich Physik, Humboldt-Universität Berlin, Berlin, Germany

Tomohiko Yamaguchi Meiji Institute for Advanced Study of Mathematical Sciences (MIMS), Nakano-ku, Tokyo, Japan

Meihua Yang School of Mathematics and Statistics, Huanzhong University of Science and Technology, Wuhan, China

Steven Yuvan Department of Physics, East Carolina University, Greenville, North Carolina, USA

Miodrag Zukovic Faculty of Technical Sciences, Centre of Excellence for Vibro-Acoustic Systems and Signal Processing, University of Novi Sad, Novi Sad, Serbia

Abbreviations

AAFT	Amplitude-adjusted Fourier transform (surrogate data)
ADP	Adenosine diphosphate
AEP	Auditory evoked potential
AI	Association-induction (hypothesis)
ALE	Asymptotic Lyapunov exponent
ARA	Attractor reconstruction analysis
ATP	Adenosine triphosphate (molecule that carries energy within cells)
AV	Atrioventricular (node)
AWR	Awareness with recall
BF	Blood flux
BIS™	Commercial anaesthetic monitor manufactured by Medtronic, Minneapolis
BMBF	Federal Ministry of Education and Research
BMI	Body mass index
BOLD	Blood-oxygen-level-dependent
BP	Blood pressure
BRACCIA	Brain, respiration and cardiac causalities in anæthesia (an FP6 project)
BSR	Burst suppression rate
cGMP	Cyclic guanosine monophosphate (a cyclic nucleotide)
CNS	Central nervous system
CPC	Cardiopulmonary coupling
CRPS	Cardiorespiratory phase synchronization
CSA	Central sleep apnea
CT	Computerised tomography
CT	Core temperature
CVD	Cardiovascular disease
CWT	Continuous wavelet transform
DBP	Diastolic blood pressure
DFA	Detrended fluctuation analysis

DFG	Deutsche Forschungsgemeinschaft (German research funding agency)
DFT	Discrete Fourier transform
DNA	Deoxyribonucleic acid (the molecule carrying the genetic information)
DoA	Depth of anaesthesis
DSA	Density spectral array
DU145	Imortalised human prostate cancer cell line, used in research
DVT	Deep venous thrombosis
ECG	Electrocardiogram
EDHF	Endothelium-derived hyperpolarizing factor
EDR	Electrocardiographically derived respiration signal
EEG	Electroencephalograph
EMG	Electromyogram
EOG	Electrooculogram
EPSRC	Engineering and Physical Sciences Research Council (UK)
ETC	Effort to compress
FFT	Fast Fourier transform
FHN	FitzHugh-Nagumo
FM	Febrile malaria
fMRI	Functional magnetic resonance imaging
FTD	Fronto-temporal dementia
FTLE	Finite-time Lyapunov exponents
GA	General anaesthesia
GIF	German-Israeli Foundation
GLUT	Glucose transporter
GSTFT	Generalized short time Fourier transform
HeLa	Imortalised human cell line derived from Henrietta Lacks, used in research
HF	High frequency (0.15–0.4 Hz)
HFC	High-frequency coupling
HR	Heart rate
HRV	Heart rate variability
IAAFT	Iterative amplitude-adjusted Fourier transform (surrogate data)
IHR	Instantaneous heart rate
IHTE	Iterative Hilbert transform embeddings
ILE	Instantaneous Lyapunov exponent
IPC	Intermittent pneumatic compression (of the microvasculature)
iPRC	Infinitesimal phase response curve
IR	Infrared
IRR	Instantaneous respiration rate
LDF	Laser Doppler flowmetry
LE	Lyapunov exponent
LF	Low frequency (0.04–0.15 Hz)
LFC	Low-frequency coupling (LFC)

L-NNA	Nω-Nitro-L-arginine (L-NNA)
LOC	Loss of consciousness
LZC	Lempel-Ziv complexity
MEG	Magnetoencephalography
MLZC	Multiscale Lempel-Ziv complexity
MRI	Magnetic resonance imaging
MSE	Multiscale entropy
NAD	Nicotinamide adenine dinucleotide
NADH	Reduced NAD
NFM	Non-febrile malaria
NH	Normally hyperbolic
NIRS	Near infrared spectroscopy
NM	Non-malaria (i.e., healthy)
NMBA	Neuromuscular blocking agent
NMD	Nonlinear mode decomposition
NOL^{TM}	Nociception level (index)
ODE	Ordinary differential equation
OSA	Obstructive sleep apnea
oxyHb	Oxyhaemoglobin
PCV	Packed cell volume (in blood)
PDE	Partial differential equation
PET	Positron emission tomography
PFK	Phosphofructokinase
PK	Pyruvate kinase
PRC	Phase response curve
preBötC	Pre-Bötzinger complex, in the brainstem
PSD	Power spectral density
PSG	Polysomnography
PSI	Patient State Index
PU	Perfusion units (arbitrary)
qCON^{TM}	Commercial anaesthetic monitor manufactured by Quantium Medical, Barcelona
RBC	Red blood cell
RD	Reaction-diffusion
RDA	Relative dispersional analysis
RDT	Rapid diagnostic test (for malaria)
REM	Rapid eye movement (during dreams)
RSA	Respiratory sinus arrhythmia
SampEn	Sample entropy
SBF	Spontaneous breathing frequency
SBP	Systolic blood pressure
SG	Savitzky-Golay (filter)
SL	Stuart-Landau (oscillator)
SQI	Signal quality index
SRBD	Sleep-related breathing disorders

ST	Skin temperature
TIVA	Total intravenous anaesthesia
VLF	Very low frequency (below 0.04 Hz)
WEKA	Waikato environment for knowledge analysis
WPC	Wavelet phase coherence
WT	Wavelet transform

Chapter 1
Introduction

Peter V. E. McClintock and Aneta Stefanovska

Abstract To set the subject of book in context, a short discussion of oscillatory dynamical systems with non-constant frequencies is provided. Such oscillators are widespread, especially (but not only) in biology. It is pointed out that they can be considered as thermodynamically open (physics) or non-autonomous (mathematics). The difficulty of treating and analysing data derived from such systems is that most earlier work, and most of the well-established methods, refer to dynamics where the natural frequencies remain constant. Recent progress is discussed in five sections corresponding to Parts of the book. They cover respectively theory, model-driven and data-driven approaches, biological oscillators, applications, and the future. Ways of using the book are suggested.

There are numerous oscillatory systems that are not periodic. In striking contrast to the simple pendulum, which so often introduces the physics student to oscillation theory, their characteristic frequencies vary in time. Such oscillators are found universally in biology, and they also appear in other contexts too. Understanding their dynamics is challenging, not least because physicists new to the area must be willing to discard, or modify, many cherished notions dating back to their schooldays.

The problem is non-trivial, because in practice the origin of the time variability is often unknown (unlike e.g. heart-rate variability where respiration modulates the heart rhythm, or the diurnal rhythm). In mathematical terms, the oscillations are non-autonomous, reflecting the physics of open systems where the function of each oscillator is affected by its environment. Time-frequency analysis is essential. Recent approaches, including wavelet phase coherence analysis and nonlinear mode decomposition, were described during the Workshop and form parts of several of

P. V. E. McClintock (✉) · A. Stefanovska
Department of Physics, Lancaster University, LA1 4YB Lancaster, UK
e-mail: p.v.e.mcclintock@lancaster.ac.uk

A. Stefanovska
e-mail: aneta@lancaster.ac.uk

A. Stefanovska and P. V. E. McClintock (eds.), *Physics of Biological Oscillators*, Understanding Complex Systems,
https://doi.org/10.1007/978-3-030-59805-1_1

the contributions that follow. These methods are not yet in widespread use, and one purpose of the book (and of the Workshop before it) is to help to promulgate them.

Science is, of course, seamless and indivisible but, for the convenience of readers, we have divided the book into four Parts covering: theory; model-driven and data-driven approaches; biological oscillators; and applications. These are not rigidly separated topics but, rather, an indication of emphasis. The applications chapters, for example, draw freely on the ideas discussed in the first three Parts.

1.1 Theory

The theory Part opens with two chapters devoted to different aspects of phase reduction, applied to autonomous oscillatory systems, an approach that will be key to most of what follows on non-autonomous oscillators. The underlying idea is to reduce a multi-dimensional dynamical equation describing a nonlinear limit cycle oscillator to a one-dimensional phase equation. Many rhythmic phenomena can in practice be considered as nonlinear limit cycle oscillators, and hence described in terms of their phase dynamics, usually amounting to an enormous simplification. This approach is particularly useful in relation to the analysis of synchronising oscillators. In real-world situations the oscillators are of course subject to external perturbations that take the system away from its limit cycle temporarily, and much interest attaches to what happens when two such systems interact with each other. Note however that the core of the book involves consideration of the situation that arises when one or more of the oscillators is non-autonomous, so that the frequency of the limit cycle itself is being perturbed by external agency. Chapter 2 by Nakao makes use of a recently-introduced extension of the classical phase reduction method that also includes amplitude degrees of freedom. He considers phase-amplitude reduction in a spatially-extended reaction-diffusion system exhibiting stable oscillatory patterns, and its entrainment by optimized periodic forcing with additional stabilization by feedback. Chapter 3 by Pietras and Daffertshofer shows how different reduction techniques applied to a network of interacting neural oscillators can lead to different dynamics of the reduced network, thereby identifying some delicate issues in the application of the method. They demonstrate that an accurately-derived phase model can properly capture the collective dynamics and they discuss the effect of biologically plausible connectivity structures on the network behaviour.

In Chap. 4, Kloeden and Yang outline relevant ideas from the mathematical theory of non-autonomous attractors, explaining that the nature of time in a non-autonomous dynamical system is very different from that in autonomous systems. They point out that this difference has profound consequences in terms of the interpretation of dynamical behaviour, and that many of the familiar concepts developed for autonomous dynamical systems are either too restrictive, or invalid, in the non-autonomous context. Chapter 5 by MacKay presents a view of a non-autonomous oscillator as a mapping from input functions of time to a circle of possible solutions (state functions of time). The author indicates how this view encompasses chrono-

taxic systems and provides a picture of synchronisation in networks of oscillators, whether autonomous or not.

In Chap. 6, Lucas et al. start from the viewpoint that the concept of thermodynamic openness is key to the functioning of living systems. The authors model openness in coupled oscillators through an external driving force with time-varying parameters. They consider a single, driven oscillator with a periodic, noisy frequency and a time-varying driving frequency, followed by driven networks with time-varying frequency and coupling. They characterise system stability by short- and long-time Lyapunov exponents, both analytically and numerically, and they also describe the different dynamical regimes in time-frequency representations. They show that time-variation of parameters can enlarge the parameter space within which synchronous behaviour is stable, as well as yielding additional phenomena such as intermittent synchronisation. The authors also demonstrate that the stabilising effect of deterministic non-autonomous driving is similar to that of bounded noise over longer times, although the short-time dynamics is very different.

Chapter 7 by Newman et al. addresses the question of non-asymptotic-time dynamics where the usual assumption of long-time-asymptotic properties like traditionally defined notions of stability and neutral stability, as well as asymptotic Lyapunov exponents, are inapplicable. By consideration of the non-autonomous Adler equation with slowly-varying forcing, they illustrate three limitations of the traditional approach. They then propose an alternative, "finite-time slow-fast" approach, that is more suitable for slowly time-dependent one-dimensional phase dynamics, and likely to be suitable for describing the dynamics of open systems involving two or more timescales.

In the final chapter of the Theory Part, Yuvan and Bier discuss synchronisation phenomena from yet another point of view. They come to the topic through a consideration of phase transitions in large systems of interacting units, leading to a mathematical description of an order parameter's power-law behaviour near the critical temperature of the system. The authors also discuss the phenomenon from an entropy point of view and indicate implications for real-life experiments on the oscillatory behaviour of yeast cells (cf. Chap. 13).

1.2 Model-Driven and Data-Driven Approaches

The relationship between (often idealised and abstract) mathematical theory and phenomena measured in the real world almost invariably involves modelling, the usual aim being to build the simplest possible model capable of encompassing the observations. Sometimes the model is created mainly on the basis of physical intuition, and several may be considered before arriving at the seemingly optimal one. In other cases, the model can emerge directly from the observations i.e. from the data that are measured. Part II comprises four chapters in which modelling plays a key role.

In Chap. 9 Kovačič et al. introduce a mechanics perspective by considering the oscillations on a chain of masses connected by linear springs and focus, in partic-

ular, on localised modes where only parts of the chain oscillate. They relate their model to the mechanical oscillations of trees, where the branches move but usually not the trunk. Chapter 10 by Ben-Tal presents some thoughts on the (sometimes controversial) question of how non-autonomous model systems can be converted to autonomous ones by application of an appropriate transformation. The author discusses the procedure, not only for periodic forcing, but also for other special cases. In Chap. 11, Stankovski offers an overview of the coupling functions that can be used to model the interactions between oscillatory systems and which mediate the non-autonomous effects seen in a particular system under examination. He focuses on the use and suitability of coupling functions in neuroscience and their use in accounting for neuronal oscillations and brain (EEG) waves. The final contribution to Part II, Chap. 12 by Gengel and Pikovsky, tackles one of the central questions confronting an experimentalist making measurements on an oscillatory system, not necessarily a biological one: how best can the recorded time series be analysed to illuminate understanding of the underlying dynamics? The authors show that *iterated Hilbert transform embedding* provides a good reconstruction of the phase dynamics, provided that the amplitude variations are relatively small.

1.3 Biological Oscillations

Although the biological oscillators of Part III are not the only examples of non-autonomous oscillatory systems, they are overwhelmingly the most widespread and important. Living systems are inherently non-autonomous on account of the internal interactions between their component parts, in addition to the influence of the external environment. Each oscillator affects some of the other oscillators, thus giving rise to the time-variations in frequency and amplitude that are observed. Furthermore, living systems are never stationary but, rather, are in a state of continuous evolution from birth until death, with corresponding evolution of their characteristic parameter values.

Chapter 13 by Folke Olsen and Lunding is devoted to oscillations in yeast glycolysis. These have been known about for over six decades, but their mechanism remains uncertain and their purpose is still a mystery. The authors present experimental evidence that many variables, seemingly unrelated to glycolysis, oscillate in synchrony with glycolytic intermediates. They suggest that the function of metabolic oscillations is to maintain the cell in a state of constant low entropy. In Chap. 14 Lloyd provides a general discussion of biological oscillations, including yeast cell oscillations, and he too considers what their purpose may be. He discusses a model in which ultradian (faster than circadian) rhythms are the synchronizing signatures that organize the coherence of the living state. Chapter 15 by Amemiya et al. addresses glycolytic oscillations in cancer cells. It reviews the first direct observation of glycolytic oscillations in HeLa cervical and DU145 prostate cancer cells. The authors propose a mathematical model to account for the oscillation mechanism, show that it can reproduce the experimental results, and consider the wider implications. They

find that, the greater the malignancy of the cells, the more they tend to exhibit glycolytic oscillations and the higher the frequency becomes.

In Chap. 16, Jacobsen and Aalkjaer provide a brief review of vasomotion. These are oscillations that occur in the tone or diameter of arteries and lead to the phenomenon of flowmotion, where the flow of blood into tissue occurs in an oscillatory manner. They discuss the mechanisms and how these can be studied. The authors hypothesise that vasomotion is beneficial because it ensures more efficient delivery of oxygen and removal of waste products, but point out that there is still a need for confirmatory experimental evidence. Chapter 17, by Colantuoni and Lapi provides another succinct review of research on vasomotion, but from an historical perspective, focusing on the seminal contributions made by their own research group.

The next two chapters relate to oscillations observed in skin blood flow. Chapter 18 by Tankanag et al. describes an investigation of paced and depth-controlled respiration in which they measured the phase coherence between skin blood flow oscillations at the pacing frequency in the left and right index fingers. They find that pacing the respiration results in a significant increase in phase coherence compared to spontaneous respiration. They attribute these results to the effect of the autonomic nervous system on vascular tone regulation under controlled breathing. In Chap. 19, Thanaj et al. review non-linear complexity-based approaches to the analysis of microvascular blood flow oscillations, with a particular focus on the extent to which they are able to identify changes in microvascular function. They conclude that, although such approaches have utility in understanding the fundamental mechanistic contributors to microvascular (dys)function, it has yet to be demonstrated that they can usefully discriminate between different (patho)physiological states in order to inform treatment regimens or to predict clinical outcomes.

Chapter 20, by Penzel et al., examines the changes in cardiovascular and electroencephalograph (EEG) oscillations that take place during sleep. The autonomous nervous system is regulated in totally different ways during slow-wave (non-REM) and REM sleep, so that analysis of instantaneous heart-rate variations allows for automatic scoring of sleep stages. The authors also find it possible, to some extent, to track transitions from wakefulness to sleep solely by analysis of heart-rate variations. ECG and heart rate analysis allow assessment of sleep disorders as well.

The final chapter in Part III, Chap. 21 by Vuksanović, reviews current knowledge of the modular properties of brain networks, as derived from *in vivo* neuroimaging of cortical morphology (e.g. thickness, surface area), and their relationship to function. The focus is on the cross-level and cross-modal organisational units of the brain, and the relationships to their modular topology. Recent approaches in network science enable the formation of bridges across different scales and properties, and suggest that cross-modal neuroimaging and analysis may provide a tool for understanding brain disorders at the system level.

1.4 Applications

One of the main impediments to widespread use of physiological oscillations in diagnostics and medical instrumentation has, arguably, been their inherently non-autonomous character and variability. Traditionally, these features have been extremely hard to model. However, the substantial progress currently being made towards an understanding of such processes—forming the main *raison d'être* of the book—shows that this problem is being overcome so that faster progress in the development of useful applications in medicine may now be anticipated. In Part IV we consider some examples, both actual and potential.

In Chap. 22, Lehnertz provides an update on the use of EEG oscillations to predict epileptic seizures. These are usually associated with an overly-synchronized firing of neurons, as detected from the observed EEG oscillations, which often appears via a transformation of otherwise normal brain rhythms. The aim is therefore to apply methods from nonlinear dynamics, statistical physics, synchronization and network theory to identify precursor rhythms that can be used to warn the patient of an impending seizure. It is a long-term project that has been running for more than three decades. The author discusses progress to date and recent developments, including implantable devices for seizure prediction and prevention, and considers the remaining problems still to be solved.

The next two chapters both deal with anaesthesia and, in particular, exploitation of the changes in physiological oscillations that occur between the awake and anaesthetised states to provide a quantitative measure of the *depth of anaesthesia*, i.e. how close the patient is to becoming aware. There is obvious potential for preventing the unintentional awareness that still occurs occasionally, and which can be very distressing for everybody involved, not just the patient. In Chap. 23, Raeder reports on the European project BRACCIA (brain, respiration and cardiac causalities in anaesthesia). Although publication of the results has not yet been completed, it has already been shown that, even without inclusion of EEG data, measurements of the oscillations in ECG, respiration, skin temperature, and skin conductivity, coupled with the use of a classification analysis based on an optimal set of discriminatory parameters, can distinguish with 95% success between the awake and anaesthetised states. Chapter 24, by Martínez-Vázquez et al. describes an anaesthetic monitor that is already on the market: the qCON™ from Quantium Medical (Barcelona). Like the market leader BIS™, its operation is based on the analysis of EEG oscillations. The authors describe the main EEG activity changes induced by hypnotic anaesthetic agents, and the analysis perspectives. They also discuss the design principles, minimal necessary validation requirements, current limitations and challenges yet to be overcome.

In Chap. 25, Thorn and Shore review medical products that have been developed to enhance the oscillatory nature of blood circulation through the external application of intermittent pneumatic compression (IPC). They remark that further research is required, at a microcirculatory level, to understand and optimise the observed clinical benefits of IPC.

Chapter 26, by Abdulhameed et al. discusses recent work on cardiovascular oscillations in malaria. In particular, the authors show how a non-autonomous dynamics approach, using time-resolved analyses of power spectra and phase coherence, reveals significant differences between malaria patients and a healthy control group. These differences appear to be attributable to the specific effects of malaria on red blood cells, which cause them to stiffen and to stick to the endothelial lining of the blood vessels, markedly altering the flow properties of the blood. Following this approach leads to a classification accuracy of 88% in distinguishing malaria patients from healthy subjects, and may provide the basis for a new noninvasive diagnostic test. Further work will, however, be needed to compare the physical findings in malaria with those in other febrile infections.

1.5 Outlook

Finally, in Chap. 27, MacKay et al. take note of the contributions made in the preceding chapters, and address the question of where the subject is going. It is now well appreciated that understanding living systems requires more than just traditional dynamical systems theory. In taking account of the fact that they function far from equilibrium, the authors comment that the minimum entropy production rate, valid near equilibrium, needs to be replaced. They discuss other principles that are potentially more relevant, and the possibility that a reformulation and mesoscopic interpretation of thermodynamics itself may be needed.

1.6 Using the Book

As will be apparent from the summary remarks above, the chapters that follow are highly diverse in character although they all, whether explicitly or implicitly, grapple with aspects of non-autonomous dynamics. They range from relatively abstruse mathematics, which will mean little to most biologists and many physicists, to the practical details of physiological experiments which will mostly be lost on the theoretical physicists and mathematicians. Only a small minority of readers will start at the beginning and peruse the entire book from beginning to end. Most readers will probably prefer to pursue in detail topics that are of particular interest to them, in just a few chapters, while remaining aware of the larger reality presented by the rest of the book, and moving out into the latter when needed.

Each chapter is written by an expert, or experts, in the relevant subfield and each of them provides an extensive bibliography. So readers should have no difficulty in following up topics that are important to them.

Part I
Theory

Chapter 2
Phase and Amplitude Description of Complex Oscillatory Patterns in Reaction-Diffusion Systems

Hiroya Nakao

Abstract Spontaneous rhythmic oscillations are widely observed in various real-world systems. In particular, biological rhythms, which typically arise via synchronization of many self-oscillatory cells, often play important functional roles in living systems. One of the standard theoretical methods for analyzing synchronization dynamics of oscillatory systems is the phase reduction for weakly perturbed limit-cycle oscillators, which allows us to simplify nonlinear dynamical models exhibiting stable limit-cycle oscillations to a simple one-dimensional phase equation. Recently, the classical phase reduction method has been generalized to infinite-dimensional oscillatory systems such as spatially extended systems and time-delayed systems, and also to include amplitude degrees of freedom representing deviations of the system state from the unperturbed limit cycle. In this chapter, we discuss the method of phase-amplitude reduction for spatially extended reaction-diffusion systems exhibiting stable oscillatory patterns. As an application, we analyze entrainment of a reaction-diffusion system exhibiting limit-cycle oscillations by an optimized periodic forcing and additional feedback stabilization.

2.1 Introduction

There are abundant examples of spontaneous rhythmic oscillations in living systems, ranging from microscopic oscillations of cardiac cells and spiking neurons to macroscopic oscillations of heartbeats and brainwaves [5, 6, 28, 32, 34, 39]. In many cases, macroscopic oscillations result from synchronized collective dynamics of many microscopic cells and play essentially important functional roles in the survival of living systems. Regular rhythmic dynamics of the cells are typically modeled as limit-cycle oscillations in nonlinear dynamical systems. A representative example of such dynamical systems is the Hodgkin-Huxley model of spiking neurons, which

H. Nakao (✉)
Department of Systems and Control Engineering, Tokyo Institute of Technology, Tokyo 152-8552, Japan
e-mail: nakao@sc.e.titech.ac.jp

A. Stefanovska and P. V. E. McClintock (eds.), *Physics of Biological Oscillators*, Understanding Complex Systems,
https://doi.org/10.1007/978-3-030-59805-1_2

is a 4-dimensional ordinary differential equations (ODEs) with complex nonlinear terms representing the dynamics of the membrane potential and channel variables [5].

Due to nonlinearity, analytical solutions of limit cycles are rarely available, requiring approximate theoretical approaches to their synchronization dynamics. The phase reduction [3–5, 7, 15, 16, 21, 24, 27, 31] is a classical and standard theoretical method for analyzing weakly perturbed limit-cycle oscillators, which approximately describes the oscillator state by using only a single phase value and simplifies the multidimensional nonlinear dynamical equations of the oscillator to a one-dimensional phase equation. It has been successfully used in analyzing, e.g., nonlinear waves and collective oscillations in populations of weakly coupled limit-cycle oscillators.

Recently, the method of phase reduction has been extended in several ways. In particular, (i) generalization to infinite-dimensional systems such as partial differential equations (PDEs) [25] and delay-differential equations [13, 26] and (ii) inclusion of amplitude degrees of freedom representing deviations of the system state from the unperturbed limit cycle [30, 35, 38] have been formulated. The first extension is important in analyzing collective oscillations that arise e.g. in spatially extended populations of dynamical units described by PDEs. The second extension, which gives reduced amplitude equations in addition to the phase equation, is relatively recent even for ODEs, but it is necessary for describing transient relaxation dynamics of the perturbed system state to the limit cycle and can be used e.g. for stabilizing the oscillations by introducing feedback control of the amplitudes.

In this chapter, we formulate the method of phase and amplitude reduction for stable oscillatory patterns arising in spatially extended reaction-diffusion systems.

2.2 Phase-Amplitude Reduction of Limit-Cycle Oscillators

We first review the method of phase-amplitude reduction [30, 35, 38] for finite-dimensional limit-cycle oscillators described by ODEs of the form

$$\dot{\mathbf{X}}(t) = \mathbf{F}(\mathbf{X}(t)), \tag{2.1}$$

where $\mathbf{X}(t) \in \mathbb{R}^n$ is a n-dimensional oscillator state at time t and $\mathbf{F} : \mathbb{R}^n \to \mathbb{R}^n$ is a sufficiently smooth vector field representing the system dynamics. We assume that Eq. (2.1) has an exponentially stable limit-cycle solution $\mathbf{X}_0(t)$ of natural period T and frequency $\omega = 2\pi/T$, satisfying $\mathbf{X}_0(t + T) = \mathbf{X}_0(t)$. We denote this limit-cycle attractor as χ and its basin of attraction as $B \subseteq \mathbb{R}^n$.

In the conventional method of phase reduction, the essential step is the introduction of the *asymptotic phase* [39] (see Fig. 2.1 for a schematic diagram). Namely, we assign a scalar phase value $\theta \in [0, 2\pi)$ to the oscillator state $\mathbf{X} \in B$ which eventually converges to the limit cycle χ. We denote this assignment as $\theta = \Theta(\mathbf{X})$, where $\Theta : B \to [0, 2\pi)$ is a phase function, and require that the phase θ always increases with a constant frequency ω as the oscillator state $\mathbf{X}$ evolves according to Eq. (2.1), namely, the function Θ satisfies

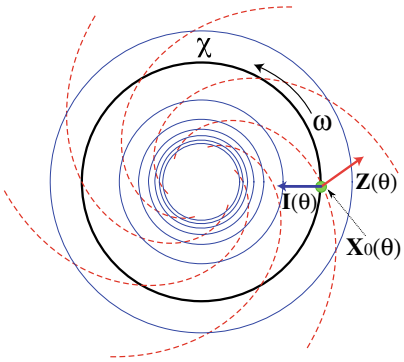

Fig. 2.1 Phase and amplitude of a limit cycle. Limit cycle χ (thick black circle), isochrons (red dashed curves), and isostables (thin blue circles). The green dot shows the oscillator state $\mathbf{X}_0(\theta)$, red arrow the phase sensitivity function $\mathbf{Z}(\theta)$, and the blue arrow the amplitude sensitivity function $\mathbf{I}(\theta)$ at phase θ, respectively

$$\dot{\theta} = \dot{\Theta}(\mathbf{X}) = \nabla_{\mathbf{X}}\Theta(\mathbf{X}) \cdot \dot{\mathbf{X}} = \mathbf{F}(\mathbf{X}) \cdot \nabla_{\mathbf{X}}\Theta(\mathbf{X}) = \omega \tag{2.2}$$

for $\mathbf{X} \in B$, where $\nabla_{\mathbf{X}}\Theta(\mathbf{X}) \in \mathbb{R}^n$ is the gradient vector of Θ and $\cdot$ represents the ordinary dot product between two vectors. The level sets of Θ are called *isochrons*.

The phase function Θ satisfying Eq. (2.2) can be obtained as follows. For the state $\mathbf{X}_0(t)$ at time t started from a reference state $\mathbf{X}_R$ at time 0 on χ, the phase function can be taken as $\Theta(\mathbf{X}_0(t)) = \omega t \pmod{2\pi}$, where $\mathbf{X}_R$ gives the origin of the phase, $\Theta(\mathbf{X}_R) = 0$. This assigns a phase value $\theta \in [0, 2\pi)$ to each point on χ. In what follows, we denote the state on χ as $\mathbf{X}_0(\theta)$ as a function of θ. Note that $\theta = \Theta(\mathbf{X}_0(\theta))$ holds. To the state $\mathbf{X}$ not on χ, we assign a phase value $\Theta(\mathbf{X}) = \theta$ if it converges to the same state on χ as $\mathbf{X}_0(\theta)$, namely, if $\lim_{\tau\to\infty} \|S^\tau\mathbf{X} - S^\tau\mathbf{X}_0(\theta)\| \to 0$, where $\|\cdot\|$ is the Euclidean norm and S^τ represents the time-τ flow of Eq. (2.1), satisfying $S^\tau\mathbf{X}(t) = \mathbf{X}(t+\tau)$. The phase function Θ defined as above satisfies Eq. (2.2) for $\mathbf{X} \in B$.

Next, we consider the amplitude degrees of freedom, representing deviations of the state $\mathbf{X}$ from the limit cycle χ. The linear stability of χ is characterized by the Floquet exponents, $0, \lambda_2, \ldots, \lambda_n$ in decreasing order of their real parts, where 0 is associated with the phase direction, namely, the neutral tangential direction along χ, and the real parts of all other exponents $\lambda_2, \ldots, \lambda_n$ are negative. For n-dimensional oscillators, there are generally $n-1$ amplitudes associated with $\lambda_2, \ldots, \lambda_n$, but we focus only on the dominant, slowest-decaying amplitude associated with λ_2 and denote this exponent as λ (< 0), which we assume simple and real for simplicity.

In a similar way to the phase θ, it is useful to assign a scalar amplitude $r = R(\mathbf{X})$ to the state $\mathbf{X} \in B$ and assume that r obeys a simple equation, where $R : B \to \mathbb{R}$ is an amplitude function. A natural assumption is that r exponentially decays to 0 as $\dot{r} = \lambda r$ when $\mathbf{X}$ converges to χ. Here, the decay rate is given by the Floquet exponent λ and $r = 0$ when $\mathbf{X}$ is on χ. Thus, we require R to satisfy $R(\mathbf{X}_0(\theta)) = 0$ and

$$\dot{r} = \dot{R}(\mathbf{X}) = \nabla_{\mathbf{X}}R(\mathbf{X}) \cdot \dot{\mathbf{X}} = \mathbf{F}(\mathbf{X}) \cdot \nabla_{\mathbf{X}}R(\mathbf{X}) = \lambda R(\mathbf{X}) = \lambda r. \tag{2.3}$$

Recent developments in the Koopman operator approach to nonlinear dynamical systems [18–20] have shown that the above definition is actually natural in the sense that R is given by an eigenfunction of the infinitesimal Koopman operator $\mathbf{F}(\mathbf{X}) \cdot \nabla_{\mathbf{X}}$ associated with the eigenvalue λ, and such R has been calculated e.g. for the van der Pol oscillator. The level sets of R are called *isostables*, in a similar sense to the isochrons for the asymptotic phase. In general, we have $n-1$ amplitudes, or principal Koopman eigenfunctions, associated with Floquet exponents $\lambda_2, \ldots, \lambda_n$, which can take complex values. Accordingly, the range of the amplitudes should be taken as $\mathbb{C}$ rather than $\mathbb{R}$. It is easy to show that the exponential of the phase function, $\Phi = e^{i\Theta}$, is also an eigenfunction of $\mathbf{F}(\mathbf{X}) \cdot \nabla_{\mathbf{X}}$ with eigenvalue $i\omega$. Thus, the Koopman operator approach gives a unifying viewpoint on the phase-amplitude description, or global linearization, of the flows around stable limit cycles.

Having defined the phase $\theta = \Theta(\mathbf{X})$ and the amplitude $r = R(\mathbf{X})$ for $\mathbf{X} \in B$, we can derive approximate phase and amplitude equations for a weakly perturbed limit-cycle oscillator described by

$$\dot{\mathbf{X}}(t) = \mathbf{F}(\mathbf{X}(t)) + \epsilon \mathbf{p}(\mathbf{X}(t), t), \tag{2.4}$$

where $\mathbf{p} \in \mathbb{R}^n$ represents the perturbation applied to the oscillator and $\epsilon > 0$ is a small parameter. The equation for the phase can be expressed as $\dot{\theta} = \nabla_{\mathbf{X}}\Theta(\mathbf{X}) \cdot \dot{\mathbf{X}} = \nabla_{\mathbf{X}}\Theta(\mathbf{X}) \cdot \mathbf{F}(\mathbf{X}) + \epsilon \nabla_{\mathbf{X}}\Theta(\mathbf{X}) \cdot \mathbf{p} = \omega + \epsilon \nabla_{\mathbf{X}}\Theta(\mathbf{X}) \cdot \mathbf{p}$, which still depends on $\mathbf{X}$. To obtain an equation closed in θ, we use the fact that $\mathbf{X}$ is near $\mathbf{X}_0(\theta)$ on χ and approximate $\mathbf{X}$ as $\mathbf{X} = \mathbf{X}_0(\theta) + O(\epsilon)$. Then, up to the lowest-order $O(\epsilon)$ in ϵ, the phase θ obeys

$$\dot{\theta}(t) \simeq \omega + \epsilon \mathbf{Z}(\theta(t)) \cdot \mathbf{p}(\mathbf{X}_0(\theta(t)), t), \tag{2.5}$$

where we defined the *phase sensitivity function* $\mathbf{Z}(\theta) = \nabla_{\mathbf{X}}\Theta(\mathbf{X})|_{\mathbf{X}=\mathbf{X}_0(\theta)}$. Likewise, the amplitude obeys $\dot{r} = \nabla_{\mathbf{X}} R(\mathbf{X}) \cdot \dot{\mathbf{X}} = \nabla_{\mathbf{X}} R(\mathbf{X}) \cdot \mathbf{F}(\mathbf{X}) + \epsilon \nabla_{\mathbf{X}} R(\mathbf{X}) \cdot \mathbf{p} = \lambda r + \epsilon \nabla_{\mathbf{X}} R(\mathbf{X}) \cdot \mathbf{p}$ and, by assuming that $\mathbf{X}$ is in the neighborhood of $\mathbf{X}_0(\theta)$, we obtain

$$\dot{r}(t) \simeq \lambda r(t) + \epsilon \mathbf{I}(\theta(t)) \cdot \mathbf{p}(\mathbf{X}_0(\theta(t)), t), \tag{2.6}$$

which is again correct up to $O(\epsilon)$. We here defined $\mathbf{I}(\theta) = \nabla_{\mathbf{X}} R(\mathbf{X})|_{\mathbf{X}=\mathbf{X}_0(\theta)}$, which we call the *amplitude sensitivity function*.

It is difficult to fully determine the phase function $\Theta(\mathbf{X})$ and the amplitude function $R(\mathbf{X})$ for all $\mathbf{X} \in B$ even numerically in multidimensional systems. However, if we are interested in the weakly perturbed case, Eq. (2.4), we only need the functions $\mathbf{Z}$ and $\mathbf{I}$. It can be shown that these quantities are given by 2π-periodic solutions to the following *adjoint* linear ODEs [3, 5, 16, 24, 30, 38]:

$$\omega \frac{d}{d\theta}\mathbf{Z}(\theta) = -J(\theta)^\top \mathbf{Z}(\theta), \quad \omega \frac{d}{d\theta}\mathbf{I}(\theta) = -[J(\theta)^\top - \lambda]\mathbf{I}(\theta), \tag{2.7}$$

where $J(\theta) = D\mathbf{F}(\mathbf{X})|_{\mathbf{X}=\mathbf{X}_0(\theta)} \in \mathbb{R}^{n\times n}$ is a Jacobian matrix of $\mathbf{F}$ at $\mathbf{X} = \mathbf{X}_0(\theta)$ on χ and $\top$ denotes transpose. The matrix components of $J(\theta)$ are given by $J_{ij}(\theta) = \partial F_i/\partial X_j|_{\mathbf{X}=\mathbf{X}_0(\theta)}$ for $i, j = 1, \ldots, n$, where F_i and X_i are vector components of $\mathbf{F}$ and $\mathbf{X}$, respectively. To be consistent with the definition of the asymptotic phase, $\mathbf{Z}$ should be normalized as $\mathbf{Z}(\theta) \cdot \mathbf{F}(\mathbf{X}_0(\theta)) = \omega$ for $\forall\theta \in [0, 2\pi)$. The normalization of $\mathbf{I}$, which determines the scale of r, can be chosen arbitrarily. These adjoint equations can be derived by expanding $\Theta(\mathbf{X})$ and $R(\mathbf{X})$ around $\mathbf{X}_0(\theta)$ to the first order in $\mathbf{X} - \mathbf{X}_0(\theta)$ and plugging them into Eqs. (2.2) and (2.3) [3, 16, 30].

Equations (2.5) and (2.6) give the lowest-order phase-amplitude description of the weakly perturbed limit-cycle oscillator Eq. (2.4), from which we can predict the dynamics of the phase θ and amplitude r and in turn use them to predict the oscillator state near χ.[1] Note that θ is decoupled from r at the lowest-order approximation. Higher-order approximations can also be developed, which yield coupling between θ and r and more precisely describe the oscillator dynamics [14, 37]. In this chapter, we consider the simplest nontrivial lowest-order case and generalize it to PDEs.

2.3 Phase-Amplitude Reduction of Reaction-Diffusion Systems

We now consider spatially extended reaction-diffusion (RD) systems described by

$$\frac{\partial \mathbf{X}(\mathbf{x}, t)}{\partial t} = \mathbf{F}(\mathbf{X}(\mathbf{x}, t); \mathbf{x}) + D\nabla^2\mathbf{X}(\mathbf{x}, t), \tag{2.8}$$

where $\mathbf{X}(\mathbf{x}, t) \in \mathbb{R}^n$ is a n-dimensional field variable at position $\mathbf{x} \in V \subseteq \mathbb{R}^d$ in a d-dimensional spatial domain V and at time t, representing e.g. concentrations of chemical species involved in the reaction, $\mathbf{F} : \mathbb{R}^n \times \mathbb{R}^d \to \mathbb{R}^n$ represents position-dependent reaction dynamics of $\mathbf{X}(\mathbf{x}, t)$, $D \in \mathbb{R}^{n\times n}$ is a matrix of diffusion coefficients, and ∇^2 is a Laplacian operator representing the diffusion of $\mathbf{X}$. Appropriate boundary conditions, e.g., periodic boundary conditions, are assumed for V. Note that Eq. (2.8) is an infinite-dimensional dynamical system whose system state at t is given by $\mathbf{X}(\mathbf{x}, t)$ for $\mathbf{x} \in V$, which we denote as $\mathbf{X}(\cdot, t) \in C$, where C is some appropriate space of smooth vector-valued functions. We assume that Eq. (2.8) possesses an exponentially stable limit-cycle solution $\mathbf{X}_0(\cdot, t)$ of natural period T and frequency $\omega = 2\pi/T$, satisfying $\mathbf{X}_0(\mathbf{x}, t + T) = \mathbf{X}_0(\mathbf{x}, t)$ for $\forall\mathbf{x} \in V$. We again denote this limit-cycle attractor in C as χ and its basin of attraction as $B \subseteq C$. Note that this

[1] The system state can be approximately represented as $\mathbf{X} \simeq \mathbf{X}_0(\theta) + \epsilon r\mathbf{u}(\theta)$ up to $O(\epsilon)$, where $\mathbf{u}(\theta)$ is a 2π-periodic Floquet eigenfunction with Floquet exponent λ satisfying $\omega(d/d\theta)\mathbf{u}(\theta) = [J(\theta) - \lambda]\mathbf{u}(\theta)$. See e.g. [16, 24] for details. This also holds true for the RD system discussed later in Sect. 2.3, namely, $\mathbf{X}(\mathbf{x}, t) \simeq \mathbf{X}_0(\mathbf{x}, \theta) + \epsilon r\mathbf{u}(\mathbf{x}, \theta)$ where the Floquet eigenfunction $\mathbf{u}(\mathbf{x}, \theta)$ is 2π-periodic in θ and satisfies $\omega(\partial/\partial\theta)\mathbf{u}(\mathbf{x}, \theta) = [J(\mathbf{x}; \theta) - \lambda + D\nabla^2]\mathbf{u}(\mathbf{x}, \theta)$.

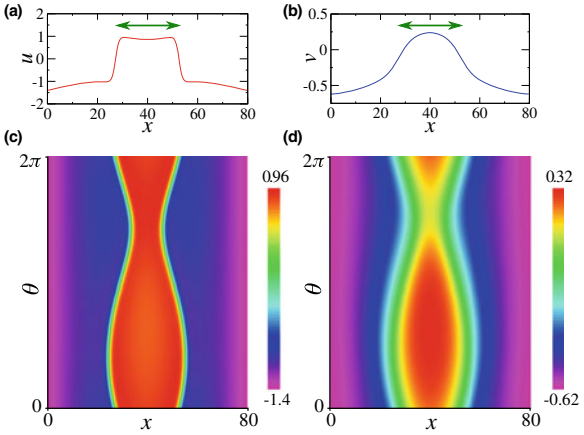

Fig. 2.2 Oscillating-spot solution of the FitzHugh-Nagumo model. **a**, **b** Spatial profiles of the u and v components, $\mathbf{X}(x,0) = (u(x,0), v(x,0))^\top$, at $\theta = 0$. **c**, **d** One-period evolution of the u and v components, $\mathbf{X}(x,\theta) = (u(x,\theta), v(x,\theta))^\top$, for $0 \le \theta < 2\pi$

assumption excludes continuous translational symmetries other than the temporal one along the limit cycle. Thus, the system possesses only a single phase variable.

Typical examples of limit-cycle solutions of the RD systems are traveling pulses on a ring, oscillating spots, target patterns, and spiral waves in spatially one or two-dimensional systems [15, 25]. Figure 2.2 shows the oscillating-spot solution of the FitzHugh-Nagumo (FHN) model on a 1-dimensional interval, where $x \in [0, L]$ with $L = 80$ represents the spatial position instead of the vector $\mathbf{x}$ (see Sect. 2.5 for details). Such complex oscillatory patterns in RD systems are difficult to analyze because of their nonlinearity and infinite-dimensionality. However, if we are interested in the vicinity of the limit cycle, namely, if we focus on the cases that the oscillatory patterns are only weakly perturbed, we can approximately describe their infinite-dimensional dynamics by simple finite-dimensional phase-amplitude equations in a similar way to the case of ODEs. In what follows, generalizing the method of phase reduction formulated in Ref. [25], we formulate a method of phase-amplitude reduction for RD systems exhibiting stable limit-cycle oscillations.

To this end, we need to introduce the phase θ and amplitude r of the infinite-dimensional state $\mathbf{X}(\cdot, t)$ of the RD system. Because we map the field variable to scalars, they should be given by *functionals* of $\mathbf{X}(\cdot, t)$. We thus define them as $\theta(t) = \Theta[\mathbf{X}(\cdot, t)]$ and $r(t) = R[\mathbf{X}(\cdot, t)]$, where $\Theta : B \to [0, 2\pi)$ is the phase functional and $R : B \to \mathbb{R}$ is the amplitude functional, respectively. Here, we again focus on the slowest-decaying amplitude associated with the largest non-zero Floquet exponent λ (< 0), which we assume simple, real, and distant from 0 with a finite spectral gap.

As in the ODE case, we require that these θ and r obey simple equations, i.e., $\dot{\theta} = \omega$ and $\dot{r} = \lambda r$. Then, from the chain rule of the derivative of functionals,

$$\dot{\theta}(t) = \dot{\Theta}[\mathbf{X}(\cdot, t)] = \int_V \left.\frac{\delta\Theta[\mathbf{X}(\cdot)]}{\delta\mathbf{X}(\mathbf{x})}\right|_{\mathbf{X}(\mathbf{x})=\mathbf{X}(\mathbf{x},t)} \cdot \frac{\partial\mathbf{X}(\mathbf{x}, t)}{\partial t} d\mathbf{x} = \omega, \tag{2.9}$$

$$\dot{r}(t) = \dot{R}[\mathbf{X}(\cdot, t)] = \int_V \left.\frac{\delta R[\mathbf{X}(\cdot)]}{\delta\mathbf{X}(\mathbf{x})}\right|_{\mathbf{X}(\mathbf{x})=\mathbf{X}(\mathbf{x},t)} \cdot \frac{\partial\mathbf{X}(\mathbf{x}, t)}{\partial t} d\mathbf{x} = \lambda r(t) \tag{2.10}$$

should hold. Here, $\partial\mathbf{X}(\mathbf{x}, t)/\partial t$ is given by Eq. (2.8) and $\delta A[\mathbf{X}(\cdot)]/\delta\mathbf{X}(\mathbf{x})|_{\mathbf{X}(\mathbf{x})=\mathbf{X}(\mathbf{x},t)} \in \mathbb{R}^n$ $(A = \Theta, R)$ represents the functional derivative of the functional $A[\mathbf{X}]$ with respect to $\mathbf{X}(\mathbf{x})$ evaluated at $\mathbf{X}(\mathbf{x}) = \mathbf{X}(\mathbf{x}, t)$. Such phase and amplitude functionals can, in principle, be defined as in the ODE case. We denote the system state on χ as $\mathbf{X}_0(\cdot, \theta)$ as a function of the phase $\theta \in [0, 2\pi)$. Note that $\Theta[\mathbf{X}_0(\cdot, \theta)] = \theta$ and $R[\mathbf{X}_0(\cdot, \theta)] = 0$ hold.

Thus, Eqs. (2.2) and (2.3) for ODEs can formally be generalized to spatially extended RD systems, where the vector gradient is replaced by the functional derivative. We can also interpret R and $\Phi = e^{i\Theta}$ as eigenfunctionals of the infinitesimal Koopman operator for RD systems [22, 23]. We note here that the explicit forms of the functionals Θ and R, which are difficult to obtain, are not necessary in the following derivation of the phase and amplitude equations near the limit-cycle solution.

Let us now consider the case that the RD system Eq. (2.8) is weakly perturbed as

$$\frac{\partial\mathbf{X}(\mathbf{x}, t)}{\partial t} = \mathbf{F}(\mathbf{X}(\mathbf{x}, t); \mathbf{x}) + D\nabla^2\mathbf{X}(\mathbf{x}, t) + \epsilon\mathbf{p}(\mathbf{X}(\cdot, t), \mathbf{x}, t), \tag{2.11}$$

where $\epsilon > 0$ is a small parameter and $\mathbf{p}(\mathbf{X}(\cdot, t), \mathbf{x}, t) \in \mathbb{R}^n$ is the applied perturbation that can depend on the state $\mathbf{X}$, position $\mathbf{x}$, and time t. In a similar way to the case of ODEs, using the phase and amplitude functionals Θ and R satisfying Eqs. (2.9) and (2.10), we can reduce Eq. (2.11) to a set of approximate phase-amplitude equations as

$$\dot{\theta} = \int_V \left.\frac{\delta\Theta[\mathbf{X}(\cdot)]}{\delta\mathbf{X}(\mathbf{x})}\right|_{\mathbf{X}(\mathbf{x})=\mathbf{X}(\mathbf{x},t)} \cdot \frac{\partial\mathbf{X}(\mathbf{x}, t)}{\partial t} d\mathbf{x} \simeq \omega + \epsilon \int_V \mathbf{Z}(\mathbf{x}, \theta) \cdot \mathbf{p}(\mathbf{X}_0(\cdot, \theta), \mathbf{x}, t) d\mathbf{x}, \tag{2.12}$$

$$\dot{r} = \int_V \left.\frac{\delta R[\mathbf{X}(\cdot)]}{\delta\mathbf{X}(\mathbf{x})}\right|_{\mathbf{X}(\mathbf{x})=\mathbf{X}(\mathbf{x},t)} \cdot \frac{\partial\mathbf{X}(\mathbf{x}, t)}{\partial t} d\mathbf{x} \simeq \lambda r + \epsilon \int_V \mathbf{I}(\mathbf{x}, \theta) \cdot \mathbf{p}(\mathbf{X}_0(\cdot, \theta), \mathbf{x}, t) d\mathbf{x}, \tag{2.13}$$

where $\partial\mathbf{X}(\mathbf{x}, t)/\partial t$ is given by Eq. (2.11). Here, in the last expression in each equation, we have approximately evaluated the functional derivatives and perturbations in the integral at $\mathbf{X}_0(\mathbf{x}, \theta)$ rather than at $\mathbf{X}(\mathbf{x}, t)$, assuming that the system state is sufficiently close to χ, and introduced the phase and amplitude sensitivity functions

$$\mathbf{Z}(\mathbf{x}, \theta) = \left.\frac{\delta\Theta[\mathbf{X}(\cdot)]}{\delta\mathbf{X}(\mathbf{x})}\right|_{\mathbf{X}(\mathbf{x})=\mathbf{X}_0(\mathbf{x},\theta)}, \quad \mathbf{I}(\mathbf{x}, \theta) = \left.\frac{\delta R[\mathbf{X}(\cdot)]}{\delta\mathbf{X}(\mathbf{x})}\right|_{\mathbf{X}(\mathbf{x})=\mathbf{X}_0(\mathbf{x},\theta)}, \tag{2.14}$$

which now depend also on the position $\mathbf{x}$. The approximate equations (2.12) and (2.13) are correct up to $O(\epsilon)$ like Eqs. (2.5) and (2.6) in the ODE case.

Though it is difficult to obtain the functionals Θ and R explicitly, it can be shown that the sensitivity functions $\mathbf{Z}$ and $\mathbf{I}$ are given by 2π-periodic solutions to the following adjoint linear PDEs [22, 25]:

$$\begin{aligned}\omega\frac{\partial \mathbf{Z}(\mathbf{x},\theta)}{\partial\theta} &= -J(\mathbf{x};\theta)^\top \mathbf{Z}(\mathbf{x},\theta) - D^\top\nabla^2\mathbf{Z}(\mathbf{x},\theta),\\ \omega\frac{\partial \mathbf{I}(\mathbf{x},\theta)}{\partial\theta} &= -[J(\mathbf{x};\theta)^\top - \lambda]\mathbf{I}(\mathbf{x},\theta) - D^\top\nabla^2\mathbf{I}(\mathbf{x},\theta),\end{aligned} \tag{2.15}$$

where $J(\mathbf{x};\theta) = D\mathbf{F}(\mathbf{X}(\mathbf{x},t);\mathbf{x}) \in \mathbb{R}^{n\times n}$ is the Jacobian matrix of $\mathbf{F}$ evaluated at position $\mathbf{x}$. The normalization for $\mathbf{Z}$ is now given by $\int_V \mathbf{Z}(\mathbf{x},\theta)\cdot\{\mathbf{F}(\mathbf{X}_0(\mathbf{x},\theta) + D\nabla^2\mathbf{X}_0(\mathbf{x},\theta)\}d\mathbf{x} = \omega$ for $\forall\theta \in [0,2\pi)$. These equations are straightforward generalization of the adjoint equations (2.7) and the normalization condition for the

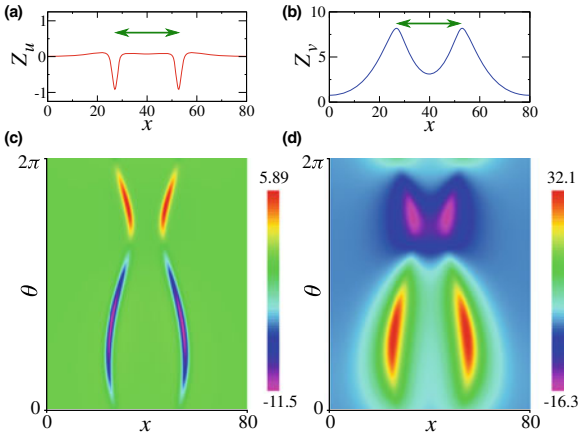

Fig. 2.3 Phase sensitivity function of the oscillating-spot solution of the FitzHugh-Nagumo model. **a**, **b** Spatial profiles of the u and v components, $\mathbf{Z}(x,0) = (Z_u(x,0), Z_v(x,0))^\top$, at $\theta = 0$. **c**, **d** One-period evolution of the u and v components, $\mathbf{Z}(x,\theta) = (Z_u(x,\theta), Z_v(x,\theta))^\top$, for $0 \le \theta < 2\pi$

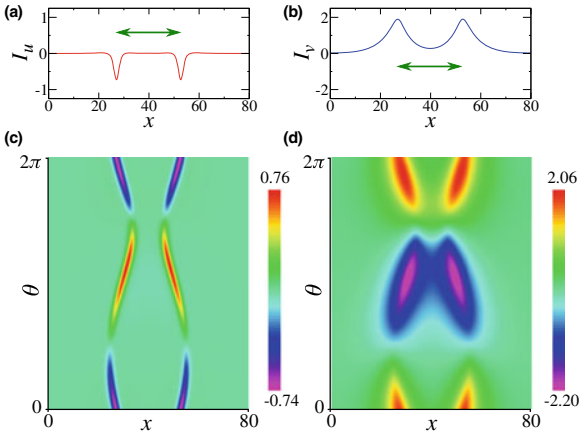

Fig. 2.4 Amplitude sensitivity function of the oscillating-spot solution of the FitzHugh-Nagumo model. **a**, **b** Spatial profiles of the u and v components, $\mathbf{I}(x,0) = (I_u(x,0), I_v(x,0))^\top$, at $\theta = 0$. **c**, **d** One-period evolution of the u and v components, $\mathbf{I}(x,\theta) = (I_u(x,\theta), I_v(x,\theta))^\top$, for $0 \le \theta < 2\pi$

ODE case. Figures 2.3 and 2.4 show the phase and amplitude sensitivity functions of the oscillating-spot solution of the FHN model, respectively (see Sect. 2.5 for details).

Thus, by defining the phase and amplitude functionals, we can reduce the weakly perturbed RD system, Eq. (2.11), to a set of ODEs (2.12) and (2.13) for the phase and amplitude. The reduced phase-amplitude equations are much simpler than the original RD system and facilitate detailed analysis of the oscillatory patterns. In Ref. [25], the phase equation has been used to analyze synchronization between a pair of mutually coupled RD systems. In the next section, we analyze optimal entrainment with feedback stabilization of RD systems using the phase and amplitude equations.

2.4 Optimal Entrainment of Oscillatory Patterns with Feedback

As an application of the reduced phase-amplitude equations, we analyze entrainment of a RD system exhibiting oscillatory patterns by an optimized periodic forcing, generalizing Ref. [40] for limit-cycle oscillators described by ODEs. The model is

$$\frac{\partial \mathbf{X}(\mathbf{x}, t)}{\partial t} = \mathbf{F}(\mathbf{X}(\mathbf{x}, t); \mathbf{x}) + D\nabla^2 \mathbf{X}(\mathbf{x}, t) + \epsilon K \mathbf{q}(\mathbf{x}, \Omega t), \tag{2.16}$$

where $\mathbf{q}(\mathbf{x}, \Omega t) \in \mathbb{R}^n$ represents a temporally periodic smooth forcing pattern of frequency Ω satisfying $\mathbf{q}(\mathbf{x}, \Omega t + 2\pi) = \mathbf{q}(\mathbf{x}, \Omega t)$ and $K = \mathrm{diag}\{K_1, \ldots, K_n\} \in \mathbb{R}^{n \times n}$ is a constant diagonal matrix representing the effect of $\mathbf{q}$ on $\mathbf{X}$ (e.g., $K_1 \neq 0$ and $K_{2,\ldots,n} = 0$ when only the 1st component of $\mathbf{X}$ is driven by the forcing). We assume that the forcing frequency Ω is sufficiently close to the natural frequency ω of the system, namely, the frequency mismatch $\omega - \Omega$ is a small value of $O(\epsilon)$ and denote it as $\epsilon\Delta$ where $\Delta = O(1)$. The reduced approximate phase-amplitude equations are

$$\begin{aligned} \dot{\theta}(t) &= \omega + \epsilon \int_V \mathbf{Z}(\mathbf{x}, \theta(t)) \cdot K \mathbf{q}(\mathbf{x}, \Omega t) d\mathbf{x}, \\ \dot{r}(t) &= \lambda r(t) + \epsilon \int_V \mathbf{I}(\mathbf{x}, \theta(t)) \cdot K \mathbf{q}(\mathbf{x}, \Omega t) d\mathbf{x}. \end{aligned} \tag{2.17}$$

For the linear stability analysis of the entrained state, we only need the phase equation. Following the standard procedure [15], we consider the phase difference $\phi = \theta - \Omega t$ between the system and periodic forcing, which obeys

$$\dot{\phi}(t) = \epsilon\Delta + \epsilon \int_V \mathbf{Z}(\mathbf{x}, \phi(t) + \Omega t) \cdot K \mathbf{q}(\mathbf{x}, \Omega t) d\mathbf{x}. \tag{2.18}$$

Because the right-hand side is $O(\epsilon)$, ϕ is a slowly varying quantity and the right-hand side can be averaged over one period of the forcing with fixed ϕ. We thus obtain

$$\dot{\phi}(t) = \epsilon[\Delta + \Gamma(\phi(t))], \tag{2.19}$$

which is correct up to $O(\epsilon)$, where we defined a 2π-periodic *phase coupling function*

$$\Gamma(\phi) = \frac{1}{2\pi}\int_0^{2\pi}\int_V \mathbf{Z}(\mathbf{x}, \phi+\psi)\cdot K\mathbf{q}(\mathbf{x}, \psi)d\mathbf{x}d\psi = \langle \mathbf{Z}(\mathbf{x}, \phi+\psi)\cdot K\mathbf{q}(\mathbf{x}, \psi)\rangle. \tag{2.20}$$

Here, we introduced the abbreviation $\langle A(\mathbf{x}, \psi)\rangle = (2\pi)^{-1}\int_0^{2\pi}\left\{\int_V A(\mathbf{x}, \psi)d\mathbf{x}\right\}d\psi$. Equation (2.19) can possess a stable fixed point $\phi^* \in [0, 2\pi)$ satisfying $\Delta + \Gamma(\phi^*) = 0$ and $\Gamma'(\phi^*) < 0$ when Δ is in an appropriate range, whose linear stability is given by the slope $\Gamma'(\phi^*) = d\Gamma(\phi)/d\phi|_{\phi=\phi^*}$ of $\Gamma(\phi)$ at ϕ^*. The oscillatory pattern can be entrained to the periodic forcing when such a stable fixed point ϕ^* exists.

We seek the optimal periodic forcing $\mathbf{q}(\mathbf{x}, \psi)$ for stable entrainment, which minimizes $\Gamma'(\phi^*)$ under the constraint that the power of $\mathbf{q}(\mathbf{x}, \psi)$ is fixed at $P > 0$, i.e., $\langle\|\mathbf{q}(\mathbf{x}, \psi)\|^2\rangle = P$, and also under the constraint that Eq. (2.19) has a fixed point at given ϕ^*, i.e., $\Delta + \Gamma(\phi^*) = 0$ holds. Thus, we solve an optimization problem

$$\text{maximize } -\Gamma'(\phi^*) \quad \text{subject to } \langle\|\mathbf{q}(\mathbf{x}, \psi)\|^2\rangle = P,\ \Delta + \Gamma(\phi^*) = 0. \tag{2.21}$$

To this end, we define an objective functional,

$$S[\mathbf{q}(\cdot, \psi)] = -\Gamma'(\phi^*) + \zeta\left\{\langle\|\mathbf{q}(\mathbf{x}, \psi)\|^2\rangle - P\right\} + \mu\{\Delta + \Gamma(\phi^*)\}, \tag{2.22}$$

where ζ and μ are Lagrange multipliers. Solving the stationarity condition, $\delta S/\delta\mathbf{q}(\mathbf{x}, \psi) = 0$, and eliminating μ by using the second constraint as well as the 2π-periodicity of $\mathbf{Z}(\mathbf{x}, \theta)$ in θ, the optimal periodic forcing can be obtained as

$$\mathbf{q}_{\text{opt}}(\mathbf{x}, \psi) = \frac{1}{2\zeta}K^\top\partial_\psi\mathbf{Z}(\phi^*+\psi) - \frac{\Delta}{\langle\|K^\top\mathbf{Z}(\mathbf{x}, \phi^*+\psi)\|^2\rangle}K^\top\mathbf{Z}(\phi^*+\psi) \tag{2.23}$$

and the optimized stability exponent as

$$\Gamma'_{\text{opt}}(\phi^*) = \frac{1}{2\zeta}\langle\|K^\top\partial_\psi\mathbf{Z}(\phi^*+\psi)\|^2\rangle, \tag{2.24}$$

where the multiplier ζ is calculated from the first constraint as

$$\zeta = -\frac{1}{2}\left(\frac{\langle\|K^\top\partial_\psi\mathbf{Z}(\mathbf{x}, \phi^*+\psi)\|^2\rangle}{P - \Delta^2/\langle\|K^\top\mathbf{Z}(\mathbf{x}, \phi^*+\psi)\|^2\rangle}\right)^{1/2}. \tag{2.25}$$

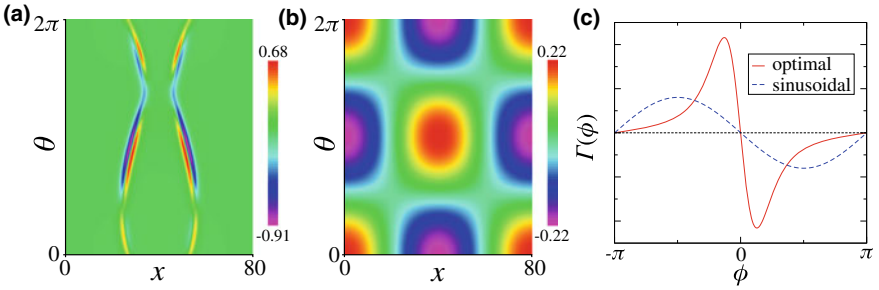

Fig. 2.5 Forcing patterns and phase coupling functions. **a**, **b** One-period evolution of the u component of the **a** optimal forcing $\mathbf{q}_{\rm opt}(x, \theta)$ and **b** sinusoidal forcing $\mathbf{q}_{\rm sin}(x, \theta)$ for $0 \le \theta < 2\pi$. **c** Phase coupling functions $\Gamma(\phi)$ for the optimal and sinusoidal forcing patterns

Figure 2.5 shows the optimized forcing, together with a spatiotemporally sinusoidal forcing for comparison, and the resulting phase coupling functions for the oscillating-spot solution of the FHN model (see Sect. 2.5 for details).

As we demonstrate in the next section, the optimized forcing $\mathbf{q}_{\rm opt}$ gives higher stability of the entrained state than the sinusoidal forcing pattern $\mathbf{q}_{\rm sin}$ of the same power. However, it can also happen that the optimized pattern perturbs the system too efficiently and kicks the system state far away from the limit cycle, where the reduced equations are no longer accurate. If so, we may need to decrease the forcing power and may not be able to improve the stability of the entrainment as desired.

In order to cope with this problem, we consider a simple feedback stabilization of the oscillatory pattern, which suppresses the deviation of the system state from the unperturbed limit cycle χ. To this end, we evaluate the phase $\theta = \Theta[\mathbf{X}(\cdot, t)]$ of the system state $\mathbf{X}(\cdot, t)$, calculate the difference vector $\mathbf{y}(\mathbf{x}, t) = \mathbf{X}(\mathbf{x}, t) - \mathbf{X}_0(\mathbf{x}, \theta)$, and apply a feedback forcing of the form $-\alpha\mathbf{y}(\mathbf{x}, t)$ to the RD system, Eq. (2.16), as

$$\frac{\partial \mathbf{X}(\mathbf{x}, t)}{\partial t} = \mathbf{F}(\mathbf{X}(\mathbf{x}, t); \mathbf{x}) + D\nabla^2\mathbf{X}(\mathbf{x}, t) + \epsilon K\mathbf{q}(\mathbf{x}, \Omega t) - \epsilon\alpha\mathbf{y}(\mathbf{x}, t), \tag{2.26}$$

where $\alpha > 0$ is the feedback gain.[2]

When $\mathbf{X}$ is sufficiently close to χ, we can show that this $\mathbf{y}$ is (bi-)orthogonal to the phase sensitivity function $\mathbf{Z}$. Indeed, we can express the phase of $\mathbf{X}$ as

$$\theta = \Theta[\mathbf{X}(\cdot, t)] = \Theta[\mathbf{X}_0(\cdot, \theta) + \mathbf{y}(\mathbf{x}, t)] \simeq \Theta[\mathbf{X}_0(\cdot, \theta)] + \int_V \mathbf{Z}(\mathbf{x}, \theta) \cdot \mathbf{y}(\mathbf{x}, t) d\mathbf{x} \tag{2.27}$$

by retaining the lowest-order functional Taylor expansion of Θ in $\mathbf{y}$. Therefore, $\int_V \mathbf{Z}(\mathbf{x}, \theta) \cdot \mathbf{y}(t) d\mathbf{x} = 0$ holds at the lowest order because $\theta = \Theta[\mathbf{X}_0(\cdot, \theta)]$. Thus,

[2] We here simply assume that the whole spatial pattern can be directly observed. This may not be realistic in practical control problems and some approximate methods may have to be devised.

the reduced phase equation of Eq. (2.26) is the same as that for Eq. (2.16) and the feedback forcing term $-\epsilon\alpha\mathbf{y}(\mathbf{x}, t)$ does not affect the phase dynamics of the system at the lowest order. On the other hand, the amplitude r of $\mathbf{X}(\cdot, t)$ is expressed as

$$r = R[\mathbf{X}(\cdot, t)] = R[\mathbf{X}_0(\cdot, \theta) + \mathbf{y}(\mathbf{x}, t)] \simeq \int_V \mathbf{I}(\mathbf{x}, \theta) \cdot \mathbf{y}(\mathbf{x}, t) d\mathbf{x} \tag{2.28}$$

where $R[\mathbf{X}_0(\cdot, \theta)] = 0$ by definition. Therefore, at the lowest order, the amplitude equation for Eq. (2.26) is given by

$$\dot{r}(t) = (\lambda - \epsilon\alpha) r(t) + \int_V \mathbf{I}(\mathbf{x}, \theta(t)) \cdot K\mathbf{q}(\mathbf{x}, \Omega t) d\mathbf{x}. \tag{2.29}$$

Thus, by introducing the feedback term $-\alpha\mathbf{y}(\mathbf{x}, t)$, we can improve the linear stability of χ from λ to $\lambda - \epsilon\alpha$ and keep the system state closer to χ while not affecting the phase dynamics, which allows us to apply periodic forcing with larger power.

2.5 Example: Oscillating Spot in the FitzHugh-Nagumo Model

As an example of the RD system possessing a stable limit cycle, we consider the FitzHugh-Nagumo model in one dimension, which exhibits a localized oscillating-spot pattern (see Ref. [25] for details). The model is given by Eq. (2.16) with

$$\mathbf{X}(x, t) = \begin{pmatrix} u \\ v \end{pmatrix}, \quad \mathbf{F}(\mathbf{X}; x) = \begin{pmatrix} u(u - \beta(x))(1 - u) - v \\ \epsilon(u - \gamma v) \end{pmatrix}, \quad D = \begin{pmatrix} \kappa & 0 \\ 0 & \delta \end{pmatrix}, \tag{2.30}$$

where $u(x, t)$ and $v(x, t)$ are the activator and inhibitor field variables at time t and position x ($0 \le x \le L$), respectively, $\beta(x)$, ϵ, and τ are parameters, and κ and δ are diffusion coefficients of u and v. We consider a system of length $L = 80$ and assume no-flux boundary conditions $\partial\mathbf{X}(0, t)/\partial x = \partial\mathbf{X}(L, t)/\partial x = 0$ at $x = 0$ and L. In order to pin the spot to the center $x = L/2$ of the system, we assume that $\beta(x)$ is position-dependent and is given by $\beta(x) = \beta_0 + (\beta_1 - \beta_0)(x/L - 1/2)^2$ with $\beta_0 = -1.1$ and $\beta_1 = -1.6$. The other parameters are $\gamma = 2$ and $\epsilon = 0.0295$, and the diffusion coefficients are $\kappa = 1$ and $\delta = 2.5$. By choosing an appropriate initial condition, this system converges to a stable limit cycle $\chi : \mathbf{X}_0(x, \theta) = (u_0(x, \theta), v_0(x, \theta))^\top$ ($0 \le x \le L, 0 \le \theta < 2\pi$) with natural period $T \simeq 196.5$ and frequency $\omega \simeq 0.032$ corresponding to the oscillating spot. The second Floquet exponent of χ is real and evaluated as $\lambda \simeq -0.387$. Using the adjoint equations (2.15), we can calculate the phase and amplitude sensitivity functions $\mathbf{Z}$ and $\mathbf{I}$ of χ.

Figure 2.2 shows the snapshot and one period evolution of the limit-cycle solution $\mathbf{X}_0$, and Figs. 2.3 and 2.4 show the snapshot and one-period evolution of the phase

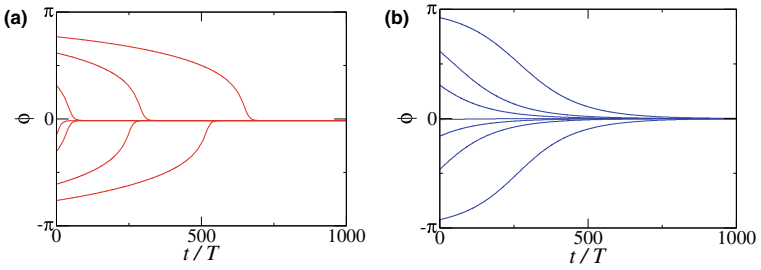

Fig. 2.6 Entrainment by the **a** optimized and **b** sinusoidal forcing. Evolution of the phase difference $\phi = \theta - \Omega t$ between the system and the periodic forcing, started from different initial conditions

and amplitude sensitivity functions $\mathbf{Z}$ and $\mathbf{I}$, respectively. It can be seen that both sensitivity functions take large values near the domain walls of the oscillating spot, indicating that perturbations given to the domain walls have strong influence on the phase and amplitude of the system. Reflecting the difference in the diffusion coefficients, the patterns of the u component are sharper than those of v.

We consider entrainment of this oscillating-spot solution by the optimized periodic forcing. For simplicity, we assume that the forcing frequency Ω is equal to the natural frequency ω of the system, i.e., $\Delta = 0$. In this case, we can set the value of ϕ^* arbitrarily by shifting the origin of the phase, and we fix it as $\phi^* = 0$. We set $\epsilon = 0.01$ and $K = \mathrm{diag}\{K_1, K_2\} = \mathrm{diag}\{0.05, 0\}$, namely, we apply the periodic forcing only to the u component of the system. We calculate the optimal forcing $\mathbf{q}_{\mathrm{opt}}(x, \psi) = (q^u_{\mathrm{opt}}(x, \psi), 0)^\top$ of power $P = 1$ by Eq. (2.23), and also a spatiotemporally sinusoidal forcing $\mathbf{q}_{\sin}(x, \psi) \propto (\cos(2\pi x/L) \sin\psi, 0)^\top$ of the same power, and drive the system periodically with these forcing patterns.

Figures 2.5a, b show the u component of the forcing patterns $\mathbf{q}_{\mathrm{opt}}(x, \psi)$ and $\mathbf{q}_{\sin}(x, \psi)$ for one period of oscillation, respectively, and Fig. 2.5c shows the resulting phase coupling functions $\Gamma(\phi)$. It can be seen that the optimal forcing pattern selectively perturbs the domain walls where the system's phase sensitivity is high, and the slope $\Gamma'(0)$ determining the linear stability of the entrained state $\phi^* = 0$ is much larger in the optimized case than in the sinusoidal case.

Figure 2.6 shows the actual convergence of the phase difference $\phi = \theta - \Omega t$ between the system and periodic forcing to $\phi^* = 0$ from several different initial conditions, obtained by direct numerical simulations of Eq. (2.16). It can be confirmed that the asymptotic convergence to the fixed point at $\phi^* = 0$ is faster and the entrainment is established earlier in the optimized case.

Now, as we discussed in the previous section, when the periodic forcing is not sufficiently small, it may kick the system state far away from the unperturbed limit cycle and can lead to breakdown of the lowest-order phase-amplitude description. By introducing the feedback stabilization, we may be able to keep the system state close to the limit cycle and apply stronger forcing. In order to confirm this, we numerically simulate Eq. (2.26) with the feedback forcing term. In the numerical calculation, the phase θ of the system state $\mathbf{X}$ is evaluated by using the procedure described below

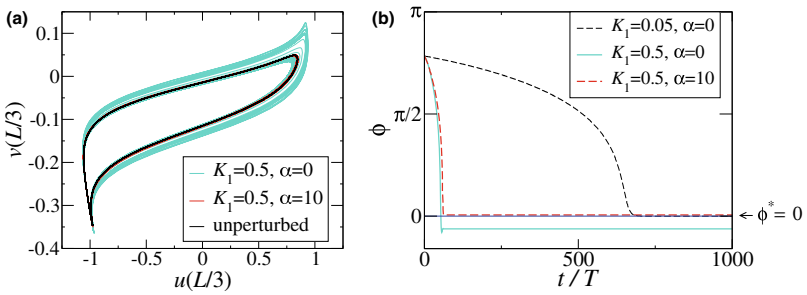

Fig. 2.7 Effect of strong forcing and feedback. **a** Trajectories of the system state $(u(x,t), v(x,t))^\top$ at $x = L/3$ for the cases with (i) no forcing, (ii) strong forcing without feedback ($K_1 = 0.5, \alpha = 0$), and (iii) strong forcing with feedback ($K_1 = 0.5$, $\alpha = 10$). **b** Convergence of the phase difference $\phi = \theta - \Omega t$ for the case only with weak forcing, $K_1 = 0.05$, and for the cases (ii) and (iii)

Eq. (2.2) in Sect. 2.2, which also applies to the RD case, and then the amplitude r of $\mathbf{X}$ is evaluated using Eq. (2.28) with $\mathbf{y}(\mathbf{x}, t) = \mathbf{X}(\mathbf{x}, t) - \mathbf{X}_0(\mathbf{x}, \theta)$ within linear approximation (note that $\mathbf{X}$ is in the neighborhood of $\mathbf{X}_0(\cdot, \theta)$ when the perturbation is weak).

Figure 2.7a shows the trajectory of the field variable $(u, v)^\top$ at $x = L/3$ obtained by direct numerical simulations of Eq. (2.26) for the cases with (i) no forcing (black), (ii) strong forcing $K_1 = 0.5$ without feedback, $\alpha = 0$ (light blue), and (iii) strong forcing $K_1 = 0.5$ with feedback gain $\alpha = 10$ (red, overlaps with the black curve). The curve for the case (i) corresponds to the unperturbed limit cycle χ. We can observe that the strong forcing without feedback drives the system state away from χ in the case (ii), but the introduction of the feedback keeps the system state close to χ in the case (iii). Figure 2.7b shows the convergence of the phase difference ϕ for the cases (ii) and (iii). For comparison, the evolution of ϕ under weak forcing $K_1 = 0.05$ without feedback is also shown. In the case (ii) without feedback, the final phase difference is considerably different from the target value $\phi^* = 0$ because of the large deviation of the system state from χ.[3] In contrast, in the case (iii) with feedback, ϕ converges to the correct target value $\phi^* = 0$ even though the forcing is 10 times stronger. Thus, the feedback stabilization allows us to apply much stronger periodic forcing and realize faster entrainment.

2.6 Summary

We have formulated the method of phase and amplitude description for limit-cycle oscillations in spatially extended RD systems subjected to weak perturbations. Though the RD systems are infinite-dimensional dynamical systems, we can still

[3] In this case, the system state converges to a spurious periodic orbit after initial transient, which is induced by the effect of the strong periodic forcing and larger than the original limit cycle χ.

approximately describe them by a set of phase and amplitude equations in the vicinity of the unperturbed limit cycle, which can be used for the analysis and control of complex oscillatory dynamics in RD systems. As an application, we have considered entrainment of the oscillatory pattern with optimized periodic forcing and feedback stabilization, which allows us to apply stronger forcing while keeping the approximate phase-amplitude description valid and thereby realizing more stable entrainment.

The method of phase reduction for infinite-dimensional dynamical systems has also been developed for delay-differential equations exhibiting limit-cycle oscillations [13, 26], for nonlinear Fokker-Planck (integro-differential) equation describing populations of coupled oscillators and excitable elements [11, 12], and also for fluid systems exhibiting stable oscillatory convection [8–10, 33]. As we have formulated for the RD systems, we can derive the amplitude equation also for such systems, which can be used for analyzing their transient relaxation properties.

In this chapter, we have presented the theory only for a single oscillatory system in the simplest lowest-order approximation with a single phase and a single amplitude. Generalization to more complex cases is also possible along the lines presented in this chapter. In general, even a single system may possess two or more phase variables when it has additional continuous translational symmetries e.g. in spatial directions [2, 10] and possesses a torus solution rather than a limit-cycle solution. We may also need to consider two or more amplitude variables and consider the case of complex Floquet eigenvalues. Moreover, although the phase is decoupled from the amplitude at the lowest-order phase-amplitude description considered in this chapter, this is not the case if we proceed to the next order; nonlinear phase-amplitude interactions can arise within a single system and, if coupled systems are considered, phase and amplitude interactions of three- or more systems can generally arise. Such higher-order interactions can be a source of intriguing complex dynamics in nonlinear oscillatory systems; see, e.g., Refs. [1, 4, 14, 17, 29, 36, 37] for various types of higher-order descriptions and their consequences.

Macroscopic oscillatory systems in the real world are often made up of spatially distributed populations of interacting microsystems and modeled by PDEs including the RD equations. Development of the phase-amplitude framework for such systems, together with the recent advance in the Koopman operator approach to nonlinear dynamical systems [23], will provide us with a unified viewpoint and practical methods for the analysis, control, and design of such complex oscillatory systems.

Acknowledgements The author is grateful to A. Stefanovska and P. V. E. McClintock for invitation to write this chapter and for their kind advice. This work is financially supported by JSPS KAKENHI Grants JP17H03279, 18K03471, JP18H03287, and JST CREST JPMJCR1913.

References

1. P. Ashwin, A. Rodrigues, Hopf normal form with SN symmetry and reduction to systems of nonlinearly coupled phase oscillators. Phys. D **325**, 14–24 (2016)
2. I.V. Biktasheva, D. Barkley, V.N. Biktashev, G.V. Bordyugov, A.J. Foulkes, Computation of the response functions of spiral waves in active media Phys. Rev. E **79**, 056702 (2009)
3. E. Brown, J. Moehlis, P. Holmes, On the phase reduction and response dynamics of neural oscillator populations. Neural Comput. **16**, 673 (2004)
4. B. Ermentrout, Y. Park, D. Wilson, Recent advances in coupled oscillator theory. Phil. Trans. Roy. Soc. A **377**, 20190092 (2019)
5. G.B. Ermentrout, D.H. Terman, *Mathematical Foundations of Neuroscience* (Springer, New York, 2010)
6. L. Glass, M.C. Mackey, *From Clocks to Chaos—The Rhythms of Life* (Princeton University Press, Princeton, 1988)
7. F.C. Hoppensteadt, E.M. Izhikevich, *Weakly Connected Neural Networks* (Springer, New York, 1997)
8. M. Iima, Jacobian-free algorithm to calculate the phase sensitivity function in the phase reduction theory and its applications to Kármán's vortex street. Phys. Rev. E **99**, 062203 (2019)
9. Y. Kawamura, H. Nakao, Collective phase description of oscillatory convection. Chaos **23**, 043129 (2013)
10. Y. Kawamura, H. Nakao, Phase description of oscillatory convection with a spatially translational mode. Phys. D **295–296**, 11–29 (2015)
11. Y. Kawamura, H. Nakao, K. Arai, H. Kori, Y. Kuramoto, Collective phase sensitivity. Phys. Rev. Lett. **101**, 024101 (2008)
12. Y. Kawamura, H. Nakao, Y. Kuramoto, Collective phase description of globally coupled excitable elements. Phys. Rev. E **84**, 046211 (2011)
13. K. Kotani, I. Yamaguchi, Y. Ogawa, Y. Jimbo, H. Nakao, G.B. Ermentrout, Adjoint method provides phase response functions for delay-induced oscillations. Phys. Rev. Lett. **109**, 044101 (2012)
14. K. Kotani, Y. Ogawa, S. Shirasaka, A. Akao, Y. Jimbo, H. Nakao, Nonlinear phase-amplitude reduction of delay-induced oscillations. Phys. Rev. Res. **2**, 033106 (2020)
15. Y. Kuramoto, *Chemical Oscillations, Waves, and Turbulence* (Dover, New York, 2003)
16. Y. Kuramoto, H. Nakao, On the concept of dynamical reduction—the case of coupled oscillators. Phil. Trans. Roy. Soc. A **377**, 20190041 (2019)
17. I. León, D. Pazó, Phase reduction beyond the first order: The case of the mean-field complex Ginzburg-Landau equation. Phys. Rev. E **100**, 012211 (2019)
18. A. Mauroy, I. Mezić, Y. Susuki (eds), The Koopman operator in systems and control. Lecture Notes in Control and Information Sciences, vol. 484, (Springer, Cham, 2020)
19. A. Mauroy, I. Mezić, Global stability analysis using the eigenfunctions of the Koopman operator. IEEE Trans. Autom. Control **61**, 3356–3369 (2016)
20. A. Mauroy, I. Mezić, Global computation of phase-amplitude reduction for limit-cycle dynamics. Chaos **28**, 073108 (2018)
21. B. Monga, D. Wilson, T. Matchen, J. Moehlis, Phase reduction and phase-based optimal control for biological systems: a tutorial. Biol. Cybern. **113**, 11–46 (2019)
22. Nakao, H., Mezić, I.: Koopman eigenfunctionals and phase-amplitude reduction of rhythmic reaction—diffusion systems, in *Proceedings of the SICE Annual Conference* (2018), pp. 74–77
23. H. Nakao, I. Mezić, Spectral Analysis of the Koopman Operator for Partial Differential Equations. Chaos **30**, 113131 (2020)
24. H. Nakao, Phase reduction approach to synchronization of nonlinear oscillators. Contemp. Phys. **57**, 188–214 (2016)
25. H. Nakao, T. Yanagita, Y. Kawamura, Phase reduction approach to synchronization of spatiotemporal rhythms in reaction-diffusion systems. Phys. Rev. X **4**, 021032 (2014)
26. V. Novičenko, K. Pyragas, Phase reduction of weakly perturbed limit cycle oscillations in time-delay systems. Phys. D **241**, 1090–1098 (2012)

27. B. Pietras, A. Daffertshofer, Network dynamics of coupled oscillators and phase reduction techniques. Phys. Rep. **819**, 1–105 (2019)
28. A. Pikovsky, M. Rosenblum, J. Kurths, *Synchronization: A Universal Concept in Nonlinear Sciences* (Cambridge University Press, Cambridge, 2001)
29. M. Rosenblum, A. Pikovsky, Numerical phase reduction beyond the first order approximation. Chaos **29**, 011105 (2019)
30. S. Shirasaka, W. Kurebayashi, H. Nakao, Phase-amplitude reduction of transient dynamics far from attractors for limit-cycling systems. Chaos **27**, 023119 (2017)
31. T. Stankovski, T. Pereira, P.V.E. McClintock, A. Stefanovska, Coupling functions: universal insights into dynamical interaction mechanisms. Rev. Mod. Phys. **89**, 045001 (2017)
32. S. Strogatz, *Sync: The Emerging Science of Spontaneous Order* (Penguin Books, London, 2004)
33. K. Taira, H. Nakao, Phase-response analysis of synchronization for periodic flows. J. Fluid Mech. **846**, R2 (2018)
34. P.A. Tass, *Phase Resetting in Medicine and Biology: Stochastic Modeling and Data Analysis* (Springer, Berlin, 2007)
35. K.C.A. Wedgwood, K.K. Lin, R. Thul, S. Coombes, Phase-amplitude descriptions of neural oscillator models. J. Math. Neurosci. **3**, 2 (2013)
36. D. Wilson, Phase-amplitude reduction far beyond the weakly perturbed paradigm. Phys. Rev. E **101**, 022220 (2020)
37. D. Wilson, B. Ermentrout, Phase models beyond weak coupling. Phys. Rev. Lett. **123**, 164101 (2019)
38. D. Wilson, J. Moehlis, Isostable reduction of periodic orbits. Phys. Rev. E **94**, 052213 (2016)
39. A.T. Winfree, *The Geometry of Biological Time* (Springer, New York, 2001)
40. A. Zlotnik, Y. Chen, I.Z. Kiss, H.-A. Tanaka, J.-S. Li, Optimal waveform for fast entrainment of weakly forced nonlinear oscillators. Phys. Rev. Lett. **111**, 024102 (2013)

Chapter 3
Reduced Phase Models of Oscillatory Neural Networks

Bastian Pietras and Andreas Daffertshofer

Abstract Phase reduction facilitates the analysis of networks of (weakly) coupled oscillators. Synchronization regions can be uncovered and also non-trivial network behavior can be foreseen via the reduced phase dynamics. Phase models have become an essential tool for describing and analyzing rhythmic neural activity. It is widely accepted that in oscillatory neural networks, phase synchronization is crucial for information processing and information routing. Accurately deriving the phase dynamics of interacting neural oscillators is far from trivial. We demonstrate how different reduction techniques of a network of interacting Wilson-Cowan neural masses can lead to different dynamics of the reduced networks of phase oscillators. We pinpoint caveats and sensitive issues in the derivation of the phase dynamics and show that an accurately derived phase model properly captures the collective dynamics. We finally investigate the influence of strong interactions and biologically plausible connectivity structures on the network behavior.

3.1 Introduction

Oscillatory behavior abounds across many different scales of the human brain [17, 18, 80]. To trace and describe these neural oscillations, the development and design of recording techniques and models have benefitted from mutual interaction between experimental and theoretical neuroscientists. Still, linking recordings of brain activity to the underlying neuronal mechanisms remains an urgent challenge. A promising approach to model large-scale brain dynamics builds on networks of

B. Pietras (✉)
Institute of Mathematics, Technische Universität Berlin & Bernstein Center for Computational Neuroscience, Berlin, Germany
e-mail: pietras@tu-berlin.de

A. Daffertshofer
Faculty of Behavioural and Movement Sciences, Amsterdam Movement Sciences & Institute for Brain and Behaviour Amsterdam, Vrije Universiteit Amsterdam, Amsterdam, The Netherlands
e-mail: a.daffertshofer@vu.nl

A. Stefanovska and P. V. E. McClintock (eds.), *Physics of Biological Oscillators*, Understanding Complex Systems,
https://doi.org/10.1007/978-3-030-59805-1_3

interacting neural oscillators. By focusing on the corresponding phase dynamics, it is possible to analyze synchronization properties of the network.

As revealed by a plethora of experimental studies relying on both invasive and non-invasive neuroimaging techniques, information processing in the brain is intrinsically linked to synchronization phenomena of oscillatory dynamics [37, 55]. Non-invasive EEG and MEG studies typically depict distributed cortical activity as of large-scale brain networks. Although M/EEG recordings have high temporal resolution, they reflect activity on rather coarse spatial scales given that signals to be perceivable require synchronous neuronal currents of a large number of neurons, commonly of the order of 10^4 to 10^5 cells. The resulting time series of the recordings are duly and extensively analyzed for their extracted phase and amplitude dynamics. Emerging synchronization patterns in the data are then assigned to particular brain functions corresponding to the underlying hypothesis or the behavioral observations. Research on the phase dynamics of cortical oscillatory activity is rather recent compared to amplitude modulations in the M/EEG. However, there are several reports indicating that the phase dynamics play a crucial role for information processing and inter-cortical communication [22, 64, 74, 75, 82, 84].

Phase synchronization also plays an integral part in defining functional connectivity structures of the brain. The technological advance of modern brain imaging methods has led to elucidate the interplay of structural and functional brain connectivity. The structure of anatomical connections between brain areas is widely believed to facilitate temporal synchronization of neural activity, and can lead to spatial patterns of functional connectivity [9, 15, 24, 48]. Yet, the extent to which structure shapes function is still unclear [36, 44]. To unveil functional brain connectivity and communication pathways [10, 33, 54], it is crucial to identify functional modules consisting of remote but synchronized neuronal populations. This can be achieved by analyzing the phase dynamics of the different brain areas.

While extensive data analysis may establish important synchronization properties across the human brain, a comprehensive understanding of the underlying neural mechanisms also requires theoretical models that can be validated and tested against experimental data. Often, heuristic phase models are used as guidelines for inferring neural network dynamics from data. But without a proper derivation of these heuristic models, the results may become questionable. Phase reduction [32, 35, 45, 46, 51, 60, 67, 77] provides a powerful tool to derive phase models from biophysiologically realistic models and to link parameters from the more complex with those from the simpler model in order to identify the key factors for a particular behavioral paradigm. Unfortunately, there is not "the" phase reduction, but one has to choose from a variety of techniques – a recent review can be found in [67]. Even worse, different phase reductions can lead to qualitatively different phase models, that is, reduced phase models may predict different network behavior. For an accurate derivation of a phase model, reduction techniques have to be tailored to the targeted macroscopic observable and the parameter regime under study. Only then one can exploit the full strengths of the reduced phase model. Finally, a word of caution is in order. Phase reduction is strictly valid only for a number of necessary assumptions. Therefore,

one always ought to keep in mind the limitations and range of applicability of an accurately reduced phase model.

In the following, we will demonstrate these aspects in more detail. We will guide our presentation along the example of a network of interacting Wilson-Cowan neural masses, which will be introduced in Sect. 3.2. We will present different phase reduction techniques for a network of weakly coupled oscillators in Sect. 3.3 and show that they may indeed result in different predictions about the collective dynamics. We reported these results previously in an extensive review on network dynamics and phase reduction techniques [67]. Here we add to this by highlighting possible limitations of phase reduction for oscillatory networks in Sects. 3.4 and 3.5. Particular focus lies on network topologies, especially when considering a realistic brain network connectivity structure, and on coupling strengths beyond the weakly perturbed paradigm. We demonstrate why in these cases a reduced phase model may (not) provide valuable information about the actual network dynamics.

3.2 Networks of Wilson-Cowan Neural Masses

Considering large-scale oscillatory brain networks, the elementary network components, or nodes, can be assumed to be neural populations consisting of a large number of neurons. From the variety of neural population, or neural mass, models, the seminal Wilson-Cowan neural mass model [88] serves as an exquisite example to derive the phase dynamics in great detail. The Wilson-Cowan model describes the dynamics of the mean firing rates of neuronal populations. At every node $k = 1, \ldots, N$ of the network, we placed properly balanced pairs of excitatory and inhibitory populations with mean firing rates $E_k = E_k(t)$ and $I_k = I_k(t)$, respectively. The nodes are coupled to other nodes through the connections between their excitatory populations [21, 23, 76]. The connection weigths are typically given by a coupling matrix $C = \{C_{jk}\}_{j,k=1,\ldots,N}$. We illustrate the basic structure of this network in Fig. 3.1.

The dynamics at node k takes on the form

$$\begin{aligned} \dot{E}_k &= -E_k + \mathcal{S}\left[a_E\left(c_{EE}E_k - c_{EI}I_k - \Theta_E + \frac{\kappa}{N}\sum_{j=1}^{N} C_{kj}\, g(E_j)\right)\right] \\ \dot{I}_k &= -I_k + \mathcal{S}\left[a_I\left(c_{IE}E_k - c_{II}I_k - \Theta_I\right)\right]. \end{aligned} \tag{3.1}$$

The function $\mathcal{S}[x] = (1 + e^{-x})^{-1}$ is a sigmoid function with thresholds Θ_E and Θ_I that need to be exceeded by the total input into neural mass k to elicit firing; the parameters a_E and a_I describe the slopes of the sigmoids. The constants $c_{EE}, c_{EI}, c_{IE}, c_{II}$ quantify the coupling strengths within each (E/I) node and $\kappa \ll 1$ scales the coupling between different nodes. Pairwise interaction between different nodes is mediated through the coupling function $g(E)$, which we choose as $g(E) = E(t) - E^0$. By subtracting an average E^0 (typically, the unstable fixed point

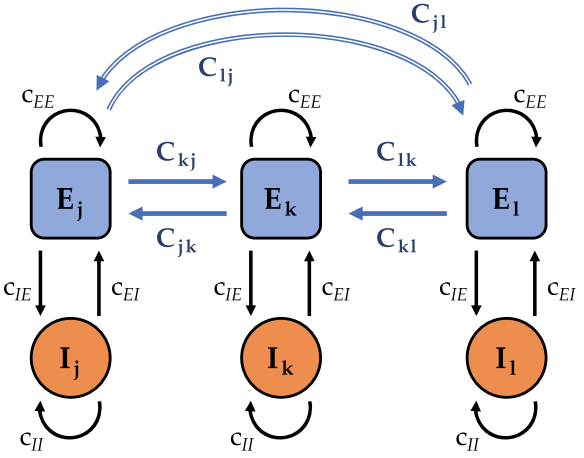

Fig. 3.1 Network of three coupled Wilson-Cowan neural masses. Each node contains excitatory and inhibitory populations, E_k and I_k, that are internally coupled with strengths c_{ij}, $i, j \in \{E, I\}$. Interaction between two neural masses $k \neq j$ occurs via their respective excitatory populations, where C_{kj} denotes the connectivity whether node k receives input from node j

within a stable limit cycle) from the actual firing rate $E = E(t)$, we avoid spurious contributions from other neural masses when they are all synchronized. In general, the interaction within and between different nodes may be time-delayed due to finite signal transmission of, in particular, long-range connections. Allowing for time delays between nodes, or for spatial interaction kernels, yields more intricate coupling dynamics, see, e.g., [47, 73]. For the sake of legibility we here restrict our analysis to instantaneous interactions. We note, however, that phase reduction can also be employed in face of time delays [67, Sect. 10.3.2].

Depending on the choice of parameters, the Wilson-Cowan model Eq. (3.1) can exhibit rich dynamics such as self-sustained oscillations and multi-stability, see, e.g., [14, 45, 67, 88]. Here, we restrict the parameter values (see *Appendix*) to the dynamical regime in which every isolated ($\kappa = 0$) node displays stable limit cycle oscillations. Each point on this stable limit cycle can, in general, be described in terms of a phase and an amplitude. If the attraction towards the limit cycle is sufficiently fast, it is possible to ignore the amplitude dynamics so that the one-dimensional phase variable ϕ_k reliably describes the state of the oscillator not only on the limit cycle, but also in its close vicinity. Moreover, assuming weak coupling between nodes, we can then capitalize on the theory of weakly coupled oscillators [32, 45, 67] to extract the phase dynamics of each node $k = 1, \ldots, N$ in form of

$$\dot{\phi}_k = \omega_k + \frac{\kappa}{N} \sum_{j=1}^{N} C_{kj} \Gamma(\phi_k - \phi_j) \tag{3.2}$$

with a natural frequency term ω_k and a phase interaction function $\Gamma(\psi)$ that depends on the phase difference $\phi_k - \phi_j$ between two nodes $k \neq j$. The phase interaction function $\Gamma(\psi)$ is typically periodic in ψ and can thus be expanded in a Fourier series:

$$\Gamma(\psi) = a_0 + a_1 \cos(\psi) + b_1 \sin(\psi) + a_2 \cos(2\psi) + b_2 \sin(2\psi) + \cdots \tag{3.3}$$

The phase dynamics Eqs. (3.2 and 3.3) can subsequently be analyzed with respect to the synchronization behavior of the network. A useful macroscopic observable to describe the network dynamics is the *Kuramoto order parameter* [51]

$$z = R\mathrm{e}^{i\Psi} = \frac{1}{N}\sum_{k=1}^{N} \mathrm{e}^{i\phi_k} , \tag{3.4}$$

whose absolute value $R = |z|$ takes on values between 0 and 1. $R = 0$ indicates an incoherent state, whereas $R = 1$ indicates a fully synchronized state. Values $0 < R < 1$ indicate partially synchronous collective dynamics. Furthermore, the Fourier coefficients a_n, b_n of the phase interaction function Eq. (3.3) are indicative for particular network behavior. For example, if we consider only the first two harmonics in $\Gamma(\psi)$, i.e. $a_n = b_n = 0$ for $n > 2$, and global coupling, $C_{kj} = 1$ for all $k \neq j$, then it can be shown [20, 49, 67] that the phase model exhibits

- a fully synchronized state for $\kappa b_1 > 0$,
- a balanced two-cluster state for $\kappa b_1 < 0$ and $\kappa b_2 > 0$, and
- slow switching behavior of oscillators between two unbalanced clusters for $\kappa b_1 < 0$, $\kappa b_2 < 0$ and b_1 is comparable in size to b_2.

There may exist additional attractors such as, e.g., three-cluster states or the so-called self-consistent partially synchronous state [20], but general conditions for their existence in terms of the Fourier coefficients $b_{1,2}$ are elusive, so that we rather concentrate on the three regimes above as well as on the incoherent state for $\kappa b_1 < 0$. One can use these insights to predict the collective dynamics of the full network. An accurately reduced phase model is capable of forecasting the transition between synchronous and asynchronous network behavior. Moreover, when focussing on higher harmonics of the phase interaction function $\Gamma(\psi)$, also non-trivial collective dynamics in the original model can be explained with the help of a reduced phase model.

3.3 Phase Reduction of Oscillatory Neural Networks

The ultimate goal of phase reduction is to rigorously establish the mapping between the full dynamics Eq. (3.1) and the reduced phase model Eq. (3.2) by expressing the natural frequency and the phase interaction function in terms of the parameters of the original model Eq. (3.1). Central to phase reductions of weakly coupled neural oscillators is Malkin's theorem [45, 56, 77], which provides a recipe to reduce a dynamical system of the form

$$\dot{\boldsymbol{x}}_k = \boldsymbol{f}(\boldsymbol{x}_k) + \kappa \boldsymbol{g}_k(\boldsymbol{x}_1, \ldots, \boldsymbol{x}_N), \quad \boldsymbol{x}_k \in \mathbb{R}^n, k = 1, \ldots, N, \tag{3.5}$$

into a phase model Eq. (3.2). As the form of the Wilson-Cowan model Eq. (3.1) does not comply with that of Eq. (3.5), it is compulsory to first transform the original dynamics appropriately. Only then we can employ standard methods [67] to retrieve the phase model Eq. (3.2). We note that the "pre-processing" step can be achieved either numerically or analytically [67, Sects. 4 and 6], giving rise to classifying different phase reduction approaches as either analytic or numerical reduction techniques.

Numerical approaches tend to be more accurate. But their software implementation often computes the necessary properties for phase reduction internally, which leaves the link between the original and the phase model parameters unclear. By contrast, analytic approaches build on subsequent algebraic transformations that yield a rigorous representation of the phase model parameters in terms of the original parameters, although such a representation may become convoluted. The pre-processing of the full dynamics Eq. (3.1) into Eq. (3.5) is based on the idea that close to a particular bifurcation, different models exhibit similar dynamics. Given that the Wilson-Cowan model Eq. (3.1) exhibits oscillatory behavior close to a Hopf bifurcation, we thus aim at transforming Eq. (3.1) into the simplest model that captures the essence of the dynamics close to a Hopf bifurcation point. This simplest model is called Hopf normal form and we can obtain it with a so-called normal form, or center manifold, reduction [45, 59, 67]. There is, however, a caveat. Since we consider not only a single isolated neural oscillator but a network of coupled neural oscillators, we require a *network Hopf normal form*: That is, not only the uncoupled part $\boldsymbol{f}(\boldsymbol{x})$ in Eq. (3.5) has to be brought into Hopf normal form, but also the coupling function $\boldsymbol{g}_k(\boldsymbol{x}_1, \ldots, \boldsymbol{x}_N)$ has to be identified accordingly subject to all symmetry constraints that are inherent to multiple Hopf bifurcations. Although there is a mathematical proof for such a network Hopf normal form, to the best of our knowledge, no general and exact algorithm for deriving it is at hand. Instead, two approximative schemes have proven fruitful to retain the simplified network Hopf normal form: Kuramoto's reductive perturbation approach and Poincaré's nonlinear transform approach, for details we refer to [67].

Stepping over these often laborious algebraic transforms, there is an alternative analytic approach which becomes exact for weakly coupled oscillators that follow a circular limit cycle: Haken's reduction via averaging [41, 67], see also [13, 40]. For planar oscillatory dynamics close to a Hopf bifurcation, the Jacobian of the uncoupled Wilson-Cowan dynamics Eq. (3.1) evaluated at the unstable fixed point (E_k^0, I_k^0) has a pair of complex conjugate eigenvalues $\lambda_\pm = \mu \pm i\omega$ with positive real part, $\mu > 0$, which corresponds to the distance to the Hopf bifurcation point.[1] We then express the dynamics in terms of the deviations $\boldsymbol{x}_k = \big(E_k - E_k^0(\mu), I_k - I_k^0(\mu)\big)$ around the unstable fixed points. Approximating the sigmoidal activation function $\mathcal{S}$ up to third order and applying some laborious algebraic transforms [67], one can derive a fairly generic form of the dynamics Eq. (3.1) that reads

[1] Typically, one measures this distance in parameter space, e.g., in parameter Θ_E such that $\mu = \Theta_E - \Theta_E^H$, where the Hopf bifurcation occurs at $\Theta_E = \Theta_E^H$.

$$\dot{\boldsymbol{x}}_k = \boldsymbol{L}\boldsymbol{x}_k + \boldsymbol{T}^{-1}\boldsymbol{f}\left(\boldsymbol{T}\boldsymbol{x}_k; \mu\right) + \kappa \boldsymbol{T}^{-1} \sum_{j=1}^{N} \boldsymbol{g}\left(\boldsymbol{T}\boldsymbol{x}_k, \boldsymbol{T}\boldsymbol{x}_j\right). \tag{3.6}$$

Here, $\boldsymbol{L}$ is the Jordan real form of the dynamics' Jacobian $\boldsymbol{J}$, $\boldsymbol{T}$ the matrix containing the eigenvectors of $\boldsymbol{J}$. The function $\boldsymbol{f}$ includes all components within node k that contribute to its dynamical change and $\boldsymbol{g}$ covers all the between-node interaction, i.e. the last term of the right-hand side of the $\dot{E}_k$ dynamics in Eq. (3.1) now given as coupling between the nodes $\boldsymbol{x}_k$ and $\boldsymbol{x}_j$. The dynamics Eq. (3.6) exhibits qualitatively the same behaviour as Eq. (3.1), but due to the Jordan real form, a circular symmetry of the limit cycle is imposed on the full dynamics.

In the immediate vicinity of the Hopf bifurcation point, one can exploit the separation of time scales of phase and amplitude dynamics and readily transform Eq. (3.6) into $\boldsymbol{x}_k = (x_k, y_k) = (r_k \cos(\phi_k), r_k \sin(\phi_k))$, where r_k and $\phi_k = \Omega t + \theta_k$ are amplitude and phase (deviations) of the oscillations at node k, which are slowly varying with respect to the (mean) frequency Ω [42], here defined over the eigenvalues at the Hopf point, $\Omega = \omega(\mu = 0)$. Near the onset of oscillations through a supercritical Hopf bifurcation, $r_k \ll 1$ is small and, thus, the right-hand side of Eq. (3.6) is at least of order $\mathcal{O}(r_k)$. Given the slower time scales of r_k and $\theta_k = \phi_k - \Omega t$, one can average over one cycle $T = 2\pi/\Omega$. In line with [21], this direct averaging of the dynamics Eq. (3.6) yields the drastically reduced phase model Eq. (3.2 and 3.3)

$$\dot{\phi}_k = \omega_k + \frac{\kappa}{N} \sum_{k=1}^{N} C_{kj} a_1 \sin(\phi_k - \phi_j) \tag{3.7}$$

with natural frequency $\omega_k = a_E a_I c_{IE} c_{EI} S'_E S'_I - \frac{1}{4}(a_E c_{EE} S'_E + a_I c_{II} S'_I)^2$, first Fourier amplitude $a_1 = \frac{1}{2} a_E S'_E \Lambda_k C_{kj} (R_j/R_k)$, and all other amplitudes vanish: $a_0 = a_n = 0$ for $n > 1$ as well as $b_n = 0$ for all $n \geq 1$. We abbreviated $\Lambda_k^2 = 1 + \rho_k^2$ with $\rho_k = \frac{1}{\omega_k}(a_E c_{EE} S'_E + a_I c_{II} S'_I)$ and $S'_{E/I}$ denotes the first derivative of the sigmoid $\mathcal{S}$ evaluated at the fixed points E_k^0/I_k^0 of Eq. (3.1).

In summary, we have four different phase reduction techniques:

1. Reductive perturbation approach
2. Nonlinear transform approach
3. Direct averaging
4. Numerical/adjoint.

The first two are the analytic approaches that build on a pre-processing step to bring the dynamics in network Hopf normal form. Then, there is Haken's approach that circumvents a rigorous normal form reduction by applying averaging directly to presumably circular dynamics close to the Hopf bifurcation. And finally, one can employ a numerical approach, which capitalizes on Malkin's theorem and provides numerical values for the reduced phase model by solving an associated adjoint problem [16, 29, 31, 32, 45], which has, e.g., been automatized in the software packages XPPAUT [28] or MatCont [26]. In order to compare the different approaches, we will

apply the four different phase reduction techniques to the network of Wilson-Cowan neural masses Eq. (3.1). In the resulting phase models Eq. (3.2), we will concentrate on the reduced natural frequency term ω_k and the first two Fourier harmonics in the phase interaction function Eq. (3.3). Their amplitudes will serve as a quantitative measure of how accurate the phase models are, whereas their relationships with one another provide a qualitative measure indicating whether the reduced phase models result in the correctly predicted collective dynamics; see the end of Sect. 3.2 for a classification of the network's phase dynamics in terms of the Fourier coefficients.

Phase reduction is highly parameter-sensitive

A first litmus test concerns the accuracy of the different phase reduction techniques close to a bifurcation boundary. Center manifold and normal form theory prescribe the exact form of the phase interaction function $\Gamma(\psi)$, see [16]. For the regime near a supercritical Hopf bifurcation, the topological normal form [53] of the dynamics yields a purely sinusoidal phase interaction function, that is, all Fourier coefficients but b_1 in Eq. (3.3) will vanish. The topological Hopf normal form requires further algebraic transformations than the conventional (Poincaré) Hopf normal form, but its essence remains the same: the first Fourier harmonics dominates and higher harmonics tend to zero. In Table 3.1 we show the results of the different phase reduction techniques when the distance to the Hopf bifurcation is as small as $\mu = 0.0003$; here, we chose Θ_E as the bifurcation parameter so that $\mu := \Theta_E - \Theta_E^H$ with Θ_E^H the parameter value where the supercritical Hopf bifurcation occurs. All four reduction techniques can reliably retrieve the correct shape of the phase interaction function with dominant first harmonics and a positive first odd Fourier coefficient $b_1 > 0$, which indicates a fully synchronized state. Moreover, the natural frequency terms coincide for all reduction techniques. Note that the quantitative differences do not influence the qualitative predictions of the network behavior.

When increasing the distance to the Hopf bifurcation point, however, the phase models start to diverge. In Table 3.2, we show exemplary results of the phase model parameters for $\mu = 0.1663$. Only the numerical/adjoint method captures the change of slope of the phase interaction function (whose derivative at $\psi = 0$ is dominated by b_1) and predicts that the fully synchronized state becomes unstable in this parameter region. The other three reduction techniques still predict the synchronous solution,

Table 3.1 Phase models derived with different reduction techniques infinitesimally close to the Hopf bifurcation ($\mu = 0.0003$). The oscillators' natural frequency is ω, and a_n, b_n are the amplitudes of the Fourier components of the phase interaction function Γ

Approach	ω	a_1	b_1	a_2	b_2
Reductive perturbation	0.701	–0.9505	1.1555	–0.0001	0.0013
Nonlinear transform	0.701	–0.9457	1.1382	–0.0009	0.0013
Direct averaging	0.701	–0.6940	0.2140	–	–
Numerical/adjoint	0.701	–0.0472	0.3843	–0.0001	0.0002

Table 3.2 Phase models derived with different reduction techniques away from the Hopf bifurcation ($\mu = 0.1663$). The oscillators' natural frequency is ω, and a_n, b_n are the amplitudes of the Fourier components of the phase interaction function Γ

Approach	ω	a_1	b_1	a_2	b_2
Reductive perturbation	0.728	–0.9505	1.1555	–0.2470	0.3657
Nonlinear transform	1.023	–0.4905	0.1383	–0.0604	0.0503
Direct averaging	1.330	–0.4733	0.2390	–	–
Numerical/adjoint	0.939	–0.4447	–0.2668	–0.0635	–0.0451

although the reduced phase models differ with respect to the amplitude of the harmonics. Compared to the numerical/adjoint method, Poincaré's reduction via nonlinear transforms yields the same orders of magnitude, whereas Kuramoto's reductive perturbation overestimates the second harmonics and the direct averaging by construction does not contain any higher harmonics at all. Strong first harmonics of the phase interaction function will amplify the coupling and thus result in faster (de-)synchronization, depending on the sign of the sinusoidal component. Second and higher harmonics may play a crucial role for clustering. An over- or underestimation of the amplitudes of higher harmonics may hence lead to erroneous predictions of multiple- or one-cluster states.

Accurate phase models capture the true collective dynamics

The farther one moves away from particular bifurcation boundaries, the more the reduced phase models will diverge. Naturally, one seeks a phase reduction technique that reliably recovers the (collective) behavior of the original (network) dynamics. While the accuracy of analytic phase reduction techniques scales with the distance to the bifurcation point (due to the normal form reduction inherent to these two-step reduction approaches [67]), numerical phase reduction techniques, in general, do not suffer this shortcoming and can retain the accuracy across parameter space. For this reason, we will probe the numerical phase reduction and test whether it captures the collective dynamics of the Wilson-Cowan network, indeed.

Following the literature [43, 45], we choose Θ_E and Θ_I as bifurcation parameters and, first, investigate the transition to synchrony as predicted by the slope $\Gamma'(0)$ of the phase interaction function changing from positive (fully synchronous state) to negative values (synchrony becomes unstable). In line with previous results,[2] our findings confirm the general picture that for large parameter regions the fully synchronous state is stable, see the yellow/red regions in Fig. 3.2. In particular, synchrony is stable close to the Hopf bifurcation boundaries of the isolated Wilson-Cowan dynamics (dashed lines in Fig. 3.2).

Second, we try to elucidate the dynamics in parameter regions where the fully synchronized state is no longer stable, see the blue regions and the inset in Fig. 3.2,

[2] Hlinka and Coombes [43] showed that the predictions based on the derivative of the numerically reduced phase interaction function agreed almost perfectly with the synchronization properties of the original network, cf. their Figs. 3.6 and 3.7.

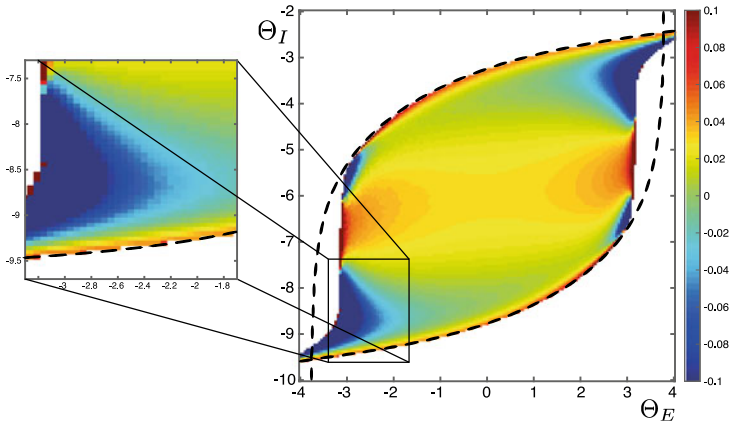

Fig. 3.2 Oscillatory regime of the Wilson-Cowan neural mass model Eq. (3.1) with parameters Eq. (3.8). The colored region of oscillatory behavior lies within the Hopf bifurcation boundaries (black dashed curves) for a single isolated Wilson-Cowan neural mass. The color coding indicates the derivative of the phase interaction function Γ at $\psi = 0$ determining the stability of the fully synchronized state: if $\Gamma'(0) > 0$ the fully synchronized state is stable, and unstable otherwise.We used the numerical/adjoint reduction method to generate this figure

and where previous results did not predict the actual dynamics correctly. Close to the Hopf bifurcation boundary the slope $\Gamma'(0) \approx b_1$ of the phase interaction function is positive and correctly predicts synchronization. Moving upwards in parameter space by increasing Θ_I leads to a change of signs in $\Gamma'(0)$, and we are in the deep blue region in Fig. 3.2, where the fully synchronous state is no longer stable. We fix the parameter $\Theta_E = -3$ and analyze the numerically reduced phase interaction function with respect to higher harmonics for different values of Θ_I. At $\Theta_I = -9.3$, we find that $b_1 > 0$ (stable fully synchronous solution). At $\Theta_I = -8.9$, $b_1 < 0$ and $b_2 < 0$, predicting that the oscillators are evenly spread along the limit cycle, which is also called a stable anti-cluster state. For larger $\Theta_I = -8.7$, the balanced two-cluster state becomes stable ($b_1 < 0$ and $b_2 > 0$); for the exact numerical values see the *Appendix*. To test the predictions of the reduced phase model, we simulated a network of $N = 30$ Wilson–Cowan neural masses with global coupling, $C_{kj} = 1$ for all $k \neq j$, and coupling strength $\kappa = 0.15$. As can be seen in Fig. 3.3, the simulations confirmed the predicted (a) fully synchronized state, (b) an anti-cluster state, i.e. incoherence, and (c) a stable two-cluster state, respectively. The other phase reduction techniques did not only fail to predict the existence of two-cluster states, but they also missed the transition from synchrony to incoherence; cf. Table 3.2.

We can thus conclude that an accurately reduced phase model within its range of applicability can correctly predict collective dynamics of a network of neural oscillators across parameter space. Numerical techniques outperform analytical approaches with respect to accuracy. Still, analytical approaches can yield a direct link between original model parameters and the constituents of the reduced phase model that allow for an immediate prediction of the network state. It is, however, crucial to verify the

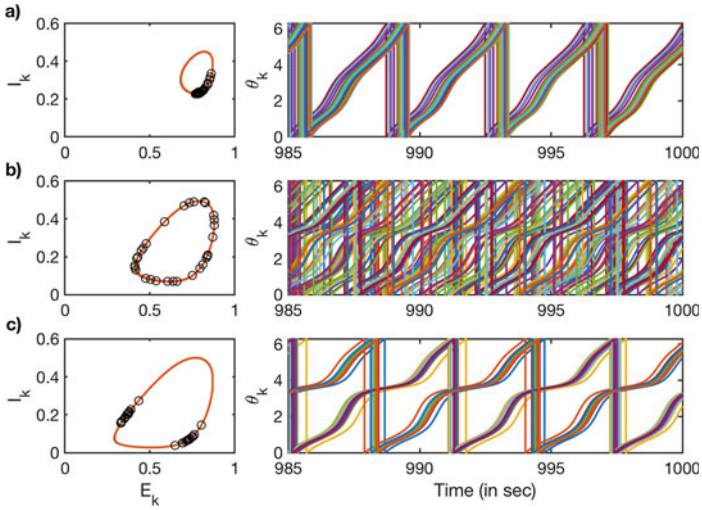

Fig. 3.3 Non-trivial network dynamics of $N = 30$ coupled Wilson-Cowan neural masses. The different network states **a** global synchronization, **b** incoherence, and **c** a balanced two-cluster state were predicted by the reduced phase model using the numerical/adjoint method. Displayed are final ($T_{\text{end}} = 1000$ seconds) conditions ('o') on the uncoupled limit cycle (left column) and the extracted phases (right) for the last 15 seconds. We fixed the coupling strength at $\kappa = 0.15$ and the simulations started from uniformly distributed initial conditions along the uncoupled limit cycle. Parameter values of (Θ_E, Θ_I) are **a** $(-3, -9.3)$, **b** $(-3, -8.9)$ and **c** $(-3, -8.7)$

parameter region where the analytical approaches are applicable. For this reason, we advocate a combination of numerical and analytical phase reduction techniques to provide an accurate picture of the network dynamics and its phase synchronization properties by means of a reduced phase model.

3.4 Phase Reduction in Face of Strong Coupling

The reduction of phase dynamics from a network of coupled oscillators retains its mathematical justification as long as the theory of weakly coupled oscillators applies. However, no rigorous definition of weak coupling exists, nor a concrete limit of the coupling strength at which the character of interaction switches from weak to strong. Usually, phase reduction is achieved with the tacit understanding that each isolated dynamical system already displays stable limit cycle oscillations, which is a necessary condition for the theory of weakly coupled oscillators to hold [5, 45]. However, in some cases it is the coupling between systems that induces oscillations. Smale was among the first to investigate the emergence of oscillations via a Hopf bifurcation due to diffusive coupling [79]. On the other hand, coupling between systems can also make oscillations cease. Ermentrout and Kopell reported this kind

of oscillation death for a chain of Wilson-Cowan neural masses [30], see also the work by Daffertshofer and van Wijk on a (heterogeneous) network of Wilson-Cowan neural masses [23]. Those coupling-induced effects only occur for reasonably large coupling strengths, and a straightforward identification of the phase dynamics as within the theory of weak coupling is not possible. While sufficiently weak coupling ensures that the shape and the frequency of the limit-cycle orbits remain almost unchanged, strong coupling leads to non-negligible amplitude effects. These can destabilize synchronized states, quench oscillations, or cause collective chaos, and a phase reduction has only been proposed for quite restrictive assumptions; see [52] and the references therein. Hence, phase-amplitude reductions [19, 78, 87], see also [57, 67] for reviews, have to be employed that also take interactions between phase and amplitude dynamics into account. The theory of weakly coupled oscillators additionally requires that the actual trajectories of the oscillators are always close to the isolated limit-cycle solution. While reduction methods exist that allow for a phase reduction farther away from the underlying periodic orbit, see, e.g., [57, 67, 89], we here try to answer the question whether appropriate conventional phase models can still capture coupling-induced collective dynamics.

Oscillation birth and clustering

To investigate coupling-induced behavior, it appears illustrative to start with two coupled identical Wilson-Cowan neural masses. In Fig. 3.4 we show the bifurcation diagram with respect to the coupling strength. Without coupling, $\kappa = 0$, the dynamics Eq. (3.1) feature only one stable stationary solution (black solid line). Increasing the coupling strength induces oscillations through a (double) Hopf bifurcation (red dot). The critical coupling strength κ_H can also be determined analytically, see the *Appendix* but also [4]. In our example, it is considerably small with $\kappa_H = 0.00531$ (note that we did not rescale the coupling by a factor $1/N$). In this coupling-induced oscillatory regime, the initial conditions can have a major impact on the resulting dynamics. For small coupling strengths $\kappa < 0.6$ (see green dot), the two Wilson-Cowan neural masses evolve from any initial conditions either into the same limit cycles or into the low activity resting state (blue solid curve). For larger coupling strengths, however, only identical initial conditions result into the same (red) limit cycles. Different initial conditions for the two coupled neural masses may still lead to stable oscillations, but the respective limit cycles of each neural mass can differ in amplitude and shape (cf. the green curves in Fig. 3.4). Moreover, these distinct oscillations that resulted from distinct initial conditions are stable beyond a critical coupling strength at which those oscillations from identical initial conditions have ceased to exist (through a fold bifurcation of limit cycles, see the inset in Fig. 3.4). From the point of view of oscillation quenching mechanisms [50], the onset of (identical) limit-cycle oscillations of the two Wilson-Cowan neural masses for small coupling strengths is a mechanism inverse to amplitude death. Larger coupling induces a symmetry breaking from two identical to two distinct limit cycles, and thus drives the system into an oscillation death-related regime. Note, however, that the Wilson-Cowan neural masses keep oscillating around the same, spatially uniform center,

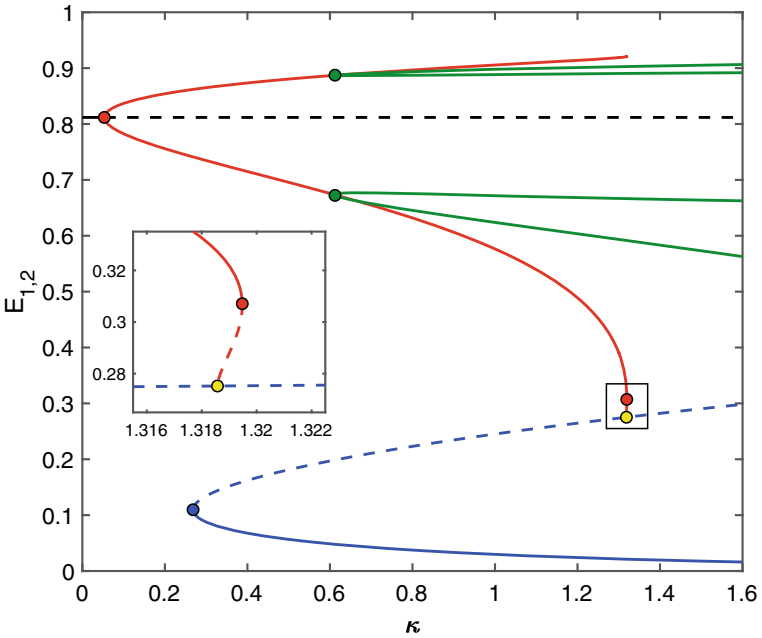

Fig. 3.4 Bifurcation diagram of two coupled identical Wilson-Cowan neural masses with parameters $(\Theta_E, \Theta_I) = (-3, -9.4)$. At low coupling, the units are at rest (black solid curve). Oscillations emerge at a double Hopf bifurcation (red dot), where the resting state becomes unstable (black dashed). The red curves display upper and lower limit of the limit cycles. Beyond the green dot, identical initial conditions of the two units evolve towards identical limit cycles (red curve) that are destroyed through a fold bifurcation of limit cycles (second red dot), whereas non-identical initial conditions lead to two distinct oscillatory solutions (with upper/lower limits on either the outer or inner branches of the green curves) that remain stable for large coupling strengths, for which identical initial conditions lead into a low-activity resting state (blue solid).The yellow dot represents a homoclinic bifurcation, induced through the unstable saddle (blue dashed) that emerged through a saddle-node bifurcation of fixed points (blue dot)

and that beyond a critical coupling strength, oscillations cease and give rise to a homogeneous steady state, which is coined amplitude death in the literature [50].

Based on the brief analytic insights concerning two coupled oscillators, we anticipate that coupling-induced effects will increase the intricacy of larger networks of strongly coupled oscillators. To illustrate this, we simulated a fully connected network of 30 identical Wilson-Cowan neural masses with random initial conditions. Figure 3.5 displays the network behavior for different coupling strengths. Without coupling, the dynamics evolve from random initial conditions towards the stationary solution given by the fixed point in Fig. 3.5 (top left panel). The dynamics of the (absolute value of the) Kuramoto order parameter R reflects the transient oscillatory dynamics from the initial conditions into the fixed point solution, where the phases of

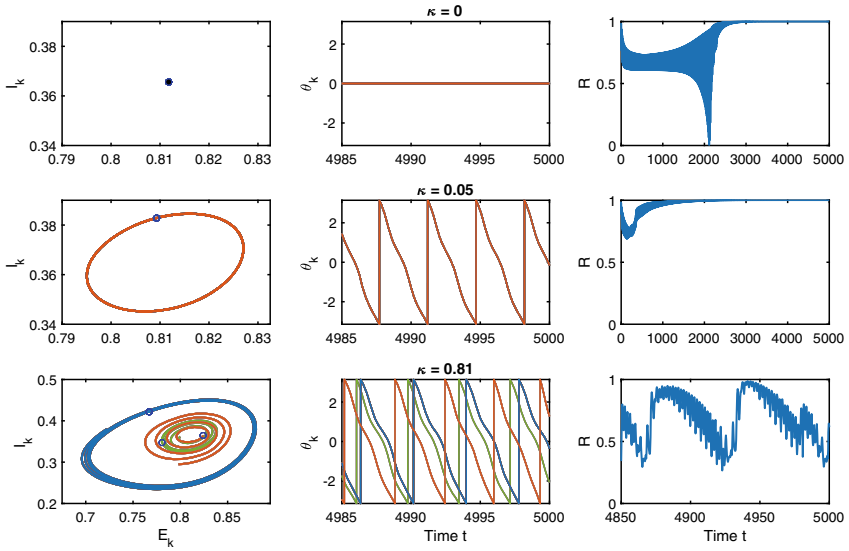

Fig. 3.5 Coupling-induced behavior of $N = 30$ globally coupled identical Wilson-Cowan neural masses with parameters $(\Theta_E, \Theta_I) = (-3, -9.4)$. Without coupling (top row), only the resting state is stable. At low coupling strength $\kappa = 0.05$ (middle row), all neural masses synchronize on the same limit cycle. At high coupling strength $\kappa = 0.81$ (bottom row), the neural masses form three clusters on distinct limit cycles and show intermittent synchronization. Left: dynamics of all neural masses in the $E_k - I_k$ plane for the last $t = 15$ seconds. Middle: extracted phases of all neural masses. Right: absolute value of the Kuramoto order parameter displaying phase synchronization of the network. See the *Appendix* for details about the network simulation and analysis.

the oscillators stay constant (after $t \approx 2500$s). For $\kappa = 0.05$, the coupling is already strong enough to lead to maintained oscillatory dynamics. The Wilson-Cowan neural masses become fully synchronized and oscillate on identical limit cycles (middle row in Fig. 3.5). For even stronger coupling, the coupling-induced oscillations become more complex. Clusters of oscillators emerge, which evolve on distinct oscillatory trajectories. In Fig. 3.5 (bottom row), the oscillatory neural masses have formed three groups that consist of different numbers of oscillators. Within each group, all oscillators are perfectly synchronized and follow the same (quasiperiodic) dynamics (see the middle and left panel, respectively). These dynamics differ, however, across groups. Note that although the Kuramoto order parameter exhibits complex oscillatory dynamics around a value that may indicate some partially synchronous state, it is impossible to infer from it the correct network behavior of three oscillating clusters.

Quenching of oscillations and quasiperiodic dynamics

To investigate the quenching of oscillations, we chose parameters such that (a) a single isolated Wilson-Cowan neural mass exhibits stable limit-cycle oscillations and

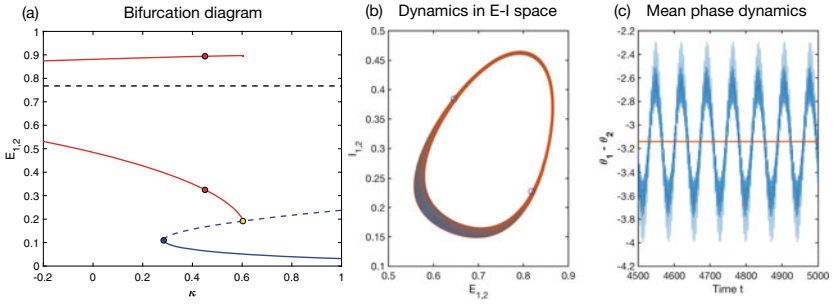

Fig. 3.6 Amplitude death and quasiperiodic behavior of two coupled identical Wilson-Cowan neural masses. **a** Bifurcation diagram similar to Fig. 3.4, but starting with stable limit cycle oscillations without coupling. Oscillation death occurs via a homoclinic bifurcation (yellow dot) for identical initial conditions. The red dots denote the emergence of quasiperiodic behavior for distinct initial conditions. In **b** quasiperiodic behavior of the two Wilson-Cowan neural masses (final condition of the two limit cycles shown as 'o') is depicted for coupling strength $\kappa = 0.475$. **c** The phase difference $\psi(t) = \theta_1(t) - \theta_2(t)$ (blue line) fluctuates around the mean $\bar{\psi}(t) = -\pi$ (orange), which indicates an incoherent state.

(b) weak global coupling leads to an incoherent, that is, asynchronous solution. The bifurcation diagram for two coupled identical oscillators with respect to the coupling strength is shown in Fig. 3.6. For identical initial conditions, the red curves represent the upper and lower limit of the amplitude of identical limit cycles, on which the two oscillators are phase-locked with a constant phase difference of $|\theta_1(t) - \theta_2(t)| = \pi$, as expected for weak coupling. The oscillations cease via a homoclinic bifurcation (yellow dot), in contrast to the fold bifurcation of limit cycles in the previous example. For distinct initial conditions, we find again two different oscillatory regimes: at low coupling strengths, the anti-phase periodic solutions evolve on the same limit cycle. However, for coupling strengths larger than $\kappa \approx 0.45$ (red dot) each neural mass exhibits quasiperiodic behavior (Fig. 3.6b). Remarkably, the mean phase difference $\bar{\psi}(t) = \lim_{T\to\infty} \int_0^T |\theta_1(t) - \theta_2(t)|dt = \pi$ stays constant, see orange line in Fig. 3.6c, which underlines that the oscillators remain incoherent.

As before, we simulated the network dynamics and confirmed the analytic predictions extrapolated from two coupled Wilson-Cowan neural masses to a larger network. Results are shown in Fig. 3.7. The parameters Θ_E, Θ_I are chosen such that the reduced phase model predicts asynchronous network dynamics for low coupling strengths, as is demonstrated by the simulations (top row). Increasing the coupling strength leads, first, to a general increase in network synchronization as indicated by the Kuramoto order parameter and, then, to quasiperiodic dynamics (middle row). The oscillators follow the same quasiperiodic trajectories spanning an annulus-shaped region in state space (similar to the behavior as shown in Fig. 3.6b). Note that although the phases of the oscillators tend to get closer to each other, the coupling is not strong enough to completely synchronize them also with respect to their amplitudes. Increasing the coupling strength even more, eventually results in destroying the network oscillations: the oscillatory dynamics of the individual

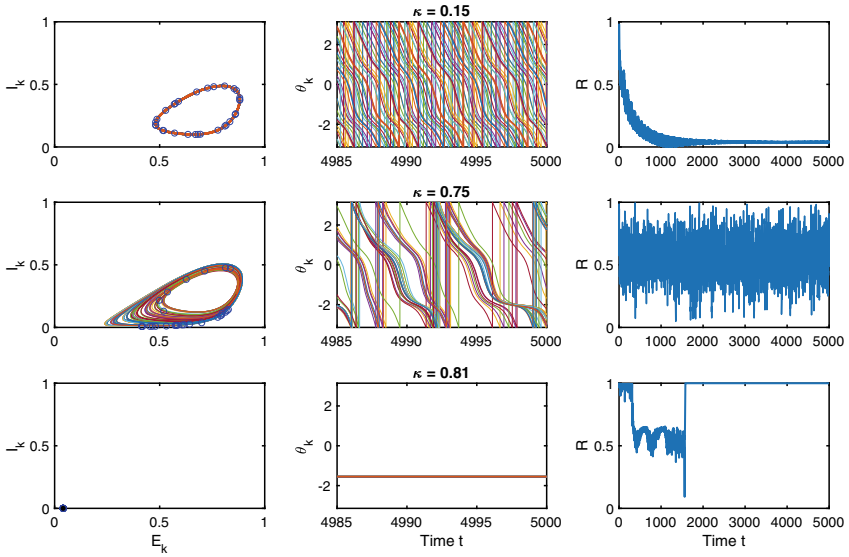

Fig. 3.7 Coupling-induced behavior of $N = 30$ globally coupled identical Wilson-Cowan neural masses with parameters $(\Theta_E, \Theta_I) = (-3, -9)$. At low coupling strength $\kappa = 0.15$ (top row), all neural masses desynchronize on the same limit cycle as predicted by the phase model. At intermediate coupling strength $\kappa = 0.75$ (middle row), oscillators move along quasiperiodic trajectories and tend to synchronize. At very high coupling strength $\kappa = 0.81$ (bottom row), oscillation death occurs and the neural masses run into a low activity resting state. Left: dynamics of all neural masses in the $E_k - I_k$ plane for the last $t = 15$ seconds. Middle: extracted phases of all neural masses. Right: absolute value of the Kuramoto order parameter displaying phase synchronization of the network. See the *Appendix* for details about the network simulation and analysis.

Wilson-Cowan neural masses collapse into the same low activity state (bottom row in Fig. 3.7). As before, the oscillation quenching mechanism is amplitude death [50]. Time-delayed interactions can also induce amplitude death, typically by stabilizing a specific homogeneous state [50]. Incorporating time delays in our setup will affect the bifurcation structure and may lead to interesting new phenomena, especially for large coupling strengths. For weak coupling, we hypothesize that the predictions on network synchronization based on a properly reduced phase model remain valid—given that time delays are taken into account during the phase reduction as, e.g., in [67, Sect. 10.3.2].

3.5 Phase Reduction in Face of Complex Structural Connectivity

Up to now, we have only considered globally coupled Wilson-Cowan neural masses with a trivial connectivity matrix, $C_{kj} = 1$ for all $k \neq j$. A realistic connectivity

structure in neural networks can have significant consequences for the collective dynamics, see, e.g., [1–3, 7, 11, 12, 27, 38, 61, 62, 68, 71, 72, 81]. A network topology, i.e. how the nodes of the network are connected, that deviates from global, all-to-all coupling, may render many results about predicted network behavior no longer valid. In some cases, the reduced phase interaction function Γ in combination with the connectivity matrix can still provide important information about the collective dynamics of a realistically connected network, e.g., about (remote) synchronization, see [25, 34, 58, 63, 69]. The Kuramoto model of phase oscillators where $\Gamma(\psi) = \sin(\psi)$ has been extensively studied on complex networks, see, e.g., the review by Rodrigues et al. [70]. More recently, it could also be shown how time delays shape the phase relationships in oscillatory networks with realistic connectivity structure [65, 66]. Some questions, however, still remain unanswered, e.g., how structure shapes function, what the constituents for synchrony are, or what drives a network into a chaotic state.

To illustrate how realistic structural connectivity—as derived, e.g., from diffusion tensor imaging (DTI)—adds to the complexity of the dynamics of neural networks, we compared the dynamics of the full Wilson-Cowan model Eq. (3.1) with the reduced phase model Eq. (3.2) for three different coupling topologies: a fully connected homogeneous network, an anatomical network reported by Hagmann and co-workers [39], and a network with small-world topology generated by the Watts-Strogatz model [86]. For the fully connected homogeneous network (i.e. global connectivity), we considered the adjacency values $C_{kj} = 1$ for all $k \neq j$, but set $C_{kk} = 0$ to exclude self-connections. For the Hagmann network, we used a DTI dataset to build a realistic network topology of the human cerebral cortex as described by Hagmann et al. [39]. To extract the "structural core" of anatomical connections, the original 998 cortical regions were assigned to a 66-node parcellation scheme and averaged over five subjects. The binary coupling matrix $C = \{C_{kj}\}$ was obtained by subsequently thresholding the weighted and undirected network gained through parcellation and

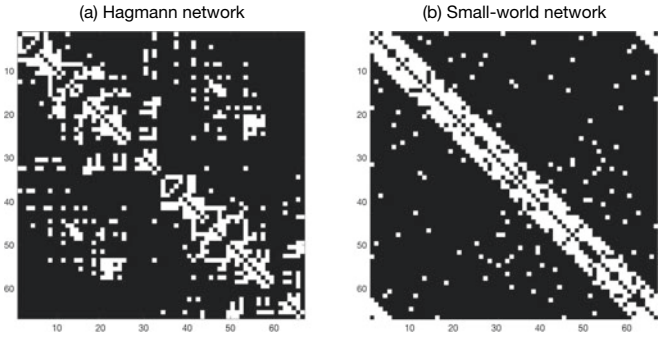

Fig. 3.8 Coupling matrices $C = \{C_{kj}\}$ for **a** the Hagmann dataset and **b** the small-world topology with $N = 66$ nodes. We generated the small-world network by using the same graph-theoretical properties as of the Hagmann network (average degree = 10, rewiring probability = 0.2). White pixels denote a link between nodes k and j, $C_{kj} = 1$

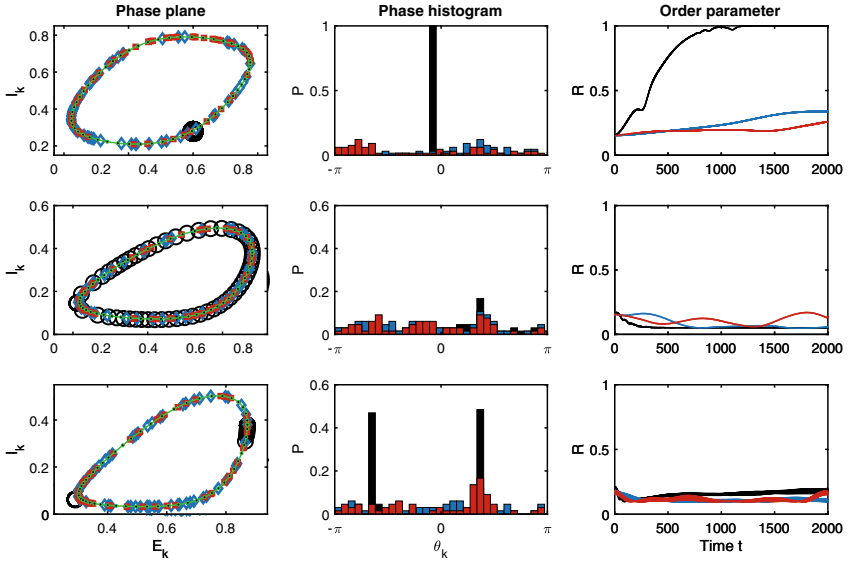

Fig. 3.9 Simulation of the Wilson-Cowan dynamics at coupling strength $\kappa = 0.15$ for regimes as predicted by the numerically reduced phase model: synchronization (top row), asynchrony (middle) and two-cluster state (bottom); see Tables 3.3, 3.4 and 3.5 in the *Appendix*. Left: final ($T = 2000$) position of all $N = 66$ Wilson-Cowan oscillators on the unperturbed limit cycle (green) with random initial conditions (black dots). Middle: histogram of the phases extracted from the final positions of the oscillators. Right: phase synchronization of the network measured in terms of the absolute value of the Kuramoto order parameter with a moving average of 20 seconds. Colors indicate full connectivity (black, circles), small world (blue, diamonds), and Hagmann (red, squares)

averaging, see Fig. 3.8 (panel a) [23, 83]. Analyzing the coupling matrix C further showed that the Hagmann network featured characteristics of a small-world network with average node-degree 10. For comparison, we thus generated a small-world network artificially by employing the procedure as introduced by Watts and Strogatz [86]: starting from an ordered network on a ring lattice with nodes connected to only a few direct neighbors, we subsequently rewired connections to random nodes with a certain probability (in our case 0.2) until we obtained a small-world network with the same average node-degree, see Fig. 3.8 (panel b). In other words, by adding a few random nodes in an ordered network, we thus created a small-world network featuring high clustering and low path length, which yields particular dynamical and synchronization properties that are appealing for their use in neuroscience [3, 6, 8, 85].

We then simulated the Wilson-Cowan networks with the three different coupling matrices. We chose parameter sets for which the reduced phase model (with global coupling) predicted synchronization, incoherence and cluster states. In Fig. 3.9 we show the network simulations for each of the three parameter regimes (top row: synchronization, middle: incoherence, bottom: balanced two-cluster state) and for each of the three coupling matrices (black: homogeneous coupling, blue: small-word, red:

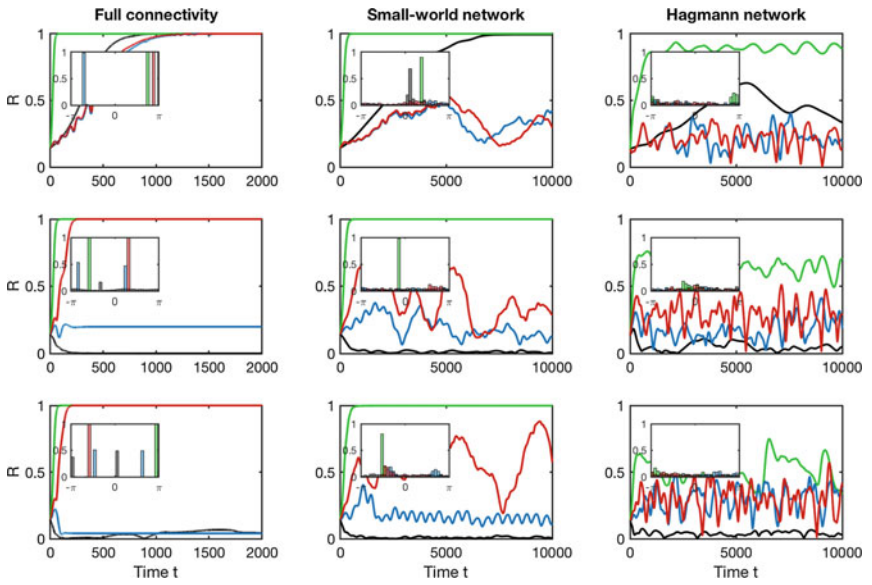

Fig. 3.10 Simulation of the reduced phase models as given in Tables 3.3, 3.4 and 3.5 at coupling strength $\kappa = 0.25$ with full (left column), small-world (middle) and Hagmann network connectivity (right) for parameter regimes where the numerically reduced phase model with global coupling predicts synchronization (top row), asynchrony (middle) and two-cluster state (bottom) Insets show histograms at final ($T = 2000$ for full connectivity, and $T = 10000$ otherwise) phase distribution for $N = 200$ oscillators ($N = 66$ for Hagmann network). Colors correspond to numerical reduction approach (black), direct averaging (green), reductive perturbation approach (red), and nonlinear transform approach (blue)

Hagmann). The more complex connectivity structures lead to macroscopic dynamics that become indistinguishable from one another; cf. the red and blue graphs corresponding to small-world and Hagmann networks, respectively. Only in the case of a fully connected homogeneous network (black graphs), the actual dynamics match the predictions of the (numerically) reduced phase model. Furthermore, we simulated the different phase models as derived with each of the four reduction techniques. The numerically reduced phase dynamics (black graphs) correctly captures the original Wilson-Cowan dynamics for full connectivity, see the left column in Fig. 3.10. For non-trivial connectivity structures, however, none of the phase models can follow the predictions based on the phase interaction function Γ. While for the small-world network (middle column) the simulations hint slightly at the synchronous, asynchronous and two-cluster regimes, respectively from top to bottom, the observed dynamics on the Hagmann network appear arbitrary. Note that the direct averaging technique (green graphs) leads to synchronous collective dynamics for almost all parameter settings and connectivity structures. The two analytic techniques diverge for full connectivity: the reductive perturbation approach (red) leads to a fully synchronized state, whereas the nonlinear transform approach (blue) results in a two-cluster state,

cf. the phase histograms of the final conditions (insets in Fig. 3.10). But for the small-world and Hagmann networks, these two techniques converge to the same resulting behavior. For details about the simulations see the *Appendix*.

In a nutshell, we can conclude that topology effects overcome otherwise precise predictions of the phase model such that even the least accurate direct averaging method does not perform worse than the other techniques.

3.6 Conclusion

Phase reduction is a powerful tool to simplify the dynamics of complex networks of neural oscillators. The reduced phase model allows a reliable prediction of various network behavior. Not only the transition between an incoherent state and a fully synchronized state can be revealed, but, by taking higher harmonics of the reduced phase interaction function into account, also non-trivial collective behavior can be forecast such as cluster states or slow-switching between clusters.

There does not, however, exist "the" phase reduction, but one has to choose from a variety of phase reduction techniques. The different reduction methods can broadly be classified as numerical and analytical phase reduction techniques. We compared different phase reduction techniques of oscillatory neural networks and showed that close to a particular bifurcation boundary, all reduction techniques retrieve the same qualitative results. Further away from bifurcation boundaries, different techniques start to diverge and one has to pay careful attention to whether, e.g., an analytically reduced phase model indeed captures the correct network behavior. We advocate a combination of numerical and analytical approaches to ensure the sought-for accuracy of the phase model while, at the same time, allowing for a direct mapping between the parameters of the neural network model with those of the reduced phase model. By this, one can identify key parameters of the neural network that have major influence on the synchronization properties of the network.

Furthermore, we showed that phase reduction has important limitations when facing strong coupling and realistic connectivity structure. Although augmented phase reduction and phase-amplitude reduction techniques for single oscillators have seen strong advances in recent years [57, 67], their extension to oscillatory networks has yet to be achieved. We illustrated some peculiar characteristics of coupling-induced behavior, such as birth and death of oscillations, and highlighted how insights about the dynamics of two strongly-coupled oscillators can be used to explain network effects such as clustering into groups of various sizes and quasiperiodic dynamics on a network level. For small coupling strengths, predictions by the reduced phase model remain valid. For stronger coupling, the validity of the reduced phase model breaks down. A reasonably good proxy for a critical coupling strength beyond which the phase model loses validity, can be obtained from the dynamics of two coupled identical systems. We hypothesize that this critical coupling strength is exceeded once the coupling-induced behavior becomes more complex, that is, when identical initial conditions result in distinct oscillatory dynamics of the two oscillators.

As to connectivity effects, we have to conclude that a reduced phase model cannot account for changes in the underlying network topology. Realistic structural connectivity has devastating impact on the network dynamics in that the collective behavior drastically differs from that for homogeneous connectivity. Even the numerically reduced phase model was no longer capable of capturing the actual network dynamics and could also no longer outperform the other reduction techniques. All phase reduction techniques performed equally well. Neither the Kuramoto order parameter dynamics nor the phase diagrams were informative for the network states with realistic structural connectivity. It may hence be helpful to first identify meaningful observables that link structure and dynamics of the network. Once this has been achieved for networks of general oscillators vis-á-vis networks of phase oscillators, we may be able to answer the question whether a reduced phase model retains the same structural-dynamical properties of the full network and can thus be used to predict also exotic network effects that arise due to complex structural connectivity.

Appendix

Following the literature [43, 45], we considered Θ_E and Θ_I as bifurcation parameters and fixed the other parameters of the Wilson-Cowan neural mass model Eq. (3.1) as

$$a_E = 1, a_I = 1, c_{EE} = c_{EI} = c_{IE} = 10, c_{II} = -2. \tag{3.8}$$

The numerical phase reduction technique correctly predicts the stability of the globally synchronized state for parameters $(\Theta_E, \Theta_I) = (-3, -9.38)$, of the incoherent state for $(\Theta_E, \Theta_I) = (-3, -8.9)$, and of the balanced two-cluster state for $(\Theta_E, \Theta_I) = (-3, -8.7)$. Tables 3.3, 3.4 and 3.5 provide the numerical values of the Fourier coefficients of the numerically reduced phase interaction function $\Gamma(\psi)$, Eq. (3.3), together with those derived along the analytic phase reduction techniques.

Coupling induced behavior
We investigated the birth and death of oscillations due to the strength of coupling between oscillators. The bifurcation diagrams in Figs. 3.4 and 3.6 were created with MatCont [26] for two identical Wilson-Cowan neural masses following the dynamics

Table 3.3 Phase models derived for different approaches at $\Theta_E = -3$, $\Theta_I = -9.38$

Approach	ω	a_1	b_1	a_2	b_2
Reductive perturbation	1.800	–0.3666	0.0251	–0.0006	0.0015
Nonlinear transform	1.800	–0.3675	0.0260	–0.0006	0.0015
Direct averaging	1.800	–0.1280	0.5739	–	–
Numerical/adjoint	1.800	–0.0413	0.0339	–0.0002	–0.0001

Eq. (3.1). The coupling-induced Hopf bifurcation can be determined analytically by inspecting the eigenvalues of the Jacobian of the (high-activity) resting state (E^0, I^0). The Jacobian has the form

$$J = \begin{pmatrix} -1 + c_{EE}S_{E1} & -c_{EI}S_{E1} & \kappa S_{E1} & 0 \\ c_{IE}S_{I1} & -1 - c_{II}S_{I1} & 0 & 0 \\ \kappa S_{E1} & 0 & -1 + c_{EE}S_{E1} & -c_{EI}S_{x1} \\ 0 & 0 & c_{IE}S_{I1} & -1 - c_{II}S_{I1} \end{pmatrix}$$

where we introduced the abbreviations $S_{E1} = a_E S' \left[a_E \left(c_{EE}E^0 - c_{EI}I^0 - \Theta_x\right)\right]$ and $S_{I1} = a_I S' \left[a_I \left(c_{IE}E^0 - c_{II}I^0 - \Theta_y\right)\right]$ and (E^0, I^0) denotes the fixed point solution. The eigenvalues $\lambda_{1,2,3,4}$ of J can readily be found and the Hopf bifurcation point at $\mathrm{Re}(\lambda_{1,2}) = 0$, $\mathrm{Re}(\lambda_{3,4}) < 0$ identified. The critical coupling strength is $\kappa_H \approx 0.053$, in perfect agreement with our computations using MatCont [26].

Network simulations

The network simulations for Fig. 3.3 of $N = 30$ globally coupled, identical Wilson-Cowan neural masses have been initialized by choosing initial conditions on the uncoupled limit cycle such that the phase synchronization (real-valued Kuramoto order-parameter) was $R = 0.15$. The dynamics Eq. (3.1) have then been run with parameter values given by Eq. (3.8) and coupling strength $\kappa = 0.15$ using an Euler-Mayurama scheme over $T = 1000s$ ($T = 5000$s for panels b and c) with stepsize $dt = 0.001s$ and noise strength $\sigma = 10^{-8}$.

For the network simulations in Figs. 3.5 and 3.7, we used again $N = 30$ globally coupled identical Wilson-Cowan neural masses and set the coupling strength as indicated in the captions. We chose random initial conditions in the basin of attrac-

Table 3.4 Phase models derived for different approaches at $\Theta_E = -3$, $\Theta_I = -8.9$

Approach	ω	a_1	b_1	a_2	b_2
Reductive perturbation	1.276	–0.3666	0.0251	–0.0381	0.0868
Nonlinear transform	1.263	–0.4592	0.0908	–0.0194	0.0562
Direct averaging	1.276	–0.2283	0.4600	–	–
Numerical/adjoint	1.267	–0.4436	–0.1244	–0.0077	-0.0184

Table 3.5 Phase models derived for different approaches at $\Theta_E = -3$, $\Theta_I = -8.7$

Approach	ω	a_1	b_1	a_2	b_2
Reductive perturbation	1.078	–0.3666	0.0251	–0.0522	0.1187
Nonlinear transform	1.079	–0.4945	0.1217	–0.0191	0.0574
Direct averaging	1.078	–0.2649	0.4245	–	–
Numerical/adjoint	1.062	–0.5877	–0.2324	–0.0304	0.0135

tion of the attracting high-activity resting state, and of the attracting limit-cycles, respectively, and found the same behavior for a range of different random selections of initial conditions. We simulated Eq. (3.1) over $T = 1000s$ with a time-step $dt = 0.0005s$ using an Euler-forward scheme. Simulations using a Runge-Kutta fourth order scheme resulted in the same dynamics. We extracted the phases from each Wilson-Cowan node (E_k, I_k) using the function $\theta_k = atan2(x_k, y_k)$, where $x_k = E_k - E^0$ and $y_k = I_k - I^0$ denote the deviations from the unstable fixed point. The degree of synchronization is measured as phase coherence in terms of the real-valued Kuramoto order parameter, $|z(t)| = |\sum_k \exp(i\theta_k(t))|$. Both the phase values as well as the Kuramoto order parameter have been extracted on a coarser time scale with $dt = 0.1s$.

For the network simulations in Fig. 3.9, we simulated the dynamics Eq. (3.1) for $N = 66$ identical Wilson-Cowan neural masses with coupling strength $\kappa = 0.15$ over $T = 2000s$ with a time step of $dt = 0.0005s$ using an Euler-forward scheme, and extracted the phases and the Kuramoto order parameter as described above. We used a moving average of $20s$ to better compare the evolution of the degree of synchronization for the different networks. We also simulated the corresponding phase dynamics Eq. (3.2) of the reduced phase models on the different network structures and in the three dynamical regimes. The Fourier coefficients for the respective phase models are listed in Tables 3.3, 3.4 and 3.5. Since amplitude effects cannot occur in the phase model, we set the coupling strength to $\kappa = 0.25$, to accelerate possible synchronization transitions and to better identify transient dynamics. Moreover, we increased the network size for full and small-world network connectivity to $N = 200$ to reduce finite-size effects. The phase dynamics were simulated for $T = 10000s$ with a time step $dt = 0.001s$ using an Euler-forward scheme. We computed the Kuramoto order parameter for each time step $dt = 0.1s$ and showed the final phase distribution in a histogram plot with 31 bins.

References

1. G. Ansmann, R. Karnatak, K. Lehnertz, U. Feudel, Extreme events in excitable systems and mechanisms of their generation. Phys. Rev. E **88**, 052911 (2013)
2. G. Ansmann, K. Lehnertz, U. Feudel, Self-induced switchings between multiple space-time patterns on complex networks of excitable units. Phys. Rev. X **6**, 011030 (2016)
3. A. Arenas, A. Díaz-Guilera, J. Kurths, Y. Moreno, C. Zhou, Synchronization in complex networks. Phys. Rep. **469**(3), 93 (2008)
4. D.G. Aronson, G.B. Ermentrout, N. Kopell, Amplitude response of coupled oscillators. Phys. D **41**(3), 403 (1990)
5. P. Ashwin, S. Coombes, R. Nicks, Mathematical frameworks for oscillatory network dynamics in neuroscience. J. Math. Neurosci. **6**(1), 2 (2016)
6. M. Barahona, L.M. Pecora, Synchronization in small-world systems. Phys. Rev. Lett. **89**(5), 054101 (2002)
7. A. Barrat, M. Barthélemy, A. Vespignani, *Dynamical Processes on Complex Networks* (Cambridge University Press, Cambridge, 2008)
8. D.S. Bassett, E.T. Bullmore, Small-world brain networks revisited. Neuroscientist **23**(5), 499 (2016)

9. D.S. Bassett, O. Sporns, Network neuroscience. Nat. Neurosci. **20**(3), 353 (2017)
10. D.S. Bassett, P. Zurn, J.I. Gold, On the nature and use of models in network neuroscience. Nat. Rev. Neurosci. **19**(9), 566 (2018)
11. S. Boccaletti, V. Latora, Y. Moreno, M. Chavez, D.U. Hwang, Complex networks: structure and dynamics. Phys. Rep. **424**(4–5), 175 (2006)
12. S. Boccaletti, J. Almendral, S. Guan, I. Leyva, Z. Liu, I. Sendiña-Nadal, Z. Wang, Y. Zou, Explosive transitions in complex networks' structure and dynamics: percolation and synchronization. Phys. Rep. **660**, 1 (2016)
13. N.N. Bogoliubov, I.A. Mitropol'skii, Y.A. Mitropolsky, *Asymptotic Methods in the Theory of Non-Linear Oscillations*, vol. 10 (CRC Press, 1961)
14. R.M. Borisyuk, A.B. Kirillov, Bifurcation analysis of a neural network model. Biol. Cybern. **66**(4), 319 (1992)
15. M. Breakspear, Dynamic models of large-scale brain activity. Nat. Neurosci. **20**(3), 340 (2017)
16. E. Brown, J. Moehlis, P. Holmes, On the phase reduction and response dynamics of neural oscillator populations. Neural Comput. **16**(4), 673 (2004)
17. G. Buzsáki, *Rhythms of the Brain* (Oxford University Press, Oxford, 2006)
18. G. Buzsáki, A. Draguhn, Neuronal oscillations in cortical networks. Science **304**(5679), 1926 (2004)
19. O. Castejón, A. Guillamon, G. Huguet, Phase-amplitude response functions for transient-state stimuli. J. Math. Neurosci. **3**(1), 13 (2013)
20. P. Clusella, A. Politi, M. Rosenblum, A minimal model of self-consistent partial synchrony. New J. Phys. **18**(9), 093037 (2016)
21. A. Daffertshofer, R. Ton, B. Pietras, M.L. Kringelbach, G. Deco, Scale-freeness or partial synchronization in neural mass phase oscillator networks: pick one of two? NeuroImage (2018)
22. A. Daffertshofer, B. Pietras, Phase synchronization in neural systems, in *Encyclopedia of Complexity and Systems Science*, ed. by R.A. Meyers (Springer, Berlin Heidelberg, 2020), pp. 1–14
23. A. Daffertshofer, B. van Wijk, On the influence of amplitude on the connectivity between phases. Front. Neuroinformatics **5**, 6 (2011)
24. G. Deco, V.K. Jirsa, A.R. McIntosh, Emerging concepts for the dynamical organization of resting-state activity in the brain. Nat. Rev. Neurosci. **12**(1), 43 (2011)
25. R. Delabays, P. Jacquod, F. Dörfler, The Kuramoto model on oriented and signed graphs. SIAM J. Appl. Dyn. Syst. **18**(1), 458 (2019)
26. A. Dhooge, W. Govaerts, Y.A. Kuznetsov, H.G. Meijer, B. Sautois, New features of the software MatCont for bifurcation analysis of dynamical systems. Math. Comput. Model. Dyn. Syst. **14**(2), 147 (2008)
27. S.N. Dorogovtsev, A.V. Goltsev, J.F. Mendes, Critical phenomena in complex networks. Rev. Mod. Phys. **80**(4), 1275 (2008)
28. B. Ermentrout, *Simulating, Analyzing, and Animating Dynamical Systems: A Guide to XPPAUT for Researchers and Students* (SIAM, 2002)
29. G.B. Ermentrout, N. Kopell, Frequency plateaus in a chain of weakly coupled oscillators, I. SIAM J. Math. Anal. **15**(2), 215 (1984)
30. G. Ermentrout, N. Kopell, Oscillator death in systems of coupled neural oscillators. SIAM J. Appl. Math. **50**(1), 125 (1990)
31. G.B. Ermentrout, N. Kopell, Multiple pulse interactions and averaging in systems of coupled neural oscillators. J. Math. Biol. **29**(3), 195 (1991)
32. G.B. Ermentrout, D.H. Terman, *Mathematical Foundations of Neuroscience*, vol. 35 (Springer, New York, 2010)
33. H. Finger, R. Gast, C. Gerloff, A.K. Engel, P. König, Probing neural networks for dynamic switches of communication pathways. PLoS Comput. Biol. **15**(12), 1 (2019)
34. L.V. Gambuzza, A. Cardillo, A. Fiasconaro, L. Fortuna, J. Gómez-Gardeñes, M. Frasca, Analysis of remote synchronization in complex networks. Chaos **23**(4), 043103 (2013)
35. S. Gherardini, S. Gupta, S. Ruffo, Spontaneous synchronisation and nonequilibrium statistical mechanics of coupled phase oscillators. Contemp. Phys. **59**(3), 229 (2018)

36. A. Ghosh, Y. Rho, A.R. McIntosh, R. Kötter, V.K. Jirsa, Noise during rest enables the exploration of the brain's dynamic repertoire. PLoS Comput. Biol. **4**(10), e1000196 (2008)
37. C.M. Gray, Synchronous oscillations in neuronal systems: mechanisms and functions. J. Comput. Neurosci. **1**(1–2), 11 (1994)
38. S. Grossberg, Nonlinear neural networks: principles, mechanisms, and architectures. Neural Netw. **1**(1), 17 (1988)
39. P. Hagmann, L. Cammoun, X. Gigandet, R. Meuli, C.J. Honey, V.J. Wedeen, O. Sporns, Mapping the structural core of human cerebral cortex. PLoS Biol. **6**(7), e159 (2008)
40. H. Haken, *Advanced Synergetics: Instability Hierarchies of Self-organizing Systems and Devices*. Springer Series in Synergetics (Springer, Berlin, 1983)
41. H. Haken, *Synergetics: Introduction and Advanced Topics* (Springer Science & Business Media, 2013)
42. H. Haken, *Synergetics: Introduction and Advanced Topics* (Springer, Berlin, 2004)
43. J. Hlinka, S. Coombes, Using computational models to relate structural and functional brain connectivity. Eur. J. Neurosci. **36**(2), 2137 (2012)
44. C.J. Honey, R. Kötter, M. Breakspear, O. Sporns, Network structure of cerebral cortex shapes functional connectivity on multiple time scales. Proc. Natl. Acad. Sci. **104**(24), 10240 (2007)
45. F.C. Hoppensteadt, E.M. Izhikevich, *Weakly Connected Neural Networks* (Springer, New York, 1997)
46. E.M. Izhikevich, *Dynamical Systems in Neuroscience* (MIT press, 2007)
47. V.K. Jirsa, Neural field dynamics with local and global connectivity and time delay. Philos. Trans. R. Soc. Lond. A: Math., Phys. Eng. Sci. **367**(1891), 1131 (2009)
48. A.N. Khambhati, A.E. Sizemore, R.F. Betzel, D.S. Bassett, Modeling and interpreting mesoscale network dynamics. NeuroImage **180**, 337 (2018)
49. H. Kori, Y. Kuramoto, S. Jain, I.Z. Kiss, J.L. Hudson, Clustering in globally coupled oscillators near a Hopf bifurcation: theory and experiments. Phys. Rev. E **89**(6), 062906 (2014)
50. A. Koseska, E. Volkov, J. Kurths, Oscillation quenching mechanisms: amplitude versus oscillation death. Phys. Rep. **531**(4), 173 (2013)
51. Y. Kuramoto, *Chemical Oscillations, Turbulence and Waves* (Springer, Berlin, 1984)
52. W. Kurebayashi, S. Shirasaka, H. Nakao, Phase reduction method for strongly perturbed limit cycle oscillators. Phys. Rev. Lett. **111**(21), 214101 (2013)
53. Y.A. Kuznetsov, *Elements of applied bifurcation theory* (Springer, New York, 1998)
54. C.W. Lynn, D.S. Bassett, The physics of brain network structure, function and control. Nat. Rev. Phys. **1**(5), 318 (2019)
55. W.A. MacKay, Synchronized neuronal oscillations and their role in motor processes. Trends Cogn. Sci. **1**(5), 176 (1997)
56. I. Malkin, *Methods of Poincaré and Liapunov in Theory of Non-Linear Oscillations* (Gostexizdat, Moscow, 1949)
57. B. Monga, D. Wilson, T. Matchen, J. Moehlis, Phase reduction and phase-based optimal control for biological systems: a tutorial. Biol. Cybern. (2018)
58. J.Y. Moon, J. Kim, T.W. Ko, M. Kim, Y. Iturria-Medina, J.H. Choi, J. Lee, G.A. Mashour, U. Lee, Structure shapes dynamics and directionality in diverse brain networks: mathematical principles and empirical confirmation in three species. Sci. Rep. **7**, 46606 EP (2017)
59. J. Murdock, *Normal Forms and Unfoldings for Local Dynamical Systems* (Springer Science & Business Media, 2006)
60. H. Nakao, Phase reduction approach to synchronisation of nonlinear oscillators. Contemp. Phys. **57**(2), 188 (2016)
61. M. Newman, *Networks* (Oxford University Press, Oxford, 2018)
62. M. Newman, A.L. Barabási, D.J. Watts, *The Structure and Dynamics of Networks*, vol. 19 (Princeton University Press, Princeton, 2011)
63. V. Nicosia, M. Valencia, M. Chavez, A. Díaz-Guilera, V. Latora, Remote synchronization reveals network symmetries and functional modules. Phys. Rev. Lett. **110**(17), 174102 (2013)
64. J.M. Palva, S. Palva, K. Kaila, Phase synchrony among neuronal oscillations in the human cortex. J. Neurosci. **25**(15), 3962 (2005)

65. S. Petkoski, V.K. Jirsa, Transmission time delays organize the brain network synchronization. Philos. Trans. R. Soc. A **377**(2153), 20180132 (2019)
66. S. Petkoski, J.M. Palva, V.K. Jirsa, Phase-lags in large scale brain synchronization: methodological considerations and in-silico analysis. PLoS Comput. Biol. **14**(7), e1006160 (2018)
67. B. Pietras, A. Daffertshofer, Network dynamics of coupled oscillators and phase reduction techniques. Phys. Rep. **819**, 1 (2019)
68. M.A. Porter, J.P. Gleeson, Dynamical systems on networks. Front. Appl. Dyn. Syst.: Rev. Tutor. **4**, (2016)
69. J.G. Restrepo, E. Ott, B.R. Hunt, Synchronization in large directed networks of coupled phase oscillators. Chaos **16**(1), 015107 (2006). https://doi.org/10.1063/1.2148388
70. F.A. Rodrigues, T.K.D. Peron, P. Ji, J. Kurths, The Kuramoto model in complex networks. Phys. Rep. **610**, 1 (2016)
71. A. Rothkegel, K. Lehnertz, Recurrent events of synchrony in complex networks of pulse-coupled oscillators. Europhys. Lett. **95**(3), 38001 (2011)
72. A. Rothkegel, K. Lehnertz, Irregular macroscopic dynamics due to chimera states in small-world networks of pulse-coupled oscillators. New J. Phys. **16**(5), 055006 (2014)
73. P. Sanz-Leon, S.A. Knock, A. Spiegler, V.K. Jirsa, Mathematical framework for large-scale brain network modeling in the virtual brain. NeuroImage **111**, 385 (2015)
74. P. Sauseng, W. Klimesch, What does phase information of oscillatory brain activity tell us about cognitive processes? Neurosci. Biobehav. Rev. **32**(5), 1001 (2008)
75. B. Schack, S. Weiss, Quantification of phase synchronization phenomena and their importance for verbal memory processes. Biol. Cybern. **92**(4), 275 (2005)
76. H. Schuster, P. Wagner, A model for neuronal oscillations in the visual cortex. Biol. Cybern. **64**(1), 77 (1990)
77. M.A. Schwemmer, T.J. Lewis, The Theory of Weakly Coupled Oscillators, in *Phase Response Curves in Neuroscience: Theory, Experiment, and Analysis*, ed. by N.W. Schultheiss, A.A. Prinz, R.J. Butera (Springer Science & Business Media, New York, NY, 2012), pp. 3–31
78. S. Shirasaka, W. Kurebayashi, H. Nakao, Phase-amplitude reduction of transient dynamics far from attractors for limit-cycling systems. Chaos **27**(2), 023119 (2017)
79. S. Smale, *A Mathematical Model of Two Cells Via Turing's Equation, in The Hopf Bifurcation and Its Applications* (Springer, New York, 1976), pp. 354–367
80. M. Steriade, Cellular substrates of brain rhythms, in *Electroencephalography Basic Principles, Clinical Applications, and Related Fields*, ed. by E. Niedermeyer, F. Lopes Da Silva (Lippincott Williams & Wilkins, Philadelphia, 2005), pp. 31–84
81. S.H. Strogatz, Exploring complex networks. Nature **410**(6825), 268 (2001)
82. G. Thut, C. Miniussi, J. Gross, The functional importance of rhythmic activity in the brain. Curr. Biol. **22**(16), R658 (2012)
83. R. Ton, G. Deco, A. Daffertshofer, Structure-function discrepancy: inhomogeneity and delays in synchronized neural networks. PLoS Comput. Biol. **10**(7), e1003736 (2014)
84. F. Varela, J.P. Lachaux, E. Rodriguez, J. Martinerie, The brainweb: phase synchronization and large-scale integration. Nat. Rev. Neurosci. **2**(4), 229 (2001)
85. X.F. Wang, G. Chen, Synchronization in small-world dynamical networks. Int. J. Bifurc. Chaos **12**(01), 187 (2002)
86. D.J. Watts, S.H. Strogatz, Collective dynamics of 'small-world' networks. Nature **393**(6684), 440 (1998)
87. K.C. Wedgwood, K.K. Lin, R. Thul, S. Coombes, Phase-amplitude descriptions of neural oscillator models. J. Math. Neurosci. **3**(1), 2 (2013)
88. H.R. Wilson, J.D. Cowan, Excitatory and inhibitory interactions in localized populations of model neurons. Biophys. J. **12**(1), 1 (1972)
89. D. Wilson, B. Ermentrout, Greater accuracy and broadened applicability of phase reduction using isostable coordinates. J. Math. Biol. (2017)

Chapter 4
Nonautonomous Attractors

Peter E. Kloeden and Meihua Yang

Abstract The nature of time in a nonautonomous dynamical system is very different from that in autonomous systems, which depend on the time that has elapsed since starting rather on the actual time. This requires new concepts of invariant sets and attractors. Pullback and forward attractors as well as forward omega-limit sets will be reviewed here in the simpler setting of nonautonomous difference equations. Both two-parameter semi-group and skew product flow formulations of nonautonomous dynamical systems are considered.

Keywords Nonautonomous difference equations · Process · Two-parameter semi-group · Skew product flows · Pullback attractor · Forward attractor · Omega limit points

4.1 Introduction

Autonomous dynamical systems are now a very well established area of mathematics. Although nonautonomous systems have been investigated in an ad hoc way for many years, a mathematical theory of nonautonomous dynamical systems has only been developed systematically in recent decades. Time has a very different role in nonautonomous dynamical systems than in autonomous systems, which depend only on the time that has elapsed since starting rather on the actual time. This has some profound consequences in terms of definitions and the interpretation of dynamical

Dedicated to Aneta Stefanovska on her 60th birthday.

P. E. Kloeden (✉)
Mathematische Institut, Universität Tübingen, 72076 Tübingen, Germany
e-mail: kloeden@na.uni-tuebingen.de

M. Yang
School of Mathematics and Statistics, Huanzhong University of Science and Technology, Wuhan, China
e-mail: yangmeih@hust.edu.cn

A. Stefanovska and P. V. E. McClintock (eds.), *Physics of Biological Oscillators*, Understanding Complex Systems,
https://doi.org/10.1007/978-3-030-59805-1_4

behaviour, so many of the concepts that have been developed and extensively investigated for autonomous dynamical systems are either too restrictive or no longer valid or meaningful in the nonautonomous context [2, 4, 17].

A new feature of nonautonomous dynamical systems is that invariant sets are in fact families of sets that are invariant in the sense that they mapped onto each other as time evolves. Another important new feature is that limiting temporal behaviour must now be characterised in two ways. For a discrete time autonomous dynamical system, the elapsed time $n - n_0 \to \infty$ if either $n \to \infty$ with n_0 fixed or if $n_0 \to -\infty$ with n fixed. In the nonautonomous case the limits obtained may be different, if they exist.

The former, called forward convergence, involves information about the future of the system, whereas the latter, called pullback convergence, uses information from the past. Two types of nonautonomous attractors arise from these convergences, a forward and a pullback attractor. These consist of families of nonempty compact subsets that are invariant in the above generalised sense and attract other sets (or even families of sets) with respect to the corresponding convergence.

The results given below have appeared in published papers over the past twenty years. They are developed systematically in monographs Kloeden and Rasmussen [15] and Kloeden and Yang [17] as well as [19] which focuses on nonautonomous difference equations. See also the monographs [2, 4].

Nonautonomous dynamical systems have many applications, especially in the biological sciences [14]. Aneta Stefanovska has been a pioneer in their use in cardiology and physics, see [1, 5, 22, 23, 28, 29].

4.2 Nonautonomous Difference Equations

A nonautonomous difference equation on $\mathbb{R}^d$ has the form

$$x_{n+1} = f_n(x_n) \tag{4.1}$$

with mappings $f_n : \mathbb{R}^d \to \mathbb{R}^d$ which may vary with time n. They are assumed to be continuous here. Define

$$\mathbb{Z}^2_{\geq} := \{(n, n_0) \in \mathbb{Z}^2 \ : \ n \geq n_0\},$$

The nonautonomous difference equation (4.1) generates a solution mapping

$$\phi : \mathbb{Z}^2_{\geq} \times \mathbb{R}^d \to \mathbb{R}^d$$

through iteration, i.e.,

$$\phi(n, n_0, x_0) := f_{n-1} \circ \cdots \circ f_{n_0}(x_0)$$

for all $n > n_0$ with $n_0 \in \mathbb{Z}$, and each $x_0 \in \mathbb{R}^d$ with the initial value $\phi(n_0, n_0, x_0) := x_0$.

These solution mappings of nonautonomous difference equations (4.1) generate an abstract discrete time nonautonomous dynamical system formulated as a 2-parameter semigroup or process [7, 8] on the state state space $\mathbb{R}^d$ and time set $\mathbb{Z}$.

Definition 4.1 A *(discrete time) process* on the state space $\mathbb{R}^d$ is a mapping $\phi : \mathbb{Z}^2_{\geq} \times \mathbb{R}^d \to \mathbb{R}^d$ which satisfies the following initial value, 2-parameter evolution and continuity properties:

(i) $\phi(n_0, n_0, x_0) = x_0$ for all $n_0 \in \mathbb{Z}$ and $x_0 \in \mathbb{R}^d$,
(ii) $\phi(n_2, n_0, x_0) = \phi(n_2, n_1, \phi(n_1, n_0, x_0))$ for all $n_0 \leq n_1 \leq n_2$ in $\mathbb{Z}$ and $x_0 \in \mathbb{R}^d$,
(iii) the mapping $x_0 \mapsto \phi(n, n_0, x_0)$ of $\mathbb{R}^d$ into itself is continuous for all $(n, n_0) \in \mathbb{Z}^2_{\geq}$.

Entire solutions, which are defined for all $n \in \mathbb{Z}$, play an important role in dynamical systems. An entire solution solution χ^* of a process satisfies

$$\phi(n, n_0, \chi^*_{n_0}) = \chi^*_n \quad \text{for all } (n, n_0) \in \mathbb{Z}^2_{\geq}.$$

The obvious idea of convergence of other solutions to an entire solution χ^* reads

$$\left\| \phi(n, n_0, x_0) - \chi^*_n \right\| \to 0 \quad \text{as } n \to \infty \quad (n_0 \text{ fixed}). \tag{4.2}$$

It involves a moving target and is called *forward convergence* (Fig. 4.1).

To obtain convergence to the point χ^*_n for a particular time n one has to start progressively earlier, i.e.,

$$\left\| \phi(n, n_0, x_0) - \chi^*_n \right) \| \to 0 \quad \text{as } n_0 \to -\infty \quad (n \text{ fixed}). \tag{4.3}$$

It is called *pullback convergence*.

Note that pullback convergence does not involve the system running backwards in time, rather it runs forwards from an ever earlier starting time. Pullback convergence has long been used under other names, e.g., to construct entire solutions [20], probability measures, e.g., [6], or by Kolmogorov under the name absolute probability (Fig. 4.2).

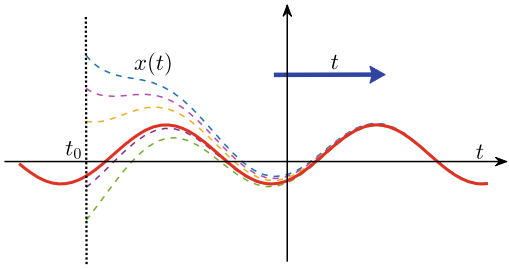

Fig. 4.1 Forward convergence as $t \to \infty$

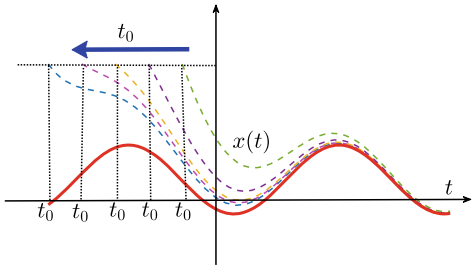

Fig. 4.2 Pullback attraction as $t_0 \to -\infty$

Forward and pullback convergence coincide in an autonomous system, but are independent of each other in a nonautonomous one. Consequently, two types of nonautonomous attractors arise from these convergences, a forward attractor and a pullback attractor.

4.3 Invariant Sets and Attractors of Processes

The nonautonomous case differs crucially from the autonomous one and requires the introduction of new concepts The following definitions and results are taken from the monographs [15, 17], see also the papers [3, 19, 24, 25].

Definition 4.2 A family $\mathscr{A} = \{A_n : n \in \mathbb{Z}\}$ of nonempty subsets of $\mathbb{R}^d$ is ϕ-*invariant* if

$$\phi\left(n, n_0, A_{n_0}\right) = A_n, \quad \text{for all } (n, n_0) \in \mathbb{Z}^2_{\geq},$$

or, equivalently, if $f_n(A_n) = A_{n+1}$ for all $n \in \mathbb{Z}$. It is said to be uniformly bounded if there exists a bounded subset B of $\mathbb{R}^d$ such that $A_n \subset B$ for all $n \in \mathbb{Z}$.

A uniformly bounded ϕ-invariant family is characterised by the bounded entire solutions.

Proposition 4.1 *A uniformly bounded family $\mathscr{A} = \{A_n : n \in \mathbb{Z}\}$ is ϕ-invariant if and only if for every pair $n_0 \in \mathbb{Z}$ and $x_0 \in A_{n_0}$ there exists a bounded entire solution χ such that $\chi_{n_0} = x_0$ and $\chi_n \in A_n$ for all $n \in \mathbb{Z}$.*

Forward and pullback convergences can be used to define *two distinct types* of nonautonomous attractors for a process ϕ. Define

$$\operatorname{dist}_{\mathbb{R}^d}(x, B) := \inf_{b \in B} \|x - b\|, \qquad \operatorname{dist}_{\mathbb{R}^d}(A, B) := \sup_{a \in A} \operatorname{dist}_{\mathbb{R}^d}(a, B)$$

for nonempty subsets A, B of $\mathbb{R}^d$.

Definition 4.3 A ϕ-invariant family $\mathscr{A} = \{A_n : n \in \mathbb{Z}\}$ of nonempty compact subsets of $\mathbb{R}^d$ is called a *forward attractor* if it forward attracts bounded subsets D of $\mathbb{R}^d$, i.e.,

$$\operatorname{dist}_{\mathbb{R}^d}\left(\phi\left(n, n_0, D\right),\ A_n\right) \to 0 \quad \text{as } n \to \infty \quad (n_0 \text{ fixed}) \tag{4.4}$$

and a *pullback attractor* if it pullback attracts bounded subsets D of $\mathbb{R}^d$, i.e.,

$$\operatorname{dist}_{\mathbb{R}^d}\left(\phi\left(n, n_0, D\right),\ A_n\right) \to 0 \quad \text{as } n_0 \to -\infty \quad (n \text{ fixed}). \tag{4.5}$$

Random attractors [6] of random dynamical systems and *snapshot attractors* in physics [26] are essentially pullback attractors.

The existence of a pullback attractor follows from that of a pullback absorbing family.

Definition 4.4 A family $\mathscr{B} = \{B_n : n \in \mathbb{Z}\}$ of nonempty compact subsets of $\mathbb{R}^d$ is called *pullback absorbing* if for every bounded subset D of $\mathbb{R}^d$ and $n \in \mathbb{Z}$ there exists an $N(n, D) \in \mathbb{N}$ such that

$$\phi\left(n, n_0, D\right) \subseteq B_n \quad \text{for all } n_0 \leq n - N(n, D).$$

It is said to be ϕ-*positively invariant* if $\phi\left(n, n_0, B_{n_0}\right) \subseteq B_n$ for all $(n, n_0) \in \mathbb{Z}^2_{\geq}$.

The following theorem generalises of a well-known theorem on the existence of an autonomous global attractor. The assumption about a ϕ-positively invariant pullback absorbing family is not a serious restriction, since one can always be constructed given a general pullback absorbing family [19].

Theorem 4.1 *Suppose that a process ϕ has a ϕ-positively invariant pullback absorbing family $\mathscr{B} = \{B_n : n \in \mathbb{Z}\}$.*

Then there exists a global pullback attractor $\mathscr{A} = \{A_n : n \in \mathbb{Z}\}$ with component sets determined by

$$A_n = \bigcap_{j \geq 0} \phi\left(n, n - j, B_{n-j}\right) \quad \textit{for all } n \in \mathbb{Z}. \tag{4.6}$$

Moreover, if $\mathscr{A}$ is uniformly bounded, then it is unique.

4.4 Construction of Forward Attractors

The situation is somewhat more complicated for forward attractors than for pullback attractors due to some peculiarities of forward attractors [25], e.g., they need not be unique.

Example 4.1 For each $r \geq 0$ the process generated by

$$x_{n+1} = f_n(x_n) := \begin{cases} x_n, & n \leq 0, \\ \frac{1}{2}\, x_n, & n > 0 \end{cases} \tag{4.7}$$

has a forward attractor $\mathscr{A}^{(r)}$ with component subsets

$$A_n^{(r)} = \begin{cases} r\,[-1,1], & n \le 0, \\ \frac{1}{2^n}\,r\,[-1,1], & n > 0. \end{cases} \tag{4.8}$$

These forward attractors are not pullback attractors.

For a long time there was no counterpart of Theorem 4.1 for nonautonomous forward attractors. In fact, such construction (4.6) was shown by Kloeden and Lorenz [12, 13] to hold within any positively invariant family, but provides only a candidate for a forward attractor; other conditions must also hold. A key observation for the construction of a forward attractor is provided by the next theorem [13]. It is based on the following important property of forward attractors [13], which requires the following definition of a forward absorbing family. See also [12].

Definition 4.5 A family $\mathscr{B} = \{B_n : n \in \mathbb{Z}\}$ of nonempty compact subsets of $\mathbb{R}^d$ is called *forward absorbing* if for every bounded subset D of $\mathbb{R}^d$ and $n \in \mathbb{Z}$ there exists an $N(n, D) \in \mathbb{N}$ such that

$$\phi\,(n, n_0, D) \subseteq B_n \quad \text{for all } n \ge n_0 + N(n, D).$$

Proposition 4.2 *A uniformly bounded forward attractor $\mathscr{A} = \{A_n : n \in \mathbb{Z}\}$ in $\mathbb{R}^d$ has a ϕ-positively invariant family $\mathscr{B} = \{B_n : n \in \mathbb{Z}\}$ of nonempty compact subsets with $A_n \subset B_n$ for $n \in \mathbb{Z}$, which is forward absorbing.*

Theorem 4.2 *Suppose that a process ϕ on $\mathbb{R}^d$ has a ϕ-positively invariant family $\mathscr{B} = \{B_n : n \in \mathbb{Z}\}$ of nonempty compact subsets of $\mathbb{R}^d$.*

Then ϕ has a maximal ϕ-invariant family $\mathscr{A} = \{A_n : n \in \mathbb{Z}\}$ in $\mathscr{B}$ of nonempty compact subsets determined by

$$A_n = \bigcap_{n_0 \le n} \phi\left(n, n_0, B_{n_0}\right) \quad \textit{for each} \quad n \in \mathbb{Z}. \tag{4.9}$$

In view of Proposition 4.2, the components sets of any *forward attractor can be constructed in this way. Note that nothing is assumed here about the dynamics* outside *of the family $\mathscr{B}$.*

4.4.1 A Counterexample

Consider the piecewise autonomous equation

$$x_{n+1} = \frac{\lambda_n\, x_n}{1 + |x_n|}, \qquad \lambda_n := \begin{cases} \lambda, & n \ge 0, \\ \lambda^{-1}, & n < 0 \end{cases} \tag{4.10}$$

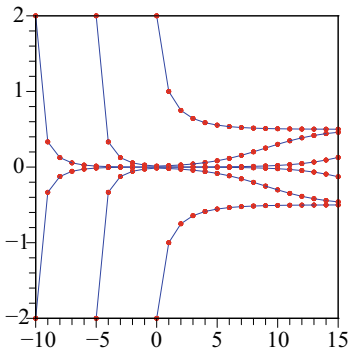

Fig. 4.3 Trajectories of the piecewise autonomous equation (4.10) with $\lambda = 1.5$

for some $\lambda > 1$, which corresponds to a switch between the two autonomous problems at $n = 0$. Its pullback attractor $\mathscr{A}$ of the resulting nonautonomous system has component sets $A_n \equiv \{0\}$ for all $n \in \mathbb{Z}$ corresponding to the zero entire solution (Fig. 4.3).

The pullback attractor is not a forward attractor in this example. In fact, this example does not even have a bounded forward attractor. This is not surprising since pullback attraction depends on the past behaviour of the system and not on its behaviour in the distant future. See [18].

4.4.2 A Condition Ensuring Forward Convergence

The above counterexample shows that a ϕ-invariant family $\mathscr{A} = \{A_n, n \in \mathbb{Z}\}$ constructed in Theorem 4.2 need *not* be a forward attractor, even when the ϕ-positively invariant family $\mathscr{B} = \{B_n, n \in \mathbb{Z}\}$ is a forward absorbing family. Another important observation is that there should be no ω-limit points from inside the family $\mathscr{B}$ that are not ω-limit points from inside the family $\mathscr{A}$.

For each $n_0 \in \mathbb{Z}$, the forward ω-limit set with respect to $\mathscr{B}$ is defined by

$$\omega_{\mathscr{B}}(n_0) := \bigcap_{m \geq n_0} \overline{\bigcup_{n \geq m} \phi(n, n_0, B_{n_0})}.$$

Suppose that the B_n are uniformly bounded in a compact set B, i.e., $B_n \subset B$. Then $\omega_{\mathscr{B}}(n_0)$ is nonempty and compact as the intersection of nonempty nested compact subsets and

$$\lim_{n \to \infty} \operatorname{dist}_{\mathbb{R}^d} \left(\phi(n, n_0, B_{n_0}),\ \omega_{\mathscr{B}}(n_0) \right) = 0 \quad (\text{fixed } n_0).$$

Since $A_{n_0} \subset B_{n_0}$ and $A_n = \phi(n, n_0, A_{n_0}) \subset \phi(n, n_0, B_{n_0})$

$$\lim_{n\to\infty} \operatorname{dist}_{\mathbb{R}^d}\left(A_n,\ \omega_{\mathscr{B}}(n_0)\right) = 0 \quad \text{(fixed } n_0\text{)}. \tag{4.11}$$

Moreover, $\omega_{\mathscr{B}}(n_0) \subset \omega_{\mathscr{B}}(n_0') \subset B$ for $n_0 \le n_0'$. Hence the set

$$\omega_{\mathscr{B}}^{\infty} := \overline{\bigcup_{n_0\in\mathbb{Z}} \omega_{\mathscr{B}}(n_0)}$$

is a nonempty and compact subset of B. From (4.11) it is clear that

$$\lim_{n\to\infty} \operatorname{dist}_{\mathbb{R}^d}\left(A_n,\ \omega_{\mathscr{B}}^{\infty}\right) = 0. \tag{4.12}$$

The ω-limit points for dynamics starting inside the family of sets $\mathscr{A}$ are defined by

$$\omega_{\mathscr{A}}^{\infty} := \bigcap_{n_0\in\mathbb{Z}} \overline{\bigcup_{n\ge n_0} A_n} = \bigcap_{n_0\in\mathbb{Z}} \overline{\bigcup_{n\ge n_0} \phi(n, n_0, A_{n_0})} \subset B,$$

which is nonempty and compact as a family of nested compact sets. Obviously, $\omega_{\mathscr{A}}^{\infty} \subset \omega_{\mathscr{B}}^{\infty} \subset B$. The example below shows that the inclusions may be strict.

The following result was proved in [13].

Theorem 4.3 *$\mathscr{A}$ is forward attracting from within $\mathscr{B}$ if and only if $\omega_{\mathscr{A}}^{\infty} = \omega_{\mathscr{B}}^{\infty}$. If $\mathscr{B}$ is forward absorbing, then $\mathscr{A}$ will then be a forward attractor.*

4.5 Forward Attracting Sets

Forward attraction (4.4) is very different conceptually from pullback attraction (4.5) in that it is about what happens in the distant future and not in actual time, i.e., current time. Pullback convergence, is in this sense the natural generalisation of convergence in autonomous systems, which depends only on the elapsed time since starting, so its limit sets exist, in fact, in actual time. Moreover, as seen in system (4.7) above, forward attractors need not be unique.

A curious feature of forward attractors in the sense of Definition 4.3 is that they require the entire past history of the system to be known. Indeed, its construction in Theorem 4.2 is based on pullback convergence, although forward convergence is about the distant future and should be independent of the past. In fact, forward convergence should not even require the system to be defined in the past.

The future limiting dynamics in (4.10) is contained in the omega limit set $\omega_{\mathscr{B}}^{\infty}$. It includes what Haraux [9] and Vishik [30] called a *uniform attractor*, i.e., a compact set which attracts the forward dynamics of the system uniformly in the initial time and is minimal in the sense that it is contained in all sets with this property.

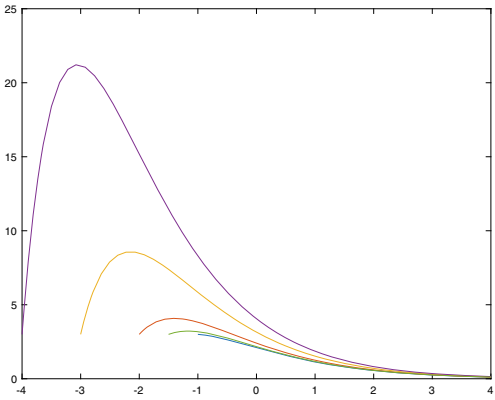

Fig. 4.4 Solutions of $x_{n+1} = \frac{1}{2}x_n + e^{-n}$ with different initial conditions. The set $\{0\}$ is not invariant but looks more and more more invariant for later starting times n_0, i.e., asymptotically invariant

However the definition of $\omega^{\infty}_{\mathscr{B}}$ does not require the system to be defined in the distant past or for the attraction to be uniform in the initial time. Moreover, nothing is said about invariance in this definition. For this reason (4.10), $\omega^{\infty}_{\mathscr{B}}$ will be called the *forward attracting set.*

In the piecewise autonomous system, (4.10), $\omega^{\infty}_{\mathscr{B}} = [1-\lambda, \lambda - 1]$ is positively invariant for all time, but only invariant for negative time. The situation can be more complicated (Fig. 4.4).

4.5.1 Asymptotic Invariance

Asymptotic invariance means that a set becomes more and more invariant the later one starts, [10, 11, 16, 21].

Definition 4.6 A set A is said to be *asymptotically positively invariant* if for any monotonic decreasing sequence $\varepsilon_p \to 0$ as $p \to \infty$ there exists a monotonic increasing sequence $N_p \to \infty$ as $p \to \infty$ such that

$$\phi(n, n_0, A) \subset B_{\varepsilon_p}(A), \quad n \geq n_0,$$

for each $n_0 \geq N_p$, where

$$B_{\varepsilon_p}(A) := \{x \in \mathbb{R}^d \ : \ \mathrm{dist}_{\mathbb{R}^d}(x, A) < \varepsilon\}.$$

Definition 4.7 A set A is said to be *asymptotically negatively invariant* if for every $a \in A$, $\varepsilon > 0$ and $N > 0$, there exist n_ε and $a_\varepsilon \in A$ such that

$$\|\varphi(n_\varepsilon, n_\varepsilon - N, a_\varepsilon) - a\| < \varepsilon.$$

Some additional assumptions about the future behaviour of the system are needed to ensure asymptotical positive or negative invariance.

Assumption 4.1 There exists a ϕ-positive invariant compact subset B in $\mathbb{R}^d$ such that for any bounded subset D of $\mathbb{R}^d$ and every $n_0 \geq N^*$ there exists a $N_D \geq 0$ for which

$$\phi(n, n_0, x_0) \in B \quad \forall n \geq n_0 + N_D, x_0 \in D.$$

Assumption 4.2 The process is Lipschitz continuous in initial conditions in B on finite time integer intervals $[n_0, n_0 + N]$ uniformly in $n_0 \geq N^*$, i.e., there exists a constant $L_B > 0$ independent of $n_0 \geq N^*$ such that

$$\|\varphi(n, \tau, x_0) - \varphi(n, \tau, y_0)\| \leq \|x_0 - y_0\| \, e^{L_B(n-\tau)} \leq \|x_0 - y_0\| \, e^{L_B N}$$

for all $x_0, y_0 \in B$ and $N^* \leq \tau < n \leq \tau + N$.

Theorem 4.4 *Let Assumption 4.1 hold, then $\omega_{\mathscr{B}}^{\infty}$ is asymptotically positively invariant. If, in addition, Assumptions 4.2 holds, then ω_B^{∞} is also asymptotically negatively invariant.*

Assumption 4.2 holds for a nonautonomous difference equation if the functions the $f_n : \mathbb{R}^d \to \mathbb{R}^d$ are Lipschitz continuous on B uniformly in $n \geq N^*$, i.e., only in the distant future.

4.6 Skew Product Flows

The formulation of a skew product flow is more complicated than that of a process, but it includes more information about how the system changes in time [11]. It consists of an *autonomous dynamical system* θ (full group) on a base space P, which is the source of the nonautonomity in a *cocycle mapping* φ acting on the state space $\mathbb{R}^d$. The autonomous dynamical system here is often called the *driving system*.

Definition 4.8 A discrete time *skew product flow* (θ, φ) on $P \times \mathbb{R}^d$ consists of a discrete time autonomous dynamical system $\theta = \{\theta_n\}_{n \in \mathbb{Z}}$ acting on a metric space (P, d_P), which is called the *base space*, i.e.,

$$(i) \ \theta_0(p) = p, \qquad (ii) \ \theta_{n+m}(p) = \theta_n \circ \theta_m(p), \qquad (iii) \ (n, p) \mapsto \theta_n(p) \ \text{ continuous}$$

for all $p \in P$ and $s, t \in \mathbb{Z}$, and a *cocycle mapping* $\varphi : \mathbb{Z}^+ \times P \times \mathbb{R}^d \to \mathbb{R}^d$ acting on a metric space $(\mathbb{R}^d, d_{\mathbb{R}}^d)$, which is called the *state space*, i.e.,

(1) *initial condition*: $\varphi(0, p, x) = x$ for all $p \in P$ and $x \in \mathbb{R}^d$,
(2) *cocycle property*: $\varphi(n + m, p, x) = \varphi(s, \theta_m(p), \varphi(m, p, x))$ for all $n, m \in \mathbb{Z}^+$, $p \in P$ and $x \in \mathbb{R}^d$,
(3) *continuity*: $(p, x) \mapsto \varphi(n, p, x)$ is continuous for each $n \in \mathbb{Z}^+$.

The cocycle property is a generalisation of both the semi-group property and the 2-parameter semi-group property.

Remark 4.1 Note that we have used ϕ to denote a process and φ to denote the cocycle mapping of a skew product flow. A process ϕ can be written as a skew product flow with the driving system given by the left shift operator $\theta(n_0) = n_0 + 1$ on the base space $P = \mathbb{Z}$ and the cocycle mapping defined by $\varphi(n, n_0, x_0) = \phi(n + n_0, n_0, x_0)$.

Remark 4.2 The base system θ serves as a driving system which makes the cocycle mapping nonautonomous. It is like a clock which keeps track of time.

Skew product flows often have very nice properties when the base space P is compact. This occurs when the driving system is, for example, periodic or almost periodic. It provides more detailed information about the dynamical behaviour of the system. George Sell, a pioneering researcher in the area, e.g., see [27], described the effect of a compact base space as being equivalent to *compactifying time*.

4.6.1 An Example

Consider a nonautonomous difference equation on $\mathbb{R}^d = \mathbb{R}$ given by

$$x_{n+1} = f_{j_n}(x_n), \qquad n \in \mathbb{Z},$$

where the functions $f_1, \ldots, f_N$ are continuous and the j_n are the components of a bi-infinite sequence $\mathbf{s} = (\ldots, j_{-1}, j_0, j_1, j_2, \ldots)$. Let $P = \{1, \ldots, N\}^{\mathbb{Z}}$ be the totality of all such bi-infinite sequences. Then

$$d_P(\mathbf{s}, \mathbf{s}') := \sum_{n=-\infty}^{\infty} 2^{-|n|} \left| j_n - j_n' \right|$$

defines a metric on P and(P, d_P) is a compact metric space.

Let θ be the *left shift operator* on P, i.e., $(\theta \mathbf{s})_n = j_{n+1}$ for $n \in \mathbb{Z}$. Define $\theta_n = \theta^n$, the n-fold composition of θ when $n > 0$ and of its inverse θ^{-1} when $n < 0$. Then $\{\theta_n\}_{n \in \mathbb{Z}}$ is a group under composition on P and the $\theta_n : P \to P$ are continuous in (P, d_P).

Moreover, the mapping $\varphi : \mathbb{Z}^+ \times P \times \mathbb{R}^d \to P$ defined by

$$\varphi(n, \mathbf{s}, x_0) = f_{j_{n-1}} \circ \cdots \circ f_{j_0}(x_0)$$

for $n \geq 1$ is a discrete-time cocycle mapping. It is clear that the mapping $x_0 \mapsto \varphi(n, \mathbf{s}, x_0)$ is continuous due to the continuity of the composition of continuous functions. One can also show that the mappings $\mathbf{s} \mapsto \varphi(n, \mathbf{s}, x_0)$ are continuous on P, see [15].

4.6.2 Attractors of Skew Product Flows

Then definition of invariance and pullback and attractors for attractors generalise to skew product flows. Essentially, $\theta^n(p_0)$ replaces the actual time $n + n_0$ and p_0 replaces the initial time n_0.

Definition 4.9 A family $\mathscr{A} = \{A_p : p \in P\}$ of nonempty subsets of $\mathbb{R}^d$ is called *φ-invariant* for a skew-product system (θ, φ) on $P \times X$ if

$$\varphi(n, p, A_p) = A_{\theta_n(p)} \quad \text{for all } n \in \mathbb{Z}^+,\ p \in P.$$

It is called φ- positively invariant if

$$\varphi(n, p, A_p) \subseteq A_{\theta_n(p)} \quad \text{for all } n \in \mathbb{Z}^+,\ p \in P.$$

Definition 4.10 A family $\mathscr{A} = \{A_p : p \in P\}$ of nonempty compact subsets of $\mathbb{R}^d$ is called *pullback attractor* of a skew-product system (θ, φ) on $P \times \mathbb{R}^d$ if it is φ-invariant and pullback attracts bounded sets, i.e.,

$$\operatorname{dist}_{\mathbb{R}^d}\left(\varphi(j, \theta_{-j}(p), D), A_p\right) = 0 \quad \text{for } j \to \infty \tag{4.13}$$

for all $p \in P$ and all bounded subsets D of $\mathbb{R}^d$.

It is called a *forward attractor* if it is φ-invariant and forward attracts bounded sets, i.e.,

$$\operatorname{dist}_{\mathbb{R}^d}\left(\varphi(j, p, D), A_{\theta_j(p)}\right) = 0 \quad \text{for } j \to \infty. \tag{4.14}$$

As with processes, the existence of a pullback for skew-product systems ensured by that of a pullback absorbing system.

Definition 4.11 A family $\mathscr{B} = \{B_p : p \in P\}$ of nonempty compact subsets of $\mathbb{R}^d$ is called a pullback absorbing family for a skew-product system (θ, φ) on $P \times \mathbb{R}^d$ if for each $p \in P$ and every bounded subset D of $\mathbb{R}^d$ there exists an $N_{p,D} \in \mathbb{Z}^+$ such that

$$\varphi\left(j, \theta_{-j}(p), D\right) \subseteq B_p \quad \text{for all } j \geq N_{p,D},\ p \in P.$$

The following result generalises the theorem for autonomous semidynamical systems and Theorem 4.1 for processes. The proof is similar in the latter case, essentially

with n and $\theta_{-n(p)}$ changed to n_0 and $n_0 - n$, respectively, but additional complications due to the fact that the pullback absorbing family is no longer assumed to be φ-positively invariant here.

Theorem 4.5 *Let (P, d_P) be a complete metric space and suppose that a skew-product system (θ, φ) on $P \times \mathbb{R}^d$ has a pullback absorbing set family $\mathscr{B} = \{B_p : p \in P\}$. Then there exists a pullback attractor $\mathscr{A} = \{A_p : p \in P\}$ with component sets determined by*

$$A_p = \bigcap_{n \geq 0} \overline{\bigcup_{j \geq n} \varphi\left(j, \theta_{-j}(p), B_{\theta_{-j}(p)}\right)}. \tag{4.15}$$

This pullback attractor is unique if its component sets are uniformly bounded.

The pullback attractor of a skew-product system (θ, φ) has some nice properties when its component subsets are contained in a common compact subset or if the state space P of the driving system is compact. See [31].

Proposition 4.3 *Suppose that $A(P) := \overline{\bigcup_{p \in P} A_p}$ is compact for a pullback attractor $\mathscr{A} = \{A_p : p \in P\}$. Then the set-valued mapping $p \mapsto A_p$ is upper semi-continuous in the sense that*

$$\operatorname{dist}_{\mathbb{R}^d}\left(A_q, A_p\right) \to 0 \quad \text{as } q \to p.$$

On the other hand, if P is compact and the set-valued mapping $p \mapsto A_p$ is upper semi-continuous, then $A(P)$ is compact.

Pullback attractors are in general not forward attractors. However, when the state space P of the driving system is compact, then one has the following partial forward convergence result for the pullback attractor [31].

Theorem 4.6 *In addition to the assumptions of Theorem 4.5, suppose that P is compact and suppose that the pullback absorbing family $\mathscr{B}$ is uniformly bounded by a compact subset C of X. Then*

$$\lim_{n \to \infty} \sup_{p \in P} \operatorname{dist}_{\mathbb{R}^d}\left(\varphi(n, p, D), A(P)\right) = 0 \tag{4.16}$$

for every bounded subset D of X, where $A(P) := \overline{\bigcup_{p \in P} A_p}$, which is compact.

If the pullback attractor here consists of singleton sets corresponding to a periodic entire trajectory, then $A(P)$ represents the limit cycle and the convergence (4.16) corresponds to *orbital stability*.

4.6.3 Skew Product Flows as Semi-dynamical Autonomous Systems

A skew product flow (θ, φ) on $P \times \mathbb{R}^d$ is an autonomous semi-dynamical system Π on the extended state space $\mathbb{X} := P \times \mathbb{R}^d$ with the metric

$$\mathrm{dist}_{\mathbb{X}}\left((p_1, x_1), (p_2, x_2)\right) = d_P(p_1, p_2) + \|(x_1 - x_2\|,$$

where $\Pi : \mathbb{T}^+ \times \mathbb{R}^d \to \mathbb{R}^d$ is defined by

$$\Pi\left(t, (p_0, x_0)\right) = \left(\theta_t(p_0), \varphi(t, p_0, x_0)\right).$$

The initial condition and continuity properties of Π are straightforward. The semi-group property follows from that of θ and the cocycle property of φ:

$$\begin{aligned}\Pi\left(s + t, (p_0, x_0)\right) &= \left(\theta_{s+t}(p_0), \varphi(s + t, p_0, x_0)\right)\\ &= \left(\theta_s \circ \theta_t(p_0), \varphi(s, \theta_t(p_0), \varphi(t, p_0, x_0))\right)\\ &= \Pi\left(s, (\theta_t(p_0), \varphi(t, p_0, x_0))\right) = \Pi\left(s, \Pi\left(t, (p_0, x_0)\right)\right).\end{aligned}$$

This representation as an autonomous semi-dynamical system is useful since it provides insights into how one could define invariant sets and attractors for nonautonomous systems.

Proposition 4.4 *Suppose that $\mathscr{A}$ is a uniform attractor (i.e., uniformly attracting in both the forward and pullback senses) of a skew-product system (θ, φ) and that $\bigcup_{p\in P} A_p$ is precompact in $\mathbb{R}^d$.*

Then the union $\mathbb{A} := \bigcup_{p\in P}\{p\} \times A_p$ is the global attractor of the autonomous semidynamical system Π.

Without uniform attraction as in Proposition 4.4 a pullback attractor need not give a global attractor, but the following result does hold.

Proposition 4.5 *If $\mathscr{A}$ is a pullback attractor for a skew-product system (θ, φ) and $\bigcup_{p\in P} A_p$ is precompact in $\mathbb{R}^d$, then $\mathbb{A} := \bigcup_{p\in P}\{p\} \times A_p$ is the maximal invariant compact set of the autonomous semidynamical system Π.*

The set $\mathbb{A}$ here need not be the global attractor of Π. In the opposite direction, the global attractor of the associated autonomous semidynamical system always forms a pullback attractor of the skew-product system.

Proposition 4.6 *If the autonomous semidynamical system Π has a global attractor*

$$\mathbb{A} = \bigcup_{p\in P}\{p\} \times A_p,$$

then $\mathscr{A} = \{A_p : p \in P\}$ is a pullback attractor for the skew-product system (θ, φ).

4.7 Concluding Remark

The asymptotic behaviour of nonautonomous dynamical systems is much more complicated than for autonomous dynamical systems. Pullback attractors have attracted a lot of attention in the past three decades and play an important role, but they do not not completely characterize the asymptotic behaviour of nonautonomous dynamical systems. They are just part of the picture.

When a pullback attractor is also forward attracting, then we have the ideal situation. But this situation usually does not hold. Then we still have the forward omega limit sets, which are more general than the Vishik uniform attractor since they do not require a rate of attraction that is uniform in the initial time, which is unrealistic in many contexts. Each of these concepts provides us with useful information about the asymptotic behaviour of a nonautonomous dynamical system. Taken together they give us the complete picture.

Acknowledgements This work was partly supported by Chinese NSF grant 11971184.

References

1. M.L. Barabash Y.F. Suprunenko, A. Stefanovska, Chronotaxic systems: a simple paradigm to treat time-dependent oscillatory dynamics stable under continuous perturbation. Nonlinear Phenom. Comp. Syst. **8**, 392–400 (2015)
2. A.N. Carvalho, J.A. Langa, J.C. Robinson, *Attractors of Infinite Dimensional Nonautonomous Dynamical Systems* (Springer, Berlin, 2012)
3. D. Cheban, P.E. Kloeden, B. Schmalfuß, The relationship between pullback, forwards and global attractors of nonautonomous dynamical systems. Nonlinear Dynam. Syst. Theory **2**, 9–28 (2002)
4. V.V. Chepyzhov, M.I. Vishik, *Attractors for Equations of Mathematical Physics* (American Mathematical Society, Providence, Rhode Island, 2002)
5. P. Clemson, B. Petkoski, T. Stankovski, A. Stefanovska, Coupled nonautonomous oscillators, in *Nonautonomous Dynamical Systems in the Life Sciences*, vol. 2102, ed. by P.E. Kloeden, C. Pötzsche (Springer LMS, 2014), pp. 163–197
6. H. Crauel, P.E. Kloeden, Nonautonomous and random Attractors. Jahresbericht der Deutschen Mathematiker-Vereinigung **117**, 173–206 (2015)
7. C.M. Dafermos, An invariance principle for compact processes. J. Different. Eqs. **9**, 239–252 (1971)
8. J.K. Hale, *Asymptotic Behavior of Dissipative Systems* (American Mathematical Society, Providence, 1988)
9. A. Haraux, *Systemes dynamiques dissipatifs et applications, Research in Applied Mathematics*, vol. 17 (Masson, Paris, 1991)
10. P.E. Kloeden, Asymptotic invariance and limit sets of general control systems. J. Different. Eqs. **19**, 91–105 (1975)
11. P.E. Kloeden, Asymptotic invariance and the discretisation of nonautonomous forward attracting sets. J. Comput. Dynam. **3**, 179–189 (2016)
12. P.E. Kloeden, T. Lorenz, Pullback and forward attractors of nonautonomous difference equations, in *Proceedings of ICDEA Wuhan*, vol. 2015, ed. by M. Bohner, Y. Ding, O. Dosly (Springer, Heidelberg, 2014), pp. 37–48

13. P.E. Kloeden, T. Lorenz, Construction of nonautonomous forward attractors, to appear in Proc. Amer. Mat. Soc. **144**(1), 259–268 (2016)
14. P.E. Kloeden, C. Pötzsche (eds.), *Nonautonomous Systems in the Life Sciences*. Springer Lecture Notes in Mathematics, Mathematical Biosciences Subseries, vol. 2102 (Springer, Heidelberg, 2014)
15. P.E. Kloeden, M. Rasmussen, *Nonautonomous Dynamical Systems* (American Mathematical Society, Providence, 2011)
16. P.E. Kloeden, M. Yang, Forward attraction in nonautonomous difference equations. J. Difference Eqs. Appl. **22**, 513–525 (2016)
17. P.E. Kloeden, M. Yang, *Introduction to Nonautonomous Dynamical Systems and their Attractors* (World Scientific Publishing Co. Inc., Singapore, 2021)
18. P.E. Kloeden, C. Pötzsche, M. Rasmussen, Limitations of pullback attractors of processes. J. Difference Eqs. Appl. **18**, 693–701 (2012)
19. P.E. Kloeden, C. Pötzsche, M. Rasmussen, Discrete-time nonautonomous dynamical systems, in *Stability and Bifurcation Theory for Non-autonomous Differential Equations*. CIME Lecture Notes in Mathematics, vol. 2065, ed. by R. Johnson, M.P. Pera (Springer, Heidelberg, 2012), pp. 35–102
20. M.A. Krasnosel'skii, *The Operator of Translation along Trajectories of Differential Equations*. Translations of Mathematical Monographs, vol. 19 (American Mathematical Society, Providence, R.I., 1968)
21. V. Lakshmikantham, S. Leela, Asymptotic self-invariant sets and conditional stability, in *Proceedings of International Symposium of Differential Equations and Dynamical Systems*, Puerto Rico 1965 (Academic Press, New York, 1967)
22. M. Lucas, D. Fanelli, A. Stefanovska, Nonautonomous driving induces stability in network of identical oscillators. Phys. Rev. E **99**, 012309 (2019)
23. M. Lucas, J. Newman, A. Stefanovska, Stabilization of dynamics of oscillatory systems by nonautonomous perturbation. Phys. Rev. E **97**, 042209 (2014)
24. C. Pötzsche, *Geometric Theory of Discrete Nonautonomous Dynamical Systems*. Lecture Notes in Mathematics, vol. 2002 (Springer, Heidelberg, 2010)
25. M. Rasmussen, *Attractivity and Bifurcation for Nonautonomous Dynamical Systems*. Lecture Notes in Mathematics, vol. 1907 (Springer, Heidelberg, 2007)
26. F. Romeiras, C. Grebogi, E. Ott, Multifractal properties of snapshot attractors of random maps. Phys. Rev. A **41**, 784–799 (1990)
27. G.R. Sell, *Topological Dynamics and Ordinary Differential Equations* (Van Nostrand Reinhold Mathematical Studies, London, 1971)
28. Y. Suprunenko, A. Stefanovska, Generalized chronotaxic systems: time-dependent oscillatory dynamics stable under continuous perturbation. Phys. Rev. E **90**, 032921 (2014)
29. Y. Suprunenko, P. Clemson, A. Stefanovska, Chronotaxic systems: a new class of self-sustained non-autonomous oscillators. Phys. Rev. Lett. **111**, 024101 (2013)
30. M.I. Vishik, *Asymptotic Behaviour of Solutions of Evolutionary Equations* (Cambridge University Press, Cambridge, 1992)
31. W. Yejuan, L. Desheng, P.E. Kloeden, On the asymptotical behavior of nonautonomous dynamical systems. Nonlinear Anal. TMA **59**, 35–53 (2004)

Chapter 5
Normal Hyperbolicity for Non-autonomous Oscillators and Oscillator Networks

Robert S. MacKay

Abstract In this chapter, non-autonomous oscillators are considered as mappings from input functions of time to a circle's worth of functions giving the state as a function of time. This view is justified using the theory of normally hyperbolic submanifolds of dynamical systems. It illuminates the phenomena of phase-locking, synchronisation and chimera; it allows an extension of the concept of coupling; and it allows a hierarchical aggregation treatment of synchronisation in networks of oscillators. The view extends to excitable and chaotic oscillators.

5.1 Introduction

Aneta Stefanovska expressed a vision "to build a self-consistent theory of non-autonomous oscillators" (June 2014). In this direction she introduced the class of "chronotaxic" systems [27], defined as "oscillatory systems with time-varying, but stable, amplitudes and frequencies".

This chapter presents a view of a non-autonomous oscillator as a mapping from input functions of time to a circle of possible solutions (state functions of time). It indicates how this view encompasses chronotaxic systems and enables one, at least conceptually, to understand the extent of synchronisation in networks of oscillators, whether autonomous or not. For the latter a hierarchical aggregation scheme is introduced.

The approach is based on the theory of normal hyperbolicity [10, 15]. This theory is the mathematical expression of Haken's slaving principle [13], the idea that

R. S. MacKay (✉)
Mathematics Institute and Centre for Complexity Science, University of Warwick, Coventry CV4 7AL, UK
e-mail: R.S.MacKay@warwick.ac.uk

A. Stefanovska and P. V. E. McClintock (eds.), *Physics of Biological Oscillators*, Understanding Complex Systems,
https://doi.org/10.1007/978-3-030-59805-1_5

some variables for a dynamical system might contract relatively rapidly onto some invariant submanifold in the state space, and then it suffices to study the dynamics on the submanifold. Two key results of normal hyperbolicity theory are: (i) conditions guaranteeing existence of such a submanifold, called a normally hyperbolic (NH) submanifold, and (ii) their smooth persistence of normally hyperbolic (NH) submanifolds as parameters are varied smoothly. It was developed before Haken's slaving principle and deserves to be better known in the physics community. It is a generalisation of centre manifold theory, which is the main mathematical tool Haken used, but has much wider scope. An obstacle is that it demands considerable technical expertise in mathematical analysis. Yet the obstacles are genuine: it turns out that NH submanifolds are differentiable some number r times, depending on the ratio between normal and tangential contraction rates, but typically not more than r times. This is important to recognise, as there is a tendency in physics to consider such functions as pathologies (though physicists do understand that there can be fractal functions).

It is a project on which I have been working for many years, notably with Ph.D. student Stephen Gin (2006–13). It was prompted initially by Mohammad Ghaffari Saadat in 2003, who had formulated a limit-cycle model for a bipedal robot walking down a slope [28] and asked me how much non-uniformity of slope it could cope with. I proposed to tackle this problem by fitting it into the framework of the non-autonomous version of the theory of NH submanifolds, where the result of a not too large forcing function on an oscillator is a circle of possible trajectories. Gin and I attempted to develop good versions of the proofs of normal hyperbolicity results to produce realistic conditions guaranteeing the outcome [12]. Our approach is still incomplete, but I present here the key ideas.

In the world of conservative dynamics, an oscillator is considered to be a Hamiltonian system with an elliptic equilibrium point; this view has fundamental importance but is not the appropriate one for present purposes.

Outside the world of conservative dynamics, an oscillator is usually considered to be an autonomous dynamical system with an attracting periodic orbit. The concept has been extended to cater for chaotic oscillators, but I will postpone treating that extension until near the end of this chapter.

This concept of oscillator as a system with an attracting limit-cycle, however, fails to include the many situations where it is subject to time-dependent forcing. Also, in a network of oscillators, each is subject to input from others, in general time-dependent, so even if the network is autonomous it is useful to consider time-dependent forcing on each of its oscillators.

So I propose a view of an oscillator as a mapping from input functions f of time to a circle's worth of solutions for its state x as a function of time. Each input function f (possibly with more than one component) causes a response x_θ (a function of time) with a phase $\theta \in S^1$ labelling the different possible responses. This view is justified by the theory of normal hyperbolicity, at least for not too strong forcing. It is also my interpretation of chronotaxic systems.

The idea is to consider a non-autonomous system $\dot{x} = v(x, t)$ on a state space X as an autonomous system in the extended state space $X \times \mathbb{R}$, with the real line $\mathbb{R}$

representing time. The dynamics has the form

$$\begin{aligned} \dot{x} &= v(x, s) \\ \dot{s} &= 1. \end{aligned} \tag{5.1}$$

First suppose the vector field $v = v_0$ is independent of s and $\dot{x} = v_0(x)$ has a limit cycle γ (in the strong sense of a periodic orbit with no Floquet multipliers[1] on the unit circle). The most relevant case for applications might be the attracting case (all Floquet multipliers inside the unit circle), but one can allow the more general situation. Then in $X \times \mathbb{R}$, the extended system (5.1) has an extended version of γ, namely an invariant cylinder $\gamma \times \mathbb{R}$. The trajectories form helices on the cylinder, representing the same periodic solution but shifted in s.

This cylinder is an example of a NH submanifold. In general, a *NH submanifold* for a C^1 dynamical system is an invariant C^1 submanifold for which the linearised normal dynamics decomposes into components which contract exponentially in forward or backward time respectively, and faster than the linearised tangential dynamics. Note that the use of the word "normal" might suggest perpendicular, but actually, a normal vector to a submanifold is defined to be an equivalence class of vectors at a point modulo vectors tangent to the submanifold at that point. In the above case, the linearised tangential dynamics neither contracts nor expands on average, because the phase difference between any pair of the helices remains constant. The linearised normal dynamics decomposes into exponentially contracting components in forward and backward time, corresponding to the Floquet multipliers inside and outside the unit circle, respectively.

Now allow v to depend weakly on s. The key result for NH submanifolds is that they persist under C^1-small perturbation. Thus the perturbed system has a C^1-nearby invariant cylinder, no longer in general of product form but diffeomorphic to $S^1 \times \mathbb{R}$. Furthermore, the vector field on it is close to that on the unperturbed cylinder, and the normal dynamics is close to that for the unperturbed case. The solutions on the perturbed cylinder are not in general just a family of periodic solutions differing by phase. In particular, there may be solutions on the cylinder to which all nearby ones converge in forward time. There may also be solutions to which all nearby ones converge in backward time. Or neither may happen. In any case, there is a circle's worth of solutions on the cylinder, which one could label by the intersections of the cylinder with $s = 0$ for example.

In particular, if $v(x, t) = v_0(x) + f(t)$ then the forcing function f produces a circle's worth of state functions x of time on the cylinder. In general a forcing function f should be allowed to depend on the state x too, so $v = v_0(x) + f(x, t)$, and by normal hyperbolicity theory, the same conclusion holds.

As an illustration, consider a model of a quasiperiodically forced limit-cycle oscillator from [6]:

[1] The Floquet multipliers of a periodic orbit are the eigenvalues of the derivative of the return map to a transverse section.

$$\begin{aligned}\dot{x} &= -qx - \omega y \\ \dot{y} &= \omega x - qy + \gamma f(t),\end{aligned} \tag{5.2}$$

with $q = \alpha(\sqrt{x^2+y^2} - a)$, $f(t) = \sin 2\pi t + \sin 4t$, $\alpha, a > 0$, $\gamma \geq 0$ (more natural would be $q = \alpha(x^2 + y^2 - a^2)$ because it makes the dynamics smooth at the origin, but the interest is in the behaviour for $r = \sqrt{x^2+y^2}$ near a). In polar coordinates (r, θ) and extended state-space, this is

$$\begin{aligned}\dot{r} &= -\alpha r(r-a) + \gamma f(s)\sin\theta \\ \dot{\theta} &= \omega - \frac{\gamma}{r} f(s)\cos\theta \\ \dot{s} &= 1.\end{aligned} \tag{5.3}$$

For $\gamma = 0$ there is an invariant cylinder $r = a$. It attracts exponentially with exponent $-\alpha a$ and the motion on the cylinder is $\dot{\theta} = \omega, \dot{s} = 1$, which has Lyapunov exponents 0. So the cylinder is NH and persists to a deformed invariant cylinder for small enough γ. A rough estimate of the range of γ for which persistence is guaranteed is given by the range for which tangential contraction is weaker than normal contraction on the unperturbed cylinder. The normal contraction rate (onto the unperturbed cylinder) is still αa. The tangential contraction (or expansion if negative) $-\frac{\partial\dot{\theta}}{\partial\theta} = -\frac{\gamma}{r} f(s)\sin\theta$. This is smaller than αa for all s, θ iff $2\gamma < \alpha a^2$. Thus one can expect the NH cylinder to persist for γ up to something of the order of $\alpha a^2/2$.

When γ exceeds $\alpha a^2/2$ one can not expect the invariant cylinder to persist. It is shown numerically in [6] that the cylinder is replaced by a (non-autonomous) chaotic attractor with one unstable Lyapunov exponent (coming from the s, θ for which the tangential dynamics is expanding). For a class of examples where a NH submanifold (in fact two 2-tori) can be proved to break up, see [2]. In this chapter, however, I will concentrate on regimes of weak enough coupling that NH submanifolds persist.

As an aside, this view of an oscillator fits in Willems' "behavioural approach" to systems and control [29]. His view was that the description of a dynamical system should be considered to be the restrictions on the set of possible functions of time for all variables. Normal hyperbolicity strikes me a key tool for delivering his approach. On the other hand, he also proposed that one should go beyond the idealisation of inputs and outputs by treating all coupling as two-way, a line that I shall not follow consistently.

In this chapter I will explain how this view of an oscillator illuminates the phenomena of phase-locking, synchronisation and chimera [1], allows to extend the concept of coupling, and allows a hierarchical reduction treatment of synchronisation in networks of oscillators. I will extend the results to allow excitable oscillators and chaotic oscillators. I will outline how the theory of normal hyperbolicity underlies the results. There is a huge literature on synchronisation, e.g. [22], and much of what I will say will be familiar but the important emphasis here is on synchronisation in aperiodically forced systems, which has been treated much less.

Perhaps this direction is not what Aneta had in mind, but I believe it provides a self-consistent theory for non-autonomous oscillators and I hope that it will be useful.

5.2 Phase-Locking

It is well-known that an oscillator may phase-lock to some features of its inputs. Indeed, this is the principle of phase-locked loops in electronic engineering [5] and of synchronous generators and motors in AC electrical networks.

My definition of phase-locking of an oscillator to forcing is that the NH cylinder (assumed attracting) has an attracting trajectory on it and the initial condition is in its basin of attraction.

Any discussion of attractors for non-autonomous systems requires care because the dynamics is unbounded in the time-direction of extended state-space, so there are inequivalent choices of neighbourhoods of a trajectory. For example, for the 2D system $\dot{x} = x, \dot{s} = 1$, any trajectory has a neighbourhood of attraction, despite looking unstable, e.g. for the solution $x = 0$ just take neighbourhood of the form $|x| < \varepsilon e^{2s}$. So I make precise here that by "attracting trajectory" I mean the case with zero unstable space of a uniformly hyperbolic trajectory in the non-autonomous sense. To explain what this means would take some space, so I refer the reader to [4] (with my Ph.D. student Zahir Bishnani), but the important feature is to choose a notion of distance in extended state-space that is uniform in time (so that one does not allow neighbourhoods like that in the above example). There might be a bundle of trajectories which all converge together in forward time, but in general there is only one trajectory in the bundle that has a uniform-in-time neighbourhood of attraction. It is a pullback attractor (for this concept, see the contribution by Kloeden in this volume). My concept of attracting trajectory is distinct, however, from that of pullback attractor, because it can also occur that a pullback attractor is not uniformly hyperbolic (it may be repelling after some time).

An alternative way to describe phase-locking is that the oscillator is synchronised to its inputs. I use "synchronise" in a weak sense: that to a given input function of time there is a locally unique forwards asymptotic solution (the strong sense applies to systems of identical oscillators with a symmetry of the coupling that maps any oscillator to any other, and consists in all oscillators doing the same; for an example, see [31]). Note that a forced oscillator may have more than one such attracting trajectory; this would allow different synchronisations to the same input.

This is in contrast to non-synchronisation, where there is a circle's worth of solutions that do not converge asymptotically to a discrete subset. The strongest version of non-synchronisation is when there is a time-dependent choice of C^1 coordinate ϕ around the cylinder, replacing an initial coordinate θ, such that $\dot{\phi} = \omega(t)$, a positive function of t only, and $\frac{\partial \phi}{\partial \theta}$ and its inverse are bounded. Then with a new time τ defined by $d\tau/dt = \omega(t)$, we obtain $d\phi/d\tau = 1$. It would be interesting to investigate the probability of this case with respect to a distribution of oscillator frequencies

for given weak forcing, perhaps obtaining a sort of non-autonomous KAM result,[2] extending the theory of reducibility of cocycles (see [7] for an early example).

The main conclusion of this section is that synchronisation of an oscillator to its inputs is dimension-reduction. In particular, if there is no immediate feedback from the oscillator to any of its inputs, then one could delete that oscillator, replacing its outputs by some modifications of the outputs from its inputs.

5.3 Synchronisation of Two Oscillators

Let us start with two autonomous oscillators $x_i = v_i(x_i)$, $i = 1, 2$, meaning each has a limit cycle γ_i, and couple them in the standard sense of a modification to the vector field of the product system, depending on the state of each but not too strongly, so

$$\dot{x}_i = v_i(x_i) + g_i(x_1, x_2), \tag{5.4}$$

with g_i C^1-small. Then the product system has a NH 2-torus, being a small perturbation of $\gamma_1 \times \gamma_2$.

If the difference of the frequencies of the uncoupled limit cycles is smaller in a suitable dimensionless sense than the coupling then the NH torus has an attracting limit cycle on it, which makes one turn in the γ_2 direction for each turn in the γ_1 direction. I say the two oscillators have gone into $1:1$ synchronisation. Recall Huygens' clocks. The torus may have more than one attracting limit cycle on it, in which case several synchronised solutions are possible. It may also have unstable limit cycles on it.

Similarly, if the frequencies are close to being in (coprime) integer ratio $m:n$ then coupling might produce an attracting $m:n$ limit cycle on the NH torus, which makes m revolutions in the γ_1 direction and n in the γ_2 direction per period. On the other hand, for weak coupling and smooth enough dynamics, the non-synchronised situation occurs with high probability. More precisely, if one adds a free parameter varying the unperturbed frequency ratio, then KAM theory gives a set of parameter values of nearly full measure for which the dynamics is conjugate to a constant vector field on a 2-torus with irrational frequency ratio (e.g. [17] for a version by my Ph.D. student João Lopes Dias). Thus synchronisation does not always result.

Now consider the non-autonomous situation, where one or both of the oscillators is subject to external forcing. If the forcing is not too strong then the resulting system has a NH submanifold in extended state space, diffeomorphic to $\gamma_1 \times \gamma_2 \times \mathbb{R}$, which I call a torus-cylinder. More generally, for any manifold M I define an M-cylinder to be a manifold diffeomorphic to $M \times \mathbb{R}$. Thus an ordinary cylinder can be called a circle-cylinder. If the unperturbed frequencies are close to integer ratio $m:n$ then the NH submanifold might contain a NH attracting submanifold diffeomorphic to a

[2] The original KAM theory gives a set of invariant tori for near-integrable Hamiltonian systems, the measure of whose complement goes to zero as the perturbation from integrability goes to zero.

circle cross time, being a perturbation of the product of a $m : n$ synchronised limit cycle for the autonomous system and time. In this situation the non-autonomous pair of oscillators can be replaced by a single one.

So again, synchronisation of two oscillators is a dimension-reduction.

5.4 What is Coupling?

In the previous section I used the standard dynamical systems notion for coupling as a perturbation of the product of two vector fields. One might want, however, to allow more general forms of coupling, for example incorporating time-delays or coupling via an intermediate dynamical system. Furthermore, suppose one achieved a dimension-reduction as in Sect. 5.2 or 5.3 and then wants to consider how the new effective oscillator is coupled to others that originally were coupled to one or both of the pair of oscillators. This is no longer describable as a standard perturbation of the product of vector fields.

So I generalise the notion of coupling of two non-autonomous oscillators. As already defined, a non-autonomous oscillator is a non-autonomous system with NH cylinder on which the dynamics can be described by one phase θ with $\dot{\theta} = f(\theta, t)$. A coupling of two non-autonomous oscillators is a non-autonomous system with a NH torus-cylinder on which the dynamics can be described by two phases $\theta = (\theta_1, \theta_2)$ with $\dot{\theta}_i = \tilde{f}_i(\theta, t)$ and $\tilde{f}_i(\theta, t)$ close to $f_i(\theta_i, t)$ for some f_i.

Then the dynamics on the NH torus-cylinder may contain a NH attracting circle-cylinder, as in the more restricted case of the previous section. If the trajectory is in its basin of attraction, I say the two oscillators synchronise.

5.5 Synchronisation of N Oscillators

Not too strong coupling of N non-autonomous oscillators produces a NH N-torus-cylinder. The dynamics on it might contain an attracting NH d-torus-cylinder for some $d < N$. If $d = 1$ the whole group is synchronised and can be replaced by a single effective non-autonomous oscillator. If $d = 0$ the whole group is phase-locked to its inputs and can be eliminated.

Once again, synchronisation, whether partial or complete, means dimension-reduction.

5.6 Hierarchical Aggregation

In a network of oscillators, the above dimension-reductions can in principle be iterated. First one identifies groups of oscillators which synchronise or phase-lock to

their inputs. One reduces to a new network of effective oscillators. Then one repeats, if possible. The end result is a decomposition into synchronised clusters.

Although I did not find out about his work until after I'd proposed this, it is a direct example of Willems' "tearing, zooming, linking" approach [29].

One should note that the end result is not necessarily complete synchronisation. Indeed, it could well be a chimera [1], meaning a system in which some of the oscillators are synchronised but others behave chaotically. The chaotic ones force the synchronised ones and the synchronised ones force the chaotic ones, but our approach of non-autonomous oscillators caters for both of these. There is now a huge literature on chimera. To me the phenomenon was not a surprise because it fits in my framework, but without the framework it can admittedly be considered surprising.

5.7 Normal Hyperbolicity Estimates

To achieve the above dimension-reductions requires good normal hyperbolicity estimates, i.e. results guaranteeing existence of NH submanifolds.

The easiest case, namely, 1D submanifolds, which are just uniformly hyperbolic trajectories of non-autonomous systems, was already treated in [4] (incidentally, it was formulated with attracting trajectories in mind, but another application would be to the unstable trajectories of geophysical flows that form boundaries between trajectories of different classes, e.g. [11]). So that takes care of the case of phase-locking.

Higher-dimensional NH submanifolds, however, require more theory. The classic references are [10, 15]. They are not particularly well adapted to producing practical estimates. Thus I set Stephen Gin onto developing a better way. His Ph.D. thesis [12] gives the outcome, but it is not a complete treatment. So here, I sketch an approach to NH estimates that I believe will be useful. It is in the classic dynamical systems setting of a vector field on the product of state space and time, but hopefully could be extended to take care of the more general forms of coupling that I have described here.

I restrict attention to submanifolds that are torus-cylinders, but of arbitrary dimension $m+1$. So suppose

$$\begin{aligned} \dot{\theta} &= \Theta(\theta, r, t) \\ \dot{r} &= R(\theta, r, t), \end{aligned} \tag{5.5}$$

for $\theta \in \mathbb{T}^m$, $r \in U$, a neighbourhood of $0 \in \mathbb{R}^p$. I suppose that the product $|R_\theta||\Theta_r|$ is small (where subscript denotes derivatives), the r-dynamics is hyperbolic, and the Green function for linearised normal dynamics decays faster than any contraction that may occur in θ-dynamics.

Given a Lipschitz graph $r = \rho(\theta, t)$, a candidate for an invariant submanifold, construct a new one, $T\rho$, by the following steps:

(1) For all (θ_0, t_0), let $\theta()$ be the trajectory of $\dot{\theta}(t) = \Theta(\theta, \rho(\theta, t), t)$ from $\theta(t_0) = \theta_0$.
(2) Solve $\dot{r}(t) = R(\theta(t), r(t), t)$ for the unique function $r()$ such that $r(t)$ is near $\rho(\theta(t), t)$ for all t.
(3) Set $(T\rho)(\theta_0, t_0) = r(t_0)$.

To achieve the second step, I assume that $L : C^1(\mathbb{R}, \mathbb{R}^p) \to C^0(\mathbb{R}, \mathbb{R}^p)$ defined by

$$L[x](t) = \dot{x}(t) - R_r(\theta(t), r(t), t)x(t)$$

on infinitesimal displacements x in r has bounded inverse. This is equivalent to the first part of the NH condition, namely a splitting of the normal bundle into exponentially contracting backwards and forwards subspaces.

Having thus constructed the "graph transform" T, I want to prove that it is a contraction on a suitable space of graphs and hence has a unique fixed point there, which will be an invariant graph. In the direction of achieving this, define a *slope* to be a linear map σ from displacements in θ to displacements in r. For an approximation $\tilde{\sigma}$ to the expected derivative ρ_θ, define $M_{\tilde{\sigma}} : W^{1,\infty}(\mathbb{R}, \mathbb{R}^{mp}) \to W^{0,\infty}(\mathbb{R}, \mathbb{R}^{mp})$ by

$$M_{\tilde{\sigma}}[\sigma] = \dot{\sigma} - R_r\sigma + \sigma(\Theta_\theta + \Theta_r\tilde{\sigma})$$

on slope functions σ of t, where $W^{s,\infty}$ are the spaces of functions with essentially bounded s^{th} derivative. Suppose that $M_{\tilde{\sigma}}$ has bounded inverse. This is the second part of the NH condition, namely faster normal contraction than tangential contraction.

Then T should be a contraction in the space of C^0 functions with an a priori Lipschitz constant. So it would have a unique fixed point ρ. Any fixed point is invariant and actually C^1 with slope ρ_θ being the fixed point of the contraction map $\sigma \mapsto M_\sigma^{-1}[R_\theta]$.

To complete this programme requires detailed estimates. Formulated in terms of contraction maps as here, it should be possible to obtain excellent estimates, along the lines of the uniformly hyperbolic case in [4]. We might do best to follow the approach of [14] (cf. [8]), but replacing their exponential hypotheses by our hypotheses of invertibility of L and M and modifying their exponentially weighted norm to use the linearised tangential flow. I would like to finish this one day.

5.8 Extension to Class 1 Neurons

So far, I have considered the simplest type of oscillator, namely limit cycles, but the treatment can be extended to class I neurons (or excitable oscillators). These are dynamical systems with an attracting invariant cylinder in the autonomous case and dynamics on it in simplest form given by

$$\dot{\theta} = \mu + 1 - \cos\theta \qquad (5.6)$$
$$\dot{\mu} = 0.$$

Since μ is constant, one could think of it as an external parameter, but I wish to consider it as a state variable because coupling from another neuron can make μ change in time. It is best to think of μ as bounded, so the attracting cylinder can be considered an invariant annulus.

They arise in modelling of "excitable neurons" whose frequency goes to zero as a parameter (μ) is varied and then settle at a μ-dependent resting state, or in reverse go from a resting state to large amplitude periodic spiking. An example is the Morris-Lecar model [21], but it was [9] who identified the phenomenon as the unfolding of a saddle-node on a cycle (I proposed this independently to physiologist H.Barlow in the same year and then in 1991 proposed to C. Koch the extension to allow crossover at a "saddle-node loop" [25] to the unfolding of a homoclinic orbit to a saddle). Thus the non-autonomous version has an attracting NH annulus-cylinder.

I had an undergraduate student study networks of such neurons in 1989/90, with the state μ of each neuron driven by the spiking of some others (with time-delay kernels), which produced periodic bursting [19].

Two class I neurons coupled not too strongly have a NH attracting annulus$\times$ annulus-cylinder. Generic bifurcation diagrams in the autonomous case were given in [3]. The dynamics on it has attracting submanifolds of various types. The non-autonomous case has non-autonomous versions of them.

The theory of this paper applies just as well to class I neurons as to ordinary oscillators, with the addition of the μ-direction for each class I neuron.

5.9 Extension to Chaotic Oscillators

The approach can also be extended to chaotic oscillators if they have an attracting NH submanifold containing the attractor. For example, think of a Rössler attractor [24], which is contained in a solid torus in $\mathbb{R}^3$. Then the non-autonomous system has a solid-torus-cylinder. A Rössler attractor can be phase-locked to forcing, meaning that the dynamics is attracted onto a disk-cylinder (a solid torus is the product of a disk and a circle). This should be quite easy because the Rössler attractor was observed to be nearly phase-coherent. I interpret that as meaning that there is a cross-section with nearly constant return time (equivalently, for a given cross-section Σ there is a constant $c > 0$ and a function $b : \Sigma \to \mathbb{R}$ such that the return time $\tau(x) = c + b(f(x)) - b(x)$, where $f : \Sigma \to \Sigma$ is the return map).

Synchronisation of chaotic attractors with NH cylinders of dimensions $N_1 + 1, N_2 + 1$ means there is a NH cylinder for the coupled system with dimension less than $N_1 + N_2 + 1$.

Even better, the theory of NH submanifolds extends to NH laminations [15]. A lamination is a topological space in which each point has a neighbourhood home-

omorphic to the product of a Euclidean space with a general topological space. It decomposes into leaves, which are locally submanifolds but in general only injectively immersed, so a leaf may accumulate onto itself. The theory of NH laminations requires a C^1-structure in addition, but is basically the same as for NH submanifolds. In particular, a NH lamination persists under C^1-small perturbation.

This means one can treat some chaotic attractors in greater detail. In particular, imagine we start with a non-trivial uniformly hyperbolic attractor of an autonomous system, for example a suspension of a Plykin attractor [23]. This is perhaps less familiar than Rössler's attractor but deserves to be better known, as the simplest uniformly hyperbolic attractor after equilibria and periodic orbits. The Plykin attractor was constructed for a discrete-time system, but the map is isotopic to the identity so one can realise it as the first return map of an associated continuous-time system. My Ph.D. student Tim Hunt showed an explicit way to realise it in a system of three ODEs, extended by another Ph.D. student Linling Ru, and less cumbersome ways have been proposed (though not yet with rigorous justification) [16]. It is a NH lamination, whose leaves are its unstable manifolds (of dimension two: one expanding dimension and one time-dimension) and they form a Cantor set transversally. Under time-dependent forcing, it persists to a Cantor set of 3D leaves whose tangent space is spanned by one expanding dimension and two near-neutral dimensions. The persistence is highly robust, requiring only that any tangential contraction be slower than any transverse contraction. Then one can ask what happens on the leaves. The dynamics might collapse onto a 2D subleaf with the same expanding dimension-one neutral dimension. I would say the attractor has synchronised to the forcing.

Similarly, one could couple a suspended Plykin attractor to a limit-cycle oscillator. It produces an attractor with a Cantor set of 3D leaves (the product of the 2D leaves of the chaotic attractor with the limit cycle). The dynamics of each leaf might collapse onto 2D subleaves. I would say the Plykin attractor and limit cycle synchronise together.

More generally, one could couple a continuous-time autonomous uniformly hyperbolic attractor with M unstable dimensions to N limit cycle oscillators and obtain an attractor with a mixture of chaos and nearly quasiperiodic behaviour. It would have M unstable dimensions, N nearly quasiperiodic dimensions, and the flow dimension, with the remaining dimensions contracting onto the leaves. By the theory of NH laminations, such attractors persist for small smooth perturbations, though the dynamics in the quasiperiodic dimensions cannot be expected to remain quasiperiodic. Nonetheless, it will have small Lyapunov exponents for those dimensions and perhaps there is a non-autonomous KAM theory that would even give truly quasiperiodic motion for a set of nearly full measure of parameters. I propose this as an explanation of the scenario reported recently by [30].

As a final note, one might ask about physical realisation of attractors like Rössler's. I designed an electronic oscillator back in 1981, principally to demonstrate period-doubling sequences [18], but moving the parameter further it exhibited a Rössler type of attractor. Model equations for the voltages at three points have the form

$$\begin{aligned} \dot{x} &= ax - by \\ \dot{y} &= cx - ez \\ \dot{z} &= -fy - g(z), \end{aligned} \tag{5.7}$$

with a, b, c, e, f positive constants of which a was adjustable by a 10-turn potentiometer, and g an approximately odd cubic nonlinearity produced with a pair of transistors. Interestingly, as I increased a further, the Rössler attractor turned into what Chua later called a double-scroll attractor [20]. Indeed, Chua's equations turn out to be equivalent to mine after minor changes of variable.

5.10 Conclusion

I have shown that the behaviour of networks of oscillators, autonomous or not, can be aided by identifying normally hyperbolic submanifolds. This allows a deeper understanding of synchronisation of oscillators to forcing and to each other, especially in the aperiodic case. There are many studies on synchronisation in autonomous or periodically forced systems (for one example, see [26]) but relatively few on the aperiodically forced case. The fundamental feature of synchronisation is dimension-reduction of an associated normally hyperbolic submanifold. In a network of oscillators, even if autonomous, the inputs that an individual oscillator sees are in general aperiodic. This motivates a hierarchical aggregation scheme for understanding the dynamics of a network of oscillators: oscillators that synchronise to their inputs can be eliminated, groups of oscillators that synchronise together can be replaced by a single effective oscillator. All this depends on generalising the notion of oscillator from a limit cycle of an autonomous dynamical systems to a mapping from input functions of time to a circle of solutions and generalising the notion of coupling. Finally, I extended the treatment from limit-cycle oscillators to excitable oscillators and chaotic oscillators.

References

1. D.M. Abrams, S.H. Strogatz, Chimera states for coupled oscillators. Phys. Rev. Lett. **93**, 174102 (2004)
2. C. Baesens, R.S. MacKay, Resonances for weak coupling of the unfolding of a saddle-node periodic orbit with an oscillator. Nonlinear **20**, 1283–1298 (2007)
3. C. Baesens, R.S. MacKay, Interaction of two systems with saddle-node bifurcation on invariant circle: part I. Nonlinearity **26**, 3043–3076 (2013)
4. Z. Bishnani, R.S. MacKay, Safety criteria for aperiodically forced systems. Dyn. Syst. **18**, 107–129 (2003)
5. P.V. Brennan, *Phase Locked Loops—Principles and Practice* (Macmillan, 1996)
6. P.T. Clemson, A. Stefanovska, Discerning non-autonomous dynamics. Phys. Rpts. **542**, 297–368 (2014)
7. E.I. Dinaburg, Y.G. Sinai, The one-dimensional Schrödinger equation with a quasi-periodic potential. Funkts. Anal. Prilozh. **9**, 8–21 (1975)

8. J. Eldering, *Normally Hyperbolic Invariant Manifolds—The Noncompact Case* (Springer, 2013)
9. B. Ermentrout, N. Kopell, Parabolic bursting in an excitable system coupled with a slow oscillation. SIAM J. Appl. Math. **46**, 233–253 (1986)
10. N. Fenichel, Persistence and smoothness of invariant manifolds for flows. Indiana U Math. J. **21**, 193–226 (1971)
11. G. Froyland, K. Padberg, M.H. England, A.M. Treguier, Detection of coherent oceanic structures via transfer operators. Phys. Rev. Lett. **98**, 224503 (2007)
12. A.H. Gin, Aperiodically forced oscillators. Ph.D. Thesis, Univ Warwick, 2013
13. H. Haken, Generalised Ginzburg-Landau equations for phase transition-like phenomena in lasers, nonlinear optics, hydrodynamics and chemical reactions. Z. Phys. B **21** 105 (1975)
14. D. Henry, *Geometric Theory of Semilinear Parabolic Equations* (Springer, 1981)
15. M.W. Hirsch, C.C. Pugh, M. Shub, *Invariant manifolds*. Lecture Notes in Mathematics, vol. 583 (Springer, 1977)
16. S.P. Kuznetsov, Dynamical chaos and uniformly hyperbolic attractors: from mathematics to physics. Phys. Uspekhi **54**(2), 119–144 (2011)
17. J. Lopes Dias, Renormalisation scheme for vector fields on $\mathbb{T}^2$ with a Diophantine frequency. Nonlinearity **15**, 665–679 (2002)
18. R.S. MacKay, Renormalisation in area-preserving maps, 1982 Princeton. Ph.D. Thesis, revised version published by World Scientific Publishing Co (1992)
19. R.S. MacKay, Dynamics of networks, in: *Stochastic and Spatial Structures of Dynamical Systems*, ed. by S van Strien, S. Verduyn Lunel (1996), pp. 81–104
20. T. Matsumoto, L.O. Chua, M. Komuro, The double scroll. IEEE Trans. Circ. Syst. CAS-32, 798–818 (1985)
21. C. Morris, H. Lecar, Voltage oscillations in the barnacle giant muscle fiber. Biophys. J. **35**, 193–213 (1981)
22. A. Pikovsky, M. Rosenblum, J. Kurths. Synchronisation (CUP, 2001)
23. R.V. Plykin, Sources and sinks of A-diffeomorphisms of surfaces. Math. USSR Sbornik **23** 233 (1974)
24. O. Rössler, An equation for continuous chaos. Phys. Lett. A **57**, 397–398 (1976)
25. S. Schecter, The saddle-node separatrix-loop bifurcation. SIAM J. Math. Anal. **18**, 1142–1156 (1987)
26. A. Shilnikov, L. Shilnikov, D. Turaev, On some mathematical topics in classical synchronization. A tutorial. Int. J .Bif. Chaos **14**, 2143–2160 (2004)
27. Y.F. Suprunenko, P.T. Clemson, A. Stefanovska, Chronotaxic systems: a new class of self-sustained nonautonomous oscillators. Phys. Rev. Lett. **111**, 024101 (2013)
28. A. Tehrani Safa, M. Ghaffari Saadat, M. Naraghi, Passive dynamic of the simplest walking model: replacing ramps with stairs. Mech. Mach. Theory **42**, 1314–1325 (2007)
29. J.C. Willems, The behavioral approach to open and interconnected systems. IEEE Control Syst. Mag. (Dec 2007)
30. J.F. Yamagishi, K. Kaneko, Chaos on a high-dimensional torus. Phys Rev Res **2**, 023044 (2020)
31. R. Yamapi, R.S. MacKay, Stability of synchronisation in a shift-invariant ring of mutually coupled oscillators. Discr. Conts. Dyn .Syst. B **10**, 973–96 (2008)

Chapter 6
Synchronisation and Non-autonomicity

Maxime Lucas, Julian M. I. Newman, and Aneta Stefanovska

Abstract Thermodynamic openness is key to the long-term stability of living systems and can yield rich dynamical behaviours. Here, we model openness in coupled oscillator systems by introducing an external driving with time-varying parameters. Five systems of increasing complexity are considered: three cases of single driven oscillators followed by two cases of driven networks. We show how the time-varying parameters can enlarge the range of other parameters for which synchronous behaviour is stable. In addition, it can yield additional behaviours such as intermittent synchronisation. The stability of these systems is analysed via short- and long-time Lyapunov exponents, both analytically and numerically. The different dynamical regimes are also described via time-frequency representation. Finally, we compare the stabilising effect of deterministic non-autonomous driving to that of bounded noise. All in all, we give an overview of some effects time-varying parameters can have on synchronisation. These effects could be a key to understand how living systems maintain stability in the face of their ever-changing environment.

6.1 Introduction

Many systems in nature are thermodynamically open, i.e. they exchange energy and matter with their environment. In fact, their openness is often key to their maintenance of life. How could an organism survive isolated from its environment? Without external supplies of nutrients and the ability to get rid of waste products of metabolism

M. Lucas (✉)
Aix-Marseille University, Marseille, France
e-mail: maxime.lucas.1@univ-amu.fr

J. M. I. . Newman
Exeter University, Exeter, UK
e-mail: J.M.I.Newman@exeter.ac.uk

A. Stefanovska
Lancaster University, Lancaster, UK
e-mail: aneta@lancaster.ac.uk

A. Stefanovska and P. V. E. McClintock (eds.), *Physics of Biological Oscillators*, Understanding Complex Systems,
https://doi.org/10.1007/978-3-030-59805-1_6

and internal toxins, there would be no sustained life. The idea that one needs to model living systems as open has indeed been expressed by E. Schrödinger in his book "What is life?" [51].

Traditionally, the effect of external influences on a system is modelled either by a very simple deterministic input—i.e. constant or strictly periodic—or for more complicated-looking cases, by noise defined in terms of stochastic processes. Sometimes, external influences are themselves modelled by an autonomous dynamical system, such that the system with its external influence can be modelled together as one autonomous dynamical system. However, here, we demonstrate what can be achieved by using deterministic non-autonomous models [25] to describe a system subject to external influences. Such models have been argued to be especially useful to describe living systems [24, 30], but have been used in other areas such as climate dynamics [11, 16, 17].

Living systems exhibit two properties of particular interest. Firstly, they maintain overall stability over long timescales (their lives) despite the input from their environment that is ever-changing in a non-trivial fashion. Secondly, due to this input, their shorter-timescale macroscopic properties, e.g. the moment-by-moment characteristics of the response to perturbation, vary in time. An example of such time-variability can be seen when the heartbeat is recorded over time—even for healthy subjects in repose. The frequency of the heartbeat varies continuously, modulated by the oscillations corresponding to breathing [8] and other low-frequency oscillatory processes resulting from neurovascular regulation of the heartbeat [52]. We emphasise that, in fact, dynamics on such shorter timescales can play a crucial role in the functioning of the system. For example, it has been shown that transitions in cardio-respiratory synchronization occur during anaesthesia [53], and it has been proposed that, in the brain, transient synchrony between neurons can improve information routing [43].

Here, we focus on systems of coupled oscillators. Such systems can exhibit synchronisation [49], where all oscillators in the system behave mutually coherently. The study of synchronisation gained interest with the works of Winfree [61] and Kuramoto [26] and the many extensions of the Kuramoto model, in particular to complex network topologies [4].

The effect of non-autonomicity on coupled oscillatory systems has started to attract attention in recent years. Low-dimensional examples include studies [56, 57], motivated by the cardiovascular system, which coined the term *chronotaxicity* to define a class of non-autonomous systems with time-varying frequencies, able to maintain stability against generic external perturbation. Inverse methods for detection of chronotaxic dynamics in experimental data were also developed [29]? and applied successfully to real biological systems [30]. Theoretical phase reduction for non-autonomous oscillators has also been developed [27, 28, 44].

Apart from the chronotaxicity studies [56, 57], a few other theoretical works have looked into non-autonomous oscillatory systems. In [22], Jensen considered one-dimensional non-autonomous Adler equations and described their changing dynamics in the limit of slow variation, and determined how slow the modulation needs to be for the analysis to hold. In [13], the same system was studied specifically in the case of periodic forcing, with particular focus on the existence and properties of periodic

orbits. More recently, Hagos and coworkers investigated the effect of time-variability of coupling functions when the total coupling strength is kept constant [18]. At the network level, the solution of the Kuramoto model with slow frequency and coupling modulations was obtained analytically in [45], and the Ott-Antonsen theory was then extended for time-varying parameters in [46]. Recent work on synchronisation in temporal networks includes [12, 33].

Bifurcation in non-autonomous systems has been considered from a mathematical viewpoint [2], including in finite-time dynamical systems [50]. In [5, 31], non-autonomicity in the form of a parameter-shift that can pass through critical bifurcation values is considered, and it is shown that the rate and the actual shape of the parameter-shift can have a dramatic impact on the resulting dynamics.

Building on the aforementioned studies, especially [22, 56], we have shown for a low-dimensional system that the non-autonomicity can enlarge the region of stability in parameter space [35, 40]. The results were then extended to driven networks of identical oscillators [34]. In the present chapter, we provide a synthesis of this recent work, and also build on this with a new result on time-varying coupling in networks.

The chapter is organised as follows. In Sect. 6.2, we define non-autonomous systems and discuss their relation to thermodynamically open systems. In Sect. 6.3, we review some methods of analysing the behaviour of dynamical systems on both short and long timescales. In Sect. 6.4, we present an analysis of five theoretical systems of increasing complexity. Finally, in Sect. 6.5, we summarise the results and discuss potential future directions.

6.2 Non-autonomicity

In this section, we discuss the relation between the thermodynamic classification of a system and the types of dynamical systems to model it.

6.2.1 Thermodynamically Open Versus Isolated

From the perspective of thermodynamics, the universe is the sum of two things: the *system* under consideration, and its *environment*, i.e. everything else [9]. The system can be of one of three classes, based on the nature of the system-environment interactions: open, closed, and isolated. A system is called *isolated* if it does not exchange anything with its environment—neither energy, nor matter. An *open* system, on the contrary, exchanges both energy and matter with its environment. Finally, a *closed* system exchanges only energy and not matter with its environment. Figure 6.1a shows a sketch of an isolated system whereas Fig. 6.1b, c depict an open one.

Isolated systems have proven useful as an idealised concept, but truly isolated systems are virtually non-existent in nature. Living systems are an example that, by nature, cannot be seen as isolated, and need to be modelled as open, as argued above.

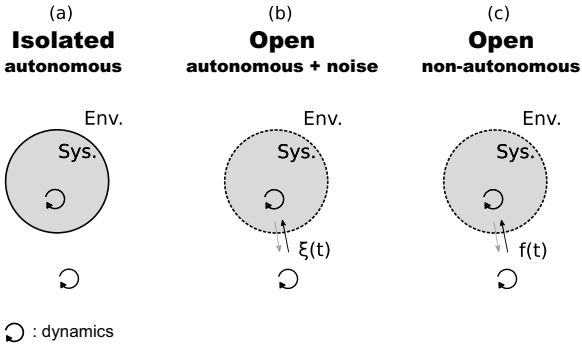

Fig. 6.1 Three typical approaches to model systems that interact with their environment

Their exchanges of energy and matter with their environment is crucial to their survival: without the ability to feed and waste, any living system would quickly die. The distinction between isolated and non-isolated systems manifests in an important way for dynamical systems, namely in the distinction between autonomous dynamical systems and dynamical systems that are either noise-driven or nonautonomous. We now discuss these different types of dynamical systems.

6.2.2 Autonomous Versus Non-autonomous

An *autonomous* dynamical system is one that evolves according to a time-independent law [55]. The evolution of its state $\boldsymbol{x}(t)$ over time can be written in general as

$$\dot{\boldsymbol{x}} = \boldsymbol{f}(\boldsymbol{x}), \tag{6.1}$$

where the function $\boldsymbol{f}$ encodes the time-independent evolution law. By definition, autonomous dynamical systems are well-defined over infinite time.

Autonomous systems are conceptually related to isolated systems: as illustrated in Fig. 6.1a, the system's evolution is independent of any external influence from its environment, as reflected in Eq. (6.1) where the evolution of $\boldsymbol{x}$ only depends on itself. How can we include external influences in the description of a dynamical system? Two main choices exist: describe the external influence as deterministic, or as a noisy process. We start with the deterministic case.

A *non-autonomous* dynamical system is one that evolves according to a time-dependent law [25]. The evolution of its state $\boldsymbol{x}(t)$ over time can be written in general as

$$\dot{\boldsymbol{x}} = \boldsymbol{f}(\boldsymbol{x}, t), \tag{6.2}$$

where the deterministic function $\boldsymbol{f}$ now explicitly depends on time.

Thus, non-autonomous systems are conceptually related to non-isolated systems such as open systems: as illustrated in Fig. 6.1c, the system's evolution depends on its own internal dynamics but also on external influences, which can come in many forms, as reflected in Eq. (6.2) by the explicit dependence of the evolution of $\boldsymbol{x}$ on t.

The formal study of non-autonomous dynamical systems started in the mathematical community [25] with early works on their stability including [1, 32, 38] and more recently [21]. Even though it is a much younger field than that of autonomous dynamical systems, it started being used sparingly in other disciplines such as physics [56] and biology [30]. In parallel, more and more researchers have included time-variability in recent years, without necessarily using the word "non-autonomous" or its associated formalisms and methods. As an example, temporal networks, i.e. networks with links that are time-dependent, have been applied successfully to diverse areas [19, 20].

Noisy processes are a second way to describe the external influence of the environment on the system. For example, as

$$\dot{\boldsymbol{x}} = \boldsymbol{f}(\boldsymbol{x}) + \xi(t), \tag{6.3}$$

where the internal (autonomous) dynamics is determined by the deterministic function $\boldsymbol{f}$, and the external time-dependent influence is modelled as noise $\xi(t)$.

By construction, such noisy models are also conceptually related to non-isolated systems such as open systems, as illustrated in Fig. 6.1b. The difference from non-autonomous systems is that the external influence is here modelled as a noisy process. Such stochastic models have been studied and used successfully for decades [47], and an arsenal of methods is available to treat them.

The noise term in Eq. (6.3) can arise as the result of a mesoscale description in terms of a few slow degrees of freedom, of a system containing many fast degrees of freedom [15]. The original Langevin equation to describe Brownian motion is a good example of this: the collective effect of the microscopic motion of the many independent fluid molecules can be described as a noise term that acts on the macroscopic movement of a bigger particle. More details about the assumptions needed for such a description to hold can be found in [14].

We have presented three types of models: autonomous, non-autonomous, and autonomous plus noise. Each type of model has strengths and weaknesses, and is best suited to describe a given system or to answer a given question. Autonomous models can be used in many cases as a useful approximation, when the interaction with the environment is negligible. Their relative simplicity often makes them mathematically tractable, and decades of research have provided us with a good understanding of the appropriate methods to study them. However, autonomous models are ill-suited to describe open systems in which the external influence of the environment is crucial, such as living systems. That influence can be modelled by noise, for which we also have many methods available. Noisy processes are useful, for example, as a mesoscopic description, when we do not have enough information about the underlying microscopic mechanisms. When possible, non-autonomous models of open systems provide us with a more time-resolved description of the systems. They are however

harder to treat analytically in general. Before closing this section, we mention that we consider, in this chapter, cases where the nonautonomicity comes from either time-varying frequencies or coupling strength.

6.3 Methods

We now briefly present existing methods for the analysis of non-autonomous dynamical systems. We discuss the assumptions made in each case, and describe their strengths and limitations when dealing with time-varying systems.

6.3.1 Asymptotic

First, we present traditional time-asymptotic methods that were historically developed for autonomous dynamical systems. For these methods, it is assumed that the model considered is defined over infinite time. We restrict ourselves to methods relevant for the rest of the present work. Other methods can be found e.g. in [54] for a theoretical approach, and in [10] for a signal processing approach.

6.3.1.1 Lyapunov Exponents

The stability of a trajectory $x(t)$ of a dynamical system (which could be autonomous, noise-diven, or nonautonomous) is often assessed in terms of the asymptotic Lyapunov exponents (ALEs) associated to it [48]. For a trajectory $x(t)$ and a unit vector v_0 corresponding to a direction of initial perturbation at time 0, we define the corresponding ALE as follows: letting $x_\delta(t)$ denote the solution starting at $x(0) + \delta v_0$ for each $\delta \in \mathbb{R}$, the ALE $\lambda^{(\infty)}$ is given by

$$\lambda^{(\infty)} = \lim_{t\to\infty} \lim_{\delta\to 0} \frac{1}{t} \ln\left(\frac{\|x_\delta(t) - x(t)\|}{|\delta|}\right) \tag{6.4}$$

if this limit exists. This measures the exponential separation rate between $x(t)$ and a nearby trajectory: a positive value corresponds to exponentially growing separation, while a negative value corresponds to exponential attraction between the trajectories. This heuristic notion of "infinitely close trajectories" can be made mathematically rigorous in terms of suitable calculus notions. If the dynamical system has a d-dimensional state space, we define a spectrum of d ALEs associated to a trajectory $x(t)$, typically ordered as $\lambda_{\max} = \lambda_1 \geq \lambda_2 \geq \cdots \geq \lambda_d$, each one corresponding to a different direction of the initial infinitesimal separation $\delta x(0)$. Assuming the system is sufficiently well behaved, the maximal ALE $\lambda_{\max}$ is obtained in Eq. (6.4) for a generic v_0. The maximal ALE indicates the stability of the trajectory $x(t)$: if $\lambda_{\max} > 0$

then the trajectory is *unstable*, i.e. exhibits sensitive dependence to changes in initial condition; if $\lambda_{\max} < 0$ then the trajectory is *stable* against small perturbations; in the intermediate case $\lambda_{\max} = 0$, the trajectory is said *neutrally stable*. The presence of positive ALEs for the trajectories of a dynamical system is commonly accepted as an indicator of *chaos*.

Two key assumptions of Definition (6.4) are that (i) the dynamical system being analysed must be defined over infinite time and (ii) the formal limit $t \to \infty$ in Definition (6.4) exists. The first assumption can be satisfied by either an autonomous system, or a non-autonomous system. Not all non-autonomous systems need be defined over infinite time, however, as discussed in chapter [40] of this volume and references therein. As for the second condition, Oseledets' multiplicative ergodic theorem [41] provides conditions for the existence of the limit, and hence of the spectrum of ALEs described above. For an autonomous system, ALEs are typically well-defined, but with some exceptions [42]. The same holds for non-autonomous systems with simple forms of non-autonomicity such as periodic variation; but for arbitrary aperiodic variation, the limit in Eq. (6.4) will typically not exist.

The ALE has the important property of being coordinate-invariant: it does not depend on the choice of coordinates for the state space of the dynamical system.

6.3.1.2 Fourier Spectrum

The realisation of a physical process can be represented in the time domain, by a time series, or in the frequency domain, e.g. by the Fourier spectrum of this time series. The two representations give different insight into the underlying system, and the frequency content of a time series is a precious tool to understand the system, especially if it is oscillatory. A typical frequency domain representation is the discrete Fourier transform (DFT) of a time series $\{x_k\}$ where the index $k = 1, \ldots, n$ represents time. The DFT is defined as the function

$$F_\omega = \sum_{k=0}^{n-1} x_k e^{i 2\pi \omega k/n}. \tag{6.5}$$

This formula allows one to go from the time domain to a frequency domain representation for a given process. If the time series includes a prominent component with a given frequency ω, the DFT will then exhibit a peak around that frequency ω. For example, a sine function with frequency ω will exhibit a single peak in its DFT at ω. The coefficients are often plotted as either the amplitude of the spectrum $|F_\omega|$ or the power $|F_\omega|^2$.

6.3.2 *Finite-Time*

In this section, we present methods that are time-resolved counterparts of the ones described above. Here, the output of the methods is the evolution of measured properties over time, allowing one to observe the time-variable dynamics.

6.3.2.1 Finite-Time Lyapunov Exponents

Stability can be considered over finite time. In particular, given a time-window $[t, t+T]$, for a trajectory $x(\cdot)$ and a unit vector v_t corresponding to a direction of perturbation at time t, we define the corresponding FTLE as follows: letting $x_\delta(\cdot)$ denote the solution coinciding with $x(t) + \delta v_t$ at time t for each $\delta \in \mathbb{R}$, the FTLE $\lambda_T(t)$ is given by

$$\lambda_T(t) = \lim_{\delta \to 0} \frac{1}{T} \ln \left(\frac{\|x_\delta(t) - x(t)\|}{|\delta|} \right). \tag{6.6}$$

The length T of the time-window is of crucial importance, as different lengths will reveal features of the dynamics over different timescales. The choice of window-length thus depends on the system at hand and the timescale of interest; a longer time-window will average out faster-timescale variations of time-localised stability. For $T \to \infty$, one recovers the ALE; for $T \to 0$, one obtains an *instantaneous Lyapunov exponent* (ILE). In numerical computation of an ALE via direct simulation, one is really just computing a FTLE over a very long time-window.

Contrary to ALEs, FTLEs are not coordinate-invariant. The FTLE has the advantage that it does not rely on the aforementioned assumptions (i) and (ii) relative to the definition of the model and the existence of the limit $t \to \infty$. The FTLE can be applied to any model, autonomous or non-autonomous, defined over finite or infinite time.

Note that an ALE for a direction of initial perturbation v_0 is an infinite-time average of the ILE $\lambda(t)$ in the direction $v_t := \lim_{\delta \to 0+} \frac{x_\delta(t) - x(t)}{\|x_\delta(t) - x(t)\|}$ where $x_\delta(0) = x(0) + \delta v_0$. (In one dimension, this simply means that the single ALE is the infinite-time average of the ILE.) Therefore, the maximal ALE only measures the average stability of a trajectory, but does not give any indication about how it might change over time. Often, in real-world systems, and especially in living systems, finite-time properties are of crucial importance to their maintaining of vital functions and of life itself. For the heart to keep beating, the mutual synchrony of its cells must be stable at all times, not just on average.

6.3.2.2 Wavelet Transform

Just as the ALE only gives an average measure of stability without time resolution, the DFT only shows a static picture of the frequency content of a time series. To overcome this limitation, one can use time-frequency representation which gives how the frequency content of a trajectory evolves over time.

The continuous wavelet transform (CWT) is a time-frequency representation that was developed to obtain a good time-frequency resolution simultaneously across a broad range of timescales. The idea is to perform frequency analysis in a time-window whose width is scaled in proportion with the timescale being investigated The CWT of a signal $x(t)$ is given by

$$W(s,t) = \frac{1}{s^p} \int_{-\infty}^{\infty} \Psi\left(\frac{u-t}{s}\right) x(u)\,\mathrm{d}u, \tag{6.7}$$

where s is a scaling factor, p is number typically chosen as either 1 or $\frac{1}{2}$, and Ψ is the "wavelet function" which represents mathematically the time-localisation used for the frequency analysis. Different types of wavelet function can be used. In this chapter, the Morlet wavelet is used, which has good time-frequency resolution [10]. Taking the scaling factor s as reciprocally proportional to frequency ω, we can obtain the power in a frequency interval $[\omega - \frac{\delta\omega}{2}, \omega + \frac{\delta\omega}{2}]$ around each frequency ω at time t as

$$P_W(\omega,t) = \int_{\omega-\frac{\delta\omega}{2}}^{\omega+\frac{\delta\omega}{2}} |W(\omega,t)|^2\,\mathrm{d}\omega \tag{6.8}$$

for $p = \frac{1}{2}$. A more detailed presentation of the CWT can be found in [10] and references therein. The wavelet transform has been used e.g. in [10, 29, 30].

6.4 Systems Analysis

In this section, we present a succession of coupled oscillators models, in increasing order of complexity. Figure 6.2 illustrates the different systems considered and the relationship between them. In Sect. 6.4.1, we start with the simplest case: a periodically driven phase oscillator. Then, we present two models in which the driving is made aperiodic: noisy, in Sect. 6.4.2, and deterministic with a time-varying driving frequency, in Sect. 6.4.3. Finally, we present results of the former case generalised to networks, in Sect. 6.4.4, for which we also present the case of a deterministic time-varying coupling strength. For each model, we apply the methods described in the previous section, and report results about the stability of the system.

Numerical integration of the systems is performed with a Runge-Kutta 4 scheme with a timestep of 0.01 s. The time-frequency representations are computed according to the Morlet wavelet transform ($p = 1$) from the PyMODA package [7].

6.4.1 Single Oscillator: Periodic Driving

We start with the following driven phase oscillator system

$$\dot{\theta}_1 = \omega + \gamma \sin[\theta_1 - \theta_0(t)], \tag{6.9}$$

where the driving has strength γ, phase $\theta_0(t)$, and a constant frequency

$$\dot{\theta}_0 = \omega_0. \tag{6.10}$$

System (6.9)–(6.10) is well known in the literature, see for example [49], and it is schematically shown in Fig. 6.2a. We nonetheless present the parts of its analysis that are relevant for the remainder of the present chapter.

System (6.9) with its driving given by Eq. (6.10) is more conveniently studied in the reference frame of the driving. The phase difference $\psi = \theta_1 - \omega_0 t$ evolves according to what is known as the Adler equation

$$\dot{\psi} = \Delta\omega + \gamma \sin \psi, \tag{6.11}$$

where $\Delta\omega = \omega - \omega_0$ is called the frequency mismatch. The frequency mismatch and the driving strength determine the dynamics of the system, and in particular the stability of the driven oscillator. There are two scenarios: either Eq. (6.11) has a

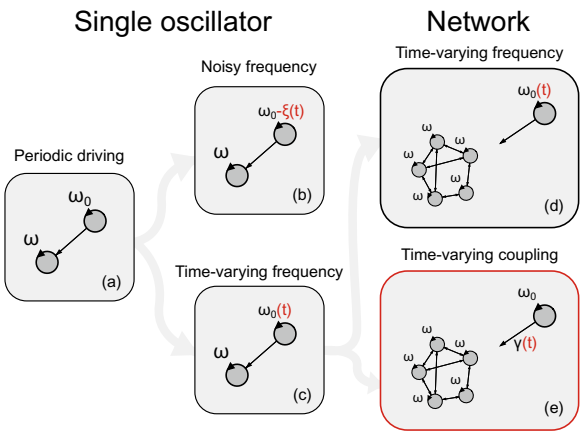

Fig. 6.2 Synchronisation in coupled oscillators with time-varying parameters: hierarchy of systems presented, in increasing complexity. **a** Single oscillator with periodic driving. **b** Single oscillator with noisy driving. **c** Single oscillator driven at a time-varying frequency. The last of these is generalised to **d** a driven network and **e** a driven network with time-varying driving strength in place of time-varying driving frequency

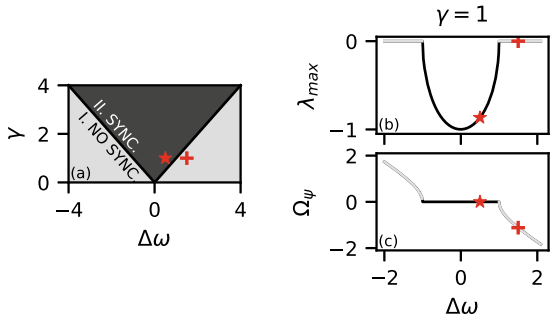

Fig. 6.3 Synchronisation versus no synchronisation, for the periodic driving case given by Eq. (6.11). **a** Region of neutral stability (region I) and region of stability (region II, also called the Arnold tongue). **b** Asymptotic Lyapunov exponent and **c** beat frequency for a fixed value of $\gamma = 1$. To help visualise how the plots in **b** and **c**relate to the two regions shown in **a**, a point is chosen from region II (with $\gamma = 1$) and marked by the red star in all three plots, and likewise a point is chosen from region I (again with $\gamma = 1$) and marked by the red plus sign in all three plots. In this periodic driving case, the region of negative Lyapunov exponent coincides with the plateau of vanishing beat frequency

stable fixed point at which ψ stays constant, or it does not and all solutions ψ exhibit unbounded monotonic growth.

The first scenario corresponds to *synchronisation*, and happens if the driving is strong enough, $\gamma > |\Delta\omega|$. This condition determines the region of synchronisation in parameter space, also called the Arnold tongue, which is illustrated as Region II in Fig. 6.3a. When the condition is fulfilled, the Adler equation has a pair of fixed points, one of which is stable, $\psi_S = \pi - \arcsin(-\Delta\omega/\gamma)$, and attracts all initial conditions apart from the unstable fixed point, see Fig. 6.4a. The phase difference ψ thus settles on the constant value ψ_S, as shown in Fig. 6.4b, and the driven oscillator is thus *phase-locked* to the driving, with the instantaneous Lyapunov exponent always being negative (and thus so is the asymptotic Lyapunov exponent), see Fig. 6.4c. Both oscillators have the same frequency (as also seen in Fig. 6.4d discussed shortly): the frequency of the driven one is *entrained* by the driving one. In this simple periodic driving case, phase-locking and frequency entrainment are equivalent, but not in other cases, as will be discussed later on.

The second scenario corresponds to there being no synchronisation, and occurs for $\gamma < |\Delta\omega|$. This is illustrated as Region I in Fig. 6.3a. In this case, the phase difference grows indefinitely as shown in Fig. 6.4f. So the oscillators are not phase-locked, as shown in Fig. 6.4e.

We now analyse the linear stability of solutions in these two cases, denoted in both cases by $\tilde{\psi}(t)$. An infinitesimal perturbation $\delta\psi$ obeys the linearised equation

$$\delta\dot{\psi} = \gamma\delta\psi\cos\tilde{\psi}(t), \tag{6.12}$$

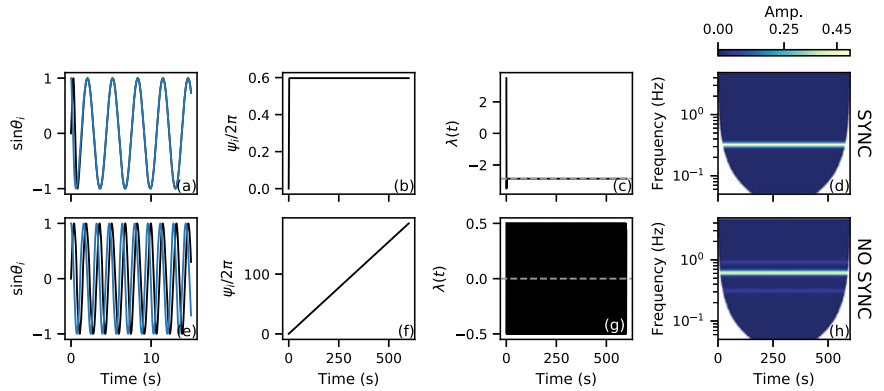

Fig. 6.4 Dynamical regimes of the single oscillator with time-varying frequency driving: synchronisation (top row, $\gamma = 3.5$ rad/s), and no synchronisation (bottom row, $\gamma = 0.5$ rad/s). For each regime, we show **a** $\sin\theta$ over time for two random initial conditions, **b** the phase difference over time, **c** the instantaneous Lyapunov exponent (black) and the asymptotic Lyapunov exponent (dashed grey), as well as a time-frequency representation of the time series $\sin\theta(t)$. Other parameters are set to $\omega_m = 0.02$ rad/s, $k = 0.5$, $\omega_0 = 2$ rad/s, and $\omega = 4$ rad/s. The time-frequency representation are computed with the Morlet wavelet transform ($p = 1$) with central frequency $f_0 = 3$

so that it grows or decays as $\delta\psi(t) = \delta\psi(0)\exp[\int_0^t \lambda(t)dt]$ with instantaneous exponential rate, i.e. instantaneous LE

$$\lambda(t) = \gamma\cos\tilde{\psi}(t). \tag{6.13}$$

In the synchronised case, we take the constant solution $\tilde{\psi}(t) = \psi_S$ to which all solutions (other than the repelling fixed point) settle. In this case, the ILE is a constant $\lambda(t) = -\sqrt{\gamma^2 - \Delta\omega^2}$, just as seen in Fig. 6.4c in black. In the non-synchronised case, however, $\tilde{\psi}(t)$ increases or decreases monotonically and unboundedly, such that the ILE $\lambda(t)$ oscillates around 0 as shown in Fig. 6.4d, also in black.

Now, the ALE can be obtained as the temporal average of the ILE

$$\lambda = \gamma\langle\cos\tilde{\psi}(t)\rangle, \tag{6.14}$$

which yields for both cases

$$\lambda = \begin{cases} -\sqrt{\gamma^2 - \Delta\omega^2} & \text{if } \gamma \geq |\Delta\omega|, \\ 0 & \text{else.} \end{cases} \tag{6.15}$$

In the synchronised case $\gamma > |\Delta\omega|$, the asymptotic and instantaneous LE are identical and negative, as shown in Fig. 6.4c in dashed grey and black respectively. So the phase of the driven oscillator θ_1 is stable by virtue of the driving from θ_0. However, in the non-synchronised case $\gamma < |\Delta\omega|$, averaging $\lambda(t)$ over each cycle

of $\tilde{\psi}(t)$ gives $\lambda = 0$ as shown in Fig. 6.4g in dashed grey, and so the phase of θ_1 is only neutrally stable.

The Lyapunov exponents tells us about the stability of the solution. We complement this information with a measure about the motion of the solution itself: the mean frequency difference, often called *beat frequency*, which is defined as

$$\Omega_\psi = 2\pi \left[\int_0^{2\pi} \frac{d\psi}{\Delta\omega + \gamma \sin\psi} \right]^{-1}, \tag{6.16}$$

and is related to the other frequencies of the system by

$$\langle \dot{\theta}_1 \rangle = \omega_0 + \Omega_\psi. \tag{6.17}$$

In the synchronised case, the driven oscillator rotates with the frequency of the driving, and hence $\Omega_\psi = 0$, otherwise it is non-zero. So, here, the region of synchronisation is equivalently characterised by the plateau $\Omega_\psi = 0$ and a negative ALE $\lambda < 0$, as illustrated in Fig. 6.3b, c by the solid black curves. This equivalence between a negative LE and a zero beat frequency no longer holds in more complicated cases, as we shall discuss in the next sections, and is illustrated by the other curves in Fig. 6.5.

One can obtain further information about the frequency content of solutions by applying a Fourier transform, for a static picture, or a wavelet transform, for a time-resolved picture. In this periodic driving case, however, both methods yield equivalent results, as shown in by the constant content of the time-frequency representation in Fig. 6.4d–h). In the synchronised case shown in Fig. 6.4d, we see only one component, namely at $\frac{\omega_0}{2\pi}$, indicating that the driven frequency is entrained to that of the driver. The non-synchronised case is shown in Fig. 6.4h. In this case, we do not have frequency entrainment; instead, the driven oscillator is quasi-periodic, containing natural frequencies of both $\frac{\omega_0}{2\pi}$ (coming from the driving) and $\frac{\Omega_\psi}{2\pi}$.

Now that we have presented the simplest case, that of a periodic (fixed-frequency) driving, we consider more complicated driving scenarios.

6.4.2 *Single Oscillator: Noisy Periodic Driving*

Time-variability due to external perturbations is often modelled in the literature with noisy processes, as described in the Introduction. For the purpose of comparison with the deterministic autonomous and non-autonomous settings (the latter presented shortly), we now describe such a case where the driving in system (6.9) has a time-variable frequency modelled as

$$\dot{\theta}_0 = \omega_0 - \xi(t), \tag{6.18}$$

where $\xi(t)$ is a noise process. This system is schematically shown in Fig. 6.2b. The phase difference $\psi = \theta_1 - \omega_0 t$ now evolves as

$$\dot{\psi} = \Delta\omega + \gamma \sin\psi + \xi(t). \tag{6.19}$$

Analysis of this equation can be found in [49], and we present here only what is relevant to the comparison with the other systems of this chapter.

When $\gamma > |\Delta\omega|$, the effect of the noise term in Eq. (6.19) is to push the trajectory away from the stable fixed point ψ_S. If at any time this noisy perturbation becomes too strong, it can push the trajectory ψ all the way to the other side of the unstable fixed point, inducing a *phase slip* where ψ makes a quick full 2π revolution before returning to the vicinity of the stable fixed point. We now consider separately the case of unbounded noise and bounded noise.

If ξ is an unbounded noise process such as stationary Gaussian white noise, then phase slips will always take place, and so overall we do not have phase-locking between the driven and driving oscillators, regardless of the values of γ and $\Delta\omega$. Defining the mean frequency difference Ω_ψ according to Eq. (6.17), the phase slips induced by unbounded noise will completely destroy the $\Omega_\psi = 0$ plateau that was observed in Fig. 6.3c to correspond to $\gamma > |\Delta\omega|$ in the case of strictly periodic driving. However, the $\lambda < 0$ region which also corresponded to $\gamma > |\Delta\omega|$ as seen in Fig. 6.3b is not destroyed; instead, the extreme opposite happens, namely that the $\lambda < 0$ region becomes the entire $(\gamma, \Delta\omega)$-parameter space (see the analytical derivation in [49]). In other words, regardless of the parameter values the trajectories ψ of Eq. (6.19) have negative ALE. Physically, this indicates that different trajectories of the driven oscillator θ_1 evolving under a common noise realisation of $\xi(t)$ but starting at different initial phases $\theta_1(0)$ will mutually converge towards each other. Synchronisation of oscillators by common noise is a well-studied phenomenon, see for example [3, 37, 39, 47].

Now suppose ξ is a bounded noise process (e.g. dichotomous Markov noise [23]), meaning that $\xi(t)$ can only take values in a bounded interval. Then the $\Omega_\psi = 0$ plateau is decreased in width compared to the scenario without noise, as shown in Fig. 6.5b, and the $\lambda < 0$ region is widened compared to the scenario without noise, as shown in Fig. 6.5a. However, if the bound on the noise strength $|\xi(t)|$ is less than the coupling strength γ, then phase slips cannot occur when $|\Delta\omega|$ is small enough, and so the $\Omega_\psi = 0$ plateau is not completely destroyed.

So we have seen that in contrast to the deterministic case of strictly periodic driving considered in Sect. 6.4.1, now for both bounded and unbounded noise, having $\Omega_\psi = 0$ is not equivalent to having $\lambda < 0$. Indeed, they have different physical interpretations: having $\Omega_\psi = 0$ indicates that the frequency of the driven oscillator is entrained to that of the driving; but having a negative ALE $\lambda < 0$ indicates that the driven oscillator loses memory of its initial phase (i.e. solutions starting at different initial phases mutually converge) due to the influence of the driver.

We will see in the next Sect. 6.4.3 how the bounded noise case relates to that of a deterministic time-varying driving frequency.

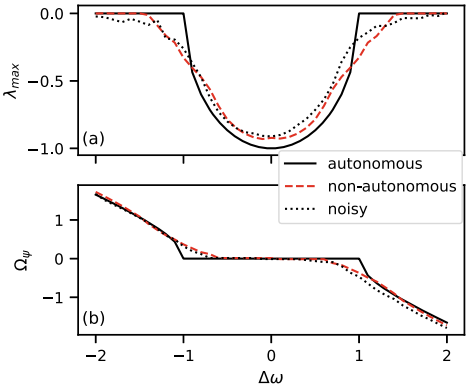

Fig. 6.5 Average quantities characterising synchronisation. **a** Asymptotic Lyapunov exponent and **b** beat frequency, for fixed-frequency driving (solid black), deterministically time-varying frequency of driving (dashed red), and noisy-frequency driving (dotted black), from systems (6.11), (6.21), and (6.19), respectively. For the noisy case, (bounded) dichotomous noise is used. Parameters are set to $\gamma = 1$ rad/s, $\omega_0 = 4$ rad/s, $k = 0.1$, dichotomous noise strength $D = 1.6\ \mathrm{s}^{-1}$ and transition constant $10\ \mathrm{s}^{-1}$

6.4.3 Single Oscillator: Time-Varying Frequency Driving

Another way to model time-variability is to use deterministic non-autonomous systems, instead of noise as in Sect. 6.4.2. We present system (6.9) with deterministic time-varying frequency, as in [35], obeying

$$\dot{\theta}_0 = \omega_0[1 + kf(\omega_m t)], \tag{6.20}$$

with modulation amplitude k, modulation frequency ω_m, and a bounded function f that determines the shape of the modulation. For the simulations in Fig. 6.7, we take $f(\cdot) = \sin(\cdot)$.

The phase difference $\psi = \theta_1 - \theta_0$ now obeys the non-autonomous equation

$$\dot{\psi} = \Delta\omega(t) + \gamma \sin\psi, \tag{6.21}$$

with time-varying frequency mismatch

$$\Delta\omega(t) = \omega - \omega_0(1 + kf(\omega_m t)) = \Delta\omega - \omega_0 kf(\omega_m t). \tag{6.22}$$

Such non-autonomous equations are generally harder to treat analytically than autonomous equations. For the remainder of this section, the frequency modulation is assumed to be very slow in comparison to the dynamics of the unmodulated system, i.e. ω_m is very small.

Recall that we presented the periodic case $k = 0$ in Sect. 6.4.1. In that case, depending on the parameters, either Eq. (6.11) has a stable fixed point and the driven

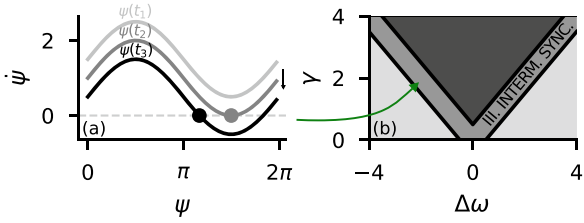

Fig. 6.6 Intermittent synchronisation in parameter space. **a** Intermittent existence of point attractor in Eq. (6.21) yields **b** the birth of region III of intermittent synchronisation in phase diagram, compared to the original diagram for periodic driving shown in Fig. 6.3

oscillator is synchronised to the driving, or Eq. (6.11) has no fixed point and the solution exhibits incoherence between the driven and the driving oscillator.

However, when we modulate the driving frequency, $k \neq 0$, as illustrated in Fig. 6.6 there are times t when the instantaneous stable fixed point $\psi_s(t) = \pi - \arcsin(-\Delta\omega(t)/\gamma)$ exists and other times when it does not. Namely, it exists when $\gamma > |\Delta\omega(t)|$ and does not exist when $\gamma < |\Delta\omega(t)|$. Since we assume a slow modulation, we have as in [22] that all trajectories converge "fast" to the slowly moving point $\psi_s(t)$ and follow it adiabatically as long as it exists, but when it does not exist the solutions exhibit unbounded growth of the phase difference, with no synchrony between the driver and driven oscillator. While $\gamma > |\Delta\omega(t)|$, the ILE $\lambda(t)$ at $\psi_s(t)$ is as in Eq. (6.13), namely $\lambda(t) = -\sqrt{\gamma^2 - \Delta\omega(t)^2}$. But while $\gamma < |\Delta\omega(t)|$, the ILE of any solution oscillates around 0.

Accordingly, we can consider in a time-localised manner the stability of the driven oscillator, by considering the FTLE $\lambda_T(t)$ over a time-window $[t, t+T]$, where T represents an intermediate timescale between the slow timescale of the driving frequency modulation and the fast timescale of the driven oscillator's internal dynamics. This intermediate-timescale FTLE will match the ALE of the differential equation obtained by freezing Eq. (6.21) at time t; that is,

$$\lambda_T(t) \approx \begin{cases} -\sqrt{\gamma^2 - \Delta\omega(t)^2} & \text{if } t : \gamma \geq |\Delta\omega(t)|, \\ 0 & \text{else.} \end{cases} \tag{6.23}$$

As a consequence of the intermittent existence of the instantaneous stable fixed point $\psi_s(t)$, three scenarios exist, as illustrated in Fig. 6.7, instead of two in the periodic case.

The first scenario is that of synchronisation at all times, and is illustrated in the top row of Fig. 6.7. This is the scenario where, even though the driving frequency changes, there exists a stable fixed point at all times: $\gamma \geq |\Delta\omega(t)|$ for all t. In this case, trajectories follow the slowly moving fixed point, as can be seen from the evolution of the phase difference $\psi(t)$, between each oscillator and the driving, in Fig. 6.7b. Physically, this means that at all times the frequency of the driven oscillator is entrained by the time-varying frequency of the driving, as shown in Fig. 6.7d. From the point of view of stability, the fixed point is always stable, hence the ILE is always negative, as shown in Fig. 6.7c. This scenario is very similar to the synchronisation scenario in the periodic case $k = 0$, except that now the oscillators' frequency and the ILE both modulate in time.

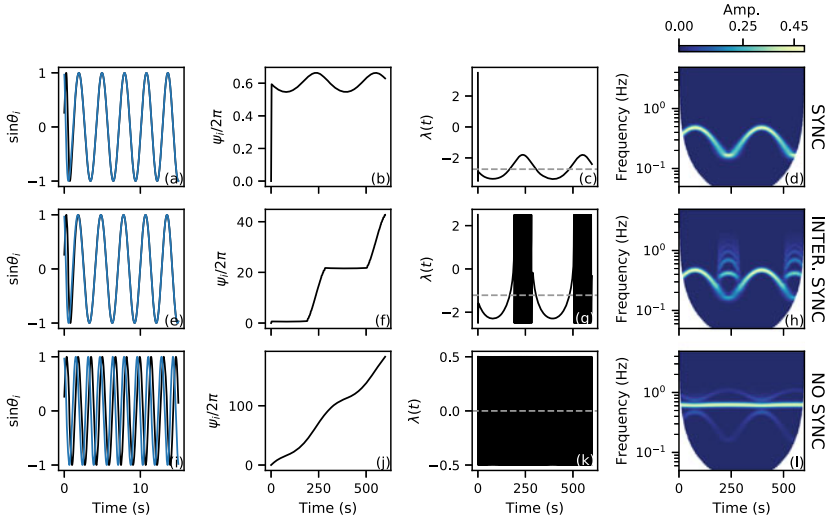

Fig. 6.7 Dynamical regimes of the single oscillator with time-varying frequency driving: synchronisation (top row, $\gamma = 3.5$ rad/s), intermittent synchronisation (middle row, $\gamma = 2.5$ rad/s), and no synchronisation (bottom row, $\gamma = 0.5$ rad/s). For each regime, we show **a** $\sin\theta$ over time for two random initial conditions, **b** the phase difference over time, **c** the instantaneous Lyapunov exponent (black) and the asymptotic Lyapunov exponent (dashed grey), as well as time-frequency representation of the time series $\sin\theta(t)$. Other parameters are set to $\omega_m = 0.02$ rad/s, $k = 0.5$, $\omega_0 = 2$ rad/s, and $\omega = 4$ rad/s. The time-frequency representation are computed with the Morlet wavelet transform ($p = 1$) with central frequency $f_0 = 3$

The second scenario is that of no synchronisation, and is illustrated in the bottom row of Fig. 6.7. This is the scenario where, even though the driving frequency changes, the fixed point does not exist at any time: $\gamma < |\Delta\omega(t)|$ for all t. In this case, there is no mutual convergence of different trajectories, as seen in Fig. 6.7i, and the phase difference $\psi(t)$, between each oscillator and the driving, exhibits unbounded monotonic growth, as seen in Fig. 6.7j. Physically, the frequency of the driven oscillator is not entrained by the time-varying frequency of the driving, and so multiple frequency modes appear in the time-frequency representation, as shown in Fig. 6.7l. From the point of view of stability, the trajectories are neutrally stable, with the ILE oscillating around 0 as shown in Fig. 6.7k. This scenario is very similar to the scenario of no synchronisation in the periodic case $k = 0$, except that now the phase difference drifts at a modulated rate, as seen in Fig. 6.7j and also reflected in the time-frequency representation in Fig. 6.7l.

The third scenario is that of intermittent synchronisation, and is illustrated in the middle row of Fig. 6.7. This is the scenario where, due to time-variability of the driving frequency, the stable fixed point exists some of the time but not all of the time. In this case, trajectories follow the slowly moving stable fixed point when it exists. As a result, the phase difference between each oscillator and the driving, $\psi(t)$ alternates between periods of drifts and periods where it is bounded, as shown in Fig. 6.7f.

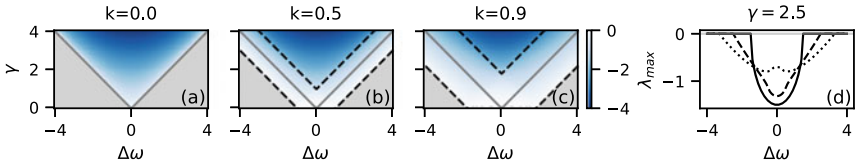

Fig. 6.8 Increase of stability region with the amplitude k of the frequency modulation. This is illustrated by the long-time (i.e. approximately asymptotic) Lyapunov exponent **a**–**c** over parameter space for increasing values of k. A negative value (shades of blue) indicates mutual convergence of trajectories, whereas a zero value (grey) does not. The grey line indicates the border of the stability region for $k = 0$, and the dashed black lines indicate the borders of regions I, II, and III. **d** The Lyapunov exponents values of panels **a**, **b**, and **c** are shown for a fixed $\gamma = 2.5$ in solid, dashed, and dotted black, respectively

Physically, this means that the frequency of the driven oscillator is entrained by the time-varying frequency of the driving only when the fixed point exists, as shown in Fig. 6.7h. From the point of view of stability, the driven oscillator exhibits time-localised stability when the fixed point exists, and time-localised neutrally stable when the fixed point does not exist. In particular, the ILE exhibits intermittency between periods where it is negative and periods where it oscillates with zero average, as in Fig. 6.7g. Even though trajectories are only intermittently synchronised to the driving, this is sufficient for different initial conditions to converge to a common trajectory, as shown in Fig. 6.7e. Indeed, trajectories mutually converge during epochs of negative ILE, but do not then diverge during the epochs where the ILE oscillates around zero. This scenario does not correspond to any dynamical behaviour that was observed in the periodic case $k = 0$. It is rather an alternation between the two previously known dynamical behaviours.

The mutual convergence of trajectories in the intermittent synchronisation scenario can also be understood from the value of the asymptotic Lyapunov exponent. Since the trajectories have an ILE that alternates between periods of being negative and periods of oscillating with zero average, the net effect is a negative ALE, signifying mutual convergence of trajectories.

As discussed in chapter [40] of this volume it is theoretically possible for the mutual synchronisation to be destroyed by canard-like phenomena where, due to an extreme "fluke" of fine-tuning of parameters, the trajectories spend time following the slow motion of the unstable fixed point and are thus re-dispersed. In such cases, we can fail to have a negative ALE. But, as one would expect, this is extremely rare.

An interesting consequence of the above analysis is that, as discussed in [35], the region in parameter space corresponding to overall stability, i.e. corresponding to the mutual convergence of trajectories towards each other, increases as the modulation amplitude k increases. As illustrated in Fig. 6.8, the region of intermittent synchronisation grows in proportion with k, while the region of perpetual synchronisation and the region of no synchronisation both diminish. Since the region of overall stability comprises of the union of the regions of perpetual synchronisation and intermittent synchronisation, this region grows with increasing k.

This stabilising effect of the external modulation can be compared to that of bounded noise illustrated in Fig. 6.5. The net effect averaged over long time is similar, such that curves showing the parameter-dependence of the ALE can be made to look similar between the case of bounded noise and the case of deterministic slow driving frequency modulation. The same is also true for the parameter-dependence of Ω_ψ, which likewise represents an average over infinite time. However, even if the effects of bounded noise and of slow deterministic modulation are similar to each other on average over long times, the actual dynamics observed in time is very different in nature. This is discussed in more detail in [35].

Now that we have described in detail the three dynamical regimes over short and long times, we generalise this to networks of oscillators in the next section.

6.4.4 *Network: Time-Varying Frequency Driving*

Now, results from the previous section are extended to networks. Instead of considering the single driven oscillator of system (6.9), we now present an arbitrary (undirected) network of N identical such oscillators, driven by the external phase $\theta_0(t)$, studied in [34]

$$\dot{\theta}_i = \omega + D\sum_{j=1}^{N} A_{ij}\sin(\theta_i - \theta_j) + \gamma\sin[\theta_i - \theta_0(t)], \tag{6.24}$$

with frequency ω, coupling constant D, symmetric adjacency matrix $\boldsymbol{A}$. Entries A_{ij} are set to 1 for connected oscillators, and 0 otherwise. All oscillators in the networks are driven with strength γ by the external oscillator $\theta_0(t)$ evolving according to Eq. (6.20) as in the previous section. As mentioned earlier, system (6.24) is a direct generalisation of Eq. (6.9) to networks.

Without external driving, $\gamma = 0$, the network converges to a fully synchronous solution $\theta_1(t) = \theta_2(t) = \cdots = \theta_N(t) = c + \omega t$ for some c, provided that the network does not have disconnected components, and that couplings are attractive, $D < 0$, see [58–60].

With external driving, $\gamma > 0$, three regimes are possible for the fully synchronous solution: it can synchronise to the external driving, or not synchronise to the external driving, or intermittently synchronise to the external driving. These regimes correspond to the three regimes of the previous section, Sect. 6.4.3, for a single driven oscillator. In fact, when all nodes in the network are in a synchronous state, they can be seen as one single node driven by the external phase. The region in parameter space for each of the regimes is also identical to the single oscillator case illustrated in Figs. 6.6 and 6.8 of Sect. 6.4.3.

For convenience, system (6.24) can be rewritten in the rotating reference frame of the driving oscillator, $\psi_i = \theta_i - \theta_0(t)$,

$$\dot{\psi}_i = \Delta\omega(t) + D\sum_{j=1}^{N} A_{ij}\sin(\psi_i - \psi_j) + \gamma\sin\psi, \tag{6.25}$$

where the time-varying frequency mismatch is $\Delta\omega(t) = \omega - \omega_0(1 + kf(\omega_m))$. When oscillators of the network are uncoupled, $D = 0$, we recover Eq. (6.21) from the single oscillator case of the previous section.

We now perform a linear stability analysis around the synchronous solution, which we denote $\tilde{\psi}(t)$. An infinitesimal heterogeneous perturbation $\delta\psi = (\delta\psi_1, \ldots, \delta\psi_N)$ evolves according to

$$\delta\dot{\psi}_i = -D\sum_{j=1}^{N} L_{ij}\delta\psi_j + \gamma\delta\psi_i\cos\tilde{\psi}(t). \tag{6.26}$$

This is an N-dimensional system, and hence the stability of these solutions is described by N Lyapunov exponents. However, it is possible to project the system onto N time-independent one-dimensional subspaces, reducing the N-dimensional problem to N one-dimensional problems. This reduction is done by using the eigenvectors ϕ_α and eigenvalues Λ_α, $\alpha = 1, \ldots, N$, of the Laplacian to project the perturbations $\delta\dot{\psi}_i = \sum_\alpha c_\alpha(\phi_\alpha)_i \exp(\int \lambda^\alpha(t)dt)$, with real constants c_α. We order these such that $\Lambda_1 \geq \Lambda_2 \geq \cdots \geq \Lambda_N$. Injecting this expression into (6.26) and solving yields for each $\alpha = 1, \ldots, N$ the ILE $\lambda^\alpha(t)$ corresponding to perturbation in the direction of ϕ_α, namely

$$\lambda^\alpha(t) = -D\Lambda_\alpha + \gamma\cos\tilde{\psi}(t). \tag{6.27}$$

The asymptotic counterpart is then given by

$$\lambda^\alpha = -D\Lambda_\alpha + \gamma\langle\cos\tilde{\psi}(t)\rangle \leq 0. \tag{6.28}$$

These Lyapunov exponents are made up of two contributions: that of the network interactions, proportional to D, and that of the external driving, proportional to γ. In the first term, the Laplacian matrix has one zero eigenvalue, $\Lambda_1 = 0$, and the rest are negative, $\Lambda_\alpha < 0$, for $\alpha \geq 2$. This implies that the first term is non-positive for any α. In the second term, the contribution is identical to that in the single oscillator case of the previous section: it is negative when the stable fixed point exists, $\gamma > |\Delta\omega(t)|$, but zero on average when it does not, $\gamma < |\Delta\omega(t)|$. So if, as in the previous section, we take an intermediate timescale T between the slow timescale of the modulation and the fast timescale of the internal dynamics of the driven oscillators θ_i, the FTLEs $\lambda_T^\alpha(t)$ over the time-window $[t, t+T]$ corresponding to perturbation in the direction of ϕ_α are given by

$$\lambda_T^1(t) \approx \begin{cases} -\sqrt{\gamma^2 - \Delta\omega^2(t)} & \text{if } t : \gamma \geq |\Delta\omega(t)|, \\ 0 & \text{else} \end{cases} \tag{6.29}$$

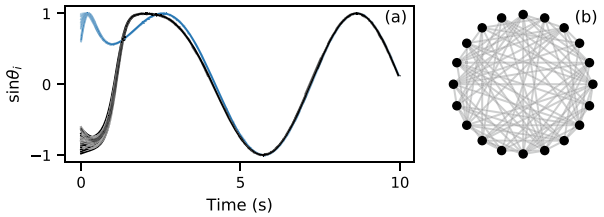

Fig. 6.9 Driven network with time-varying frequency: intermittent synchronisation yields convergence of different initial conditions. **a** Time series of two initial conditions (blue and black). The oscillators of each initial condition first synchronise between themselves, and then both initial conditions converge to the same trajectory. **b** These trajectories were simulated on a random network with wiring probability $p = 0.5$. Other parameters are set to $N = 20$, $\omega = 3$ rad/s, $\omega_0 = 1$ rad/s, $\gamma = 2$ rad/s, $D = -0.5$ rad/s, $k = 0.5$, $\omega_m = 0.02$ rad/s

and for $\alpha \geq 2$,

$$\lambda_T^{\alpha}(t) \approx \begin{cases} -D\Lambda_\alpha - \sqrt{\gamma^2 - \Delta\omega^2(t)} & \text{if } t : \gamma \geq |\Delta\omega(t)|, \\ -D\Lambda_\alpha < 0 & \text{else.} \end{cases} \tag{6.30}$$

These FTLEs for $\alpha \geq 2$ are always negative due to the attractive couplings between the oscillators in the network.

The first asymptotic Lyapunov exponent λ^1 corresponds to the eigenvector $\phi_1 = (1, \ldots, 1)^T$, i.e. a perturbation that pushes all synchronised oscillators in the same direction with the same strength. In other words, this perturbation does not affect how synchronous oscillators in network are with each other; it only affects the global phase of the fully synchronised oscillators. A zero value indicates neutral stability, and hence no synchronisation to the external driving, whereas a negative value indicates stability of the phase, i.e. synchronisation to the external driving. This is identical to the single oscillator case of the previous section, and so Fig. 6.8 is also valid for λ^1 of the present section. The subsequent ALEs, λ^α are negative, and hence ensure that the synchronous state—that is, $\theta_1(t) = \theta_2(t) = \cdots = \theta_N(t)$—is maintained in the face of any perturbation.

In conclusion, this section shows a natural generalisation of the previous section to the case of a driven network of identical oscillators. We illustrate in Fig. 6.9 the two different phenomena taking place: (1) the mutual convergence of different oscillators in the network due to the Lyapunov exponents $\lambda^\alpha < 0$ for all $\alpha \geq 2$, and (2) the mutual convergence of two different initial conditions due to $\lambda^1 < 0$. This is done in a random network, in which each link exists with probability $p = 0.5$.

6.4.5 Network: Time-Varying Driving Strength

In this section, we extend existing results to take into account a time-varying coupling strength. Here, we consider a slowly time-varying driving strength $\gamma(t)$ of the unidirectional driving of a phase oscillator θ_0 (of fixed frequency) upon a network of N identical oscillators. This is given by

$$\dot{\theta}_i = \omega + D\sum_{j=1}^{N} A_{ij}\sin(\theta_i - \theta_j) + \gamma(t)\sin[\theta_i - \omega_0 t], \tag{6.31}$$

where the driving strength varies as

$$\gamma(t) = \gamma_0 + kf(\omega_m t), \tag{6.32}$$

with very small ω_m. Similarly to the case of Sect. 6.4.4, the phase difference $\psi_i = \theta_i - \omega_0 t$ evolves as

$$\dot{\psi}_i = \Delta\omega + D\sum_{j=1}^{N} A_{ij}\sin(\psi_i - \psi_j) + \gamma(t)\sin\psi. \tag{6.33}$$

Similarly to Eq. (6.25), whenever $\gamma(t) > |\Delta\omega|$, the synchronous solution is attracted to the slowly moving point $\psi^*(t)$ given by $\psi_i^*(t) = \pi - \arcsin[-\Delta\omega/\gamma(t)]$ for all $i = 1, \ldots, N$. So once again, one can define three regions in parameter space, corresponding to the same three dynamical regimes for the synchronous solution as before: synchronisation to the driver, intermittent synchronisation to the driver, and no synchronisation to the driver. These are also based on the existence of the stable fixed point $\psi^*(t)$ at all time, some of the time, and never, respectively.

Without loss of generality we assume that $f(\omega_m t)$ is bounded in $[-1, 1]$ such that $\gamma_{\max} = \gamma_0 + k$ and $\gamma_{min} = \gamma_0 - k$. Just as in the time-varying-frequency case, the three regions are defined as satisfying the synchronisation $\gamma(t) > |\Delta\omega|$ at no times (I), at all times (II), or intermittently (III), which yields the following conditions

I.	$\gamma_0 < \lvert\Delta\omega\rvert - k$	No sync.	(6.34)
II.	$\gamma_0 > \lvert\Delta\omega\rvert + k$	Sync.	(6.35)
III.	$\lvert\Delta\omega\rvert + k > \gamma_0 > \lvert\Delta\omega\rvert - k$	Intermit. sync.	(6.36)

so that the regions are identical to the time-varying-frequency case of Sect. 6.4.4 and illustrated in Fig. 6.10.

Interestingly, the dynamics of the phase difference will vary with time even though the driving and the driven frequencies are constant, due to dynamics of the driving strength.

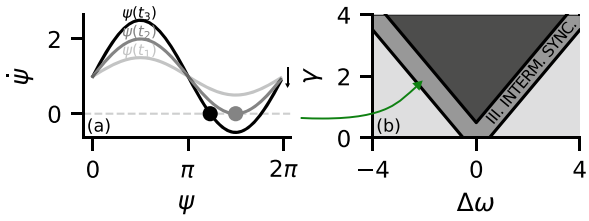

Fig. 6.10 Intermittent synchronisation in parameter space. **a** Intermittent existence of point attractor in Eq. (6.33) yields **b** the birth of region III of intermittent synchronisation in phase diagram, compared to the original diagram for periodic driving shown in Fig. 6.3

Finally, in addition to intermittent synchronisation induced from a time-varying frequency and a time-varying coupling strength, Hagos and coworkers reported that a time-varying coupling function (while keeping the total coupling strength constant), can also yield intermittent synchronisation [18].

6.5 Summary and Conclusions

In this chapter, we have reported on five models of increasing complexity, that investigate the effect of an ever-changing environment on the synchronisation of coupled oscillators. The first three models consisted of a unidirectionally coupled pair of oscillators, with the driving frequency taking different forms as a function of time. The last two models were driven networks of coupled oscillators, with (1) time-varying frequency of driving and (2) time-varying driving strength. The analysis of this last model was new.

In each of these models, we reported on the motion and stability of solutions (in particular, the synchronous solution for the last two models). In each case, the model was systematically analysed with time-resolved measures, such as finite-time Lyapunov exponents and time-frequency representations, as well as averaged quantities, such as asymptotic Lyapunov exponents. We discussed the appearance of a new dynamical regime, "intermittent synchronisation", induced by deterministic time-variability of parameters, and we also compared and contrasted this with the effect of introducing bounded noise into the driving frequency.

Including a deterministic source of temporal variation is a step closer to realistic modelling of oscillatory systems in nature. This regime of intermittent synchronisation, even though only implying intermittent time-localised stability, guarantees mutual convergence of initial conditions in the long term. For a more in-depth analysis of this long-term synchronisation of trajectories via intermittent synchronisation in the one-dimensional setting, see [40]. Intermittent synchronisation was also observed in a related but different setting in [18]. In addition, we reported on how time-varying parameters can enlarge the region in parameter space where synchronisation to the driver occurs and is stable. This mechanism could be one of the keys to understanding how living systems maintain stability in the face of their ever-changing environment. A natural future direction for this work is to develop methods of analysis of time-

series recordings for identification of such stability mechanisms in open systems, building upon the initial work of [29, 30].

In conclusion, we have studied oscillatory systems that are explicitly driven by time-variable external influences; such models aim at explicitly taking into account the thermodynamic openness that is crucial for living systems to stay alive. Modelling this openness deterministically and explicitly may be key to advancing our understanding of the underlying mechanisms at play in the stability of living systems, such as the brain [6], and even beyond, e.g. in cosmology [36].

Acknowledgements We would like to thank Joe Rowland Adams for useful feedback on the manuscript. We also would like to thank three anonymous referees for their useful comments which have helped to improve the manuscript. This study has been supported by an EPSRC Doctoral Prize Fellowship, the DFG grant CRC 701, the EPSRC grant EP/M006298/1, and the European Union's Horizon 2020 research and innovation programme under the Marie Skłodowska-Curie grant agreement No 642563.

References

1. D. Aeyels, Stability of nonautonomous systems by Liapunov's direct method. Banach Cent. Publ. **32**(1), 9–17 (1995)
2. V. Anagnostopoulou, T. Jaeger, Nonautonomous saddle-node bifurcations: random and deterministic forcing. J. Differ. Equations **253**(2), 379–399 (2012)
3. V.A. Antonov, Modeling of processes of cyclic evolution type. Synchronization by a random signal. Vestn. Leningr. Univ Mat Mekh Astron. (vyp. 2), 67–76 (1984)
4. A. Arenas, A. Díaz-Guilera, J. Kurths, Y. Moreno, C. Zhou, Synchronization in complex networks. Phys. Rep. **469**(3), 93–153 (2008)
5. P. Ashwin, S. Wieczorek, R. Vitolo, P. Cox, Tipping points in open systems: bifurcation, noise-induced and rate-dependent examples in the climate system. Phil. Trans. R Soc. A **370**(1962), 1166–1184 (2012)
6. J.D. Barrow, Conjecture about the general cosmological solution of Einstein's equations. Phys. Rev. D **102**(2), 024017 (2020)
7. P. Boškoski, D. Iatsenko, G. Lancaster, S. McCormack, J. Newman, G.V. Policharla, V. Ticcinelli, T. Stankovski, A. Stefanovska, PyMODA v0.1.0 (2020)
8. M. Bračič Lotrič, A. Stefanovska, Synchronization and modulation in the human cardiorespiratory system. Phys. A **283**(3–4), 451–461 (2000)
9. A. Carter, *Classical and Statistical Thermodynamics* (Prentice Hall, Raymond f. Boyer Library Collection, 2001)
10. P.T. Clemson, A. Stefanovska, Discerning non-autonomous dynamics. Phys. Rep. **542**(4), 297–368 (2014)
11. B. de Saedeleer, M. Crucifix, S. Wieczorek, Is the astronomical forcing a reliable and unique pacemaker for climate? A conceptual model study. Clim. Dyn. **40**(1–2), 273–294 (2013)
12. M. Faggian, F. Ginelli, F. Rosas, Z. Levnajić, Synchronization in time-varying random networks with vanishing connectivity. Sci. Rep. **9**(1), 10207 (2019)
13. P. Gandhi, E. Knobloch, C. Beaume, Dynamics of phase slips in systems with time-periodic modulation. Phys. Rev. E **92**(6), 062914 (2015)
14. C. Gardiner, *Stochastic Methods*, vol. 4 (Springer, Berlin, 2009)
15. P. Gaspard, Cycles, randomness, and transport from chaotic dynamics to stochastic processes. Chaos **25**(9), 097606 (2015)
16. M. Ghil, The wind-driven ocean circulation: applying dynamical systems theory to a climate problem. Discrete Contin. Dyn. Syst. A **37**(1), 189–228 (2017)

17. M. Ghil, M.D. Chekroun, E. Simonnet, Climate dynamics and fluid mechanics: natural variability and related uncertainties. Phys. D **237**(14–17), 2111–2126 (2008)
18. Z. Hagos, T. Stankovski, J. Newman, T. Pereira, P.V. McClintock, A. Stefanovska, Synchronization transitions caused by time-varying coupling functions. Philos. Trans. R Soc. A **377**(2160), 20190275 (2019)
19. P. Holme, Modern temporal network theory: a colloquium. Eur. Phys. J B **88**(9), 234 (2015)
20. P. Holme, J. Saramäki, Temporal networks. Phys. Rep. **519**(3), 97–125 (2012)
21. A. Iggidr, G. Sallet, On the stability of nonautonomous systems. Automatica **39**(1), 167–171 (2003)
22. R.V. Jensen, Synchronization of driven nonlinear oscillators. Am. J. Phys. **70**(6), 607–619 (2002)
23. C. Kim, E.K. Lee, P. Talkner, Numerical method for solving stochastic differential equations with dichotomous noise. Phys. Rev. E **73**(2), 026101 (2006)
24. P.E. Kloeden, C. Pötzsche, Nonautonomous dynamical systems in the life sciences, in *Nonautonomous Dynamical Systems in the Life Sciences* (Springer, 2013), pp. 3–39
25. P.E. Kloeden, M. Rasmussen, *Nonautonomous Dynamical Systems* (American Mathematical Society, Providence, 2011)
26. Y. Kuramoto, Self-entrainment of a population of coupled non-linear oscillators title, in *International Symposium on Mathematical Problems in Theoretical Physics*, Kyoto (1975), pp. 420–422
27. W. Kurebayashi, S. Shirasaka, H. Nakao, Phase reduction method for strongly perturbed limit cycle oscillators. Phys. Rev. Lett. **111**(21), 214101 (2013)
28. W. Kurebayashi, S. Shirasaka, H. Nakao, A criterion for timescale decomposition of external inputs for generalized phase reduction of limit-cycle oscillators. NOLTA **6**(2), 171–180 (2015)
29. G. Lancaster, P.T. Clemson, Y.F. Suprunenko, T. Stankovski, A. Stefanovska, Detecting chronotaxic systems from single-variable time series with separable amplitude and phase. Entropy **17**(6), 4413–4438 (2015)
30. G. Lancaster, Y.F. Suprunenko, K. Jenkins, A. Stefanovska, Modelling chronotaxicity of cellular energy metabolism to facilitate the identification of altered metabolic states. Sci. Rep. **6**, 29584 (2016)
31. J.A. Langa, J.C. Robinson, A. Suárez, Stability, instability, and bifurcation phenomena in non-autonomous differential equations. Nonlinearity **15**(3), 887 (2002)
32. J.P. LaSalle, Stability of nonautonomous systems. Technical Report, Brown Univ. Providence Ri Lefschetz Center for Dynamical Systems (1976)
33. M. Lucas, D. Fanelli, T. Carletti, J. Petit, Desynchronization induced by time-varying network. EPL **121**(5), 50008 (2018)
34. M. Lucas, D. Fanelli, A. Stefanovska, Nonautonomous driving induces stability in network of identical oscillators. Phys. Rev. E **99**(1), 012309 (2019)
35. M. Lucas, J. Newman, A. Stefanovska, Stabilization of dynamics of oscillatory systems by nonautonomous perturbation. Phys. Rev. E **97**(4), 042209 (2018)
36. D.J. Lurie, D. Kessler, D.S. Bassett, R.F. Betzel, M. Breakspear, S. Kheilholz, A. Kucyi, R. Liégeois, M.A. Lindquist, A.R. McIntosh et al., Questions and controversies in the study of time-varying functional connectivity in resting fMRI. Netw. Neurosci. **4**(1), 30–69 (2020)
37. D. Malicet, Random walks on Homeo(S^1). Commun. Math. Phys. **356**(3), 1083–1116 (2017)
38. D.R. Merkin, The stability of nonautonomous systems, in *Introduction to the Theory of Stability* (Springer, 1997)
39. J. Newman, Necessary and sufficient conditions for stable synchronization in random dynamical systems. Ergod. Theory Dyn. Syst. 1–19 (2017)
40. J. Newman, M. Lucas, A. Stefanovska, Non-asymptotic-time Dynamics. In: Physics of Biological Oscillators (Springer, Berlin, 2020)
41. V.I. Oseledets, A multiplicative ergodic theorem. Characteristic Ljapunov, exponents of dynamical systems. Tr. Mosk. Mat. Obs. **19**, 179–210 (1968)
42. W. Ott, J.A. Yorke, When Lyapunov exponents fail to exist. Phys. Rev. E **78**(5), 056203 (2008)

43. A. Palmigiano, T. Geisel, F. Wolf, D. Battaglia, Flexible information routing by transient synchrony. Nat. Neurosci. **28**(3), 1–9 (2017)
44. Y. Park, G.B. Ermentrout, Weakly coupled oscillators in a slowly varying world. J. Comput. Neurosci. **40**(3), 269–281 (2016)
45. S. Petkoski, A. Stefanovska, The Kuramoto model with time-varying parameters. Phys. Rev. E **86**(4), 046212 (2012)
46. B. Pietras, A. Daffertshofer, Ott-Antonsen attractiveness for parameter-dependent oscillatory systems. Chaos **26**(10), 103101 (2016)
47. A.S. Pikovskii, Synchronization and stochastization of array of self-excited oscillators by external noise. Radiophys. Quantum Electron. **27**(5), 390–395 (1984)
48. A. Pikovsky, A. Politi, *Lyapunov Exponents: A Tool to Explore Complex Dynamics* (Cambridge University Press, Cambridge, UK, 2016)
49. A. Pikovsky, M. Rosenblum, J. Kurths, *Synchronization: A Universal Concept in Nonlinear Sciences* (Cambridge University Press, Cambridge, UK, 2003)
50. M. Rasmussen, Finite-time attractivity and bifurcation for nonautonomous differential equations. Differ. Equ. Dynam Syst. **18**(1), 57–78 (2010)
51. E. Schrödinger, *What Is Life?* (Cambridge University Press, Cambridge, 1944)
52. A. Stefanovska, Coupled oscillators: complex but not complicated cardiovascular and brain interactions. IEEE Eng. Med. Biol. Mag. **26**(6), 25–29 (2007)
53. A. Stefanovska, H. Haken, P.V.E. McClintock, M. Hožič, F. Bajrović, S. Ribarič, Reversible transitions between synchronization states of the cardiorespiratory system. Phys. Rev. Lett. **85**(22), 4831–4834 (2000)
54. S.H. Strogatz, *Sync: The Emerging Science of Spontaneous Order* (Penguin, UK, 2004)
55. S.H. Strogatz, *Nonlinear Dynamics and Chaos: With Applications to Physics, Biology, Chemistry, and Engineering*, 2nd edn. (Westview Press, Boulder, 2014)
56. Y.F. Suprunenko, P.T. Clemson, A. Stefanovska, Chronotaxic systems: a new class of self-sustained nonautonomous oscillators. Phys. Rev. Lett. **111**(2), 024101 (2013)
57. Y.F. Suprunenko, A. Stefanovska, Generalized chronotaxic systems: time-dependent oscillatory dynamics stable under continuous perturbation. Phys. Rev. E **90**(3), 32921 (2014)
58. R. Toenjes, B. Blasius, Perturbation analysis of complete synchronization in networks of phase oscillators. Phys. Rev. E **80**(2), 026202 (2009)
59. S. Watanabe, S.H. Strogatz, Integrability of a globally coupled oscillator array. Phys. Rev. Lett. **70**(16), 2391 (1993)
60. S. Watanabe, S.H. Strogatz, Constants of motion for superconducting Josephson arrays. Phys. D **74**(3–4), 197–253 (1994)
61. A.T. Winfree, Biological rhythms and the behavior of populations of coupled oscillators. J. Theor. Biol. **16**(1), 15 (1967)

Chapter 7
Non-asymptotic-time Dynamics

Julian M. I. Newman, Maxime Lucas, and Aneta Stefanovska

Abstract Traditional analysis of dynamics concerns coordinate-invariant features of the long-time-asymptotic behaviour of a system. Using the non-autonomous Adler equation with slowly varying forcing, we illustrate three of the limitations of this traditional approach. We discuss an alternative, "slow-fast finite-time dynamical systems" approach, that is more suitable for slowly time-dependent one-dimensional phase dynamics, and is likely to be suitable for more general dynamics of open systems involving two or more timescales.

7.1 Introduction

In recent decades, the limitations of long-time-asymptotic approaches to dynamical systems analysis have been increasingly recognised, giving rise to the birth of *finite-time dynamical systems* (FTDS) theory. In this chapter, building upon considerations from the chapter [24] of this same volume, we illustrate these limitations through the dynamics of a non-autonomous Adler equation with slowly varying forcing. Furthermore, we briefly introduce the concept of dynamics analysis via a slow-fast limit of finite-time dynamical systems, which is more suitable for describing this system than traditional long-time-asymptotic analysis is.

J. M. I. Newman (✉)
Exeter University, Exeter, UK
e-mail: J.M.I.Newman@exeter.ac.uk

M. Lucas
Aix-Marseille University, Marseille, France
e-mail: maxime.lucas.1@univ-amu.fr

A. Stefanovska
Lancaster University, Lancaster, UK
e-mail: aneta@lancaster.ac.uk

A. Stefanovska and P. V. E. McClintock (eds.), *Physics of Biological Oscillators*, Understanding Complex Systems,
https://doi.org/10.1007/978-3-030-59805-1_7

7.1.1 Classical Dynamical Systems Theory

Dynamical systems theory describes the "qualitative" behaviour of processes evolving according to some given law. As a mathematical discipline, it dates back to Henri Poincaré [29] and Aleksandr Lyapunov [25]; a particular goal of this theory was to describe properties—particularly stability properties—of celestial orbits.

The fundamental assumption underlying the modelling of celestial mechanics is that each celestial body is a point particle, whose instantaneous acceleration is determined from the instantaneous configuration of the positions of all the celestial bodies, by *Newton's universal law of gravitation*. This law stipulates the existence of a universal non-time-varying constant of nature in terms of which the (similarly time-independent) mathematical relation between forces and distances is then formulated. This model of celestial mechanics means, in particular, that the future motion of celestial bodies starting from any given initial configuration of positions and velocities is in no way dependent on the *time* at which the bodies start in this initial configuration. In other words, the Newtonian formulation of celestial mechanics is, in a way, "timeless": although *increments of time* are of physical meaning and significance, *absolute times* are not. Or in the language of dynamical systems theory: the law specifying the time-evolution of the position-velocity configuration of a system of interacting celestial bodies is an *autonomous dynamical system*.

As described in the preceding chapter [24], a dynamical system is called *autonomous* if the future evolution that it specifies from any given current state has no dependence on the current time. Autonomous dynamical systems serve as mathematical models for the time-evolution of the state of an *isolated* physical system. A physical system is called isolated if it exchanges neither matter nor energy with its environment. Since the pioneering work of Poincaré and Lyapunov, the mathematical theory of autonomous dynamical systems has become extremely well-developed over the last century, and new and important advances continue to be made. This theory includes mathematical formalisms for some of the most fundamental questions that one can ask about a physical system's behaviour in time, such as *stability* or *chaos*, as well as how this behaviour depends on the system's parameters. Such mathematical formalisms include *asymptotic stability*, *stability in the sense of Lyapunov* (formalising the physical concept of "neutral stability"), various mathematical definitions of chaos, and also *asymptotic Lyapunov exponents* (ALEs) which are often used to quantify stability or chaos [24]. Two important features of these various mathematical formalisms for the questions one can ask about a system's qualitative or quantitative dynamics are as follows.

- They give the same answer after a change of coordinates of the state space of the system.
- For any finite time-interval $[0, T]$ (however large T may be), the answer is independent of the behaviour of the system on the time-interval $[0, T]$.

Properties of dynamical systems that fulfil the latter of these are referred to as *long-time-asymptotic* properties. These only make sense if the dynamical system is itself

well-defined on infinite time; but in the setting of autonomous dynamical systems, this is not generally a problem. As above, long-time-asymptotic properties include traditionally defined notions of stability and neutral stability, as well as asymptotic Lyapunov exponents.

The classical theory of autonomous dynamical systems has been applied throughout the sciences to describe the qualitative behaviour of systems given a quantitative model, and inversely to inform the inference of underlying physics from observational data [28, 34].

7.1.2 The Limitations of Long-Time-Asymptotic Analysis

The aim of the present chapter is to explore some of the ways in which long-time-asymptotic formalisms of stability can be inadequate or unsuitable when studying open systems and the parameter-dependence of their stability.

As we have seen in Chap. 6 [24], in order to model the time-evolution of a process subject to time-variable external influences (i.e. a process that does not possess the kind of "timelessness" described above for Newtonian celestial mechanics), it would not be suitable to use an autonomous dynamical system defined on the space of states of the process. Instead, *non-autonomous* [18] and *noise-perturbed* [1] dynamical systems can be used. (It is well-known that one can convert a non-autonomous system on the state space into an autonomous system on the higher-dimensional state-time space. But this does not make traditional autonomous dynamical systems theory, as developed for isolated systems, applicable to analysis of open systems: all solutions of this higher-dimensional system simply blow up to infinity as their time-coordinate blows up to infinity [18, Remark 2.5].)

Nonetheless, merely carrying over traditional long-time-asymptotic analysis methods from the classical autonomous setting to the non-autonomous setting *still* inherently limits the extent to which the free time-variability of open systems can be suitably treated. The main points that we will highlight in this chapter (see also [15, Sects. 1.1, 6]) are:

(1) that the behaviour of an open system on the finite timescales of interest need not follow (even approximately) any particular deterministic or statistical rule that can be extended indefinitely in time;
(2) that a finite-time dynamical model which admits no natural extension to infinite time may still clearly exhibit important dynamical phenomena;
(3) that even for an indefinite-time non-autonomous model, simply pursuing a long-time-asymptotic analysis of dynamics may *hinder* the recognition of physically significant dynamical phenomena.

Chapter 6 [24] highlighted how non-autonomous driving can induce stability, through the example of a phase oscillator governed by the Adler equation being driven by an external phase oscillator with time-dependent frequency, where the

frequency modulation of the driving oscillator is such that the driven oscillator intermittently synchronises with the driving oscillator. We will use this same example to illustrate the above three points; further details are presented in [27]. The physical phenomenon of phase stabilisation by time-dependent external influence has previously been described within the framework of *chronotaxic oscillators* [33], where the mathematical concept of pullback-attraction in deterministic nonautonomous dynamical systems was used to describe the stability of self-sustained oscillators with time-dependent phase dynamics. However, this requires the model of the time-dependent external forcing to be well-defined indefinitely far back into the past. This present chapter draws attention to how the same physical stabilisation effect can be understood in terms of dynamical behaviour on bounded time-intervals even when indefinite-time models are inherently irrelevant or unsuitable.

Now let us mention that the paper [27], and this present chapter, are far from being the first investigation into finite-time dynamics motivated by the limitations of long-time-asymptotic dynamics. The field of non-autonomous finite-time dynamical systems, though relatively recent, has seen important progress being made [2, 3, 5, 9, 15, 16, 21, 31]. So far, the primary application of FTDS theory has been the study of *Lagrangian coherent structures* in diverse fluid flows [10, 11, 13, 20, 26, 30, 32, 35, 36, 38]. Other examples include population dynamics [37] and activation of biochemical signalling pathways [3]. Our present contribution to this field of finite-time dynamics is the consideration of FTDS with slow-timescale driving (as formalised in Sect. 7.5). Let us mention that fast-timescale driving of the Adler equation has also been treated rigorously from a finite-time perspective in [8], in the context of synchronisation transitions induced by time-dependence of the shape of phase-coupling function.

7.1.3 Structure of the Chapter

In Sect. 7.2, we will present a general analysis of Adler equations with slowly time-dependent additive forcing, following the same line of reasoning as in the chapter [24]. In particular, in Sect. 7.2.4 we will describe the time-variability-induced stabilisation phenomenon that forms the basis of the considerations in this chapter. In Sect. 7.3, we will illustrate points (1) and (2) of Sect. 7.1.2 through the example of an Adler equation driven by a low-pass-filtered sample realisation of a Brownian bridge. In Sect. 7.4, we will illustrate point (3) of Sect. 7.1.2 through the example of an Adler equation with slow sinusoidal driving. In Sect. 7.5, we will briefly describe the framework of slow-fast FTDS that can be used to formalise the stabilisation phenomenon seen in both [24] and this chapter. In Sect. 7.6, we will summarise and conclude.

7.2 The Non-autonomous Adler Equation

As in [24], the phase difference for a unidirectionally coupled pair of phase-oscillators with Kuramoto-type coupling can be modelled by an *Adler equation* with additive forcing, i.e.

$$\dot{\theta}(t) \;=\; -a\sin(\theta(t)) + G(t). \tag{7.1}$$

Physically, if the oscillator-pair is an isolated system then the driving frequency will be constant (i.e. not time-dependent), and as a result the term $G(t)$ will simply be a constant (i.e. with no dependence on t). In this case, (7.1) is an autonomous dynamical system on the circle. But if, instead, the driving oscillator is open to external influence, then this is likely to mean that the driving frequency will be time-dependent, and as a result the term $G(t)$ will depend on t. In this case, (7.1) is a non-autonomous dynamical system on the circle. In either case, for studying dynamics, we can without loss of generality take $a > 0$.

For our consideration here, just as in the previous chapter [24], we will take the forcing term $G(t)$ to be slowly time-dependent, corresponding to slow frequency modulation of the driving oscillator. In other words, the timescale of variation of $G(t)$ is slower than the timescale of the dynamics of θ itself. (This can be formalised as in Sect. 7.5.).

7.2.1 Stability and Neutral Stability in the Autonomous Case

Before considering the non-autonomous case where $G(t)$ depends slowly on t, let us first consider the autonomous case where G is constant, in which case we can apply a classical dynamical systems analysis to (7.1).

- If $G \in (-a, a)$, all solutions $\theta(t)$ of (7.1) converge to the sink $y := \arcsin\left(\frac{G}{a}\right)$, apart from the repulsive constant solution at the source $\pi - \arcsin\left(\frac{G}{a}\right)$. Hence in particular, for any solution other than the repulsive solution, a small perturbation to the initial condition will be "forgotten over time", since eventually the solution will settle at the sink in any case. This "loss of memory of perturbation" corresponds physically to *stability*. The separation between solutions starting at different initial conditions (other than the source) will decay at an exponential rate, with exponent $-a\cos(y) = -\sqrt{a^2 - G^2}$; this is the ALE of every trajectory of (7.1) other than the single repulsive trajectory, and quantifies the system's stability.
- If $G \notin [-a, a]$, all the trajectories $\theta(t)$ of (7.1) move strictly periodically round the circle with common period $\int_0^{2\pi} \frac{d\theta}{|-a\sin(\theta)+G|} = \frac{2\pi}{\sqrt{G^2-a^2}}$. Hence, on the one hand, the separation between solutions starting at two nearby conditions does not decay as time tends to infinity, but on the other hand, the two solutions will remain nearby forever. So the effect of a small perturbation to a solution's initial condition will

not be forgotten but nonetheless it will remain small. This corresponds physically to *neutral stability*. In this case, the ALE of every trajectory is 0.

So in short, if $G \in (-a, a)$ then the system (7.1) describes a stable process, but if $G \notin [-a, a]$ then the system (7.1) describes a neutrally stable process.

Finally, let us briefly mention the *boundary between stability and neutral stability*, which occurs when $|G|$ is *exactly* equal to a. In this case, there is a unique fixed point, which is attracting from one direction but is unstable due to being repelling in the other direction, and all trajectories converge to this unstable fixed point and have an ALE of 0. For most of this chapter, we will leave out the analysis of such degenerate cases lying on the boundary between two scenarios.

7.2.2 Stability and Neutral Stability in the Non-autonomous Case

In view of the above statemets for the autonomous case, now under the assumption that $G(t)$ varies very slowly with time t, a "conceptual-level" analysis of (7.1) gives us the following:

- While $G(t) \in (-a, a)$, the trajectories move away from the vicinity of the *slowly moving source* $\pi - \arcsin\left(\frac{G(t)}{a}\right)$, and cluster together into an increasingly tight cluster near the *slowly moving sink* $y(t) := \arcsin\left(\frac{G(t)}{a}\right)$. In this clustering, the separation between different trajectories decays approximately according to an exponential decay of exponent $-a\cos(y(t)) = -\sqrt{a^2 - G(t)^2}$.
- While $G(t) \notin [-a, a]$, trajectories move approximately periodically round the circle with common approximate period $\frac{2\pi}{\sqrt{G(t)^2 - a^2}}$.
- Thus overall, over a given time-interval $[0, T]$, we have the following:

(a) If there are subintervals during which $G(t) \in (-a, a)$, then the solutions starting at different initial conditions end up clustered extremely close to each other (apart from those solutions that start extremely near the maximally repulsive solution which follows the slowly moving source while $G(t) \in (-a, a)$). So the effect of a perturbation to a solution's initial condition will eventually be forgotten over time.

(b) If there are no times at which $G(t) \in [-a, a]$ then the system does not exhibit significant separation or attraction between the trajectories of different initial conditions. So the effect of a small perturbation to a solution's initial condition will not be forgotten but on the other hand will remain small.

Once again, the loss of memory of initial condition in case (a) corresponds physically to *stability*, and the lack of significant mutual attraction or separation of solutions in case (b) corresponds physically to *neutral stability*.

The above adiabatic reasoning is precisely the reasoning behind the stabilisation phenomenon observed in Sect. 6.4.3 of the chapter [24]. Here in this chapter, we will highlight how the stabilisation arising from this inherently finite-time reasoning does not, in general, lend itself to being formalised and quantified in terms of traditional long-time-asymptotic mathematical formalisms. This stands in contrast to the noise-induced stability described in Sect. 6.4.2 of the chapter [24], the theory of which is inherently tied to the model's long-time-asymptotic dynamics.

7.2.3 *Quantitative Rate of Synchronisation of Trajectories*

As in [14], an approximate overall exponential separation rate $\Lambda \leq 0$ between solutions of (7.1) over a time-interval $[0, T]$ can be computed in accordance with the above adiabatic reasoning. Namely, recalling that there is no significant mutual separation or attraction of trajectories while $|G(t)| > a$, but that while $|G(t)| < a$ the separation between trajectories decays with exponential rate $-\sqrt{a^2 - G(t)^2}$, we obtain overall the approximate exponential separation rate

$$\Lambda \;=\; -\frac{1}{T}\int_{\{s\in[0,T]:|G(s)|<a\}} \sqrt{a^2 - G(t)^2}\, dt. \tag{7.2}$$

More precisely, this quantity Λ serves as an estimate for the *finite-time Lyapunov exponent* λ_T, over the time-window $[0, T]$, of trajectories of (7.1). Note that Λ must be either 0 or negative, with 0 corresponding to neutral stability and a negative value corresponding to stability.

7.2.4 *Transition from Neutral Stability to Stability*

In this chapter, we will consider $G(t)$ taking the form $k + Ag(t)$ where $A \geq 0$ is a parameter representing the breadth of time-variability. That is, we consider the non-autonomous Adler equation

$$\dot{\theta}(t) \;=\; -a\sin(\theta(t)) + k + Ag(t). \tag{7.3}$$

Consider $g(t)$ on a time-interval $t \in [0, T]$, and suppose that $g(t)$ takes both positive and negative values on $[0, T]$. If $k > a$, then letting

$$A_* := \frac{a-k}{\min_{t\in[0,T]} g(t)} > 0, \tag{7.4}$$

the reasoning in Sect. 7.2.2 yields the following:

- if $A < A_*$ then the trajectories of (7.3) exhibit neutral stability,
- but if $A > A_*$ then the trajectories of (7.3) exhibit stability.

In physical terms, sufficiently broadly time-variable forcing induces phase stability in an oscillatory process evolving according to the model (7.3). The chapter [24] presents the stabilisation phenomenon from the point of view of the overall region of stability in parameter space. The value A_* represents the *critical A-value* for the transition between neutral stability and stability.

7.2.5 Numerics for the Non-autonomous Adler Equation

To aid physical intuition, in the presentation of all our numerics, time t is considered as real time measured in units of seconds, and all other parameters and variables have the appropriate units accordingly. Throughout this chapter, solutions of Eq. (7.1) are simulated by numerical integration using a 4th order Runge-Kutta scheme, with a time step of 0.01 s. For the reverse-time bifurcation diagrams, to obtain the initial condition $\theta(0)$ for a given final state $\theta(T)$, the value of $\theta(T)$ was used as the initial condition $\theta_{back}(0)$ of a forward-time simulation of the differential equation $\dot{\theta}_{back}(t) = a\sin(\theta_{back}(t)) - G(T-t)$, and then $\theta(0)$ was taken as $\theta_{back}(T)$.

7.3 A Toy Model of "inherently Finite-Time" Dynamics

In this section, we use the stabilisation phenomenon described in Sect. 7.2.4 to illustrate that stability and neutral stability can be central among the physical properties of a finite-time process even if the process's dynamics cannot be described by the long-term behaviour of an infinite-time mathematical model of the process. In this case, such stability properties cannot be formalised and quantified by the traditional mathematical formalisms such as asymptotic Lyapunov exponents.

Specifically, as a finite-time adaptation of the indefinite-time ergodic Gaussian process considered in [14], we consider here the non-autonomous Adler equation (7.3) with $g(t)$ being a low-pass-filtered sample realisation of a *Brownian bridge*, as illustrated in Fig. 7.1.

7.3.1 Definition and Basic Properties of a Brownian Bridge

A Brownian bridge is a finite-time stochastic process that models the inhomogeneity of a large sample of random times selected mutually independently from the uniform distribution on a pre-specified finite time-interval. Namely, fixing a finite time-interval $[0, \tau]$ and a value $\sigma > 0$ (analogous to the *diffusion parameter* of

a Brownian motion), a *Brownian bridge* $(B_t)_{t\in[0,\tau]}$ *on* $[0,\tau]$ *with parameter* σ is approximated by taking an i.i.d. sample $S = \{T_1, \ldots, T_N\}$ of large size N from the uniform distribution on $[0,\tau]$, and setting

$$B_t \;=\; \sigma\sqrt{N\tau}\left(P_S([0,t]) - \frac{t}{\tau}\right)$$

where $P_S([0,t])$ is the proportion of the sample S that lies within $[0,t]$, i.e. $P_S([0,t]) = \frac{\#(S\cap[0,t])}{N}$. The well-definedness of the limit as $N\to\infty$ is given by *Donsker's theorem* [4, Theorem 1.1.1]. Note that $B_0 = B_\tau = 0$.

Let us now outline the connection between a Brownian bridge and a Brownian motion. A (*zero-drift*) *Brownian motion with diffusion parameter* σ is an infinite-time stochastic process $(M_t)_{t\in\mathbb{R}}$ with continuous time-dependence, such that increments in M_t over consecutive time-intervals are independent of each other, and M_t has mean 0 and standard deviation $\sigma\sqrt{|t|}$. Now given a finite time $\tau > 0$, one can construct a portion $(M_t)_{t\in[0,\tau]}$ of a Brownian motion $(M_t)_{t\in\mathbb{R}}$ with diffusion parameter σ as the sum of two independent components,

$$M_t = tX + B_t, \tag{7.5}$$

where $(B_t)_{t\in[0,\tau]}$ is a Brownian bridge on $[0,\tau]$ with parameter σ, and X is a normal random variable independent of $(B_t)_{t\in[0,\tau]}$ with mean 0 and standard deviation $\frac{\sigma}{\sqrt{\tau}}$. There is no way to define B_t for $t > \tau$ so as to extend the construction (7.5) of Brownian motion beyond time τ: for any $t > \tau$, the standard deviation $\frac{\sigma t}{\sqrt{\tau}}$ of the component tX is already larger than the standard deviation $\sigma\sqrt{t}$ of M_t.

7.3.2 *Finite-Time Non-autonomous Adler Equation*

We consider the model (7.3) with $g\colon [0,\tau]\to\mathbb{R}$ as shown in Fig. 7.1, where $\tau = 2\pi\times 10^5$ s. Since the construction of g (as detailed shortly) is based on a sample realisation of a Brownian bridge, and Brownian bridges admit no natural extension to infinite time, the model we consider exemplifies point (1) of the three main points in Sect. 7.1.2. In this section, we will compare numerical simulation of this model with the picture presented in Sect. 7.2.4 and observe clear agreement. This will serve to exemplify point (2) of the abovementioned three points in Sect. 7.1.2.

The function $g(t)$ was constructed as follows. First, a sample realisation (M_t) of a zero-drift Brownian motion with diffusion parameter $\frac{1}{\sqrt{\tau}}$ was constructed on $[0,\tau]$, by cumulative addition of independent and identically distributed Gaussian increments, with a time-step of 0.01 s. (The purpose of taking $\frac{1}{\sqrt{\tau}}$ for the diffusion is simply to help "bound" this long-duration process; it means that M_τ has a standard deviation of 1.) A corresponding sample realisation $(B_t)_{t\in[0,\tau]}$ of a Brownian bridge of parameter $\frac{1}{\sqrt{\tau}}$ was then constructed as $B_t = M_t - \frac{t}{\tau}M_\tau$. Finally, $(g(t))_{t\in[0,\tau]}$ was

obtained by passing $(B_t)_{t\in[0,\tau]}$ through a 5th order Butterworth low-pass filter with cut-off frequency $1/(2\pi \times 10^3)$ Hz, performed via cascaded second-order sections (in Python, with the function "scipy.signal.sosfilt"), and we linearly interpolated the output of the filter.

Other parameters of Eq. (7.3) are taken to be $a = \frac{1}{3}$ rad/s and $k = 1$ rad/s, and we consider how the dynamics depends on the parameter A. Due to the low-pass filter, $g(t)$ has very slow gradual time-dependence compared to the timescale of the "internal dynamics" of the system (represented by $A = 0$). Therefore, since $k > a$, the picture described in Sect. 7.2.4 can be applied, and we will now see this picture confirmed by numerics. Figure 7.2b shows a "numerical bifurcation diagram" of (7.3) where for each A-value, the trajectories at time τ of 50 evenly spaced initial conditions are shown. Despite the non-existence of infinite-time dynamics for this system, we clearly see in Fig. 7.2b a transition from neutrally stable dynamics, where trajectories fill the circle, to stable dynamics, where trajectories cluster around a point (implying loss of memory of initial condition). We see this transition occurring at the value A_* defined by (7.4) with $T = \tau$, which is marked in dashed black in plots (a), (b) and (c) of Fig. 7.2. Thus, the picture seen in Fig. 7.2b is exactly in accordance with the description in Sect. 7.2.4.

As in [24], the stability can also be assessed in terms of finite-time Lyapunov exponents (FTLEs). The FTLE for a trajectory $\theta(t)$ of (7.3) over a time-window $[0, T]$ is computed as

$$\lambda_T = \frac{1}{T}\int_0^T -a\cos(\theta(t))\,dt. \tag{7.6}$$

We consider the FTLEs for trajectories of (7.3) over the whole time-window $[0, \tau]$. The values of λ_τ for the trajectories of 50 initial conditions are shown in Fig. 7.2a. For each A-value, we see that the 50 trajectories share indistinguishably the same FTLE value, being indistinguishable from 0 for $A < A_*$ and clearly negative for $A > A_*$. Again, this suggests a transition from neutral stability to stability at A_*.

For further illustration, let us now consider the dynamics not over the whole time-interval, but rather over the subinterval $[0, \tau']$ with $\tau' = \pi \times 10^4$ s. Figure 7.2e shows the numerical bifurcation diagram for simulation only up to time τ'. Here, we see the critical transition from neutral stability to stability occurring at the new value of A_* where in (7.4), we take $T = \tau'$ rather than $T = \tau$. Note that A_* is now significantly larger than what it was when we considered the whole time-interval $[0, \tau]$. This is

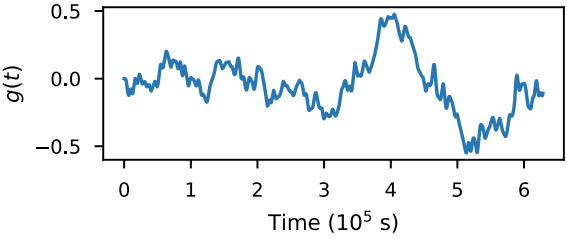

Fig. 7.1 Graph of $g(t)$, obtained by passing a sample realisation of a Brownian bridge on [0 s, $2\pi \times 10^5$ s] through a low-pass filter

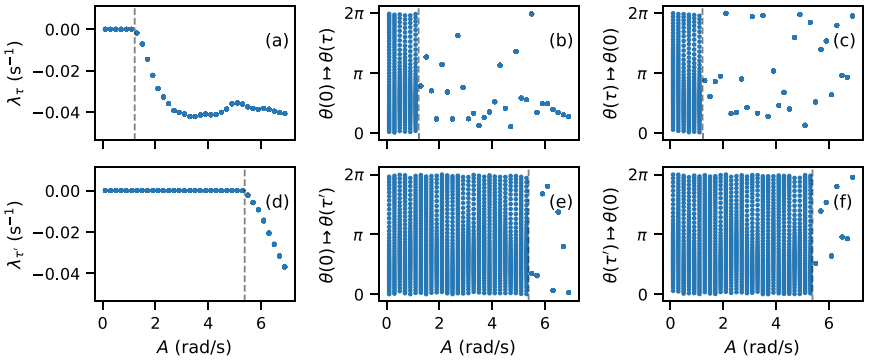

Fig. 7.2 Dynamics of (7.3) with g as in Fig. 7.1, with varying A, over the time-interval $[0\text{ s}, 2\pi \times 10^5\text{ s}]$ of duration $\tau = 2\pi \times 10^5$ s in (**a**)–(**c**), and over the shorter time-interval $[0\text{ s}, \pi \times 10^4\text{ s}]$ of duration $\tau' = \pi \times 10^4$ s in (**d**)–(**f**). Other parameters are $a = \frac{1}{3}$ rad/s and $k = 1$ rad/s. In (**a**–**e**), for each A-value, results for the evolution $\theta(t)$ of 50 equally spaced initial conditions $\theta(0) = \frac{2\pi i}{50}$, $i = 0, \ldots, 49$, are shown: (**a**, **d**) shows the finite-time Lyapunov exponents λ_T, as defined by (7.6), for these trajectories, with $T = \tau$ in (**a**) and with $T = \tau'$ in (**d**); (**b**, **e**) shows the positions $\theta(T)$ of these trajectories at time $T = \tau$ in (**b**) and $T = \tau'$ in (**e**). In (**c**, **f**), for each A-value, the positions of $\theta(0)$ for the 50 trajectories ending at the points $\theta(T) = \frac{2\pi i}{50}$, $i = 0, \ldots, 49$, are shown, with $T = \tau$ in (c) and $T = \tau'$ in (**f**). In (**a**)–(**c**), the value A_* as defined in (7.4) with $T = \tau$ is marked in dashed black. In (**d**)–(**f**), the value A_* as defined in (7.4) with $T = \tau'$ is marked in dashed black

because $g(t)$ reaches significantly more negative values during $t \in (\tau', \tau]$ than it manages to reach during $t \in [0, \tau']$. FTLEs of trajectories over the time-window $[0, \tau']$ are shown in Fig. 7.2d, and again they show a transition from 0 to negative at the new A_* value.

For the whole time-interval $[0, \tau]$ and the subinterval $[0, \tau']$, reverse-time bifurcation diagrams are shown in plots (c) and (f) of Fig. 7.2 respectively. In plots (b) and (c), and likewise in plots (e) and (f), we see that if A is above the critical value then trajectories are repelled away from the very small vicinity of a repulsive initial condition and are mutually attracted into a very small cluster; thus, the critical transitions that we see in Fig. 7.2 are strongly resemblant of a classical saddle-node bifurcation of autonomous dynamical systems. But this bifurcation cannot be formalised in terms of the long-time-asymptotic dynamics of any reasonable extension of the model (7.3) to infinite time. Indeed, this is highlighted by the fact that critical parameter-value A_* for this bifurcation is *different* between when the system is considered over $[0, \tau']$ and when the system is considered over $[0, \tau]$. The conclusion we draw from these observations is that for a physical process subject to time-dependent external influences, important stabilisation phenomena can be completely indetectable by all theoretical or experimental approaches that assume the well-definedness of long-time-asymptotic dynamical properties such as asymptotic stability or asymptotic Lyapunov exponents.

7.4 The Adler Equation with Sinusoidal Driving

In order to illustrate point (3) of the three main points in Sect. 7.1.2, we now consider the Adler equation with slow-timescale sinusoidal driving (just as was used for the numerical illustrations in the chapter [24]). The strict periodicity of the driving means that the theoretical analysis in Sect. 7.2, as well as numerics of the kind presented in Sect. 7.3, can now be compared with a long-time-asymptotic analysis of stability.

We consider the system (7.3) with $g(t) = \cos(\omega t)$, i.e.

$$\dot{\theta}(t) \;=\; -a\sin(\theta(t)) + k + A\cos(\omega t), \tag{7.7}$$

with $a, k, \omega > 0$ and $A \geq 0$. We assume slow time-dependence of the driving, specifically in the sense that both ω and the product $A\omega$ are very small. We will also mostly focus on the case that $k > a$, so that the picture in Sect. 7.2.4 is applicable.

Let us first present the basic results of a classical stability analysis.

7.4.1 An Initial Long-time-asymptotic Analysis of Dynamics

The case that $A = 0$ is the autonomous case for which a classical stability analysis was carried out in Sect. 7.2.1 (with $k = G$), as well as in Sect. 6.4.1 of the chapter [24]. We now address the general case from the same classical point of view.

The ALE of a trajectory $\theta(t)$ of (7.7) is precisely the limit as $T \to \infty$ of the FTLE λ_T given by (7.6). Now let Ω be the "mean frequency" $\langle\dot{\theta}\rangle$ of trajectories of (7.7), namely

$$\Omega = \lim_{T\to\infty} \frac{1}{T}\int_0^T \dot{\theta}(t)\,dt,$$

which does not depend on the initial condition $\theta(0)$ of the trajectory $\theta(t)$, but does depend on the system parameters a, k, A and ω. For the autonomous case $A = 0$, as in [24, Sect. 6.4.1] we have $\Omega = 0$ in the stable scenario ($k < a$), but $\Omega = \sqrt{k^2 - a^2} > 0$ in the neutrally stable scenario ($k > a$).

Proposition 1 *For any given parameter values a, k, A, ω in Eq. (7.7), exactly one of the following three statements holds.*

(A) Equation (7.7) exhibits neutral stability in the following sense:

- *There is a finite bound $M > 0$ such that for any two distinct solutions $\theta_1(t)$ and $\theta_2(t)$ of (7.7), for all time $t \in \mathbb{R}$,*

$$\frac{1}{M} \leq \frac{distance\,between\,\theta_1(t)\,and\,\theta_2(t)}{distance\,between\,\theta_1(0)\,and\,\theta_2(0)} \leq M.$$

- *The ALE of every trajectory is 0.*

(B) Equation (7.7) exhibits stability in the following sense:

- *There is a $\frac{2\pi}{\omega}$-periodic solution $p(t)$ that attracts all solutions as $t \to \infty$, apart from a single repulsive periodic solution $\pi - p(-t)$.*
- *The ALE of every trajectory other than the repulsive trajectory $\pi - p(-t)$ is a negative number λ.*

(C) Equation (7.7) lies "on the boundary between stability and neutral stability", in the following sense: There is a unique $\frac{2\pi}{\omega}$-periodic solution, which is attracting from one direction but is unstable due to being repulsive in the other direction, and all solutions converge to this solution as $t \to \infty$ and have an ALE of 0.

Furthermore, if the mean frequency Ω is not an integer multiple of ω, then we must be in case (A).

This proposition is essentially Theorems 1 and 4 of [12]. So we see that the set of possible behaviours for the periodically forced Adler equation is directly analogous to the set of possible behaviours for the autonomous Adler equation in Sect. 7.2.1. (This is quite a special property of Adler equations, that does not generalise to other one-dimensional phase-oscillator models [6].)

For the case that $k > a$, we emphasise the following corollary of Proposition 1.

Corollary 1 *Assume $k > a$, and fix any $A \geq 0$. There are intervals of ω-values arbitrarily close to 0 for which Eq. (7.7) exhibits neutral stability in the sense of Proposition 1(A).*

Proof For any trajectory $\theta(t)$, since

$$k - a + A\cos(\omega t) \leq \dot{\theta}(t) \leq k + a + A\cos(\omega t)$$

for all t, and since the term $A\cos(\omega t)$ has an average of 0, it follows that

$$k - a \leq \Omega \leq k + a.$$

Now Ω depends continuously on the parameters of Eq. (7.7) [17, Proposition 11.1.6]. Hence, since Ω is constrained to the interval $[k-a, k+a] \subset (0, \infty)$, it follows that as $\omega \to 0$, there will always be intervals of ω-values for which Ω is not an integer multiple of ω.

Note that Corollary 1 applies to every $A \geq 0$: whatever the value of A, it is possible for the time-dependence of the driving $G(t) := k + A\cos(\omega t)$ to be arbitrarily slow (corresponding to arbitrarily small ω) and yet for the system to exhibit neutral stability in the sense of Proposition 1(A). In both the statements and the proofs of Proposition 1 and Corollary 1, no distinction whatsoever appears between the situation that $G(t)$ remains forever outside $[-a, a]$ and the situation that there are times t when $G(t) \in (-a, a)$, as considered in Sect. 7.2.2. In particular, the statement and proof of Corollary 1 recognise no distinction between A-values less than a critical value A_* and A-values larger than a critical value A_*.

7.4.2 Analysis Based on Sect. 7.2

Assume $k > a$. Considering (7.7) over an arbitrary time-interval $[0, T]$ with $T \geq \frac{\pi}{\omega}$, the critical A-value A_* as defined in (7.4) is simply given by $A_* = k - a$. So as in Sect. 7.2.4 we have the following: if $A < k - a$ then, by the reasoning of Sect. 7.2.2, the trajectories of (7.7) exhibit neutral stability; and if $A > k - a$ then by the same reasoning of Sect. 7.2.2, the trajectories of (7.7) exhibit stability.

As in Sect. 7.2.3, one can quantify the level of stability using the adiabatically derived FTLE estimate Λ defined in Eq. (7.2). If T is an integer multiple of $\frac{\pi}{\omega}$ then this is given by

$$\Lambda = \begin{cases} 0 & A \leq k - a \\ -\frac{1}{\pi} \int_{\arccos\left(\frac{a-k}{A}\right)}^{\pi} \sqrt{a^2 - (k + A\cos(t))^2}\, dt & k - a < A \leq k + a \\ -\frac{1}{\pi} \int_{\arccos\left(\frac{a-k}{A}\right)}^{\arccos\left(-\frac{k+a}{A}\right)} \sqrt{a^2 - (k + A\cos(t))^2}\, dt & A > k + a. \end{cases} \tag{7.8}$$

We emphasise that this quantity Λ has no dependence on ω and no dependence on T, within the constraint that T is an integer multiple of $\frac{\pi}{\omega}$.

7.4.3 Numerics

We fix the time-interval $[0\text{ s}, 2\pi \times 10^5\text{ s}]$ of duration $T = 2\pi \times 10^5$ s, and fix $\omega = 10^{-3}$ rad/s, so that $T = \frac{200\pi}{\omega}$, i.e. T corresponds to exactly 100 periods of the driving $k + A\cos(\omega t)$. Figure 7.3 shows the FTLEs and forward- and reverse-time numerical bifurcation diagrams for the system, analogous to the plots in Fig. 7.2. Once again, the value of A_* is marked, which is now simply equal to $k - a$ as stated in Sect. 7.4.2. But additionally, on the FTLE plot, the adiabatically derived FTLE approximation Λ given in (7.8) is shown in grey.

In all these plots, we see exactly the same stabilisation phenomenon as was observed in Sect. 7.3.2. We furthermore observe extremely good agreement between Λ and the numerically obtained FTLE values. So overall, the numerical picture in Fig. 7.3 confirms the analysis in Sect. 7.4.2.

Many further numerical simulation results for the sinusoidally driven Adler equation can be found in the chapter [24] and in [27], all confirming the conceptual analysis in Sect. 7.2.2 and the stabilisation phenomenon in Sect. 7.2.4.

7.4.4 Comparison of the Above Analyses

We have seen clearly that for $k > a$, the same critical transition from neutral stability to stability occurs in the slowly sinusoidally forced Adler equation (7.7) as was

seen to occur for the model in Sect. 7.3.2. Furthermore, for $A > k - a$ the FTLEs are indistinguishable from the negative value $\Lambda < 0$ given in Eq. (7.8). However, Corollary 1 says that whatever the value of A, it is possible for ω to be arbitrarily small and still for (7.7) to have neutrally stable dynamics where the ALE of every trajectory is 0.

So the question arises of how to reconcile these two seemingly conflicting descriptions of the dynamics of (7.7). Now it turns out that when $A > k - a$, the width of the ω-intervals of neutral stability is extremely small compared to the separation between them; this is proved rigorously in [7] for $A = a$ and $k \in (a, 2a)$. So, in other words, while this neutral stability can occur for all A-values as in Corollary 1, nonetheless it is an extremely fine-tuned phenomenon in the case that $A > k - a$. In these narrow ω-intervals of neutral stability for $A > k - a$, the mechanism for the breakdown of the conceptual analysis in Sect. 7.2.2 is a kind of canard-like phenomenon: at some of the times when the forcing $G(t) := k + A\cos(\omega t)$ starts to re-enter the interval $(-a, a)$, the previously formed cluster of mutually synchronised trajectories happens to spend too much time tracking the motion of the *slowly moving source* $z(t) := \pi - \text{arc sin}\left(\frac{G(t)}{a}\right)$ and is thus de-synchronised.

However, the mathematical tools needed to obtain Proposition 1 and Corollary 1 neither reveal the narrowness of the ω-intervals of neutral stability when $A > k - a$, nor hint at the existence of an adiabatic mechanism of stability for $A > k - a$ (namely as described in Sect. 7.2.2) which needs some other peculiar mechanism of destabilisation to undo.

So in conclusion:

- We have seen in Fig. 7.3 a clear and physically important qualitative change in the behaviour of the model (7.7) as A crosses from below $k - a$ to above $k - a$, and we have explained this in terms of very simple non-asymptotic-time reasoning, of exactly the same kind as was applied to the model in Sect. 7.3.2.
- But simply pursuing a classical approach to stability analysis risks *positively hindering* the recognition of this important qualitative change.

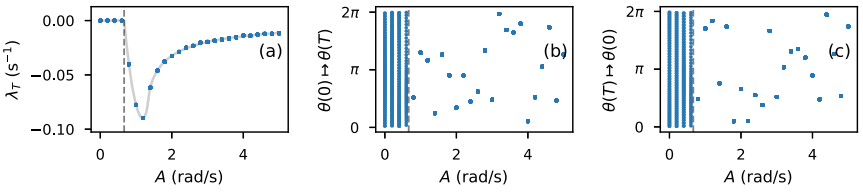

Fig. 7.3 Dynamics of (7.7) with varying A, for $\omega = 10^{-3}$ rad/s, from time 0 s up to time $T = 2\pi \times 10^5$ s $= \frac{200\pi}{\omega}$. Other parameters are $a = \frac{1}{3}$ rad/s and $k = 1$ rad/s. In (**a**) and (**b**), for each A-value, results for the evolution $\theta(t)$ of 50 equally spaced initial conditions $\theta(0) = \frac{2\pi i}{50}$, $i = 0, \ldots, 49$, are shown: **a** shows the finite-time Lyapunov exponents λ_T, as defined by (7.6), for these trajectories, and also shows Λ (defined in (7.8)) in grey; (**b**) shows the positions $\theta(T)$ of these trajectories at time T. In (**c**), for each A-value, the positions of $\theta(0)$ for the 50 trajectories of (7.7) with $\theta(T) = \frac{2\pi i}{50}$, $i = 0, \ldots, 49$, are shown. The value $k - a = \frac{2}{3}$ rad/s is marked by the black dashed line

7.5 Slow-Fast Finite-Time Dynamical Systems

In view of the conclusions at the end of Sects. 7.3 and 7.4, a natural question is whether there might be other approaches to formally defining concepts of stability and neutral stability other than the long-time-asymptotic approaches introduced by Aleksandr Lyapunov.

For any physical process in the real world, time is a finite parameter just like all other parameters, and we are interested in the behaviour on finite timescales. The philosophy behind traditional long-time-asymptotic dynamics analysis is that for many physical processes, what is practically observed on such finite timescales of interest matches the theoretical limiting behaviour of a suitable mathematical model of the process as $t \to \infty$. However, we propose that for the kinds of slowly time-dependent systems that we have been studying in this chapter, an appropriate approach is not to treat *time* as the special parameter that can be approximated by an infinite limit, but instead to treat the *timescale separation* as the special parameter that can be approximated by an infinite limit. We do anticipate (as evidenced numerically in [27]) that the timescale separation will often not need to be very great in order for the infinite-limit approximation to give a suitable description of dynamics.

For one-dimensional phase-oscillator models, our proposed approach means that we consider finite-time differential equations of the form

$$\dot{\theta}(t) \;=\; F(\theta(t), \varepsilon t), \qquad t \in [0, \tfrac{1}{\varepsilon}] \tag{7.9}$$

for some function $F\colon \mathbb{R} \times [0, 1] \to \mathbb{R}$ that is 2π-periodic in its first input, and we consider the limiting behaviour as $\varepsilon \to 0$. For example, non-autonomous Adler equation models could take the form

$$\dot{\theta}(t) \;=\; -a \sin(\theta) + \tilde{G}(\varepsilon t)$$

for some $\tilde{G}\colon [0, 1] \to \mathbb{R}$, and one can consider the limiting behaviour as $\varepsilon \to 0$.

The study of limiting dynamical behaviour as timescale separation tends to infinity is the subject of *slow-fast dynamical systems* [19]. Here, we are combining this slow-fast approach with the philosophy of FTDS theory, by restricting the slow time εt to the unit interval. In the paper [27], we use this "slow-fast FTDS" approach to define notions of stability and neutral stability that are analogous to those seen in scenarios (A) and (B) of Proposition 1 but from an "$\varepsilon \to 0$ perspective" in place of a "$t \to \infty$ perspective". We use these definitions to address rigorously the stabilisation phenomenon that we have discussed in this chapter.

This chapter has focused on stabilisation of one-dimensional phase dynamics. But as seen in [22, 24] and also numerically evidenced in [23], similar dynamical phenomena are likely to be prevalent in higher-dimensional multiple-timescale non-autonomous systems as well.

7.6 Conclusion

We have studied slowly time-varying one-dimensional phase dynamics to illustrate the physical limitations of traditional mathematical formalisms of dynamical systems analysis that have their roots in the study of isolated systems. For processes subject to slowly time-dependent forcing, we have proposed an alternative framework of "slow-fast finite-time dynamical systems" for mathematical analysis of physical concepts such as stability. More generally, we argue that a finite-time perspective on dynamical behaviour may be crucial to the correct identification and explanation of dynamical phenomena occurring in open systems studied throughout the sciences.

Acknowledgements We are grateful for the comments of three anonymous referees, which have led to considerable improvement of this manuscript. This study has been supported by an EPSRC Doctoral Prize Fellowship, the DFG grant CRC 701, the EPSRC grant EP/M006298/1, and the European Union's Horizon 2020 research and innovation programme under the Marie Skłodowska-Curie grant agreement No 642563. Codes for the numerics carried out in this chapter are available upon request and are deposited on the Lancaster Publications and Research system Pure.

References

1. L. Arnold, *Random Dynamical Systems, Springer Monographs in Mathematics* (Springer, Berlin, 1995)
2. A. Berger, T.S. Doan, S. Siegmund, Nonautonomous finite-time dynamics. Discret. Contin. Dyn. Sys. B **9**(3 & 4), 463–492 (2008)
3. L.H. Duc, J.P. Chávez, T.S. Doan, S. Siegmund, Finite-time Lyapunov exponents and metabolic control coefficients for threshold detection of stimulus-response curves. J. Biol. Dyn. **10**(1), 379–394 (2016)
4. R.M. Dudley, *Uniform Central Limit Theorems*. Cambridge Studies in Advanced Mathematics. Cambridge University Press (1999)
5. P. Giesl, J. McMichen, Determination of the area of exponential attraction in one-dimensional finite-time systems using meshless collocation. Discret. Contin. Dyn. Sys. B **23**(4), 1835–1850 (2018)
6. A. Glutsyuk, L. Rybnikov, On families of differential equations on two-torus with all phase-lock areas. Nonlinearity **30**(1), 61–72 (2016)
7. J. Guckenheimer, Y.S. Ilyashenko, The duck and the devil: canards on the staircase. Mosc. Math. J. **1**(1), 27–47 (2001)
8. Z. Hagos, T. Stankovski, J. Newman, T. Pereira, P.V.E. McClintock, A. Stefanovska, Synchronization transitions caused by time-varying coupling functions. Philos. T. R. Soc. A **377**(2160), 20190275 (2019)
9. G. Haller, Finding finite-time invariant manifolds in two-dimensional velocity fields. Chaos **10**(1), 99–108 (2000)
10. G. Haller, Lagrangian coherent structures. Annu. Rev. Fluid Mech. **47**(1), 137–162 (2015)
11. G. Haller, G. Yuan, Lagrangian coherent structures and mixing in two-dimensional turbulence. Phys. D **147**(3), 352–370 (2000)
12. Y.S. Ilyashenko, D.A. Ryzhov, D.A. Filimonov, Phase-lock effect for equations modeling resistively shunted Josephson junctions and for their perturbations. Funct. Anal. Appl. **45**(3), 192 (2011)
13. S. Ivić, I. Mrša Haber, T. Legović, Lagrangian coherent structures in the Rijeka Bay current field. Acta Adriat. **58**(3), 373–389 (2017)

14. R.V. Jensen, Synchronization of driven nonlinear oscillators. Am. J. Phys. **70**(6), 607–619 (2002)
15. D. Karrasch, Linearization of hyperbolic finite-time processes. J. Differ. Equ. **254**(1), 256–282 (2013)
16. B. Kaszás, U. Feudel, T. Tél, Leaking in history space: a way to analyze systems subjected to arbitrary driving. Chaos **28**(3), 033,612 (2018)
17. A. Katok, B. Hasselblatt, *Introduction to the Modern Theory of Dynamical Systems, Encyclopedia of Mathematics and its Applications* (Cambridge University Press, Cambridge, 1995)
18. P.E. Kloeden, M. Rasmussen, *Nonautonomous Dynamical Systems* (American Mathematical Society, Providence, 2011)
19. C. Kuehn, *Multiple Time Scale Dynamics, Applied Mathematical Sciences*, vol. 191 (Springer, Cham, 2015)
20. Y. Lehahn, F. d'Ovidio, M. Lévy, E. Heifetz, Stirring of the northeast Atlantic spring bloom: A Lagrangian analysis based on multisatellite data. J. Geophys. Res. C **112**(C8) (2007)
21. F. Lekien, S.C. Shadden, J.E. Marsden, Lagrangian coherent structures in n-dimensional systems. J. Math. Phys. **48**(6), 065,404 (2007)
22. M. Lucas, D. Fanelli, A. Stefanovska, Nonautonomous driving induces stability in network of identical oscillators. Phys. Rev. E **99**(1), 012,309 (2019)
23. M. Lucas, J. Newman, A. Stefanovska, Stabilization of dynamics of oscillatory systems by nonautonomous perturbation. Phys. Rev. E **97**(4), 042,209 (2018)
24. M. Lucas, J.M.I. Newman, A. Stefanovska, Synchronisation and non-autonomicity. In: Stefanovska A., McClintock P.V.E. (eds) *Physics of Biological Oscillators. Understanding Complex Systems*, pp. 85–110, (Springer, Cham, 2021). https://doi.org/10.1007/978-3-030-59805-1_6
25. A.M. Lyapunov, The general problem of the stability of motion. Int. J. Control **55**(3), 531–534 (1992)
26. R.L. Moorcroft, S.M. Fielding, Criteria for shear banding in time-dependent flows of complex fluids. Phys. Rev. Lett. **110**(8), 086,001 (2013)
27. J. Newman, M. Lucas, A. Stefanovska, Stabilisation of cyclic processes by slowly varying forcing (2019). Submitted
28. A. Pikovsky, M. Rosenblum, J. Kurths, *Synchronization: A Universal Concept in Nonlinear Sciences*, vol. 12 (Cambridge University Press, Cambridge, UK, 2003)
29. H. Poincaré, *Mémoire sur les courbes définies par une équation différentielle* (J. Math, Pures Appl, 1881)
30. A.G. Ramos et al., Lagrangian coherent structure assisted path planning for transoceanic autonomous underwater vehicle missions. Sci. Rep. **8**, 4575 (2018)
31. M. Rasmussen, Finite-time attractivity and bifurcation for nonautonomous differential equations. Differ. Equ. Dynam. Syst. **18**(1), 57–78 (2010)
32. S.C. Shadden, J.O. Dabiri, J.E. Marsden, Lagrangian analysis of fluid transport in empirical vortex ring flows. Phys. Fluids **18**(4), 047,105 (2006)
33. A. Stefanovska, P.T. Clemson, Y.F. Suprunenko, Introduction to chronotaxic systems – systems far from thermodynamics equilibrium that adjust their clocks. In: Wunner G., Pelster A. (eds) *Selforganization in Complex Systems: the Past, Present, and Future of Synergetics. Understanding Complex Systems*, pp. 227–246, (Springer, Cham, 2016). https://doi.org/10.1007/978-3-319-27635-9_14
34. S.H. Strogatz, *Nonlinear Dynamics and Chaos: With Applications to Physics, Biology, Chemistry, and Engineering*, 2nd edn. (Westview Press, Boulder, 2014)
35. E. Tew Kai, V. Rossi, J. Sudre, H. Weimerskirch, C. Lopez, E. Hernandez-Garcia, F. Marsac, V. Garçon, Top marine predators track Lagrangian coherent structures. PNAS **106**(20), 8245–8250 (2009)
36. J. Töger, M. Kanski, M. Carlsson, S.J. Kovács, G. Söderlind, H. Arheden, E. Heiberg, Vortex ring formation in the left ventricle of the heart: analysis by 4D flow MRI and Lagrangian coherent structures. Ann. Biomed. Eng. **40**(12), 2652–2662 (2012)

37. M. Ushio, C.H. Hsieh, R. Masuda, E.R. Deyle, H. Ye, C.W. Chang, G. Sugihara, M. Kondoh, Fluctuating interaction network and time-varying stability of a natural fish community. Nature **554**(7692), 360 (2018)
38. N. Wang, U. Ramirez, F. Flores, S. Datta-Barua, Lagrangian coherent structures in the thermosphere: Predictive transport barriers. Geophys. Res. Lett. **44**(10), 4549–4557 (2017)

Chapter 8
Synchronization of Coupled Oscillators—Phase Transitions and Entropy Production

Steven Yuvan and Martin Bier

Abstract Over the last half century, a good understanding of liquid-gas phase transitions and magnetization phase transitions has been developed. After an order parameter, r, is defined, it can be derived how $r = 0$ for $T > T_c$ and how $r \propto (T_c - T)^{\gamma}$ at lowest order for $T < T_c$. Here T is the temperature and T_c represents a critical temperature. The value of γ appears to not depend on physical details of the system, but very much on dimensionality. No phase transitions exist for one-dimensional systems. For systems of four or more dimensions, each unit is interacting with sufficiently many neighbors to warrant a mean-field approach. The mean-field approximation leads to $\gamma = 1/2$. In this article we formulate a realistic, nonequilibrium system of coupled oscillators. Each oscillator moves forward through a cyclic 1D array of n states and the rate at which an oscillator proceeds from state i to state $i + 1$ depends on the populations in states $i + 1$ and $i - 1$. We study how the phase transitions occur from a homogeneous distribution over the states to a clustered distribution. A clustered distribution means that oscillators have synchronized. We define an order parameter and we find that the critical exponent takes on the mean-field value of 1/2 for any number of states n. However, as n increases, the phase transition occurs for ever smaller values of T_c. We present rigorous mathematics and simple approximations to develop an understanding of the phase transitions in this system. We explain why and how the critical exponent value of 1/2 is expected to be robust and we discuss a wet-lab experimental setup to substantiate our findings.

S. Yuvan · M. Bier (✉)
Department of Physics, East Carolina University, Greenville, NC 27858, USA
e-mail: bierm@ecu.edu

A. Stefanovska and P. V. E. McClintock (eds.), *Physics of Biological Oscillators*, Understanding Complex Systems,
https://doi.org/10.1007/978-3-030-59805-1_8

8.1 Introduction

8.1.1 The Liquid-Gas Phase Transition

A small correction to the Ideal Gas Law suffices to capture most of the phenomenology of the liquid-gas phase transition. In the Van der Waals Equation [19],

$$\left(P + \frac{a}{v^2}\right)(v - b) = k_B T, \tag{8.1}$$

P denotes the pressure, v is the volume per molecule, k_B is Boltzmann's constant, and T is the temperature. The "b" takes into account that the involved molecules are not points, but have finite size. The "a" is associated with the attractive force between molecules. There is a v^2 in the denominator for the following reasons. (i) For each molecule the amount of interaction with other molecules is proportional to the number of molecules in a specified volume around the molecule and thus to the density $\rho = 1/v$. (ii) For the pressure on the wall of the container, the number of molecules in a layer-volume near the wall is what is significant. The molecules in that layer-volume are only attracted in the direction away from the wall. The number of molecules in the layer-volume is again proportional to $\rho = 1/v$. Effects (i) and (ii) together result in the a/v^2 term in Eq. (8.1).

Equation (8.1) leads to the isotherms depicted in Fig. 8.1a. The equation is readily turned into a 3rd order polynomial in v. There are values of T for which there is only one value of v for every P. But for sufficiently small T there are 3 values of

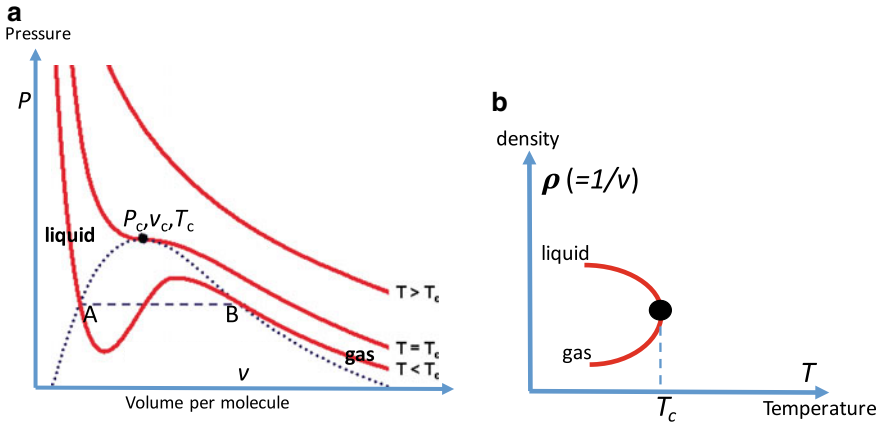

Fig. 8.1 **a** The P-v diagram according to the Van der Waals Equation (Eq. 8.1). In the area inside the dotted curve, there is coexistence of liquid and gas phases. The critical point (P_c, v_c, T_c) is a unique point where there is no distinction between liquid and gas phase. **b** But lowering the temperature at constant pressure, such distinction emerges and follows a power law: $\rho_{\text{liquid}} - \rho_{\text{gas}} \propto (T_c - T)^{\gamma}$, where γ is the critical exponent

v for a sufficiently small value of P. The area inside the dotted curve in Fig. 8.1a is where the multivaluedness occurs. The $T = T_c$ isotherm is the border curve that divides the P-v diagram into the two regions. The part of the $T < T_c$ curve where $dP/dv > 0$ is not realistic. It was James Clerk Maxwell who realized that, between the points A and B on the dotted curve (cf. Fig. 8.1a), the isotherm has to be replaced by a horizontal segment (dashed in Fig. 8.1a). It is along this line that liquid and gas coexist and that the phase transition takes place: as volume is increased, pressure stays the same and the system responds by evaporating more liquid.

On the $T = T_c$ curve there is a point where $d^2P/dv^2 = dP/dv = 0$. This is the so-called critical point. It is a unique point (P_c, v_c, T_c) in P, v, T-space where the liquid phase and the gas phase are not distinguishable. In the vicinity of the critical point, the different physical quantities follow power laws. From the Van der Waals Equation it can be derived that at leading order $\left(v_{\text{gas}} - v_{\text{liquid}}\right) \propto (T_c - T)^{1/2}$ or, in terms of the density $\rho = 1/v$:

$$\rho_{\text{liquid}} - \rho_{\text{gas}} \propto (T_c - T)^{1/2} . \tag{8.2}$$

In other words, as the temperature is brought from T_c to a small ΔT below the critical temperature, the liquid and gas densities start to differ proportionally to $\sqrt{\Delta T}$. This is a symmetry breaking and Fig. 8.1b illustrates how it occurs. The liquid phase occupies a smaller volume and therefore a smaller phase-space volume than the gas phase. A smaller phase-space volume means fewer microstates and therefore, following the traditional Boltzmann definition [19], a lower entropy. The quantity $(\rho_{\text{liquid}} - \rho_{\text{gas}})$, cf. Eq. (8.2), can therefore be taken as an order parameter.

The critical behavior described by Eq. (8.2) does not depend on a or b. The exponent $1/2$ is therefore expected to apply universally. Experiment does show universality. However, it appears that the actual exponent is not $1/2$, but close to $1/3$ [10, 13].

8.1.2 Magnetization

Magnetization is less omnipresent in daily life than evaporation. However, as a phase transition it is easier to model than the transition from liquid to gas. Figure 8.2a shows a 2D Ising model. On each lattice point there is an atom whose spin, s, can be pointed either upward ($s = 1$) or downward ($s = -1$). Parallel spins ($\uparrow\uparrow$) have less energy than spins with opposite orientation ($\uparrow\downarrow$). Assuming that an individual spin only interacts with its four nearest neighbors and that there is no external magnetic field, we have for the magnetic energy of the entire system

$$H = -J \sum_{\langle i,j \rangle} s_i s_j , \tag{8.3}$$

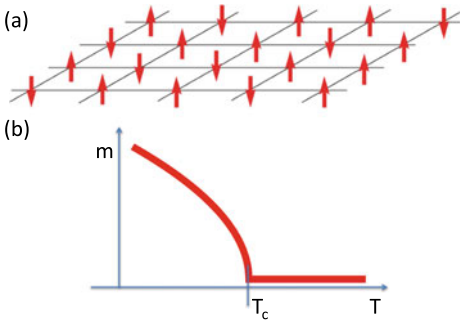

Fig. 8.2 **a** In the 2D Ising model each spin interacts only with its four nearest neighbors. **b** Ising models of two and more dimensions exhibit a phase transition. Above a critical temperature, T_c, there is no magnetization. At the critical temperature there is a discontinuity in the first derivative and below the critical temperature we have $m \propto (T_c - T)^{\gamma}$, where γ is the critical exponent

where $\langle i, j \rangle$ denotes a summation over all neighbor-neighbor interactions and $-J$ and J are the energies of the parallel and antiparallel orientation, respectively.

If the temperature is finite, then there is a competition in the system between thermally driven randomization and the "desire" of the system to go to the lowest energy by aligning spins. The solution is readily found if we assume that, through its four neighbors, each individual spin just "feels" the average magnetization of the entire system. This is called the mean-field approximation. If we let p and $1 - p$ be the probabilities of "spin up" and "spin down," then we can identify the magnetization of the system, m, with the average value of the spin: $m = p(1) + (1 - p)(-1) = 2p - 1$. With the mean-field approximation, the above sum for the energy, Eq. (8.3), simplifies: it becomes a sum over all the individual spins and each spin in the system can either be parallel or antiparallel with m. The energy difference between the parallel and the antiparallel orientation is $2Jm$. The probability p of a spin being parallel to m is then given by a Boltzmann ratio [19]: $p/(1 - p) = \exp[2Jm/(k_B T)]$, where k_B denotes Boltzmann's constant. With $m = 2p - 1$, we eliminate p and derive that $m = \tanh[Jm/(k_B T)]$. This equation has three solutions for small T and one solution for large T. As in the case of the liquid-gas transition, the critical temperature T_c marks the border between these two domains. In the vicinity of the critical temperature we take $J/(k_B T) = 1 + \varepsilon$. Expanding the hyperbolic tangent up to third order in ε, we can solve for the magnetization m. It is found that $|m| \propto \varepsilon^{1/2}$ (cf. Fig. 8.2b). It is obvious that $|m|$ can be seen as an order parameter for the system and that a symmetry breaking occurs if the temperature drops below T_c.

As in the case of the liquid-gas transition, the estimate of $1/2$ for the critical exponent turns out to be higher than what experiments show. Real critical exponents associated with the onset of magnetization cover a range between $1/3$ and $1/2$ [1, 11, 17].

8.1.3 Universality in Phase Transitions

For both the liquid-gas transition and the magnetization there is a "competition" between the system's tendency to settle in the lowest energy arrangement and the thermal agitation due to $k_B T$. A phase transition occurs when the system exhibits a discontinuity upon variation of temperature. Though the physical details and the basic equations are different for the magnetization and the liquid-gas transition, in both cases we observed that simple theory predicts a value of 1/2 for an exponent that actual experiment finds to be significantly lower.

The reason for the discrepancy is the same in both cases. The mean-field approach is not justified in a 3D space where each particle only interacts with a limited number of other particles. The mean-field approximation replaces the product of the two spins, $s_i s_j$, in Eq. (8.3) with the product of the average spins, i.e. m^2. We can actually rewrite $s_i s_j = (m + \delta_i)(m + \delta_j)$, where δ can only take the values $(1 - m)$ and $(-1 - m)$. What the mean field approximation essentially does is neglect all the $\delta_i \delta_j$ products in Eq. (8.3). This will lead to incorrect energies particularly if there are clusters with parallel spins.

Our treatment of the liquid-gas phase transition was fully based on the Van der Waals Equation. This equation does not acknowledge local density variations. The mean-field approximation was therefore implicit when the critical exponent of $1/2$ was derived.

Through analytical solutions and approximations, series expansions, and numerical simulations, the critical exponents for the Ising model in spaces of different dimensionality have been obtained [10]. There is no phase transition at finite temperature in 1D. In 2D and 3D the critical exponents are $1/8$ and 0.32, respectively. It turns out, finally, that in case of more than three dimensions the number of neighbors is sufficiently large for the mean-field approximation to apply and obtain $1/2$ for the critical exponent.

8.1.4 Phase Transitions for Coupled Oscillators

Already in the 17th century Christiaan Huygens noticed that two clocks, when hanging side-by-side on a wall, will synchronize their ticking over time. For a modern scientist or engineer it is not hard to understand that such clocks are mechanically coupled through little shockwaves that propagate through the wall. A contemporary and animate version of Huygens' clocks occurred when the London Millenium Footbridge across the Thames was opened in June of 2000. Pedestrians walking across the bridge began to synchronize their stepping leading the bridge to sway with alarming and unforeseen amplitude [12].

Setups with N coupled oscillators are commonly modelled with a system due to Kuramoto [26]:

$$\dot{\theta}_i = \omega_i + \frac{K}{N}\sum_{j=1}^{N}(\theta_j - \theta_i). \tag{8.4}$$

Here θ and ω represent the phase and innate frequency of each oscillator. K denotes the coupling strength between the oscillators. The last term on the right-hand-side describes a force that drives each oscillator towards the average phase. As each oscillator "feels" the average of the other oscillations, it is obvious that this is a mean-field model. There is no Brownian noise in this model. The competition here is between the coupling strength and the distribution of the innate frequencies. For the Kuramoto model it has indeed been derived and observed that a phase transition occurs as K goes up [26].

It is not just mechanical oscillations that synchronize. In an anaerobic environment yeast cells turn glucose into ethanol. Under certain conditions the throughput of the glucose-ethanol metabolic chain will oscillate with a period of about a minute. One of the metabolites in the chain, acetaldehyde, can freely permeate the cell membrane. Yeast cells in a suspension thus share the bath's acetaldehyde concentration and this leads to a mean-field coupling. Experiment and mathematical analysis both show how, in the course of several cycles, the yeast cells in a suspension synchronize their oscillations [4].

Just such a chemically-inspired system of coupled oscillators will be our focus. The setup in Fig. 8.3a depicts an n-state cycle. Only counterclockwise transitions are possible. A large population of oscillators is going through the cycle. We take p_i to be the fraction of the total population that is in state i. We let the transition rate k_i from state i to $(i+1)$ depend on p_{i+1} and p_{i-1}, i.e. on the populations in the state ahead and the state behind state i (cf. Fig. 8.3a):

$$k_i = k_0 \exp\left[\alpha\,(p_{i+1} - p_{i-1})\right]. \tag{8.5}$$

The constant k_0 is the same for all transitions and can be absorbed in the timescale; we will leave it out in the remainder of this article. The idea of Eq. (8.5) is that the population in state $(i+1)$ increases the transition rate k_i and thus pulls the population in state i forward to state $(i+1)$. At the same time, the population in state $(i-1)$ decreases k_i and thus pulls back on the population in state i. For $\alpha > 0$, Eq. (8.5) describes a tendency of the entire population to cluster in one or more states. That tendency increases with α. We choose to put the populations in the exponent as the transition rate, k, generally depends exponentially on the height E of the activation barrier associated with the transition, i.e. $k \propto \exp[-E]$. In Refs. [28–31] a 3-state model with $k_i = k_0 \exp\left[\alpha\,(p_{i+1} - p_i)\right]$ is the basis for the analysis, i.e., not the population in the previous state $(i-1)$, but the population in state i itself is impeding the forward transition from i to $(i+1)$.

The system in Fig. 8.3a with Eq. (8.5) can be taken to model a number of real-life systems. Ion pumps in cell membranes go through a sequence of conformational states as they go through their catalytic cycle. An example is the well-known Na,K-ATPase. This is an ion pump that hydrolyzes ATP and uses the released energy to

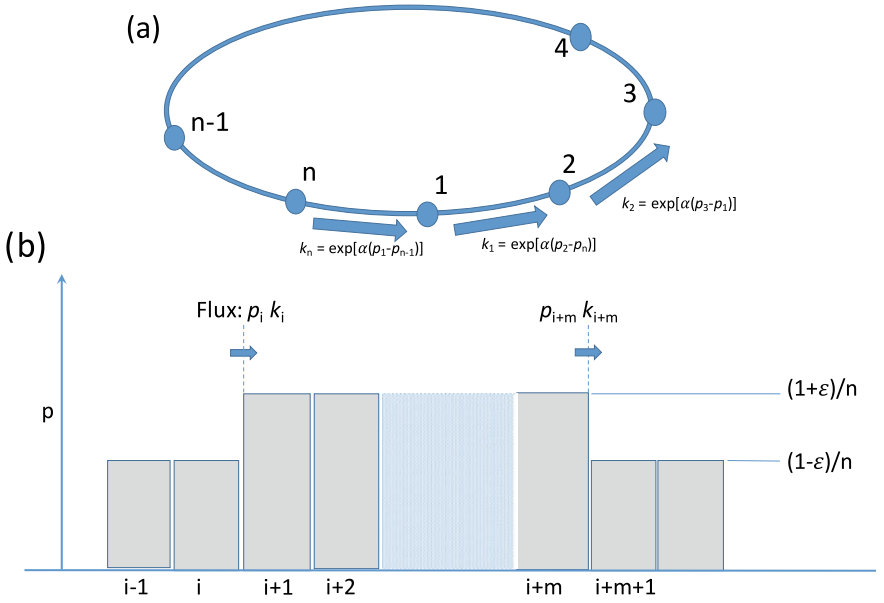

Fig. 8.3 **a** Our n-state model of coupled oscillators. Each oscillator moves through the n-state cycle in the counterclockwise direction. The transition rate, k_i, from state i to state $i+1$ depends on populations in states $i-1$ and $i+1$. **b** For sufficiently low values of the coupling parameter, α, there is a homogeneous distribution over the states, i.e. $p_i = 1/n \; \forall \, i$. For values just above the critical value, α_c, we construct a model in which we assume that the population in a state is either $(1+\varepsilon)/n$ or $(1-\varepsilon)/n$, where ε is small

pump sodium and potassium ions through the membrane against the electrochemical potential [18]. Na,K-ATPase can be present in the membrane in large concentrations. These proteins are very polar and they can be coupled through dipole-dipole interaction. But they can also interact as they change shape in the course of the catalytic cycle and thus deform the cytoskeleton and bilayer membrane. Through these couplings and the mechanism of Fig. 8.3, the pumps can synchronize their catalytic cycles.

A more provocative example of the dynamics of Fig. 8.3a and Eq. (8.5) can be found in bicycle racing. On a flat road with a smooth asphalt surface, more than 95% of the effort goes into overcoming air resistance. Due to aerodynamic drag, bicycle racers that ride in a group put in a smaller effort as compared to when they ride alone [6, 9]. The larger the group, the smaller the power that has to be produced by an individual rider. Bicycle racers thus tend to cluster in groups where they share the burden. However, when the road goes uphill, work against gravity has to be done. Furthermore, on a surface of cobblestones or gravel, the rolling resistance takes on more significance. Work against gravity or rolling resistance cannot be shared and the "racers' coupling," the α in our model, thus goes down. This is why it is generally on hill climbs or on cobblestones that the peleton in a bicycle race breaks up [7].

There is no explicit Brownian noise in the system of Fig. 8.3a. However, a constant rate out of a state implies that an individual oscillator has an exponentially distributed waiting time in that state. Effectively, this gives the system a stochasticity and a temperature: for $\alpha = 0$ the n-state system will, over time, forget any initial distribution over the n states and evolve towards a homogeneous distribution over the states, i.e. $p_i = 1/n$ where $i = 1, 2, \ldots n$. The parameter α denotes the coupling strength. For $\alpha = 0$ there is no coupling. As in the case of the gas-liquid transition and the magnetization, the randomization is opposed by a coupling that drives the system to an ordered state.

There is a fundamental difference between the liquid-gas transition (Fig. 8.1) and the magnetization (Fig. 8.2) on the one hand and our setup (Fig. 8.3a) on the other hand. With the first two systems we are looking at a thermal equilibrium. The system in Fig. 8.3a, however, goes through a chemical cycle. As there are no clockwise transitions, there is no detailed balance and there is continuous production of entropy.

8.2 Numerical Simulation and Mathematical Analysis

8.2.1 A Heuristic Approach

A simple heuristic model for the behavior close to the phase transition leads to some concise formulae that well approximate the actual behavior. The simple model can, furthermore, help build intuition for the mechanisms behind the phase transition. A less general form of the model was also presented in Ref. [5] in the context of $n = 4$, i.e., oscillators going through a 4-state cycle.

As was mentioned before, when α is small the probability distribution over the n states will over time approach $p_i = 1/n$ for all initial conditions. For sufficiently large values of α, clusters as in Fig. 8.3b will persist. For the clustering and the homogenization to be in balance, a "bump of length m" as in Fig. 8.3b needs to have as much influx ($J_i^{\text{in}} = p_i k_i$) as outflux ($J_{i+m}^{\text{out}} = p_{i+m} k_{i+m}$). We are interested in the region near the phase transition, so we consider values of the probability variation, ε (cf. Fig. 8.3b), that are small relative to 1. For simplicity, we allow two values for p_i: $(1 + \varepsilon)/n$ and $(1 - \varepsilon)/n$. Each value is taken on by half of the probabilities in the distribution. In the vicinity of the phase transition, equating the fluxes into and out of the "bump" leads to:

$$\frac{1-\varepsilon}{n} \exp\left[2\alpha\varepsilon/n\right] \approx \frac{1+\varepsilon}{n} \exp\left[-2\alpha\varepsilon/n\right]. \tag{8.6}$$

This formula is only valid for a bump that consists of two or more neighboring states with a population $(1 + \varepsilon)/n$. Furthermore, to the left of this bump there need to be at least two neighboring states with a population $(1 - \varepsilon)/n$. Expressing α/n in terms of

ε, we find from Eq. (8.6): $\alpha/n \approx 1/(4\varepsilon)\log[(1+\varepsilon)/(1-\varepsilon)]$. Expanding the right-hand-side for small ε up to second order, we next obtain $\alpha/n \approx (1/2) + (1/6)\varepsilon^2$. From the latter expression, we solve for ε and thus derive an approximation for the amplitude, ε, as a function of the coupling parameter α:

$$\varepsilon \approx \sqrt{\frac{6}{n}}\sqrt{\alpha - \frac{n}{2}}. \tag{8.7}$$

In order to quantify to what extent a distribution on a cycle as in Fig. 8.3a is homogeneous, an order parameter, r, is commonly defined as:

$$re^{i\psi} = \sum_{k=1}^{n} p_k \exp\left[\frac{2i\pi k}{n}\right], \tag{8.8}$$

where the "i" in the numerator of both exponents denotes $\sqrt{-1}$. This definition is due to Lord Rayleigh [2, 26]. It is obvious that we get $r = 0$ if there is no synchronization and all the p_k's are identical. We have $r = 1$ if there is maximal synchronization and all molecules are in the same state j, i.e. $p_k = 1$ if $k = j$ and $p_k = 0$ if $k \neq j$. We consider our model (Fig. 8.3) for a large value of n and we again take a simple approach to come to an upper bound for the value of the order parameter. Imagine that $p_k = (1+\varepsilon)/n$ for $1 \leq k \leq n/2$ and $p_k = (1-\varepsilon)/n$ for $n/2 < k \leq n$. The sum on the right-hand-side of Eq. (8.8) now reduces to $(2\varepsilon)\sum_{k=1}^{n/2}(1/n)\exp[2i\pi k/n]$. For large n we can approximate the summation with an integral over a half of a period L: $(1/L)\int_{x=0}^{L/2}\exp[2i\pi x/L]\,dx = i/\pi$. With this result and with Eq. (8.7), we derive for the order parameter as a function of α:

$$r = 0 \text{ if } \alpha < n/2 \quad \text{and} \quad r \approx \frac{3}{2}\sqrt{\frac{1}{n}}\sqrt{\alpha - n/2} \text{ if } \alpha > n/2, \tag{8.9}$$

where we took $2\sqrt{6}/\pi \approx 3/2$. Equation (8.9) makes strong statements about the phase transition. As the number of states in the cycle, n, increases, the phase transition occurs for ever larger values of the coupling parameter as $\alpha_c \approx n/2$, where α_c stands for the *critical value* of α. However, the square root over the $(\alpha - n/2)$-term means that the *critical exponent* maintains its mean-field value of 1/2 (cf. Eq. (8.2)) for all values of n. In the next section we will verify some of these predictions with both analytical and numerical work. In the Conclusions and Discussion section of this article we will put these results in the larger phase-transition context.

8.2.2 The System of ODEs

The system of coupled ordinary differential equations associated with the setup shown in Fig. 8.3a is:

$$\begin{aligned}
\dot{p}_1 &= k_n p_n - k_1 p_1, \\
\dot{p}_2 &= k_1 p_1 - k_2 p_2, \\
&\ldots \\
\dot{p}_n &= k_{n-1} p_{n-1} - k_n p_n.
\end{aligned} \tag{8.10}$$

Here the k's represent the transition rates (cf. Eq. (8.5)) and a dot above a symbol denotes differentiation with respect to time, i.e. $\bullet \equiv d/dt$. The periodic boundary conditions imply $k_n = \exp\left[\alpha\left(p_1 - p_{n-1}\right)\right]$ and $k_1 = \exp\left[\alpha\left(p_2 - p_n\right)\right]$. The point $p_j = 1/n \; \forall j$ is the obvious fixed point. As in an ordinary Taylor series, the behavior of the system in the close vicinity of a point is determined by the lowest order terms, generally the linear terms, in an expansion. This leads to an $n \times n$ matrix; the so-called Jacobian matrix [8]. The j-th row of this matrix lists the values of the derivatives of $(k_{j-1} p_{j-1} - k_j p_j)$ at the fixed point. The expression $(k_{j-1} p_{j-1} - k_j p_j)$ is the right-hand-side of the j-th equation in Eq. (8.10). Along a row of the matrix, derivatives are taken with respect to p_1, p_2, ..., p_n, respectively. We obtain for the Jacobian matrix in our case:

$$\mathbf{J} = \begin{bmatrix}
\left(\frac{\alpha}{n} - 1\right) & -\frac{\alpha}{n} & 0 & 0 & \ldots & 0 & -\frac{\alpha}{n} & \left(\frac{\alpha}{n} + 1\right) \\
\left(\frac{\alpha}{n} + 1\right) & \left(\frac{\alpha}{n} - 1\right) & -\frac{\alpha}{n} & 0 & 0 & \ldots & 0 & -\frac{\alpha}{n} \\
-\frac{\alpha}{n} & \left(\frac{\alpha}{n} + 1\right) & \left(\frac{\alpha}{n} - 1\right) & -\frac{\alpha}{n} & 0 & \ldots & 0 & 0 \\
0 & -\frac{\alpha}{n} & \left(\frac{\alpha}{n} + 1\right) & \left(\frac{\alpha}{n} - 1\right) & -\frac{\alpha}{n} & 0 & \ldots & 0 \\
\vdots & 0 & \ddots & \ddots & \ddots & \ddots & 0 & \vdots \\
\vdots & \vdots & 0 & \ddots & \ddots & \ddots & \ddots & 0 \\
0 & 0 & \ldots & 0 & -\frac{\alpha}{n} & \left(\frac{\alpha}{n} + 1\right) & \left(\frac{\alpha}{n} - 1\right) & -\frac{\alpha}{n} \\
-\frac{\alpha}{n} & 0 & 0 & \ldots & 0 & -\frac{\alpha}{n} & \left(\frac{\alpha}{n} + 1\right) & \left(\frac{\alpha}{n} - 1\right)
\end{bmatrix}. \tag{8.11}$$

The eigenvalues of this $n \times n$ matrix will tell us whether $p_j = 1/n \; \forall j$ is an attractor or a repeller [8]. For sufficiently small α the real parts of all eigenvalues are negative and the point $p_j = 1/n \; \forall j$ is then an attractor. The phase transition to synchronization occurs when, upon increasing α, the real part of just one eigenvalue turns positive. At that value of α, $p_j = 1/n \; \forall j$ becomes an unstable solution.

The matrix $\mathbf{J}$ (cf. Eq. (8.11)) is a tetradiagonal circulant matrix. In a circulant matrix each row is rotated one element to the right relative to the preceding row. The eigenvalues are the values of λ that solve the equation:

$$\det\left(\mathbf{J} - \lambda \mathbf{I}\right) = 0. \tag{8.12}$$

A standard formula is available for the eigenvalues of a circulant matrix [25]. For the present system with only four possible nonzero elements in the matrix, we obtain after some algebra:

$$\lambda_j = \left(\frac{\alpha}{n} - 1\right) - \frac{\alpha}{n}\exp\left[2\pi i\frac{j}{n}\right] - \frac{\alpha}{n}\exp\left[-4\pi i\frac{j}{n}\right] + \left(\frac{\alpha}{n} + 1\right)\exp\left[-2\pi i\frac{j}{n}\right], \quad j = 0, 1, \ldots, n-1. \tag{8.13}$$

Considering only the real parts, we have:

$$\mathrm{Re}[\lambda_j] = \frac{\alpha}{n}\left(1 - \cos\left[4\pi\frac{j}{n}\right]\right) - 1 + \cos\left[2\pi\frac{j}{n}\right]. \tag{8.14}$$

Note that $\lambda_0 = 0$. This zero eigenvalue is associated with the zero determinant of the above matrix, Eq. (8.11), and ultimately with the normalized total population, $\sum_{j=1}^{n} p_j = 1$. It is obvious from Eq. (8.14) that all eigenvalues for $j \geq 1$ have negative real parts for sufficiently small α. Real parts are zero for $\alpha = (n/4)\sec^2(\pi j/n)$. The smallest values of $\sec^2(x)$, and hence the first eigenvalues to become positive, occur for arguments furthest away from the asymptote at $x = \pi/2$. This happens simultaneously for $j = 1$ and $j = n - 1$ and leads to a critical point point at $\alpha_c = (n/4)\sec^2(\pi/n)$. For large values of n, the secant squared will approach unity. We thus have $\lim_{n\to\infty} \alpha_c = n/4$. The heuristic approach of the previous section led to $\alpha_c \approx n/2$. Even though the proportionality factors differ by a factor of two, the heuristic treatment and the analytical result of this section agree in that they both have α_c increase in directly proportionality to n.

Figure 8.4 shows the results of numerical simulations of Eq. (8.10); for different values of the number of states, n, the order parameter, r, is plotted as a function of the coupling parameter α. It appears that the critical exponent follows the $\gamma = 1/2$ prediction of the heuristic approach to very good accuracy. A critical exponent $\gamma = 1/2$ was already established for $n = 4$ in Ref. [5]. We also obtained the plots for $n = 6$ and $n = 8$. For these values we likewise found a critical exponent of 1/2. For values $n \gtrapprox 10$ the numerical simulations become inaccurate, especially in the vicinity of the phase transition. There are therefore insufficient data to verify the $3/(2\sqrt{n})$ prefactor in Eq. (8.9).

8.2.3 The Temperature Dependence

If transitions as in Eq. (8.5) are thermally activated, then the transition rate k generally follows an Arrhenius dependence and features the temperature, T, in the denominator of the exponent, i.e. $k \propto \exp[-b/T]$, where b is positive [19]. This means that the coupling parameter α in Eq. (8.5) should be replaced by α/T if we wish to include temperature dependence. We can now see how the system behaves in the experimentally more likely scenario where the temperature is varied while coupling constants are fixed and constant. Equation (8.7) has the form $r \propto \sqrt{\alpha - \alpha_c}$, where α_c denotes the critical value of α. For a constant $\alpha = \alpha_0$ and a varying temperature T, this formula takes the form $r \propto \sqrt{\alpha_0/T - \alpha_0/T_c} \propto \sqrt{1/T - 1/T_c}$. When T is close to T_c, the latter expression is well approximated by $r \propto \sqrt{T_c - T}$. This is the same

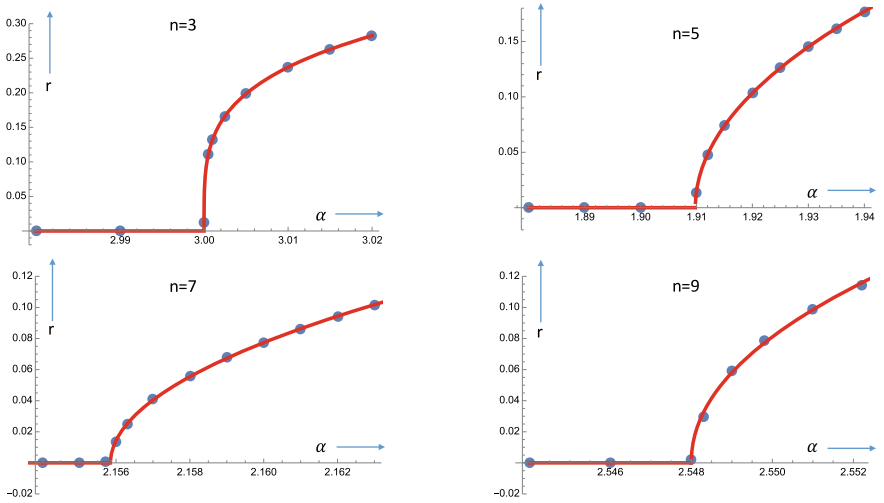

Fig. 8.4 The order parameter, r (cf. Eq. (8.8)), as a function of the coupling parameter α. Shown are the results of numerical simulation of the ODEs (cf. Eq. (8.10)) with *Mathematica* for 3, 5, 7, and 9 states. Each dot represents the result of a simulation of a million units of time. After the order parameter had relaxed to a constant value, the average over 100,000 units of time was taken. The red curves result from fitting a power law, $r = q(\alpha - \alpha_c)^\gamma$ to the blue dots, where α_c is the critical value $\alpha_c = (n/4)\sec^2(\pi/n)$. Let (q_n, γ_n) be the result of this fit for the n-state system. For $n = 3$, we find $(q_3, \gamma_3) = (0.77, 0.25)$. For $n = 5$, $n = 7$, and $n = 9$ we gathered data up to $r \approx 0.1$ so as to identify just the leading order behavior. The results were $(q_5, \gamma_5) = (1.0, 0.50)$, $(q_7, \gamma_7) = (1.2, 0.51)$, and $(q_9, \gamma_9) = (1.6, 0.48)$. The values of the prefactor q_n appear of the order of magnitude of the $(3/2)\sqrt{1/n}$-prediction (cf. Eq. (8.9)), but do not show the $\propto \sqrt{1/n}$ decrease with n

mean-field temperature dependence of the order parameter that we discussed earlier in the context of the gas-liquid transition (cf. Fig. 8.1) and the onset of magnetization (cf. Fig. 8.2).

8.3 Conclusions and Discussion

8.3.1 The Phase Transition as the Number of States Is Increased

The system of Fig. 8.3a with $n = 3$ has already been a starting point for much research [28–31]. What we observe for $n = 3$ is a critical exponent of 1/4 (see Fig. 8.4). A bifurcation with a critical exponent of 1/4 occurs in $\dot{x} = x(\mu - x^4)$ as the system crosses $\mu = 0$. For our system in case of $n = 3$, the nonlinear system of three coupled first-order equations is highly coupled; each of the three equations contains nonlinear terms that contain all of the three dependent variables. It should furthermore be pointed out that this system of three coupled first-order ordinary

differential equations actually readily reduces to second order. This is because of the fixed and normalized total population, i.e. $p_1 + p_2 + p_3 = 1$.

For $n = 4$ each state is coupled to two of the four others states. In Ref. [5] the system of ODEs is numerically solved and, in addition, stochastic simulations are performed and a heuristic derivation is presented. The critical exponent comes out to be 1/2. For $n = 4$, we still face a highly structured dynamical system and it is remarkable that the statistical approach and the associated mean-field prediction apparently already apply.

In the system of Fig. 8.3a, each state "interacts" with its two neighbor states. So for general n, each oscillator effectively connects with a fraction of about $2/n$ of the entire population. It appears that for $n = 4$, the fraction of 1/2 is sufficiently high to warrant a mean-field approach. As n is increased, we expect the legitimacy of the mean-field approach to break down. In Ref. [5] the continuum limit, $n \to \infty$, of the system in Fig. 8.3a is investigated. In that limit the flow of probability density around the cycle in Fig. 8.3a is described by a PDE that, after some manipulation, appears equivalent to a Burgers' Equation [15]. It turns out that for $n \to \infty$, a phase transition no longer occurs as α is varied. The results presented in Sect. 8.2 of this article are consistent with this observation: in the $n \to \infty$ limit, the phase transition is pushed to the $\alpha \to \infty$ limit. Going to $n = 10$ with our numerical simulations, we did not observe a change of the mean-field exponent of 1/2. All in all, both the simple heuristic approach and the full simulation of the ODEs show that the critical exponent of the phase transition keeps the mean-field value of 1/2, but that the phase transition occurs for ever higher values of the coupling parameter, α, as the number of states, n, is increased. We will come back to this in the penultimate subsection.

8.3.2 *Entropy and Dissipative Structures*

As was mentioned before, our system as depicted in Fig. 8.3 has irreversible transitions. Unlike the systems discussed in Sects. 8.1.1 and 8.1.2, it is not at equilibrium. Our system produces entropy and in this subsection we will come to a quantitative assessment of the involved entropies.

One oscillator with a probability p_k of being in state k, comes with an associated entropy of $S = -\sum_{k=1}^{n} p_k \log p_k$. For the case of a homogeneous distribution, i.e. $p_k = 1/n \ \forall k$, it is readily found that $S = \log n$. If we have $p_k = (1 + \varepsilon)/n$ for half of the n states and $p_k = (1 - \varepsilon)/n$ for the other half, then we find $S \approx \log n - \varepsilon^2/2$ after we use the approximation $\log(1 \pm \varepsilon) \approx \pm\varepsilon - \varepsilon^2/2$. In other words, the nonhomogeneous distribution of oscillators over states leads to an entropy decrease. Clustering decreases entropy.

Consider again the "bump" in Fig. 8.3b. If the probability in each state were $1/n$, then the flux from each state to the next would be $J_{i\to(i+1)} = p_i k_i = 1/n$. However, when there is a jump as in Fig. 8.3b, the two fluxes adjacent to the jump carry nonzero exponents (cf. Eq. (8.5)). From state i to $i + 1$, the probability goes from $(1 - \varepsilon)/n$ to $(1 + \varepsilon)/n$. This leads to $J_{i\to(i+1)} = (1/n)(1 - \varepsilon) \exp[2\alpha\varepsilon/n]$

and $J_{(i+1)\to(i+2)} = (1/n)(1+\varepsilon)\exp[2\alpha\varepsilon/n]$. Upon going from state $(i+m)$ to state $(i+m+1)$, there is a probability decrease from $(1+\varepsilon)/n$ to $(1-\varepsilon)/n$. This leads to $J_{(i+m)\to(i+m+1)} = (1/n)(1+\varepsilon)\exp[-2\alpha\varepsilon/n]$ and $J_{(i+m+1)\to(i+m+2)} = (1/n)(1-\varepsilon)\exp[-2\alpha\varepsilon/n]$. The remaining fluxes along the horizontal axis in Fig. 8.3b are $(1+\varepsilon)/n$ and $(1-\varepsilon)/n$ in the elevated and lowered part, respectively. They average to $1/n$ as there are just as many elevated as lowered probabilities. It is readily verified that the four fluxes adjacent to the upward and downward jump average to $(1/n)\cosh[2\alpha\varepsilon/n]$. For any nonzero real value of x, we have $\cosh x > 1$. This means that having a "bump" leads to a higher throughput for the cycle in Fig. 8.3a and to a larger production of entropy.

The phase transition from a homogeneous distribution to one with "bumps" constitutes a symmetry breaking and an establishment of an order. However, this lower entropy structure leads to a larger throughput and a larger entropy production for the system as a whole. We can thus view the bumps as a self-organized dissipative structure as described by Prigogine in the 1970s [20].

The increase of four fluxes from an average of $1/n$ to an average of $(1/n)\cosh[2\alpha\varepsilon/n]$ for every bump can help us understand why the phase transition is pushed out to $\alpha \to \infty$ for $n \to \infty$. We have $|\varepsilon| < 1$. So for $n \to \infty$, the argument $2\alpha\varepsilon/n$ vanishes (leading to $(1/n)\cosh[2\alpha\varepsilon/n] \to 1/n$) and the enhanced flux disappears, *unless* α changes proportionally with n.

The subject matter of this subsection can be the starting point for ample mathematical analysis. There is, for instance, a large body of work on how the flux through an entire cycle as in Fig. 8.3a is affected if just a few transitions are speeded up [14, 16]. As Eq. (8.7) is a rough approximation already, it would be somewhat excessive to substantially elaborate in this direction.

8.3.3 Why Mean-Field Works for a 1D System

It may at first seem surprising that a 1D system as in Fig. 8.3a gives rise to a value of the critical exponent that is characteristic of the mean-field approximation. After all, the 1D Ising model features no phase transition at all if the number of involved spins, N, is finite. Only if the 1D Ising array has infinitely many spins is there a phase transition, but it occurs at the $T \to 0$ limit if $N \to \infty$.

However, upon closer consideration our mean-field result makes sense. With the system in Fig. 8.3a we face a large number of oscillators, N_{tot}, that is distributed over n states. For the mass action approach of Eq. (8.10) to apply, we need $N_{tot} \gg n$. Let N_i be the number of oscillators in state i. We then have $p_i = N_i/N_{tot}$. The rate of change of N_i depends on the numbers N_{i-2}, N_{i-1}, N_i, and N_{i+1}. In this way every individual oscillator is interacting with infinitely many other oscillators. The legitimacy of the mean-field approach can thus be understood.

The 1D Ising model can be evaluated analytically and the pertinent derivation is shown in many authoritative textbooks [10, 22, 24]. A rigorous treatment shows that at finite temperature, the magnetization (which is taken as an order parameter in

Ising models) is zero in the absence of an external field. However, as the temperature T goes to zero, a singularity is approached. Complete alignment, i.e. $r = 1$, occurs at $T = 0$ [22]. Lev Landau gave a good intuitive explanation of this behavior [24]. We will give an explanation in the same vein for our coupled oscillators, but before doing so it is instructive to reiterate Landau's account.

Let $-J$ and $+J$ be the energies for neighboring spins in the parallel and antiparallel alignment, respectively. Next imagine a cyclic 1D array of N spins all in parallel alignment. We randomly pick two non-neighboring spins on this cycle. There are $W = N(N-3)$ ways to make this choice. The chosen spins divide the cycle into two segments. After flipping all the magnets in one of the segments, we have two magnetic domains. The flipping involves two interfaces where the energy increases from $-J$ to $+J$ and thus requires $4J$ of free energy. However, it is also associated with an entropy increase of $\Delta S = k_B \ln W \approx 2k_B \ln N$. For finite T and $N \to \infty$, we always have $T\Delta S \gg 4J$. This means that no finite coupling energy is sufficient to overcome the thermal noise and give full alignment of all spins. Only at $T = 0$ is it possible to achieve $r > 0$.

Going back to the system depicted in Fig. 8.3a, a similar line of reasoning is found to apply. Assume we add one oscillator to the system with N_{tot} oscillators. The randomization over n states is associated with an entropy of $S = k_B \ln n$. This quantity obviously increases with n. As was mentioned before, the energy that is driving the transitions features in the exponents of the transition rates k_i (cf. Eq. (8.5)). If an oscillator is added to state i, there is a change in the quantities $\alpha(p_{i+2} - p_i)$ and $\alpha(p_i - p_{i-2})$ that are in the exponents of k_{i+1} and k_{i-1}, respectively. For an increasing number of states, one oscillator is coupled to an ever smaller fraction of the entire population of oscillators. The changes in the coupling energy will therefore become ever more insignificant upon increase of n when compared to $k_B T \ln n$, i.e. the free energy change due to entropy effects. This explains why the value of the coupling constant α at which the phase transition occurs increases with n. Equivalently, the value of T at which the phase transition occurs decreases with n and we have $T_c \to 0$ as $n \to \infty$.

The resiliency of the critical exponent value of 1/2 would be an interesting venue for future research. We have shown that in a nonequilibrium setting as in Fig. 8.3a, the value of 1/2 persists for any number of states. But what would happen if, for instance, we let the rates k_i, where $i = 1...n$, depend on time, i.e., k_i goes up or down as an oscillator spends more time in state i? How much can we modify the system in Fig. 8.3a before we find another critical behavior?

8.3.4 Implications for Coupled Oscillators in the Wet Lab

We have seen and come to understand that the 2nd order phase transition with a critical exponent of 1/2 is very robust. The mean-field value of the critical exponent arises because the mass action (Eq. (8.10)) implies that each oscillator in the system is coupled to infinitely many other oscillators. Coupling an oscillator to a smaller

fraction of the total number of oscillators pushes the phase transition to a higher value of the coupling coefficient or, equivalently, to a smaller value of the temperature. With this insight we expect that the critical exponent value of 1/2 will also persist if the transition rates in Fig. 8.3a are made to vary along the cycle or if other mathematical forms for the population dependencies of the the transition rates are tried.

There is autocatalysis or product stimulation in the system depicted in Fig. 8.3a, i.e., the product of the $j \rightarrow j+1$ transition increases the rate of the $j \rightarrow j+1$ transition. Product stimulation is a form of positive feedback and it is commonly the underlying driving force behind biochemical oscillations [21]. In the system in Fig. 8.3a, the parameter α can be seen as a measure for the strength of the positive feedback. Product stimulation is a key feature in the glycolytic oscillations that were already mentioned in Sect. 8.1.4 [3]. The product stimulation in glycolytic oscillations is twofold. ATP binding and hydrolysis is the first step in this metabolic chain, but subsequently ATP is produced again at several steps in the chain. Furthermore, early in the chain energy that is harvested from the breakdown of glucose is stored in NAD reduction: $NAD^+ + H^+ + 2e^- \rightarrow NADH$. For the final step in the chain, the conversion from acetaldehyde to ethanol, the necessary energy is derived from the oxidation of NADH, i.e. the reverse reaction: $NADH \rightarrow NAD^+ + H^+ + 2e^-$. The glycolysis consists of about ten enzyme-mediated steps and because ATP and NADH are products as well as substrates in the chain, the chain can be seen as a cycle much like the one in Fig. 8.3a.

In a suspension of oscillating yeast cells there is a synchronized oscillation inside every cell. The number of oscillators inside each cell, N_{in}, is different for each cell. The catalyzing enzymes process the substrate molecules one-by-one and it is substrate concentrations and the number of enzymes in each cell that ultimately determine an effective N_{in} and a characteristic frequency for each cell.

As was mentioned before, acetaldehyde can freely permeate the membrane of the yeast cell. The oscillations are thus coupled through the shared acetaldehyde concentration. It is obvious that for a suspension with a small density of yeast cells, the acetaldehyde concentration will be close to zero and not lead to any coupling. Reference [27] models the suspension of oscillating yeast cells with a Kuramoto model, where the shared acetaldehyde concentration provides the coupling between the M cells. Figure 8.5a is from Ref. [27] and shows the order parameter as a function of the density. The order parameter r is experimentally determined by simultaneously following the fluorescing behavior of individual cells that have been fixed in their location. The measurements are not very precise, but appear consistent with the phase transition and the critical exponent of 1/2 that are predicted by the Kuramoto model. A model as in Fig. 8.3a, which also predicts a critical exponent of 1/2, may be more chemically realistic than the Kuramoto model as it explicitly includes positive feedbacks that underlie the oscillations.

There is still a measure of controversy about the oscillations of yeast cells in a suspension. Reference [27] reports the observation that individual cells still oscillate even when they are in a solution that is too dilute for coupling. In Ref. [23], on the other hand, similar measurements were described and there it was found that cells in a diluted solution no longer oscillate. The authors of Ref. [23] describe how

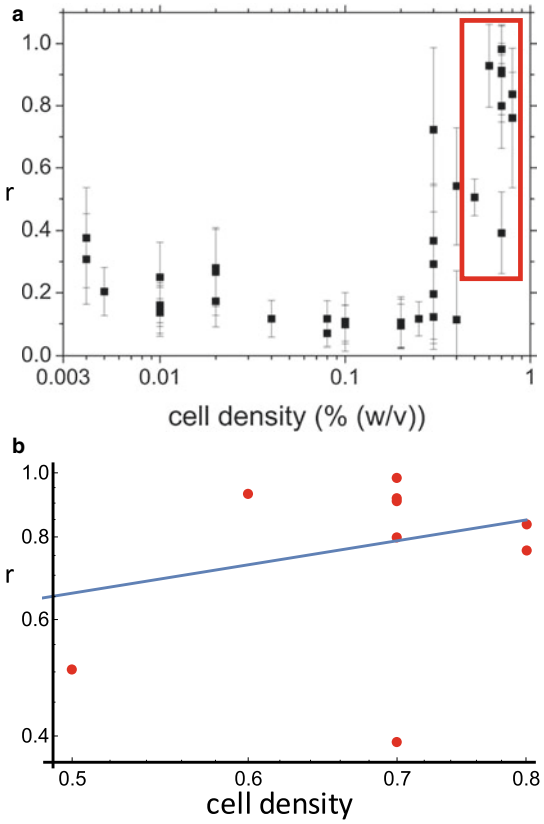

Fig. 8.5 **a** The top graph is from Ref. [27]. Yeast cells in a suspension synchronize their glycolytic oscillations, but do so more effectively if the density of the cells in the suspension is higher. The horizontal axis (note the logarithmic scale) gives the density of the yeast cells in the suspension. On the vertical axis r gives the resulting order parameter for the coupled oscillating cells (cf. Eq. (8.8)). From a density of about 0.5% on, we observe a rapid increase of r and what appears like a phase transition. The bottom graph shows the data points in the red rectangle and giving the vertical axis a logarithmic scale, we find for the best fitting straight line a slope of 0.54. The margins of error are large and data points exhibit a wide spread, but this result appears consistent with the 1/2 that the Kuramoto model and our theory predict

a suspension of cells ultimately uses the acetaldehyde concentration for "quorum sensing." Only when a quorum is met, i.e. when the cell density and the ensuing bath-acetaldehyde concentration are sufficiently high, do oscillations commence. A Kuramoto model is in that case no longer appropriate. Quorum-sensing can be consistent with a model as in Fig. 8.3a. In a very dilute solution acetaldehyde effectively diffuses away and disappears from the cell as soon as it is formed. The conversion to ethanol and the accompanying NADH consumption then no longer take place. Instead of an NADH-NAD feedback loop, we would get NADH accumulation. Upon increase of the cell density, the NADH-NAD feedback loop gets established. Once

the quorum is met, a mean-field approach applies and a phase transition with a critical exponent of 1/2 once again occurs.

Acknowledgements We are grateful to Katja Lindenberg, Hans Westerhoff, and Bartek Lisowski for very useful feedback on earlier versions of this manuscript.

References

1. S. Arajs, B.L. Tehan, E.E. Anderson, A.A. Stelmach, Critical magnetic behavior of nickel near the Curie point. Phys. Stat. Sol. **41**(2), 639–648 (1970)
2. E. Batschelet, *Circular Statistics in Biology* (Academic Press, New York, 1981), pp. 54–58
3. M. Bier, B. Teusink, B.N. Kholodenko, H.V. Westerhoff, Control analysis of glycolytic oscillations. Biophys. Chem. **62**(1), 15–24 (1996)
4. M. Bier, B.M. Bakker, H.V. Westerhoff, How yeast cells synchronize their glycolytic oscillations: a perturbation analytic treatment. Biophys. J. **78**(3), 1087–1093 (2000)
5. M. Bier, B. Lisowski, E. Gudowska-Nowak, Phase transitions and entropies for synchronizing oscillators. Phys. Rev. E **93**(1), 012143 (2016)
6. B. Blocken, T. van Druenen, Y. Toparlar, F. Malizia, P. Mannion, T. Andrianne, T. Marchal, G.J. Maas, J. Diepens, Aerodynamic drag in cycling pelotons: new insights by CFD simulation and wind tunnel testing. J. Wind Eng. Ind. Aerod. **179**, 319–337 (2018)
7. E. Borysewicz, *Bicycle Road Racing: The Complete Program for Training and Competition* (Velo-News, Boulder, CO, 2005)
8. W. Boyce, R. DiPrima, *Elementary Differential Equations*, 10th edn. (Wiley, Hoboken, NJ, 2012)
9. J.P. Broker, C.R. Kyle, E.R. Burke, Racing cyclist power requirements in the 4000-m individual and team pursuits. Med. Sci. Sports Exerc. **31**(11), 1677 (1999)
10. P.M. Chaikin, T.C. Lubensky, *Principles of Condensed Matter Physics* (Cambridge University Press, Cambridge, UK, 1995)
11. K. Dhahri, N. Dhahri, J. Dhahri, K. Taibi, E.K. Hlil, Critical phenomena and estimation of the spontaneous magnetization from a mean field analysis of the magnetic entropy change in $La_{0.7}Ca_{0.1}Pb_{0.2}Mn_{0.95}Al_{0.025}Sn_{0.025}O_3$. RSC Adv. **8**(6), 3099–3107 (2018)
12. B. Eckhardt, E. Ott, S.H. Strogatz, D.M. Abrams, A. McRobie, Modeling walker synchronization on the Millennium Bridge. Phys. Rev. E **75**(2), 021110 (2007)
13. E.A. Guggenheim, The principle of corresponding states. J. Chem. Phys. **13**(7), 253–261 (1945)
14. R. Heinrich, T.A. Rapoport, A linear steady-state treatment of enzymatic chains. Eur. J. Biochem. **42**(1), 89–95 (1974)
15. E.A. Jackson, *Perspectives of Nonlinear Dynamics*, vol. 2 (Cambridge University Press, New York, 1991)
16. H. Kacser, The control of flux. Symp. Soc. Exp. Biol. **27**, 65–104 (1973)
17. L.P. Kadanoff, W. Götze, D. Hamblen, R. Hecht, E.A.S. Lewis, V.V. Palciauskas, M. Rayl, J. Swift, D. Aspnes, J. Kane, Static phenomena near critical points: theory and experiment. Rev. Mod. Phys. **39**(2), 395–431 (1967)
18. P. Läuger, *Electrogenic Ion Pumps* (Sinauer Associates Inc., Sunderland, MA, 1991)
19. W. Moore, *Physical Chemistry*, 5th edn. (Prentice-Hall, Englewood, New Jersey, 1974)
20. G. Nicolis, I. Prigogine, *Self-organization in Non-Equilibrium Systems: From Dissipative Structures to Order Through Fluctuations* (Wiley, New York, 1977)
21. B. Novák, J.J. Tyson, Design principles of biochemical oscillators. Nat. Rev. Mol. Cell Biol. **9**(12), 981–991 (2008)
22. M. Plischke, B. Bergersen, *Equilibrium Statistical Physics*, 2nd edn. (World Scientific Publishing, Singapore, 1994)

23. A.K. Poulsen, M.Ø. Petersen, L.F. Olsen, Single cell studies and simulation of cell–cell interactions using oscillating glycolysis in yeast cells. Biophys. Chem. **125**(2), 275–280 (2007)
24. S. Salinas, *Introduction to Statistical Physics*, 1st edn. (Springer, New York, 2001), pp. 257–276
25. G. Seber, *A Matrix Handbook For Statisticians* (Wiley, Hoboken, NJ, 2008), p. 153
26. S.H. Strogatz, From Kuramoto to Crawford: exploring the onset of synchronization in populations of coupled oscillators. Physica D **143**(1), 1–20 (2000)
27. A. Weber, Y. Prokazov, W. Zuschratter, M.J.B. Hauser, Desynchronisation of glycolytic oscillations in yeast cell populations. PLoS ONE **7**(9), e43276 (2012)
28. K. Wood, C. Van den Broeck, R. Kawai, K. Lindenberg, Critical behavior and synchronization of discrete stochastic phase-coupled oscillators. Phys. Rev. E **74**(3), 031113 (2006)
29. K. Wood, C. Van den Broeck, R. Kawai, K. Lindenberg, Universality of synchrony: critical behavior in a discrete model of stochastic phase-coupled oscillators. Phys. Rev. Lett. **96**(14), 145701 (2006)
30. K. Wood, C. Van den Broeck, R. Kawai, K. Lindenberg, Continuous and discontinuous phase transitions and partial synchronization in stochastic three-state oscillators. Phys. Rev. E **76**(4), 041132 (2007)
31. K. Wood, C. Van den Broeck, R. Kawai, K. Lindenberg, Effects of disorder on synchronization of discrete phase-coupled oscillators. Phys. Rev. E **75**(4), 041107 (2007)

Part II
Model-Driven and Data-Driven Approaches

Chapter 9
On Localised Modes in Bio-inspired Hierarchically Organised Oscillatory Chains

Ivana Kovacic, Dragi Radomirovic, and Miodrag Zukovic

Abstract This study is concerned with bio-inspired hierarchically organised oscillatory chains from the viewpoint of a localisation phenomenon, when only certain parts of the chain oscillate. The chain consists of block masses attached mutually via tension-extension Hookean springs. The first- and second-order hierarchy are considered to determine their modes and modal frequencies, with the focus on localised modes. Then, a chain with an arbitrary number of masses is dealt with. A theorem is presented that defines the number of its localised modes in terms of the order of hierarchy.

Keywords Spring-mass system · Coupling · Localisation phenomenon

9.1 Introduction

Mechanical aspects of trees' static and dynamic behaviour and the role of branches have been intriguing researchers not only for decades, but for centuries. Even Galileo [1] noted 'that an oak two hundred cubits high would not be able to sustain its own branches if they were distributed as in a tree of ordinary size.' Branches of trees belong to slender structures, but cope reasonably well both with small and large-amplitude oscillations caused by a variety of excitations, unlike man-made slender structures, which are not so robust. Understanding the underlying physical principle of their behaviour is of interest both for plant science [2] and also for biomimetics when they are modelled as coupled oscillators [3], as they can be beneficially utilised in many engineering applications [3, 4].

Of interest for this work are mechanical models of branched trees as biological oscillators. These mechanical models created and examined so far have been either

I. Kovacic (✉) · M. Zukovic
Faculty of Technical Sciences, Centre of Excellence for Vibro-Acoustic Systems and Signal Processing, University of Novi Sad, Novi Sad, Serbia
e-mail: ivanakov@uns.ac.rs

D. Radomirovic
Faculty of Agriculture, University of Novi Sad, Novi Sad, Serbia

A. Stefanovska and P. V. E. McClintock (eds.), *Physics of Biological Oscillators*, Understanding Complex Systems,
https://doi.org/10.1007/978-3-030-59805-1_9

discrete or continuous, with only few multi-degree-of-freedom models of branched trees with discrete masses. In [5, 6], each structural element of a tree—the trunk and branches—are treated as oscillating masses attached mutually via springs arranged in parallel. The model is simple and potentially useful for biomimetic applications, especially related to tuned mass-dampers [3]. However, its dynamic behaviour has not been explored deeply. This work contributes to this shortcoming from the viewpoint of the appearance of localised modes, when only a part of the structure oscillates, but the main mass, i.e. the trunk stays at rest.

9.2 Model with First-Order Branches

A discrete model of a trunk with two branches is shown in Fig. 9.1: the trunk (main mass) is of mass m and it is attached first to the fixed base via one linear spring of stiffness k as well as via two parallel linear springs of stiffness k_1 to two subsequent masses m_1, which mimic the branches. Such model is suggested in [6], but no analyses of its modal characteristics have been presented. Thus, such analyses are provided subsequently. The generalised coordinates are chosen to be the absolute displacements x, y_1, y_2 of each mass measured from the respective equilibria (Fig. 9.1). The chain from Fig. 9.1 has the following equations of motion per each mass:

$$m\ddot{x} + (k + 2k_1)x - k_1 y_1 - k_1 y_2 = 0, \tag{9.1}$$

$$m_1\ddot{x}_1 - k_1 x + k_1 y_1 = 0, \tag{9.2}$$

$$m_1\ddot{x}_1 - k_1 x + k_1 y_1 = 0. \tag{9.3}$$

In order to determine natural (mode) frequencies ω, one can assume the solutions as $x = A\cos\omega t$, $y_1 = B_1\cos\omega t$, $y_2 = B_2\cos\omega t$, where the amplitudes A, B_1, B_2 and ω are unknown. Substituting these forms into the equations of motion, the corresponding characteristic equation [7] can be derived:

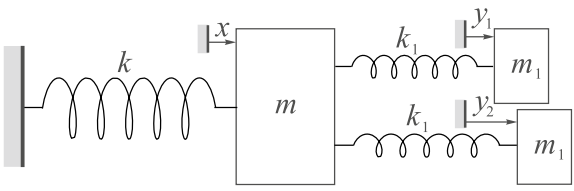

Fig. 9.1 Mechanical model of a trunk and first-order branches

$$\Delta_{21} = \begin{vmatrix} k + 2k_1 - m\omega^2 & -k_1 & -k_1 \\ -k_1 & k_1 - m_1\omega^2 & 0 \\ -k_1 & 0 & k_1 - m_1\omega^2 \end{vmatrix} = 0. \tag{9.4}$$

This equation can be represented as $\Delta_{21} = \Delta_{21,1}\ \Delta_{21,2} = 0$, where

$$\Delta_{21,1} = \left(k_1 - m_1\omega^2\right), \tag{9.5}$$

$$\Delta_{21,2} = \left[kk_1 - (k_1 m + km_1 + 2k_1 m_1)\omega^2 + mm_1\omega^4\right] = 0. \tag{9.6}$$

Based on previous experiments that the masses and stiffness reduce with a new order of hierarchy, the corresponding reduction laws are taken as follows: $\frac{m_1}{m} = \left(\frac{1}{2}\right)^{\frac{4}{3}}$, $\frac{k_1}{k} = \kappa$ (see [3] and the references cited there). The parameter κ represent the stiffness ratio.

Three resulting modal frequencies are calculated from Eqs. (9.5)–(9.6) and plotted versus the stiffness ratio in Fig. 9.2.

Note that the modal frequencies are normalised with respect to the natural frequency of the trunk, i.e. the first mass m and the spring k, where this natural frequency is $\sqrt{(k/m)}$. The second modal frequency ω_{II} is obtained by equating Eq. (9.5) to zero as $\frac{\omega_{\mathrm{II}}^2}{\left(\frac{k}{m}\right)} = \frac{k_1}{m_1}$, while the first ω_{I} and third frequency ω_{III} are calculated by making Eq. (9.6) equal to zero. Note that $\frac{\omega_{\mathrm{I}}}{\sqrt{k/m}} \to 0.75$ when $\kappa \to \infty$,

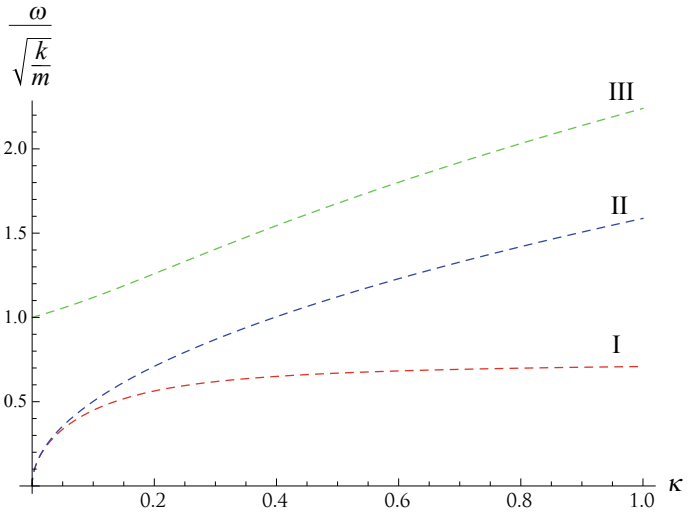

Fig. 9.2 Modal frequencies I, II and III of the model with first-order branches calculated from Eqs. (9.5) and (9.6)

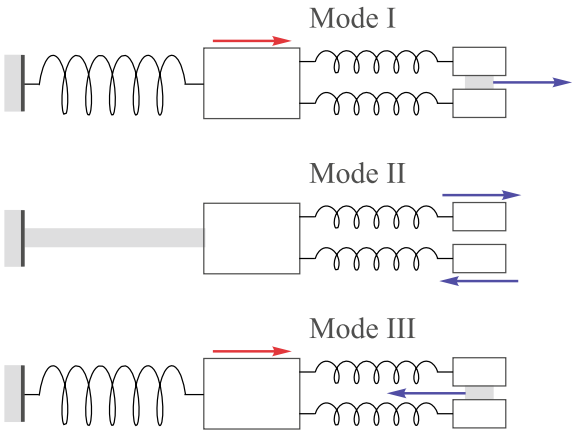

Fig. 9.3 Mode shapes I–III of the model with first-order branches

which implies that the first modal frequency has an asymptotic value equal to 75% of the natural frequency of the trunk.

Three mode shapes describing the behaviour at each frequency, i.e. the ratios of the amplitudes of masses at each frequency, are shown in Fig. 9.3 qualitatively. In the first mode, all the masses move in-phase and the amplitudes of the smaller masses are equal ($B_1 = B_2$), which indicates that they behave as rigidly attached to each other (Mode I, Fig. 9.3). Note that the direction of motion is depicted by the arrows. The second mode that corresponds to the frequency ω_{II} is characterised by the fact that the first mass does not move ($A = 0$), while the smaller masses move out-of-phase ($B_1 = -B_2$) (Mode II, Fig. 9.3), i.e. the mode is localised in these branches, while the trunk stays at rest. In the third mode shape, the main mass and the smaller ones move out-of-phase, but the amplitudes of the smaller masses are equal ($B_1 = B_2$), so they again behave as rigidly attached to each other (Mode III, Fig. 9.3).

9.3 Models with Second-Order Branches

The model with two block masses arranged in parallel that are attached to the main mass (Fig. 9.1) is enriched now with the second-order hierarchy (Fig. 9.4), where

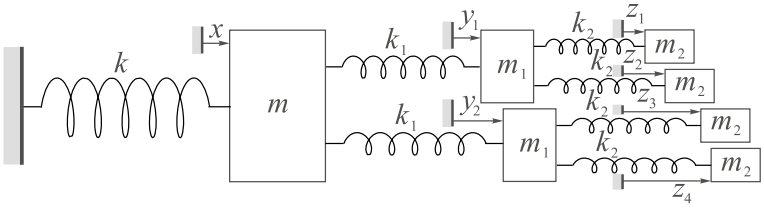

Fig. 9.4 Mechanical model with second-order branches

two pairs of block masses m_2 are attached to two masses m_1 by parallel linear springs of equal stiffness k_2.

Following the algorithm from the previous section, it is assumed that the reduction of the parameters follows the laws: $\frac{m_1}{m} = \frac{m_2}{m_1} = \left(\frac{1}{2}\right)^{\frac{4}{3}}$, $\frac{k_1}{k} = \frac{k_2}{k_1} = \kappa$ [3]. Four absolute generalised coordinates z_1–z_4 are introduced (Fig. 9.4). Deriving the equations of motion as in Sect. 9.2, assuming the harmonic solutions for each coordinate, the following corresponding characteristic equation [7] can be obtained:

$$\Delta_{22} = \Delta_{22,1}\Delta_{22,2}\Delta_{22,3} = 0, \tag{9.7}$$

where:

$$\Delta_{22,1} = \left(k_2 - m_2\omega^2\right)^2, \tag{9.8}$$

$$\Delta_{22,2} = k_1k_2 - (k_2m_1 + k_1m_2 + 2k_2m_2)\omega^2 + m_1m_2\omega^4, \tag{9.9}$$

$$\begin{aligned}\Delta_{22,3} = {} & kk_1k_2 - (k_1k_2m + kk_2m_1 + 2k_1k_2m_1 + kk_1m_2 + 2kk_2m_2 + 4k_1k_2m_2)\omega^2 \\ & + (k_2mm_1 + k_1mm_2 + 2k_2mm_2 + km_1m_2 + 2k_1m_1m_2)\omega^4 - mm_1m_2\omega^6,\end{aligned} \tag{9.10}$$

with ω again standing for the unknown frequency of each mode. The solutions of the characteristic equation (9.7), normalised with $\sqrt{k/m}$ are presented in terms of the stiffness ratio in Fig. 9.5. As seen from Eq. (9.8), one modal frequency is double: $\omega_{\mathrm{II}}^2 = k_2/m_2$. The order of modal frequencies III = IV and V changes for $\kappa \approx 0.59$.

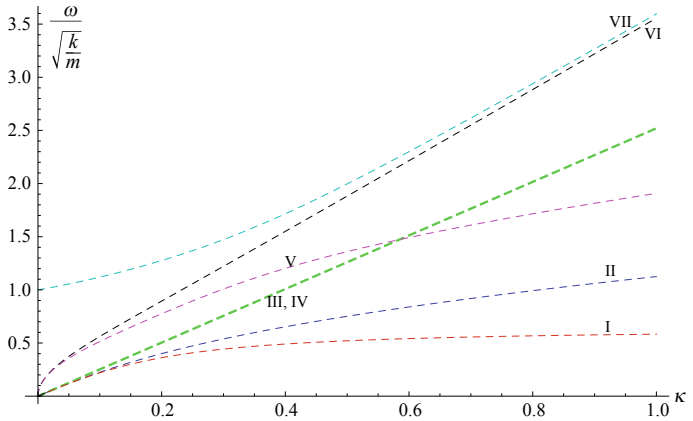

Fig. 9.5 Modal frequencies I–VII of the system with second-order branches calculated from Eqs. (9.8)–(9.10)

Two penultimate frequencies (VI and VII) become close to each other for higher κ. Note that for certain κ, frequencies III, IV can become equal to V.

Mode shapes that correspond to the behaviour at each of these frequencies are shown in Fig. 9.6 for $\kappa = 0.3$. Modes I, V and VII affect the whole chain of oscillators. Modes II and VI are localised in all branches, while Modes III = IV are localised in the second-order branches. The case plotted is when two groups of these branches move in the opposite direction (note that the green arrows in Fig. 9.6 can have opposite directions, so this is counted as a double mode).

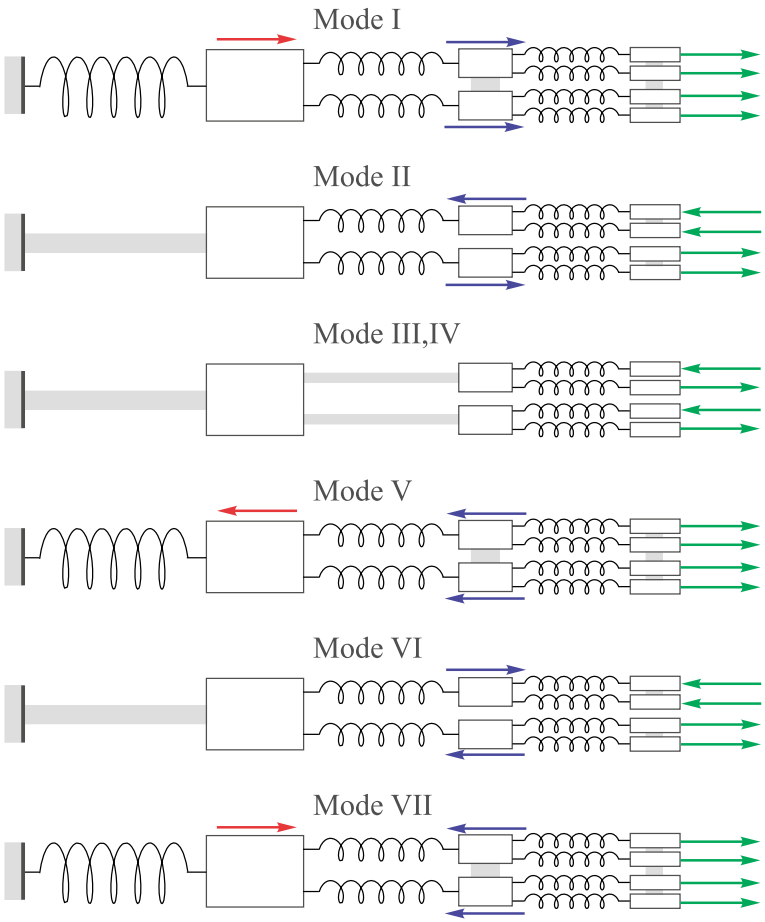

Fig. 9.6 Mode shapes for of the system with second-order branches for $\kappa = 0.3$

9.4 Model with a Chain of Arbitrary Order of Hierarchy

The models presented previously can be extended to an arbitrary order of hierarchy by adding two new subsequent masses to each mass, attaching them via two linear springs arranged in parallel (Fig. 9.7). The number of masses n in a chain is equal to the number of degrees of freedom, and is given by:

$$n = \sum_{i=0}^{\mathrm{N}} 2^{\mathrm{N}-i}. \tag{9.11}$$

where N stands for the order of hierarchy, i.e. the number of groups of equal masses arranged in parallel. So, the main mass corresponds to the zeroth order of hierarchy (N = 0, $n = 1$); two masses attached to it belongs to the first-order of hierarchy (N = 1, $n = 3$); there are four masses in the second-order of hierarchy (N = 2, $n = 7$); there are eight masses in the third order of hierarchy (N = 3, $n = 15$), and so on. Considering the equilibrium in each hierarchical order, one can distinguish several possibilities for the appearance of the localisation phenomenon:

Group 1: One pair of masses of the highest hierarchy oscillate, while the lower order of the structure is at rest (Fig. 9.8a). As the masses m_{N} oscillate with the same magnitude but in the opposite direction, the corresponding spring forces have also the same magnitude and the opposite directions. Consequently, the resulting force

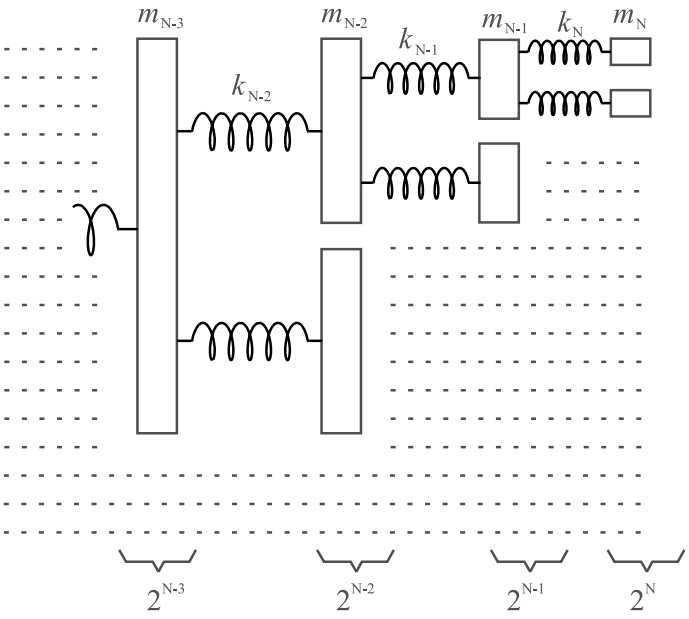

Fig. 9.7 Chain of hierarchically organised oscillators

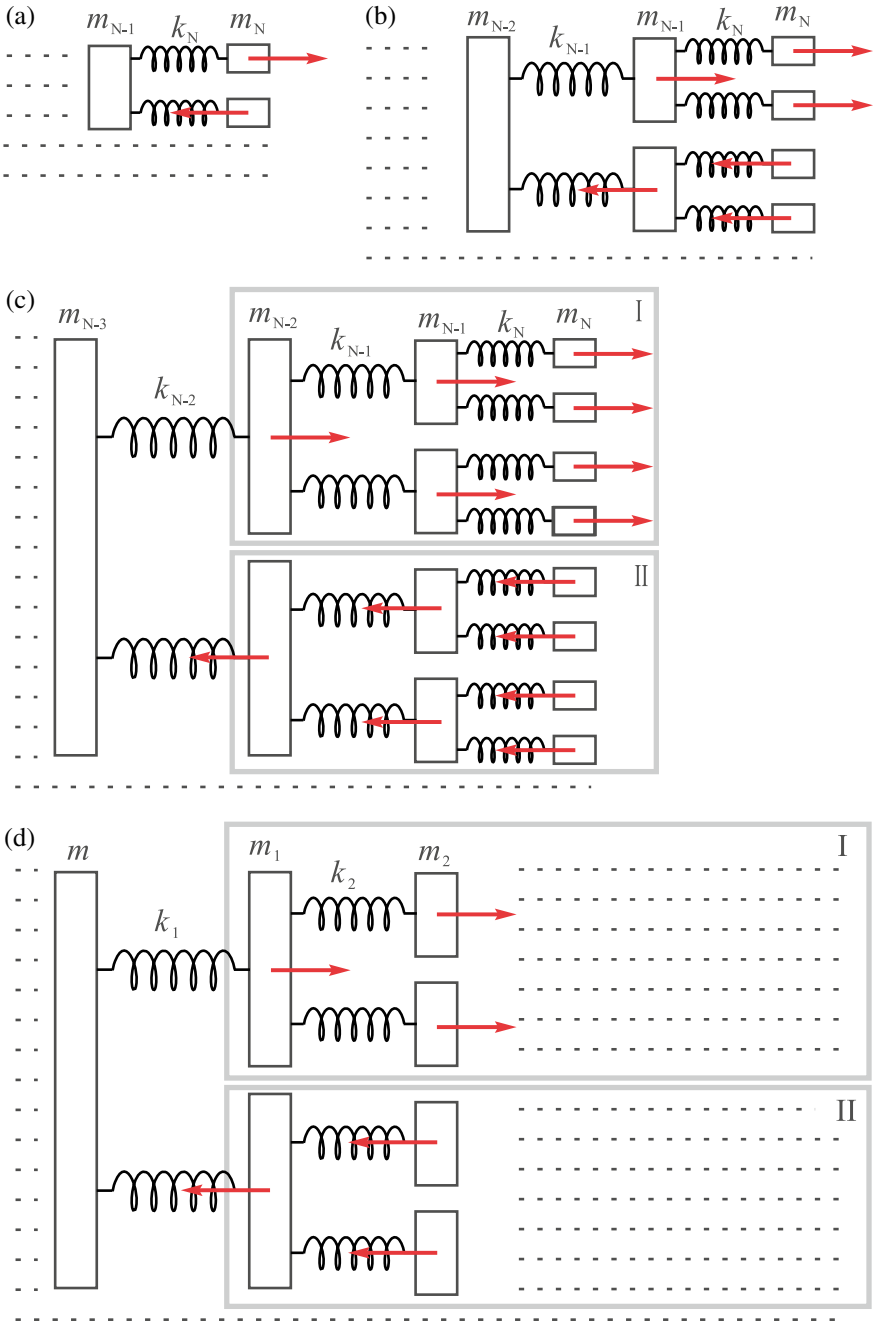

Fig. 9.8 Localised modes in: **a** Group 1; **b** Group 2; **c** Group 3; **d** Group 4

that acts on the mass m_{N-1} is equal to zero and this mass does not oscillate. The frequency of vibration corresponds to the natural frequency of the masses from the highest order of hierarchy and is equal to $\sqrt{k_N/m_N}$. The number of the localised modes n_1 that appear at this frequency corresponds to the number of the pairs of masses of the highest hierarchy: $n_1 = 1$ group* 2^N masses/2 in each pair $= 2^{N-1}$.

Group 2: This group includes the case when the masses from the penultimate and ultimate order of hierarchy oscillate (Fig. 9.8b). One mass m_{N-1} and two masses m_N attached to it move in one direction, while the other mass m_{N-1} and two masses m_N attached to it move in the opposite direction. Thus, the spring forces that act on the mass m_{N-2} cancel out and this mass stays at rest. This case is characterised by two modal shapes and two natural frequencies. The overall number of this type of modal shapes n_2 is equal to: $n_2 = 2$ groups * 2^{N-2} modal shape $= 2^{N-1}$.

Group 3: There are oscillations of the masses from the three highest orders of hierarchy (note that one existing group is presented in Fig. 9.8c). There are two sets of such masses, numbered by I and II in Fig. 9.8c. They move in the identical way but in the opposite directions, yielding a zero-valued resulting force acting on the mass m_{N-3}, so that this mass stays at rest. This case is characterised by three modal shapes and three modal frequencies. The overall number of this type of modal shapes n_3 is defined by: $n_3 = 3$ groups * 2^{N-3} modal shape.

Group 4: This class contains the modes when all masses besides the main one m (Fig. 9.8d) oscillate. There are two sets of such masses. One set contains N masses and is characterised by N modal shapes. The overall number of these modal shapes n_N is: $n_N = N$ groups * 2^{N-N} modal shape $= N$.

The following Theorem can now be formulated.

Theorem [8] *A chain consisting of the main spring-mass system to which* N *hierarchically organised parallel systems of spring-masses is attached* (Fig. 9.7) *is characterised by localised modes whose number is defined by the difference between the number of degrees of freedom and the number of masses in the hierarchy including the main mass, i.e.*

$$\sum_{i=1}^{N} i \cdot 2^{N-i} = \sum_{i=1}^{N+1} 2^{N+1-i} - (N+1) \tag{9.12}$$

This Theorem is given here without the proof, which can be found in [8]. Instead of giving the proof, the claim of the theorem is compared with the results presented in Sects. 9.2 and 9.3.

So, when $N = 1$, only one localised mode exists: the masses m_1 oscillate, but the main mass does not. This coincides with the case obtained in Sect. 9.2, illustrated in Fig. 9.3.

When $N = 2$, Theorem implies that there are four localised modes. Two modes are localised in the highest-order of hierarchy and two modes are localised in the penultimate and ultimate order of hierarchy and corresponds to different frequencies. This agrees with the findings from Sect. 9.3, presented in Fig. 9.6.

Using Theorem for the case $N = 3$, one can calculate that 11 localised modes will appear. Four modes are localised in the highest-order of hierarchy. There are two groups of two localised in the penultimate and ultimate order of hierarchy and, consequently, two doubled frequencies. In addition, there are also three modes appearing at a different frequency. It should be pointed out that this chain with the third-order hierarchy is characterised by one quadrilateral and two double modal frequencies.

9.5 Conclusions

A chain of bio-inspired hierarchically organised masses on linear springs has been considered, where the trunk is modelled as a main mass, while branches are symmetrically attached to the masses in pairs via linear springs. The mass and stiffness properties are reduced in each order of hierarchy. This model is characterised by localised modes, when only certain parts of the chain oscillate while the main mass stays at rest. So, in the case of a trunk and the first-order branches, only one localised mode exists: the main mass does not oscillate, while the branches do. In the model with second-order branches, there are two modes localised in the second-order branches and two in all branches. As the order of hierarchy increases, the number of localised modes increases, too. One potential applications of these findings is the case when the trunk is excited at the frequency tuned to the one that corresponds to a localised modes Although excited, the trunk will not oscillate, as this case corresponds to the concept of dynamic absorbers or tuned mass-dampers [3, 7].

Acknowledgements The authors acknowledge support of the Ministry of Education and Science of Serbia (the project no. 451-03-68/2020-14/200156).

References

1. G. Galilei, *Dialogues Concerning Two New Sciences, 1638* (trans. H. Crew and A. de Salvio) (Dover Publications, Mineola, New York, USA, 1954)
2. E. De Langre, Plant vibrations at all scales: a review. J. Exp. Bot. **70**, 3521–3531 (2019)
3. I. Kovacic, M. Zukovic, D. Radomirovic, Sympodial tree-like structures: from small to large-amplitude vibrations. Bioinspir. Biomim. **13**, Paper No 026002 (20 pp.) (2018)
4. I. Kovacic, M. Zukovic, Coupled purely nonlinear oscillators: normal modes and exact solutions for free and forced responses. Nonlinear Dyn. **87**, 713–726 (2017)
5. K. James, Dynamic loading of trees. J. Arboric. **29**, 165–171 (2003)
6. K.R. James, *A Dynamic Structural Analysis of Trees Subject to Wind Loading*. PhD thesis, University of Melbourne, 2010
7. I. Kovacic, D. Radomirovic, *Mechanical Vibrations: Fundamentals with Solved Examples* (Willey, 2017)
8. I. Kovacic, M. Zukovic, D. Radomirovic, On a localization phenomenon in two types of bio-inspired hierarchically organised oscillatory systems. Nonlinear Dyn. **99**, 679–706 (2020)

Chapter 10
Useful Transformations from Non-autonomous to Autonomous Systems

Alona Ben-Tal

Abstract Every non-autonomous vector field can be viewed as autonomous by treating the time as another dependent variable and augmenting the dynamical system with an additional differential equation. This standard transformation of non-autonomous vector fields to autonomous is, arguably, of little use in that common techniques for the study of autonomous systems, such as looking for stationary solutions, cannot be applied. This chapter presents alternative ways of transforming a non-autonomous system to autonomous in the special case of periodic forcing, but it also makes the argument that this could be done in other special cases. The argument is inspired by mathematical modelling. Two examples of alternative transformations are given, one in a system of ordinary differential equations and one in a Boolean network.

10.1 Introduction

Analysis of autonomous systems of ordinary differential equations, $\dot{\mathbf{x}} = \mathbf{f}(\mathbf{x})$, where $\mathbf{x} \in \mathbb{R}^n$, $\dot{\mathbf{x}}$ is the derivative of $\mathbf{x}$ with respect to time and $\mathbf{f}(\mathbf{x})$ is a vector of functions, usually starts by finding stationary solutions and their stabilities [13, 25]. The stationary solutions, $\mathbf{x}^*$, are solutions for which $\mathbf{x}(t) = \mathbf{x}^*$ for all time t. In other words, they satisfy the equation $\mathbf{f}(\mathbf{x}^*) = 0$. The stability of each stationary solution can often be found by calculating the eigenvalues of the $(n \times n)$ Jacobian $\frac{\partial f_i}{\partial x_j}\Big|_{\mathbf{x}=\mathbf{x}^*}$ where $i, j \in \{1, \ldots, n\}$. As an example, consider the simple, damped pendulum with mass m and length L (see Fig. 10.1a). The rates of change of the angle, θ, and the angular velocity, z are given by:

A. Ben-Tal (✉)
School of Natural and Computational Sciences, Massey University, Private Bag 102904, 0745 North Shore, Auckland, New Zealand
e-mail: a.ben-tal@massey.ac.nz

A. Stefanovska and P. V. E. McClintock (eds.), *Physics of Biological Oscillators*, Understanding Complex Systems,
https://doi.org/10.1007/978-3-030-59805-1_10

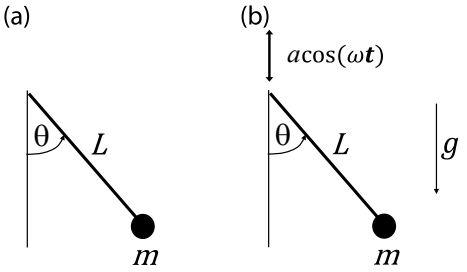

Fig. 10.1 Examples of autonomous and non-autonomous systems. **a** The simple pendulum is an autonomous system. **b** A periodically forced pendulum is a non-autonomous system

$$\begin{aligned} \frac{d\theta}{dt} &= z \\ \frac{dz}{dt} &= -\frac{g}{L}\sin\theta - \mu z \end{aligned} \tag{10.1}$$

where g is the gravitational acceleration and μ is a damping coefficient.

Here, $n = 2$ and $\mathbf{x} = [\theta, z]$. The stationary solutions are $\mathbf{x}_1^* = [0, 0]$ and $\mathbf{x}_2^* = [\pi, 0]$. The Jacobians can be calculated as:

$$\frac{\partial f_i}{\partial x_j}\Big|_{\mathbf{x}_1^*} = \begin{bmatrix} 0 & 1 \\ -\frac{g}{L} & -\mu \end{bmatrix}, \quad \frac{\partial f_i}{\partial x_j}\Big|_{\mathbf{x}_2^*} = \begin{bmatrix} 0 & 1 \\ \frac{g}{L} & -\mu \end{bmatrix} \tag{10.2}$$

from which it can be deduced that $\mathbf{x}_1^*$ is stable and $\mathbf{x}_2^*$ is unstable [13].

Consider now a periodically forced pendulum with a vertical acceleration of its base (expressed as $a\cos(\omega t)$ in Fig. 10.1b). In this case, the rates of change of θ, and z are given by (see also [9]):

$$\begin{aligned} \frac{d\theta}{dt} &= z \\ \frac{dz}{dt} &= -\frac{g}{L}\sin\theta - \mu z - \frac{a}{L}\cos(\omega t)\sin\theta \end{aligned} \tag{10.3}$$

Time appears now explicitly on the right hand side of the equations, so $\dot{\mathbf{x}} = \mathbf{f}(\mathbf{x}, t)$, and the system is non-autonomous. The standard way of transforming the non-autonomous system to autonomous is to define a new variable $\phi = t$ and augment the original system by adding a new differential equation [15, 25]:

$$\frac{d\phi}{dt} = 1 \tag{10.4}$$

The new system of differential equations, $\dot{\mathbf{y}} = \bar{\mathbf{f}}(\mathbf{y})$, is now autonomous with $n = 3$ and $y = [\theta, z, \phi]$. The standard transformation shows that the explicit appearance of time, adds another dimension to the system. This extra dimension could add significant complexity to the behavior of solutions. In particular, a two dimensional non-autonomous system could exhibit chaos, whereas, a two-dimensional autonomous

system of ordinary differential equations could not (assuming continuity and smoothness of $\mathbf{f}(\mathbf{x})$) [15]. Indeed, the forced pendulum exhibits complicated motions (see for example, [9, 10, 17, 26]). Arguably, this is where the usefulness of this transformation ends. The most basic analysis that can be done in native autonomous systems (i.e. finding stationary solutions) cannot be done in the transformed system—there is no solution to the equation $\mathbf{f}(\mathbf{y}) = 0$. One could argue that the absence of stationary solutions in non-autonomous systems is not surprising - solutions of non-autonomous systems are expected to be time-dependent. It could also be argued that techniques used to study time-dependent solutions of autonomous systems, could be used to study solutions of non-autonomous systems (for example, Poincaré map [16, 25], averaging and perturbation methods [15–17]). Nevertheless, we show in Sect. 10.3 that in special cases, there exist other transformations from non-autonomous systems to autonomous that are more useful than the standard transformation in that they allow analysis of the transformed system using theoretical results derived for native autonomous systems. Our approach is inspired by mathematical modelling and we begin by looking at a specific example: modelling the cardio-respiratory system.

10.2 Appearance of Oscillations in Mathematical Modelling of the Cardio-Respiratory System

The main function of the cardio-respiratory system is to ensure an adequate delivery of oxygen to every cell in the body and the removal of carbon dioxide [11]. Over a short period of time (several minutes), this is achieved by adjusting the breathing pattern and the heart rate via a neural network located in the brainstem [12, 14, 21]. Assuming the external environment is large enough and insulated, conditions outside the body practically stay constant over a short period of time (e.g. temperature, concentrations of oxygen and carbon dioxide). Hence, we can assume that there are no external sources of time-dependent signals. Under these conditions, the cardio-respiratory system (and indeed the whole body) can be viewed as an autonomous system. However, due to its complexity, parts of the system are often modeled separately. This leads to two sources of oscillations: intrinsic and forced.

10.2.1 Intrinsic Oscillations

Intrinsic oscillations can be found in mathematical models of the respiratory neural system [7, 8, 18, 20, 23]. As an example, consider a model of a single neuron in an area of the brainstem called the pre Bötzinger Complex (preBötC) which drives breathing [7]:

$$\frac{dv}{dt} = f_1\left(v, n, h_p\right) \tag{10.5}$$

$$\frac{dn}{dt} = f_2\left(v, n\right) \tag{10.6}$$

$$\frac{dh_p}{dt} = f_3\left(v, h_p\right) \tag{10.7}$$

where v is the neuron membrane potential, n is the gating of potassium, h_p is the gating of persistent sodium and f_1, f_2, f_3 are specific functions (see [4, 7] for more details). The system can generate a bursting signal (Fig. 10.2). A typical analysis of this system and the underlying mechanism of the bursting generation is shown in Fig. 10.3. Equations 10.5 and 10.6 are treated as a fast subsystem and the variable h_p is treated as a parameter. The steady state solutions and their stabilities can then be calculated for different values of h_p. These solutions are shown as a bifurcation diagram of the fast subsystem in Fig. 10.3a. Solid blue lines represent stable equilibria, dashed blue lines represent unstable equilibria, solid red line represents periodic solutions and the dashed red line represents unstable periodic solutions. The periodic solutions in Fig. 10.3a appear through a sub-critical Hopf bifurcation [22]. This is when the stability of the equilibrium solution changes from unstable to stable and an unstable periodic solution appears. Figure 10.3b shows a smaller area of Fig. 10.3a with a solution of the full system (Eqs. 10.5–10.7) superimposed on it in green. The rate of change of h_p is positive when the solution of the full system is near the stable equilibrium of the fast sub-system and negative when it is near the stable periodic solution of the sub-system. Hence, the solution of the full system moves to the right along the equilibrium of the fast sub-system and to the left along the periodic solution of the sub-system. When the stable equilibrium of the sub-system terminates, the solution of the full system moves to the periodic solution and vice versa, creating bursting.

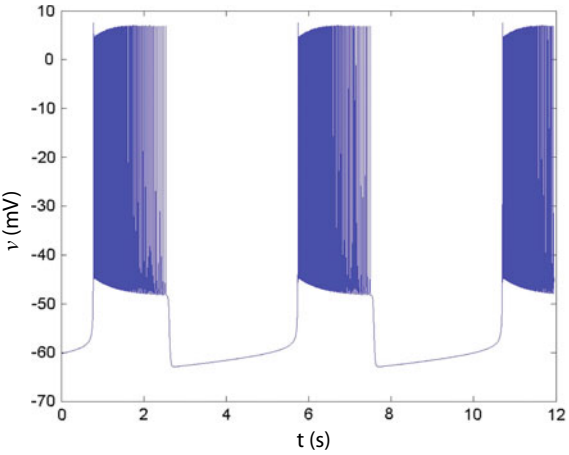

Fig. 10.2 A bursting signal generated by Eqs. 10.5–10.7. The underlying mechanism of the bursting generation can be explained by Fig. 10.3

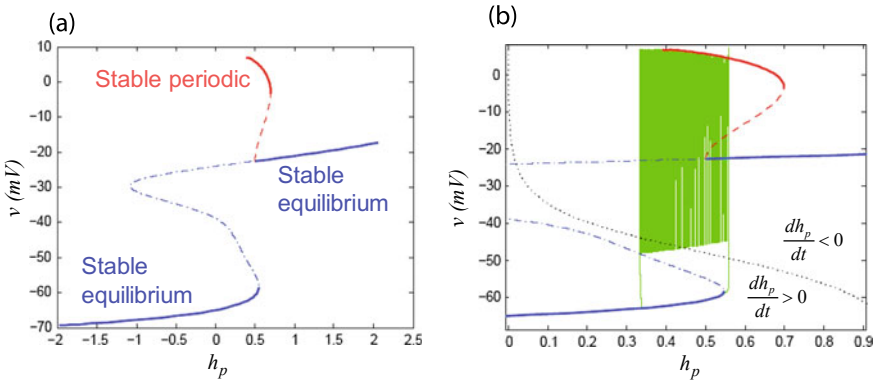

Fig. 10.3 A typical analysis of the underlying mechanism of bursting generation. **a** A bifurcation diagram of Eqs. 10.5–10.6 (the fast subsystem) when h_p is taken as a parameter. Solid blue lines represent stable equilibria, dashed blue lines represent unstable equilibria, solid red line represents periodic solutions and dashed red line represents unstable periodic solutions. **b** A smaller area of the bifurcation diagram in (**a**) with a solution of the full system (Eqs. 10.5–10.7, see Fig. 10.2) superimposed on it in green

10.2.2 Forced Oscillations

As we have seen in the previous section, the neural respiratory circuitry generates intrinsic oscillations, usually in the form of bursting. These neural signals excite the respiratory muscles, causing the muscles to contract during the active phase of the bursting and relax during the quiet phase (under normal conditions, [12]). When modeling other parts of the cardio-respiratory system, it is often convenient to ignore the neural circuitry and replace it with some given oscillations (called "forced oscillations"). As an example consider a simple model of the mammalian lungs (Fig. 10.4) [3]. The lungs here are modeled as a single container with a moving plate. The plate is connected to a spring with a constant k_s. Spring compression represents lung inflation. The lung elastance E is equivalent to k_s/s^2 where s is the area of the plate. The pressure inside the container is P_A and the volume of the container is V_A. The pressure outside is P_m (assumed to be constant), the air flow is q and the resistance to flow is R. The pleural pressure $P_L(t)$ is a given function of time. When the pleural pressure drops, P_A drops and air flows into the lungs. When the pleural pressure increases, P_A increases and air flows out. The rate of change of the lung volume can be described by the following equation [3]:

$$\frac{dV_A}{dt} = -\frac{E}{R}V_A + \frac{1}{R}\left(P_m - P_L(t)\right) \tag{10.8}$$

This equation is clearly non-autonomous. In this case, because it is a linear ordinary differential equation, $V_A(t)$ can be expressed as [19]:

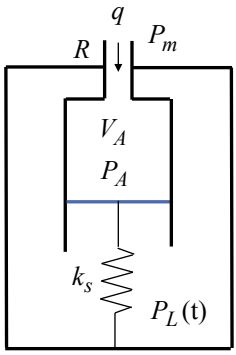

Fig. 10.4 A simple model of the lungs. The lungs is modeled as a single container with a moving plate. The plate is connected to a spring with a constant k_s. The pressure inside the container is P_A and the volume of the container is V_A. The pressure outside is P_m (assumed to be constant), the air flow is q and the resistance to flow is R. The pleural pressure, $P_L(t)$, is a given function of time. Figure adapted from [3]

$$V_A(t) = V_A(0)e^{-\frac{E}{R}t} + e^{-\frac{E}{R}t}\int_0^t \frac{1}{R}\left(P_m - P_L(\tau)\right)e^{\frac{E}{R}\tau}d\tau \tag{10.9}$$

If $P_L(t)$ is periodic then $V_A(t)$ in steady state is periodic too.

Another example of forced oscillations can be found in a model of heart rate control (Fig. 10.5) [5]. The heart period is controlled by the parasympathetic nerve which itself is affected by the baroreceptors, central respiratory drive and stretch receptors. There are nine equations in this model and the exact details are not essential. Therefore, the equations are not given here (see [5] for the details). The important thing to note in Fig. 10.5 is that the signal $A(t)$ (the central respiratory drive, Fig. 10.5a) is an input to the model. This signal is a simplification of the bursting signal shown in Fig. 10.2. In principle, had we known more about the operation of the respiratory neural circuitry and how it responds to feedback signals, we could have closed the loop on respiration and create an autonomous model for the short-term control of the cardio-respiratory system.

10.3 Alternative Transformations

The modeling examples illustrated in Sect. 10.2 demonstrated that for modeling convenience, intrinsic oscillations in an autonomous system can be replaced by forced oscillations, creating non-autonomous systems. Inspired by the modeling examples we suggest that, in special cases, the process can be reversed. That is, the non-autonomous systems can be transformed to "native" autonomous. We show two examples of how this can be done. Clearly there are many other examples to be found.

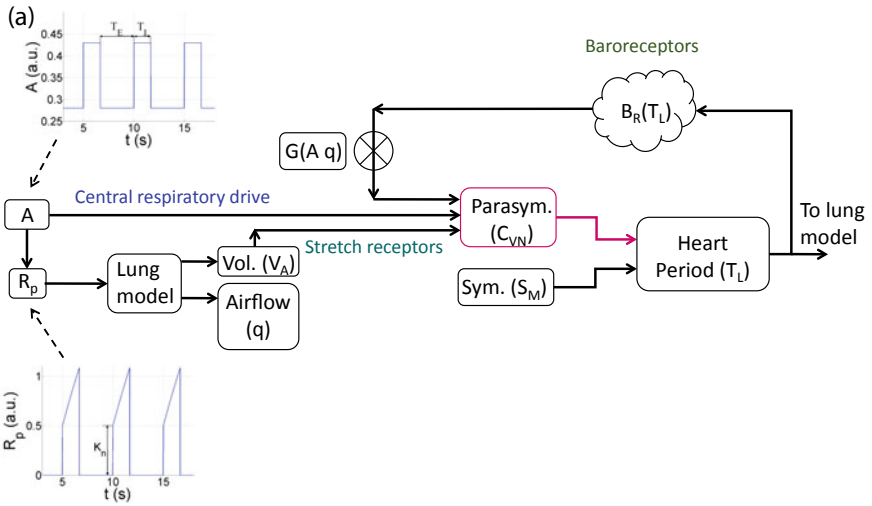

Fig. 10.5 A model of heart rate control (figure adapted from [5]). The heart period is affected by the sympathetic nerve (assumed to be constant in this model) and the parasympathetic nerve. The parasympathetic nerve is affected by the baroreceptors which are modulated by the central respiratory drive $A(t)$ and air flow q through a gating function G. The baroreceptors are represented by a function of the heart period, B_R. The parasympathetic nerve is also affected by stretch receptors represented by lung volume. The central respiratory drive $A(t)$ shown in (**a**) is an input to the model and the main reason the model is non-autonomous. This signal is a simplification of the bursting shown in Fig. 10.2. It drives respiration and also affects the parasympathetic nerve. See [5] for more details

10.3.1 *Transforming a System of Ordinary Differential Equations with Sinusoidal Inputs*

Consider a general description of a system with sinusoidal inputs:

$$\frac{d\mathbf{x}}{dt} = \mathbf{f}(\mathbf{x}) + \mathbf{g}(a\cos(\omega t), a\sin(\omega t), \mathbf{x}) \tag{10.10}$$

where $\mathbf{x} \in \mathbb{R}^n$, $\mathbf{g} = [g_1(a\cos(\omega t), a\sin(\omega t), \mathbf{x}), \ldots, g_n(a\cos(\omega t), a\sin(\omega t), \mathbf{x})]^T$ and $a \geq 0$. We further assume that $\mathbf{g}(a = 0) = [0, \ldots, 0]^T$. That is, we assume that without the sinusoidal inputs, the system is autonomous.

Let $u = a\cos(\omega t)$ and $v = a\sin(\omega t)$. Equation (10.10) can then be written as:

$$\begin{aligned}\frac{d\mathbf{x}}{dt} &= \mathbf{f}(\mathbf{x}) + \mathbf{g}(u, v, \mathbf{x}) \\ \frac{du}{dt} &= -\omega v \\ \frac{dv}{dt} &= \omega u\end{aligned} \tag{10.11}$$

The system of Eq. (10.11) can be written as $\dot{\mathbf{y}} = \bar{\mathbf{f}}(\mathbf{y})$ where $\mathbf{y} = [\mathbf{x}, u, v]$ and is subjected to the constraint $u^2 + v^2 = a^2$. Hence it has only one extra dimension compared to the original non-autonomous system. The system has equilibrium points at $\mathbf{f}(\mathbf{x}) = 0, u = 0$ and $v = 0$, that is, the same equilibrium points of the system when there is no forcing ($a = 0$). The Jacobian is given by:

$$\frac{\partial \bar{f}_i}{\partial y_j} = \begin{bmatrix} \left(\frac{\partial f_i}{\partial x_j} + \frac{\partial g_i}{\partial x_j}\right) & \begin{pmatrix} \frac{\partial g_1}{\partial u} & \frac{\partial g_1}{\partial v} \\ \vdots & \vdots \\ \frac{\partial g_n}{\partial u} & \frac{\partial g_n}{\partial v} \end{pmatrix} \\ \begin{pmatrix} 0 \dots 0 \\ 0 \dots 0 \end{pmatrix} & \begin{pmatrix} 0 & -\omega \\ \omega & 0 \end{pmatrix} \end{bmatrix} \tag{10.12}$$

As an example consider the forced pendulum in Eq. (10.3). The transformed system is given by:

$$\begin{aligned} \frac{d\theta}{dt} &= z \\ \frac{dz}{dt} &= -\frac{g}{L}\sin\theta - \mu z - \frac{u}{L}\sin\theta \\ \frac{du}{dt} &= -\omega v \\ \frac{dv}{dt} &= \omega u \end{aligned} \tag{10.13}$$

subject to $u^2 + v^2 = a^2$. The Jacobian at the fixed point $[0, 0, 0, 0]$ is given by:

$$\frac{\partial \bar{f}_i}{\partial y_j}\Big|_{(0,0,0,0)} = \begin{bmatrix} \begin{pmatrix} 0 & 1 \\ -\frac{g}{L} & -\mu \end{pmatrix} & \begin{pmatrix} 0 & 0 \\ 0 & 0 \end{pmatrix} \\ \begin{pmatrix} 0 & 0 \\ 0 & 0 \end{pmatrix} & \begin{pmatrix} 0 & -\omega \\ \omega & 0 \end{pmatrix} \end{bmatrix} \tag{10.14}$$

The eigenvalues of the Jacobian in Eq. (10.14) are the eigenvalues of the two matrices along the diagonal of the Jacobian. This gives two eigenvalues with negative real parts (the eigenvalues of the original unforced system at the equilibrium point which is known to be stable) and two additional eigenvalues that are purely imaginary. This means that the stability of the equilibrium point cannot be determined by this analysis (a linearization around the equilibrium point), however, the center manifold theorem [15, 25] can be applied. From it we can conclude that if a is very small (that is, the forcing is weak), the system will oscillate in steady state around the original equilibrium point with the same direction and period as the forcing (in this example, vertical movement with period $2\pi/\omega$) and the same stability as the original equilibrium point. Note that, in this example, if the initial conditions are such that

$[\theta, z] = [0, 0]$ or $[\theta, z] = [\pi, 0]$ the vertical movement around these points will be sustained even for large a. However, for other initial conditions, our result predicts that, for very small a, the vertical oscillations around $\theta = 0$ will be stable but the vertical oscillations around $\theta = \pi$ will be unstable. This result, has been found using other methods for the forced damped pendulum [9, 10] and for other forced oscillators [2, 15]. The idea for the transformation presented here was first introduced in [2]. It was also used there to conclude that if $x \in \mathbb{R}$, the oscillations in steady state will always have the period of the forcing even if a is large, provided $f(x)$ is not periodic (see [2] for a proof).

10.3.2 *Transformation of a Non-autonomous Boolean Network*

We now divert from differential equations and look at a Boolean network. The nodes in a Boolean network could take only two values "1" or "0" and the connection between nodes could be excitatory or inhibitory (see Fig. 10.6). The state of the nodes can change according to a set of rules. As an example consider the following set of rules adapted from [1, 24]:

- A node will be "1" in the next step if at least one activator is "1" in the current step and all the inhibitors are "0".
- A node will be "0" in the next step if there are no activators which are "1" in the current step.
- A node will be "0" in the next step if at least one of the inhibitors is "1" in the current step, regardless of the state of the activators.

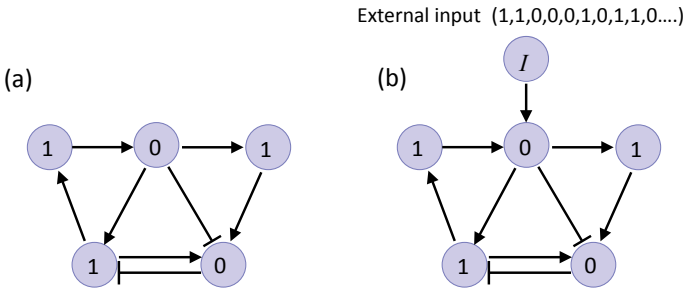

Fig. 10.6 Examples of Boolean networks. The nodes could take only two values: "1" or "0". Connections between nodes could be excitatory (→) or inhibitory (⊣). The figure shows the current state of the nodes. These can change in the next step according to a set of rules (see text). **a** An autonomous Boolean network—the states of the nodes in the next step depend only on their current state. **b** A non-autonomous Boolean network—due to the external input, the states of the nodes in the next step depend on their current state as well as the step number

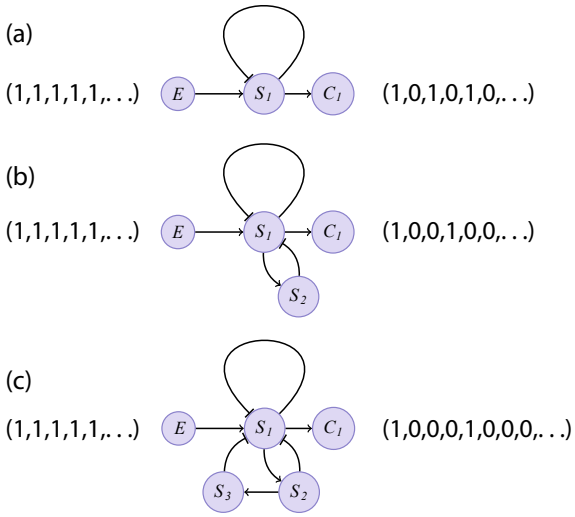

Fig. 10.7 Examples of autonomous Boolean networks that can generate periodic signals. **a** Period 2. **b** Period 3. **c** Period 4. In all cases, a constant source of energy (the node E) is required. Figure adapted from [6]

This set of rules relies on knowing the current state of the nodes and can be applied to autonomous Boolean networks (for example, Fig. 10.6a). However, it is not enough for non-autonomous Boolean networks (for example, Fig. 10.6b) because we cannot know the state of I without knowing the step number.

However, if the input signal I could be replaced by an autonomous Boolean network that produces the same signal as its output, it will transform the non-autonomous network to autonomous. We show in [6] how this can be done when I is periodic (we define the trajectory $(10\cdots010\cdots0...) \equiv (\overline{\underbrace{10\cdots0}_{p}})$ as periodic with period p).

Figure 10.7 shows autonomous networks that can produce signals with periods 2, 3 and 4. A similar idea was used to prove that for any given periodic signal there exists an autonomous Boolean network that can generate the signal.

We used the Boolean framework to study the control of bursting in the respiratory neural network [6]. Within this framework, the bursting signal in Fig. 10.2 could be represented by the signal $(1111000011110000...) \equiv (\overline{11110000})$ where "1" represents an action potential and "0" no action potential. Input signals to the neural network were taken as periodic with period p where p was a control parameter. The transformation described in Fig. 10.7 enabled us to conclude that a trajectory of a non-autonomous Boolean network with a periodic forcing will eventually repeat a certain pattern. This is because an autonomous and deterministic Boolean network has a finite number of nodes and hence a finite number of states. Therefore, trajectories will eventually come back to one of the states they have visited before. Our ability to use rules for an autonomous system, to study a non-autonomous system, enabled us to show how inspiration and expiration times can be controlled *selectively* at the level of the neural circuitry.

10.4 Conclusions

This chapter presented two alternative transformations from non-autonomous systems to autonomous in the special case of periodic forcing. The alternative transformations enabled the use of theorems derived for native autonomous systems which otherwise, under the standard transformation, could not be utilized. The transformations presented are inspired by mathematical modeling which also suggests that transformations for other special cases exist.

References

1. R. Albert, H.G. Othmer, The topology of the regulatory interactions predicts the expression pattern of the segment polarity genes in drosophila melanogaster. J. Theor. Biol. **223**(1), 1–18 (2003)
2. A. Ben-Tal, A study of symmetric forced oscillators. Ph. D. thesis, University of Auckland, New Zealand (2001)
3. A. Ben-Tal, Simplified models for gas exchange in the human lungs. J. Theor. Biol. **238**(2), 474–95 (2006)
4. A. Ben-Tal, I.G. Kevrekidis, Coarse-graining and simplification of the dynamics seen in bursting neurons. SIAM J. Appl. Dyn. Syst. **15**(2), 1193–1226 (2016)
5. A. Ben-Tal, S.S. Shamailov, J.F.R. Paton, Central regulation of heart rate and the appearance of respiratory sinus arrhythmia: new insights from mathematical modeling. Math. Biosci. **255**, 71–82 (2014)
6. A. Ben-Tal, Y.J. Wang, M.C.A. Leite, The logic behind neural control of breathing pattern. Sci. Rep. **9** (2019)
7. R.J. Butera, J. Rinzel, J.C. Smith, Models of respiratory rhythm generation in the pre-bötzinger complex. I. bursting pacemaker neurons. J. Neurophys. **81**, 382–397 (1999)
8. R.J. Butera, J. Rinzel, J.C. Smith, Models of respiratory rhythm generation in the pre-bötzinger complex. II. populations of coupled pacemaker neurons. J. Neurophys. **81**, 398–415 (1999)
9. D. Capecchi, S.R. Bishop, Periodic oscillations and attracting basins for a parametrically excited pendulum. Dyn. Stab. Syst. **9**(2), 123–143 (1994)
10. M.J. Clifford, S.R. Bishop, Inverted oscillations of a driven pendulum. Proc. R. Soc. A-Math. Phys. Eng. Sci. **454**(1979), 2811–2817 (1998)
11. J.H. Comroe, *Physiology of Respiration*, 2nd edn. (Year Book Medical Publishers, Inc., 1977)
12. C.A. Del Negro, G.D. Funk, J.L. Feldman, Breathing matters. Nat. Rev. Neurosci. **19**(6), 351–367 (2018)
13. L. Edelstein-Keshet, Mathematical models in biology. Soc. Ind. Appl. Math. (2005)
14. M. Elstad, E.L. O'Callaghan, A.J. Smith, A. Ben-Tal, R. Ramchandra, Cardiorespiratory interactions in humans and animals: rhythms for life. Am. J. Phys. Heart Circ. Phys. **315**(1), H6–H17 (2018)
15. J. Guckenheimer, P. Holmes, Nonlinear oscillations, dynamical systems and bifurcations of vector fields. *Applied Mathematical Sciences*, vol. 42, (Springer-Verlag, New York, 1996)
16. D. Jordan, P. Smith, *Nonlinear Ordinary Differential Equations: An Introduction for Scientists and Engineers*. (Oxford University Press, 2007)
17. S. Lenci, E. Pavlovskaia, G. Rega, M. Wiercigroch, Rotating solutions and stability of parametric pendulum by perturbation method. J. Sound Vib. **310**(1–2), 243–259 (2008)
18. B.G. Lindsey, I.A. Rybak, J.C. Smith, Computational models and emergent properties of respiratory neural networks. Compr. Phys. **2**, 1619–1670 (2012)

19. J.C. Robinson, *An Introduction to Ordinary Differential Equations*. (Cambridge University Press, 2004)
20. J.E. Rubin, N.A. Shevtsova, G.B. Ermentrout, J.C. Smith, I.A. Rybak, Multiple rhythmic states in a model of the respiratory central pattern generator. J. Neurophys. **101**(4) (2009). https://doi.org/10.1152/jn.90958.2008
21. J.C. Smith, A.P.L. Abdala, A. Borgmann, I.A. Rybak, J.F.R. Paton, Brainstem respiratory networks: building blocks and microcircuits. Trends. Neurosci. **36**(3), 152–62 (2013)
22. S.H. Strogatz, *Nonlinear Dynamics and Chaos*. (Perseus Books, 1994)
23. N. Toporikova, R.J. Butera, Two types of independent bursting mechanisms in inspiratory neurons: an integrative model. J. Comput. Neurosci. **30**(3), 515–528 (2011)
24. Y. Wang, K. Chilakamarri, D. Kazakos, M.C. Leite, Relations between the dynamics of network systems and their subnetworks. Aims Math. **2**(3), 437–450 (2017)
25. S. Wiggins, Introduction to applied nonlinear dynamical systems and chaos. *Texts in Applied Mathematics 2*. (Springer-Verlag, 1990)
26. J.A. Wright, M. Bartuccelli, G. Gentile, Comparisons between the pendulum with varying length and the pendulum with oscillating support. J. Math. Anal. Appl. **449**(2), 1684–1707 (2017)

Chapter 11
Coupling Functions in Neuroscience

Tomislav Stankovski

Abstract Neural interactions play one of the central roles in the brain mediating various processes and functions. They are particularly important for the brain as a complex system that has many different functions from the same structural connectivity. When studying such interactions coupling functions are very suitable, as inherently they can reveal the underlaying functional mechanism. This chapter overviews some recent and widely used aspects of coupling functions for studying neural interactions. Coupling functions are discussed in connection to two different levels of brain interactions—that of neuron interactions and brainwave cross-frequency interactions. Aspects relevant to this from both, theory and methods, are presented. Although the discussion is based on neuroscience, there are strong implications from, and to, other fields as well.

11.1 Introduction

Many systems in nature are found to interact, between each other or with the environment. The interaction can cause gradual or sudden changes in their qualitative dynamics, leading to their grouping, self-organizing, clustering, mutual coordinated synchronization, even to some extremes when their very existence is suppressed [20, 37, 55, 74, 75, 84]. An important class of such dynamical systems are oscillators, which also often interact resulting in a quite intricate dynamics.

On the quest to untangle and better understand interactions, one could study several complementary aspects [14]. One is structural connectivity, where physical actual connection is studied. Often this is not directly observable, or it exist but it is not active and dynamic all the time. Further on, one could study functional connectivity i.e. if a functional dependence (like correlation, coherence or mutual information)

T. Stankovski (✉)
Faculty of Medicine, Ss. Cyril and Methodius University in Skopje, Skopje, North Macedonia
e-mail: t.stankovski@ukim.edu.mk

Department of Physics, Lancaster University, Lancaster, UK

A. Stefanovska and P. V. E. McClintock (eds.), *Physics of Biological Oscillators*, Understanding Complex Systems,
https://doi.org/10.1007/978-3-030-59805-1_11

exist between the observed data. Finally, one could study the causal relations between dynamical models and observe the effective connectivity. In this way, the interactions can be reconstructed in terms of coupling functions which define the underlaying interaction mechanism.

With their ability to describe the interactions in detail, coupling functions have received a significant attention in the scientific community recently [69, 70]. Three crucial aspects of coupling functions were studied: the theory, methods and applications. Various methods have been designed for reconstruction of coupling functions from data [15, 33, 35, 39, 66, 80]. These have enabled applications in different scientific fields including chemistry [32], climate [41], secure communications [44, 68], mechanics [34], social sciences [56], and oscillatory interaction in physiology for cardiorespiratory and cardiovascular interactions [26, 35, 40, 59, 79].

Arguably, the greatest current interest for coupling functions is coming from neuroscience. This is probably because the brain is a highly-connected complex system [51], with connections on different levels and dimensions, many of them carrying important implications for characteristic neural states and diseases. Coupling functions are particularly appealing here because they can characterize the particular neural mechanisms behind these connections. Recent works have encompassed the theory and inference of a diversity of neural phenomena, levels, physical regions, and physiological conditions [4, 13, 47, 49, 61, 71, 73, 76–78, 81, 86].

The chapter gives an overview of the topic of coupling function, with particular focus on their use and suitability to neuroscience. This will be explained through observations on two levels of brain connectivity—the neurons and the brainwaves level. The relationship between the appropriate theory and methods will be also given. On systemic level, the focus will be on neuronal oscillations, thus positioning around and complementing the main topic of the book—biological oscillators. The chapter will finish by outlook and some thoughts on the future developments and uses of coupling function in neuroscience. However, before going into greater detail, first the basics of what coupling functions are discussed briefly bellow.

11.1.1 Coupling Function Basics

The system setup to be studied is one of an interacting dynamical systems, with the focus of coupled oscillators. Then, *coupling functions describe the physical rule specifying how the interactions occur and manifest*. Because they are directly connected with the functional dependencies, coupling functions focus not only on *if* the interactions exist, but more on *how* they appear and develop. For example, when studying phase dynamics of coupled oscillators the magnitude of the phase coupling function affects directly the oscillatory frequency and will describe how the oscillations are being accelerated or decelerated by the influence of the other oscillator. Similarly, if one considers the amplitude dynamics of interacting dynamical systems, the magnitude of coupling function will prescribe how the amplitude is increased or decreased due to the interaction.

First we consider two coupled dynamical systems given in the following general form:

$$\begin{aligned} \dot{x} &= f_1(x) + g_1(x, y) \\ \dot{y} &= f_2(y) + g_2(x, y), \end{aligned} \tag{11.1}$$

where the functions $f_1(x)$ and $f_2(y)$ describe the inner dynamics, while $g_1(x, y)$ and $g_2(x, y)$ describe the coupling functions in the state space. Then, given that the two dynamical systems are oscillators, and under the assumption that they are weakly nonlinear and weakly coupled, one can apply the phase reduction theory [37, 45, 53]. This yields simplified approximative systems where the full (at least two dimensional) state space domain is reduced to a one dimensional phase dynamics domain:

$$\begin{aligned} \dot{\phi}_1 &= \omega_1 + q_1(\phi_2, \phi_1) \\ \dot{\phi}_2 &= \omega_2 + q_2(\phi_1, \phi_2), \end{aligned} \tag{11.2}$$

where ϕ_1, ϕ_2 are the phase variables of the oscillators, ω_1, ω_2 are their natural frequencies, and $q_1(\phi_2, \phi_1)$ and $q_2(\phi_1, \phi_2)$ *are the coupling functions* in phase dynamics domain. For example, in the Kuramoto model [37] they were prescribed to be sine functions from the phase differences:

$$\begin{aligned} \dot{\phi}_1 &= \omega_1 + \varepsilon_1 \sin(\phi_2 - \phi_1) \\ \dot{\phi}_2 &= \omega_2 + \varepsilon_2 \sin(\phi_1 - \phi_2), \end{aligned} \tag{11.3}$$

where $\varepsilon_1, \varepsilon_2$ are the coupling strength parameters. Apart from this example of sinusoidal form, the coupling functions $q_1(\phi_2, \phi_1)$ and $q_2(\phi_1, \phi_2)$ can have very different and more general functional form, including a decomposition on a Fourier series. Given in the phase dynamics like this Eq. 11.2, the coupling functions $q_1(\phi_2, \phi_1)$ and $q_2(\phi_1, \phi_2)$ are additive to the frequency parameters ω_1, ω_2, meaning that their higher or lower values will lead to acceleration or deceleration of the affected oscillations, respectively.

Coupling function can be described in terms of its *strength* and *form*. The coupling strength is a relatively well-studied quantity, and there are many statistical methods which detect measures proportional to it (e.g., the mutual-information based measures, transfer entropy and Granger causality). It is the functional form of the coupling function, however, that has provided a new dimension and perspective probing directly the mechanisms of the interactions. Where, the *mechanism* is defined by the functional form that gives the rule and process through which the input values are translated into output values i.e. for the interactions it prescribes how the input influence from one system is translated into the output effect on the affected or the coupled system.

In this way a coupling function can describe the qualitative transitions between distinct states of the systems e.g., routes into and out of synchronization, oscillation

death or network clustering. Moreover, depending on the known form of the coupling function and the detected quantitative inputs, one can even predict transitions to synchronization. Decomposition of a coupling function provides a description of the functional contributions from each separate subsystem within the coupling relationship. Hence, by describing the mechanisms, coupling functions reveal more than just investigating correlations and statistical effects.

11.2 Suitability of Coupling Functions for Neuroscience

The human brain is an intriguing organ, considered to be one of the most complex systems in the universe. The adult human brain is estimated to contain 86 ± 8 billion neurons, with a roughly equal number (85 ± 10 billion) of non-neuronal cells [3]. Out of these neurons, 16 billion (19%) are located in the cerebral cortex, and 69 billion (80%) are in the cerebellum. One of the main features of the brain is how the neurons are connected, and when and how they are active in order to process information and to produce various functionalities.

In neuroscience, the brain connectivity is classified in three different types of connectivity. That is, the brain connectivity refers to a pattern of links ("structural, or anatomical, connectivity"), of statistical dependencies ("functional connectivity") or of causal model interactions ("effective connectivity") between distinct units within a nervous system [14, 25, 60]. In terms of graph theory of the brain, the units correspond to nodes, while the connectivity links to edges [23]. The connectivity pattern between the units is formed by structural links such as synapses or fiber pathways, or it represents statistical or causal relationships measured as cross-correlations, coherence, information flow or the all-important *coupling function*. In this way, therefore, the brain connectivity is crucial to understand how neurons and neural networks process information.

The units can correspond to individual neurons, neuronal populations, or anatomically segregated brain regions. Taking aside the anatomically structural brain regions, the other two—the neurons and their populations—are of particular interest from a system neuroscience point of view. Moreover, for certain conditions these systems may operate in the oscillatory regime for some time. When having an oscillatory nature their dynamics and connectivity can be modeled as coupled oscillators (see for example Fig. 11.1). In this constellation, a coupling function with its functional form can be very suitable effective connectivity measure through which much can be learned about the mechanisms and functionality of the brain.

As the two connectivity units, the neurons and the neuronal populations, are of particular interest to the focus of coupling functions and oscillatory dynamics, bellow they will be discussed separately in light of the utility of coupling functions.

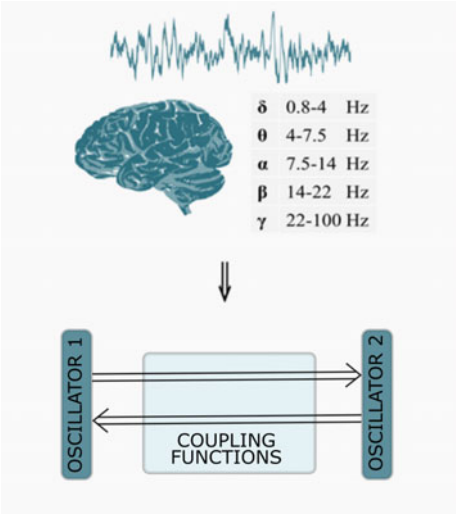

Fig. 11.1 A schematic example of the brain, an electroencephalography (EEG) signal recording as a measure of the neural population electrical activity, and the schematic model of two oscillators and their coupling functions which can be used to model a particular brainwave activity. The five distinct brainwave ($\delta, \theta, \alpha, \beta, \gamma$) frequency intervals are also given on the right of the figure

11.2.1 Coupling Functions on Neuronal Level

The neurons are archetypical cells which act as basic units from which the structure of the brain is realized. Existing in great numbers, they are interconnected in various network configurations giving rise to different functions of the brain. One should note that besides neurons other cell types may also contribute to the brain overall function [21]. As such the brain is a complex system which can perform large number of neural functions from relatively static structure [51]. For comparison, in terms of functions the brain is much more complex than for example the heart, which performs generally only one function—pumping blood to other parts of the body. Importantly for the brain, the neurons are electrically excitable cells, which are active only in the act of performing certain function.

Based on their function, neurons are typically classified into three types: sensory neurons, motor neurons and interneurons. Number of neuron *models* exist which describe various features, including but not limited to the Hodgkin-Huxley, the Integrate-and-fire, the FitzHugh-Nagumo, the Morris-Lecar and the Izhikevich neuronal model [18, 24, 27, 42, 58]. These models describe the relationship between neuronal membrane electrical currents at the input stage, and membrane voltage at the output stage. Notably, the most extensive experimental description in this category of models was made by Hodgkin and Huxley [24], which received the 1963 Nobel Prize in Physiology or Medicine. The mathematical description of the neuronal models is usually represented by a set of ordinary or stochastic differential equations, describing dynamical systems which under specific conditions exhibit nonlinear *oscillatory* dynamics.

Importantly, the neurons are highly interconnected forming a complex brain network. Their interactions give rise to different neural states and functions. In terms of system interactions, such brain interactions could lead to qualitative transitions like synchronization and clustering, on the whole or part of the brain network. When observing the neuronal models as dynamical systems, the mechanisms of the interactions are defined by the neuronal coupling functions. On this level, coupling functions have been studied extensively, although more in an indirect way through the neuronal phase response curve (PRC) [2, 10]. Namely, coupling function is a convolution between two functions, the phase response curve and the perturbation function [37] i.e. one function of how an oscillator responds to perturbations and the second function defining the perturbations from the second oscillator, respectively. There are generally two types of such response curves, type I with all positive, and type II with positive and negative values. Different types of phase response curves were studied (especially theoretically) forming different types of neuronal models [6, 11, 48]. The phase response curves are typically defined for weakly coupled units [45, 53].

An important feature of the neuronal oscillations are that they are excitable and have non-smooth spike-like trajectories. Such dynamics of the neuronal oscillations are highly nonlinear. For many applications, the neuronal activity is studied completely through the timing of the spike events [17]. In general, such spike-like oscillations act similar as a delta function, hence the phase response curves will have a similar delta function-like form [12]. This can have direct effect when observing the coupling function which can be a convolution between the a delta-like functions.

In terms of methods for neuronal coupling functions, a number of methods exist for reconstructing the neuronal phase response curves and the associate coupling functions [16, 77]. However, there are many open problems on this task and many applications on different types of signals from interacting neurons are yet to be resolved.

11.2.2 Coupling Functions on Brainwave Level

Studying some kind of property of a large number of neurons at once, as a whole or region of the brain, scales up the observation on higher level. In this way the resultant measurement of the brain, or region of the brain, is in a way some kind of mean field, a sum of all the functional activities of the individual neurons in a group, ensemble or network. For example such measurements include the neural EEG, iEEG, NIRS, MRI, CT and PET, which measure different characteristics like the electrical activity, the hemodynamic activity, the perfusion etc. of the whole brain or on specific spatially localized brain regions.

Arguably, the most used high level observable is the EEG. Electroencephalography (EEG) is a noninvasive electrophysiological monitoring method to record electrical activity of the brain. EEG measures voltage fluctuations resulting from ionic current within the neurons of the brain [46]. EEG measures electrical activity over a period of time, usually recorded from multiple electrodes placed on the scalp

according to some widely accepted protocols, like the International 10–20 system [31] (internationally recognized protocol to describe and apply the location of scalp electrodes).

At first sight the EEG signal looks random-like and complex (see e.g., Fig. 11.1), however, a detailed spectral analysis reveals that there are number of distinct oscillating intervals—called *brainwaves*. The most commonly studied brainwaves include the delta δ, theta θ, alpha α, beta β and gamma γ neural oscillation [7]. The frequency intervals of these brainwaves are also given in Fig. 11.1. Apart from these, there are also other brainwaves, including the mu μ, faster gamma1 γ_1 and gamma2 γ_2 brainwaves, and other more characteristic oscillations like the sleep spindles, thalamocortical oscillations, subthreshold membrane potential oscillations, cardiac cycle etc. The brainwaves are often linked to specific brain functions and mechanisms, though not all of them are known and they are still a very active field of research. The existence and strength of the brainwave oscillations are usually determined by spectral Fourier or Wavelet analysis.

The brainwave oscillations emanate from the dynamics of large-scale cell ensembles which oscillate synchronously within characteristic frequency intervals. The different ensembles communicate with each other to integrate their local information flows into a common brain network. One of the most appropriate ways of describing communication of that kind is through *cross-frequency coupling*, and there has been a large number of such studies in recent years to elucidate the functional activity of the brain underlying e.g., cognition, attention, learning and working memory [9, 29, 30, 43, 82]. The different types of cross-frequency coupling depend on the dynamical properties of the oscillating systems that are coupled, e.g., phase, amplitude/power and frequency, and different combinations of brainwaves have been investigated, including often the δ-α, θ-γ and α-γ cross-frequency coupling relation. These types of investigation are usually based on the statistics of the cross-frequency relationship e.g., in terms of correlation or phase-locking, or on a quantification of the coupling amplitude.

Recently, a new type of measure for brain interactions was introduced called *neural cross-frequency coupling functions* [73]. This measure is one of the central aspects in this chapter. The neural cross-frequency coupling functions describe interactions which are cross-frequency coupling i.e. between brainwaves but now describing not only the coupling existence and strength but also the form of coupling function. This functional form acts as another dimension of the coupling with the ability to describe the mechanisms, or the functional law, of the underlying coupling connection in question [69]. In simple words, not only *if*, but also *how* the neural coupling takes place.

When studying brainwave interactions the neural cross-frequency coupling functions are very suitable. Namely, the fact that the brainwaves are described by oscillations can be used to model the interacting dynamics with the coupled phase oscillator model [37]. In this way one can have a direct 1:1 correspondence between the number of observables and the dimensions of the measured signals—having a 1D signal and 1D model for the phase dynamics for each system i.e. there will be no hidden

dimensions. To illustrate the steps of the analysis an example of δ-to-α phase neural coupling function is considered:

- First one needs to extract the δ and α oscillation signals—this is done with standard filtering of the EEG signals.
- After this, one needs to detect the instantaneous phase signals from the oscillations, which can be done by Hilbert transform, and further transforming this with protophase-to-phase transformation [34].
- Such phases $\phi_\delta(t)$ and $\phi_\alpha(t)$ are then inputs to a method for dynamical inference which can infer a model of two coupled phase oscillators where the base functions are represented by Fourier series (set of sine and cosine functions of the $\phi_\delta(t)$ and $\phi_\alpha(t)$ arguments). In our calculations we used the method for dynamical Bayesian inference [66] and Fourier series as base function up to the second order.
- The resulting inferred model explicitly gives the desired neural coupling functions.
- After reconstructing the neural coupling functions of interest, one can use them to perform coupling function analysis in order to extract and quantify unique characteristics.

The phase coupling functions give the precise mechanism of how one oscillation is accelerated or decelerated as an effect of another oscillation. For example, let us consider the δ-to-α phase neural coupling function. Figure 11.2 presents such δ-to-α coupling function $q_\alpha(\phi_\delta(t), \phi_\alpha(t))$ from three studies involving resting state and anaesthesia, from single electrode or from spatially distributed electrodes [71–73]. Figure 11.2a shows the coupling existence, strength and significance in respect of surrogates, while the Fig. 11.2b shows the all-important neural coupling function $q_\alpha(\phi_\delta(t), \phi_\alpha(t))$. Observing closely the 3D plot in Fig. 11.2 describes that the $q_\alpha(\phi_\delta(t), \phi_\alpha(t))$ coupling function which is evaluated in the $\phi_\alpha(t)$ dynamics changes mostly along the $\phi_\delta(t)$ axis, meaning it is a predominantly direct coupling from δ oscillations. Detailed description of the direct form of coupling function, which is not analytical for non-parametric functional form, are presented elsewhere [72]. The specific form of the coupling function describes the coupling mechanism that when the δ oscillations are between 0 and π the coupling function is negative and the α oscillations are decelerated, while when the δ oscillations are between π and 2π the coupling function is positive and the α oscillations are accelerated. The rest of the figures tell similar story—Fig. 11.2c present three cases of $q_\alpha(\phi_\delta(t), \phi_\alpha(t))$ coupling functions for awake and anaesthetized subjects (with propofol and sevoflurane anaesthetics, respectively), while Fig. 11.2d, e present the $q_\alpha(\phi_\delta(t), \phi_\alpha(t))$ in spatial distribution on the cortex and its average value. The 3D plots present the qualitative description, while for quantitative analysis one can extract two measures—the coupling strength and the similarity of form of coupling function [69].

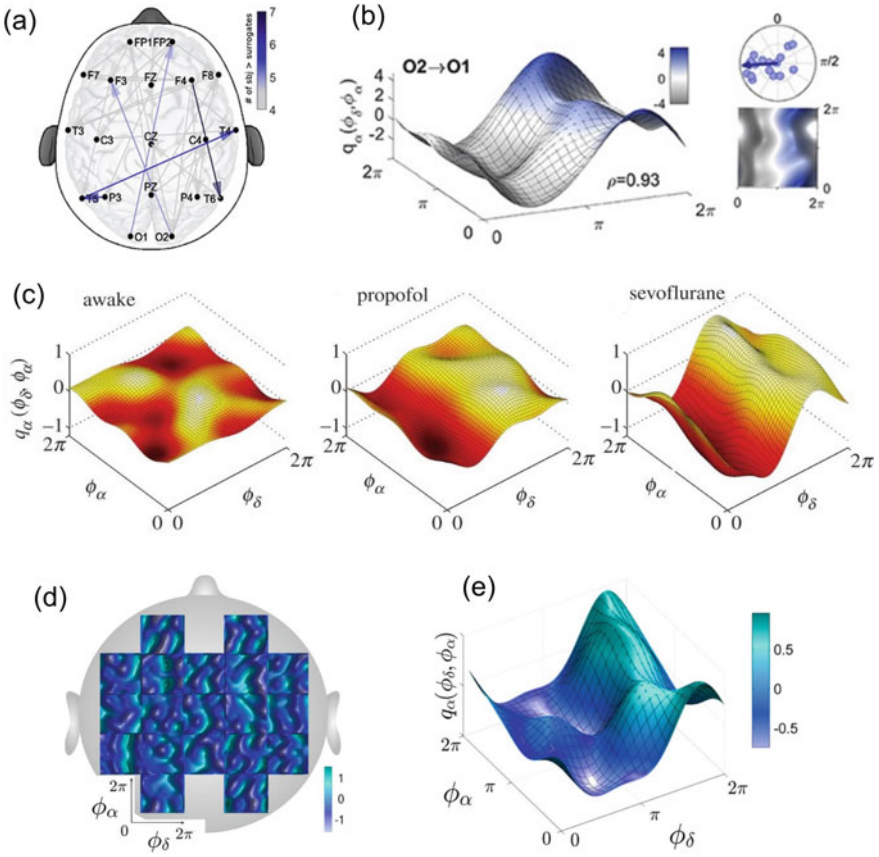

Fig. 11.2 Examples of δ-α neural coupling functions. **a** The coupling strength spatial distribution and significance in respect of surrogates. **b** The δ-α phase coupling functions of resting state—with 3D and 2D plots and a polar index of coupling function similarity. **c** The effect of anaesthesia on the δ-α coupling functions—the three group functions are for the awake, anesthetised with propofol and anesthetized with sevoflurane states. **d** and **e** depict the spatial distribution and the average resting state δ-α coupling function, respectively. **a** and **b** are from [73], **c** is from [71], **d** and **e** are from [72]

11.3 Theory and Methods for Coupling Functions in Neuroscience

The theory and methods for studying coupling functions of brain interactions are developed unsymmetrically. Namely, it seems that theoretical studies are more developed for the neuronal level, while the methods are largely developed for studying the large-scale (brainwaves) systems. Of course, this is not a black-and-white division, however the predominance of the two aspects certainly seems to be like this.

The large populations of interacting neurons, in form of ensembles and networks, have been studied extensively in theory. The celebrated Kuramoto model [36, 37] has been exploited in particular. It is a model of large population of phase oscillators, one which has an exact analytic solution for the synchronization state of the whole ensemble. The coupling functions is a simple sine function of the phase difference. Kuramoto discussed that this coupling function is not very physical, however his interest was in finding an analytically solvable model. The Kuramoto model has been particularly popular in neuroscience with its ability to describe analytically the synchronous states of large populations of neurons [1, 5, 52]. Other two recently introduced approaches, known as the Ott and Antonsen [50] and Watanabe and Strogatz [83] reductions, provide reduced model equations that exactly describe the collective dynamics for each subpopulation in the neural oscillator network via few collective variables only. A recent review provides a comprehensive and updated overview on the topic [4]. The theoretical studies on the large-scale brainwave interactions are often performed through the common framework of two or few coupled oscillatory systems [55].

To infer coupling functions from data one needs to employ methods based on dynamical inference. These are class of methods which can reconstruct a model of ordinary or stochastic differential equations from data. The coupling functions are integral part of such models. In this chapter examples were shown from the use of a specific method based on dynamical Bayesian inference [64, 66, 67]; however any other method based on dynamical inference (often referred to also as dynamic modelling or dynamic filtering) can also be used [15, 33, 35, 39, 80]. The differences between the results of these methods in terms of the coupling functions are minor and not qualitatively different. Often, there is a need for coupling functions to be inferred from networks of interacting systems, and several methods have been applied in this way [39, 54, 72]. In neuroscience, such methods have been used mainly on two to several brainwave oscillation systems, and it has been argued that the precision and feasibility are exponentially reduced as the number of systems increases and it is recommended not to go beyond $N > 10$ [57]. For this reason and due to the exponentially increasing demand for larger number of systems, there are not many effective methods for inference of coupling functions in low-level large populations of neuronal interactions.

In terms of methodology and analysis, few other aspects are important when analysing coupling functions. One is that once coupling functions are inferred they give the qualitative mechanisms but for any quantitative evaluations and comparisons (for example in a multisubject neuroscience study) one can conduct coupling function analysis i.e. it can calculate the coupling strength and the similarity of the form of coupling function [35, 69, 79]. Also, of paramount importance is to validate if the inferred coupling functions are statistically significant in respect of surrogate time series [38, 63]. Usually one tests whether the strengths of the coupling functions are significantly higher than the coupling strengths of a large number of randomized

surrogate time series which have similar statistical properties to those of the original data. Also one should be careful when analysing neural coupling functions as it has been shown that they can be time-varying [19, 65, 73], hence this should be taken into account in the analysis.

11.4 Conclusions and Discussions

In summary, this chapter gives an overview of how coupling functions are relevant and useful in neuroscience. They bring an additional dimension—the form of coupling function—which revels the mechanism of the neural interactions. This is relevant in neuroscience, as it can describe and be linked to the many different brain functions.

Two largely studied levels of neural interactions were discussed, the low-level individual neurons and the high-level systemic processes like the brainwave oscillations. Of course, these two levels are not exclusive but they are closely related, i.e. the brainwaves are like mean-field averages of the activities of billions of neurons. In fact studies exist where the brainwave oscillations are modeled as Kuramoto ensembles but the large-scale cross-frequency couplings for the modelling are inferred from data [5, 62]. Needless to say, coupling functions have implications for other levels and depths of the brain other than the two discussed here.

The focus was on phase coupling functions, though the interactions can be in amplitude, or combine phase-amplitude based domains [8, 29, 30]. Many modeling methods used in neuroscience actually inferred dynamical systems where coupling functions were an integral part [15, 28]. In such cases coupling functions were implicit, and they were not treated as separate entities, nor were they assesses and analysed separately. These tasks are yet to be developed properly for the amplitude and the phase-amplitude domains.

As an outlook, with all their advantages one could expect that coupling functions will continue to play an important role in future neuroscience studies, maybe even to extend their current use. The ever demanding computational power for calculations on large populations of neuron interactions will be more accessible in future, as new improved and faster methods will be developed. The artificial neural networks take on increasing importance recently, with many application across different disciplines and industries [22, 85]. The coupling function theory and the different findings in many neuroscience studies could play an important role in establishing improved and more efficient artificial neural networks. Also, the models could be extended and generalized further for easier applications on amplitude and phase-amplitude domains. The theory needs to follow closer the new discoveries from neural coupling functions analysis. The coupling function developments in other fields, especially in physics, could play an important role for neuroscience tasks, and vice versa.

References

1. J.A. Acebrón, L.L. Bonilla, C.J. Pérez Vicente, F. Ritort, R. Spigler, The Kuramoto model: a simple paradigm for synchronization phenomena. Rev. Mod. Phys. **77**, 137–185 (2005)
2. S. Achuthan, C.C. Canavier, Phase-resetting curves determine synchronization, phase locking, and clustering in networks of neural oscillators. J. Neurosci. **29**(16), 5218–5233 (2009)
3. F.A. Azevedo, L.R. Carvalho, L.T. Grinberg, J.M. Farfel, R.E. Ferretti, R.E. Leite, W.J. Filho, R. Lent, S. Herculano-Houzel, Equal numbers of neuronal and nonneuronal cells make the human brain an isometrically scaled-up primate brain. J. Comparat. Neurol. **513**(5), 532–541 (2009)
4. C. Bick, M. Goodfellow, C.R. Laing, E.A. Martens, Understanding the dynamics of biological and neural oscillator networks through exact mean-field reductions: a review. J. Mathemat. Neurosci. **10**, 9 (2020)
5. M. Breakspear, S. Heitmann, A. Daffertshofer, Generative models of cortical oscillations: neurobiological implications of the Kuramoto model. Front. Human Neurosci. **4**, 190 (2010)
6. E.N. Brown, J. Moehlis, P. Holmes, On the phase reduction and response dynamics of neural oscillator populations. Neur. Comp. **16**(4), 673–715 (2004)
7. G. Buzsáki, A. Draguhn, Neuronal oscillations in cortical networks. Science **304**, 1926–1929 (2004)
8. R.T. Canolty, E. Edwards, S.S. Dalal, M. Soltani, S.S. Nagarajan, H.E. Kirsch, M.S. Berger, N.M. Barbaro, R.T. Knight, High gamma power is phase-locked to theta oscillations in human neocortex. Science **313**(5793), 1626–1628 (2006)
9. R.T. Canolty, R.T. Knight, The functional role of cross-frequency coupling. Trends Cognit. Sci. **14**(11), 506–515 (2010)
10. B. Ermentrout, Type I membranes, phase resetting curves, and synchrony. Neural Comput. **8**(5), 979–1001 (1996)
11. B. Ermentrout, D. Saunders, Phase resetting and coupling of noisy neural oscillators. J. Comput. Neurosci. **20**(2), 179–190 (2006)
12. G.B. Ermentrout, B. Beverlin, T. Netoff, Phase response curves to measure ion channel effects on neurons, in *Phase Response Curves in Neuroscience* (Springer, 2012), pp. 207–236
13. A.S. Etémé, C.B. Tabi, J.F.B. Ateba, H.P.F. Ekobena, A. Mohamadou, T.C. Kofane, Neuronal firing and DNA dynamics in a neural network. J. Phys. Comms. **2**(12), 125004 (2018)
14. K.J. Friston, Functional and effective connectivity: a review. Brain. Connect. **1**(1), 13–36 (2011)
15. K.J. Friston, L. Harrison, W. Penny, Dynamic causal modelling. Neuroimage **19**(4), 1273–1302 (2003)
16. R.F. Galán, G.B. Ermentrout, N.N. Urban, Efficient estimation of phase-resetting curves in real neurons and its significance for neural-network modeling. Phys. Rev. Lett. **94**, 158101 (2005). https://doi.org/10.1103/PhysRevLett.94.158101
17. W. Gerstner, W.M. Kistler, *Spiking Neuron Models: Single Neurons, Populations, Plasticity* (Cambridge University Press, 2002)
18. W. Gerstner, R. Naud, How good are neuron models? Science **326**(5951), 379–380 (2009)
19. Z. Hagos, T. Stankovski, J. Newman, T. Pereira, P.V.E. McClintock, A. Stefanovska, Synchronization transitions caused by time-varying coupling functions. Philoso. Trans. R. Soc. A **377**(2160), 20190275 (2019)
20. H. Haken, *Synergetics, An Introduction* (Springer, Berlin, 1983)
21. R. Haseloff, I. Blasig, H.C. Bauer, H. Bauer, In search of the astrocytic factor (s) modulating blood-brain barrier functions in brain capillary endothelial cells in vitro. Cell. Molecul. Neurobiol. **25**(1), 25–39 (2005)
22. M.H. Hassoun et al., *Fundamentals of Artificial Neural Networks* (MIT Press, 1995)
23. Y. He, A. Evans, Graph theoretical modeling of brain connectivity. Current Opin. Neurol. **23**(4), 341–350 (2010)
24. A.L. Hodgkin, A.F. Huxley, Currents carried by sodium and potassium ions through the membrane of the giant axon of loligo. J. Physiol. **116**(4), 449–472 (1952)

25. B. Horwitz, The elusive concept of brain connectivity. Neuroimage **19**(2), 466–470 (2003)
26. D. Iatsenko, A. Bernjak, T. Stankovski, Y. Shiogai, P.J. Owen-Lynch, P.B.M. Clarkson, P.V.E. McClintock, A. Stefanovska, Evolution of cardio-respiratory interactions with age. Phil. Trans. R. Soc. Lond. A **371**(1997), 20110622 (2013)
27. E.M. Izhikevich, Simple model of spiking neurons. IEEE Trans. Neural Netw. **14**(6), 1569–1572 (2003)
28. A. Jafarian, P. Zeidman, V. Litvak, K. Friston, Structure learning in coupled dynamical systems and dynamic causal modelling. Phil. Trans. R. Soc. A **377**, 20190048 (2019)
29. O. Jensen, L.L. Colgin, Cross-frequency coupling between neuronal oscillations. Trends Cognit. Sci. **11**(7), 267–269 (2007)
30. V. Jirsa, V. Müller, Cross-frequency coupling in real and virtual brain networks. Front. Comput. Neurosci. **7**, 78 (2013)
31. V. Jurcak, D. Tsuzuki, I. Dan, 10/20, 10/10, and 10/5 systems revisited: their validity as relative head-surface-based positioning systems. Neuroimage **34**(4), 1600–1611 (2007)
32. I.Z. Kiss, C.G. Rusin, H. Kori, J.L. Hudson, Engineering complex dynamical structures: sequential patterns and desynchronization. Science **316**(5833), 1886–1889 (2007)
33. I.Z. Kiss, Y. Zhai, J.L. Hudson, Predicting mutual entrainment of oscillators with experiment-based phase models. Phys. Rev. Lett. **94**, 248301 (2005)
34. B. Kralemann, L. Cimponeriu, M. Rosenblum, A. Pikovsky, R. Mrowka, Phase dynamics of coupled oscillators reconstructed from data. Phys. Rev. E **77**(6, Part 2), 066205 (2008)
35. B. Kralemann, M. Frühwirth, A. Pikovsky, M. Rosenblum, T. Kenner, J. Schaefer, M. Moser, In vivo cardiac phase response curve elucidates human respiratory heart rate variability. Nat. Commun. **4**, 2418 (2013)
36. Y. Kuramoto, Self-entrainment of a population of coupled non-linear oscillators, in *Lecture Notes in Physics*, vol. 39, ed. by H. Araki (Springer, New York, 1975), pp. 420–422
37. Y. Kuramoto, *Chemical Oscillations, Waves, and Turbulence* (Springer, Berlin, 1984)
38. G. Lancaster, D. Iatsenko, A. Pidde, V. Ticcinelli, A. Stefanovska, Surrogate data for hypothesis testing of physical systems. Phys. Rep. (2018)
39. Z. Levnajić, A. Pikovsky, Network reconstruction from random phase resetting. Phys. Rev. Lett. **107**, 034101 (2011). https://doi.org/10.1103/PhysRevLett.107.034101
40. D. Lukarski, M. Ginovska, H. Spasevska, T. Stankovski, Time window determination for inference of time-varying dynamics: application to cardiorespiratory interaction. Front. Physiol. **11** (2020)
41. W. Moon, J.S. Wettlaufer, Coupling functions in climate. Phil. Trans. R. Soc. A **377**(2160), 20190006 (2019)
42. C. Morris, H. Lecar, Voltage oscillations in the barnacle giant muscle fiber. Biophys. J. **35**(1), 193–213 (1981)
43. B. Musizza, A. Stefanovska, P.V.E. McClintock, M. Paluš, J. Petrovčič, S. Ribarič, F.F. Bajrović, Interactions between cardiac, respiratory, and EEG-δ oscillations in rats during anæsthesia. J. Physiol. (London) **580**(1), 315–326 (2007)
44. G. Nadzinski, M. Dobrevski, C. Anderson, P.V.E. McClintock, A. Stefanovska, M. Stankovski, T. Stankovski, Experimental realization of the coupling function secure communications protocol and analysis of its noise robustness. IEEE Trans. Info. Forens. Secur. **13**(10), 2591–2601 (2018)
45. H. Nakao, Phase reduction approach to synchronisation of nonlinear oscillators. Contem. Phys. **57**(2), 188–214 (2016)
46. E. Niedermeyer, F.L. da Silva, *Electroencephalography: Basic Principles, Clinical Applications, and Related Fields* (Lippincott Williams & Wilkins, 2005)
47. T. Onojima, T. Goto, H. Mizuhara, T. Aoyagi, A dynamical systems approach for estimating phase interactions between rhythms of different frequencies from experimental data. PLoS Comput. Biol. **14**(1), e1005928 (2018)
48. S.A. Oprisan, A.A. Prinz, C.C. Canavier, Phase resetting and phase locking in hybrid circuits of one model and one biological neuron. Biophys. J. **87**(4), 2283–2298 (2004)

49. P. Orio, M. Gatica, R. Herzog, J.P. Maidana, S. Castro, K. Xu, Chaos versus noise as drivers of multistability in neural networks. Chaos **28**(10), 106321 (2018)
50. E. Ott, T.M. Antonsen, Low dimensional behavior of large systems of globally coupled oscillators. Chaos **18**(3), 037113 (2008)
51. H.J. Park, K. Friston, Structural and functional brain networks: from connections to cognition. Science **342**(6158), 1238411 (2013)
52. S. Petkoski, V.K. Jirsa, Transmission time delays organize the brain network synchronization. Philoso. Trans. R. Soc. A **377**(2153), 20180132 (2019)
53. B. Pietras, A. Daffertshofer, Network dynamics of coupled oscillators and phase reduction techniques. Phys. Rep. **819**, 1–105 (2019)
54. A. Pikovsky, Reconstruction of a random phase dynamics network from observations. Phys. Lett. A **382**(4), 147–152 (2018)
55. A. Pikovsky, M. Rosenblum, J. Kurths, *Synchronization–A Universal Concept in Nonlinear Sciences* (Cambridge University Press, Cambridge, 2001)
56. S. Ranganathan, V. Spaiser, R.P. Mann, D.J.T. Sumpter, Bayesian dynamical systems modelling in the social sciences. PLoS ONE **9**(1), e86468 (2014)
57. T. Rings, K. Lehnertz, Distinguishing between direct and indirect directional couplings in large oscillator networks: partial or non-partial phase analyses? Chaos **26**(9), 093106 (2016)
58. C. Rocsoreanu, A. Georgescu, N. Giurgiteanu, *The FitzHugh-Nagumo Model: Bifurcation and Dynamics*, vol. 10 (Springer Science & Business Media, 2012)
59. M. Rosenblum, M. Frühwirth, M. Moser, A. Pikovsky, Dynamical disentanglement in an analysis of oscillatory systems: an application to respiratory sinus arrhythmia. Phil. Trans. R. Soc. A **377**(2160), 20190045 (2019)
60. M. Rubinov, O. Sporns, Complex network measures of brain connectivity: uses and interpretations. Neuroimage **52**(3), 1059–1069 (2010)
61. A. Sanz-Garcia, T. Rings, K. Lehnertz, Impact of type of intracranial EEG sensors on link strengths of evolving functional brain networks. Physiol. Meas. **39**(7), 074003 (2018)
62. H. Schmidt, G. Petkov, M.P. Richardson, J.R. Terry, Dynamics on networks: the role of local dynamics and global networks on the emergence of hypersynchronous neural activity. PLoS Comput. Biol. **10**(11) (2014)
63. T. Schreiber, A. Schmitz, Surrogate time series. Phys. D **142**(3–4), 346–382 (2000)
64. V.N. Smelyanskiy, D.G. Luchinsky, A. Stefanovska, P.V.E. McClintock, Inference of a nonlinear stochastic model of the cardiorespiratory interaction. Phys. Rev. Lett. **94**(9), 098101 (2005)
65. T. Stankovski, Time-varying coupling functions: dynamical inference and cause of synchronization transitions. Phys. Rev. E **95**(2), 022206 (2017)
66. T. Stankovski, A. Duggento, P.V.E. McClintock, A. Stefanovska, Inference of time-evolving coupled dynamical systems in the presence of noise. Phys. Rev. Lett. **109**, 024101 (2012)
67. T. Stankovski, A. Duggento, P.V.E. McClintock, A. Stefanovska, A tutorial on time-evolving dynamical Bayesian inference. Eur. Phys. J. Special Topics **223**(13), 2685–2703 (2014)
68. T. Stankovski, P.V.E. McClintock, A. Stefanovska, Coupling functions enable secure communications. Phys. Rev. X **4**, 011026 (2014)
69. T. Stankovski, T. Pereira, P.V.E. McClintock, A. Stefanovska, Coupling functions: universal insights into dynamical interaction mechanisms. Rev. Mod. Phys. **89**(33), 045001 (2017)
70. T. Stankovski, T. Pereira, P.V.E. McClintock, A. Stefanovska, Coupling functions: dynamical interaction mechanisms in the physical, biological and social sciences. Phil. Trans. R. Soc. A **377**, 20190039 (2019)
71. T. Stankovski, S. Petkoski, J. Raeder, A.F. Smith, P.V.E. McClintock, A. Stefanovska, Alterations in the coupling functions between cortical and cardio-respiratory oscillations due to anaesthesia with propofol and sevoflurane. Phil. Trans. R. Soc. A **374**(2067), 20150186 (2016)
72. T. Stankovski, V. Ticcinelli, P.V.E. McClintock, A. Stefanovska, Coupling functions in networks of oscillators. New J. Phys. **17**(3), 035002 (2015)
73. T. Stankovski, V. Ticcinelli, P.V.E. McClintock, A. Stefanovska, Neural cross-frequency coupling functions. Front. Syst. Neurosci. **11**(33), https://doi.org/10.3389/fnsys.2017.00033 (2017)

74. A. Stefanovska, Coupled oscillators: complex but not complicated cardiovascular and brain interactions. IEEE Eng. Med. Bio. Magazine **26**(6), 25–29 (2007)
75. S. Strogatz, *Nonlinear Dynamics and Chaos* (Westview Press, Boulder, 2001)
76. H. Su, C. Huo, B. Wang, W. Li, G. Xu, Q. Liu, Z. Li, Alterations in the coupling functions between cerebral oxyhaemoglobin and arterial blood pressure signals in post-stroke subjects. PloS One **13**(4), e0195936 (2018)
77. K. Suzuki, T. Aoyagi, K. Kitano, Bayesian estimation of phase dynamics based on partially sampled spikes generated by realistic model neurons. Front. Comput. Neurosci. **11**, 116 (2018)
78. C.N. Takembo, A. Mvogo, H.P.E. Fouda, T.C. Kofané, Effect of electromagnetic radiation on the dynamics of spatiotemporal patterns in memristor-based neuronal network. Nonlin. Dyn. 1–12 (2018)
79. V. Ticcinelli, T. Stankovski, D. Iatsenko, A. Bernjak, A. Bradbury, A. Gallagher, P.B.M. Clarkson, P.V.E. McClintock, A. Stefanovska, Coherence and coupling functions reveal microvascular impairment in treated hypertension. Front. Physiol. **8**, 749 (2017)
80. I.T. Tokuda, S. Jain, I.Z. Kiss, J.L. Hudson, Inferring phase equations from multivariate time series. Phys. Rev. Lett. **99**, 064101 (2007)
81. G. Uribarri, G.B. Mindlin, Resonant features in a forced population of excitatory neurons. arXiv:1902.06008 (2019)
82. B. Voytek, R.T. Canolty, A. Shestyuk, N.E. Crone, J. Parvizi, R.T. Knight, Shifts in gamma phase–amplitude coupling frequency from theta to alpha over posterior cortex during visual tasks. Front. Hum. Neurosci. **4**, Art. No. 191 (2010)
83. S. Watanabe, S.H. Strogatz, Integrability of a globally coupled oscillator array. Phys. Rev. Lett. **70**(16), 2391 (1993)
84. A.T. Winfree, Biological rhythms and the behavior of populations of coupled oscillators. J. Theor. Biol. **16**(1), 15 (1967)
85. B. Yegnanarayana, *Artificial neural networks* (PHI Learning Pvt, Ltd, 2009)
86. A. Yeldesbay, G.R. Fink, S. Daun, Reconstruction of effective connectivity in the case of asymmetric phase distributions. J. Neurosci. Methods **317**, 94–107 (2019)

Chapter 12
Phase Reconstruction with Iterated Hilbert Transforms

Erik Gengel and Arkady Pikovsky

Abstract We discuss theoretical and practical issues of data-driven phase reconstruction approaches for nonlinear oscillatory systems by means of the geometric technique of embeddings and protophase-to-phase transformation. In this chapter, we introduce a natural extension of the well-studied Hilbert transform by iteration. The novel approach, termed iterated Hilbert transform embeddings, implements central assumptions underlying phase reconstruction and allows for exact demodulation of purely phase modulated signals. Here, we examine the performance of the novel method for the more challenging situation of generic phase-amplitude modulated signals of a simple nonlinear oscillatory system. In particular we present the benefits of the approach for secondary phase analysis steps illustrated by reconstruction of the phase response curve. Limitations of the approach are disussed for a noise-driven phase dynamics.

E. Gengel · A. Pikovsky (✉)
Institute for Physics and Astronomy, Universit of Potsdam, Karl-Liebknecht-Str. 24/25, 14476 Potsdam, Germany
e-mail: pikovsky@uni-potsdam.de

E. Gengel
e-mail: egengel@uni-potsdam.de

E. Gengel
Friedrich-Ebert Stiftung, Bonn, Germany

A. Pikovsky
Higher School of Economics, Nizhny Novgorod, Russia

Department of Control Theory, Institute of Information Technologies, Mathematics and Mechanics, Lobachevsky University Nizhny Novgorod, Nizhny Novgorod, Russia

A. Stefanovska and P. V. E. McClintock (eds.), *Physics of Biological Oscillators*, Understanding Complex Systems,
https://doi.org/10.1007/978-3-030-59805-1_12

12.1 Introduction and Overview

This chapter deals with the art of phase reconstruction. We focus on Hilbert transforms, however, much of the introduced methodology is not bound to Hilbert transforms alone.

In general, three approaches to signal analysis of oscillatory signals can be identified. The first approach applies statistical methods to extract information from observations assuming no further model [2, 22, 34]. The second approach takes the theory of dynamical systems into account and analyses the signals in terms of the phase and the amplitude notions provided in this theory [1, 7, 9, 17–19, 24, 29, 30, 37]. In an intermediate methodology, a phase and an amplitude are extracted from the data and then analysed in terms of statistical quantities. These methods may or may not take an underlying theory into account [15, 23, 25, 28, 36, 42, 43] Alternatively, one applies machine learning techniques to obtain equations of motion directly from observations [6, 41].

Here we focus on signal analysis approaches suitable for oscillating systems. The basic assumption is that the signal originates from a dynamical oscillating system, interacting with other systems and/or with the environment, and the goal is to understand the dynamics. This task is especially important and challenging in life science, where a theoretic description of the oscillators is in many cases lacking, because the underlying mechanisms are not clear. On the other hand, measurements of the full phase space dynamics are impossible, or would destroy the system itself. The latter aspect introduces the common setting where measurements of the systems are passive, i.e., an observer collects data from the free running system and may only apply weak perturbations to prevent damage. For such passive observations, we pursue here the approach inspired by the dynamical system theory: we try to extract the phases from the signals, with the aim to build models as close to theoretical descriptions as possible.

The ideas of the phase dynamics reconstruction has been widely used in physics, chemistry, biology, medicine and other areas [4, 20, 31, 35] to understand properties of oscillators and coupling between them (see also Chaps. 2, 3 and 11 of this book). The reason for this, as we discuss below, is that the phase is sensitive to interactions and external perturbations. In particular, many studies apply Hilbert transforms to reconstruct the phase from data (for example see [3, 14, 38, 43] and references therein). However, several fundamental issues in the process of phase reconstruction are unresolved, long standing and mostly omitted in the community. One issue deals with the role of the amplitudes [8, 21]. And from the view point of pure signal processing: how to deal with phase-amplitude mixing in Hilbert transforms [10, 13]. The latter issue will be discussed in particular here and we describe a solution by virtue of *iterative Hilbert transform embeddings* (IHTE) [12].

First, we describe the theoretical concepts. We then discuss the art of phase reconstruction with a focus on IHTE. We illustrate this method by presenting results for a Stuart-Landau non-linear oscillator, including reconstruction of the *infinitesimal phase response curve* (iPRC). Finally, we discuss difficulties of application in case of noisy oscillations.

12.2 Nonlinear Oscillators and Phase Reduction

Here we briefly review the phase reduction of driven limit cycle oscillators, for more details see [26, 27]. An autonomous oscillator is described by N state variables $\mathbf{y}$ which evolve according to a system of differential equations $\dot{\mathbf{y}} = \mathbf{f}(\mathbf{y})$. One assumes that this system has a stable limit cycle $\mathbf{y}_0(t) = \mathbf{y}_0(t + T)$ describing periodic (period T) oscillations. In the basin of attraction of the cycle one can always introduce a phase variable φ which grows uniformly in time

$$\dot{\varphi} = \omega = \frac{2\pi}{T}. \tag{12.1}$$

On the limit cycle, only the phase varies, so that $\mathbf{y}_0(\varphi) = \mathbf{y}_0(\varphi + 2\pi)$, which means that the value of the phase uniquely determines the point on the limit cycle.

If the autonomous oscillator is perturbed, i.e., it is driven by a small external force $\dot{\mathbf{y}} = \mathbf{f}(\mathbf{y}) + \varepsilon \mathbf{p}(\mathbf{y}, t)$, then the system slightly (of order $\sim \varepsilon$) deviates from the limit cycle, and additionally the phase does not grow uniformly, but obeys (in the first order in ε) the equation

$$\dot{\varphi} = \omega + \varepsilon Q(\varphi, t), \tag{12.2}$$

where Q can be expressed via $\mathbf{f}$, $\mathbf{p}$ (see [26] for details). Equation (12.2) contains only the phase and not the amplitude, it can be viewed as a result of the *phase reduction*. The dynamics of the phase according to (12.2) allows for studying different important effects of synchronization, etc. In the case when the oscillator is forced by another one, the force $\mathbf{p}(\eta)$ can be viewed as a function of the phase $\eta(t)$ of this driving oscillator, so the function $Q(\varphi, \eta)$ becomes the coupling function depending on two phases. In experimental situations it is quite common to perturb just one variable of the system. In that case, if the forcing term is scalar and does not depend on the system variables, one can factorize $Q(\varphi, t) = Z(\varphi)P(t)$ into the iPRC $Z(\varphi)$ and the (scalar) external driving $P(t)$ [5, 39].

Example: Forced Stuart-Landau Oscillator. In this contribution we consider as an example the perturbed Stuart-Landau oscillator (SL)

$$\dot{a} = (\mu + i\nu)a - (1 + i\alpha)a|a|^2 + i\varepsilon P(t), \qquad P(t) = \cos(r\omega t) \tag{12.3}$$

where $a(t) := R(t)\exp[i\phi(t)]$ is the complex amplitude. Parameter μ determines the amplitude ($\sqrt{\mu}$) and stability of the limit cycles, α is the nonisochronicity parameter. It is easy to check that

$$\varphi(t) = \phi(t) - \alpha \ln[R(t)] \tag{12.4}$$

is the proper phase, rotating, independently of amplitude R, with uniform frequency $\omega = \nu - \mu\alpha$. The frequency of the forcing is $r\omega$, where parameter r is the ratio of the external frequency to the base frequency ω. In the first order in ε, the amplitude and the phase dynamics read

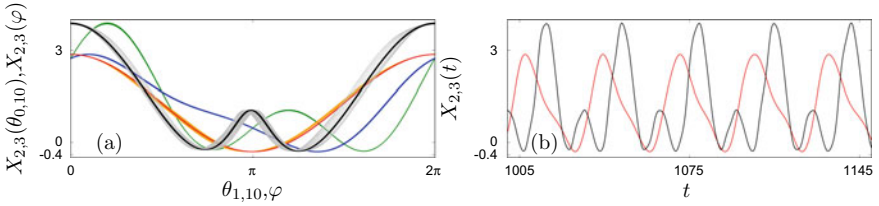

Fig. 12.1 Panel **a**: Observables X_2 (blue points) and X_3 (green points) as functions of the true phase φ. The fact that these sets are not distiguishable from a line demonstrates validity of the phase description for the SL oscillator (i.e. the amplitude modulation is indeed small). The same observables as functions of the first protophase θ_1 are not lines but broad sets (orange points for $X_2(\theta_1)$ and grey points for $X_3(\theta_1)$). The same observables become good function of the protophase θ_{10} after 10-th iteration of our procedure (red and black points, corerspondingly). Panel **b**: Time series for observables $X_{2,3}(t)$ (red,black). Simulation parameters are $\mu = 8, \alpha = 0.1, \nu = 1, \varepsilon = 0.1$ and $r = 1.8$ (for $X_2(t)$) and $r = 5.6$ (for $X_3(t)$). In this scale, small amplitude and phase modulations are hardly seen

$$\begin{aligned} \dot{R} &= R(\mu - R^2) + \varepsilon P(t)\sin(\varphi), \\ \dot{\varphi} &= \omega + \varepsilon\mu^{-1/2}(\cos(\varphi) - \alpha\sin(\varphi))P(t). \end{aligned} \tag{12.5}$$

Here, the iPRC is

$$Z(\varphi) = (\cos(\varphi) - \alpha\sin(\varphi))\mu^{-1/2}. \tag{12.6}$$

One can see that for small ε the dynamics of the SL is nearly periodic, with small ($\sim \varepsilon$) amplitude and phase modulations. Below in this paper we will consider three different scalar observables of the SL dynamics: $X_1(t) = \mathrm{Re}[a(t)]$, $X_2(t) = 0.1(\mathrm{Im}[a])^2 + 0.2(\mathrm{Re}[a])^2 + 0.3\mathrm{Im}[a] + 0.4\mathrm{Re}[a]$, and $X_3(t) = X_2(t) + 0.3\mathrm{Re}[a]\mathrm{Im}[a]$. The observable X_1 is "simple", it is a pure cosine function of time for the autonomous SL oscillator. The observable X_2 is also relatively simple (with one maximum and minimum pro period), but not a pure cosine. The observable X_3 can be viewed as a *multi-component signal* [11], with two maxima and minima pro period. Snapshots of the time series of corresponding signals $X_{2,3}(t)$ are illustrated in Fig. 12.1b.

12.3 Phase Reconstruction and Iterative Hilbert Transform Embeddings

12.3.1 Waveform, Phase and Demodulation

In Sect. 12.2 we introduced the phase dynamics concept for weakly perturbed oscillators. It is based on the equations of the original oscillator's dynamics. In the context of

data analysis, one faces a problem of the phase dynamics reconstruction solely from the observations of a driven oscillator. From the time series of a scalar observable, one wants to reconstruct the phase dynamics equation (12.2).

The first assumption we make is that the phase modulation of the process observed is much stronger than the amplitude modulation. Although, according to the theory, amplitude perturbations appear already in the leading order $\sim \varepsilon$ (cf. Eq. (12.5)), these variations could be small if the stability of the limit cycle is strong. Indeed, like example Eq. (12.5) shows, perturbations of the amplitude are inverse proportional to the stability of the limit cycle $\sim \varepsilon/\mu$, and are additionally small for μ large. Thus, for the rest of this chapter we assume that the dynamical process under reconstruction is solely determined by the dynamics of the phase.

Generally, a time series emanates from an observable $X[\mathbf{y}(t)]$ of the systems dynamics. According to the assumption above, we neglect amplitude modulation which means that we assume $\mathbf{y} = \mathbf{y}_0$, so that the scalar signal observed is purely phase modulated

$$X(t) = X[\mathbf{y}_0(\varphi(t))] =: S(\varphi(t)). \tag{12.7}$$

Here a 2π-periodic function $S(\varphi) = X[\mathbf{y}_0(\varphi)]$ is unknown, we call it the waveform. The reconstruction problem for the signal $X(t)$ is that of finding the waveform $S(\varphi)$ and the phase $\varphi(t)$. In Fig. 12.1a, we illustrate these waveforms for the observables $X_{2,3}$ of the SL oscillator. Plotting $X_{2,3}$ as functions of φ with dots, one gets extremely narrow lines which indicate that for chosen large stability of the limit cycle the amplitude dynamics can be neglected and decomposition is possible. On the contrary, if the observed signals possess essential amplitude modulation, $X(\varphi)$ would look like a band. In that case the above representation (12.7) is not adequate.

We stress here that a decomposition into the waveform and the phase is not unique. Indeed, let us introduce a new monotonous "phase" $\theta(t)$ according to an arbitrary transformation

$$\theta = \Theta(\varphi), \quad \Theta(\varphi + 2\pi) = \Theta(\varphi) + 2\pi, \quad \Theta' > 0. \tag{12.8}$$

Then the signal can be represented as $X(t) = S(\Theta^{-1}(\theta)) = \tilde{S}(\theta)$ with a new waveform $\tilde{S} = S \circ \Theta^{-1}$. Variables $\theta(t)$ are called protophases [17, 18]. Examples for mappings Eq. (12.8) are depicted in Fig. 12.4. To see the difference between protophases and true phase $\varphi(t)$, let us consider the non-driven, non-modulated dynamics. Here the phase $\varphi(t)$ grows uniformly $\dot{\varphi} = \omega$, while the protophase $\theta(t)$ grows non-uniformly, as

$$\dot{\theta} = \Theta'(\varphi)\omega = \omega\Theta'(\Theta^{-1}(\theta)) = f(\theta). \tag{12.9}$$

However, having a protophase and the function $f(\theta)$ governing its dynamics, one can transform to the true phase $\varphi(t)$ by inverting relation (12.8):

$$\frac{d\varphi}{d\theta} = \frac{1}{\Theta'(\varphi)} = \frac{\omega}{f(\theta)}, \quad \varphi = \int_0^\theta \frac{\omega d\theta'}{f(\theta')}. \tag{12.10}$$

Note that Eq. (12.10) is well defined as by construction, $\dot{\theta} = f(\theta) > 0$. In the case one observes driven oscillations, one approximately estimates $f(\theta) = \langle\dot{\theta}\rangle$, see [18] for details.

According to the discussion above, one can perform the phase reconstruction of an observed signal $X(t)$ in two steps:
(i) Find a decomposition $X(t) = \tilde{S}(\theta(t))$ into a waveform and a protophase, satisfying conditions

$$\text{(I):}\ \forall t, \dot{\theta}(t) > 0, \qquad \text{(II):}\ \tilde{S}(\theta) = \tilde{S}(\theta + 2\pi). \tag{12.11}$$

(ii) Perform a transformation from a protophase to the phase, so that the latter grows on average uniformly in time

$$\text{(III):}\ \langle\dot{\varphi}\rangle = \text{const}. \tag{12.12}$$

Conditions [I, II] ensure that the reconstructed protophase is monotonous and 2π-periodic. Condition [III] selects the phase as a variable uniformly growing in time, in contrast to other protophases which according to (12.9) grow with a rate that is protophase-dependent (with 2π-periodicity). Below we discuss in details the methods allowing for accomplishing steps (i) and (ii).

12.3.2 *Embeddings, Hilbert Transform, and Phase-Amplitude Mixing*

The first task, a decomposition into a waveform and a protophase, is trivial, if two scalar observables $\{X(t) = X[\mathbf{y}_0(t)], Y(t) = Y[\mathbf{y}_0(t)]\}$ of the oscillator's dynamics are available (of course, these observables should be not fully dependent). In this case, on the $\{X, Y\}$ plane one observes a *closed* continuous curve, parametrized by the phase, and the trajectory rotates along this curve. Any parametrization of the curve, normalized by 2π, will then provide a protophase as a function of time. After this, one has only to accomplish the step (ii), i.e. to transform the protophase to the phase.

An intrinsically non-trivial problem appears, if only one scalar observable, $X(t)$, is available. The goal is to perform a two-dimensional embedding of the signal $X(t)$, by generating from it the second variable $Y(t)$. There exist several approaches for this task. The most popular ones are the delay-embedding $Y(t) = X(t - \tau)$ [16], the derivative embedding $Y(t) = \dot{X}(t)$ [32], and the Hilbert transform (HT) embedding $Y(t) = \hat{H}[X](t)$, where (on a finite interval $[t_0, t_m]$)

$$\hat{H}[X](t) := \frac{\text{p.v.}}{\pi} \int_{t_0}^{t_m} \frac{X(\tau)}{t - \tau} d\tau. \tag{12.13}$$

It is an observation of practice, that the latter approach based on the HT often gives the most stable results. A reason for this is that the HT produces minimal distortions to the signal's spectrum. Indeed, all the methods mentioned are linear transformations, which in Fourier space correspond to multiplications with factors $e^{i\Omega\tau}$, $i\Omega$, and $i\ \mathrm{sign}(\Omega)$, respectively. The factor for HT depends on frequency in a "minimal" way, and does not have, contrary to the delay embedding, a parameter. However, the HT provides only an approximate embedding, due to a mixing of phase and amplitude modulations [13].

Indeed, only for a non-modulated, i.e. for a purely periodic signal $X(t)$, the HT transform provides a periodic $Y(t)$, so that on the $\{X, Y\}$ plane one observes a perfect closed loop. If the signal $X(t)$ is phase-modulated, then on the $\{X, Y = \hat{H}[X(t)]\}$ plane one observes a non-closed trajectory (which only approximately can be considered as a loop), the width of the band gives the size of the appearing amplitude modulation (see Figs. 12.1a and 12.2). (Also if one has a purely amplitude-modulated signal, its HT will provide spurious phase modulation - but this is not relevant for our problem). It should be noted that the spurious amplitude modulation arises solely due to the spectral properties of the Hilbert transform, and is not related to the length of the observation data. Usually, already 20–30 observed periods suffice to overcome boundary effects. Instead, the spectral content of the phase modulation heavily influences the appearance of amplitude modulation, and hence the accuracy of reconstruction [12].

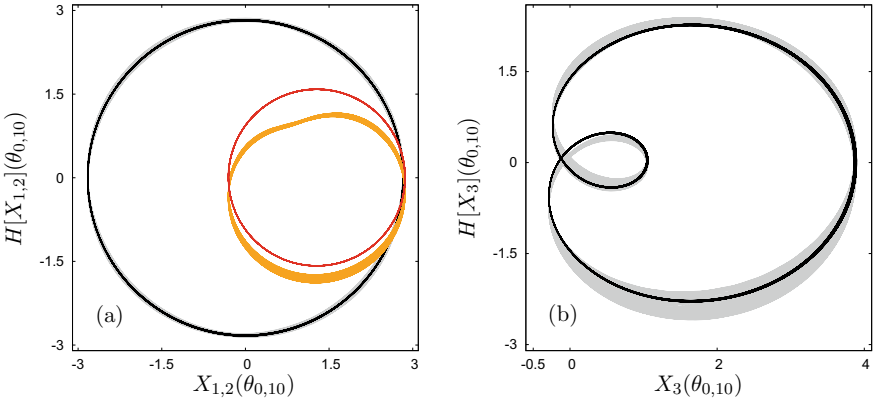

Fig. 12.2 IHTE for a periodically driven SL oscillator Eq. (12.3) with harmonic driving $P(t) = \cos(r\omega t)$. Parameters: $\mu = 8$, $\alpha = 0.1$, $\nu = 1$, $\varepsilon = 0.1$. In panel **a** observables $X_1(t)$ (for frequency ratio $r = 5.6$) and $X_2(t)$ (for $r = 1.8$) are used. Shown are the first step of the IHTE hierarchy in grey and orange, and step ten in black and red for X_1 and X_2, respectively. In panel **b** the observable $X_3(t)$ with $r = 5.6$ is used where grey corresponds to the first embedding and black corresponds to the embedding in step ten. Embeddings at the first iteration yield wide bands, which indicates for an "artificial" modulation of the amplitude, while at the 10th iteration the embeddings are nearly perfect lines, which means that the observed signals are nearly perfect phase modulated ones. Note that the embedding of X_1 has a circular shape, the embeddings of $X_{2,3}$ are distorted from a circle causing non-uniform protophases. In case of X_3, the embedding shows a loop (panel (**b**))

In the next section we describe a method to circumvent this problem by virtue of *iterated HT embeddings* (IHTE) [12], illustrating the procedure with different observables of the SL oscillator.

12.3.3 Iterated HT Embeddings

As discussed above, the HT embedding $\{X(t), \hat{H}[X(t)]\}$ although does not provide a closed looped line, allows one for an approximate determination of the protophase. To accomplish this, one needs to define a variable monotonously growing along the trajectory and gaining 2π at each approximate loop. A naive analytic-signal-based protophase $\arg(X + iY)$ would work only for cosine-like waveforms like $X_{1,2}$. Therefore we employ another definition of the protophase, based on the trajectory length [18]

$$L(t) = \int_0^t \sqrt{\dot{X}^2(\tau) + \dot{Y}^2(\tau)}d\tau. \tag{12.14}$$

This length grows monotonously also in the case when the embedding has loops (cf. Fig. 12.2), in which case the analytic-signal-based definition obviously fails.

Having calculated the length $L(t)$, we can transform it to a protophase by interpolation. For this, we define in the signal features which we attribute to the zero (modulo 2π) protophase, and define the corresponding time instants t_j. In the simplest case, one can define a protophase $\theta(t)$ on the interval (t_j, t_{j+1}) as a linear function of the length $\theta(t) = 2\pi j + 2\pi(L(t) - L(t_j))/(L(t_{j+1}) - L(t_j))$. However, such a protophase will be discontinuous in the first derivative. A better transformation is achieved via splines: one constructs a spline approximation for the function $\theta(L)$, provided one knows the values of this function at the signal features: $\theta(t_j) = 2\pi j$ at $L(t_j)$.

Constructed in this way, the protophase $\theta(t)$ is only approximate, because $X(\theta + 2\pi) \neq X(\theta)$. Visually, on the plane $\{X, \hat{H}[X]\}$ one observes a band instead of a single loop (see Fig. 12.2). Also, when X is plotted versus θ, one observes not a single-valued function, but a band (see Fig. 12.1a).

Recently, in Ref. [12], we proposed to use iterative Hilbert transform embeddings (IHTE) to improve the quality of the protophase definition above. Our idea is to perform subsequent Hilbert transforms based on the previously calculated protophases $\theta_n(t)$, where n denotes the step of iteration (see Fig. 12.3). Intuitively, the advantage of iterations can be understood as follows: The widely used first iteration already presents an approximation to the protophase, although not a perfect one. This means, that the function $X(\theta_1)$ still has modulation, but less than $X(t)$. Now, if we take θ_1 as a new time and again perform a demodulation by virtue of the Hilbert transform embedding, we expect $\theta_2(t)$ to be better than $\theta_1(t)$, etc. A detailed analysis performed in Ref. [12] shows that this procedure indeed converges to perfect demodulation.

In terms of iterations, the protophase $\theta(t)$ discussed above is the first iteration $\theta_1(t)$, while the time variable can be considered as the "zero" iteration $\theta_0(t)$. At each

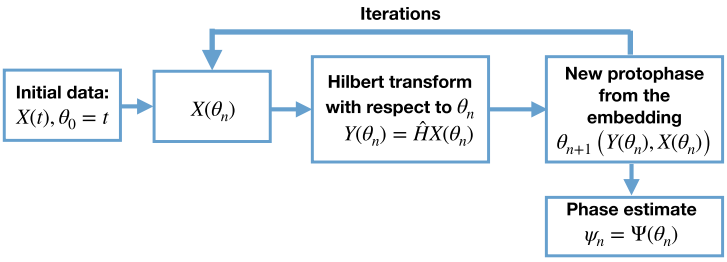

Fig. 12.3 Here we schematically explain the iterative Hilbert tranform embeddings. Typically only one iteration is performed, and the protophase $\theta_1(t)$ is used for further analysis. We show in this chapter, how the quality of the phase reconstruction improves with the iterative embeddings

iteration step we use the obtained protophase as a new "time" with respect to which the next HT is performed:

$$Y_{n+1}(\theta_n) = \hat{H}[X(\theta_n)] := \frac{\text{p.v.}}{\pi} \int_{\theta_n(t_0)}^{\theta_n(t_m)} \frac{X(\theta'_n)}{\theta_n - \theta'_n} d\theta'_n. \tag{12.15}$$

An implementation of this integral is given in [12]. Basically there are two challenges here: first, the integration has to be performed on a non-uniform grid and second, one has to take care of the singularity at $\theta'_n = \theta_n$.

The iteration process will be as follows (see Fig. 12.3):

1. Having $X(\theta_n) = X(t(\theta_n))$, we calculate $Y_{n+1}(\theta_n) = \hat{H}[X(\theta_n)]$ according to (12.15).
2. Next, we construct the embedding $\{X, Y_{n+1}\}$ and find the length $L(\theta_n)$ from (12.14).
3. After defining signal features, we calculate, using splines, the new protophase θ_{n+1} as a function of $L(\theta_n)$, which gives the new protophase θ_{n+1} as a function of the old one θ_n.

The steps 1–3 are repeated, starting from $\theta_0 = t$. After n iterations, we obtain a waveform and a protophase

$$\tilde{S}(\theta_n) = X(t(\theta_n)) \tag{12.16}$$

As has been demonstrated in Ref. [12], the procedure converges to a proper protophase, fulfilling conditions [I, II] above. For a purely phase modulated signal, at large n the errors (12.17) reach very small values limited by accuracy of integration. The convergence rate depends heavily on the complexity of the waveform and on the level and frequency of modulation, but typically at $\hat{n} \approx 10$ a good protophase is constructed.

Summarizing, the IHTE solve the problem of constructing a protophase $\theta(t) = \theta_{\hat{n}}(t)$ and the corresponding waveform $\tilde{S}(\theta)$ from a scalar phase-modulated signal $X(t)$; this protophase fulfills conditions (12.11)-[I, II]. Indeed, one observes in Fig. 12.4 that the first mapping $\Theta_1(\varphi)$ is not purely 2π-periodic (blue bands). Instead,

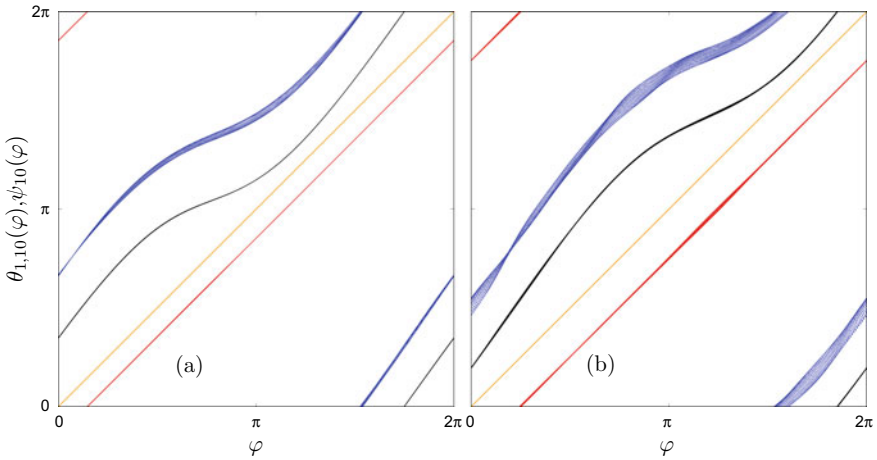

Fig. 12.4 Depicted are the phase-to-protophase maps Eq. (12.8) for $X_2[.]$ (panel **a**) and $X_3[.]$ (panel **b**) based on the embeddings shown in Fig. 12.2. Colours correspond to $\Theta_1(\varphi)$ (blue, this data form a rather wide band indicating that the protophase at the first iteration is not precise), $\Theta_{10}(\varphi)$ (black, this data forms a narrow line indicating for a good protophase reconstruction), $\psi_{10}(\varphi)$ (red, this narrow line is straight indicating for a good phase reconstruction). The orange line is the diagonal. For better visibility the curves are shifted vertically

after ten iterations, $\Theta_{10}(\varphi)$ effectively has become a line (black) indicating that a protophase is reconstructed. The same can be seen in Fig. 12.1a, where bands of values $X_{2,3}(\theta_1)$ are transformed to narrow lines $X_{2,3}(\theta_{10})$ after ten iterations.

As the final step in obtaining a close estimate $\psi(t)$ of the proper phase $\varphi(t)$, we have to perform the protophase-to-phase transformation, as described in Ref. [18]. The transformation is based on relation (12.10), where the Fourier components of the density of the protophase are estimated according to $F_k = t_m^{-1} \int_0^{t_m} \exp[-ik\theta(t)]\, dt$; these components are used to perform the transformation as $\psi = \theta + \sum_{k\neq 0} F_k (ik)^{-1} [\exp(ik\theta) - 1]$. Indeed, one observes in Fig. 12.4 (red lines) that $\psi(t)$ is, up to estimation errors, resembling the dynamics of $\varphi(t)$. However, we want to stress here that determination of the protophase-to-phase transformation is based on a statistical evaluation of the probability density of the protophase. Hence, in order to achieve a proper reconstructions with small distortions in the protophase-to-phase mapping, one needs long time series.

We can check for the similarity of $\theta_n(t)$ or $\psi_n(t)$ to the true phase $\varphi(t)$ by calculating a phase and a frequency error as the standard deviations

$$\mathrm{STD}_n^{\mathbf{q}} = \sqrt{\frac{1}{\hat{N}_1} \int_{t_{\min}}^{t_{\max}} [\mathbf{q}_n(\tau) - \varphi(\tau)]^2 d\tau} \qquad \mathrm{STD}_n^{\dot{\mathbf{q}}} = \sqrt{\frac{1}{\hat{N}_2} \int_{t_{\min}}^{t_{\max}} [\dot{\mathbf{q}}_n(\tau) - \dot{\varphi}(\tau)]^2 d\tau}$$

$$\hat{N}_1 = \int_{t_{\min}}^{t_{\max}} (\varphi(\tau) - \tilde{\omega}\tau)^2 d\tau \qquad \hat{N}_2 = \int_{t_{\min}}^{t_{\max}} [\dot{\varphi}(\tau) - \tilde{\omega}]^2 d\tau. \tag{12.17}$$

$\mathrm{STD}_n^{\mathbf{q},\dot{\mathbf{q}}}$ tend to zero only, if the reconstructed protophases and transformed protophases $\mathbf{q}_n = \{\theta_n(t), \psi_n(t)\}$ are close to the true phase $\varphi(t)$ of the system (see Eq.(12.4)). In the integration, we skip the outer ten percent at the beginning and at the end of the time series, to avoid boundary effects. Estimations of the instantaneous frequency $\varphi(t)$ and $\dot{\mathbf{q}}_n(t)$ are performed by a 12th order polynomial filter (Savitzky-Golay filter) with a window of 25 points and four times repetition [33] denoted as SG(12,25,4). Throughout the chapter we use a sampling rate of $dt = 0.01$, such that the smoothing window has a width of $dt = 0.25$, corresponding to roughly 11% of the fastest forcing period ($r = 14.3$). The estimated average growth rate $\tilde{\omega}$ is obtained by linear regression. Note that the normalization integral $\hat{N}_1$ is suitable for all phases where the average growth is linear.

12.4 Numerical Experiments

12.4.1 Deterministic Oscillations

Here we consider the SL system (12.3) with $\mu = 8$, $\alpha = 0.1$, $\nu = 1$. As the observables we explore functions $X_{1,2,3}[a(t)]$ defined above. The system is forced harmonically by $\varepsilon P(\eta) = \varepsilon \cos(\eta(t))$ with amplitude $\varepsilon = 0.1$. The external force phase is $\eta(t) = r\omega t$, for the explored range of driving frequencies $r\omega$ the SL operated in the asynchronous regime. We observe 100 periods with a time step of $dt = 0.01$.

In Fig. 12.6 the phase and the frequency errors according to Eq. (12.17) for the first 20 iteration steps are shown. While for slow modulations ($r < 1$), the reconstruction is already accurate in the first step, for fast forcing frequencies ($r > 1$) indeed several iterations are needed for precise reconstruction. The reason for this is that for high-frequency modulations iterative HT embeddings first shift high-frequency Fourier components of the phase modulation to lower frequencies, where they eventually disappear. This mechanism is closely related to the Bedrosian identities [40] and is explained in detail in [12]. For the reconstruction of phases in case of $X_{2,3}[a(t)]$, we have to calculate the transformed phase $\psi(t)$, because here the protophases deviate from uniform growth. The results show, that IHTE combined with the protophase-to-phase transformation provides proper phase reconstructions for the fairly stable limit cycle oscillator under study.

Figure 12.5 presents comparisons of the inferred modulation $u_n(t) := \psi_n(t) - \tilde{\omega}t$ with the true one $q(t) = \varphi - \omega t$, and of the inferred instantaneous frequencies $\dot{\theta}_n(t)/\dot{\psi}_n(t)$ with $\dot{\varphi}$, for a quite fast external force $r = 5.6$ (black bold dots in Fig. 12.6). While the first iterate is by far not accurate, iterations provide the reconstructed estimation of the phases $\psi_{20}(t)$ which is very close to $\varphi(t)$.

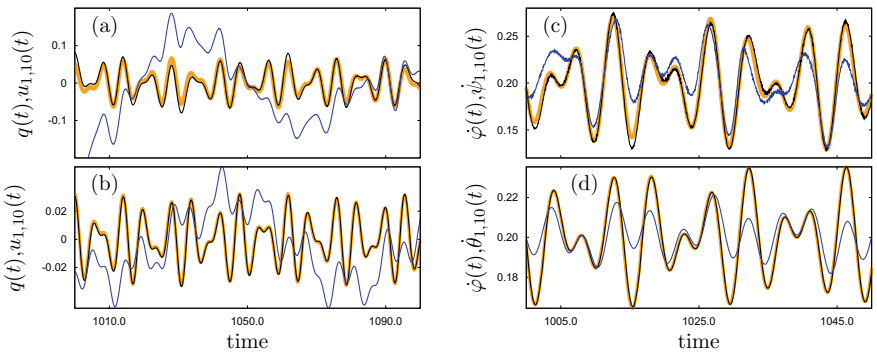

Fig. 12.5 Comparison of true modulation $q(t)$ and of true instantaneous frequency $\dot{\varphi}$ (orange) with the corresponding iteration results $u_n(t)$ in the first step (blue) and in the 10th step (black) for the observables $X_1(t)$ (b, d) and $X_3(t)$ (a, c). Parameters are $\mu = 8$, $\alpha = 0.1$, $\nu = 1$, $\varepsilon = 0.1$ and $r = 5.6$. For calculation of the derivative $\dot{\varphi}(t)$ we use a SG(12,25,4) filter

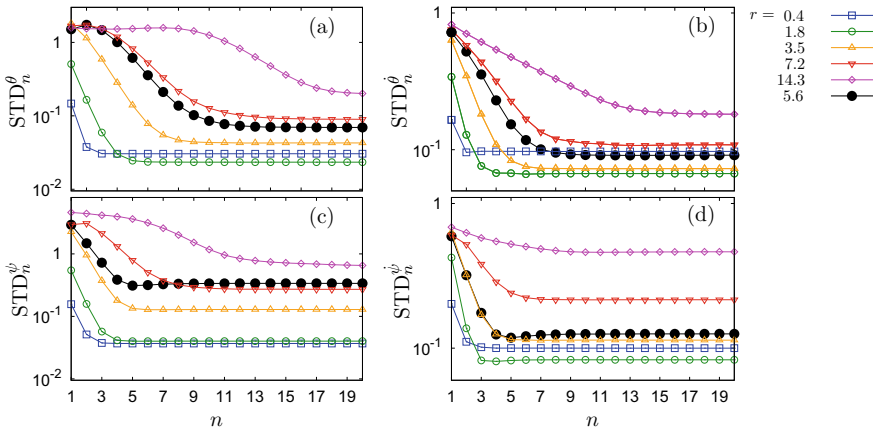

Fig. 12.6 Phase and frequency errors for observables $X_1(t)$ (a, b) and $X_2(t)$ (c, d) for different forcing frequencies $r\omega$. Also shown in (c, d black doted line) is the reconstruction error for $X_3(t)$, where the use of $L(t)$ for phase calculation is crucial. Slow modulations are essentially reconstructed in the first step while fast modulations need at least several iterations. With increased forcing frequency, $\theta_n(t)$ differs significantly from $\varphi(t)$ and the number of needed iterative steps grows

12.4.2 Reconstruction of the Phase Response Curve from Observation

Here, we present the advantage of using the IHTE for the reconstruction of the coupling functions and the iPRC. As an example we consider the SL oscillator with harmonic driving and parameters $r = 5.6$, $\mu = 8$, $\alpha = 0.1$, $\nu = 1$ and $\varepsilon = 0.1$ observed via variable $X_1[.]$. The coupling function is reconstructed by a kernel-density fit. Namely, we use a kernel $\mathbb{K}(x, y) = \exp[\kappa(\cos(x) + \cos(y) - 2)]$ and

$\kappa = 200$ to construct $\dot{\theta}(\varphi, \eta)$. We apply a simple iterative method described in [19]. After K iterative steps, the extracted coupling function $\tilde{Q}_{K,n}(\varphi, \eta) := \dot{\theta}_n(\varphi, \eta) - \tilde{\omega}$ is factorized into $\tilde{Z}_K(\varphi)$ and $\tilde{P}_K(\eta)$. In Fig. 12.8, the improvement due to IHTE is evident. We used $K = 30$ factorization steps and recover the actual coupling function with pretty high accuracy for different frequencies of forcing depicted in Fig. 12.7.

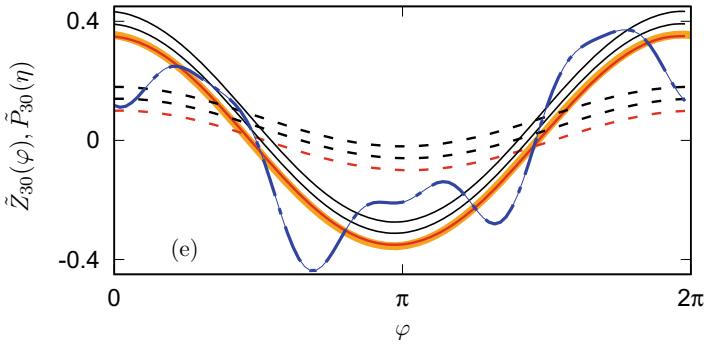

Fig. 12.7 The phase response curve $Z(\varphi)$ (orange). The blue unevenly dashed line depicts the estimation $\tilde{Z}_{30}(\varphi)$ based on $\theta_1(t)$. Also shown are the estimations $\tilde{Z}_{30}(\varphi)$ (solid line) and $\tilde{P}_{30}(\eta)$ (dashed line) based on $\theta_{10}(t)$ for $r = [0.06, 4.5, 5.6]$ (top to bottom). Red lines refer to the coupling functions Fig. 12.8

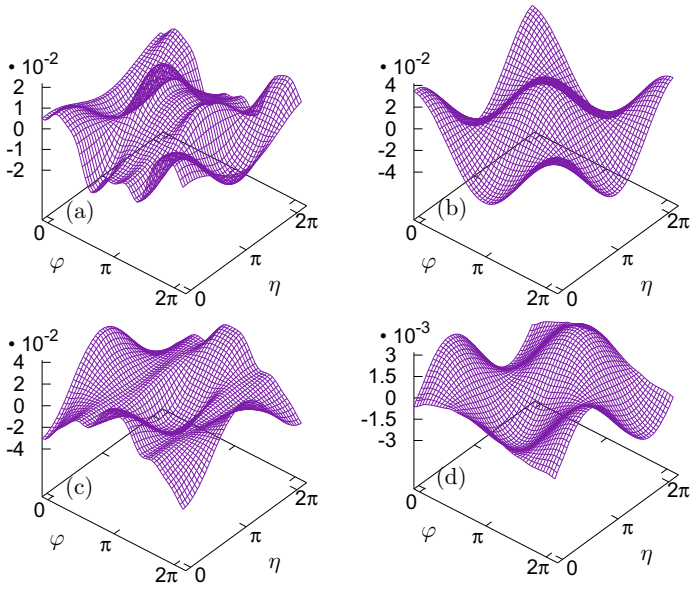

Fig. 12.8 Reconstructed coupling functions $\tilde{Q}_{30,1}(\varphi, \eta)$ (panel (a)) and $\tilde{Q}_{30,10}(\varphi, \eta)$ (panel (b)) based on $\theta_1(t)$ and $\theta_{10}(t)$, respectively. The reconstruction error for the first iteration $Q_{30,1}(\varphi, \eta) - Q(\varphi, \eta)$ is shown in panel (c), and for the 10th iteration $Q_{30,10}(\varphi, \eta) - Q(\varphi, \eta)$ in panel (d). Noteworthy, the vertical scale in panel (d) is more than ten times smaller than in panel (c)

12.4.3 Noisy Oscillations

In this section we discuss applicability of the described method to noisy signals. We assume that the SL oscillator is driven by an external force containing a deterministic and a stochastic (white noise) component

$$\varepsilon P(t) = \varepsilon \cos(\omega r t) + \xi(t), \qquad \langle \xi \rangle = 0, \langle \xi(t), \xi(t') \rangle = \sigma^2 \delta(t - t') \tag{12.18}$$

with $\mu = 8$, $\alpha = 0.1$, $\nu = 1$, $\varepsilon = 0.2$, $r = 5.6$ and different noise levels $\sigma = [0.1, 0.08, 0.06]$. We assume a "perfect" observation according to $X_1(t)$ (i.e., there is no observational noise). Due to the stochastic forcing, the signal's spectrum has infinite support. In the time domain, $X(t)$ contains an infinite amount of local maxima and minima which will cause infinitely many but small loops in the embedding (see Fig. 12.9b). Strictly speaking, we can not obtain phase from such a signal by calculating the length of the embedded curve, because the latter is a fractal curve.

Therefore, we can not deal with the raw signal $X(t)$. Instead, as a preprocessing, we smooth out fast small-scale fluctuations of $X(t)$ by a SG [4, 12, 25] filter, effectively cutting the spectrum of the signal at high frequencies. In such a setting with a finite-width spectrum, we expect that IHTE can improve the phase reconstruction.

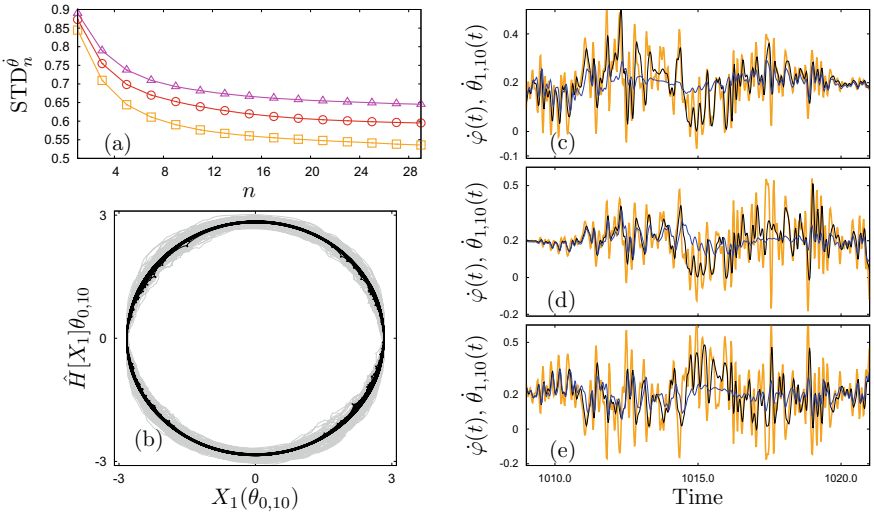

Fig. 12.9 Phase reconstruction for the SL system with $\mu = 8, \alpha = 0.1, \nu = 1, \varepsilon = 0.2$ and $r = 5.6$ and observable $X_1[.]$. Panel (a): the errors of frequency reconstruction for $\sigma = [0.06, 0.08, 0.1]$ (squares, circles, triangles). Panel (b): The first Hilbert embedding (grey) and the last embedding at 10th step (black). Note that the small scale loops as a result of the remaining noise influence in $X_1(t)$. Panels (c, d, e): Depicted are snapshots of the instantaneous frequency $\dot\varphi(t)$ (orange), and of the reconstructed frequencies $\dot\theta_1(t)$ (blue) and $\dot\theta_{10}(t)$ (black) for $\sigma = [0.06, 0.08, 0.1]$, respectively. Note that $\dot\varphi(t)$ can be negative as an effect of noise, while all reconstructions obey (12.11)-[I]

The results in this case have to be interpreted relative to the smoothing parameters which are chosen in such a way that they preserve essential local features of the dynamics. Indeed, we observe negative instantaneous frequencies $\varphi(t)$ pointing to the need of a high polynomial order of smoothing (see Fig. 12.9c, d, e). Also, the noise causes diffusion of phase (see Fig. 12.9).

From the viewpoint of phase extraction via embeddings, the white noise forcing represents a "worst case". On the contrary, in all situations where coloured noise with a bounded spectrum is present, we expect IHTE to be the more easily applicable. Depending on the spectral composition of noise, small-scale loops in the embedding may be not present at all, or may be eliminated with minimal filtering. If the noise has only relatively low-frequency component, the embedding will be relatively smooth, and no additional processing is needed.

Our method is restricted to the conditions (12.11). Since all of these conditions are not fulfilled in this example, the actual phase dynamics is only partly reconstructed, as can be seen also from Fig. 12.9a where the reconstruction error decay is much less pronounced than in Fig. 12.6. In view of this, the presented example can be considered as a proof of concept for IHTE of noisy signals. The method improves the estimation of the phase, as the examples of Fig. 12.9 show, by factor up to 2.

We add the following preprocessing to IHTE:

1. Given $X(t)$, apply a high-order SG-filter making the signal smooth with a large number of inflection points.
2. Next, smooth $\varphi(t)$ by the same SG-filter.
3. Proceed signal $X(t)$ with IHTE as described in Sect. 12.3.3.

12.5 Conclusion and Open Problems

In summary, the IHTE approach solves the problem of phase demodulation for purely phase modulated signals. Here, we present results for a dynamical system, where the amplitude dynamics is also present and linked to the dynamics of $\varphi(t)$. We have demonstrated that IHTE indeed provides a good reconstruction of the phase dynamics, if the amplitude variations are relatively small (see Fig. 12.4, 12.6, 12.5). We show that iterations drastically improve the reconstruction of the phase, in comparison to the previously employed approach based on a single Hilbert transform (see Fig. 12.5) and $Z(\varphi)$ (see Fig. 12.8). However, the analysis of the performance of IHTE in the case of larger amplitude variations is a question to be discussed in the future.

An important issue in the phase reconstruction is the protophase-to-phase transformation. It is particularly relevant for generic observables like $X_3[.]$, with complex waveforms. While handling such observables in the framework of IHTE does not state a problem, influence of amplitude variations may depend drastically on the complexity of the waveform. It should be stressed here, that while construction of the protophase via IHTE is almost exact, the protophase-to-phase transformation is

based on some assumption about the dynamics, which typically are only approximately fulfilled. This topic certainly deserves further studies.

Biological systems are noisy. We have given an example here, where IHTE also improves the reconstruction of the phase in presence of fluctuations (see Fig. 12.9). However, the very concept of a monotonously growing phase should be reconsidered for noisy signals. Here we largely avoided problems by smoothing the observed signal, but in this approach some features of the modulation might be lost.

Acknowledgements Both authors thank Aneta Stefanovska and Peter McClintock for the kind invitation to contribute to this interdisciplinary work. Erik Gengel thanks the Friedrich-Ebert-Stiftung for financial support. This paper was supported by the RSF grant 17-12-01534. The analysis in Sec. 3.3 was supported by the Laboratory of Dynamical Systems and Applications NRU HSE, of the Russian Ministry of Science and Higher Education (Grant No. 075-15-2019-1931).

References

1. A. Bahraminasab, F. Ghasemi, A. Stefanovska, P.V.E. McClintock, H. Kantz, Direction of coupling from phases of interacting oscillators: a permutation information approach. Phys. Rev. Lett. **100**, 084101 (2008)
2. H. Balzter, N.J. Tate, J. Kaduk, D. Harper, S. Page, R. Morrison, M. Muskulus, P. Jones, Multi-scale entropy analysis as a method for time-series analysis of climate data. Climate **3**(1), 227–240 (2015)
3. D. Benitez, P. Gaydecki, A. Zaidi, A. Fitzpatrick, The use of the Hilbert transform in ECG signal analysis. Comput. Biol. Med. **31**(5), 399–406 (2001)
4. K.A. Blaha, A. Pikovsky, M. Rosenblum, M.T. Clark, C.G. Rusin, J.L. Hudson, Reconstruction of two-dimensional phase dynamics from experiments on coupled oscillators. Phys. Rev. E **84**(4), 046201 (2011)
5. E. Brown, J. Moehlis, P. Holmes, On the phase reduction and response dynamics of neural oscillator populations. Neural Comput. **16**(4), 673–715 (2004)
6. S.L. Brunton, J.N. Kutz, *Data-Driven Science and Engineering: Machine Learning, Dynamical Systems, and Control* (Cambridge University Press, 2019)
7. R. Cestnik, M. Rosenblum, Reconstructing networks of pulse-coupled oscillators from spike trains. Phys. Rev. E **96**(1), 012209 (2017)
8. R. Chestnik, M. Rosenblum, Inferring the phase response curve from observation of a continuously perturbed oscillator. Sci. Rep. **8**(1), 13606 (2018)
9. L. Cimponeriu, M. Rosenblum, A. Pikovsky, Estimation of delay in coupling from time series. Phys. Rev. E **70**, 046213 (2004)
10. L. Cohen, P. Loughlin, D. Vakman, On an ambiguity in the definition of the amplitude and phase of a signal. Sig. Process. **79**(3), 301–307 (1999)
11. M. Feldman, *Hilbert Transform Applications in Mechanical Vibration* (Wiley, 2011)
12. E. Gengel, A. Pikovsky, Phase demodulation with iterative Hilbert transform embeddings. Sig. Process. **165**, 115–127 (2019)
13. R. Guevara Erra, J.L. Perez Velazquez, M. Rosenblum, Neural synchronization from the perspective of non-linear dynamics. Front. Comput. Neurosci. **11**, 98 (2017)
14. N.-H. Holstein-Rathlou, K.-P. Yip, O.V. Sosnovtseva, E. Mosekilde, Synchronization phenomena in nephron–nephron interaction. Chaos: Interdiscip. J. Nonlinear Sci. **11**(2), 417–426 (2001)
15. N. Jajcay, S. Kravtsov, G. Sugihara, A.A. Tsonis, M. Paluš, Synchronization and causality across time scales in El Niño Southern Oscillation. NPJ Clim. Atmos. Sci. **1**(1), 1–8 (2018)

16. H. Kim, R. Eykholt, J. Salas, Nonlinear dynamics, delay times, and embedding windows. Phys. D **127**(1–2), 48–60 (1999)
17. B. Kralemann, L. Cimponeriu, M. Rosenblum, A. Pikovsky, R. Mrowka, Uncovering interaction of coupled oscillators from data. Phys. Rev. E **76**(5 Pt 2), 055201 (2007)
18. B. Kralemann, L. Cimponeriu, M. Rosenblum, A. Pikovsky, R. Mrowka, Phase dynamics of coupled oscillators reconstructed from data. Phys. Rev. E **77**(6), 066205 (2008)
19. B. Kralemann, M. Frühwirth, A. Pikovsky, M. Rosenblum, T. Kenner, J. Schaefer, M. Moser, In vivo cardiac phase response curve elucidates human respiratory heart rate variability. Nat. Commun. **4**, 2418 (2013)
20. B. Kralemann, A. Pikovsky, M. Rosenblum, Reconstructing phase dynamics of oscillator networks. Chaos **21**(2), 025104 (2011)
21. C. Letellier, J. Maquet, L. Le Sceller, G. Gouesbet, L. Aguirre, On the non-equivalence of observables in phase-space reconstructions from recorded time series. J. Phys. A: Math. Gen. **31**(39), 7913 (1998)
22. D. Li, X. Li, Z. Liang, L.J. Voss, J.W. Sleigh, Multiscale permutation entropy analysis of EEG recordings during sevoflurane anesthesia. J. Neural Eng. **7**(4), 046010 (2010)
23. M. Paluš, Multiscale atmospheric dynamics: cross-frequency phase-amplitude coupling in the air temperature. Phys. Rev. Lett. **112**(7), 078702 (2014)
24. M. Paluš, A. Stefanovska, Direction of coupling from phases of interacting oscillators: An information-theoretic approach. Phys. Rev. E **67**, 055201 (2003)
25. Z. Peng, W.T. Peter, F. Chu, An improved Hilbert-Huang transform and its application in vibration signal analysis. J. Sound Vib. **286**(1–2), 187–205 (2005)
26. B. Pietras, A. Daffertshofer, Network dynamics of coupled oscillators and phase reduction techniques. Phys. Rep. (2019)
27. A. Pikovsky, M. Rosenblum, J. Kurths, *Synchronization: A Universal Concept in Nonlinear Sciences* (Cambridge University Press, 2001)
28. T. Rings, K. Lehnertz, Distinguishing between direct and indirect directional couplings in large oscillator networks: partial or non-partial phase analyses? Chaos: Interdiscip. J. Nonlinear Sci. **26**(9), 093106 (2016)
29. M. Rosenblum, L. Cimponeriu, A. Pikovsky, Coupled oscillators approach in analysis of physiological data. Conf. Proc. IEEE Eng. Med. Biol. Soc. **1**, 441–4 (2006)
30. M. Rosenblum, A. Pikovsky, Detecting direction of coupling in interacting oscillators. Phys. Rev. E **64**(4), 045202(R) (2001)
31. M. Rosenblum, A. Pikovsky, Synchronization: from pendulum clocks to chaotic lasers and chemical oscillators. Contemp. Phys. **44**(5), 401–416 (2003)
32. T. Sauer, J.A. Yorke, M. Casdagli, Embedology. J. Stat. Phys. **65**(3–4), 579–616 (1991)
33. A. Savitzky, M.J. Golay, Smoothing and differentiation of data by simplified least squares procedures. Anal. Chem. **36**(8), 1627–1639 (1964)
34. A. Schlemmer, S. Berg, T. Lilienkamp, S. Luther, U. Parlitz, Spatiotemporal permutation entropy as a measure for complexity of cardiac arrhythmia. Front. Phys. **6**, 39 (2018)
35. T. Stankovski, T. Pereira, P.V.E. McClintock, A. Stefanovska, Coupling functions: universal insights into dynamical interaction mechanisms. Rev. Mod. Phys. **89**, 045001 (2017)
36. T. Stankovski, S. Petkoski, J. Raeder, A.F. Smith, P.V. McClintock, A. Stefanovska, Alterations in the coupling functions between cortical and cardio-respiratory oscillations due to anaesthesia with propofol and sevoflurane. Philos. Trans. R. Soc. A: Math., Phys. Eng. Sci. **374**(2067), 20150186 (2016)
37. Ç. Topçu, M. Frühwirth, M. Moser, M. Rosenblum, A. Pikovsky, Disentangling respiratory sinus arrhythmia in heart rate variability records. Physiol. Meas. **39**(5), 054002 (2018)
38. A.B. Tort, R. Komorowski, H. Eichenbaum, N. Kopell, Measuring phase-amplitude coupling between neuronal oscillations of different frequencies. J. Neurophysiol. **104**(2), 1195–1210 (2010)
39. A.T. Winfree, *The Geometry of Biological Time*, vol. 12 (Springer Science & Business Media, 2001)

40. Y. Xu, D. Yan, The Bedrosian identity for the Hilbert transform of product functions. Proc. Am. Math. Soc. **134**(9), 2719–2728 (2006)
41. E. Yeung, S. Kundu, N. Hodas,Learning deep neural network representations for Koopman operators of nonlinear dynamical systems, in *2019 American Control Conference (ACC)* (IEEE, 2019), pp. 4832–4839
42. H. Yu, F. Li, T. Wu, R. Li, L. Yao, C. Wang, X. Wu, Functional brain abnormalities in major depressive disorder using the Hilbert-Huang transform. Brain Imaging Behav. **12**(6), 1556–1568 (2018)
43. D.A. Zappalà, M. Barreiro, C. Masoller, Uncovering temporal regularity in atmospheric dynamics through Hilbert phase analysis. Chaos: Interdiscip. J. Nonlinear Sci. **29**(5), 051101 (2019)

Part III
Biological Oscillators

Chapter 13
Oscillations in Yeast Glycolysis

Lars Folke Olsen and Anita Lunding

Abstract Oscillations in yeast glycolysis have been known for more than six decades. In spite of intensive experimental and model studies there are still gaps in our understanding of these glycolytic oscillations, e.g. the mechanisms by which they arise, why they have been preserved throughout evolution, and what their potential functions in the cell could be. In the current paper new experimental observations will be presented showing that many variables, that were hitherto considered unrelated to glycolysis, oscillate synchronously with glycolytic intermediates. Furthermore, a strong coupling between glycolysis and the polarisation of intracellular water is presented, suggesting that water has a strong influence on metabolism. This challenges our current understanding of the mechanism behind the glycolytic oscillations. Finally, it is proposed that the function of metabolic oscillations is to maintain the cell in a state of constant low entropy.

13.1 Introduction

Glycolysis is the conversion of glucose to smaller substances such as lactic acid or ethanol in both prokaryotic and eukaryotic cells. The main function of glycolysis is to provide the cell with ATP when respiration is inhibited or absent. In dense suspensions of starved non-growing cells of the yeast *Saccharomyces cerevisiae* temporal oscillations in glycolysis can be observed [58]. These oscillations were discovered more than 60 years ago by Duysens [20]. The oscillations manifest themselves as oscillations in not only concentrations of metabolites in the glycolytic pathway (e.g. hexose phosphates), the redox active coenzyme NADH and adenylates (e.g. ATP) [59], but also in many other extensive (scale linearly with system size) and intensive (independent on system size) thermodynamic variables [2, 19, 46, 47, 63–66], all with the same frequency. In intact yeast cells the frequency of glycolytic oscillations

L. F. Olsen (✉) · A. Lunding
PhyLife, Institute of Biochemistry and Molecular Biology, University of Southern Denmark, Campusvej 55, 5230 Odense M, Denmark
e-mail: lfo@bmb.sdu.dk

A. Stefanovska and P. V. E. McClintock (eds.), *Physics of Biological Oscillators*, Understanding Complex Systems,
https://doi.org/10.1007/978-3-030-59805-1_13

is almost constant and only shows significant variation in response to changes in temperature or in cell density [1] or to partially replacing H_2O by D_2O [64]. The reason for this robustness of frequency is not known and cannot be reproduced by most mathematical models of the pathway. While it is generally accepted that the enzyme *phosphofructokinase* plays a central role in the mechanism responsible for the oscillations, recent evidence has shown that also a number of enzymes and proteins, normally considered unrelated to glycolysis, contribute to the mechanism [61, 65].

Thus, glycolytic oscillations seem to involve a plethora of cellular processes. Here, we will present new evidence that the dynamics of intracellular water also plays an important role in the mechanism of the oscillations. These results seem to be general and may be carried over to other oscillatory processes and ultimately suggest that intracellular water may have a key role in cell metabolism and signal transduction in cells. The function of the glycolytic oscillations is not known, but nevertheless they have been preserved throughout evolution. Several roles of the oscillations have been proposed, e.g. that they constitute an inevitable side effect in the tradeoff between hard robustness and efficiency [13] or they increase the thermodynamic efficiency of glycolysis [60]. Here we propose an alternative function for the oscillations, namely that they serve to maintain the cell in a state of constant low entropy.

13.2 Variables Measured in Oscillating Glycolysis

Oscillations in glycolysis are typically measured as oscillations in the autofluorescence of NADH. Most other metabolites in glycolysis are optically "silent" and therefore cannot be measured in real time, but only after quenching of cell metabolism, extraction of cell content and subsequent analysis by off-line assays [22, 40, 41, 59]. NADH oscillations in intact cells may be observed using fluorescence spectroscopy to measure oscillations in cell suspensions [9, 23] or fluorescence microscopy [4, 12] to measure oscillations in single cells [12]. A typical experiment which shows oscillations of NADH fluorescence in a suspension of yeast cells can be seen in Fig. 13.1a. Oscillations in NADH fluorescence are induced by addition of first glucose and then 60 s later potassium cyanide to a suspension of starved yeast cells.

However, more recently time-resolved measurements of other variables such as intracellular pH [19, 46], mitochondrial membrane potential [2], intracellular potassium ion [47] and water dynamics [64, 65] have been made. For example, it has long been known that mitochondria contribute to the regulation of glycolytic oscillations [3], and more recently oscillations in mitochondrial and other intracellular membrane potentials were directly measured using membrane potential-sensitive fluorescent dyes and shown to oscillate synchronously with NADH [2]. Figure 13.1 shows simultaneous measurements of NADH, intracellular ATP, mitochondrial membrane

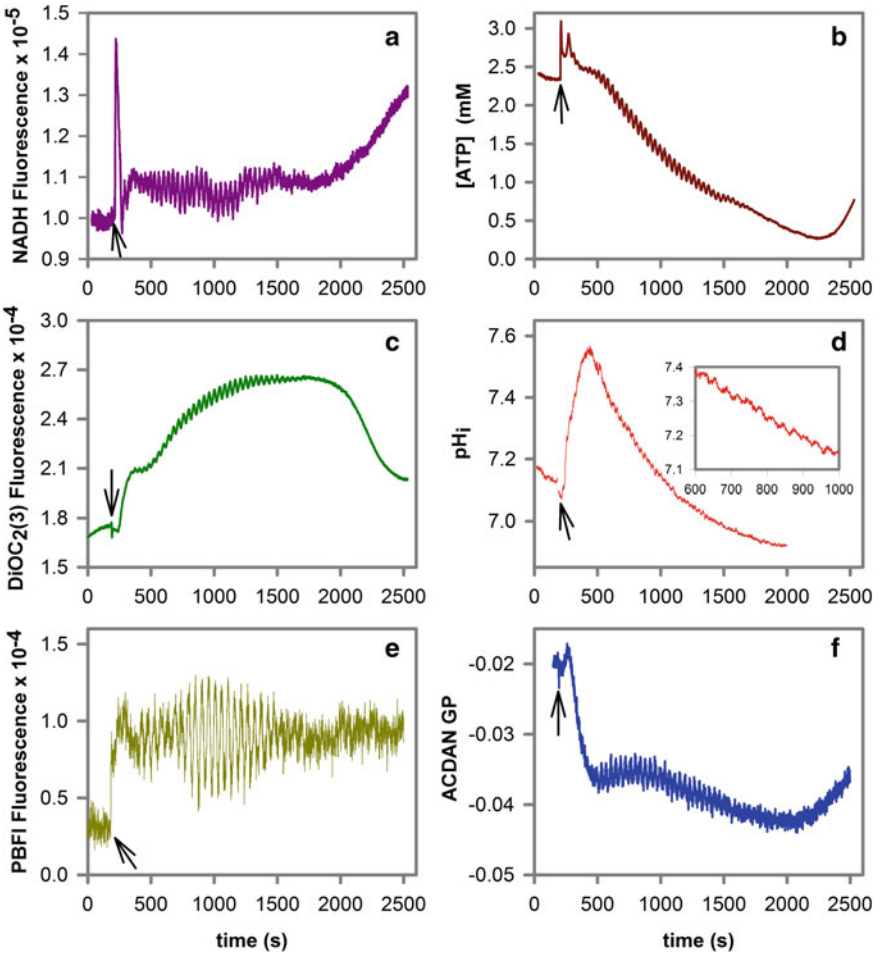

Fig. 13.1 Measurements of oscillations in **a** NADH, **b** intracellular ATP concentration (measured using an ATP-sensitive optical nanosensor [50]), **c** mitochondrial membrane potential (measured as the fluorescence of the membrane potential-sensitive dye $DiOC_2(3)$), **d** intracellular pH, **e** potassium ion concentration (measured as the fluorescence of the potassium sensitive fluorophore PBFI) and **f** the physical state of water (measured as ACDAN GP, see Sect. 13.3) in a suspension of *S. cerevisiae* BY4743 cells. The cells were suspended in 100 mM potassium phosphate buffer, pH 6.8, to a density of 10% (w/v). Oscillations in glycolysis were induced by addition of 30 mM glucose at the indicated arrows and 60 s later 5 mM potassium cyanide (KCN)

potential, intracellular pH, K^+ concentration and water dynamics (see Sect. 13.3) in a suspension of yeast cells supplied with glucose and KCN. The main function of KCN is to inhibit respiration. Intracellular glucose was shown to be essentially constant and non-oscillating at a concentration of about 0.5 mM [56] (not shown in Fig. 13.1).

ATP was shown to oscillate in antiphase with NADH [50, 59] (see also Fig. 13.2a). At the same time the ATP concentration decreases slowly (Fig. 13.1b) until the added glucose is used up and then starts to rise again up to the initial level. It is somewhat puzzling that after starvation of the cells intracellular ATP is not zero, but relatively high. The (slow) decline in ATP observed after addition of glucose and KCN indicates that the consumption of ATP is higher than its production. Mitochondrial membrane potential (Fig. 13.1c) shows a rapid rise immediately after addition of glucose and KCN followed by a slower increase with superimposed oscillations until a plateau is reached. When glucose is exhausted the potential drops to its initial value. Intracellular pH shows an initial fast rise followed by a slower decline (Fig. 13.1d). On top of this are pH oscillations with a very small amplitude as seen in the inset in Fig. 13.1d. The initial rise in pH_i will be smaller if inhibitors of the plasma membrane H^+-ATPase Pma1p are added before glucose and KCN [46]. Inhibition of this enzyme

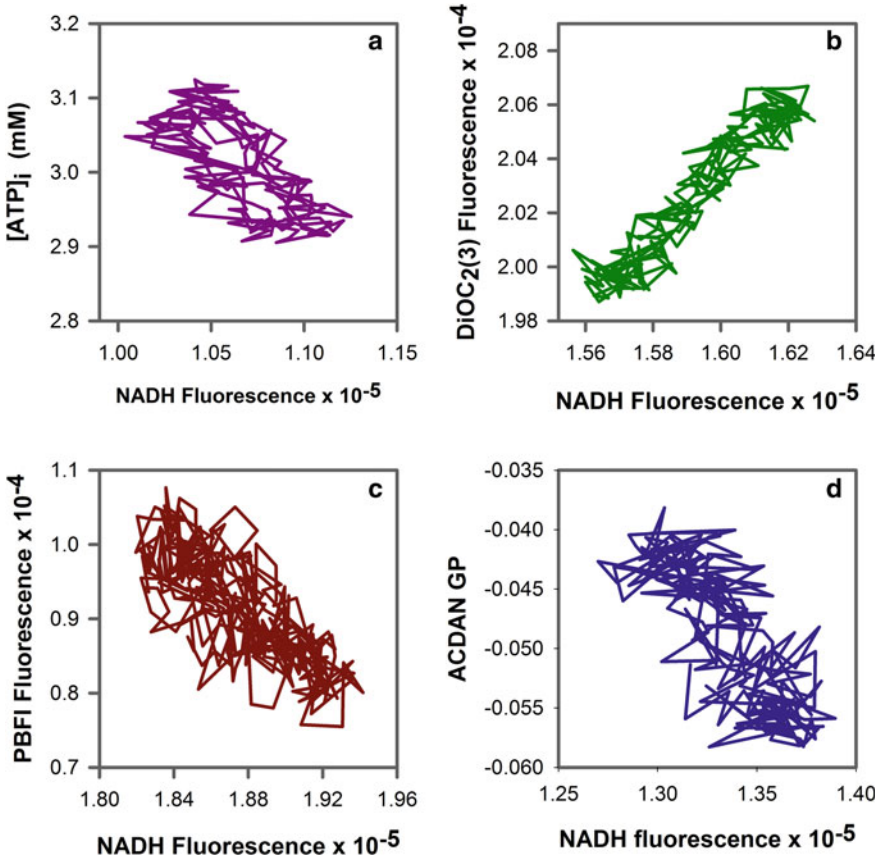

Fig. 13.2 Phase plots of **a** intracellular ATP concentration, **b** mitochondrial membrane potential, **c** potassium concentration and **d** ACDAN GP against the fluorescence of NADH

will also reduce the slow decline in intracellular ATP [74]. Oscillations in intracellular K^+ concentration can also be measured as shown in Fig. 13.1e using the potassium-sensitive fluorescent probe PBFI [43]. Interestingly, these measurements suggest that the concentration of *free* intracellular potassium ion is on the order of 20 mM or below [47], which contrasts with the up to 300 mM total intracellular concentration of this ion in yeast [72]. This suggests that most intracellular potassium ion may be bound to proteins and other negatively charged groups in the cell [47].

Recently, our group has explored a new class of fluorescent dyes, which has allowed us to measure a new and hitherto overlooked physical property linked to glycolytic oscillations. These dyes are the so-called 6-acyl-2-(dimethylamino)naphtalene (DAN) probes, which are polarity-sensitive molecules that can be used to measure the dynamics of intracellular water. These probes, originally introduced by G. Weber [39, 70], were designed to measure dipolar relaxation times of the environment (water in particular) [6, 39, 70]. When these probes are added to yeast cells with oscillating glycolysis it was shown that their fluorescence oscillates synchronously with NADH fluorescence (Fig. 13.1f) [64, 65]. This suggests that the dynamics of water and metabolism (glycolysis) are tightly coupled as will be discussed further in Sect. 13.3.

A useful way to analyse multiple simultaneous time series from oscillating reactions is to perform phase plots of the variables. Such phase plots are shown in Fig. 13.2 for some of the data shown in Fig. 13.1. From these phase plots we may infer, e.g., that intracellular ATP, K^+ concentration and ACDAN GP (see Sect. 13.3) all oscillate in phase.

Other variables that have been measured in oscillating glycolysis in intact yeast cells include carbon dioxide production [55], heat flux [63], temperature and cell volume [66] (see Sect. 13.4).

The fact that so many different and seemingly unrelated intensive and extensive thermodynamic variables were found to oscillate in synchrony suggest that numerous cellular processes, and not just enzymes in the glycolytic pathway, contribute to the mechanism of the oscillations.

13.3 The Dynamics of Intracellular Water Modulate Glycolytic Oscillations

13.3.1 Macromolecular Crowding and the Dynamics of Intracellular Water

Water is the most abundant component of the cell and plays important roles in many cellular processes as a solvent for macromolecules, small molecules and ions, but also as a substrate in hydrolysis reactions. Traditionally, intracellular water has been considered to be in a liquid state [27, 69]. In fact, essentially all previous biochemical models of glycolytic oscillations assume mass action kinetics, which is only strictly

valid in dilute solutions. However, due to the molecular crowding of the cytoplasm caused by the high intracellular concentrations of biological macromolecules [16, 17, 32, 38, 54, 73] the state of intracellular water may be different from that in dilute solution. The overall concentration of macromolecules in the cytoplasm amounts to a volume fraction of 40%, and this and the large polar surface areas of intracellular lipid membranes may facilitate the binding of water molecules and restrict their motion, challenging the view that intracellular water is mainly in a fluid state [14, 21, 75]. This creates a gap in our current understanding of metabolism and its regulation, mainly because enzymes may have different properties in the crowded environment inside a cell [15, 53]. In some cases this *macromolecular crowding* is referred to as an "excluded volume effect" [15] where crowding has no effect on the physical-chemical properties of water. However, recent studies using molecular dynamics simulations have indicated that the mobility of water molecules is very heterogeneous and that a large fraction of intracellular water molecules is essentially immobilised in long-lived water bridges between proteins [37].

13.3.2 Coupling of Dynamics of Intracellular Water to Glycolysis

The discovery of biomolecular condensates has spurred new interest in intracellular water [7]. These phase-separated concentrates of proteins and nucleic acids may offer additional cellular compartmentalization on top of that provided by organelles and may provide a special aqueous environment for temporal and spatial control of cellular biochemistry [62]. Interestingly—and relevant here—the liquid-like droplets may show viscous fluid dynamics and their apparent viscosity is ATP-dependent [10]. Recently it was found that the dynamics of intracellular water has a strong influence on glycolytic oscillations [64]. For example adding increasing concentrations of D_2O (up to 50%) to a suspension of yeast cells results in a decrease in the frequency of the oscillations. As stated above the oscillation frequency is otherwise generally insensitive to changes in experimental conditions [11, 57]. The effect of D_2O is not due to its physicochemical properties (e.g. density and viscosity) because ACDAN and PRODAN show exactly the same emission peaks in pure H_2O and D_2O [6, 64]. Instead, the effect of D_2O on the frequency of glycolytic oscillations was interpreted as a secondary isotope effect [64], i.e. the presence of deuterium affects the rates of physicochemical processes even if deuterated bonds are not themselves involved [68].

Further evidence that the solvent (H_2O or D_2O) is involved in the mechanism of oscillation comes from the use of the so-called DAN (6-acyl-2-(dimethylamino) naphtalene) probes, specifically ACDAN, PRODAN and LAURDAN [64]. These probes were developed as polarity sensitive fluorescent probes to study nanosecond relaxation processes in biological systems [70]. LAURDAN is, because of its long hydrophobic side chain, not soluble in water, whereas the two other probes (ACDAN and PRODAN), because of their shorter side chains, are very soluble in water and

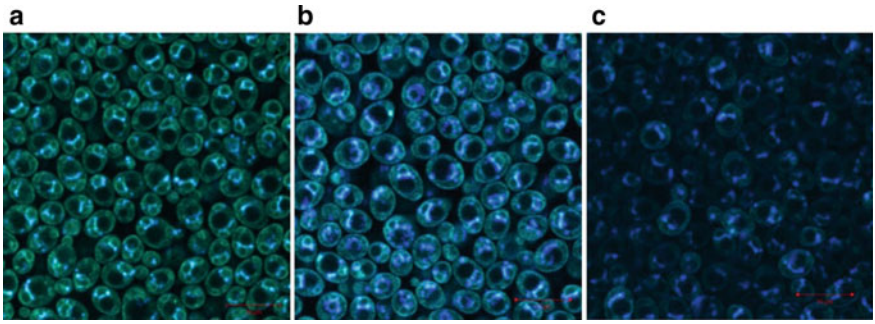

Fig. 13.3 Confocal fluorescence images of S. cerevisia BY4743 cells stained with **a** ACDAN, **b** PRODAN and **c** LAURDAN

hence also in the cytoplasm of cells. For years these probes (primarily LAURDAN) have been used to study phase transitions in model lipid membranes [5, 52]. Here, it was found that the probes mainly respond to the dipolar relaxation of water molecules present at the membrane interface. If relaxation of the solvent molecules is relatively fast the emission spectrum of the DAN probes exhibits a red shift and if the relaxation of the solvent is relatively slow the spectrum exhibits a blue shift. This approach can be generalised to all the DAN probes [6] such that ACDAN, which is hydrophilic and water soluble responds in a similar way to the surrounding solvent (water) molecules. Confocal images of yeast cells stained with DAN probes are shown in Fig. 13.3. The regions exhibiting blue and green fluorescence represent domains with slow relaxation of water, while the dark regions represent domains with fast relaxation of water. The two major dark intracellular regions in Fig. 13.3a, b (low or no fluorescence) represent the vacuole (largest dark region) and the nucleus. It is not possible from such images to quantify how much of the total intracellular water is represented by the blue and green fluorescence. However, a recent report on intracellular water in yeast suggests that about 20% of intracellular water is "slow" water, bound mostly to proteins [69]. The remaining 80% were reported to be in a fluid state. This number is compatible with what we observe in Fig. 13.3a, b since a large fraction of intracellular water is present in intracellular vacuoles and the nucleus where it is in a fluid state and therefore optically "silent".

To quantify the spectral data from the DAN probes a so-called "Generalized Polarization function" (GP) was developed and defined as [6, 51]:

$$GP = \frac{I_{440} - I_{490}}{I_{440} + I_{490}} \tag{13.1}$$

where I_{440} and I_{490} are the measured fluorescence intensities at 440 nm and 490 nm, respectively, for an excitation wavelength of 365 nm. It is easily seen from Eq. 13.1 that the value of GP must fall in the interval $-1 \leq GP \leq +1$. The closer the GP gets to +1 the slower is the relaxation of water. We have previously reported that the GP value for ACDAN (ACDAN GP), and hence the dynamics of intracellular

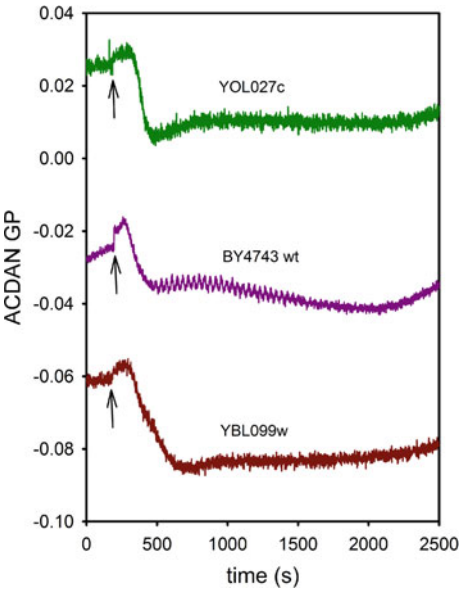

Fig. 13.4 Time series of ACDAN GP in the BY4743 wild type strains and two strains with a mutation in the F_1F_0 ATPase complex (YBL099w) and the mitochondrial H^+/K^+ transporter mdm38 (YOL027c). Glucose was added at the time indicated by the arrows and KCN was added 60 s later

water, oscillate synchronously with other intensive variables in glycolysis and that all the green and blue regions in Fig. 13.3a oscillate in complete phase, i.e. the oscillations are cell wide with no time delay between different aqueous regions in the cell [64]. To investigate further the coupling between glycolytic oscillations and the state of intracellular water a number of *S. cerevisiae* strains with null mutations in various enzymes and proteins in glycolysis and other metabolic pathways were stained with ACDAN and the fluorescence spectra and temporal behaviour were recorded [65]. Figure 13.4 shows the time series of ACDAN GP in the wild type strain and two strains with null mutations in the Atp1p subunit of the F_1F_0-ATPase or in the protein Mdm38p mitochondrial H^+/K^+ transporter. Neither of the two mutant strains exhibits glycolytic oscillations. We note that the ACDAN GP in the two mutants is either higher (Mdm38pΔ mutant) or lower (Atp1pΔ mutant) than the GP in the wild type strain. This could indicate that there is an optimal GP value for observing glycolytic oscillations in yeast. Therefore, more than 20 additional strains with various null mutations were examined for their ability to show glycolytic oscillations and their ACDAN GP values were measured in the resting state before addition of glucose and KCN. A plot of the oscillation amplitude and the frequency against the ACDAN GP value showed that there is indeed a range of GP values (from about 0.0 to −0.06) for which oscillations occur [65]. Thus, the physical state of intracellular water seems to have a tremendous effect on glycolytic oscillations. This does not fit very well to the hypothesis that intracellular water is always in a fluid state. However, a recent model based on equilibrium statistical mechanics [67] is capable of reproducing and explaining the coupling of oscillations in glycolysis to oscillations in dynamics of intracellular water. This model is based on the so-

called Association-Induction hypothesis developed by Gilbert Ling [26, 30–32], which, among other things, predicts that intracellular water is in a polarised state and that the concentration of *free* intracellular K^+ is low due to binding to intracellular proteins.

13.4 A Potential Role of Glycolytic Oscillations

Homeostasis implies that a variable, e.g. a concentration or temperature, is actively regulated to be maintained nearly constant. The concept was originally proposed by French physiologist Claude Bernard [8]. In biochemistry homeostasis is synonymous with the term steady state. The idea that biological systems operate at a steady state has survived to this date. Oscillatory dynamics do not fit very well to the steady state concept. It is interesting that glycolytic oscillations have been found in multiple yeast strains and thus seems to have been preserved throughout evolution. Furthermore, many other metabolic and signalling pathways in yeast and other organisms show oscillatory behaviour [23, 24, 34, 36]. Therefore, it is tempting to speculate that instead of homeostasis one should consider the normal state of the cell as a homeodynamic state [35, 71]. Homeodynamics consider the living organism as operating not far from equilibrium on a low duty cycle and with only some constituent processes being far from equilibrium. Since metabolic oscillations seem to be so widespread it is natural to ask: what are their functions? So far no definite answer has been given. One possible explanation for the existence of metabolic oscillations is that the ability to exhibit oscillatory dynamics constitutes a harmless side-effect of the complex regulatory mechanisms controlling the activities of glycolytic enzymes [18]. Another explanation could be that the glycolytic oscillations have evolved as an inevitable side effect of hard trade-offs between robustness and efficiency [13]. According to these two views oscillations have no function at all. On the other hand, it has also been proposed that the mechanisms responsible for the oscillations have evolved to reduce the dissipation of energy [60]; that is, oscillations make metabolic pathways more energy efficient. Here we shall propose a radically new hypothesis for the glycolytic oscillations, namely that they reflect a living organism's quest for maintaining a low-entropy state [66].

Oscillating (bio)chemical processes are considered to be non-linear dissipative thermodynamic processes [28, 44, 45]. This is in contrast to many oscillating systems in classical physics, which are non-dissipative adiabatic processes. Traditionally, irreversible processes have been described by Onsager's phenomenological equations [48, 49], which assume a symmetric linear coupling matrix between fluxes and forces. Onsager-type equations yield fluxes that can be written as $\underline{J} = \underline{\underline{L}} \cdot \underline{X}$ where $\underline{\underline{L}}$ is an arbitrary matrix. As demonstrated in a recent study [25] any such matrix can be separated into a symmetric ($\underline{\underline{L}}^S$) and an antisymmetric ($\underline{\underline{L}}^A$) matrix. Since the antisymmetric matrix does not contribute to dissipation, entropy production is exclusively governed by the symmetric matrix [48, 49]. This situation is illustrated

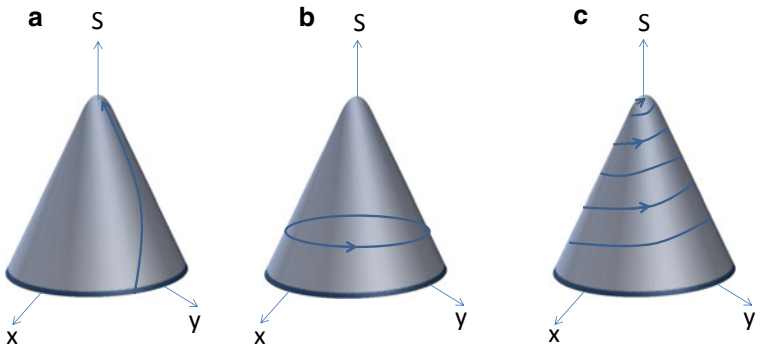

Fig. 13.5 Schematic representation of **a** dissipation, **b** isentropic oscillation and **c** a real process with both oscillation and dissipation. Entropy (S) is plotted against two state variables x and y. Adapted from [25]

in Fig. 13.5a. However, as shown in [25] it is not generally justified to omit the antisymmetric terms. Furthermore, it can be shown that the antisymmetric matrix may lead to oscillations where entropy is conserved as exemplified by an oscillating piston or an electrical LC-circuit [25]. In addition, it was shown that this formalism can be extended to other processes, including oscillating (bio)chemical systems. In such entropy conserving thermodynamic systems all extensive and intensive variables including temperature can display oscillations [25]. This situation is illustrated in Fig. 13.5b. Thus, the combination of the symmetric and the antisymmetric matrix may lead to damped oscillations as illustrated in Fig. 13.5c. A strong indicator for an entropy conserving adiabatic process will be a *periodic change in temperature*.

As for glycolysis in intact yeast cells it has been shown that the oscillations in NADH concentration are accompanied by oscillations in a multitude of extensive and intensive thermodynamic variables (see Sect. 13.2), including heat production [63], electrical conductivity [42], cell volume and temperature [66] as predicted by the revision of Onsager's theory [25]. It is important to note that the observed temperature oscillations evidence both heat absorption and heat release as expected for an adiabatic process [66]. The fact that so many extensive and intensive thermodynamic variables oscillate in synchrony could indicate that glycolytic oscillations are isentropic or close to being isentropic, and hence may not be that far from equilibrium.

13.5 Concluding Remarks

Our studies of glycolytic oscillations cannot be explained in terms of current views on cell physiology where cells are assumed to be in a far from equilibrium steady state and cell cytoplasm is assumed to be a fluid aqueous solution in which ions and macromolecules diffuse freely. However, our results are in accordance with

the Association-Induction (AI) hypothesis developed by Gilbert Ling [26, 29, 30, 32, 33], which treats the cellular interior in a resting cell as a highly structured near-equilibrium system. According to the AI hypothesis intracellular water is in a polarised state and most intracellular potassium ions are bound to cytoskeletal proteins [32]. Interestingly the AI hypothesis, while largely ignored, has never been refuted and we suggest that it may be relevant for all cellular types.

Acknowledgements The authors acknowledge the Danish Molecular Biomedical Imaging Centre (DaMBIC, University of Southern Denmark) for the use of the bioimaging facilities. LFO was supported by a grant from the Danish Council for Independent Research, Natural Sciences (DFF 4002-00465).

References

1. J. Aldridge, E. Pye, Cell density dependence of oscillatory metabolism. Nature **259**(5545), 670–671 (1976)
2. A.Z. Andersen, A.K. Poulsen, J.C. Brasen, L.F. Olsen, On-line measurements of oscillating mitochondrial membrane potential in glucose-fermenting Saccharomyces cerevisiae. Yeast **24**(9), 731–739 (2007)
3. M. Aon et al., Dynamic regulation of yeast glycolytic oscillations by mitochondrial functions. J. Cell Sci. **99**(2), 325–334 (1991)
4. M. Aon, S. Cortassa, H. Westerhoff, K. van Dam, Synchrony and mutual stimulation of yeast-cells during fast glycolytic oscillations. J. Gen. Microbiol. **138**(10), 2219–2227 (1992)
5. L.A. Bagatolli, Laurdan fluorescence properties in membranes: a journey from the fluorometer to the microscope, in *Fluorescent Methods to Study Biological Membranes*, ed. by Y. Mely, G. Duportail (Springer, Berlin, Heidelberg, 2013), pp. 3–35
6. L.A. Bagatolli, R.P. Stock, The use of 6-acyl-2-(dimethylamino)naphthalenes as relaxation probes of biological environments, in *Perspectives on Fluorescence: A Tribute to Gregorio Weber*, Springer Series in Fluorescence, ed. by D.M. Jameson (Springer, Heidelberg, 2016), pp. 197–216
7. S.F. Banani, H.O. Lee, A.A. Hyman, M.K. Rosen, Biomolecular condensates: organizers of cellular biochemistry. Nature Rev. Mol. Cell Biol. **18**(5), 285–298 (2017)
8. C. Bernard, *Introduction a l'etude de la medicine experimentale* (Macmillan, New York, 1927)
9. A. Betz, B. Chance, Influence of inhibitors and temperature on oscillation of reduced pyridine nucleotides in yeast cells. Arch. Biochem. Biophys. **109**(3), 579–584 (1965)
10. C.P. Brangwynne, T.J. Mitchison, A.A. Hyman, Active liquid-like behavior of nucleoli determines their size and shape in xenopus laevis oocytes. Proc. Natl. Acad. Sci. **108**(11), 4334–4339 (2011)
11. B. Chance, R. Estabrook, A. Ghosh, Damped sinusoidal oscillations of cytoplasmic reduced pyridine nucleotide in yeast cells. Proc. Natl. Acad. Sci. USA **51**(6), 1244+ (1964)
12. B. Chance et al., Synchronization phenomena in oscillations of yeast cells and isolated mitochondria, in *Biological and Biochemical Oscillators*, ed. by B. Chance (Academic Press, New York, 1973), pp. 285–300
13. F.A. Chandra, G. Buzi, J.C. Doyle, Glycolytic oscillations and limits on robust efficiency. Science **333**(6039), 187–192 (2011)
14. M. Chaplin, Do we underestimate the importance of water in cell biology? Nat. Rev. Mol. Cell Biol. **7**(11), 861–866 (2006)
15. N.A. Chebotareva, B.I. Kurganov, N.B. Livanova, Biochemical effects of molecular crowding. Biochemistry (Moscow) **69**(11), 1239–1251 (2004)

16. J. Clegg, Properties and metabolism of the aqueous cytoplasm and its boundaries. Am. J. Physiol. **246**(2), R133–R151 (1984)
17. R.M. Davidson, A. Lauritzen, S. Seneff, Biological water dynamics and entropy: a biophysical origin of cancer and other diseases. Entropy **15**(9), 3822–3876 (2013)
18. H. Degn, Oscillating chemical reactions in homogeneous phase. J. Chem. Educ. **49**(5), 302–307 (1972)
19. B.J.T. Dodd, J.M. Kralj, Live cell imaging reveals pH oscillations in Saccharomyces cerevisiae during metabolic transitions. Sci. Rep. **7**, 13992 (2017)
20. L. Duysens, J. Amesz, Fluorescence spectrophotometry of reduced phosphopyridine nucleotide in intact cells in the near-ultraviolet and visible region. Biochim. Biophys. Acta **24**, 19–26 (1957)
21. R. Ellis, Macromolecular crowding: obvious but underappreciated. Trends Biochem. Sci. **26**(10), 597–604 (2001)
22. A. Ghosh, B. Chance, Oscillations of glycolytic intermediates in yeast cells. Biochem. Biophys. Res. Commun. **16**(2), 174–181 (1964)
23. A. Goldbeter, *Biochemical Oscillations and Cellular Rhythms: The Molecular Bases of Periodic and Chaotic Behaviour* (Cambridge University Press, Cambridge, 1996)
24. A. Goldbeter, C. Gerard, D. Gonze, J.C. Leloup, G. Dupont, Systems biology of cellular rhythms. FEBS Lett. **586**(18, SI), 2955–2965 (2012)
25. T. Heimburg, Linear nonequilibrium thermodynamics of reversible periodic processes and chemical oscillations. Phys. Chem. Chem. Phys. **19**(26), 17331–17341 (2017)
26. G. Karreman, Cooperative specific adsorption of ions at charged sites in an electric field. Bull. Math. Biophys. **27**, 91–104 (1965)
27. H. Knull, A.P. Minton, Structure within eukaryotic cytoplasm and its relationship to glycolytic metabolism. Cell Biochem. Funct. **14**(4), 237–248 (1996)
28. D. Kondepudi, I. Prigogine, *Modern Thermodynamics: From Heat Engines to Dissipative Structures* (Wiley, New York, 1998)
29. G. Ling, The association-induction hypothesis. Tex. Rep. Biol. Med. **22**, 244–265 (1964)
30. G.N. Ling, The physical state of water in living cell and model systems. Ann. N. Y. Acad. Sci. **2**, 401–417 (1965)
31. G. Ling, Diphosphoglycerate and inosine hexaphosphate control of oxygen binding by hemoglobin: a theoretical interpretation of experimental data. Proc. Natl. Acad. Sci. USA **67**, 296–301 (1970)
32. G.N. Ling, *Life at the Cell and Below-cell Level: The Hidden History of a Fundamental Revolution in Biology* (Pacific Press, New York, NY, 2001)
33. G. Ling, What is life answered in terms of properties and activities of autocooperative assemblies of molecules, atoms, ions, and electrons called nano-protoplasm. Physiol. Chem. Phys. Med. NMR **42**, 1–64 (2012)
34. D. Lloyd, D. Murray, The temporal architecture of eukaryotic growth. FEBS Lett. **580**(12, SI), 2830–2835 (2006)
35. D. Lloyd, M.A. Aon, S. Cortassa, Why homeodynamics, not homeostasis. Sci. World J. **1**, 133–145 (2001)
36. D. Lloyd, S. Cortassa, B. O'Rourke, M.A. Aon, What yeast and cardiomyocytes share: ultradian oscillatory redox mechanisms of cellular coherence and survival. Integr. Biol. **4**(1), 65–74 (2012)
37. C. Lu, D. Prada-Gracia, F. Rao, Structure and dynamics of water in crowded environments slows down peptide conformational changes. J. Chem. Phys. **141**(4), 045101 (2014)
38. K. Luby-Phelps, Cytoarchitecture and physical properties of cytoplasm: volume, viscosity. diffusion, intracellular surface area. Int. Rev. Cytol. **192**, 189–221 (2000)
39. R.B. Macgregor, G. Weber, Fluorophores in polar media: spectral effects of the Langevin distribution of electrostatic interactions. Ann. N. Y. Acad. Sci. **366**, 140–154 (1981)
40. P.K. Maitra, Pulsating glucose flux in yeast. Biochem. Biophys. Res. Commun. **25**(4), 462–467 (1966)

41. P.K. Maitra, R.W. Estabrook, Fluorometric method for enzymic determination of glycolytic intermediates. Anal. Biochem. **7**(4), 472–484 (1964)
42. T. Male, J. Feder, G.N. Giaever, I. Giaever, Oscillations in yeast observed electrically. Biol. Rhythm Res. **30**(4), 361–370 (1999)
43. A. Minta, R. Tsien, Fluorescent indicators for cytosolic sodium. J. Biol. Chem. **264**(32), 19449–19457 (1989)
44. G. Nicolis, J. Portnow, Chemical oscillations. Chem. Rev. **73**(4), 365–384 (1973)
45. G. Nicolis, I. Prigogine, *Self-organization in Nonequilibrium Systems: From Dissipative Structures to Order Through Fluctuatons* (Wiley, New York, 1977)
46. L.F. Olsen, A.Z. Andersen, A. Lunding, J.C. Brasen, A.K. Poulsen, Regulation of glycolytic oscillations by mitochondrial and plasma membrane H+-atpases. Biophys. J. **96**(9), 3850–3861 (2009)
47. L.F. Olsen, R.P. Stock, L. Bagatolli, Glycolytic oscillations and intracellular K+ concentration are strongly coupled in the yeast Saccharomyces cerevisiae. Arch. Biochem. Biophys. **681**, 108257 (2020)
48. L. Onsager, Reciprocal relations in irreversible processes. I. Phys. Rev. **37**(4), 405–426 (1931)
49. L. Onsager, Reciprocal relations in irreversible processes. II. Phys. Rev. **38**(12), 2265–2279 (1931)
50. V.C. Özalp, T.R. Pedersen, L.J. Nielsen, L.F. Olsen, Time-resolved measurements of intracellular ATP in the yeast Saccharomyces cerevisiae using a new type of nanobiosensor. J. Biol. Chem. **285**(48), 37579–37588 (2010)
51. T. Parasassi, G. De Stasio, R. Rusch, E. Gratton, A photophysical model for diphenylhexatriene fluorescence decay in solvents and in phospholipid-vesicles. Biophys. J. **59**(2), 466–475 (1991)
52. T. Parasassi, E. Krasnowska, L. Bagatolli, E. Gratton, LAURDAN and PRODAN as polarity-sensitive fluorescent membrane probes. J. Fluoresc. **8**(4), 365–373 (1998)
53. V.A. Parsegian, R.P. Rand, R.C. Rau, Osmotic stress, crowding, preferential hydration, and binding: a comparison of perspectives. Proc. Natl. Acad. Sci. USA **97**, 3987–3992 (2000)
54. G. Pollack, *Cells, Gels and the Engines of Life. (A New, Unifying Approach to Cell Function)*, 1st edn. (Ebner and Sons, Seattle, 2001)
55. A.K. Poulsen, F.R. Lauritsen, L.F. Olsen, Sustained glycolytic oscillations—no need for cyanide. FEMS Microbiol. Lett. **236**(2), 261–266 (2004)
56. A.K. Poulsen, A.Z. Andersen, J.C. Brasen, A.M. Scharff-Poulsen, L.F. Olsen, Probing glycolytic and membrane potential oscillations in Saccharomyces cerevisiae. Biochemistry **47**(28), 7477–7484 (2008)
57. K. Reijenga et al., Control of glycolytic dynamics by hexose transport in Saccharomyces cerevisiae. Biophys. J. **80**(2), 626–634 (2001)
58. P. Richard, The rhythm of yeast. FEMS Microbiol. Rev. **27**(4), 547–557 (2003)
59. P. Richard, B. Teusink, M.B. Hemker, K. van Dam, H.V. Westerhoff, Sustained oscillations in free-energy state and hexose phosphates in yeast. Yeast **12**(8), 731–740 (1996)
60. P. Richter, J. Ross, Concentration oscillations and efficiency—glycolysis. Science **211**(4483), 715–717 (1981)
61. T.D. Schrøder, V.C. Özalp, A. Lunding, K.D. Jernshøj, L.F. Olsen, An experimental study of the regulation of glycolytic oscillations in yeast. FEBS J. **280**(23), 6033–6044 (2013)
62. W. Stroberg, S. Schnell, Do cellular condensates accelerate biochemical reactions? Lessons from microdroplet chemistry. Biophys. J. **115**(1), 3–8 (2018)
63. B. Teusink et al., Synchronized heat flux oscillations in yeast cell populations. J. Biol. Chem. **271**(40), 24442–24448 (1996)
64. H.S. Thoke et al., Tight coupling of metabolic oscillations and intracellular water dynamics in Saccharomyces cerevisiae. PLoS ONE **10**(2), e0117308 (2015)
65. H.S. Thoke, S. Thorsteinsson, R.P. Stock, L.A. Bagatolli, L.F. Olsen, The dynamics of intracellular water constrains glycolytic oscillations in Saccharomyces cerevisiae. Sci. Rep. **7**, 16250 (2017)
66. H.S. Thoke et al., Is a constant low-entropy process at the root of glycolytic oscillations? J. Biol. Phys. **44**, 419–431 (2018)

67. H.S. Thoke, L.A. Bagatolli, L.F. Olsen, Effect of macromolecular crowding on the kinetics of glycolytic enzymes and the behaviour of glycolysis in yeast. Integr. Biol. **10**(10), 587–597 (2018)
68. J. Thomson, *Biological Effects of Deuterium* (Macmillan, New York, 1963)
69. M. Tros et al., Picosecond orientational dynamics of water in living cells. Nat. Commun. **8**, 904 (2017)
70. G. Weber, F.J. Farris, Synthesis and spectral properties of a hydrophobic fluorescent probe: 6-propionyl-2-(dimethylamino)naphthalene. Biochemistry **18**(14), 3075–3078 (1979)
71. F.E. Yates, Homeokinetics/homeodynamics: a physical heuristic for life and complexity. Ecol. Psychol. **20**(2), 148–179 (2008)
72. L. Yenush, Potassium and sodium transport in yeast, in *Yeast Membrane Transport*, Advances in Experimental Medicine and Biology, ed. by J. Ramos, H. Sychrova, M. Kschischo, vol. 892 (2016), pp. 187–228
73. H. Yoo, E. Nagornyak, R. Das, A.D. Wexler, G.H. Pollack, Contraction-induced changes in hydrogen bonding of muscle hydration water. J. Phys. Chem. Lett. **5**(6), 947–952 (2014)
74. C.K. Ytting et al., Measurements of intracellular ATP provide new insight into the regulation of glycolysis in the yeast Saccharomyces cerevisiae. Integr Biol. **4**(1), 99–107 (2012)
75. S. Zimmerman, S. Trach, Estimation of macromolecule concentrations and excluded volume effects for the cytoplasm of Escherichia-coli. J. Mol. Biol. **222**(3), 599–620 (1991)

Chapter 14
Oscillations, Rhythms and Synchronized Time Bases: The Key Signatures of Life

David Lloyd

Abstract The dynamic complexity of the living state as evident on viewing cells microscopically defies immediate comprehension. Experiment and theory now allows us to approach some of the problems of this organized complexity (and one that embraces inherent functional purpose) characterizing the phenomenon of life. In an irreducible whole, and in a not so far from equilibrium open system, for the most part it works on a low-duty cycle. We can distinguish many types of time-dependent behaviour: e.g., oscillatory, rhythmic, clock-like timekeeping (and synchronized), deterministically chaotic, and self-similar or fractal), all simultaneously proceeding on many time scales. Self-synchronized continuous cultures of yeast represent, until now, the most characterized example of in vivo elucidation of time structure. The predominantly oscillatory behavior of network components becomes evident, with spontaneously synchronized cellular respiration cycles between discrete periods of increased oxygen consumption (oxidative phase) and decreased oxygen consumption (reductive phase). This temperature-compensated ultradian 'clock' provides coordination, linking temporally partitioned functions by direct feedback loops between the energetic and redox state of the cell and its growing ultrastructure. This model system represents a basic framework is proposed as a universal cellular principle whereby ultradian rhythms are the synchronizing signatures that organize the coherence of the living state. The current challenge is to devise ever increasingly powerful, but non-invasive (or minimally perturbing) techniques to investigate the living organism.

Keywords Time-structure · Oscillations · Rhythms · Ultradian · Mitochondria · Metabolism · Energetics · Oxygen · Dynamics · Synchrony · Signal-processing

D. Lloyd (✉)
School of Biosciences, and of Engineering, Cardiff University, Sir Martin Evans Building, Park Place, Cathays Park, Cardiff CF10 3AX, Wales, UK
e-mail: lloydd@cardiff.ac.uk

A. Stefanovska and P. V. E. McClintock (eds.), *Physics of Biological Oscillators*, Understanding Complex Systems,
https://doi.org/10.1007/978-3-030-59805-1_14

14.1 Introduction: Life as a Complex System

> 'You can never know what to expect from the real nightingale, but everything is determined in the artificial bird. It will be so-and so, and no different! You can explain it; you can open it up and show the human thought - how the cylinders are placed, how they work, and how one follows the other.'
>
> Andersen [3] 'The Nightingale'.

Physicists and engineers deal with universal uniformity of mechanisms, usually reducible to relatively simple systems, whereas the evolution of organisms has used an almost infinite range of quality controls on the test-beds of vitality and survival over a period of >2 billions of years leading to colossal variety. Biology has come to expect a great diversity of form, each example of which is invested with its own individual functional efficiency. The coherent unit (cell and/or, for an unicellular example, whole organism) has to self-organize (coherently control) its energetics, informational signaling, and mass increase during its growth [22]. It then has to reproduce exact copies of each and every one of its almost infinite molecular components and partition them to the progeny, often then to develop new structures during adaptation to environmental changes, signals and stresses, whilst still maintaining form and function (perhaps over many years) until death. Functional order requires temporally ordered sequences of processes and events repeatedly performed in successive discreet time intervals and on time scales from atto-seconds to years.

There is a simplistic current zeal for equating an organism to a machine that can be understood, and with a life story that can be predicted if its DNA is completely sequenced. Although analogies with robotic machines and their informational contents have become commonplace, these prove more useful to the man-made constructs of engineers ('biomimetics') than to the attempts of biologists to fathom the purposeful organized complexity of life [100]. Furthermore, the non-reducibility of the living order to its constituent parts is one of its implicit properties: Hans Christian Andersen got it right!

14.1.1 Thermodynamics of the Living State

The living state in exchanging matter and energy with its surroundings is an open thermodynamic system, but close analogies cannot be made with far-from equilibrium physical (Bénard instabilities), or chemical (Belousov-Zhabotinsky oscillator) systems. Living organisms perform with their constituent enzyme reactions on a low duty-cycle whereby ΔG values are small (some exceptions occur where ionophores are involved) [162]. Thus overall they are at not-so-far from equilibrium states. Heimburg [60] asserts that 'In isoentropic thermodynamic systems all extensive and intensive variables including temperature can display oscillations reminiscent of adiabatic waves'. This suggests [156] that the oscillatory propensity of the living state is a consequence of the necessity for continued performance of metabolic activity

at a maintained low entropy condition; it also questions the proposal that metabolic reactions are essentially dissipative.

14.1.2 Metabolic Fluxes, Flows and Turnover of Constituents and Component Organelles

Claude Bernard's classic monograph ([9], translated in 1927) of the control mechanisms dictating the constancy of the milieu intérieur, set a standard for physiologists considering the persistent and robust maintenance of a mean composition of body fluids. This philosophy was perpetuated and developed by Cannon [14] as 'the wisdom of the body' and he introduced the useful concept of 'homeostasis' as an overarching natural balanced consequence. However, Yates [162] has emphasised the essentially dynamic condition of enzyme-catalysed reactions in networks and cycles, and advocated the term, homeodynamic to more precisely describe living systems [100].

14.1.3 Time Domains of Living Systems

A dynamic concept at the whole cell level was analysed by Gilbert [33], and hypothetical relationships between differentiation, the cell division cycle, and oncogenesis were modeled with a mathematical rigour. At this date it was also proposed that in early sea urchin embryos, the observed hourly rhythms of amino acid incorporation into proteins could be ascribed to mechanisms involving cytoplasmic regulators, e.g., non-protein thiols [116, 117].

The postulate of 'homeostasis' has overshadowed the recognition of the fundamental and basic importance of the 'harmonious organization' of life, [61, 62], whereby the simplistic static condition concept is refined to indicate the ceaseless dynamism of the 'milieu intérieur' as oscillatory states on many temporal scales. Thus it must be realised that 'constancy' is a relative term [100], and that time-scales must be considered; oscillatory performance is common.

Figure 14.1 indicates much of what is known of the frequency ranges (about their mean values) of the human rhythmical functions in repose, as well as under functional effort (horizontally hatched).

Sel'kov [148] revived and applied mathematical modeling to the important concept of the of redox cycling involving thiol-disulphide compounds as proposed by Rapkine [140], and extended the model to the pathophysiology of the aberrant growth of tumours. In a series of sole-authored papers, Gilbert [33–38], further developed his own highly original ideas on the living state and modeled inter-dependence of normal and cancerous states of this transition, cellular differentiation and senescence as series of dynamic bifurcations: this was a seminal series of publications.

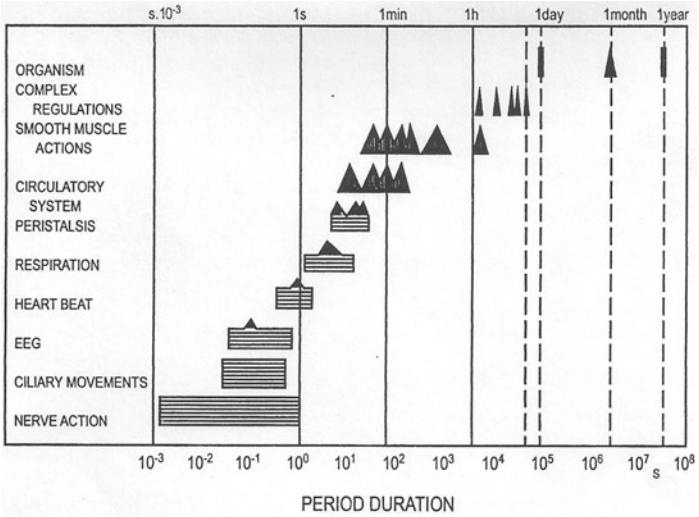

Fig. 14.1 Measurements of human physiological functions illustrating the 'harmony of the body' [61]

Examples of analytical mathematical methods used and of examples of oscillating experimental systems are to be found in Gilbert's subsequent publications with Tsilimigras [44], MacKinnon [43], Visser [45], Josting [41], Lloyd [42], Ferreira [39], and Hammond [40], and recently reviewed [47]. The dynamics and stability of mitochondrial structure and related functions in yeast was probed throughout the 1970s by the pioneering group of Luzikov (reviewed in [109]); their conclusion was that the continued activity of components of the respiratory chain require their continuous performance, and quality control of this maintenance is dictated by a host of proteolytic enzymes [110], via creative destruction.

Reich and Sel'kov [142, 143] published a useful summary of the ideas previously promulgated by Goodwin [48], that changes in controls on key parameters of oscillatory metabolism could be explanatory for differentiation of cells to form tissues, and also for changes of state leading to oncogenesis. Key concepts [33] were subsequently further developed by Goodwin [49]. A logical classification of the time domains operational in all living organisms, made the apparently incomprehensible complexity somewhat more easily understood [94, 20–22].

Figure 14.2 shows the domains of biochemical reactions underlying physiological functions on faster time scales [130] down to sub-picoseconds. Real-time fluorescence imaging (using confocal and 2-photon excitation) provide new insights into long-standing problems of cell structure and function [80, 81, 105]. Advancing imaging techniques applied to biophysical measurements lead to ever more defined resolution at single cell, organelle [164] and molecule levels.

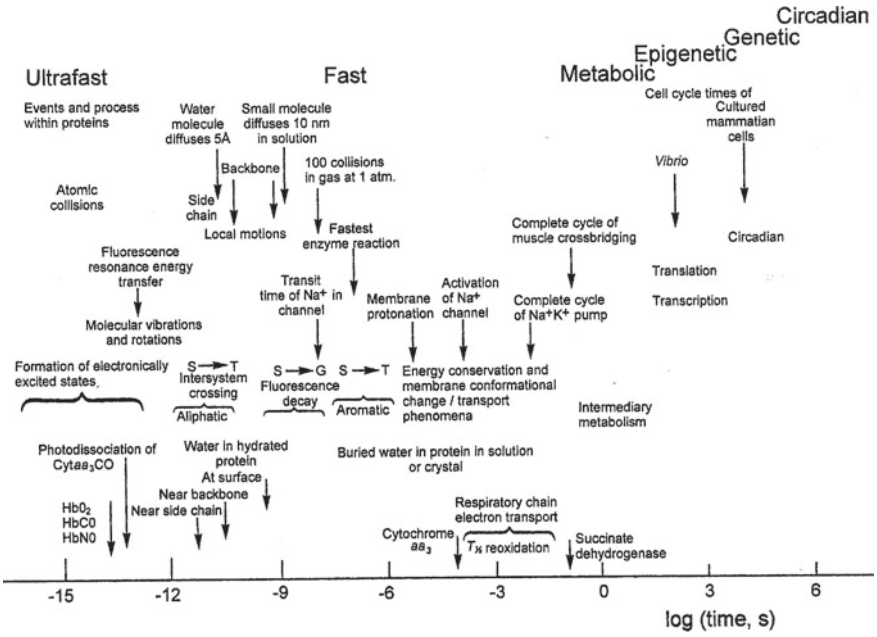

Fig. 14.2 The time domains of living systems

14.1.4 Biological Oscillations

The history of synchronizing oscillators, and the remarkable mechanisms in the heart and brain depend upon these principles, but how coherence is achieved across widespread distance these in organs is complex and not understood. Stabilization of dynamics can be achieved by non-autonomous perturbation [107], and chronotaxic systems far from equilibrium can adjust their clocks [155]. Changes in metabolic states can be described by the alterations in their chronotaxicity [78].

Reasons have been presented why oscillations should be expected in all biochemical studies [39, 163]. These articles provide practical details for setting up sampling regimes and analyzing data for confirmation of oscillatory behaviour. Our basic understanding of cell biochemistry requires extensive re-evaluation in the light of these principles. Furthermore, until the last few years, comparative neglect of the medical importance of biological rhythms has arisen because temporal anatomy is invisible by nature [123].

Lüttge and Hütt [108] have summarized why ultradian oscillations may be crucial for functional biochemical and physiological coherence: and an updated list of examples can now be formulated:

1. For the synchronization of spatially separated physiological processes, e.g. respiratory activity of mitochondria, and reactions leading to nucleotide biosynthesis [87, 89].

2. For the separation of incompatible processes within the same cellular compartment e.g., H_2S production and oxidative metabolism in a protozoon, *Acanthamoeba castellanii* [93, 99], and in yeast [72, 125, 153].
3. Oscillations in enzyme reactions lower the average concentrations involving potentially toxic reaction products (e.g. H_2O_2, superoxide, and other reactive O_2 species (e.g. in the peroxidase-oxidase reaction), Hauser et al. [58]. Superoxide radical anions (O_2^-) act as signals, but in excess are responsible for oxidative damage.
4. Oscillations may increase the thermodynamic efficiency of metabolism by lowering energy dissipation [79, 122, 123], and/or be a necessary accompaniment of the low-entropy state of cells [60].
5. Signaling: e.g., Ca^{2+} oscillations transmit stimulus-specific information to downstream signaling machinery involving Ca^{2+}dependent protein phosphorylation [120]. Protein phosphatases and protein kinases are involved in the complex and highly dynamic and specific signaling functions in normal, inflamed, [19], and cancerous cells [51–56]. Out of phase expression of multiple isoenzymes may be involved: e.g., in cultured erythroleukemia cells distinct temporal oscillatory expression of 3 isoforms have been characterized [54, 56], and in the *ras* oncogene during proliferation and differentiation [56]. Regulation of the dynamics may be crucial to the control of cell function and transformation. Oscillations may encode information (frequency-encoding is more accurate than amplitude encoding) in signal transduction chains or networks. Spatial reorganization is required during differentiation, e.g., in the segmentation of embryos and insects the 'somite clock'.
6. Synchronization of intra- and extra-cellular processes. In heart and brain synchronization of coupled oscillators is vital for concerted signaling, action and responses over wide spatial scales. Thus, time-frequency wavelet transforms of several non-invasive measurements of cardiovascular signals within and between neuronal (EEC) recordings indicate strengths and directions of interactions between the two systems and in principle can be used to assess the state of the organism under anesthesia [154].
7. Most biological receptors are phasic in their nature and therefore oscillating signals can be rapidly sensed without membrane modification [122]: i.e., speed of response can be faster from an appropriately rapidly oscillating signal.

14.1.5 Rhythms and Clock-Like Timekeepers

Rhythms are self-sustained oscillations, emergent and persistent, even if their characteristics (frequency, phase or amplitude) may become temporarily modified (as just described for oscillations). However, their unregulated and hence unperturbed "free-running" periods are robust and their periods, phase and amplitudes fully recoverable when restraints or stimuli are removed. Biological clock-like synchronisers, e.g. the

40 min ultradian clock in the yeast, *Saccharomyces cerevisiae*, like circadian clocks and physical clocks, are temperature compensated, exhibiting a Q_{10} close to 1.

The term "the Biological Clock", as often used, refers to the ~24 h period circadian clock that has evolved in almost all animals, plants, and many fungi and cyanobacteria [50, 141]. It matches many hundreds of biochemical, physiological and behavioral functions to the daily rotation of the earth. Circadian rhythms are comparatively recent innovations on the evolutionary time scale [85, 94, 163]. Although crucially important, especially in biomedical understanding and applications, they are not fundamental core characteristics of the living state: they represent the icing on the cake. Many unicellular organisms (e.g., yeasts, [86] with no 'canonical' circadian receptors or genes' can entrain to daily environmental cycles.

14.1.6 Ultradian (Circahoralian) Clocks

Clocks or timekeepers that cycle many times in a day are called ultradian (a general term), or more specifically circahoralian (~hourly ones) [11]. In baker's or brewer's yeasts e.g., some defined strains of *Saccharomyces cerevisiae*, a 40 min rhythm is a basic timer mechanism, closely linked to cycles of mitochondrial energization [15, 101, 102]. In another yeast (with a faster growth rate), this timekeeper is of shorter duration e.g., in *Candida utilis* it is 30 min [64], Lloyd et al. [93, 99], whereas in *Schizosaccharomyces pombe* longer, at 60 min [90, 135–137]. Longer period oscillations have been repeatedly described in yeasts or bacteria in continuous cultures in the earlier literature: these may stem from perturbative disturbances. Klevecz [69] has measured the mammalian quantal increments in cultured cell division times as being about 4 h. Brodsky [10, 12] has surveys showing circahoralian rhythms measured by different characteristics in a diverse range of cells, and tissues from animals as 30–80 min. Ultradian rhythms are extensively studied in plants (stem growth, leaf movements, etc. [103].

14.1.7 The Cell-Division Cycle

The cell-division cycle is not a clock but an emergent biological process hypothetically composed of multiple oscillators, check- points 'sizer' and temporal controls [48, 75, 85, 91, 94, 95, 97, 104]. It is often regarded as depending on a series of stepwise progressions, i.e., like a set of dominoes that must fall in a specific sequence, controlled at specific "checkpoints". Eukaryotes have evolved prior to the cyclin/cyclin kinase mechanism, and respiratory oscillations are sufficient to trigger and progress the cell division cycle [133]. Many other investigators have always regarded the cell cycle (and it is now evident) to be a complex process dependent on

an interwoven ensemble of oscillators, rhythms, and timekeepers acting on different time scales but integrated as a heterarchy and therefore with no dominant central control.

14.1.8 Oscillations in Glycolysis

The first report of oscillating concentrations of NADH, a cofactor in intact living organisms was in suspensions of anaerobic yeast cells by Duysens and Amesz [27]. This observation appears not to have been immediately followed up by these investigators or elsewhere until, following electrical activity in the muscle of the electric eel, transients in metabolites were analysed [115]. A decade later, [113] interest in a baker's yeast as an excellent model system for spectrophotometric and fluorometric studies was rekindled and analysed in detail were reviewed in an essential text for anyone studying oscillating biological systems [16], and their computer simulations. No clear-cut function has been assigned to glycolytic oscillatory dynamics [88]. It has however provided many insights into control mechanisms, especially in mutant strains, (e.g., [106, 114]). The recognition of feedback control and allosteric enzyme regulation has helped to elucidate the molecular mechanisms involved in some of these cases, the most clearly understood system is still the high-frequency (approximately 2 min^{-1}) glycolytically-associated oscillations in the yeast *Saccharomyces carlsbergensis*, (reclassified as a strain of *S. cerevisiae*).

Thereby yeast glycolytic oscillations are the most defined systems, as are their interactions with mitochondria and plasma membranes [131, 139]. In yeast displaying glycolytic oscillations, coupling of the dynamics of glycolytic ATP and NADH and the extent of dipolar relaxation of intracellular water is synchronized via the action of the cytoskeleton and affects membrane functions [156].

14.1.9 Cellular Respiratory Oscillations

In 1973 Mochan and Pye [121] pointed out that respiratory oscillations in yeast cultures during growth involve redox changes in mitochondrial cytochrome components.

Degn [24] suggested that oscillatory behaviour in general (e.g., not only in NADH, but also in the fluorometrically detected oxidized form of flavins [25, 26], might indicate sloppy-control under certain conditions.

In 1980, Bashford et al. [7] obtained fluorometric evidence for redox cycling in *Schizosaccharomyces pombe*, and in *Acanthamoeba castellanii*: in both organisms each of the coenzymes showed short-periods of 4.5 ± 1.0 min.

Oscillating mitochondrial membrane potentials in yeast have been observed using fluorimetry by Andersen et al. [4], and dynamically imaged by Aon et al. [5].

Rates of O_2 consumption during the respiration of the yeast cell division cycle were shown to be a discontinuous (oscillatory) process proceeding in in selection-synchronized cultures [135, 136].

Observations of short term rhythms of protein synthesis (period ~1 h) in a variety of mammalian tissues and cultured cells as noted over the previous years in the Soviet journals from 1967 was reviewed in the Western literature [10, 11]. In synchronous cultures of *Schizosaccharomyces pombe*, inhibitor sensitivities and activity of mitochondrial ATPase oscillated [29]. In *Acanthamoeba castellanii*, oscillatory respiration was accompanied by synchronized total cellular protein and RNA accumulation [30, 31], and also by accumulation of ATPase activity, enzyme protein and F_1-ATPase inhibitor [32]. Temperature compensation of these respiratory oscillations was revealed, and hence their probable functions as rhythms with timekeeping or synchronizing activities [95, 118]. Quantal increments in cell-division cycle times at decreasing temperatures from 30 to 20 °C were noted. Similar quantization of division times in cultured mammalian cells had previously been observed and modeled as a limit cycle oscillator with added noise [69, 88, 149].

14.1.10 Time Structure Discovered in Self-synchronous Yeast Continuous Cultures

Detailed mapping of the temporally organized structure of a cell and requires either the production of unperturbed populations of individuals growing and performing in synchrony [13, 63, 64, 90, 136, 150–152], or measurements made on single cells [5, 8, 133, 138]. The former method provides large enough sampled populations for physiological and biochemical assays, whereas possible time averaging from imperfect, perturbed synchrony, or specific population effects are avoided from the latter.

A pivotal development was described and implemented by the group of Hiroshi Kuriyama at Tsukuba. They first devised and perfected the conditions enabling the growth of laboratory scale self-synchronous continuous culture. These studies have enabled highly significant advances in the resolution of time structure of yeast, an invaluable experimental model system, and at present the most fully investigated of any organism [67, 68, 147]. The temperature compensated period in yeast [128] of the ~40 min period in yeast strongly suggested a time-keeping function, just as for the ultradian ~65 min rhythm in *Acanthamoeba castellanii* [95], and the circadian (~24 h) expression of bioluminescence in *Gonyaulax (now Lingulodinium) polyedra,* a dinoflagellate [57]. Glutathione is a central player in the redox cycle that sustains the respiratory oscillation [127], confirming the ideas of Rapkine [140], and that thiol cycling is the key to the generation of cellular respiratory rhythms [92]. Mitochondrial respiratory (adenylate) control [15] is also at the very core of the ultradian rhythms, not only in yeast [97, 101], but also in protists [85, 104].

Continuous monitoring of dissolved gases (O_2, CO_2 and H_2S, [96] by a submerged probe, using membrane inlet mass spectrometry proved revelatory, especially when employed in conjunction with intracellular redox state readout (NADPH, and flavins, [17]. Transcriptional analyses using microarrays have revealed a global dynamic architecture [18, 70, 71, 73], and that with respect to gene expression, the dominant period is not the cell budding cycle (90–120 min), but more commonly the ~40 min sub-multiple of that cycle period. Furthermore, wavelet analysis revealed genome-wide oscillations in expression mirroring the 40 min respiratory oscillations in the self synchronized continuous culture [72]. Two temporal clusters (4,679 of 5,329) were maximally expressed in the reductive phase of the ~40-min cycle, and the third cluster (650) in the respiratory stage [74]. Thus maximal expression of the gene super-cluster important in respiration is functionally expressed oppositely in the cycle from those genes known to be involved in reductive functions. The transcriptional cycle gates synchronous bursts of DNA replication in a constant fraction of the population at 40 min intervals. It was also suggested [74], that the separation of DNA replication into the reductive part of the ~40 min cycle represents an evolutionary important mechanism for the obviation of oxidative damage (e.g. by reactive species derived from partial reductive reactions of O_2.

More than 1600 oscillating metabolites [2, 126, 129, 146] reveal coordination with metabolic functions, organelle elaboration and function, and the cell division cycle. Redox control is central in the cellular network and implicit to its rhythmicity [129], and also to transcriptional processes and chromosome dynamics [2, 111, 112].

The detailed chronology of these coordinated research topics by collaborating groups has been reviewed [1, 86, 104].

14.1.11 Non-linear Dynamics of the Self-synchronous Culture: Chaos and Fractals

May [119] has written: 'First-order difference equations arise in many contexts in the biological, economic and social sciences. Such equations, even though simple and deterministic, can exhibit a surprising array of dynamical behaviour, from stable points, to a bifurcating hierarchy of stable cycles, to apparently random fluctuations. There are consequently many fascinating problems, some concerned with delicate mathematical aspects of the fine structure of the trajectories, and some concerned with the practical implications and applications of the bizarre behaviour exhibited by the simplest of discrete time, nonlinear systems, such as Eq. (14.1).

$$x_{t+1} = a\, x_t(1 - x_t) \tag{14.1}$$

Yet such nonlinear systems are surely the rule, not the exception, outside the physical sciences.'

One application of this Eq. (14.1) is in describing the density of individuals x_t, as a population whose growth constant is a.

Mathematical methods for exposing the complex behaviour of continuous yeast cultures has been shown to satisfy several of the criteria [46, 59, 83, 84] for deterministic chaos:

1. Under 'permittistatical' control of a continuous yeast culture, using the output from an AC impedance measuring device to regulate growth rate by the medium supply rate [23].
2. Stepwise decreased medium pH reveals increased complexities of trajectories and the uncovering of a strange attractor [124].
3. Addition to cultures of a type-A monoamine oxidase inhibitor, phenelzine, gave period 2 doubling [82, 145].
4. A long-term (3 months) culture yielding more than 36,000 points at 12 s intervals for each of 4 dissolved gases (O_2, CO_2, H_2S and Ar) using an immersed membrane inlet mass spectrometer probe indicated a low-dimensional chaotic attractor [144].

Figure 14.3a, b shows the dissolved oxygen signal versus time. The 13 h collective mode and bursts in circahoralian oscillatory activity are clearly visible in panel (a). Panel (b), is an enlargement of the boxed region in panel (a), showing the 4-min oscillations as well as the periodic re-emergence of the circahoralian rhythm. Panel (c) shows the metabolic attractor seen in an $[O_2]$, $[H_2S]$ projection, with points coloured by the (baseline- corrected) CO_2 signal. The line (which is actually a plane extending in the direction of the $[CO_2]$ axis) was obtained by a simple linear regression of the $[H_2S]$ versus $[O_2]$ data. Panel (d) shows a section through the attractor at the level of the plane in panel (c), which is used as simple way to de-trend the data and chose a plane running roughly through the middle of the attractor. These short-period oscillations were also visible in recordings from the O_2 electrode when the culture exhibited simpler dynamics.

A metabolic attractor (the set of biochemical states visited by the culture after decay of initial transients) of a time-series obtained for all three dissolved gases (normalized for variations in Ar as an inert reference gas) at 12-s intervals directly in the culture exhibited several characteristics indicative of chaotic behavior. The attractor is shown in Fig. 14.3c, d. The capacity dimension of the attractor [28], one measure of fractal dimension, was 2.09 ± 0.07 (95% confidence). A capacity dimension close to two suggests that this is neither a simple cycle ($D = 1.0$), nor a system filling a three-dimensional (3-D) region of phase space. Although the attractor looks like a mostly solid structure seen from the perspective of Fig. 14.3c, cuts through the attractor show a complex structure, with regions that are nearly completely filled, and others containing only a few points, e.g., Fig. 14.3d, which explains the dimension that is <3. A dimension of two could be compatible with a quasiperiodic attractor. However, an estimate of the Lyapunov exponent gave a value of $0.752 \pm 0.004\ h^{-1}$. A positive Lyapunov exponent implies exponential divergence of nearby trajectories, which is the signature of chaos [59]. The 3–5 min signal was also observed associated with high respiration levels in single cells [5]. Self-similar (fractal) time structure

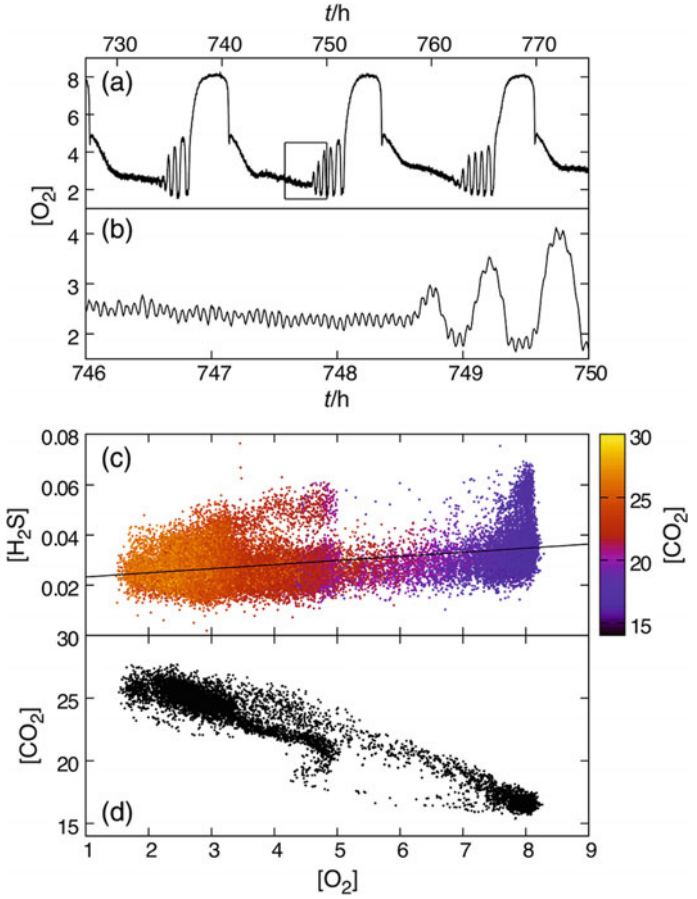

Fig. 14.3 Mass spectrometric determination of dissolved O_2, CO_2 and H_2S during complex oscillations in a yeast continuous fermentation experiment. Data are from Roussel and Lloyd [144], courtesy of Dr. MR. Roussel

across multiple time scales of the multioscillator was determined by well-established principles [6]. Thus both the dissolved O_2 and the CO_2 data gave a perfect correlation between oscillators in the 13 h, 40 min, and 4 min domains. Relative Dispersional Analysis (RDA) of double log plots gave an inverse power relationship with a fractal dimension $D_f = (1.0)$ implying that RD is constant with scale (i.e., the time series look statistically-similar on all time scales). Long-term memory from min to hours is implicit in the oscillatory behaviour, and provides for coherence of the whole system. Power spectral analysis (PSA) also indicated an inverse power law proportional to $1/f^{ß}$, with a value of $ß = 1.95$, close to that of coloured noise, and again as expected for a system that shows deterministic chaos. The basic principles underlying the fractal nature of a chaotic time series has previously been explained [84].

Advantages proposed for systems displaying chaos include innovation, the preservation of diversity, the prevention of entrainment and the dissipation of disturbance [84]. Controlled chaos may provide for flexible mechanisms for switching from one periodic orbit to another [83]. Chaotic dynamics has recently been detected in mitochondrial oxidative metabolism under stress when network stability is compromised at the 'edge' between fully functional and pathological behaviour [65, 66].

14.2 General Conclusions

Studies of ultradian oscillatory phenomena as 'the dynamic signatures of life' [163], not only in lower eukaryotes, but also in mammals [98, 132], and of declining capacities during aging [157], are playing a burgeoning part in current research [20, 21, 76, 77], as well as future diagnostic and medical practice [134, 158–161].

Acknowledgements DL would like to thank all the students and coworkers involved for permission to publish their data, and especially Dr. MR Roussel, for a figure and his interpretation of those data. Two referees kindly provided important information.

This chapter is dedicated to the memory of Robert M. May, the complex systems pioneer who died on 28 April 2020.

References

1. C. Amariei, R. Machné, K. Sasidharan, W. Gottstein, M. Tomita, T. Soga, D. Lloyd, D.B. Murray, The dynamics of cellular energetics during continuous yeast culture. Conf. Proc. IEEE Eng. Med. Biol. Soc. **2013**, 2708–2711 (2013)
2. C. Amariei, R. Machné, V. Stoic, T. Soga, M. Tomita, D. Lloyd, D.B. Murray, Time resolved DNA occupancy dynamics during the respiratory oscillation uncover a global reset point in the yeast growth program. Microb. Cell **1**(9), 279–288 (2014)
3. H.C. Andersen, The Nightingale, in *The Complete Hans Christian Andersen Fairy Tales*, trans. J. Hersholt. Canterbury Classics (G Books, Baker and Taylor, San Diego, CA, 1843), pp. 159–164
4. A.Z. Andersen, A.K. Poulsen, J.C. Brasen, L.F. Olsen, On-line measurements of oscillating mitochondrial membrane potential in glucose-fermenting *Saccharomyces cerevisiae*. Yeast **24**, 731–739 (2007)
5. M.A. Aon, S. Cortassa, K.M. Lemar, A. Hayes, D. Lloyd, Single and cell population respiratory oscillations in yeast: a 2-photon study. FEBS Lett. **58**, 6–14 (2007)
6. M.A. Aon, M.R. Roussel, S. Cortassa, B. O'Rourke, D.B. Murray, M. Beckmann, D. Lloyd, The scale-free dynamics of eukaryotic cells. PLoS ONE **3**(11), e3624 (2008)
7. C.L. Bashford, R.K. Poole, D. Lloyd, B. Chance, Oscillations of redox state in synchronized dividing cultures of *Acanthamoeba castellanii* and *Schizosaccharomyces pombe*. Biophys. J. **29**, 1–11 (1980)
8. B.L. Baumgartner, R. O'Laughlin, M. Jin, L.S. Tsimring, N. Hao, J. Hasty, Flavin-based metabolic cycles are integral features of growth and division in single cells. Sci. Rep. **8**(1), 18045 (2018)

9. C. Bernard, in *Introduction à l'Etude de la Medicine Experimentale*. H.C. Green, trans. (1927). (McMillan, New York, 1878)
10. V.Y. Brodsky, Protein synthesis rhythm. J. Theor. Biol. **55**, 167–200 (1975)
11. V.Y. Brodsky, Rhythms of protein synthesis and other circahoralian oscillations: the possible involvement of fractals, in *Ultradian Rhythms in Life Processes: An Inquiry into Fundamental Principles of Chronobiology and Psychology*, ed. by D. Lloyd, E.L. Rossi (Springer, London), pp. 24–40, (Springer Science+Business Media BV, London), pp. 85–104
12. V.Y. Brodsky, Circahoralian (ultradian) rhythms. Biochemistry (Mosc.) **79**(6), 483–495 (2014)
13. A.J. Burnetti, M. Aydin, N.E. Buchler, Cell cycle Start is coupled to entry into the yeast metabolic cycle across diverse strains and growth rates. Mol. Biol. Cell **27**, 64–74 (2016)
14. W.B. Cannon, *The Wisdom of the Body* (Norton, New York, 1932), p. 340
15. B. Chance, R. Williams, Respiratory enzymes in oxidative phosphorylation. 1. Kinetics of oxygen utilization. J. Biol. Chem. **217**(1), 383–394 (1955)
16. B. Chance, G. Williamson, I.Y. Lee, L. Mela, D. DeVault, A.K. Ghosh, E.K. Pye, Synchronization phenomena in oscillations in yeast cells and isolated mitochondria, in *Biological and Biochemical Oscillators. A Colloquium of the Johnson Foundation*, ed. by B. Chance, E.K. Pye, A.K. Ghosh, A.B. Hess (Academic Press, New York & London, 1973), pp. 285–302
17. B. Chance, V. Legallais, J. Sorge, N. Graham, A versatile time-sharing multichannel spectrophotometer, reflectometer, and fluorometer. Anal. Biochem. **66**(2), 498–514 (1975)
18. S.L. Chin, I.M. Marcus, R.R. Klevecz, C.M. Li, Dynamics of oscillatory phenotypes in *Saccharomyces cerevisiae* reveal a network of genome-wide transcriptional oscillators. FEBS J. **279**, 1119–1130 (2012)
19. P. Cohen, Targeting protein kinases for the development of anti-inflamatory drugs. Curr. Opin. Cell Biol. **21**(2), 317–324 (2009)
20. S. Cortassa, M.A. Aon, E. Marbán, R.L. Winslow, O'Rourke, An integrated model of cardiac mitochondrial metabolism. Biophys. J. **84**, 2734–2755 (2003)
21. S. Cortassa, M.A. Aon, S.J. Sollot, Control and regulation of substrate selection in cytoplasmic and mitochondrial catabolic networks. A systems biology analysis. Front Physiol. **10**, 201 (2019)
22. S. Cortassa, M.A. Aon, A.A. Iglesias, J.C. Aon, D. Lloyd, in *An Introduction to Metabolic and Cellular Engineering*, 2nd. edn. (World Scientific, Singapore, 2012), pp. xiv + 428
23. H.M. Davey, C.L. Davey, A.M. Woodward, A.N. Edmonds, A.W. Lee, D.B. Kell, Oscillatory, stochastic and chaotic growth rate fluctuations in permittistatically controlled yeast cultures. Biosystems **39**, 43–61 (1996)
24. H. Degn, Oscillating chemical reactions in homogeneous phase. J. Chem. Edu. **49**, 302–307 (1972)
25. H. Degn, D.E. Harrison, Theory of oscillations of respitation rate in continuous cultures of Klebsiella aerogenes. J. Theor. Biol. **22**(2), 238–248 (1969)
26. H. Degn, D.E. Harrison, Undamped short period oscillations of flavin in respiring non-growing bacteria. Biochem. Biophys. Res. Commun. **45**(6), 1554–1559 (1971)
27. L.N.M. Duysens, J. Amesz, Fluorescence spectrophotometry of reduced phosphopyridine nucleotide in intact cells in the near ultraviolet and visible region. Biochim. Biophys. Acta **24**(1), 19–26 (1957)
28. J.P. Eckmann, D. Ruelle, Ergodic theory of chaos and strange attractors. Rev. Mod. Phys. **57**, 617–656 (1985)
29. S.W. Edwards, D. Lloyd, Mitochondrial adenosine triphosphate of the fission yeast *Schizosaccharomyces pombe* 972 h-. Changes in activity and oligomycin sensitivity during the cell cycle of catabolite–repressed and -derepressed cells. Biochem. J. **162**, 39–46 (1977)
30. S.W. Edwards, D. Lloyd, Oscillations of respiration and adenine nucleotides in synchronous cultures of *Acanthamoeba castellanii*: mitochondrial respiratory control *in vivo*. J. Gen. Microbiol. **108**, 197–204 (1978)
31. S.W. Edwards, D. Lloyd, Oscillations in protein and RNA during synchronous growth of *Acanthamoeba castellanii:* evidence for periodic turnover of macromolecules during the cell cycle. FEBS Lett. **109**, 21–26 (1980)

32. S.W. Edwards, J.B. Evans, J.L. Williams, D. Lloyd, The mitochondrial adenosine triphosphatase of *Acanthamoeba castellanii:* oscillatory accumulation of enzyme activity, enzyme protein and F1-inhibitor during the cell cycle. Biochem. J. **202**, 453–458 (1982)
33. D.A. Gilbert, Differentiation, oncogenesis, and cellular periodicities. J. Theor. Biol. **21**(1), 113–122 (1968)
34. D.A. Gilbert, The malignant transformation as a metabolic steady state transition: the possible significance of the phasing of enzyme synthesis and related aspects. Curr. Mod. Biol. **5**(3), 128–138 (1973)
35. D.A. Gilbert, The nature of the cell cycle and the control of cell cycle proliferation. Curr. Mod. Biol. **5**(4), 197–206 (1974)
36. D.A. Gilbert, Feedback quenching as a means of effectively increasing the period of biochemical and biological oscillators. BioSystems **10**(3), 241–245 (1978)
37. D.A. Gilbert, On G_0 and cell cycle controls. BioEssays **9**, 135–136 (1988)
38. D.A. Gilbert, Ageing, oscillations and efficiency. BioSystems **36**(1), 1–5 (1995)
39. D.A. Gilbert, G.M.N. Ferreira, Problems associated with the study of cellular oscillations. Cell Biol. Int. **24**(8), 501–514 (2000)
40. D.A. Gilbert, K.D. Hammond, Phosphorylation dynamics in mammalian cells, in *Ultradian Rhythms from Molecules to Mind. A New Vision of Life*, ed. by D. Lloyd, E.L. Rossi (Springer + Business Media B.V, New York, 2008), pp. 105–128
41. D.A. Gilbert, A.C. Joosting, The inverse periodogram: a linearising inverting modification of normanalysis. BioSystems **32**(3), 191–193 (1994)
42. D.A. Gilbert, D. Lloyd, The living cell: a complex autodynamic multi-oscillator system? Cell Biol. Int. **24**(8), 569–580 (2000)
43. D.A. Gilbert, H. MacKinnon, Oscillations and cancer, in *Ultradian Rhythms in Life Processes. An Inquiry into Fundamental Principles of Chronobiology and Psychobiology*, ed. by D. Lloyd, E.L. Rossi (Springer, London, 1992), pp. 71–87
44. D.A. Gilbert, C.W.A. Tsilimigras, Cellular oscillations: the relative independence of enzyme activity rhythms and periodic variations in the amount of extractable protein. S. Afr. J. Sci. **77**, 66–72 (1981)
45. D.A. Gilbert, G.R. Visser, Insulin-induced enhancement of cell morphological dynamics: non-specific enhancement of cell morphological dynamics: non-specific biophysical mechanisms for the generalized stimulation of metabolism? BioSystems **29**, 143–149 (1993)
46. D.A. Gilbert, G. Visser, G.M. Ferreira, K.D. Hammond, Transient chaos in intracellular dynamics? Cell Biol. Int. **24**(8), 589–592 (2000)
47. K. Gilbert, K.D. Hammond, V.Y. Brodsky, D. Lloyd, An appreciation of the prescience of Don Gilbert (1930–2011): master of the theory and experimental unraveling of biochemical and cellular oscillatory dynamics. Cell Biol. Int. (2020). https://doi.org/10.1002/cbin.11341
48. B.C. Goodwin, in *Temporal Organisation in Cells: A Dynamic Theory of Cellular Control Processes* (Academic Press, London, 1963), pp. x + 163
49. B.C. Goodwin, in *Analytical Physiology of Cells and Developing Organisms: A Dynamic Theory of Cellular Control Processes* (Academic Press, London & New York, 1976), pp. x + 249
50. F. Halberg, Chronobiology: professional wallflower or paragdigm of biomedical thought and practice? Prog. Clin. Biol. Res. **227A**, 1–26 (1987)
51. K.D. Hammond, L.J. Cloutman, D.A. Gilbert, Cancer reversal: regulation of phosphotyrosine phosphatase. Biochem. Soc. Trans. **17**(6), 1048–1049 (1989)
52. K.D. Hammond, L. Cloutman, B. Mindel, D.A. Gilbert, Temporal changes in phosphoamino acid phosphatase activities in murine erythroleukaemic cells. Int. J. Biochem. **21**(2), 197–201 (1989)
53. K.D. Hammond, R. Bhoola, U. Bodalina, D.A. Gilbert, Dynamic cells: temporal organisation and control of phosphorylation. Trends Comp. Biochem. Physiol. **4**, 75–88 (1998)
54. K.D. Hammond, N. Savage, M. Littlewood, Protein kinase C in erythroleukaemia cells: temporal variations in the expression of the alpha, epsilon and zeta isoforms. Cell Biol. Int. **24**(8), 529–537 (2000)

55. K.D. Hammond, N. Savage, M. Littlewood, Rhythmic patterns in the expression of the ras oncogene in proliferating and differentiating erythroleukaemia cells. Cell Biol. Int. **24**(8), 549–557 (2000)
56. K.D. Hammond, L. Caravotas, D.A. Gilbert, Dynamic cells: temporal organisation and control of signal transducing pathways. Trends Comp. Biochem. Physiol. **7**, 47–57 (2000)
57. J.W. Hastings, B.M. Sweeney, On the mechanism of temperature independence in a biological clock. Proc. Nat. Acad. Sci. USA **49**(3), 804–811 (1957)
58. M.J.B. Hauser, U. Kummer, A.Z. Larsen, L.F. Olsen, Oscillatory dynamics protect enzymes and possibly cells against toxic substances. Faraday Disc. **120**, 215–227 (2001)
59. D.M. Heffernan, P. Jenkins, M. Daly, B.J. Hawdon, J. O'Gorman, Characterization of chaos. Int. J. Theor. Phys. **31**, 1345–1362 (1992)
60. T. Heimburg, Linear nonequilibrium thermodynamics of reversible periodic processes and chemical oscillations. Phys. Chem. Chem. Phys. **19**, 17331–17341 (2017)
61. G. Hildebrandt, Rhythmic functional order and man's emancipation from the time factor, in *A New Image of Man in Medicine*, *Vol II: Basis of an Individual Physiology*, ed. by K.E. Schaefer, G. Hildebrandt, N. Macbeth (Futura, Mount Kisco, New York, 1979), pp. 275–295
62. G. Hildebrandt, M. Moser, M. Lehofer, *Chronobiology and chronomedicine (in German)* (Hippokrates, Stuttgart, 1999)
63. M. Jules, J. François, J.L. Parrou, Autonomous oscillations in *Saccharomyces cerevisiae* during cultures on trehalose. FEBS J **272**, 1490–1500 (2005)
64. J. Kader, D. Lloyd, Respiratory oscillations and heat evolution in synchronous cultures of *Candida utilis*. J. Gen. Microbiol. **114**, 455–461 (1979)
65. J.M. Kembro, S. Cortassa, M.A. Aon, Complex oscillatory redox dynamics with signaling potential at the edge between normal and pathological mitochondrial function. Front. Physiol. **5**, 257 (2014)
66. J.M. Kembro, S. Cortassa, D. Lloyd, S.J. Sollott, M.A. Aon, Mitochondrial chaotic dynamics: redox-energetic behavior at the edge of stability. Sci. Rep. **8**, 15422 (2018)
67. M. Keulers, A.D. Satroutdinov, H. Kuriyama, Oscillations in ethanol grown *Saccharomyces cerevisiae*. FEBS Microbiol. Lett. **142**, 253–258 (1996)
68. M. Keulers, A.D. Satroutdinov, T. Suzuki, H. Kuriyama, Synchronization affector of autonomous short-period-sustained oscillation of *Saccharomyces cerevisiae*. Yeast **12**, 673–682 (1996)
69. R.R. Klevecz, Quantized generation times in mammalian cells as an expression of the cellular clock. Proc. Nat. Acad. Sci. USA **73**, 4012–4016 (1976)
70. R.R. Klevecz, A precise circadian clock from chaotic cell cycle oscillations, in *Ultradian Rhythms in Life Processes. An Inquiry into Fundamental Principles of Chronobiology and Psychology*, ed. by D. Lloyd, E.L. Rossi (Springer, London, 1992), pp. 41–69
71. R.R. Klevecz, H.B. Dowse, Tuning in the transcriptome: basins of attraction in the yeast cell cycle. Cell Prolif. **33**(4), 209–218 (2000)
72. R.R. Klevecz, D.B. Murray, Genome wide oscillations: wavelet analysis of time series analysis in yeast expression arrays uncovers the dynamic architecture of phenotype. Mol. Biol. Rep. **28**, 73–82 (2001)
73. R.R. Klevecz, C.M. Li, Evolution of the clock from yeast to man by period-doubling folds. Cold Spring Harbor Symp. Quant. Biol. **72**, 421–429 (2007)
74. R.R. Klevecz, J. Bolen, G. Forest, D.B. Murray, A genome-wide oscillation in transcription gates DNA replication and the cell cycle. Proc. Nat. Acad. Sci. USA **101**, 1200–1205 (2004)
75. R.R. Klevecz, C.M. Li, I. Marcus, P.H. Frankel, Collective behavior in gene regulation: the cell is an oscillator, the cell cycle a developmental process. FEBS J. **275**, 2372–2384 (2008)
76. F.T. Kurz, M.A. Aon, B. O'Rourke, A.A. Armoundas, Functional implications of cardiac mitochondrial clustering. Adv. Exp. Med. Biol. **982**, 1–24 (2017)
77. F.T. Kurz, J.M. Kembro, A.G. Flesia, A.A. Armoundas, S. Cortassa, M.A. Aon, D. Lloyd, Network dynamics: quantitative analysis of complex behavior in metabolism, organelles, and cells, from experiments to models and back. Wiley Interdiscip. Rev. Syst. Biol. Med. **9**(1) (2017). https://doi.org/10.1002/wsbm.1352

78. G. Lancaster, Y.F. Suprunenco, K. Jenkins, A. Stefanovska, Modelling chronotaxicity of cellular energy metabolism to facilitate the identification of altered metabolic states. Sci. Rep. **6**, 29584 (2016)
79. J.G. Lazer, J. Ross, Changes in mean concentration, phase shifts, and dissipation in a forced oscillatory reaction. Science **247**, 189–192 (1990)
80. K.M. Lemar, C.T. Müller, S. Plummer, D. Lloyd, Cell death mechanisms in the human opportunistic pathogen, *Candida albicans*. J. Eukaryot. Microbiol. **50**(Suppl.). 685–686 (2003)
81. K.M. Lemar, M.A. Aon, S. Cortassa, B. O'Rourke, C.T. Müller, D. Lloyd, Diallyl disulphide depletes glutathione in *Candida albicans:* oxidative-stress mediated cell death studied by two-photon microscopy. Yeast **24**, 695–706 (2007)
82. C.M. Li, R.R. Klevecz, A rapid genome-scale response to the transcriptional oscillator to perturbation reveals a period-doubling path to phenotypic change. Proc. Nat. Acad. Sci. USA **103**, 16254–16259 (2006)
83. A.L. Lloyd, D. Lloyd, Hypothesis: the central oscillator of the circadian clock is a controlled chaotic attractor. Biosystems **29**, 77–85 (1993)
84. A.L. Lloyd, D. Lloyd, Chaos: its significance and detection in biology. Biol. Rhythm Res. **26**(2), 233–252 (1994)
85. D. Lloyd, Intracellular time keeping: epigenetic oscillations reveal the functions of an ultradian clock, in *Ultradian Rhythms in Life Processes: An Inquiry into Fundamental Principles of Chronobiology and Psychology*, ed. by D. Lloyd, E.L. Rossi (Springer, London, 1992), pp. 5–22
86. D. Lloyd, *Saccharomyces cerevisiae:* oscillatory orchestration of growth, in *Advancing Frontiers in Mycology and Mycotechnology*, ed. by T. Satyanarayana et al. (Springer Nature, Singapore, 2019), pp. 181–214
87. D. Lloyd, F. Kippert, A temperature-compensated ultradian clock explains temperature-dependent quantal cell cycle times. Symp. Soc. Exp. Biol. **XXXXI**, 135–155. Cambridge University Press, Cambridge (1987)
88. D. Lloyd, M. Stupfel, The occurrence and functions of ultradian rhythms. Biol. Rev. **66**, 275–299 (1991)
89. D. Lloyd, F. Kippert, Intracellular coordination by the ultradian clock. Cell Biol. Int. **17**, 1047–1052 (1993)
90. D. Lloyd, F. Kippert, A temperature-compensated ultradian clock ticks in *Schizosaccharomyces cerevisiae*. Microbiology **141**, 883–890 (1995)
91. D. Lloyd, D.A. Gilbert, Temporal organization of the cell division cycle in eukaryotic microorganisms, in *Microbial Responses to Light and Time*, ed. by M.X. Caddick, S. Baumberg, D.A. Hodgson, K. Phillips-Jones (University Press, Cambridge, 1998), pp 237–278. Soc Gen Microbiol. Symp **56**
92. D. Lloyd, D.B. Murray, Redox cycling of intracellular thiols: state variables for ultradian, cell division and circadian cycles, in *Redox Behaviour of Circadian Systems*, ed. by T. Van den Driessche, J.L. Guisset, G.P. DeVries (Kluwer, Amsterdam, 2000), pp. 85–94
93. D. Lloyd, B. Kristensen, H. Degn, Oxidative detoxification of hydrogen sulphide detected by mass spectrometry in the soil amoeba, *Acanthamoeba castellanii*. Microbiology **126**(1), 166–170 (1981)
94. D. Lloyd, R.K. Poole, S.W. Edwards, in *The Cell Division Cycle: Temporal Organization and Control of Cellular Growth and Reproduction* (Academic Press: London, 1982), pp. xii + 513
95. D. Lloyd, S.W. Edwards, J.C. Fry, Temperature compensated oscillations in respiration and cellular protein content in synchronous cultures of *Acanthamoeba castellanii*. Proc. Nat. Sci. USA **79**, 3785–3788 (1982)
96. D. Lloyd, S. Bohátka, J. Szilágyi, Quadrupole mass spectrometry in the monitoring and control of fermentations. Biosensors **1**, 179–212 (1985)
97. D. Lloyd, D.B. Murray, R.R. Klevecz, J. Wolf, H. Kuriyama, The ultradian clock (~40 min) in yeast, in *Ultradian Rhythms from Molecules to Mind: A New Vision of Life*, ed. by D. Lloyd, E.L. Rossi (Springer Science + Business Media BV, London, 2008), pp. 11–42

98. D. Lloyd, S. Cortassa, B. O'Rourke, M.A. Aon, What yeast and cardiomyocytes share: ultradian oscillatory redox mechanisms of cellular coherence and survival. Integr. Biol. (Camb.) **4**, 65–74 (2012)
99. D. Lloyd, S.W. Edwards, J.L. Williams, Oscillatory accumulation of total cellular protein in *Candida utilis*. FEMS Microbiol. Lett. **12**, 295–298 (1981)
100. D. Lloyd, M.A. Aon, S. Cortassa, Why homeodynamics, not homeostasis? Sci. World **1**, 133–145 (2001)
101. D. Lloyd, L.E. Salgado, M.P. Turner, M.T.E. Suller, D.B. Murray, Cycles of mitochondrial energization driven by the ultradian clock in a culture of *Saccharomyces cerevisiae*. Microbiology **148**, 3715–3724 (2002)
102. D. Lloyd, K.M. Lemar, E.J. Salgado, T.M. Gould, D.B. Murray, Respiratory oscillations in yeast: mitochondrial reactive species, apoptosis and time: a hypothesis. FEMS Yeast Res. **3**, 333–339 (2003)
103. D. Lloyd, M.A. Aon, S. Cortassa, Rhythms, clocks and deterministic chaos in unicellular organisms, in *Rhythms in Plants*, 2nd edn, ed. by S. Mancuso, Shabala (Springer SA Sham, Switzerland, 2015), pp. 367–399
104. D. Lloyd, D.B. Murray, M.A. Aon, S. Cortassa, M.R. Roussel, M. Beckmann, R.K. Poole, Temporal metabolic partitioning of the yeast and protist cellular networks: the cell is a global scale-invariant (fractal or self-similar) multioscillator. J. Biomed. Opt. **24**(5), 051404 (2018)
105. D. Lloyd, C.O. Millet, C.F. Williams, A.J. Hayes, S.J.A. Pope, I. Pope et al., Functional imaging of a model unicell: *Spironucleus vortens* as an anaerobic but aerotolerant flagellated protist. Adv. Microb. Physiol. **76** (2020). https://doi.org/10.1016/bs.ampbs.2020.01.002
106. Z. Lobo, P.K. Maitra, Phosphofructokinase mutants of yeast. Biochemistry and genetics. J. Biol. Chem. **258**(3), 1444–1449 (1983)
107. M. Lucas, J. Newman, A. Stefanovska, Stabilization of dynamics of oscillatory systems by nonautonomous perturbation. Phys. Rev. D **97**, 042209 (2018)
108. U. Lüttge, M-Th Hütt, High frequency or ultradian rhythms in plants. Prog. Bot. **65**, 235–263 (2004)
109. V.N. Luzikov, in *Mitochondrial Biogenesis and Breakdown*, translated by A.V. Galkin, D.B. Roodyn (Consultants Bureau, New York and London, 1984)
110. V.N. Luzikov, Principles of control over formation of structures responsible for respiratory functions of mitochondria. Biochemistry (Moscow) **74**, 1443–1456 (2009)
111. R. Machné, D.B. Murray, The yin and yang of yeast transcription: elements of a global feedback system between metabolism and chromatin. PLoS One **7**(6), e 37906 (2012)
112. R. Machné, D.B. Murray, P.F. Stadler, Similarity-based segmentation of multi-dimensional signals. Sci. Rep. **7**(1), 12355 (2017)
113. P.K. Maitra, Pulsating glucose flux in yeast. Biochem. Biophys. Res. Commun. **25**(4), 462–467 (1966)
114. P.K. Maitra, Glucose and fructose metabolism in phosphoglucoisomerase-less mutant of *Saccharomyces cerevisiae*. J. Bacteriol. **107**, 759–769 (1970)
115. P.K. Maitra, A. Ghosh, B. Schoener, B. Chance, Transients in glycolytic metabolism following electrical activity in electrophorus. Biochem. Biophys. Acta. **88**, 112–119 (1964)
116. Y. Mano, Regulation system of protein synthesis in early embryogenesis in the sea urchin. Biochem. Biophys. Res. Commun. **33**, 877–882 (1968)
117. Y. Mano, Cytoplasmic regulation and cyclic variation in protein synthesis in the early cleavage stage of the sea urchin embryo. Dev. Biol. **22**, 433–460 (1970)
118. N. Marques, S.W. Edwards, J.C. Fry, F. Halberg, D. Lloyd, Temperature-compensated ultradian variation in cellular protein content of *Acanthamoeba castellanii* revisited. Prog. Clin. Biol. Res. **227A**, 105–119 (1987)
119. R.M. May, Simple mathematical models with very complicated dynamics. Nature **261**(5560), 459–467 (1976)
120. M.R. McAinsh, A.A.R. Webb, J.E. Taylor, A.M. Hetherington, Stimulus-induced oscillations in guard cell cytosolic free calcium. Plant Cell **7**(8), 1207–1219 (1995)

121. E. Mochan, K. Pye, Respiratory oscillations in adapting yeast cultures. Nature New Biol. **242**, 177–179 (1973)
122. M. Moser, M. Fruehwirth, R. Penter, R. Winker, Why life oscillates-from a topographical towards functional chronobiology. Cancer Cuses Control **17**, 591–599 (2006)
123. M. Moser, M. Fruehwirth, T. Kenner, The symphony of life-importance, interaction and visualization of biological rhythms. IEEE Eng. Med. Biol. Mag. **27**, 29–37 (2008)
124. D.B. Murray, D. Lloyd, A tunable attractor underlies yeast respiratory dynamics. Biosystems **90**, 287–294 (2007)
125. D.B. Murray, R.R. Klevecz, D. Lloyd, Generation and maintenance of synchrony in *Saccharomyces cerevisiae* continuous culture. Exp. Cell Res. **287**, 10–15 (2003)
126. D.B. Murray, M. Beckmann, H. Kitano, Regulation of yeast oscillatory dynamics. Proc. Nat. Acad. Sci. USA **104**, 2241–2246 (2007)
127. D.B. Murray, M. Keuler, F. Englen, D. Lloyd, H. Kuriyama, Involvement of glutathione in the regulation of respiratory oscillation during a continuous culture of *Saccharomyces cerevisiae*. Microbiology **145**, 2739–2745 (1999)
128. D.B. Murray, S. Roller, H. Kuriyama, D. Lloyd, Clock control of respiratory oscillations found during yeast continuous culture. J. Bacteriol. **183**, 7253–7259 (2001)
129. D.B. Murray, C. Amariei, K. Sasidharan, R. Machne, M.A. Aon, D. Lloyd, Temporal partitioning of the yeast cellular network, in *Systems Biology of Metabolic and Signaling Networks: Energy, Mass and Information Transfer*, vol. 16, ed. by M.A. Aon, V. Saks, U. Schlattner. Springer Series in Biophysics (Springer, Berlin, Heidelberg, 2014), pp. 323–349
130. M. Noite, M.W. Reimann, J.G. King, H. Markram, E.B. Müller, Cortical reliability admit noise and chaos. Nat. Commun. **10**(1), 3792 (2019)
131. L.F. Olsen, A.Z. Andersen, A. Lunding, J.C. Brasen, A.K. Poulsen, Regulation of glycolytic oscillations by mitochondria and plasma membrane H+-ATPases. Biophys. J. **96**, 3850–3886 (2009)
132. B. O'Rourke, B.M. Ramza, E. Marban, Oscillations of membrane current and excitability driven by metabolic oscillations in heart cells. Science **265**, 962–966 (1994)
133. A. Papagiannakis, B. Niebel, E.C. Wit, M. Heinemann, Autonomous metabolic oscillations robustly gate the early and late cell cycle. Mol. Cell **65**, 285–295 (2017)
134. M. Picard, D.C. Wallace, Y. Burelle, The rise of mitochondria in medicine. Mitochondrion **30**, 105–116 (2016)
135. R.K. Poole, D. Lloyd, Changes in enzyme activities in synchronously dividing cultures of *Schizosaccharomyces pombe* h–. Biochem. J. **136**, 195–207 (1973)
136. R.K. Poole, D. Lloyd, R.B. Kemp, Respiratory oscillations and heat evolution in synchronous cultures of fission yeast, *Schizosaccharomyces pombe* 972 h-. J. Gen. Microbiol. **77**, 209–290 (1973)
137. R.K. Poole, D. Lloyd, B. Chance, The development of the cell division cycle of a glucose-repressed fission yeast, *Schizosaccharomyces pombe* 972 h-. Biochem. J. **138**, 201–210 (1974)
138. A.K. Poulsen, O.M. Petersen, L.F. Olsen, Single cell studies and simulation of cell-cell interactions using oscillating glycolysis in yeast cells. Biophys. Chem. **125**(2–3), 275–228 (2007)
139. A.K. Poulsen, A.Z. Andersen, J.C. Brasen, A.M. Scharff-Poulsen, L.F. Olsen, Probing glycolytic and membrane potential oscillations. Biochemistry **47**, 7477–7484 (2008)
140. L. Rapkine, Sur les processes chimiques au course de la division cellulaire. Ann. Physiol. Physicochem. **7**, 382–418 (1931)
141. R. Refinetti, G. Cornélissen, F. Halberg, Procedures for numerical analysis of circadian rhythms. Biol. Rhythm Res. **38**(4), 275–325 (2007)
142. J.G. Reich, E.E. Sel'kov, Time hierarchy, equilibrium and non-equilibrium in metabolic systems. BioSystems **7**(1), 39–50 (1975)
143. J.G. Reich, E.E. Sel'kov, in *Energy Metabolism of the Cell: A Theoretical Treatise* (Academic Press, London, 1981), pp. viii + 345
144. M.R. Roussel, D. Lloyd, Observation of a chaotic multi-oscillatory metabolic attractor by real-time monitoring of a yeast continuous culture. FEBS J. **274**, 1011–1018 (2007)

145. E.L. Salgado, D.B. Murray, D. Lloyd, Some antidepressants (Li+, monoamine oxidase type-A inhibitors) perturb the ultradian clock in *Saccharomyces cerevisiae*. Biol. Rhythm Res. **33**, 351–361 (2002)
146. K. Sasidharan, M. Tomita, M.A. Aon, D. Lloyd, D.B. Murray, The time-structure of yeast metabolism *in vivo*. Adv. Exp. Med. Biol. **736**, 359–379 (2012)
147. A.D. Satroutdinov, H. Kuriyama, H. Kobayashi, Oscillatory metabolism of *Saccharomyces cerevisiae* in continuous culture. FEMS Microbiol. Lett. **98**, 261–268 (1992)
148. E.E. Sel'kov, Two alternative self-oscillating stationary states in thiol metabolism-two alternative, types of cell division-normal and malignant ones. Biophysika **15**, 1065–1073 (1970)
149. R.M. Shymko, R.R. Klevecz, Cell division gated by oscillatory timekeeping and critical size, in *Biomathematics and Cell Kinetics*, ed. by Rotenberg (Elsevier/North Holland Biomedical Press, Amsterdam, 1981), pp. 329–348
150. S.J. Silverman, A.A. Petti, N. Slavov, L. Parsond, R. Briehof, S.Y. Thiberge, D. Zenklusen, S.J. Gandhi, D.R. Larson, R.H. Singer, D.P. Botstein, Metabolic cycling in single yeast cells from unsynchronized steady-state populations limited on glucose or phosphate. Proc. Nat. Acad. Sci. USA **107**, 6946–6995 (2010)
151. N. Slavov, D. Botstein, Coupling among growth rate response, metabolic cycle and cell division cycle in yeast. Mol. Biol. Cell **22**, 1997–2009 (2011)
152. N. Slavov, J. Macinskas, A. Caudy, D. Botstein, Metabolic cycling without cell division in respiring yeast. Proc. Nat. Acad. Sci. USA **108**, 19090–19095 (2011)
153. H.Y. Sohn, D.B. Murray, H. Kuriyama, Ultradian oscillation of *Saccharomyces cerevisiae* during aerobic continuous culture: hydrogen sulfide mediates population synchrony. Yeast **16**, 1185–1190 (2000)
154. A. Stefanovska, Coupled oscillators—complex but not complicated cardiovascular and brain interactions. IEEE Eng. Med. Biol. Mag. **26**, 25–29 (2007)
155. A. Stefanovska, P.T. Clemson, Suprunenko, An introduction to chronotaxis systems—systems far from equilibrium that adjust their clocks, in *Self-organization in Complex Systems: The Past, the Present and the Future of Synergetics*, ed. by A. Pelster, G. Wunner (Springer, Berlin, 2013)
156. H.S. Thoke, L.F. Olsen, L. Duelund, R.P. Stock, T. Heimburg, L.A. Bagatolli, Is a constant low-entropy process at the root of glycolytic oscillations? J. Biol. Phys. **44**, 419–431 (2018)
157. V. Ticcinelli, T. Stankovski, P. McClintock, A. Stefanovsky, Aging of the couplings between cardiac, respiratory and myogenic activity in humans. IEEE Eng. Med. Biol. Soc. (2015). https://doi.org/10.1109/EMBC.2015.7320093
158. D.C. Wallace, Mitochondria and cancer. Nat. Rev. Cancer **12**, 685–698 (2012)
159. D.C. Wallace, Mitochondrial DNA in human variation and disease. Cell **163**, 33–38 (2015)
160. H.N. Xu, J. Tchou, M. Feng, H. Zhao, L.Z. Li, Optical redox imaging indices discriminate human breast cancer from normal tissues. J. Biomed. Opt. **21**(11), 114003 (2016)
161. H.N. Xu, H. Zhao, K. Chellappa, J.G. Davis, S. Nioka, J.A. Baur, L.Z. Li, Optical Redox imaging of fixed unstained muscle slides reveals useful biological information. Mol. Imaging Biol. **21**(3), 417–425 (2019)
162. F.E. Yates, Fractal applications in biology: scaling time in biochemical networks: (Numerical Methods). Meth. Enzymol. **219**, 636–676 (1992)
163. F.E. Yates, L.B. Yates, Ultradian rhythms as the dynamic signatures of life, in *Ultradian Rhythms from Molecules to Mind, A New Vision of Life*, ed. by D. Lloyd, E.L. Rossi (Springer, Dordrecht, 2008), pp. 249–260
164. K. Zand, T. Pham, A. Davila Jr., D.C. Wallace, P.J. Burke, Nanofluidic platform for single mitochondria analysis using fluorescence microscopy. Anal. Chem. **85**(12), 6018–6025 (2013)

Chapter 15
Glycolytic Oscillations in Cancer Cells

Takashi Amemiya, Kenichi Shibata, Masatoshi Watanabe, Satoshi Nakata, Kazuyuki Nakamura, and Tomohiko Yamaguchi

Abstract We highlight recently discovered glycolytic oscillations in HeLa cervical and DU145 prostate cancer cells, and discuss the individual and collective behaviors based on a mathematical model proposed previously. We found strong heterogeneities in the oscillations, indicating that glycolytic enzymatic activities are very heterogeneous in these cells. Further, the degree of synchronisation in their oscillations was very low, indicating that cell-to-cell interaction is very low during glycolysis in cancer cells. Biomedical implications obtained from the analyses of the oscillatory dynamics are also presented; more malignant cancer cells tend to exhibit glycolytic oscillations with higher frequencies than less malignant cells. Thus, glycolytic oscillations in cancer cells can be a medical indicator to detect the malignancy of cancer cells.

T. Amemiya (✉) · K. Shibata
Graduate School of Environment and Information Sciences, Yokohama National University (YNU), 79-7 Tokiwadai, Hodogaya-ku, Yokohama 240-8501, Kanagawa, Japan
e-mail: amemiya-takashi-jk@ynu.ac.jp

M. Watanabe
Graduate School of Medicine, Mie University, 2-174 Edobashi, Tsu 514-8507, Mie, Japan

S. Nakata
Graduate School of Integrated Sciences for Life, Hiroshima University, 1-3-1 Kagamiyama, Higashi-Hiroshima 739-8526, Japan

K. Nakamura
School of Interdisciplinary Mathematical Sciences, Meiji University, 4-21-1 Nakano, Nakano-ku, Tokyo 164-8525, Japan

JST, PRESTO, 4-1-8 Honcho, Kawaguchi 332-0012, Saitama, Japan

T. Yamaguchi
Meiji Institute for Advanced Study of Mathematical Sciences (MIMS), 4-21-1 Nakano, Nakano-ku, Tokyo 164-8525, Japan

A. Stefanovska and P. V. E. McClintock (eds.), *Physics of Biological Oscillators*, Understanding Complex Systems,
https://doi.org/10.1007/978-3-030-59805-1_15

15.1 Introduction

Glycolytic oscillations are spatiotemporal oscillations in the concentrations of metabolic intermediates in cells, and this phenomenon has been the focus of theoretical and experimental studies in rhythmic behaviours at the cellular level [21]. They have been reported in several cell types such as yeast cells [3, 16, 24, 44, 54, 60], pancreatic β-cells [7, 8], ventricular myocytes [66], and cancer cells [4, 5, 19, 30]. The mechanism of intracellular glycolytic oscillations and their synchronisation have been studied intensively using yeast, *Saccharomyces cerevisiae*, for almost 60 years [13].

In 1967, glycolytic oscillations in cancer cells were reported for the first time [30]. Oscillations of metabolic intermediates, such as nicotinamide adenine dinucleotide (NAD^+), fructose 1,6-bisphosphate, and adenosine triphosphate (ATP), were observed in aerobic suspensions of intact Ehrlich ascites tumour cells obtained from Swiss white mice. However, so far, no studies have reported an evidence of glycolytic oscillations in cancer cells in individual cell level, and we have previously reported the oscillations in HeLa cervical cancer cells [5].

This chapter reviews the first direct observation of glycolytic oscillations in HeLa cervical and DU145 prostate cancer cells, and presents a mathematical model to explain the mechanism of their oscillations and reproduce the experimental results. Biomedical implications obtained from the analyses of the oscillatory dynamics are also presented: the more the malignancy of cancer cells, the more they tend to exhibit glycolytic oscillations with higher frequencies.

15.2 Mechanism of Glycolytic Oscillations in Cancer Cells

The mechanism of the glycolytic oscillations in cancer cells can be compared with glycolytic control reactions in yeast as shown in Fig. 15.1. The core oscillatory mechanism is the adenosine diphosphate (ADP) dependent activation of glycolytic products via allosteric enzyme phosphofructokinase (PFK), and its subsequent inhibition by ATP. Although it is now recognized that interactions with mitochondria are extensive [34] even at low physiological and pathophysiological levels of tissue and cytosolic oxygen [36]. Our understanding of this basic oscillatory mechanism will be improved by considering interactions between cytosolic glycolytic pathway and mitochondrial oxidative phosphorylation such as reduced nicotinamide adenine dinucleotide (NADH) transport via malate-aspartate shuttle [23, 33].

It is also noted that during the period NADH fluorescence is being measured, cancer cells are not in a replicative state. The glycolytic dynamics would vary significantly in cells in replicative and non-replicative states, and so the applicability of the present studies to the non-replicative state will be limited. Nonetheless, the dynamics of glycolytic oscillations reflects glycolytic activities in cancer cells, and therefore can be applied to a biomedical diagnosis of cancer, as discussed later.

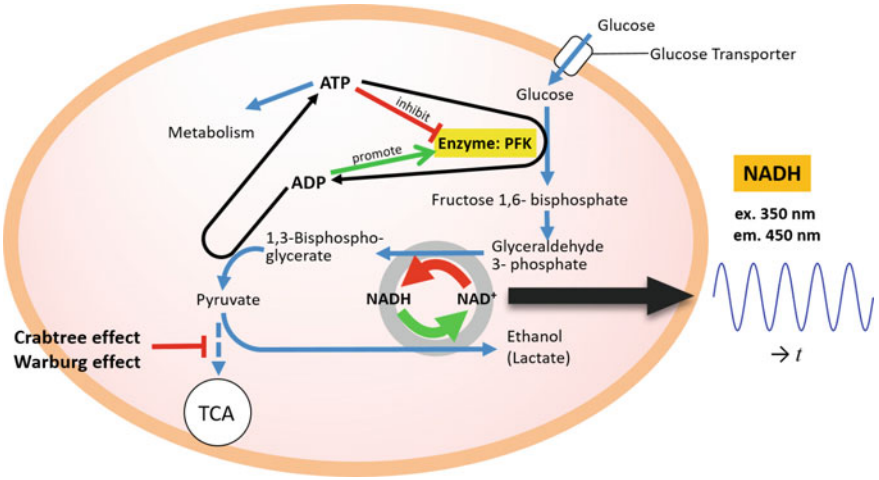

Fig. 15.1 Schematic of glycolytic pathway and mechanism for glycolytic oscillations in yeast and cancer cells. Aerobic glycolysis is enhanced because of the Crabtree effect in yeast cells and both the Crabtree and Warburg effects in cancer cells. Thus, pyruvate, the end product of glycolysis, is not used as a substrate in tricarboxylic acid cycle (TCA), but used during fermentation. Glycolytic oscillations are due to a nonlinear enzymatic reaction of phosphofructokinase (PFK), which is promoted by adenosine diphosphate (ADP) and inhibited by adenosine triphosphate (ATP). The oscillatory behaviour can be observed by auto-fluorescence of reduced nicotinamide adenine dinucleotide (NADH), the coenzyme in glycolysis

15.3 Crabtree Effect and Warburg Effect

Many yeasts including *Saccharomyces cerevisiae* are known to enhance their glycolytic pathway at high glucose concentrations and even under aerobic conditions, in a phenomenon called the Crabtree effect [15]. This metabolic character might be one of the reasons why glycolytic oscillations were studied using the budding yeast. Similarly, many types of cancer cells also exhibit the Crabtree effect, which is a short-term phenotypic adaptation, and the Warburg effect in which glycolytic ATP generation predominates over mitochondrial oxidative ATP production [38, 59]. Genetic mutations also enhance the glycolytic activity and impair oxidative phosphorylation [17]. Since the Warburg effect is a metabolic hallmark of cancer cells [28], glycolysis has been the focus of research interest, even from a therapeutic viewpoint [26]. Thus, studies on glycolysis have been carried out using both cancer and yeast cells [17].

In spite of extensive studies on glycolysis in cancer cells from mid-1900s [12, 37, 63], there have been no reports of glycolytic oscillations in cancer cells since the first report in the preliminary note [30]. The scarcity of observed glycolytic oscillations in cancer cells can be attributed to their low degree of synchronisation. To date, experiments to investigate glycolysis in yeast and cancer cells have been carried out using glucose-starved suspension cultures under aerobic conditions [16, 30, 42, 63]. In such systems, glycolytic oscillations could be observed at the population

level. However, only ambiguous oscillations will be observed if the degree of cell synchronisation is low, which will be discussed below.

15.4 Dynamical Quorum Sensing and Kuramoto Desynchronization

The cell-density dependent synchronisation behaviour in suspension culture systems is called dynamical quorum sensing [42]. Quorum sensing is a phenomenon in which microorganisms can sense a small, freely diffusible, and transient molecule, the autoinducer, that accumulates to a critical concentration in a cell-density dependent manner in the extracellular environment [27]. In suspension culture, yeast cells exhibit coherent oscillations at the population level by the exchange of a metabolite, acetaldehyde, pyruvate, H_2S, or possibly ethanol [6, 9, 31, 43, 49]; however these oscillations suddenly cease below the critical cell density, ca. 7×10^8 cells/ml. Detailed mathematical analysis of the oscillatory behaviour revealed that individual yeast cells have a coherent motion and stop oscillating in synchrony below the critical cell density. This dynamical behaviour is phenomenologically similar to the Hopf bifurcation in a single oscillator [21].

An intrinsically different type of transition to synchronised oscillatory behaviour was observed in systems of immobilised yeast cells [60]. In the immobilised systems, individual cells exhibited oscillations even at very low cell densities, ca. 1×10^5 cells/ml, however collective oscillatory behaviour did not appear due to weak coupling between cells at low densities. Whereas the collective coherent oscillations appeared at high cell densities; thus, this collective oscillatory behaviour at population level is cell-density dependent. This type of transition from oscillations to quiescence at the population level is called Kuramoto desynchronization [55, 57].

15.5 Glycolytic Oscillations in HeLa Cervical Cancer Cells

We have focused on the metabolic characteristics, namely, the Crabtree and/or Warburg effects in yeast and cancer cells, and thus carried out experiments of glycolytic oscillations in HeLa cells using systems of immobilised cells [5]. We could observe their glycolytic oscillations in individual cell level for the first time (Fig. 15.2).

Four characteristic behaviours in HeLa glycolytic oscillations can be summarised as follows [5]: (i) starvation of glucose was indispensable for the oscillations, (ii) starvation of both glucose and serum induced oscillations with longer periods and larger amplitudes than those with only glucose starvation, (iii) the oscillations were highly heterogeneous in terms of the number of oscillatory cells, periods of oscillations, and duration of oscillations in large populations of cells ($N \approx 700 - 900$),

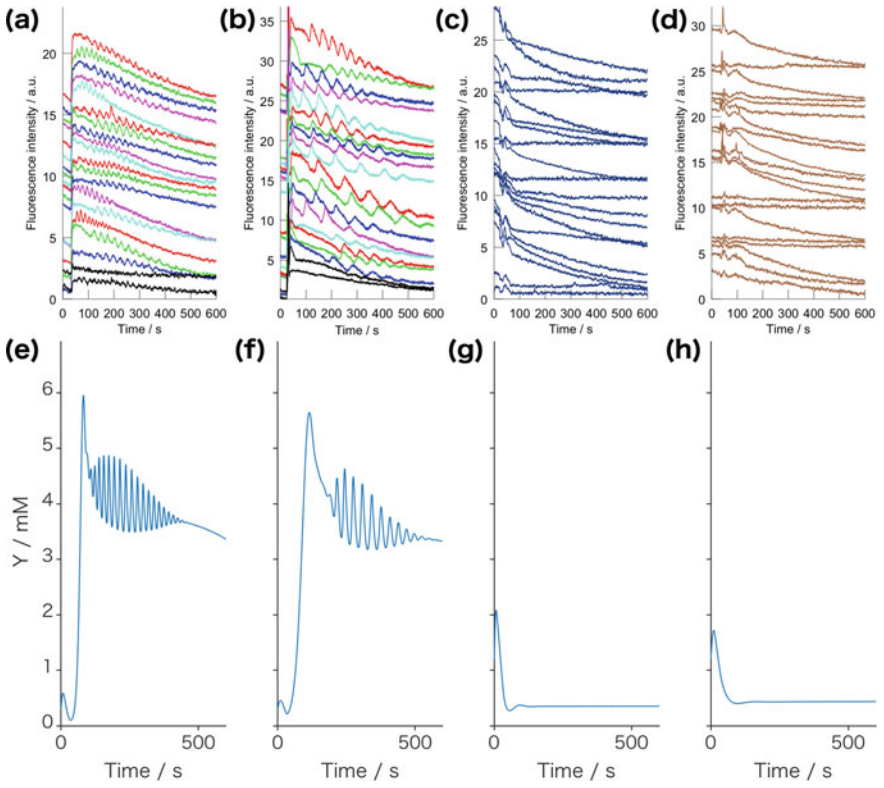

Fig. 15.2 Typical time series of experimental results with NADH fluorescence in HeLa cells and simulation results in an intermediary metabolite Y (**e–h**). The pre-incubating conditions were (**a, e**): (Glc−, FBS+); (**b, f**): (Glc− , FBS−); (**c, g**): (Glc+, FBS+); and (**d, h**): (Glc+, FBS−). HeLa cells were cultured and starved at 37 °C, and fixed to the stage of an inverted fluorescence microscope at 25 °C. The mathematical model is shown in Fig. 15.4, and parameter values for the simulation can be found in literature [4] [Reproduced from Amemiya et al., Chaos 29, 033132 (2019), with the permission of AIP Publishing]

and (iv) quantitative analysis using Kuramoto order parameter $K(t)$ [55] with values lying between 0 (all cells out of phase) and 1 (perfect synchrony) confirmed a very low degree of the intercellular synchronisation of oscillations.

As for the oscillations in individual cells, period distributions can be considered to originate from the difference in the enzymatic activity in the glycolytic pathway [4]. Contrarily, not much is known about possible synchronisation mechanisms in glycolytic oscillations in cancer cells, unlike yeast cells [13, 42, 44, 49]. Thus far, intercellular calcium waves have been found to propagate over a monolayer of HeLa cells via an extracellular signalling molecule such as ATP or through gap junctions [35, 45]. However, no studies have reported cell-to-cell communication for glycolysis in cancer cells.

15.6 Glycolytic Oscillations in Prostate Cancer Cells (DU145)

Prostate cancer, DU145 cells were also found to exhibit glycolytic oscillations for the first time as shown in Fig. 15.3. Experimental methods for the oscillations in DU145 cells were similar to those for HeLa cells [5]. We found that the periods of oscillations (46.2 ± 14.6 s) were longer and the maximum of oscillatory ratio (0.249) was smaller in DU145 cells than the periods (19.3 ± 6.30 s) and the oscillatory ratio (0.355) in HeLa cells. DU145 cells also exhibited heterogeneities in the oscillations in terms of the number of oscillatory cells, periods of oscillations, and duration of oscillations, similar to HeLa cells [4, 5].

Interestingly, the Warburg effect, a common feature of cancer cells, is not observed in prostate cancer cells [18]. In particular, early prostate cancers rely on lipids and other energetic molecules, and not on aerobic respiration, for ATP production.

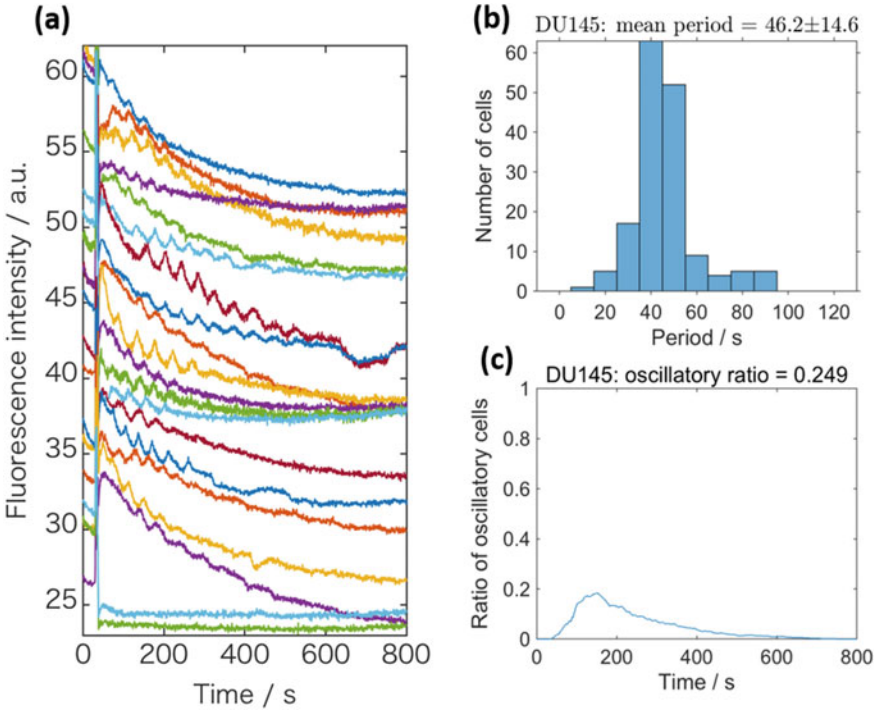

Fig. 15.3 Typical time series of experimental results of glycolytic oscillations with NADH fluorescence in DU145 prostate cancer cells (**a**), their frequency distribution (**b**), and the ratio of oscillatory cells to total cells of $N = 650$ as function of time (**c**). The mean period was 46.2 ± 14.6 s, and the maximum oscillatory ratio was 0.249. The cells were cultured at 37 °C, pre-incubated for 24 h without glucose and with serum conditions (Glc−, FBS+) at 37 °C, and 20 mM glucose was added for the experiment of glycolytic oscillations at 25 °C

Furthermore, prostate cancer cells are reported to show "reverse Warburg effect" in which cancer-associated fibroblasts (CAFs) undergo aerobic glycolysis to produce lactate, which is subsequently used as a metabolic substrate by adjacent cancer cells in tumour tissues [48].

The above metabolic characteristics in prostate cancer, namely, low glycolytic activities, were probably represented in the glycolytic oscillations in DU145 cells; the periods of oscillations were longer and the oscillatory ratio was smaller than those in HeLa cells, which exhibit the Warburg effect. In addition, prostate cancer has been reported to have high five-year survival rates, for instance, close to 99% in 2013 in the US [50]. On the other hand, cervical cancer, whose cell line (HeLa) exhibited higher glycolytic activities than DU145 cells in the oscillations, was reported to have five-year survival rates of 67% in 2009 in the US [50]. Thus, we might predict the malignancy that is directly proportional to glycolytic activities in cancer cells by using their oscillatory behaviours as a readout.

15.7 Mathematical Model for Glycolytic Oscillations in Cancer Cells

Many mathematical models have been developed to reproduce glycolytic oscillations in yeast cells based on the enzymatic reactions in cells. They include minimal models with two variables [14, 22, 51, 52], those with five to nine variables [58, 61, 62], and those with extensive mechanistic details [25, 47].

On the other hand, very detailed models for cancer glycolysis were developed to study the basic cellular physiology such as enzymatic and transport properties [32, 40, 41]; however, no glycolytic oscillations have been investigated in these models. A kinetic model was proposed recently to reproduce glycolytic oscillations of HeLa cells qualitatively [39]. The importance of interaction between glycolysis and mitochondria was also pointed out [34].

We developed a simple mathematical model, as shown in Fig. 15.4, to describe the heterogeneities in glycolytic oscillations in HeLa cells [4]. It is a six-variable model, simple enough to be applied for a mathematical analysis and capture the core of the glycolytic pathway and the activity of the glucose transporter (GLUT). We have succeeded in quantitatively simulating the heterogeneous oscillatory behaviours by considering the variations in the rate constants for the enzymatic reactions and the flux of glucose uptake through GLUT.

Briefly, it considers the upstream (ATP-consuming) reactions of hexose and the downstream (ATP-producing) reactions of triose. Allosteric reactions of PFK and pyruvate kinase (PK) represent the upstream and downstream reactions, respectively. This model describes Michaelis–Menten type mechanisms for the PFK and PK reactions, and a first-order reaction for the consumption of ATP and the final product [4]. It also considers the uptake of glucose into the cells through GLUT. Glucose uptake is reported to enhance glycolysis more than 20-fold in HeLa cells under glucose

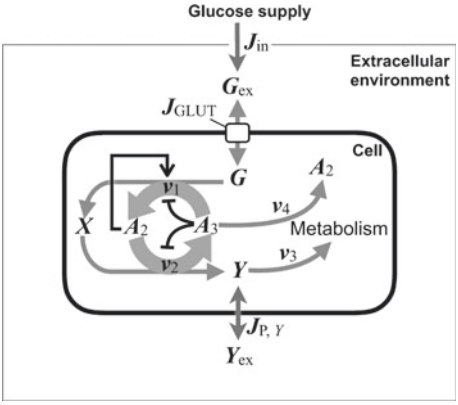

Fig. 15.4 Schematic representation of the model. Variables are G_{ex} (extracellular glucose), G (glucose), X (pools of intermediates after PFK reaction), Y (pools of intermediates after PK reaction), Y_{ex} (extracellular Y), and A_3 (ATP). Total concentration of A_2 (ADP) and A_3 is assumed to be constant: $A_2 + A_3 = A_0$. Transport processes are J_{in} (glucose supply), J_{GLUT} (glucose transporter), and $J_{P,Y}$ (exchange of Y across plasma membrane). Reaction rates of enzymatic reactions are v_1 (PFK reaction), v_2 (PK reaction), v_3 (consumption of Y), and v_4 (ATP consumption). The PKF reaction (v_1) is activated by A_2, and inhibited by A_3. The PK reaction (v_2) is inhibited by A_3 [Reproduced from Amemiya et al., Chaos 29, 033132 (2019), with the permission of AIP Publishing]

starvation [53], and its rate was found to affect the occurrence of the oscillations in the model as well.

The model reproduced the experimental results of glycolytic oscillations in HeLa cells quantitatively. First, the effect of serum-starvation (Glc−, FBS−) was reproduced by using smaller values of the rate constants of enzymatic reactions than those under only glucose starvation (Glc−, FBS+), yielding oscillations with longer periods in glucose and serum starved (Glc−, FBS−) condition (Fig. 15.2 panel b, f) than those in the glucose starved (Glc−, FBS+) condition (Fig. 15.2 panel a, e). Second, the effect of no-starvation of glucose, (Glc+, FBS+) and serum starvation (Glc+, FBS−), resulted in no oscillations; this behaviour was reproduced using a small value of V_{max}, indicating decrease in the activity of GLUT (Fig. 15.2 panel c, d, g, h). Third, different values of the rate constants yielded oscillations with different periods, and both rate constants values and initial conditions of the metabolites in the cells, yielded different starting time and duration of the oscillations. Fourth, the ratio of oscillatory cells to those of both non-oscillatory and oscillatory cells, as function of time was also reproduced well [4].

It is noted that since the Warburg effect applies in cancer cells generally, the exclusion of oxidative phosphorylation in modelling NADH dynamics is justifiable approximation here. However, oxidative phosphorylation still takes place in cancer cells [33], thus the present NADH dynamics should be remarked to be still an approximation, and to be improved in that way.

15.8 Conditions for Glycolytic Oscillations in Cancer Cells

Experiments indicated that the ratio of oscillatory cells was higher under both glucose and serum starved condition (Glc−, FBS−) than under only glucose starved condition (Glc−, FBS+) [5]. This was also reproduced by our mathematical model, which assumed that the values of rate constants of glycolytic enzymes were lower under the former condition (Glc−, FBS−) than under the latter (Glc−, FBS+). The above consideration is reasonable because both glucose and serum starvation are reported to decrease the glycolytic enzymatic activities in cancer cells [10, 29, 64, 67]. In contrast, glucose starvation induces increase in the glucose uptake rate in HeLa cells [53]. Thus, it can be said that cancer cells tend to exhibit more glycolytic oscillations with lower activities of glycolytic enzymes and higher velocities of glucose uptake. This was represented by our mathematical model under conditions of glucose and serum starvation (Glc−, FBS−) and glucose starvation (Glc−, FBS+) in our previous study [4].

Thus, we numerically examined the oscillatory conditions as functions of the activities of glycolytic enzymes (α), and the maximum velocity of glucose uptake (V_{max}); Based on these results we proposed a schematic model in Fig. 15.5. Here, a parameter α was introduced in our model [4], and has linear relationships with the

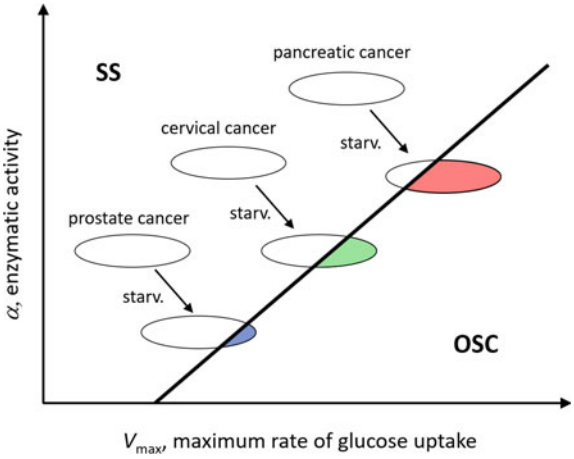

Fig. 15.5 Schematic of steady-state (SS) and oscillatory (OSC) regions spanned by enzymatic activity, α, and maximum rate of glucose uptake, V_{max}, through glucose transporter as shown in Fig. 15.4. This graph is drawn on the basis of numerical calculations of SS and OSC behaviours using the mathematical model (Fig. 15.4). We can see that cancer cells tend to oscillate more with lower enzymatic activity and higher glucose-uptake rate. Populations of three types of cancer cells, prostate, cervical, and pancreatic cancers, are indicated in the diagram by circles. These cells may exhibit glycolytic oscillations under pre-incubation without glucose (glucose-starvation); the oscillatory cells are indicated by the coloured region. On the basis of our studies of glycolytic oscillations in HeLa cervical and DU145 prostate cancer cells, and literature survey, we postulated that more malignant cancer has higher glycolytic enzymatic activity and glucose-uptake rate

values of four rate constants (k_1–k_4) of glycolytic enzymes in the model. We can see that more glycolytic oscillations tend to occur with lower enzymatic activities and the higher velocity of glucose uptake as mentioned above.

Effects of starvation of glucose, or both glucose and serum on the oscillations are represented in the diagram (Fig. 15.5). Cancer cells with no-starvation of glucose, (Glc+, FBS+) and serum starved cells (Glc+, FBS−), exhibited no glycolytic oscillations upon addition of glucose, thus the population of cells is schematically indicated by a white-outlined circle in a steady-state region (SS) in the diagram. Glucose-starvation is reported to decrease the activities of glycolytic enzymes [64, 67] and also to increase the velocity of glucose uptake [53]. On the other hand, serum-starvation is reported to decrease enzymatic activities [10, 29]. Thus, starvation of both glucose and serum totally moves the population of cells to a region indicated by a partly coloured circle where some of the cells are in an oscillatory state (OSC). The oscillatory ratio can change depending on starvation conditions and on the type of cells.

15.9 Malignancy of Cancer Cells and Glycolytic Oscillations

Based on previous studies of glycolytic oscillations in HeLa cells [4, 5], and DU145 cells presented here, and the characteristics of glycolytic activities in cancer cells as will be mentioned below, we assume that the greater the malignancy of cancer cells, the more they tend to exhibit glycolytic oscillations. Thus our operating definition of malignancy of cancer cells with relation to cellular metabolism is that more malignant cancer cells may enhance more glycolytic activities.

Multiple glycolytic enzymes are highly expressed in various types of cancers, including pancreatic cancer [65], one of the most malignant cancers, and promote metastasis [2]. By comparing two breast cancer cell lines MCF7 and MDA-MB231, highly invasive MDA-MB231 cells were reported to be more glycolytic than non-invasive MCF7 cells [20, 46]. With regard to adoptive T cell therapy, increased tumour glycolytic activity is shown to be associated with lower therapeutic response, and glycolysis-related genes are reported to be upregulated in melanoma and lung cancer patient samples that are poorly infiltrated by T cells [11]. Further, glucose-transporter 1 (GLUT1) is also reported to be highly expressed in tumour cell lines of different organs such as renal cell carcinoma, melanoma, and hepatocellular carcinoma compared to their non-malignant counterparts [56].

However, according to worldwide epidemiological survey [50], prostate cancer, whose cell line (DU145) exhibited little glycolytic oscillations in our study (Fig. 15.3), was reported to have close to 99% five-year survival rates in 2013, in the US; in contrast, pancreatic cancer showed very low five-year survival rates of 8.2%. Cervical cancer, whose cell line (HeLa) exhibited glycolytic oscillations [5], was reported to have five-year survival rates of 67% in 2009 in the US. In general,

prostate cancer has very high five-year survival rates, cervical cancer has moderate survival rates, and pancreatic, liver, and lung cancers have very low survival rates in other countries [1, 50]. Naturally, five-year cancer survival rates are affected by earlier detection and/or improved treatment, nonetheless it can be considered to be a good indicator representing malignancy of cancer.

Based on the above considerations, three types of cancer, i.e., pancreatic, cervical, and prostate cancers, are schematically plotted in the diagram (Fig. 15.5). In the diagram, populations of more malignant cancer are located in more upper right region. Upon addition of glucose after glucose starvation, or glucose and serum starvation, a certain number of these cancers may exhibit glycolytic oscillations. We hypothesise from the studies of HeLa and DU145 cells that more malignant cancer may exhibit higher oscillatory ratio. More studies using various types of cancer cells are necessary in order to verify this hypothesis regarding the relationship between malignancy and characteristics in glycolytic oscillations in cancer cells, which will be applied for diagnosis of cancer.

15.10 Summary

Fifty years after the discovery of glycolytic oscillations in Ehrlich ascites tumour cells grown in suspension, the individual and collective behaviours have been unravelled in HeLa cells due to the advancements in experimental and analytical techniques. Strong heterogeneities were found in their glycolytic oscillations, indicating that glycolytic enzymatic activities are very heterogeneous in HeLa cells. Furthermore, the degree of synchronisation in the oscillations was very low, indicating very little cell-to-cell interaction during glycolysis in HeLa cells. Nearly the same qualitative behaviours were also observed in DU145 cells.

Based on the experiments of glycolytic oscillations in HeLa and DU145 cells, and the literature available on glycolytic activities and malignancy in cancer cells, we have proposed a model indicating the relationship between malignancy of cancer cells and their glycolytic oscillation characteristics. We propose that more malignant cancer cells tend to exhibit glycolytic oscillations with shorter periods than less malignant cells. Thus, glycolytic oscillations in cancer cells may be a medical indicator to detect the malignancy of cancer cells.

Acknowledgements We are grateful to Professor Stefanovska for useful discussions on glycolytic oscillators. This study was supported in part by a grant for Cooperative Research Project to T. A. from YNU, JSPS KAKENHI Grant Numbers 17KT0123 to S. N., 19H04205 to T. A., MIMS/CMMA collaborative research symposium to T. Y. and T. A., MIMS Joint Research Project for Mathematical Sciences to T. Y, Health Labour Science Research Grant to M. W., and JST PRESTO JPMJPR1774 to K. N. We would like to thank Editage (www.editage.com) for English language editing.

References

1. C. Allemani et al., Global surveillance of cancer survival 1995–2009: analysis of individual data for 25 676 887 patients from 279 population-based registries in 67 countries (CONCORD-2). Lancet **385**, 977–1010 (2015)
2. B. Altenberg, K.O. Greulich, Genes of glycolysis are ubiquitously overexpressed in 24 cancer classes. Genomics **84**, 1014–1020 (2004)
3. T. Amemiya, K. Obase, N. Hiramatsu, K. Itoh, K. Shibata, M. Takinoue, T. Yamamoto, T. Yamaguchi, Collective and individual glycolytic oscillations in yeast cells encapsulated in alginate microparticles. Chaos **25**, 064606 (2015)
4. T. Amemiya, K. Shibata, Y. Du, S. Nakata, T. Yamaguchi, Modeling studies of heterogeneities in glycolytic oscillations in HeLa cervical cancer cells. Chaos **29**, 033132 (2019)
5. T. Amemiya, K. Shibata, Y. Itoh, K. Itoh, M. Watanabe, T. Yamaguchi, Primordial oscillations in life: direct observation of glycolytic oscillations in individual HeLa cervical cancer cells. Chaos **27**, 104602 (2017)
6. M.A. Aon, S. Cortassa, H.V. Westerhoff, K. Van Dam, Synchrony and mutual stimulation of yeast cells during fast glycolytic oscillations. J. Gen. Microbiol. **138**, 2219–2227 (1992)
7. R.K.P. Benninger, D.W. Piston, Cellular communication and heterogeneity in pancreatic islet insulin secretion dynamics. Trends Endocrinol. Metabol. **25**, 399–406 (2014)
8. R. Bertram, L.S. Satin, M.G. Pedersen, D.S. Luciani, A. Sherman, Interaction of glycolysis and mitochondrial respiration in metabolic oscillations of pancreatic islets. Biophys. J. **92**, 1544–1555 (2007)
9. A. Betz, J.U. Becker, Phase dependent phase shifts induced by pyruvate and acetaldehyde in oscillating NADH of yeast cells. J. Interdis. Cycle Res. **6**, 167–173 (1975)
10. P. Bruni, M. Farnararo, V. Vasta, A. D'Alessandro, Increase of the glycolytic rate in human resting fibroblasts following serum stimulation. FEBS Lett. **159**, 39–42 (1983)
11. T. Cascone et al., Increased tumor glycolysis characterizes immune resistance to adoptive T cell therapy. Cell Metab. **27**, 977–987 (2018)
12. B. Chance, B. Hess, Metabolic control mechanisms: IV. The effect of glucose upon the steady state of respiratory enzymes in the ascites cell. J. Biol. Chem. **234**, 2421–2427 (1959)
13. B. Chance, G. Williamson, I.Y. Lee, L. Mela, D. DeVault, A.K. Ghosh, E.K. Pye, Synchronization phenomena in oscillations in yeast cells and isolated mitochondria. In: *Biological and Biochemical Oscillators. A Colloquium of the Johnson Foundation*, ed. by B. Chance, E.K. Pye, A.K. Ghosh, A.B. Hess (Academic Press, New York & London, 1973), pp. 285–302
14. F.A. Chandra, G. Buzi, J.C. Doyle, Glycolytic oscillations and limits on robust efficiency. Science **333**, 187–192 (2011)
15. H.G. Crabtree, Observations on the carbohydrate metabolism of tumors. Biochem. J. **23**, 536–545 (1929)
16. S. Danø, P. Sørensen, F. Hynne, Sustained oscillations in living cells. Nature **402**, 320–322 (1999)
17. R. Diaz-Ruiz, M. Rigoulet, A. Devin, The Warburg and Crabtree effects: on the origin of cancer cell energy metabolism and of yeast glucose repression. Biochem. Biophys. Acta. **1807**, 568–576 (2011)
18. E. Eidelman, J. Twum-Ampofo, J. Ansari, M.M. Siddiqui, The metabolic phenotype of prostate cancer. Front. Oncol. **7**, 131 (2017)
19. L.C. Fru, E.B. Adamson, D.D. Campos, S.B. Fain, S.L. Jacques, A.J. van der Kogel, K.P. Nichel, C. Song, R.J. Kimple, M.W. Kissick, Potential role of the glycolytic oscillator in acute hypoxia in tumors. Phys. Med. Biol. **60**, 9215–9255 (2015)
20. R.A. Gatenby, R.J. Gillies, Why do cancers have high aerobic glycolysis? Nat. Rev. Cancer **4**, 891–899 (2004)

21. A. Goldbeter, *Biochemical Oscillations and Cellular Rhythms* (Cambridge University Press, United Kingdom, 1996)
22. A. Goldbeter, R. Lefever, Dissipative structure for an allosteric model. Biophys. J. **12**, 1302–1315 (1972)
23. W.V.V. Greenhouse, A.L. Lehninger, Occurrence of malate-aspartate shuttle in various tumor types. Cancer Res. **36**, 1392–1396 (1976)
24. A.-K. Gustavsson, D.D. van Niekerk, C.B. Adiels, F.B. du Preez, M. Goksör, J.L. Snoep, Sustained glycolytic oscillations in individual isolated yeast cells. FEBS J. **279**, 2837–2847 (2012)
25. B.O. Hald, P.G. Sörensen, Modeling diauxic glycolytic oscillations in yeast. Biophys. J. **99**, 3191–3199 (2010)
26. R.B. Hamanaka, N.S. Chandel, Targeting glucose metabolism for cancer therapy. J. Exp. Med. **209**, 211–215 (2012)
27. J.W. Hastings, E.P. Greenberg, Quorum sensing: the explanation of a curious phenomenon reveals a common characteristic of bacteria. J. Bacteriol. **181**(9), 2667–2668 (1999)
28. M.G.V. Heiden, L.C. Cantley, C.B. Thompson, Understanding the Warburg effect: the metabolic requirements of cell proliferation. Science **324**, 1029–1033 (2009)
29. S.Y. Hong, F.-X. Yu, Y. Luo, T. Hagen, Oncogenic activation of the PI3K/Akt pathway promotes cellular glucose uptake by downregulating the expression of thioredoxin-interacting protein. Cell. Signal. **28**, 377–383 (2016)
30. K.H. Ibsen, K.W. Schiller, Oscillations of nucleotides and glycolytic intermediates in aerobic suspensions of Ehrlich ascites tumor cells. Biochim. Biophys. Acta **131**, 405–407 (1967)
31. M. Keulers, A.D. Satroutdinov, T. Suzuki, H. Kuriyama, Synchronization affector of autonomous short-period-sustained oscillation of *Saccharomyces cerevisiae*. Yeast **12**, 673–682 (1996)
32. T. Khazaei, A. McGuigan, R. Mahadevan, Ensemble modeling of cancer metabolism. Front. Physiol. **3**, Article 135 (2012)
33. S.-Y. Kim, Cancer energy metabolism: shutting power off cancer factory. Biomol. Ther. **26**, 34–44 (2018)
34. G. Lancaster, Y.F. Suprunenko, K. Jenkins, A. Stefanovska, Modelling chronotaxicity of cellular energy metabolism to facilitate the identification of altered metabolic states. Sci. Rep. **6**, 29584 (2016)
35. G.C. Lin, J.K. Rurangirwa, M. Koval, T.H. Steinberg, Gap junctional communication modulates agonist-induced calcium oscillations in transfected HeLa cells. J. Cell Sci. **117**, 881–887 (2004)
36. D. Lloyd, C.F. Williams, Avoid excessive oxygen levels in experiments with organisms, tissues and cells. Adv. Microb. Physiol. **67**, 293–314 (2015)
37. J.W. Locasale, M.G.V. Heiden, L.C. Cantley, Rewiring of glycolysis in cancer cell metabolism. Cell Cycle **9**, 4253 (2010)
38. E.N. Maldonado, J.J. Lamasters, ATP/ADP ratio: the missing link between mitochondria and the Warburg effect. Mitochondrion **19A**, 78–84 (2014)
39. R.R. Martin, S. Montero, E. Silva, M. Bizzarri, G. Cocho, R. Mansilla, J.M. Nieto-Villar, Phase transitions in tumor growth: V what can be expected from cancer glycolytic oscillations? Physica A **486**, 762–771 (2017)
40. A. Marín-Hernández, J.C. Gallardo-Pérez, S. Rodríguez-Enríquez, R. Encalada, R. Moreno-Sánchez, E. Saavedra, Modeling cancer glycolysis. Biochem. Biophys. Acta. **1807**, 755–767 (2011)
41. A. Marín-Hernández, S.Y. López-Ramirez, I.D. Mazo-Monsalvo, J.C. Gallardo-Perez, S. Rodríguez-Enriquez, R. Moreno-Sanchez, E. Saavera, Modeling cancer glycolysis under hypoglycemia, and the role played by the differential expression of glycolytic isoforms. FEBS J. **281**, 3325–3345 (2014)
42. S. De Monte, F. d'Ovidio, S. Danø, P. Sørensen, Dynamical quorum sensing: Population density encoded in cellular dynamics. Proc. Natl. Acad. Sci. USA **20**, 18377–18381 (2007)

43. D.B. Murray, R.R. Klevecz, D. Lloyd, Generation and maintenance of synchrony in Saccharomyces cerevisiae continuous culture. Exp. Cell Res. **287**, 10–15 (2003)
44. L.F. Olsen, A.Z. Andersen, A. Lunding, J.C. Brasen, A.K. Poulsen, Regulation of glycolytic oscillations by mitochondrial and plasma membrane H^+-ATPases. Biophys. J. **96**, 3850–3861 (2009)
45. K. Paemeleire, P.E.M. Martin, S.L. Coleman, K.E. Fogarty, W.A. Carrington, L. Leybaert, R.A. Tuft, W.H. Evans, M.J. Sanderson, Intercellular calcium waves in HeLa cells expressing GFP-labeled connexin 43, 32, or 26. Mol. Biol. Cell **11**, 1815–1827 (2000)
46. H. Pelicano, W. Zhang, J. Liu, N. Hammoudi, J. Dai, R.-H. Xu, L. Pusztai, P. Huang, Mitochondrial dysfunction in some triple-negative breast cancer cell lines: role of mTOR pathway and therapeutic potential. Breast Cancer Res. **16**, 434 (2014)
47. F.B. du Preez, D.D. van Niekerk, J.L. Snoep, From steady-state to synchronized yeast glycolytic oscillations II: model validation. FEBS J. **279**, 2823–2836 (2012)
48. N. Pértega-Gomes, J.R. Vizcaíno, J. Attig, S. Jurmeister, C. Lopes, F. Baltazar, A lactate shuttle system between tumour and stromal cells is associated with poor prognosis in prostate cancer. BMC Cancer **14**, 352 (2014)
49. P. Richard, B.M. Bakker, B. Teusink, K. van Dam, H.V. Westerhoff, Acetaldehyde mediates the synchronization of sustained glycolytic oscillations in populations of yeast cells. Eur. J. Biochem. **235**, 238–241 (1996)
50. M. Roser, H. Ritchie, "Cancer" Published online at OurWorldInData.Org. https://ourworldindata.org/cancer
51. J. Schütze, J. Wolf, Spatio-temporal dynamics of glycolysis in cell layers. A mathematical model. Biosystems **99**, 104–108 (2010)
52. E.E. Sel'kov, Self-oscillations in glycolysis. 1. A simple kinetic model. Eur. J. Biochem. **4**, 79–86 (1968)
53. S.N. Shaw, H. Amos, Insulin stimulation of glucose entry in chick fibroblasts and Hela cells. Biochem. Biophys. Res. Commun. **53**, 357–365 (1973)
54. K. Shibata, T. Amemiya, Y. Kakakita, K. Obase, K. Itoh, M. Takinoue, S. Nakata, T. Yamaguchi, Promotion and inhibition of synchronous glycolytic oscillations in yeast by chitosan. FEBS J. **285**, 2679–2690 (2018)
55. S. Shinomoto, Y. Kuramoto, Phase transition in active rotator systems. Prog. Theor. Phys. **75**, 1105–1110 (1986)
56. K. Singer et al., Warburg phenotype in renal cell carcinoma: high expression of glucose-transporter 1 (GLUT-1) correlates with low $CD8^+$ T-cell infiltration in the tumor. Int. J. Caner **128**, 2085–2095 (2011)
57. S.H. Strogatz, From Kuramoto to Crawfrd: exploring the onset of synchronization in populations of coupled oscillators. Physica. D **143**, 1–20 (2000)
58. Y. Termonia, J. Ross, Oscillations and control features in glycolysis: Numerical analysis of a comprehensive model. Proc. Natl. Acad. Sci. USA **78**, 2952–2956 (1981)
59. Warburg, O., On the origin of cancer cells. Science **123**, 309–314 (1956)
60. A. Weber, Y. Prokazov, W. Zuschratter, M.J.B. Hauser, Desynchronisation of glycolytic oscillations in yeast cell populations. PLoS ONE **7**, e43276 (2012)
61. J. Wolf, R. Heinrich, Effect of cellular interaction on glycolytic oscillations in yeast: a theoretical investigation. Biochem. J. **345**, 321–334 (2000)
62. J. Wolf, J. Passarge, O.J.G. Somsen, J.L. Snoep, R. Heinrich, H.V. Westerhoff, Transduction of intracellular and intercellular dynamics in yeast glycolytic oscillations. Biophys. J. **78**, 1145–1153 (2000)
63. R. Wu, E. Racker, Regulatory mechanisms in carbohydrate metabolism. IV. Pasteur effect and Crabtree effect in ascites tumor cells. J. Biol. Chem. **234**, 1036–1041 (1959)
64. S. Wu, X. Yin, X. Fang, J. Zheng, L. Li, X. Liu, L. Chu, c-MYC responds to glucose deprivation in a cell-type-dependent manner. Cell Death Dis. **1**, 15057 (2015)

65. J. Yang, B. Ren, G. Yang, H. Wang, G. Chen, L. You, T. Zhang, Y. Zhao, The enhancement of glycolysis regulates pancreatic cancer metastasis. Cell. Mol. Life Sci. **77**, 305–321 (2019)
66. J.-H. Yang, L. Yang, Z. Qu, J.N. Weiss, Glycolytic oscillations in isolated rabbit ventricular myocytes. J. Biol. Chem. **283**, 36321–36327 (2008)
67. X.-Y. Zhong et al., CARM1 methylates GAPDH to regulate glucose metabolism and is suppressed in liver cancer. Cell Rep. **24**, 3207–3223 (2018)

Chapter 16
Mechanism and Consequence of Vasomotion

Jens Christian Brings Jacobsen and Christian Aalkjær

Abstract Oscillations in the tone or diameter of arteries is called vasomotion and leads to the phenomenon of flowmotion, where the flow of blood into a tissue is oscillating. Vasomotion occurs consequent to oscillations of the contractile state of the smooth muscle cells in the vascular wall and is present in most small arteries in the body. Vasomotion can occur via mechanisms intrinsic to the vascular wall and can consequently be studied in arteries isolated from the body and mounted in an organ chamber. The prevalence of vasomotion is highest in situations where the flow to an organ is compromised. It seems likely that vasomotion is beneficial and ensures an improved dialysis of the tissue, i.e. more efficient delivery of oxygen and removal of waste product, although there is still a need for more experimental evidence to confirm this.

This small review will discuss the oscillation in the tone of small arteries, i.e. vasomotion, and the consequent oscillation of blood flow, which is called flowmotion. However, before we get into a discussion of these oscillations we will briefly outline the main concepts of arterial structure and function.

16.1 Background Information on Small Arteries and Their Function

Arteries are the blood vessels, which lead from the heart to the organs and tissues and where the oxygenated blood is transported. These vessels deliver the oxygen and nutrients needed to sustain a normal metabolism and hence function of the organs.

J. C. B. Jacobsen (✉) · C. Aalkjær
Department of Biomedical Sciences, University of Copenhagen, Copenhagen, Denmark
e-mail: jcbrings@sund.ku.dk

C. Aalkjær
Institute of Biomedicine, University of Aarhus, Aarhus, Denmark

A. Stefanovska and P. V. E. McClintock (eds.), *Physics of Biological Oscillators*, Understanding Complex Systems,
https://doi.org/10.1007/978-3-030-59805-1_16

The arterial wall has three layers. An inner layer, which mainly consist of a single cell layer—the endothelial cells. The endothelial cells separates the other layers of the arterial wall from the blood, and produce a large number of molecules, which are important for the fluidity of the blood and for the tone of the vascular smooth muscle cells. The latter are present in the next layer of the arterial wall, the medial layer. The smooth muscle cells of the medial layer are circumferentially oriented and controls the lumen diameter and the compliance of the arterial wall through contraction and relaxation. The third layer is the adventitia, which is a connective tissue layer containing only few cells of importance for maintenance of the collagen and elastic fibers and for some immune functions of the arterial wall. The inner part of the adventitia (next to the smooth muscle cells of the media) harbors different types of nerve fibers. The activity in the nerve fibers controls the tone of the smooth muscle cells, i.e. some nerve fibers release substances, which causes contraction, while other fibers release substances that relax the smooth muscle cells. Vasoactive substances both from the endothelium and from the nerves thus affect the tone of the smooth muscle cells. In addition, molecules produced in the various organs of the body influence tone; a prominent example of this is the relaxant and hence vasodilatory effect of metabolic end-products such as e.g. CO_2.

The tone of the smooth muscle cells and hence the diameter of the arteries has a number of hemodynamical consequences. By constriction and thus reduction of vessel diameter the resistance to flow increases. By constricting some arteries and dilating others, the blood can be shunted away from one organ or region and towards another. Simultaneous constriction of a large number of arteries will also increase the total hydraulic resistance, which means that the blood pressure, i.e. the pressure in the large arteries at the level of the heart, increases. Finally, constriction of an artery will reduce the intravascular pressure in the arteries, arterioles and capillaries downstream for the constricted artery.

Arteries are conveniently divided into large and small arteries. The main function of the large arteries is to dampen the oscillations in pressure and flow, which is consequent to the pulsative action of the heart. The systole is the constriction phase of the heart muscle when blood is expelled and pressure in the arterial system rises, and the diastole is the filling phase, where the heart muscle is relaxed and arterial pressure is lower.

The small arteries (and the even smaller arterioles) is where the main hydraulic resistance resides and it is the regulation of the tone of the smooth muscle cells in the small arteries that is important for the distribution of blood and for control of blood pressure and capillary pressure. It is the small arteries, which are in focus in this review.

The tone of the vascular smooth muscle cells is controlled by (1) the electrical potential across the membrane (the membrane potential), (2) the release of Ca^{2+} from Ca^{2+}-stores in the cells, and (3) the sensitivity of the contractile proteins to Ca^{2+}. The membrane potential is generated by a combination of active transport (transport against an electrochemical gradient) of ions and passive transport of ions. The most relevant ions are Na^+, K^+, and Cl^-. In a relaxed smooth muscle the membrane potential is about -60 to -80 mV, with the inside being negative. When the membrane

depolarizes towards 0 mV Ca^{2+} selective channels open and Ca^{2+} runs into the cell down its electrochemical gradient. The resulting intracellular increase Ca^{2+} concentration activates contractile proteins and the smooth muscle cell contract. When the cell membrane repolarizes the Ca^{2+} channels closes and Ca^{2+} is pumped out of the cell. Importantly the smooth muscle cells (and also the endothelial cells) constitute an electrical syncytium because they are connected by low resistance channels (gap junctions), allowing current to flow from one cell to the next. When the cells are activated by vasoconstrictors e.g. noradrenaline from nerves in the vessel wall, Ca^{2+} is also released from stores inside the cells, which adds to the Ca^{2+} increase induced by depolarization of the membrane. The sensitivity of the contractile proteins to Ca^{2+} can be modified through a number of relatively complex biochemical pathways.

16.2 The Concept of Vasomotion

The tone of the vascular smooth muscle cells often oscillate. This leads to the phenomenon of vasomotion which is a cyclic variation in vessel diameter. Vasomotion is present in most, if not all, small arteries in both animals and humans. The first description of vasomotion was in bat wing veins [31], i.e. the blood vessels which leads from the tissues to the heart. Vasomotion of veins is a well studied phenomenon [59]. Vasomotion leads to flowmotion, where the flow into a tissue or a whole organ oscillates. Flowmotion can be seen in the intact animal or human where it can be divided and characterized within five or six different frequency bands [33, 34, 54]—from 0.008 Hz to 1–2 Hz—associated with different aspects of the vascular function (e.g. endothelium dependent, nerve dependent, smooth muscle dependent etc.). Vasomotion also occurs when an artery is removed from the body and suspended in an organ bath [16, 43], demonstrating that vasomotion is an inherent property of the vascular wall. The prevalence of vasomotion varies between different vascular beds, between blood vessel branching orders, and between arteries and veins and is changed in many pathological conditions e.g. hypertension [42, 47], diabetes [4], ischemia [49] and Alzheimer's disease [10]. Vasomotion appears to disappear in elderly people and yet, as it will be seen, we still do not fully understand what the consequences of vasomotion are.

16.3 How Does Vasomotion Develop?

For vasomotion to occur there is a requirement for an oscillator and for a mean of synchronizing the oscillations in the many smooth muscle cells in the arterial wall. There is undoubtedly a number of ways in which this can be achieved. There is, however also some mechanisms which very likely are important for most types of vasomotion. It seems likely that there is no single pacemaker cell or group of pacemaker cells which sets up the oscillation. Rather, there is evidence that at least

the Ca^{2+} concentration of all the smooth muscle cells in the wall can oscillate and it is the entrainment of these oscillations which sets up vasomotion. It is also likely that it is electrical current running between the cells via gap-junctions which is key to understanding the entrainment. This is supported by the finding that in all cases, where the membrane potential of the smooth muscle has been measured during vasomotion, the membrane potential is oscillating [9, 13, 19, 21–23, 39, 41, 53]. These oscillations occur with the same frequency as the contractions (between 2 and 20 Hz) and only slightly phase shifted relative to the latter, so the depolarizing phase of the oscillation precedes the contractile phase of the vasomotion with 1–2 s [1]. Also Ca^{2+} is oscillating synchronized in all cells when vasomotion occurs and is phase shifted less than 1 s relatively to the contraction [1]. There is thus little doubt that vasomotion in all instances is caused by oscillation of the membrane potential which sets up the oscillation of Ca^{2+} in the smooth muscle cells in turn leading to vasomotion.

There is evidence for the existence of two types of oscillators in smooth muscle cells. One where interactions between potential sensitive and/or Ca^{2+} sensitive ion channels in the membrane leads to oscillations of the membrane potential—the membrane oscillator, and one where release of Ca^{2+} from intracellular stores and slow reuptake of Ca^{2+} into these stores, sets up and oscillation of Ca^{2+}—a cytosolic oscillator. A combination of the two is also a possibility and in the following, we will provide an example of a model for vasomotion in small arteries from the rat intestine where the oscillator is based on an interaction between an intracellular oscillator and a cytosolic oscillator. This mechanism for initiation of vasomotion has been modelled in silico [29, 30].

In the smooth muscle cells of small muscular arteries, when exposed to a low concentration of noradrenaline, Ca^{2+} waves run along the cell length axis in an uncoordinated fashion [43]. After a few minutes these Ca^{2+} oscillations synchronize and become global oscillations (i.e. not waves) in cell Ca^{2+}; at this point vasomotion starts. The initial Ca^{2+} waves are caused by release of Ca^{2+} from the intracellular Ca^{2+} store, while the synchronized oscillations of global Ca^{2+} are dependent on Ca^{2+} influx from the extracellular space consequent to oscillations of the membrane potential [43]. The synchronizing step is prevented by removing the endothelial cells from the arteries [43] and it was shown that adding a constant concentration of the a membrane permeable variant of the messenger molecule cGMP to an artery where the endothelium is removed induces vasomotion [18] and synchronization of the Ca^{2+} transients [43]. Since membrane potential oscillations are critical for vasomotion, it is of interest to understand how the oscillatory Ca^{2+} transients in a cGMP dependent manner lead to oscillations of the membrane potential. Pharmacologically induced release of Ca^{2+} from the intracellular stores could induce depolarization of the membrane potential in an endothelium- and cGMP dependent manner. This would mean that a Ca^{2+}-activated and cGMP-dependent ion conductance, which provides a depolarizing current is most likely of importance. We showed that a Cl^- conductance with these characteristics is present in rat small arteries [38] and suggested that this Cl^- conductance would be important for vasomotion in these arteries [43]. This is consistent with the idea that a Cl^- conductance is also important for the rhythmic contraction

of lymph-vessels [58]. This hypothesis could be tested when the membrane proteins responsible for the Cl^- conductance were known. It turned out that two proteins were necessary for the Ca^{2+}-activated, cGMP-dependent Cl^- conductance. One is a protein called TMEM16A [7] and the other protein is called bestrophin [40]. If the Ca^{2+}-activated and cGMP-dependent Cl^- conductance is important for vasomotion, the latter should be disturbed if TMEM16A or bestrophin is knocked out. Using gene targeting approaches we performed knock-down of these two gene products in the smooth muscle cells and showed that this is associated with gross disturbance of vasomotion [5, 7]. This confirmed a model for vasomotion where a mixed cytosolic and membrane oscillator result in entrainment of oscillating smooth muscle cells to produce vasomotion. The basis for this model is a loop where Ca^{2+} released from the sarcoplasmic reticulum activates a Cl^- conductance in the cell membrane. This leads to membrane depolarization, consequent influx of Ca^{2+}, and refilling of the sarcoplasmic reticulum. A delay in this loop sets up the oscillation and the loop involves a reciprocal interaction between release of Ca^{2+} from the sarcoplasmic reticulum and the membrane potential.

It is important to emphasize that there is experimental evidence for other mechanisms leading to vasomotion as well. Some of these are not dependent on release of Ca^{2+} from the intracellular Ca^{2+} stores and solely depend on a membrane oscillator. In other situations, the endothelial cells seem to prevent vasomotion rather than promote it, as it was the case in the example discussed above.

16.4 Microvascular Networks

The small arteries connect to form networks. These are highly branched, space filling structures, permeating the tissue. Successive branching ultimately places the primary exchange vessels, the capillaries, within close proximity of any tissue cell. As described mathematically already long ago by Krogh [32] the remaining distance for nutrients and waste products can thereby be efficiently bridged by diffusion.

Microvascular networks are constantly adapting to long-term changes in structure and demand of the surrounding tissue. As e.g. skeletal muscle tissue increases in size under physical training, the microvascular supply network must change accordingly. This process, characterized by sprouting of numerous new vessels from existing ones and subsequent pruning and remodeling to form a mature network [44], (reviewed in [35]), encompasses substantial variation which is reflected in the final network structure. Hence, microvascular networks are inherently heterogeneous structures [12]. Different flow routes through the network therefore tend to have different hydraulic resistances. At normal perfusion levels, this heterogeneity will not compromise delivery of oxygen and nutrients to any tissue region, since resistance vessels upstream of the capillary bed can actively change diameter to compensate for inadequate perfusion of a given area. If e.g., perfusion pressure drops or local tissue metabolism increases, resistance vessels dilate to ensure adequate perfusion of their local region. In particular, the dependence of artery diameter on transmural pressure,

i.e. the myogenic mechanism, is important in many tissues to ensure a uniform flow (flow autoregulation) over a broad range of perfusion pressures. In addition, under low-pressure conditions accumulation of a diversity of factors in the tissue caused by inadequate oxygenation and inadequate removal of waste products will enhance vasodilatation. The latter situation however, unveils the underlying differences in hydraulic resistance of different flow routes through the network. Consequently, as pressure is reduced, regions with high resistance may increasingly lose blood-flow to regions with low resistance.

16.5 Vasomotion Depends on the Hemodynamic Status and May Have Consequences for Tissue Oxygenation

An interesting observation concerns the relation between perfusion pressure and the prevalence of flowmotion (cyclic change in blood perfusion, which is a consequence of upstream vasomotion). Smith et al. [50, 51] characterized flowmotion initiated by pressure reduction in the rabbit gastrocnemius and tenuissimus muscles. Skeletal muscle tissue displays a well-developed autoregulatory response. Below a certain pressure limit however, tissue perfusion declines almost linearly with pressure, indicating that perfusion can no longer be sustained by further reduction in myogenic tone. This lower limit coincides with onset of flowmotion. Reducing the pressure further enhances flowmotion. However, increased occurrence of flowmotion is predominantly seen within a certain range of pressures around the lower end of the autoregulatory curve. Below this range, flowmotion declines and eventually vanishes. Likely, flowmotion that originate locally in the vascular bed represents oscillations in vascular tone superimposed on the basal tone ubiquitously present under resting conditions. Complete loss of basal tone due to very low pressure therefore abolishes vasomotion altogether. In fact, one would expect flowmotion being absent no matter the cause of complete vasodilation in a tissue, be it excessively low perfusion pressure, accumulation of metabolites and/or hypoxia. Observations very similar to those of Smith et al. was made in the rat diaphragm microcirculation, in which vasomotion first become more prevalent during progressive hemorrhagic hypotension, then decline in prevalence as pressure falls below 60% of normal pressure [6].

Along the same line, a lower perfusion pressure in patients with occlusive peripheral arterial disease (PAD) appears to coincide with a higher prevalence of flowmotion as measured with laser Doppler-flowmetry [24, 46, 52]. Schmidt et al. [52] made observations in 50 healthy controls and in a total of 75 patients with PAD ranging in severity from Fontaine class I to class IV (with class IV being the most severe). Skin flowmotion was relatively rare in healthy subjects (around 10%, mean arterial pressure in the foot 132 mmHg). Its incidence (plantar side of first toe) increased to around 50% in class I and II PAD (mean arterial pressure in the foot 100 mmHg) and on to around 80% in class III and IV PAD (mean arterial pressure in the foot

75 mmHg). Furthermore, with other factors matched, skin oxygenation appeared to be better in the presences of flowmotion as compared to a situation without [49].

Similar observations were made by Hudetz et al. [25] in the rat cerebral circulation which also has a pronounced autoregulatory response. Reduction in mean arterial pressure by various methods below 90 mmHg all resulted in appearance of flow oscillations at 4–11 cpm, the amplitude of which grew with further pressure reduction. Time-averaged flow was preserved though, corresponding in this case to an intact autoregulation. Oscillations were completely abolished during cerebral vasodilatation by 5% carbon dioxide in the inspired air. Abolition of all tone by lowering pressure to very low levels was not investigated in that study, however Fujii et al. [11] found that pronounced hypotension abolishes vasomotion in another cerebral vessel, the basilar artery (for a review see [26]).

The abovementioned studies identified an association between pressure reduction and the prevalence of flowmotion, but this does not guarantee a direct causal relation between the two. Rather, some evidence point to the state within the tissue itself as a main determinant of the prevalence and characteristics of flowmotion. In the observations above from both rabbit and man, flowmotion became more prevalent as perfusion pressure was reduced. While this could be a consequence of the pressure reduction itself and its effect on the arterial wall it could also be a consequence of reduced perfusion, in turn changing the state of the tissue. That factors such as reduction in oxygen transport to the tissue may be as important a stimulus as the pressure reduction itself, was shown by Lee et al. [36]. They observed that the prevalence of flowmotion (around 3 cpm) increased from 65% under baseline conditions to 100% during hemodilution to 43% of normal hematocrit, which is equivalent to a large reduction in the oxygen transport capacity of the blood. Thorn et al. [56] noted when simultaneously recoding flow and oxygenation in the skin microcirculation of healthy individuals, that there appears to be distinct modes of flowmotion. One of these oscillations involves a fall in oxygenated hemoglobin and a simultaneous rise in deoxygenated hemoglobin. Further investigation [55], revealed what could potentially be a causal relation inducing flowmotion. A slow decline in blood mean oxygen saturation (reflected in a simultaneous rise in deoxygenated hemoglobin and fall in oxygenated hemoglobin) to a threshold value induced a consistent and rapid rise in flow, which was again followed by a slow decline. A possible interpretation of this pattern is that the tissue under resting conditions cyclically upregulates its own flow when a certain critical lower limit is approached. This must somehow involve upstream signaling, likely in the form of an electrical vascular conducted response running in the endothelium, from the capillary bed to the upstream resistance network in order to allow for a rapid and consistent increase in flow. To that end, laser-Doppler-flowmetry of flowmotion in the rabbit tenuissimus muscle has indeed been found to correlate tightly with vasomotion in upstream transverse arterioles [50].

In a different tissue, the rat testis, Lysiak et al. [37] measured flow and oxygen tension (with laser Doppler-flowmetry and an oxygen electrode) simultaneously in the interstitium and found the two signals to be completely phase-locked at 12 cpm

(although with different amplitude relative to baseline). Others have identified oscillations in the rat testis with similar characteristics, and, notably, such oscillations are local and vary in characteristics across the tissue [8]. As pointed out by Lysiak et al. [37], the normal interstitial oxygen pressure of the testis is very low (in the range of half of that found in other tissues); probably the testis interstitium is a protected environment, also when it comes to avoiding high oxygen levels which might increase production of reactive oxygen species.

These observations raises the question if, on a theoretical basis, the presence of flowmotion per se is beneficial to the tissue. Goldman and Popel [15] simulated the effect on tissue oxygenation of oscillations in blood flow velocity, in a network of skeletal muscle capillaries. Under "resting" conditions when the amount of inflowing oxygen is plenty relative to oxygen consumption rate, there is no effect of oscillations in flow velocity (in any combination of amplitude and frequency) and throughout the tissue oxygen tension remains sufficient. Increasing tissue metabolic rate while preserving the same flow increases heterogeneity in tissue oxygenation since the delivery of oxygen is not uniformly efficient in a network with a naturally heterogeneous structure. In this situation, flowmotion appear to alleviate the hypoxia of undersupplied regions. The most efficient frequency in this system was in the range 1.5–3 cpm in agreement with the abovementioned observations from skeletal muscle [50] and skin [52]. Introducing an oxygen buffer into the model in the form of myoglobin removes the beneficial effect of vasomotion, however as pointed out by the authors, many tissues have little or no myoglobin.

There are indications that vasomotion may also promote drainage of the interstitium. Sakurai and Terui [48] induced vasomotion in the rabbit ear microcirculation by electrical stimulation of the cervical sympathetic nerve and studied the clearance of radioactive Cr-EDTA injected into the interstitium. Stimulating the nerve while keeping the ambient temperature in the interval 25–35 °C consistently induced vasomotion (around 3 cpm) and a reduction in total flow. Below or above this temperature interval, stimulation caused the same reduction in total flow but without vasomotion. The radioactive isotope was however, cleared from the tissue at a double rate in the presence of vasomotion. Also based on calculations of transcapillary fluxes it has been suggested that during pressure fluctuations caused by vasomotion there will be an increased drainage of the interstitium [27]. As pointed out by Intaglietta [28] an increased drainage is required to increase intravascular volume during systemic hypotension which, as outlined above, is a state associated with increased prevalence of vasomotion. Likely, vasomotion is further stimulated in this situation due to release of the vasoactive substance vasopressin [14]. There is, however, a general need for experiments, which can critically test the hypothesis that vasomotion acts to preserve tissue homeostasis and functionality by enhancing uniform oxygen delivery and removal of waste products. Ideally, this would be experiments that could report tissue parameters that reflects deviation from normal tissue homeostasis under various conditions. The parameters measured could be e.g. oxygen- and carbon dioxide pressures, pH, interstitial lactic acid and potassium concentration etc. but also tissue function such as contractility or conductivity in electrically coupled tissues. The conditions investigated could be a gradual reduction in tissue perfusion

pressure. The intervention could be a situation with abolition of vasomotion versus control. Clearly, this requires that we fully understand the pathways which leads to vasomotion (and consequently flowmotion), in order to selectively block vasomotion without affecting tissue metabolism by the intervention itself. Such data would provide valuable input to the discussion of the consequences of vasomotion.

There are numerous examples of spontaneous or induced vasomotion in isolated vessels (e.g. Peng et al. [43], Gustafsson et al. [17, 20], Broegger et al. [5], Rahman et al. [45], reviewed in [2]). Since isolated vessels are devoid of influence from other vessels, nerves and surrounding tissue, self-sustained oscillations must, as noted above, be an intrinsic property of the vascular wall. The ubiquitous presence of vasomotion across species and tissues suggests that, rather than being a question of ability per se to oscillate it is a question of which set of conditions should be present for a given type of vessel to oscillate. Thus, the oscillatory ability may or may not, be evoked under the specific conditions that prevail in a given tissue at a given time. Simulation studies show that myogenic reactivity in a network of vessels may in itself be enough to elicit complex and self-sustained oscillatory behavior [57], and, as discussed above, indeed intraluminal pressure has been shown to modulate vasomotion characteristics [3]. When it comes to causal relations and consequences however, it is helpful that some studies report the occurrence of flowmotion (as the consequence of vasomotion) together with independently measured parameters such as tissue oxygenation or tracer clearance. For instance, it appears that flowmotion become more prevalent and pronounced as autoregulation reaches its lower limit, perfusion heterogeneity increases and the tissue experiences risk of focally insufficient oxygenation. In some tissues, a life on the edge of insufficient flow appear be the normal state although likely for different reasons in different tissues. In the skin, minimal perfusion under baseline conditions could be an adaptation to avoid heat-loss at rest, whereas in the testis it may, as described above, represent a specific adaptation to avoid high oxygen pressures. Whatever the reason, the tissue faces the same problem: with a heterogeneous distribution network, approaching the lower limit of sufficient perfusion increases the risk of some regions experiencing hypoxia for periods intolerable for the tissue cells. In this situation however, the different stimuli (e.g. accumulation of metabolites, fall in pH, fall in oxygen tension) seem to increasingly converge to push the vascular wall from a non-oscillatory and into an oscillatory domain. While, as outlines above, an oscillating flow may increase the local delivery of oxygen and drainage of the interstitium, it may also have a more direct effect. By periodically forcing the hydraulic resistance up in some parts of the network and simultaneously down in others, flow is forced along constantly shifting flow routes (briefly reviewed in [28]). In this way the effect of structural heterogeneity in the network is mitigated and the risk of some tissue areas experiencing long-lasting hypoxia or ischemia is reduced. Below a certain critical perfusion pressure however, total flow is insufficient to match total tissue demand in all cases. Eventually, as shown by Schmidt [49] and others, vasomotion/flowmotion tend to disappear when pressure becomes very low. In this situation, where the microvascular bed relaxes completely due to absence of myogenic activation and buildup of tissue waste products, flowmotion would probably be of little significance anyway.

In summary, there seem to be some evidence suggesting that vasomotion and the derived flowmotion can expand the pressure range over which a heterogeneous network can supply the surrounding tissue with sufficient flow.

References

1. C. Aalkjaer, H. Nilsson, Vasomotion: Cellular background for the oscillator and for the synchronization of smooth muscle cells. Br. J. Pharmacol. **144**(5), 605–616 (2005)
2. C. Aalkjaer, D. Boedtkjer, V. Matchkov, Vasomotion—what is currently thought? Acta. Physiol. (Oxf). **202**(3), 253–269 (2011)
3. H. Achakri, N. Stergiopulos, N. Hoogerwerf, D. Hayoz, H.R. Brunner, J.J. Meister, Intraluminal pressure modulates the magnitude and the frequency of induced vasomotion in rat arteries. J. Vasc. Res. **32**(4), 237–246 (1995)
4. L. Bernardi, M. Rossi, S. Leuzzi, E. Mevio, G. Fornasari, A. Calciati, et al., Reduction of 0.1 Hz microcirculatory fluctuations as evidence of sympathetic dysfunction in insulin-dependent diabetes. Cardiovasc. Res. **34**(1), 185–191 (1997)
5. T. Broegger, J.C. Jacobsen, D.V. Secher, D.M. Boedtkjer, H. Kold-Petersen, F.S. Pedersen, et al. Bestrophin is important for the rhythmic but not the tonic contraction in rat mesenteric small arteries. Cardiovasc. Res. **91**(4), 685–693 (2011)
6. C.W. Chen, C.H. Lee, T.R. Hsiue, H.Y. Chang, Vasomotion in rat diaphragm microcirculation at rest and during stepwise arterial pressure reduction. Acta. Physiol. Scand. **161**(3), 281–288 (1997)
7. V. Dam, D.B. Boedtkjer, J. Nyvad, C. Aalkjaer, V. Matchkov, TMEM16A knockdown abrogates two different Ca2+-activated Cl− currents and contractility of smooth muscle in rat mesenteric small arteries. Pflugers Arch. Eur. J. Physiol. **466**(7), 1391–1409 (2014)
8. J.E. Damber, O. Lindahl, G. Selstam, T. Tenland, Rhythmical oscillations in rat testicular microcirculation as recorded by laser Doppler flowmetry. Acta. Physiol. Scand. **118**(2), 117–123 (1983)
9. P.Y. der Weid, J.L. Beny, Simultaneous oscillations in the membrane potential of pig coronary artery endothelial and smooth muscle cells. J. Physiol. **471**, 13–24 (1993)
10. L.Y. Di Marco, E. Farkas, C. Martin, A. Venneri, A.F. Frangi, Is Vasomotion in cerebral arteries impaired in Alzheimer's disease? J. Alzhe. Dis. JAD **46**(1), 35–53 (2015)
11. K. Fujii, D.D. Heistad, F.M. Faraci, Vasomotion of basilar arteries in vivo. Am. J. Physiol. **258**(6 Pt 2), H1829–H1834 (1990)
12. P. Gaehtgens, Why networks? Int. J. Microcirc. Clin. Exp. **11**(2), 123–132 (1992)
13. C.J. Garland, Influence of the endothelium and alpha-adrenoreceptor antagonists on responses to noradrenaline in the rabbit basilar artery. J. Physiol. **418**, 205–217 (1989)
14. R. Gerstberger, J.U. Meyer, R. Rettig, M. Printz, M. Intaglietta, Regulatory role of vasoactive peptides in subcutaneous skin microcirculation of the hamster. Int. J. Microcirc. Clin. Exp. **7**(1), 3–14 (1988)
15. D. Goldman, A.S. Popel, A computational study of the effect of vasomotion on oxygen transport from capillary networks. J. Theor. Biol. **209**(2), 189–199 (2001)
16. T.M. Griffith, D.H. Edwards, Mechanisms underlying chaotic vasomotion in isolated resistance arteries: roles of calcium and EDRF. Biorheology **30**(5–6), 333–347 (1993)
17. H. Gustafsson, Vasomotion and underlying mechanisms in small arteries. An in vitro study of rat blood vessels. Acta. Physiol. Scand. **149**(Suppl. 614), 1–44 (1993)
18. H. Gustafsson, H. Nilsson, Rhythmic contractions of isolated small arteries from rat: role of calcium. Acta. Physiol. Scand. **149**(3), 283–291 (1993)
19. H. Gustafsson, M.J. Mulvany, H. Nilsson, Rhythmic contractions of isolated small arteries from rat: influence of the endothelium. Acta. Physiol. Scand. **148**, 153–163 (1993)

20. H. Gustafsson, A. Bulow, H. Nilsson, Rhythmic contractions of isolated, pressurized small arteries from rat. Acta. Physiol. Scand. **152**(2), 145–152 (1994)
21. R.E. Haddock, C.E. Hill, Differential activation of ion channels by inositol 1,4,5-trisphosphate (IP_3)- and ryanodine-sensitive calcium stores in rat basilar artery vasomotion. J. Physiol. **545**(Pt 2), 615–627 (2002)
22. R.E. Haddock, G.D. Hirst, C.E. Hill, Voltage independence of vasomotion in isolated irideal arterioles of the rat. J. Physiol. **540**(Pt 1), 219–229 (2002)
23. N. Hayashida, K. Okui, Y. Fukuda, Mechanism of spontaneous rhythmic contraction in isolated rat large artery. Jpn. J. Physiol. **36**(4), 783–794 (1986)
24. U. Hoffmann, U.K. Franzeck, A. Bollinger, Low frequency oscillations of skin blood flux in peripheral arterial occlusive disease. VASA Zeitschrift Fur Gefasskrankheiten **23**(2), 120–124 (1994)
25. A.G. Hudetz, R.J. Roman, D.R. Harder, Spontaneous flow oscillations in the cerebral cortex during acute changes in mean arterial pressure. J. Cereb. Blood Flow Metabol.: Offical J. Int. Soc. Cereb. Blood Flow Metabol. **12**(3), 491–499 (1992)
26. A.G. Hudetz, B.B. Biswal, H. Shen, K.K. Lauer, J.P. Kampine, Spontaneous fluctuations in cerebral oxygen supply. An introduction. Adv. Experi. Medi. Biol. **454**, 551–559 (1998)
27. M. Intaglietta, Vasomotor activity, time-dependent fluid exchange and tissue pressure. Microvasc. Res. **21**(2), 153–164 (1981)
28. M. Intaglietta, Arteriolar vasomotion: implications for tissue ischemia. Blood Vess. **28**(Suppl 1), 1–7 (1991)
29. J.C. Jacobsen, C. Aalkjaer, H. Nilsson, V. Matchkov, J. Freiberg, N.H. Holstein-Rathlou, A model of smooth muscle cell synchronization in the arterial wall. Am. J. Physiol. Heart Circ. Physiol. **293**, H229–H237 (2007)
30. J.C. Jacobsen, C. Aalkjaer, H. Nilsson, V.V. Matchkov, J. Freiberg, N.H. Holstein-Rathlou, Activation of a cGMP-sensitive calcium-dependent chloride channel may cause transition from calcium waves to whole cell oscillations in smooth muscle cells. Am. J. Physiol. Heart Circ. Physiol. **293**(1), H215–H228 (2007)
31. T.W. Jones, Discovery that the veins of the bat's wing are endowed with rhythmical contractility and that onward flow of blood is accelerated by each contraction. Phil. Trans. Roy. Soc. Lond. **142**, 131–136 (1852)
32. A. Krogh, The number and distribution of capillaries in muscles with calculations of the oxygen pressure head necessary for supplying the tissue. J. Physiol. **52**(6), 409–415 (1919)
33. P. Kvandal, S.A. Landsverk, A. Bernjak, A. Stefanovska, H.D. Kvernmo, K.A. Kirkeboen, Low-frequency oscillations of the laser Doppler perfusion signal in human skin. Microvasc. Res. **72**(3), 120–127 (2006)
34. S.A. Landsverk, P. Kvandal, A. Bernjak, A. Stefanovska, K.A. Kirkeboen, The effects of general anesthesia on human skin microcirculation evaluated by wavelet transform. Anesth. Analg. **105**(4), 1012–1019, table (2007)
35. C.Y. Lee, V.L. Bautch, Ups and downs of guided vessel sprouting: the role of polarity. Physiology (Bethesda, Md) **26**(5), 326–333 (2011)
36. C.H. Lee, H.Y. Chang, C.W. Chen, T.R. Hsiue, Vasomotion enhanced by normovolemic hemodilution in rat diaphragmatic microcirculation. J. Formosan Medi. Assoc. [Taiwan yi zhi] **104**(9), 630–638 (2005)
37. J.J. Lysiak, Q.A. Nguyen, T.T. Turner, Fluctuations in rat testicular interstitial oxygen tensions are linked to testicular vasomotion: persistence after repair of torsion. Biol. Reprod. **63**(5), 1383–1389 (2000)
38. V. Matchkov, C. Aalkjaer, H. Nilsson, A novel cGMP-dependent calcium-activated chloride current from the mesenteric resistance artery. J. Gen. Physiol. **122**, 40a (2003)
39. V.V. Matchkov, A. Rahman, H. Peng, H. Nilsson, C. Aalkjaer, Junctional and nonjunctional effects of heptanol and glycyrrhetinic acid derivates in rat mesenteric small arteries. Br. J. Pharmacol. **142**(6), 961–972 (2004)

40. V.V. Matchkov, P. Larsen, E.V. Bouzinova, A. Rojek, D.M. Boedtkjer, V. Golubinskaya et al., Bestrophin-3 (vitelliform macular dystrophy 2-like 3 protein) is essential for the cGMP-dependent calcium-activated chloride conductance in vascular smooth muscle cells. Circ. Res. **103**(8), 864–872 (2008)
41. M.J. Mulvany, H. Nilsson, J.A. Flatman, Role of membrane potential in the response of rat small mesenteric arteries to exogenous noradrenaline stimulation. J. Physiol. **332**, 363–373 (1982)
42. G. Osol, W. Halpern, Spontaneous vasomotion in pressurized cerebral arteries from genetically hypertensive rats. Am. J. Physiol. **254**(1 Pt 2), H28–H33 (1988)
43. H. Peng, V. Matchkov, A. Ivarsen, C. Aalkjaer, H. Nilsson, Hypothesis for the initiation of vasomotion. Circ. Res. **88**(8), 810–815 (2001)
44. B.M. Prior, H.T. Yang, R.L. Terjung, What makes vessels grow with exercise training? J. Appl. Physiol. (Bethesda, Md: 1985) **97**(3), 1119–1128 (2004)
45. A. Rahman, V. Matchkov, H. Nilsson, C. Aalkjaer, Effects of cGMP on coordination of vascular smooth muscle cells of rat mesenteric small arteries. J. Vasc. Res. **42**(4), 301–311 (2005)
46. M. Rossi, S. Bertuglia, M. Varanini, A. Giusti, G. Santoro, A. Carpi, Generalised wavelet analysis of cutaneous flowmotion during post-occlusive reactive hyperaemia in patients with peripheral arterial obstructive disease. Biomedi. & Pharmaco. [Biomedecine & pharmacotherapie] **59**(5), 233–239 (2005)
47. M. Rossi, A. Carpi, M.C. Di, F. Galetta, G. Santoro, Spectral analysis of laser Doppler skin blood flow oscillations in human essential arterial hypertension. Microvasc. Res. **72**(1–2), 34–41 (2006)
48. T. Sakurai, N. Terui, Effects of sympathetically induced vasomotion on tissue-capillary fluid exchange. Am. J. Physiol. Heart Circ. Physiol. **291**(4), H1761–H1767 (2006)
49. J.A. Schmidt, *Periodic Hemodynamics in Health and Disease* (Springer, Heidelberg, Berlin, 1996)
50. J.A. Schmidt, P. Borgstrom, M. Intaglietta, The vascular origin of slow wave flowmotion in skeletal muscle during local hypotension. Int. J. Microcirc. Clin. Exp. **12**(3), 287–297 (1993)
51. J.A. Schmidt, P. Borgstroem, S.P. Bruttig, A. Fronek, M. Intaglietta, Vasomotion as a flow-dependent phenomenon. Prog. Appl. Microcircul. **20**, 34–51 (1993) Basel: Karger
52. J.A. Schmidt, P. Borgström, G.P. Firestone, P.V. Wichert, M. Intaglietta, A. Fronek, Periodic hemodynamics (flow motion) in peripheral arterial occlusive disease. J. Vasc. Sur. **18**(2), 207–215 (1993)
53. S.S. Segal, J.L. Beny, Intracellular recording and dye transfer in arterioles during blood flow control. Am. J. Physiol. **263**(1 Pt 2), H1–H7 (1992)
54. A. Stefanovska, Coupled oscillators: complex but not complicated cardiovascular and brain interactions. Conf. Proc. Ann. Int. Conf. IEEE Eng. Medi. Biol. Soc. **1**, 437–440 (2006)
55. C.E. Thorn, H. Kyte, D.W. Slaff, A.C. Shore, An association between vasomotion and oxygen extraction. Am. J. Physiol. Heart Circ. Physiol. **301**(2), H442–H449 (2011)
56. C.E. Thorn, S.J. Matcher, I.V. Meglinski, A.C. Shore, Is mean blood saturation a useful marker of tissue oxygenation? Am. J. Physiol. Heart Circ. Physiol. **296**(5), H1289–H1295 (2009)
57. M. Ursino, S. Cavalcanti, S. Bertuglia, A. Colantuoni, Theoretical analysis of complex oscillations in multibranched microvascular networks. Microvasc. Res. **51**(2), 229–249 (1996)
58. D.F. Van Helden, Pacemaker potentials in lymphatic smooth muscle of the guinea-pig mesentery. J. Physiol. **471**, 465–479 (1993)
59. D.F. van Helden, M.S. Imtiaz, Venous vasomotion. Adv. Exp. Med. Biol. **1124**, 313–328 (2019)

Chapter 17
Biological Oscillations of Vascular Origin and Their Meaning: In Vivo Studies of Arteriolar Vasomotion

Antonio Colantuoni and Dominga Lapi

Abstract Oscillations in vessel diameter were reported by Jones (Circ. Res. 15:279–287, [15]) in the bat wing venular microcirculation, while Krogh (A Contribution to the Physiology of the Capillaries. Nobel Lecture, [16]) suggested the capillary recruitment to increase blood flow in muscle tissue. Nicoll and Webb (Angiology 6:291–308, [23]) were the first to define vasomotion as the outstanding motor phenomenon in the vasculature, investigating microcirculation in the bat wing. A lot of data were reported during the decades 70' and 80' of the last century. We implemented a preparation (skin fold chamber window) to observe subcutaneous vessels without anesthesia and acute surgical trauma in golden hamsters. We observed rhythmic changes in arteriolar diameter, with increase in amplitude and frequency from larger to smaller arterioles. We noted that at branchings there was a change in vasomotion frequency with significant reduction in arteriolar diameter. We further developed our in vivo preparation to investigate the microvascular networks in dorsal skin muscle (Cutaneous Maximus) in golden hamsters. We characterized the arterioles according to Strahler's ordering scheme, starting from order 1 arterioles up to largest in the preparation (order 5: 39.6 ± 5.7 μm), that were arcade arterioles, i.e. arterio-arteriolar anastomoses, functioning as a blood reservoir to feed the muscle tissue, through terminal arteriolar trees. These arterioles gave origin to the capillaries and presented vasomotion with occlusion of the lumen (0.14 ± 0.04 Hz), causing intermittent capillary blood flow. Furthermore, the arteriolar oscillations were investigated in the rat cranial window preparation, where we detected arteriolar oscillation in the same range as reported by Aneta Stefanowska in humans by the laser Doppler technique. In conclusion, the regulation of tissue perfusion takes place in the microcirculation, where arterioles induce an "opening and closing mechanism" distribution of blood flow to the capillary networks.

A. Colantuoni (✉) · D. Lapi
Department of Clinical Medicine and Surgery, Federico II University Medical School, Via Pansini 5, Naples 80131, Italy
e-mail: antonio.colantuoni@unina.it

D. Lapi
e-mail: dominga.lapi@unina.it

A. Stefanovska and P. V. E. McClintock (eds.), *Physics of Biological Oscillators*, Understanding Complex Systems,
https://doi.org/10.1007/978-3-030-59805-1_17

17.1 Historical Background

Oscillations in vessel diameter were reported as early as 1852 by Jones in the bat wing, where rhythmic contractions of venular vessels with fast frequency (more than 20 cycles per min, cpm) were described [27]. However, we had to wait until the new century, when Krogh introduced the concept of capillary recruitment in [16, 17], due to precapillary sphincters, and Clark and Clark [6] described in an in vivo preparation (rabbit ear chamber) calibre changes in minute vessels. They observed constriction and dilation of arterioles with a frequency in the range 2–3 cpm.

Chambers and Zweifach [5] reported oscillations in capillary blood flow, but the fundamental finding was the organization of the microcirculation around the metarteriole in the mesentery of frog and other experimental models. Nicoll and Webb [23] for the first time defined vasomotion as the outstanding motor phenomenon in the vasculature. They reported the rhythmic changes in diameter of venules and arterioles describing the microcirculation in the bat wing. However, the effects of arteriolar diameter changes on vascular tone were highlighted by Folkow [14], who suggested that many points in the arterial circulation endowed with peripheral pacemakers are able to regulate vascular tone through contraction of vascular smooth muscle cells.

Wiederhielm and Weston [26] reported irregular vasomotion in small arteries and arterioles, but regular activity in metarterioles and precapillary sphincters in the same model of bat wing. Further data on vasomotion or changes in blood flow were presented in the 70's and 80's of the last century in rabbit tenuissimus muscle [21], isolated sartorius muscle [25], isolated arterioles of the hamster cheek pouch [12], cremaster muscle of decerebrate rat [13]. Therefore, arteriolar vasomotion was detected in different tissues, while isolated arterioles were able to constrict and dilate: all data indicated that rhythmic changes in arteriolar diameter occur with and without anesthesia, characterized by frequencies quite in the same ranges.

17.2 Vasomotion in Hamster Dorsal Skin Fold Window Preparation

In the laboratory of Marcos Intaglietta we implemented the dorsal skin fold chamber window preparation to observe microcirculation in hamsters without anesthesia and acute surgical trauma [7, 8]. We defined the pattern of arteriolar rhythmic diameter changes along the arteriolar networks in subcutaneous tissue, while we did not detect diameter changes in venular vessels. It was of interest that branching points were present in discrete points of the arteriolar networks and from these branching points originated oscillations in vessel diameter which were effective in producing oscillations in blood flow in downstream vessels right down to the capillaries. The amplitude of these diameter changes was different according to arteriolar diameter: from the largest arterioles (15–30% of mean diameter) down to the smallest ones (85–100% of mean diameter). The frequencies of these oscillations were inversely

related to arteriolar diameter, because the smallest arterioles (7.05 ± 2.20 μm) revealed the highest frequencies (9.47 ± 2.89 cpm). Moreover, we reported that nor-epinephrine and epinephrine increase the frequency of vasomotion, and vasomotion was reduced or abolished by isoproterenol, phentolamine, adenosine and verapamil [9]. We observed, furthermore, that vasomotion frequencies changed at arteriolar bifurcations [10]. These data indicate that all arterioles presented oscillations in diameter from the largest to the smallest, where branching points appeared able to generate constriction and dilation of the vessels with complex overlapping of waves regulating capillary blood flow. However, in [4] Bouskela and Grampp reported data derived from hamster cheek pouch where they did not find any relationship between diameters and frequencies, with different changes in diameter (2–10 μm) and frequencies in the range 3–15 cpm. In this case, arteriolar vasomotion appeared as irregular vasomotor phenomenon difficult to explain. We could suggest that surgical trauma and anesthesia might have influenced vasomotion patterns. In our hamster cheek pouch preparations we did not observe regular vasomotion [11], otherwise detected in unanesthetized hamster window preparation. In this preparation we investigated the changes in arteriolar vasomotion induced by anesthesia and we observed disappearance of the arteriolar rhythmic diameter changes. After a while there was a recovery of arteriolar vasomotion in alpha-chloralose anesthetized animals [8]. However, improvements in methods of signal processing allowed us to identify all frequency components in long-lasting recordings of pial arterioles in anesthetized rats [19].

More recently, there have been several reports on vasomotion, especially in mesenteric arterioles, and the molecular mechanisms involved [1, 24], indicating that ion fluxes are able to induce vasomotion and suggesting which mechanisms are operative in vascular smooth muscle cells (a review of these mechanistic areas is beyond the scope of this chapter and is dealt with elsewhere: see Chap. 20).

We investigated the changes in arteriolar vasomotion frequency and amplitude in hamster skin fold chamber window preparation under hypoxia and hyperoxia, reporting different responses between larger and smaller arterioles [2]. Hypoxia (8, 11 and 15% oxygen gas mixture inspiration), indeed, caused an increase in vasomotion frequency, a decrease in mean diameter and in capillary blood flow. These effects were more pronounced with 8 and 11% oxygen gas mixture: high frequency vasomotion shifted from order 1 and 2 to order 3 arterioles (24 ± 4 cpm, 11% oxygen gas mixture). Hyperoxia (100% oxygen gas mixture) induced constriction of the smallest vessels (order 1 and 2), decrease in mean diameter and in vasomotion frequency, while order 3 arterioles dilated.

Improving our model, we implemented the hamster skin fold window preparation to investigate the microvascular networks in the hamster skeletal muscle (Cutaneous Maximus) [20]. We characterized the micro-arrangement of arterioles feeding the muscle, where we found arterio-arteriolar anastomoses, called arcade arterioles, just overlapping the layer of the skeletal muscle cells, from where originated the arterioles penetrating among the muscle cells and feeding the skeletal tissue. Therefore, it is reasonable to suggest that a blood reservoir (arcading system) is operative to feed blood to cells according to their metabolic requirements. The terminal branching

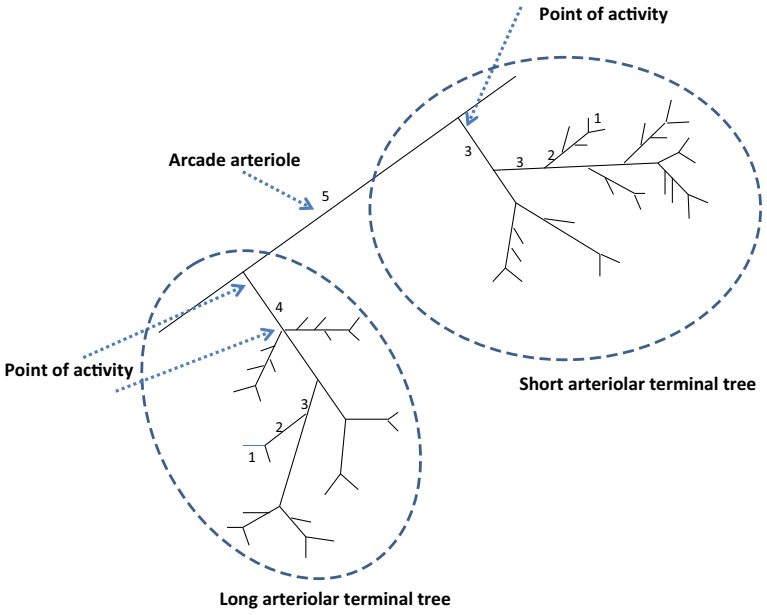

Fig. 17.1 Scheme of a microvascular network in hamster skeletal muscle (Cutaneous Maximus). The arcade arteriole is an order 5 arteriole with two branchings: the long terminal arteriolar tree and the short terminal arteriolar tree. At branching, the long and short terminal trees present an active point of contraction and dilation. In the long terminal arteriolar tree, there is at least another point of activity at the first branching of order 4 arteriole

arterioles were differentiated in short and long terminal arteriolar trees, where the long ones were characterized by larger vessels undergoing constriction and dilation from the branching point (Fig. 17.1). This activity was conducted to all daughter vessels with different amplitude (50–70% in order 4, 90–100% in order 2 and 1) and caused intermittent blood flow in capillaries, according to the constriction or dilation of the smallest arterioles. The short terminal trees were characterized by order 3 arterioles (diameter: 19.4 $\pm$ 3.0 μm) spreading from arcading arterioles (diameter: 39.6 $\pm$ 5.7 μm) and able to completely constrict, inducing opening and closing of downstream arterioles. Therefore, there was consequent intermittent blood flow in all capillaries originating from the smallest order 1 arterioles, present in the terminal tree. These rhythmic diameter changes were observed in awake animals without anaesthesia, with complex superposition of waves spreading from larger vessels up to the terminal arterioles.

The microvascular scenario could be summarized as the interplay of larger arteriolar anastomoses and the terminal branching vessels. The arcade arterioles full of blood facilitate the blood supply to the skeletal muscle cells; these vessels are characterized by slow oscillations in diameter and repeated inversion in the direction of blood flow during a minute time interval. These arterioles gave origin to terminal arteriolar trees, that presented a point of activity at their beginning, where a mechanism

"switch on and off" was effective in opening or closing the branching vessel, regulating the volume of blood perfusing the active skeletal muscle cells. The difference between terminal order 4 and order 3 arterioles, branching from arcade arterioles, was in the frequency rate, higher in order 3 than in order 4 vessels. Moreover, order 3 arterioles completely constricted during the vasomotion cycle, and this constriction wave was conducted through the daughter arterioles up to the capillaries (usually 24 ± 9, for each terminal unit). Therefore, all the capillaries presented stop and go blood flow, according to the activity of parent order 3 arteriole. The long terminal trees, conversely, originated 45 ± 6 capillaries, where the stop and go mechanism was asynchronous, due to the different points of activity in the daughter vessels spreading from the parent order 4 arteriole. These features permit to increase the blood volume supply to the tissue by 273 and 239% compared to the baseline, on the average, for the short and long terminal trees, respectively. Therefore, it is reasonable to suggest that frequency oscillations in the ranges 0.01–0.08 and 0.08–0.16 derive from arteriolar vasomotion, i.e. from mechanisms regulating the blood flow distribution to the tissues. It is worth noting that larger arterioles are densely innervated and their activity is largely influenced by sympathetic nervous system discharge, while smaller arterioles are most influenced by features of smooth muscle cells endowed in the arteriolar walls.

17.3 Vasomotion in Rat Closed Cranial Window

In another experimental preparation, the rat closed cranial window, under α-chloralose anaesthesia, we recorded rhythmic diameter changes in pial arterioles observed through the window localized on the left parietal cortex [19]. We recorded the rhythmic changes for 30 min and processed the diameter changes with the generalized short time Fourier transform (GSTFT) to evaluate the frequency components. We detected six components in the rhythmic diameter change recordings. Our aim was to characterize each component; consequently, we used many substances to stimulate or inhibit the endothelial or smooth muscle factors: acetylcholine, papaverine, Nω-Nitro-L-arginine (L-NNA), inhibitor of eNOS; indomethacin (INDO), inhibitor of prostaglandin endoperoxidase; charybdotoxin plus apamin, inhibitors of endothelium-derived hyperpolarizing factor (EDHF). We observed that under baseline conditions, the range of the first component was: 0.001–0.0095 Hz (0.06–0.57 cpm); of the second: 0.0095–0.02 Hz (0.57–1.2 cpm); of the third: 0.02–0.06 Hz (1.2–3.6 cpm); of the fourth: 0.06–0.2 Hz (3.6–12 cpm); of the fifth: 0.2–2.0 Hz (12–120 cpm) and of the sixth: 2.0–4.5 Hz (120–270 cpm) (Table 17.1). The sixth component had the highest power spectral density in order 2 and 3 arterioles (mean diameter: 23.8 ± 1.4 μm and 33.5 ± 1.8 μm, respectively), followed by the fourth, third, second and first component. In order 4 vessels (mean diameter: 43.7 ±1.4) the sixth component showed the highest spectral density, but there was an increase in the first and second components, while there was a decrease in third and fifth components. Our data indicate that acetylcholine caused an increase in

Table 17.1 The six frequency components detected in rat pial arterioles

Frequency components	Frequency range (Hz)	Frequency range (cpm)
ULF ultra low	0.001–0.0095	0.06–0.57
VLF very low	0.0095–0.02	0.57–1.2
ILF intermediate	0.02–0.06	1.2–3.6
LF low	0.06– 0.2	3.6–12
HF high	0.2–2.0	12–120
VHF very high	2.0–4.5	120–270

power spectral density of both the first and the second component. However, L-NNA after acetylcholine decreased the power spectral density of the second, compared to the first component. Charybdotoxin plus apamin were effective in blunting the power spectral density of the first component, while the second was not affected. After acetylcholine administration, charybdotoxin plus apamin were able to abolish the power spectral density of the first component, while the second was partially affected. Therefore, it is reasonable to conclude that the first component of arteriolar oscillation is related to the release of EDHF able to facilitate dilation of arterioles with nitric oxide, effective in causing the second component of arteriolar rhythmic diameter changes.

It is worth noting that the arterial rhythmic diameter changes, evaluated in rat pial microcirculation, presented the same frequency components as reported by Aneta Stefanovska and coworkers [18] in humans, processing laser Doppler recordings of cutaneous blood flow oscillations. Therefore, the oscillations in diameter of arterioles are related to the complex interactions on vascular smooth muscle cells of the different mechanisms involved in the regulation of blood flow distribution in the living bodies. The smooth muscle cells in the arteriolar walls receive stimulations from sympathetic nervous system discharge, respiration and heart rates and are responsive to EDHF and nitric oxide released from endothelial cells. The summation of all these factors produces the oscillatory patterns of vasomotion, the outstanding motor phenomenon in the vasculature.

After decades of experimental investigations and clinical studies, utilizing different techniques, such as in vivo videomicroscopy, laser-Doppler flowmetry and laser speckle imaging [22], available data indicate that oscillations in blood flow characterize peripheral circulation in living organisms. The oscillations in peripheral blood flow are due to several factors in humans, as previously reported [18]: it is worth noting that systemic sclerosis, largely affecting body circulation, is effective in abolishing most of these components, so that in the regulation of peripheral blood flow distribution only the heart rate-related component influences microvascular oscillations [3]. The remaining components are unable to modulate peripheral blood flow

during the late phases of the disease. The patterns of the oscillation frequencies are the same in both experimental models and humans in clinical settings.

17.4 Conclusions

In conclusion, the regulation of tissue perfusion takes place in the microcirculation, where the delivery of blood is controlled at the level of arterioles by "an opening and closing mechanism" that causes intermittent capillary blood flow which is effective in inducing an efficient delivery of nutrients to the tissue and washout of waste products. This regulation participates to the overall vascular tone which is subjected to complex and different control mechanisms, such as those exerted by endothelium-derived factors, sympathetic nervous system discharge and hormones.

References

1. C. Aalkjær, H. Nilsson, Vasomotion: cellular background for the oscillator and for the synchronization of smooth muscle cells. Br. J. Pharmacol. **144**, 605–616 (2005). https://doi.org/10.1038/sj.bjp.0706084
2. S. Bertuglia, A. Colantuoni, G. Coppini, M. Intaglietta, Hypoxia- or hyperoxia-induced changes in arteriolar vasomotion in skeletal muscle microcirculation. Am. J. Physiol. **260**, H362–H372 (1991)
3. S. Bertuglia, P. Leger, A. Colantuoni, G. Coppini, P. Bendayan, H. Boccalon, Different flow motion patterns in healthy controls and patients with Raynaud's phenomenon. Technol. Health Care **7**, 113–123 (1999)
4. E. Bouskela, W. Grampp, Spontaneous vasomotion in hamster cheek pouch arterioles in varying experimental conditions. Am. J. Physiol. **262**, H478–H485 (1992). https://doi.org/10.1152/ajpheart.1992.262.2.H478
5. R. Chambers, B.W. Zweifach, Topography and function of the mesentery capillary circulation. Am. J. Anat. **75**, 173–206 (1944)
6. E.R. Clark, E.L. Clark, Observation on living preformed blood vessels as seen in a chamber in the rabbit's ear. Am. J. Anat. **19**, 441–447 (1932)
7. A. Colantuoni, S. Bertuglia, M. Intaglietta, Quantitation of rhythmic diameter changes in arterial microcirculation. Am. J. Physiol. **246**, H508–H517 (1984)
8. A. Colantuoni, S. Bertuglia, M. Intaglietta, Effects of anesthesia on the spontaneous activity of the microvasculature. Int. J. Microcirc. Clin. Exp. **3**, 13–27 (1984)
9. A. Colantuoni, S. Bertuglia, M. Intaglietta, The effects of alpha- or beta-adrenergic receptor agonists and antagonists and calcium entry blockers on the spontaneous vasomotion. Microvasc. Res. **28**, 143–158 (1984)
10. A. Colantuoni, S. Bertuglia, M. Intaglietta, Variations of rhythmic diameter changes at the arterial microvascular bifurcations. Pflügers Arch. **403**, 289–295 (1985)
11. A. Colantuoni, S. Bertuglia, M. Intaglietta, Microvascular vasomotion: origin of laser Doppler flux motion. Int. J. Microcir. Clin. Exp. **14**, 151–158 (1994). https://doi.org/10.1159/000178823
12. B. Duling, The hamster cheek pouch as a model in microcirculation research. Eur. Respir. J. Suppl. **12**, 595s–600s (1973)
13. J.E. Faber, P.D. Harris, D.L. Wiegman, Anesthetic depression of microcirculation, central hemodynamics, and respiration in decerebrate rats. Am. J. Physiol. **243**, H837–H843 (1982). https://doi.org/10.1152/ajpheart.1982.243.6.H837

14. B. Folkow, Description of the myogenic hypothesis. Circ. Res. **15**(Suppl 1), 279–287 (1964)
15. T.W. Jones, Discovery that the veins of the bats wing (which are furnisched with valves) are endowed with rhythmical contractility and that outward flow of blood is accelerated by each contraction. Physiol. Trans. R. Soc. London. A **142**, 131, Part 1 (1852)
16. A. Krogh, *A Contribution to the Physiology of the Capillaries. Nobel Lecture*, 11 Dec 1920
17. A. Krogh, *The Anatomy and Physiology of the Capillaries* (Yale University Press, New Haven Connecticut, 1929)
18. P. Kvandal, S.A. Landsverk, A. Bernjak, A. Stefanovska, H.D. Kvernmo, K.A. Kirkebøen, Low-frequency oscillations of the laser Doppler perfusion signal in human skin. Microvasc. Res. **72**, 120–127 (2006)
19. D. Lapi, T. Mastantuono, M. Di Maro, M. Varanini, A. Colantuoni, Low-frequency components in rat pial arteriolar rhythmic diameter changes. J. Vasc. Res. **54**, 344–358 (2017). https://doi.org/10.1159/000478984
20. D. Lapi, M. Di Maro, T. Mastantuono, N. Starita, M. Ursino, A. Colantuoni, Arterial network geometric characteristics and regulation of capillary blood flow in hamster skeletal muscle microcirculation. Front. Physiol. **18**(9), 1953 (2019). https://doi.org/10.3389/fphys.2018.01953
21. L. Lindbom, R.F. Tuma, K.E. Arfors, Blood flow in the rabbit tenuissimus muscle Influence of preparative procedures for intravital microscopic observation. Acta Physiol. Scand. (1982). https://doi.org/10.1111/j.1748-1716.1982.tb06960.x
22. T. Mastantuono, N. Starita, L. Battiloro, M. Di Maro, M. Chiurazzi, G. Nasti, E. Muscariello, M. Cesarelli, L. Iuppariello, G. D'Addio, A. Gorbach, A. Colantuoni, D. Lapi, Laser speckle imaging of rat pial microcirculation during hypoperfusion-reperfusion damage. Front. Cell. Neurosci. **11**, 298 (2017). https://doi.org/10.3389/fncel.2017.00298
23. P.A. Nicoll, R.L. Webb, Vascular patterns and active vasomotion as determiners of flow through minute vessels. Angiology **6**, 291–308 (1955). https://doi.org/10.1177/000331975500600403
24. H. Nilsson, C. Aalkjaer, Vasomotion: mechanisms and physiological importance. Mol Interv. **3**(79–89), 51 (2003)
25. H. Schmid-Schonbein, Microrheology of erythrocytes, blood viscosity, and the distribution of blood flow in the microcirculation. Int Rev Physiol **9**, 1–62 (1976)
26. C.A. Wiederhielm, B.W. Weston, Microvascular, lymphatic and tissue pressure in unanesthetized mammal. Am. J. Physiol. **225**, 992–996 (1973)
27. M.P. Wiedeman, Preparation of the bat wing for in vivo microscopy. Microvasc. Res. **5**, 417–422 (1973). https://doi.org/10.1016/0026-2862(73)90058-7

Chapter 18
Phase Coherence of Finger Skin Blood Flow Oscillations Induced by Controlled Breathing in Humans

Arina V. Tankanag, Gennady V. Krasnikov, and Nikolai K. Chemeris

Abstract The influence of deep controlled breathing on phase coherence of respiratory-related skin blood flow oscillations of left and right finger-pad forefingers in 29 healthy young females was studied. Breathing was controlled on both rate (0.25, 0.16, 0.1, 0.07 and 0.05 Hz) and depth (40% of the maximal chest excursion). The correlation degree between the phases of respiratory-related skin blood flow oscillations of left and right fingers was estimated from the value of wavelet phase coherence . We obtained the significant increase of phase coherence for all analyzed frequencies of controlled breathing as compared to spontaneous one. The maximal increase was observed for controlled breathing at 0.25 Hz, at a frequency close to the spontaneous one. We suggest that the observed effects are primarily due to an increase of breathing depth. Under spontaneous breathing depth does not exceed 15% of the maximal chest excursion, while in the present study the breathing depth was 40%. The results obtained can be attributed to the effects of the autonomic nervous system on vascular tone regulation under controlled breathing .

18.1 Introduction

The respiration effect on vascular bed can be described as an amplitude modulation of the heart-synchronous pulsating signal. Spontaneous breathing is accompanied by variations in the intrathoracic pressure, which determines the dynamics of the breathing pump—blood venous return to the heart from the periphery [6, 12]. This causes a cyclic variation in the cardiac output, maintains the average arterial blood pressure and increases the activity of aortic and pulmonary baroreceptors. The latter leads to a cyclic variation of activity in the corresponding structures of autonomic

A. V. Tankanag (✉) · N. K. Chemeris
Institute of Cell Biophysics, Russian Academy of Sciences, Moscow region, Pushchino, Russian Federation
e-mail: tav@icb.psn.ru

G. V. Krasnikov
Tula State Lev Tolstoy Pedagogical University, Tula, Russian Federation

A. Stefanovska and P. V. E. McClintock (eds.), *Physics of Biological Oscillators*, Understanding Complex Systems,
https://doi.org/10.1007/978-3-030-59805-1_18

nervous system [8, 11]. The formation of respiratory-related oscillations in vascular blood flow is due to at least two mechanisms: a) passive spread of respiratory modulation of blood pressure, b) vasomotor reflexes caused by respiratory modulation of sympathetic nerve activity. Such oscillations were successfully recorded by means of laser Doppler flowmetry (LDF). Apart from spontaneous breathing, controlled one is of particular interest due to its influence on respiratory-related cardiovascular oscillations. Our previous study demonstrated that deep controlled breathing affects skin blood flow oscillation spectra [9]. Other authors reported that a deep inspiratory gasp induces almost complete shut-down of a microvascular blood flow which manifests itself as a decrease in LDF signals [1]. Thus, the respiratory-cardiovascular coupling is a complicated and timely problem. It is known that it depends on the frequency and deepness of breathing. In this work, we present a study of the influence of deep controlled breathing on phase coherence of respiratory-related skin blood flow oscillations of left and right finger-pad forefingers.

18.2 Methodology

18.2.1 Participants

29 healthy normotensive young females aged from 18 to 25 years (weight 58 ± 10 kg, height 166 ± 4 cm, arterial blood pressure 117 ± 11/69 ± 6 mm Hg, heart rate 71 ± 9 bpm) participated in the study. The participants had not taken any drugs for at least one week before the study. None of the participants smoked and they abstained from any alcohol- or caffeine-containing drinks for at least 12 h before the study. The exclusion criteria were previous history of cardiovascular diseases, diabetes and other acute and chronic illnesses. The study was approved by the local Committee for Human Biomedical Research Ethics and was carried out in accordance with the principles outlined in the 2002 *Declaration of Helsinki* of the World Medical Association. The study protocol and its purpose were explained in detail to each subject and informed consent was obtained from all subjects.

18.2.2 Measurements

The registration was initiated following a 20-min adaptation period. During the measurements the subjects were in sitting position in a quiet room at constant room temperature of 23 ± 1 °C. For each participant 7 successive recording sessions were carried out: first and last, at spontaneous breathing rate before and after all controlled regimes; and the five, in the regime of controlled breathing with different rates of enforced breathing and fixed depth. The following rates of controlled breathing were used: 0.25, 0.16, 0.1, 0.07 and 0.05 Hz. In the present study the breathing depth was

constant and amounted to 40% of the maximal chest excursion. The duration of all signals was 300 s.

The depth, form and rate of respiratory movements (pneumogram) were registered using a strip-chart detector fastened to the chest of the subject. The analog signal from the detector was digitized and displayed at the monitor. The subject adjusted the depth, form and rate of her chest excursions so that the breathing curve was superposed with a reference curve demonstrated on the monitor. As the reference, a sinusoidal curve with a given frequency and amplitude was used.

Skin blood perfusion was registered by laser Doppler flowmeter LAKK-02 (LAZMA, Russia) with two identical probes (wavelength 0.63 μm; emission power, 0.5 mW). The probes were fastened to the palmar surface of the distal phalanx of left and right forefingers. The frequency of LDF signals sampling was 16 Hz.

During every session three signals were recorded simultaneously: pneumogram and two LDF signals of left and right finger-pad skin (SBF_{left} and SBF_{right}, respectively). Figure 18.1 shows fragments of the signals registered in one of the participants under spontaneous and controlled breathing. Between the sessions persons were trained and adapted for 2–3 min to the corresponding breathing regime. If a participant had difficulties under controlling breathing or felt unwell at any stage of the examination the procedure was immediately stopped and the participant was removed from the study.

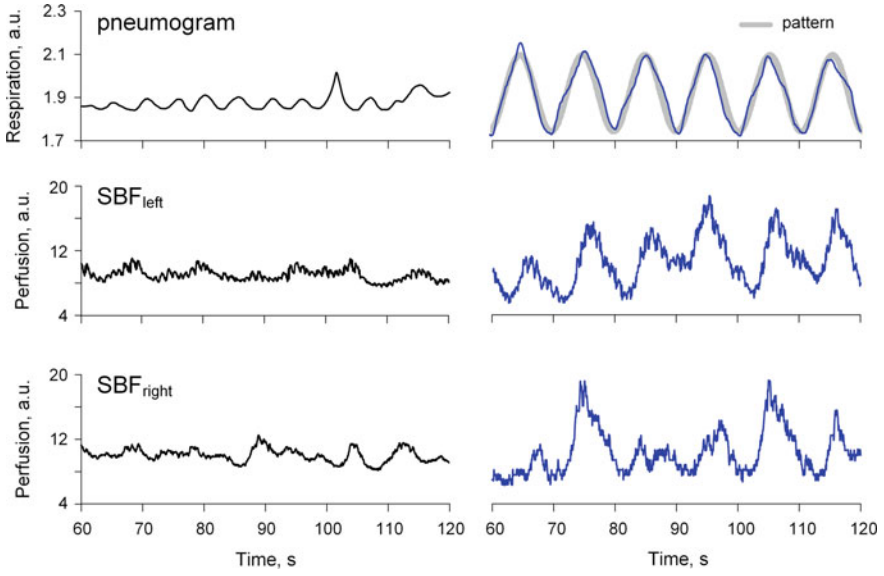

Fig. 18.1 Fragments of a pneumogram, LDF signals from left (SBF_{left}) and right (SBF_{right}) forefingers registered under spontaneous (black lines) and controlled breathing with the rate 0.1 Hz (blue lines). Drawn with the grey color on the controlled-breathing pneumogram is the reference curve defining the breathing profile

18.2.3 Data Analysis

The correlation degree between the phases of respiratory-related skin blood flow oscillations of left (SBF_{left}) and right (SBF_{right}) fingers was estimated from the value of wavelet phase coherence [3, 14, 17–19, 21, 22]. We chose the complex valued Morlet wavelet $\Psi(t) = e^{i\omega_0 t}e^{(-t^2/2)}$. For each signal a spectral function $X(\omega_k, t_n) = a_{k,n} + ib_{k,n}$ was determined, describing the spectral properties of the *x(t)* signal in the time–frequency domain. The phase difference for a pair of signals $x_1(t)$ and $x_2(t)$ at any time point t_n and frequency ω_k was calculated, where $x_1(t)$ and $x_2(t)$ were SBF_{left} and SBF_{right}, respectively. The coefficients were determined as

$$\cos(\Delta\varphi_{k,n}) = \frac{a_{1k,n}a_{2k,n} + b_{1k,n}b_{2k,n}}{\sqrt{a_{1k,n}^2 + b_{1k,n}^2}\sqrt{a_{2k,n}^2 + b_{2k,n}^2}}, \quad \sin(\Delta\varphi_{k,n}) = \frac{b_{1k,n}a_{2k,n} - a_{1k,n}b_{2k,n}}{\sqrt{a_{1k,n}^2 + b_{1k,n}^2}\sqrt{a_{2k,n}^2 + b_{2k,n}^2}},$$

and averaged over the whole signal length (N)

$$\langle\cos(\Delta\varphi_{k,n})\rangle = \frac{1}{N}\sum_{n=1}^{N}\cos(\Delta\varphi_{k,n}), \quad \langle\sin(\Delta\varphi_{k,n})\rangle = \frac{1}{N}\sum_{n=1}^{N}\sin(\Delta\varphi_{k,n}).$$

Subsequently an averaged over time wavelet phase coherence was calculated for each analyzed frequency ω_k

$$C_\varphi(\omega_k) = \sqrt{\langle\cos(\Delta\varphi_{k,n})\rangle^2 + \langle\sin(\Delta\varphi_{k,n})\rangle^2}.$$

The $C_\varphi(\omega_k)$ function takes values from 0 to 1, containing the information on the degree of phase coherence of the two signals $x_1(t)$ and $x_2(t)$ at frequency ω_k.

The statistical analysis of the results obtained was carried out with SigmaPlot 13.0 software (Systat Software, Inc., 2014). Nonparametric statistical tests were performed to avoid any assumption of normality. The Wilcoxon test was used to estimate the significance of differences between the wavelet phase coherence values obtained in spontaneous breathing and controlled regimes. The differences were considered statistically significant at $p < 0.05$.

18.3 Results

Firstly, we tested reversibility of the breathing practices. The Fig. 18.2 presented the phase coherence values for SBF_{left}–SBF_{right} pair under spontaneous breathing before and after all controlled breathing tests. There are no differences between phase coherence calculated for oscillations registered initially and after all breathing practices.

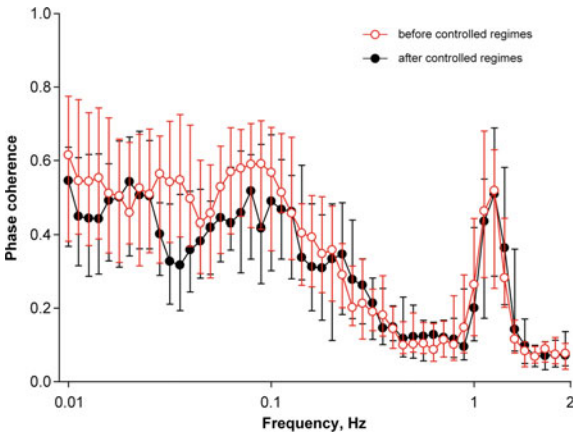

Fig. 18.2 Phase coherence of skin blood flow oscillations of left and right fingers under spontaneous breathing before (red color) and after (black color) controlled breathing practices

Below we provide the results of the analysis of the influence of controlled breathing with different frequencies on the phase coherence between SBF_{left}–SBF_{right} pair (Fig. 18.3). One can see that all breathing regimes caused a significant increase in phase coherence values at the appropriate frequency.

To estimate the influence of the controlled breathing on phase correlation between respiratory-related blood flow oscillations of left and right finger skin, we calculated the ratio of the phase coherence value at defined frequency of controlled breathing to the value at the same frequency during spontaneous breathing. The results are

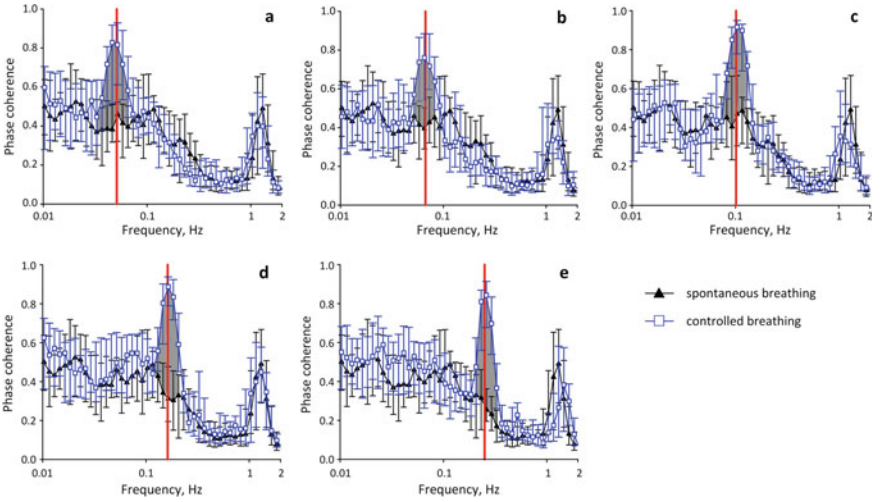

Fig. 18.3 Phase coherence of skin blood flow oscillations of left and right fingers under spontaneous (black color) and controlled (blue color) breathing with the following frequencies: 0.05 Hz (**a**), 0.07 Hz (**b**), 0.10 Hz (**c**), 0.16 Hz (**d**) and 0.25 Hz (**e**). Vertical red lines correspond breathing rates. Areas of significant changes are grey

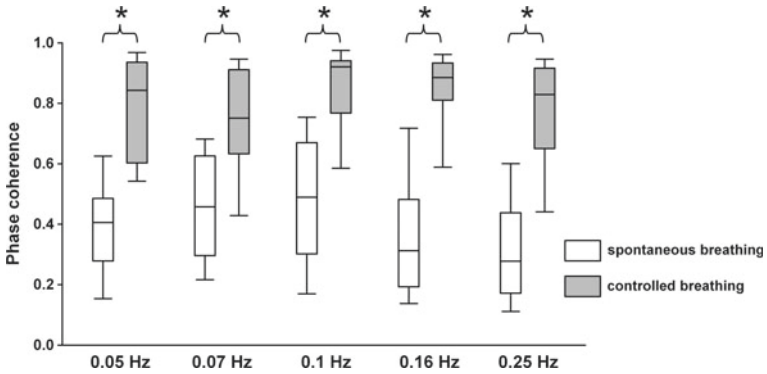

Fig. 18.4 Box-Whisker plots for the phase coherence values of skin blood flow oscillations of left and right fingers. The asterisk symbol (*) indicates statistically significant differences between spontaneous and controlled breathing ($p < 0.05$)

Table 18.1 Median values of phase coherence function between skin blood flow oscillations of left and right fingers

Frequency (Hz)	Breathing regimes	
	Spontaneous	Controlled
0.05	0.41	0.84*
0.07	0.46	0.75*
0.1	0.49	0.92*
0.16	0.31	0.89*
0.25	0.28	0.83*

*statistically significant differences between spontaneous and controlled breathing ($p < 0.05$)

presented in the Fig. 18.4 and Table 18.1. There is significant increase in phase coherence of SBF_{left}–SBF_{right} pair for all breathing regimes. The maximal increase was observed for controlled breathing at 0.25 Hz which is close to the spontaneous breathing rate. At this frequency, the median of phase coherence value was approximately three times higher under controlled breathing as compared to spontaneous one (Table 18.1).

18.4 Discussion

We obtained the significant increase of phase coherence of skin blood flow oscillations of left and right forefingers for all regimes of controlled breathing. The respiratory-related variations in peripheral hemodynamics can originate from changes in the arterial blood pressure induced by thoracic pressure changes and passively transmitted from large to small arteries [5] or from peripheral sympathetic

activity oscillations [15]. A tight relation between breathing and sympathetic nerve activity is known. In particular, the sympathetic activity increases during inhalation and becomes maximal at the last stage of inhalation and at the beginning of exhalation [7, 13, 23]. The cutaneous blood flow is regulated with vasoconstriction induced by a sympathetic nervous system. Moreover, the peripheral blood flow depends on the sympathetic activity because the arteriovenular anastomoses located in the acral parts have high sympathetic innervation. So the respiratory activity influences the peripheral blood flow indirectly, whereas the sympathetic activity induces vasoconstriction independently from the mechanical manifestation of the respiratory cycle [16]. We suggest that the described mechanisms are involved in the formation of respiratory-related oscillations in peripheral blood flow registered by LDF technique. The prevalence of the mechanism regulating blood flow is caused by the impact of an arterio-venous component on the total signal and by the regional differences in vascular sympathetic innervation. The palmar finger skin has a large number of arterio-venuous anastomoses, the tone of which is not affected by baroreceptors and is regulated exclusively by sympathetic innervation [10, 11]. Therefore, the respiratory-related skin blood flow oscillations are mainly influenced by respiratory-modulated sympathetic vasoconstriction. An addition, one of the possible mechanisms for synchronization of blood flow oscillations might rest upon the reaction of the muscular layer of the vascular wall on the pressure change - myogenic response. It is known that a decrease of arterial blood pressure results in a transient artery dilatation, while its increase leads to a constriction due to the reaction from the vascular muscle layer, the so-called Bayliss effect [4]. Thus, perhaps the pressure wave is well propagated to the periphery, as myogenic is defined as a reaction to a pressure wave. Not only may the myogenic response be involved in the synchronization of cardiovascular oscillations, but also respiratory sinus arrhythmia (RSA). RSA is heart rate variability in synchrony with respiration, associated with an increase in heart rate during inspiration and a decrease during expiration [2, 20]. RSA is a physiologic phenomenon reflecting respiratory-circulatory interactions universally observed among vertebrates. We suggest that these two mechanisms can also influence phase interactions in microvasculature. But this assumption needs further investigations.

It should be mentioned that only young females participated in the study. Apparently, the results may be different for other participants, for instance, for women of another age or for men. However, studying gender- and age-related features of phase coherence of skin blood flow oscillations is beyond the scope of this study and requires additional research.

18.5 Conclusion

In the study we present the results of investigation of phase interactions between blood flow oscillations of left and right forefinger-pad skin under breathing controlled on both rate and depth. It was obtained that controlled breathing leads to the significant

increase of phase coherence between respiratory-related blood flow oscillations of left and right fingers for all breathing regimes. The maximal increase was observed under controlled breathing at 0.25 Hz, i.e. at a frequency close to the spontaneous one. We suggest that the observed significant increase is primarily due to an increase of breathing depth. Spontaneous breathing depth does not exceed 15% of the maximal chest excursion, while in the present study the depth was 40%. We suppose that under deep breathing the role of both potential mechanisms of respiratory-related oscillation generation (venous pressure variations and vascular tone regulation via autonomic nervous system) enhance but this assumption requires additional investigation.

Acknowledgements The authors thank the participants for their time and commitment to the study. The work is supported by the Russian Foundation for Basic Research (grant # 18-015-00292).

References

1. J. Allen, J.R. Frame, A. Murray, Microvascular blood flow and skin temperature changes in the fingers following a deep nspiratory gasp. Physiol. Meas. **23**(2), 365–373 (2002). https://doi.org/10.1088/0967-3334/23/2/312
2. A. Angelone, N.A. Coulter Jr., Respiratory sinus arrhythemia: a frequency dependent phenomenon. J. Appl. Physiol. **19**, 479–482 (1964). https://doi.org/10.1152/jappl.1964.19.3.479
3. A. Bandrivskyy, A. Bernjak, P. McClintock, A. Stefanovska, Wavelet phase coherence analysis: application to skin temperature and blood flow. Cardiovasc. Eng.: Int. J. **4**(1), 89–93 (2004). https://doi.org/10.1023/B:CARE.0000025126.63253.43
4. W.M. Bayliss, On the local reactions of the arterial wall to changes of internal pressure. J. Physiol. **28**(3), 220–231 (1902). https://doi.org/10.1113/jphysiol.1902.sp000911
5. L. Bernardi, A. Radaelli, P.L. Solda, A.J. Coats, M. Reeder, A. Calciati, C.S. Garrard, P. Sleight, Autonomic control of skin microvessels: assessment by power spectrum of photoplethysmographic waves. Clin. Sci. (Lond.) **90**(5), 345–355 (1996). https://doi.org/10.1042/cs0900345
6. A. Bollinger, A. Yanar, U. Hoffmann, U.K. Franzeck, Is high-frequency flux motion due to respiration or to vasomotion activity. Progr. Appl. Micr. **20**, 52–58 (1993)
7. J.H. Costa-Silva, D.B. Zoccal, B.H. Machado, Glutamatergic antagonism in the NTS decreases post-inspiratory drive and changes phrenic and sympathetic coupling during chemoreflex activation. J. Neurophysiol. **103**(4), 2095–2106 (2010). https://doi.org/10.1152/jn.00802.2009
8. F. Khan, V.A. Spence, S.B. Wilson, N.C. Abbot, Quantification of sympathetic vascular responses in skin by laser Doppler flowmetry. Int. J. Microcirc. Clin. Exp. **10**(2), 145–153 (1991)
9. G.V. Krasnikov, M.Y. Tyurina, A.V. Tankanag, G.M. Piskunova, N.K. Chemeris, Analysis of heart rate variability and skin blood flow oscillations under deep controlled breathing. Respir. Physiol. Neurobiol. **185**(3), 562–570 (2013). https://doi.org/10.1016/j.resp.2012.11.007
10. A.I. Krupatkin, Blood flow oscillations at a frequency of about 0.1 Hz in skin microvessels do not reflect the sympathetic regulation of their tone. Hum. Physiol. **35**(2):183–191 (2009). https://doi.org/10.1134/S036211970902008X
11. H.N. Mayrovitz, E.E. Groseclose, Inspiration-induced vascular responses in finger dorsum skin. Microvasc. Res. **63**(2), 227–232 (2002). https://doi.org/10.1006/mvre.2001.2391
12. D.J. Meredith, D. Clifton, P. Charlton, J. Brooks, C.W. Pugh, L. Tarassenko, Photoplethysmographic derivation of respiratory rate: a review of relevant physiology. J. Med. Eng. Technol. **36**(1), 1–7 (2012). https://doi.org/10.3109/03091902.2011.638965

13. T. Miyawaki, J. Minson, L. Arnolda, J. Chalmers, I. Llewellyn-Smith, P. Pilowsky, Role of excitatory amino acid receptors in cardiorespiratory coupling in ventrolateral medulla. Am. J. Physiol. **271**(5 Pt 2), R1221-1230 (1996). https://doi.org/10.1152/ajpregu.1996.271.5.R1221
14. I.A. Mizeva, Phase coherence of 0.1 Hz microvascular tone oscillations during the local heating, in IOP Conference Series: Materials Science and Engineering, 208, 012027 (2017). https://doi.org/10.1088/1757-899X/208/1/012027
15. L. Nilsson, A. Johansson, S. Kalman, Macrocirculation is not the sole determinant of respiratory induced variations in the reflection mode photoplethysmographic signal. Physiol. Meas. **24**(4), 925–937 (2003). https://doi.org/10.1088/0967-3334/24/4/009
16. M. Nitzan, I. Faib, H. Friedman, Respiration-induced changes in tissue blood volume distal to occluded artery, measured by photoplethysmography. J. Biomed. Opt. **11**(4), 040506 (2006). https://doi.org/10.1117/1.2236285
17. A. Perrella, M. Sorelli, F. Giardini, L. Frassineti, P. Francia, L. Bocchi, Wavelet phase coherence between the microvascular pulse contour and the respiratory activity. Ifmbe. Proc. **68**(2), 311–314 (2019). https://doi.org/10.1007/978-981-10-9038-7_58
18. A.V. Tankanag, A.A. Grinevich, T.V. Kirilina, G.V. Krasnikov, G.M. Piskunova, N.K. Chemeris, Wavelet phase coherence analysis of the skin blood flow oscillations in human. Microvasc. Res. **95**, 53–59 (2014). https://doi.org/10.1016/j.mvr.2014.07.003
19. A.V. Tankanag, A.A. Grinevich, I.V. Tikhonova, A.V. Chaplygina, N.K. Chemeris, Phase synchronization of skin blood flow oscillations in humans under asymmetric local heating. Biophysics **62**(4), 629–635 (2017). https://doi.org/10.1134/S0006350917040212
20. J.A. Taylor, C.W. Myers, J.R. Halliwill, H. Seidel, D.L. Eckberg, Sympathetic restraint of respiratory sinus arrhythmia: implications for vagal-cardiac tone assessment in humans. Am. J. Physiol. Heart. Circ. Physiol. **280**(6), H2804-2814 (2001). https://doi.org/10.1152/ajpheart.2001.280.6.H2804
21. V. Ticcinelli, T. Stankovski, D. Iatsenko, A. Bernjak, A.E. Bradbury, A.R. Gallagher, P.B.M. Clarkson, P.V.E. McClintock, A. Stefanovska, Coherence and coupling functions reveal microvascular impairment in treated hypertension. Front. Physiol. **8**, 749 (2017). https://doi.org/10.3389/fphys.2017.00749
22. L. Xie, B. Liu, X. Wang, M. Mei, M. Li, X. Yu, Zhang J (2017) Effects of different stresses on cardiac autonomic control and cardiovascular coupling. J. Appl. Physiol. **122**(3), 435–445 (1985). https://doi.org/10.1152/japplphysiol.00245.2016
23. D.B. Zoccal, A.E. Simms, L.G. Bonagamba, V.A. Braga, A.E. Pickering, J.F. Paton, B.H. Machado, Increased sympathetic outflow in juvenile rats submitted to chronic intermittent hypoxia correlates with enhanced expiratory activity. J. Physiol. **586**(13), 3253–3265 (2008). https://doi.org/10.1113/jphysiol.2008.154187

Chapter 19
Complexity-Based Analysis of Microvascular Blood Flow in Human Skin

Marjola Thanaj, Andrew J. Chipperfield, and Geraldine F. Clough

Abstract The maintenance of an adequate microvascular perfusion sufficient to meet the metabolic demands of the tissue is dependent on neural, humoral and local vaso-mechanisms that determine vascular tone and blood flow patterns within a microvascular network. It has been argued that attenuation of these flow patterns may be a major contributor to disease risk. Thus, quantitative information on the in vivo spatio-temporal behaviour of microvascular perfusion is important if we are to understand network functionality and flexibility in cardiovascular disease. Time and frequency-domain analysis has been extensively used to describe the dynamic characteristics of Laser Doppler flowmetry (LDF) signals obtained from superficial microvascular networks such as that of the skin. However, neither approach has provided definitive and consistent information on the relative contribution of the oscillatory components of flowmotion (endothelial, neurogenic, myogenic, respiratory and cardiac) to a sustained and adequate microvascular perfusion; nor advance our understanding of how such processes are collectively modified in disease. More recently, non-linear complexity-based approaches have begun to yield evidence of a declining adaptability of microvascular flow patterns as disease severity increases. In this chapter we review the utility and application of these approaches for the quantitative, mechanistic exploration of microvascular (dys)function.

M. Thanaj · A. J. Chipperfield
Bioengineering Science Group, Faculty of Engineering and the Environment, University of Southampton, Highfield, Southampton SO17 1BJ, UK
e-mail: M.Thanaj@soton.ac.uk

A. J. Chipperfield
e-mail: a.j.chipperfield@soton.ac.uk

G. F. Clough (✉)
Human Development & Health, Faculty of Medicine, Southampton General Hospital, University of Southampton, Southampton SO16 6YD, UK
e-mail: g.f.clough@soton.ac.uk

A. Stefanovska and P. V. E. McClintock (eds.), *Physics of Biological Oscillators*, Understanding Complex Systems,
https://doi.org/10.1007/978-3-030-59805-1_19

Abbreviations

ARA	Attractor reconstruction analysis
BF	Blood flux
CVD	Cardiovascular disease
ETC	Effort to Compress
FFT	Fast Fourier transform
LDF	Laser Doppler flowmetry
LZC	Lempel-Ziv Complexity
MLZC	Multiscale Lempel-Ziv complexity
MSE	Multiscale entropy
NO	Nitric oxide
oxyHb	Oxyhaemoglobin
PSD	Power spectral density
PU	Arbitrary perfusion units
SampEn	Sample Entropy
WT	Wavelet transform

19.1 Introduction

The maintenance of an adequate blood flow through a vascular network sufficient to meet the metabolic demands of the tissue, is dependent on neural, humoral and local vaso-mechanisms that determine vascular tone and flow patterns within the microvasculature. It has been argued that attenuation of these flow patterns may be a major contributor to disease risk and that quantitative information on the temporal behaviour and spatial distribution of microvascular perfusion, in vivo, is important if we are to understand network functionality and flexibility in cardiovascular and metabolic disease.

To date, time and frequency domain analysis has been extensively used to assess network functionality and to describe the dynamic characteristics of signals derived from superficial vascular networks such as that of the skin, obtained using non-invasive laser Doppler fluximetry [24, 54]. Variations in the amplitude and relative contribution of spontaneous, rhythmic oscillatory fluctuations of local endothelial, neurogenic, and myogenic origin have become widely associated with a decline in microvascular function in a wide variety of disease states (see [19]). Impairment of spatial and temporal regulation of network perfusion by these localised mechanisms has been shown to give rise to a mismatch between perfusion and demand, particularly at times of elevated metabolic demand [30]. The consequence of such inadequate perfusion control is a compromised tissue function, such as that associated with features of the metabolic syndrome, which eventually leads to the development of retinopathy, neuropathy, skin ulcers and difficult to heal wounds [25].

More recently, the regularity and the randomness of blood flow within microvascular networks has been explored using non-linear methods such as entropy and complexity techniques [40, 53, 75, 83, 85]. Studies in humans at risk or with CVD have shown a reduced complexity of the blood flux signal using Lempel-Ziv complexity algorithms [18] and altered microvascular haemodynamics associated with diminished chaotic ischaemic flow [34]. In rodent models of cardiovascular and metabolic disease, chaotic network attractor analysis has revealed a declining adaptability of microvascular flow patterns [30] and altered spatial heterogeneity and temporal stability of network perfusion to limit the adaptive ability of the microvasculature and so compromise its function [74]. However, the relevance of these non-linear indices to the diagnosis and treatment of human cardiovascular disease (CVD) has yet to be determined.

19.2 Assessment of Microvascular Blood Flow

The microvasculature comprises the small resistance arteries, arterioles, capillaries and venules with diameter less than 200 μm that lie within the tissue parenchyma. The primary role of the microcirculation is the optimal exchange of gases, nutrients, water, and metabolites between the blood and surrounding tissues. Regulation of microvascular perfusion is predominately achieved through changes in network conductance, modulated at a local level by endothelial, neurogenic and myogenic regulatory activity [74]. Together these activities determine the cyclic oscillations of arteriolar diameter (vasomotion) [20, 77] that are related to changes in blood flow distribution in the microvascular networks (flow motion) [65].

Microcirculatory blood flow has been non-invasively investigated using techniques such as laser Doppler flowmetry (LDF) [67] laser speckle contrast imaging [11, 70], peripheral arterial tonography [28], diffuse correlation spectroscopy [3], side-stream dark field [31] and orthogonal polarisation spectral cameras [80], and nailfold capillaroscopy [89]. The microcirculation of the skin offers an accessible site in which to study the physiological mechanisms involved in the regulation of tissue perfusion [36, 67] and LDF, based on the Doppler Effect, first described by Christian Doppler in 1842 and applied by Buys Ballot in 1845 to sound waves [35], is currently the most widely used method for continuous, non-invasive monitoring of skin microcirculation under physiological and pathological conditions [24]. The LDF signal shows vigorous temporal and spatial variability and measures of this variability (and/or increased stability) can provide a rich source of information relating to the flexibility/responsiveness of the system. As LDF provides only a relative index of microvascular perfusion in the time domain it is frequently used in conjunction with a reactivity test to allow investigation of the mechanisms underlying local control of vascular tone. Reactivity tests include post occlusive reactive hyperaemia, local thermal warming and pharmacological tools such as iontophoresis of vasoactive agents. Skin microvascular responses in the time domain to these provocations are

comprehensively reviewed [24, 68, 69] and the signalling pathways underlying the responses described elsewhere [68].

19.3 Analysis of Microvascular Blood Flow Signals in the Spectral Domain

The LDF technique has been extended to explore microvascular control mechanisms within the skin through the analysis of the component frequencies of the laser Doppler signal [21, 38, 48]. Time series analysis of LDF signals shows spontaneous, local, rhythmic oscillatory fluctuations of the blood flux in the microvascular network. These periodic oscillations have been shown to reflect the influence of myogenic (~0.05–0.15 Hz) [45], neurogenic (~0.02–0.05 Hz) [78] and both endothelial nitric oxide (NO)-dependent (~0.0095–0.02 Hz) and -independent (<0.0095 Hz) [47, 49, 66] activity on vascular tone. Additionally, the haemodynamic effects of the heart beat (~0.6–2.0 Hz) and respiratory activity (~0.15–0.6 Hz) [10] may be detected in the LDF signal (Table 19.1).

The two main methods of spectral analysis that have been used to extract these oscillatory signals are based on the Fast Fourier Transform (FFT) algorithm and on a generalized wavelet transform (WT) [2].

Table 19.1 Periodic activity of the laser Doppler blood flux signal and its potential origins (From [19])

Periodic activity	Time constant (s)	Frequency (Hz)	Origin
Endothelial NO-independent	>105	<0.0095	Mechanisms other than NO-mediated originating from endothelial cells, e.g. endothelial derived hyperpolarizing factor (EDHF)
Endothelial NO-dependent	48–105	0.0095–0.02	NO production by endothelial cells
Neurogenic	19–48	0.02–0.05	Sympathetic nervous system
Myogenic	7–19	0.05–0.15	Vascular smooth muscle (VSM) cells
Respiratory	1.6–7	0.15–0.620	Breathing
Cardiac	0.5–1.6	0.60–2.00	Heartbeat

19.3.1 Fast Fourier Transform

The Fourier Transform (FT) is the decomposition of a time series into its constituent frequency components [29, 62]. Power Spectral Density (PSD) describes the contribution to the power in the frequency components across a spectrum. In FFT analysis, the PSD of flow motion waves is obtained by computing the discrete Fourier transform of the LDF signal, which itself is a discrete representation of a continuous signal. In this way FFT analysis provides an estimate of the absolute power in the signal at a given frequency and of the PSD contribution of a frequency band to the total power of the signal. This is often used to evaluate the impact of each frequency band (and their associated control mechanisms) on overall flowmotion.

19.3.2 Wavelet Transform

Generalized wavelet analysis is a scale-independent method with adjustable time and frequency resolution. It was introduced for the analysis of LDF signals by Stefanovska and colleagues [8]. While wavelets are not specifically designed for spectral analysis, spectral information can be recovered by analysis of the wavelets to produce the scalogram giving the energy contribution of each wavelet coefficient which can then be used to express the flow motion activities in AU/Hz [79]. The Wavelet Transform (WT) allows for the analysis of time and frequency contents of an oscillatory signal [56] and has the advantage over the FFT in that it provides information about changes in frequency and power of distinct oscillatory bands over time. The WT can also be averaged over time, at a particular frequency, to yield an average scalogram.

19.3.3 Application of Spectral Domain Analysis

Spectral analysis of the low frequency periodic oscillations in blood flux measurements obtained using LDF provides mechanistic information of the processes regulating microvascular perfusion [45, 71, 79]. A decline in microvascular function is widely associated with variations in the amplitude and relative contribution of the low frequency oscillations, with flow patterns differing according to the time course and severity of disease [57, 65, 66]. There is, however, a lack of consensus on the interpretation of the direction of change of the relative contributions of the oscillatory signals across the spectral bands and their mechanistic origins. Direct comparison of different studies is complicated by the choice of parameters for frequency domain analysis (e.g. window size, overlap, number of bins). Furthermore, recent work suggests that the frequency bands are not fixed and may vary, for example, with age or pathological state [33]. Most studies use fixed non-overlapping intervals

to define the spectral bands as originally described by Stefanovska and colleagues [8]. It is unlikely that the boundaries of these frequency intervals remain constant across a cohort of individuals, or for a given individual, under changing conditions of physiological stress. State-dependent fluctuations in frequency intervals may thus give rise to different spectral signatures within, and across, the cohorts studied. However, frequency domain analysis remains a valuable tool in our understanding of the processes modulating microvascular BF and their relative contribution to overall network perfusion [55].

19.4 Information and Complexity-Based Analysis of Microvascular Blood Flow Signals

While conventional time and frequency domain analysis techniques have proved valuable in the understanding of blood flow within a microvascular bed they have failed, so far, to describe mechanistically the changes in observed flow patterns between pathological conditions or haemodynamic states. Nonlinear methods, based on ideas from information theory, have been used to quantify the regularity and randomness of short lengths of physiological signals and have demonstrated the potential for diagnostic capability [6]. Recently, their application has been extended to the LDF signal from superficial microvascular networks.

Complexity analysis quantifies the degree of variability or loss of spontaneity in a time series and has been applied to a range of bio-signals, including electroencephalograms [43] and electrocardiograms [86]. The degree of variability in these signals reflects the physiological adaptability of the underlying system and is an established biomarker of overall health status [1]. There is, however, no single definition of complexity. Nagaraj and Balasubramaian [58] describe three methods of quantifying complexity which in the context of the current discussion relate to (i) how hard it is describe the information in the LDF signal, i.e. the number of unique patterns in the time series or model order, (ii) how hard it is to create or loosely compress the information and (iii) the degree of organisation or structure in the LDF signal. The most widely used measures in LDF signal analysis are Lempel-Ziv Complexity (LZC), sample entropy and effort-to-compress (ETC) complexity. All these approaches have successfully provided a measure of the information content of the LDF signal [83, 85] (Fig. 19.1).

19.4.1 Lempel-Ziv Complexity (LZC)-Based Analysis

Lempel-Ziv complexity (LZC) [50] provides a measure of how difficult it is to describe the information contained in a signal and is the length of the shortest instruction set needed to reconstruct the signal without information loss. A simple periodic

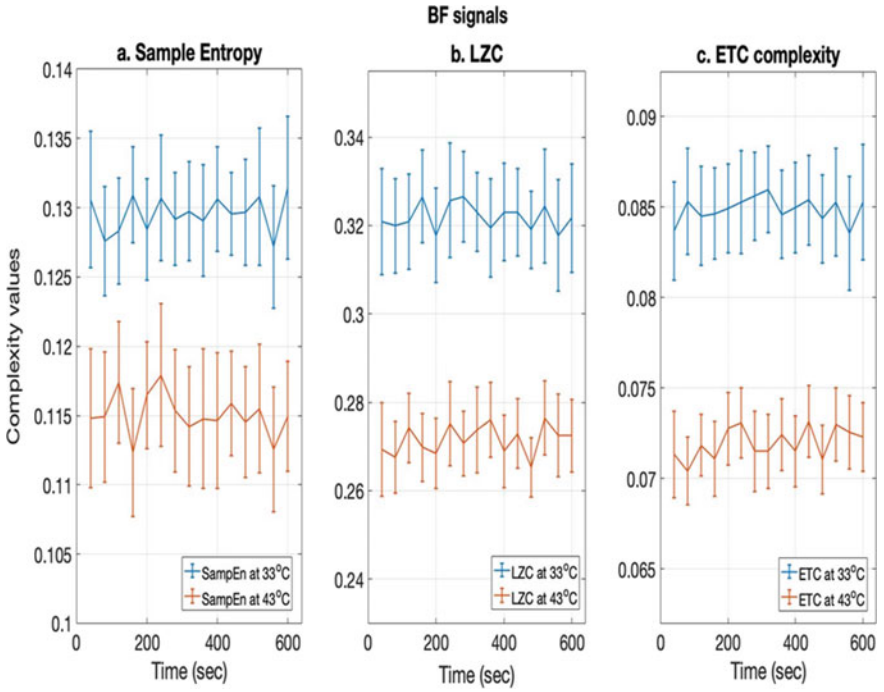

Fig. 19.1 Changes in regularity and complexity of the LDF blood flux signals captured at 40 Hz measured in the forearm of 15 healthy volunteers, in two haemodynamic steady states at 33 °C (blue) and at 43 °C (red). **a** Sample Entropy, **b** Lempel and Ziv complexity, **c** Effort to Compress complexity. Values are presented as means ± SEM. Adapted from [83]

signal would have low complexity as the same terms are repeated continually while a random signal would have high complexity as there are no rules, or repeating patterns that define it. Before LZC can be calculated the original LDF signal must be transformed to a binary sequence. This can be achieved by recording a one if a sample is greater than the median and zero otherwise [2]. Alternatively, a delta encoding method which captures more of the variability in the signal has been used [46]. In this latter approach a zero is recoded if a value is less than the previous value in the time series or a one if the value is greater than the previous value. The signal is often divided into epochs of suitable length to examine how LZC varies over time; or a sliding window is used to detect the time of rapid spontaneous changes in the signal. There are many challenges in applying complexity-based analysis methods to signals in general, such as the influence of noise, signal length and quantization method. While many of these issues are not fully resolved, there has been considerable effort in developing methodologies that can be applied in clinical practice [73, 90].

Figure 19.1b shows an example of LZC calculated for 15 × 40 s epochs of the LDF BF signal captured at 40 Hz, from the skin of the ventral surface of the forearm

in 15 healthy male volunteers. In this study signals were recorded initially with skin temperature clamped at 33 °C and then when it was raised to 43 °C. As the epochs are not synchronised, direct comparison between values at the two temperatures in a given individual, or of group values, provides little understanding of spontaneous temporal activity. However, differences in the information content of the BF signals are clearly observable, with that of signals measured at 43 °C being lower (less variable) and having fewer unique states (a lower LZC) than those at 33 °C. An LZC-index, calculated as the mean of the 15 × 40 s epochs, has been used to discriminate between haemodynamic states or between "at-risk" groups [14, 17, 18]. However, to what extent LZ based algorithms can be used as a clinical tool with which to classify disordered states within the microcirculation remains to be fully investigated. The cardiac and respiratory rhythms might be predicted to have significant but opposite influences on signal complexity due to their generally periodic nature. Skin sympathetic nerve activity is known to be modulated by respiration and cutaneous vasoconstrictor neurones are temporarily coupled to cardiac and respiratory oscillations [26]. Heart rate variability may also contribute to the complexity of the BF signal [72] and cardiac rhythm is modulated by respiration [76].

19.4.2 Entropy-Based and Effort to Compress Complexity Analysis

Sample entropy (SampEn) provides an applicable finite sequence formulation that discriminates the data sets by a measure of randomness, from totally regular to completely random. SampEn assigns non-negative patterns in time series, with larger values of entropy corresponding to more irregularity and smaller values corresponding to more regularity in the data. The regularity of the signal can be measured with the SampEn, by defining how often a short time series is repeated. A similar complexity method based on the lossless compression algorithm is the Effort to Compress (ETC) complexity, proposed by Nagaraj, Balasubramanian [59]. Similar to the LZC approach, the given sequence is also first converted to a symbolic sequence.

There have been few studies to investigate the SampEn and ETC complexity of LDF signals from human skin blood. Figure 19.1a, c taken from Thanaj et al. [83] gives one example of this. Such data provide strong evidence that, similar to LZC, these algorithms showed sensitivity to a change in haemodynamic state. Here, lower entropy and complexity indices with relatively consistent variation across the 15 epochs were observed when microvascular flow approached maximal dilation and network perfusion during heating. However, Liao et al. [53] in a similar study investigating the sample entropy indexes in response to local heating of the sacral skin blood flow in people at risk of pressure ulcers, failed to find any significant correlation with skin vasodilatory capacity. This led them to argue that nonlinear analysis is not always a consistent method for the assessment of vasodilatory function.

19.4.3 Application of Complexity-Based Analysis of Laser Doppler BF Signals

Non-linear methods such as entropy and complexity analysis have been increasingly used to explore the regularity and the randomness of blood flux signals derived from microvascular networks as a possible predictor of functional dysregulation, both in human cohorts and in animal models of human disease. One of the first of these studies was by Tigno et al. [85] who investigated the complexity of LDF signals from nondiabetic, prediabetic and diabetic primates. They report an LZC that decreased with progression of diabetes [85]. Similarly, Chipperfield et al. [18] showed that in humans with and without type 2 diabetes mellitus LZC of the LDF signal reduced as CVD risk increased. Together, these findings suggest that the impact of diabetes on spontaneous oscillations in the bio-signal derived from microvascular blood flow may be reflected in the complexity of the low frequency flowmotion activity rather than, or as well as, in their oscillatory power content. Contrary to the studies described above using LZC, Hsiu et al. [37] using approximate entropy to compare beat-to-beat cardiac rhythms in the LDF signal in nondiabetic, prediabetic and diabetic humans have shown an increased signal complexity in people with diabetes. However, the increase in complexity reported by Hsiu et al. [37] relates to complexity between consecutive high frequency heart beats rather than to low frequency (flowmotion) activity. To what extent the impact of diabetes on the microcirculation involves a decrease in complexity of the low frequency oscillations and an increase in complexity of conducted signals such as that of the cardiac rhythm requires further investigation.

Age-related changes in microvascular flows have been investigated by Humeau et al. [39] using wavelet-based representations, with Hölder exponents to measure the regularity of the LDF signal and sample entropy to assess its complexity. They showed that endothelium-related activity decreased with age while microvascular perfusion became more regular and less complex, although not significantly. Liao et al. [52] using a modified SampEn algorithm similarly found that the LDF signal showed a higher degree of regularity during thermal warming as compared to the baseline in both young (mean age 27 years) and older (mean age 72 years) individuals. The LDF signal also showed a higher degree of regularity in the older group as compared to the young group, attributed in part to enhanced cardiac oscillations.

SampEn of LDF signals has also been used to discriminate between normal and abnormal skin microvascular function in diseases affecting digits, such as Raynaud's phenomenon and systemic sclerosis [27]. These authors found that baseline entropy was significantly increased in patients with systemic sclerosis compared to those with Raynaud's phenomenon and with controls, on the finger pad but not on the forearm; consistent with the pathophysiology of the disease, which predominantly affects the digital microcirculation.

Overall, these studies appear consistent with the premise that a greater complexity (variability) of the blood flux signal may indicate a more effective microvascular system, whereas a lower variability in microvascular activity corresponds to a loss of

the system's ability to adapt to pathophysiological conditions and/or is an indicator of disease severity.

19.5 Multiscale Frequency, Complexity and Scale

Conventional entropy and complexity methods have the disadvantage that they can only study behaviour at one scale. However, the physiological processes that regulate flow motion operate across multiple temporal scales ranging from 0.001 to 2 Hz and appear to vary under a wide range of physiological and pathophysiological conditions as discussed previously. To account for these multiple and potentially varying process scales, LZ complexity and entropy has be evaluated in multiple time-scales using a coarse-graining approach. Such multiscale analyses have been shown to be effective in the general understanding of a wide range of physiological signals [15, 23, 40].

Costa et al. [22] applied multiscale entropy to the cardiac inter-beat interval to determine the regularity of the cardiac properties in the young, elderly and individuals with heart failure during both waking and sleeping periods. They found good discrimination between these periods for all groups and reported that the multiscale entropy analysis was a valid method for quantifying the complexity of biological signals across multiple spatial and temporal scales. Kalev et al. [43] using multiscale LZ complexity, were able to demonstrate an 86% classification accuracy by accounting for the different frequencies of information content in the electroencephalogram. Similarly, Papaioannou et al. [63] showed that multiscale complexity analysis of temperature signals from patients with systematic inflammation, sepsis or septic shock could be used to determine the early presence of pathology.

In this approach, the sampling frequency is altered by a scale factor τ defining the scale level used to resample the original signal reducing the scale of the time series. For the time series $\{x_1, \ldots, x_N\}$, where N is the number of samples, the coarse-grained time series, y^τ, is:

$$y_i^\tau = \frac{1}{\tau} \sum_{i=(i-1)\tau+1}^{i\tau} x_j, 1 \leq i \leq N/\tau \tag{19.5.1}$$

Thus, for an LDF signal originally sampled at 40 Hz, the LZC can be evaluated at different LDF sample rates, where the sampling frequency is $f_\tau = 40/\tau$ where τ is the scale factor. At scale $\tau = 1$ the original signal is preserved at 40 Hz and at scale $\tau = 24$ resampled to 1.67 Hz. At scale factor one, the time series y^1 is the original signal and the length of each coarse-grained time series $\{y^\tau\}$ is equal to the original signal divided by the scale factor, τ. It has been suggested that the length of signal required to obtain viable complexity measures and reported that a signal length > 1000 samples are required which equates to 10 min captured at 40 Hz at scale $\tau = 24$ [83].

An example of the application of the multiscale approach is shown in Fig. 19.2

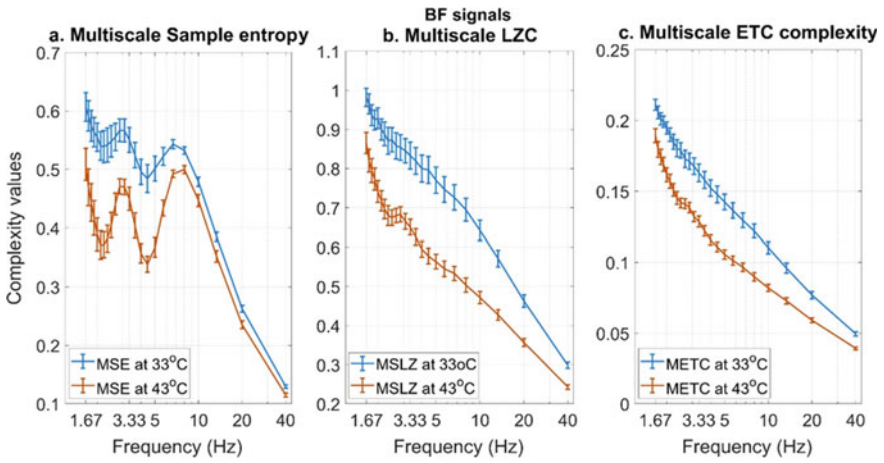

Fig. 19.2 Average multiscale analysis of skin blood flux signals measured at the forearm using laser Doppler fluximetry at 33 °C (blue) and at 43 °C (red). **a** multiscale sample entropy, **b** multiscale Lempel-Ziv complexity, **c** Multiscale Effort to Compress complexity. Values are presented as mean ± SEM for n = 15 healthy individuals. From [83]

taken from Thanaj et al. [83]. Overall, the reduction in the information content of the signals analysed across multiple sampling frequencies (lower sampling frequency corresponding to higher time-scale) seen during the vasodilator response to warming, is similar to that using conventional uni-scale analysis. However, as sampling frequency decreases LZC can also be seen to increase as does the separation between the groups until the Nyquist frequency of the original BF signal is reached or passed. Assuming the Nyquist frequency is the upper limit of the cardiac band of 1.6 Hz, then this sampling frequency will be 3.2 Hz ($\tau = 12$). Below this sampling frequency, the influence of the relatively periodic heart rate will be reduced and the information content of the signal increased. At lower sampling frequencies the resampled BF signal covers a longer time period and the lower frequencies associated with flow motion contribute proportionally more to signal variability resulting in higher complexity.

In an attempt to address the physiological interpretation of the complexity of BF signals Chipperfield et al. [18] have explored how the spectral components of the BF signal influence its information content and hence complexity. They examined the correlations between the power content of the five frequency intervals and MLZC over sampling frequencies of 40–1.67 Hz [18]. They showed that endothelial, neurogenic, myogenic and respiratory band activity all contributed positively, and the relatively regular cardiac band activity negatively, to the information content of the resting BF signal measured at the forearm. This contribution appeared to vary with haemodynamic state [14] and with pathology [18]. Used in combination with time- and frequency-domain metrics this approach could potentially discriminate between the varying mechanistic influences that determine network perfusion [17].

However, entropy measures do not show the same changes through scales as complexity. Humeau et al. [41] in a recent study of the multiscale entropy (MSE) analysis of LDF signals in healthy subjects, showed a similar behaviour of the MSE of the BF signal when filtered for the frequencies associated with heart rate (∼0.6–2 Hz). These authors suggested that the increase and then decrease of the MSE over the scales may be due to the non-periodic nature of the signals and therefore the progression of complexity in multiple scales cannot be stable [41].

19.6 Other Descriptors of Time- and Frequency-Domain Characteristics of the Microvascular Blood Flux Signal

There are a growing number of publications on the analysis of other time and frequency characteristics of LDF signals. For example, empirical mode decomposition is a method of decomposing a signal in the time domain, which may be nonlinear and non-stationary, into a set of functions allowing the varying frequencies in time to be preserved. Humeau-Heurtier and Klonizakis [42] used this approach to find instantaneous frequencies from intrinsic mode functions, in healthy subjects and patients with varicose veins. Liao and Jan [51] analysed nonlinear properties of LDF signals in subjects at risk of pressure ulcers using ensemble empirical mode decomposition to examine the self-phase synchronisation between the component frequencies of blood flow oscillations. However, two of the most promising areas of current investigation are time localised phase coherence and the use of attractor reconstruction.

19.6.1 Time Localised Phase Coherence

Phase coherence is another approach to studying interactions between different time series. High phase coherence synchronisation can be understood as connectivity/congruence between studied signals. This approach has been applied by Bernjak et al. [9] to simultaneously recorded skin blood flux and tissue oxygenation signals measured at the forearm of healthy volunteers. The phase coherence was estimated as the difference in instantaneous phases at each frequency and each time point, using a wavelet transform. A major finding using this approach was that the phase difference changed over time and with the microvascular bed sampled. The authors observed a significant phase coherence between the two signals in the low frequencies and also in the cardiac frequency band in the superficial dermal vascular bed. They reported no significant phase coherence in deeper tissues [9]. Similarly, Tankanag et al. [82] investigating wavelet phase coherence of oscillations between

two different skin sites, also in healthy individuals, demonstrated both local and central mechanisms regulating low-frequency blood flow oscillations.

19.6.2 Attractor Reconstruction

Attractor reconstruction analysis has been used previously to determine changes in the shape and variability of quasi periodic signals, achieving a two-dimensional attractor and providing features such as density and symmetry. Attractor reconstruction has been previously applied to various physiological data including blood pressure [5, 60, 61], plethysmographic [87], electroencephalographic (EEG) [88] and blood flow signals [7, 12, 32, 64]. The attractors reconstructed from these times series, using a suitable time delay and embedding dimension, contain properties that can be used to define the dynamics of the system and provide a visual representation of the system's stability [44].

In this approach, the signals are first reconstructed in three-dimensional space with a time delay, τ, computed using the mutual information analysis where the average mutual information between two instances i and $i + \tau$ reaches its first local minimum [44, 81] and the first local maximum is the average period,T, of the signal. Then, the ideal time delay will be either $\tau = T/3$ or $\tau = 2T/3$. So, for a time series $x(t)$, the two additional variables will be:

$$y(t) = x(t - \tau) \quad \text{and} \quad z(t) = x(t - 2\tau).$$

The reconstructed phase space can be now plotted as (x, y, z). Then, the variation of the time series of the (x, y, z) attractor is removed by projecting the attractor in two-dimensional space, referred as plane (v, w) perpendicular to the vector (1, 1, 1) forming two new variables:

$$v = \frac{1}{\sqrt{6}}(x + y - 2z) \quad \text{and} \quad w = \frac{1}{\sqrt{2}}(x - y).$$

The two-dimensional plane (v, w) will be defined as periodic, with period $T = 3\tau$ when a symmetric triangular shape is observed.

Recently, Aston et al. [5] have applied a new approach, attractor reconstruction analysis (ARA), which quantifies the changes in the morphology and variability of a quasi-periodic signal without affecting the signal information, to arterial blood pressure signals, photoplethysmogram signals and electrocardiogram signals captured from animals and humans. ARA provides a two-dimensional colour-scaled representation of the signal producing features like density and symmetry by which Aston and colleagues [4, 5, 16, 60] were able to identify changes in the shape and variability of the signal associated with cardiovascular function. Similarly, González et al. [32] investigating the attractors of rheoencephalographic signals in human volunteers,

found that nonlinear features derived from the attractors were able to detect the changes in the cerebral blood flow during apnoea.

LDF BF signals are also quasi-periodic and quasi-stationary and may also lend themselves to the attractor reconstruction method as a potential method by which to identify changes in the microvascular functionality. Thanaj et al. [84] showed a significant drop of the maximal density derived from the ARA, during increased flow, with a good discrimination of the blood flow signals between two functional haemodynamic states (Fig. 19.3).

For example, Fig. 19.3 shows the attractors generated from the entire BF signal obtained from one individual, under thermoneutral conditions, randomly selecting a window during a steady state at 33 °C, during transition and during a steady state at 43 °C, that illustrate the changes in different haemodynamic states. The windows of the blood flow signal in Fig. 19.3a shows the segments from the signal in Fig. 19.3b corresponding to the attractors in Fig. 19.3c. The window of the BF signal at 33 °C is shown to result in a dense attractor with many overlaps. The window at the transition time illustrates the BF signal during the last 40 s of the transition, showing the increase of the signal amplitude and therefore the attractor becomes wider and less dense. Similarly, the window at 43 °C shows the BF signal at 43 °C corresponding to larger attractor as the amplitude of the signals is increased as it represents the increased amplitude of the signal. This finding is consistent with the recent studies

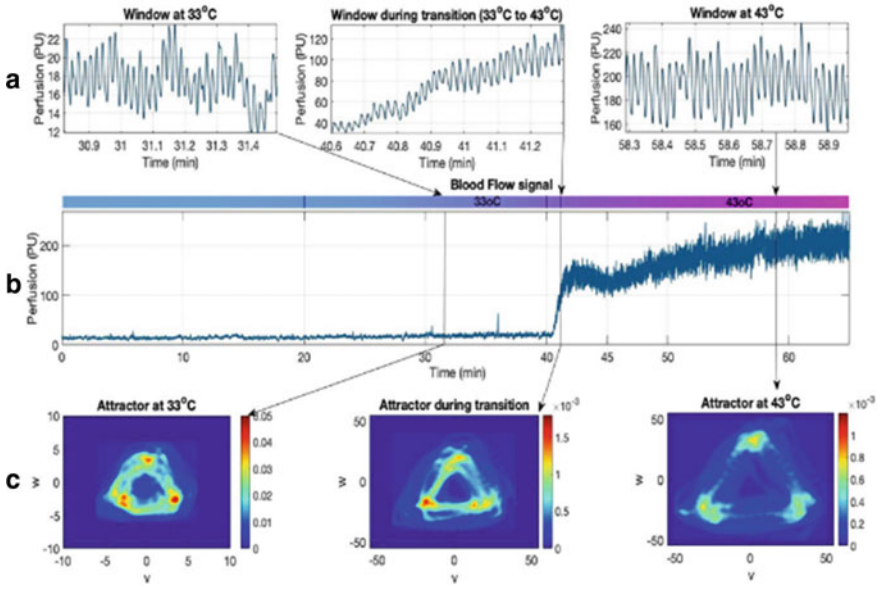

Fig. 19.3 **a** Windows of 20 s each derived from the blood flow signal at 33 °C, during transition time and at 43 °C. **b** A blood flow signal of one healthy volunteer at baseline temperature, at 33 °C, during transition time from 33 to 43 °C and during local warming at 43 °C. Lines indicate the end of each window. **c** The reconstructed attractors for each of these windows. From [84]

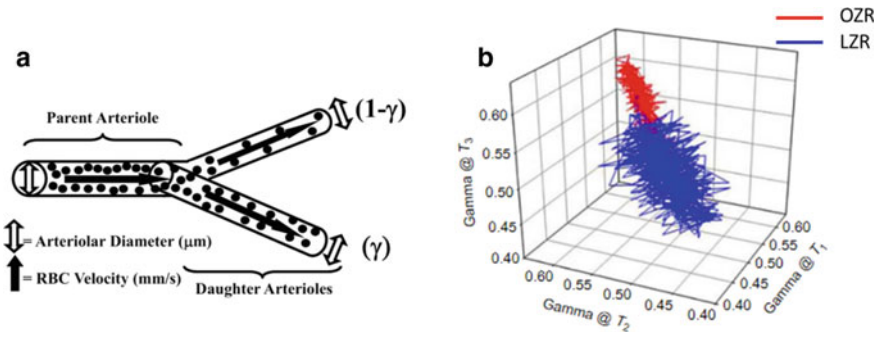

Fig. 19.4 **a** Schematic representation of an arteriolar bifurcation showing the key measured parameters of arteriolar diameter and erythrocyte velocity (measured using optical Doppler velocimetry) used to calculate blood flow volumes. Perfusion distribution volumes are given as the proportionality parameter γ and $(1 - \gamma)$ in the two daughter arterioles arising from a parent. RBC, red blood cell. **b** Presentation of the chaotic attractor describing the overall spatial-temporal behaviour of γ at 1A-2A arteriolar bifurcations in the lean Zucker rat (blue) and obese Zucker rat (red) under control conditions (A). The attractors are presented as iterated maps, where the respective value for γ is presented at multiple successive time points within that condition. Taken from Butcher et al. [13]

[4, 5, 16, 60] using attractor reconstruction analysis in arterial blood pressure signals, suggesting that the size of the attractor is related with the signal amplitude.

In a not unrelated fashion, Frisbee and colleagues, using chaotic network attractor analysis to describe perfusion heterogeneity (γ) at arteriolar bifurcations, have described the spatial and temporal shifts in perfusion distribution within the skeletal muscle microcirculation of rodents at risk of CVD (Fig. 19.4a, b for details) [13]. Frisbee et al. [30] went on to demonstrate that this attractor is a strong predictor of functional outcomes within animal models of cardiovascular and metabolic disease risk of increasing severity.

19.7 Concluding Remarks

The analysis of complex physiological time series is the focus of considerable attention as it has proved difficult to describe such signals using simple mathematical models. One such signal is that derived from the superficial microvascular network of the skin, sampled using non-invasive laser Doppler flowmetry. Time and frequency domain analysis, used to assess network functionality and to describe the dynamic characteristics of signals, has offered invaluable insight into the variations in the amplitude and relative contribution of spontaneous, rhythmic oscillatory fluctuations of local and systemic origin. Impairment of spatial and temporal regulation of network perfusion by these localised mechanisms has informed our understanding of how a mismatch between perfusion and demand, particularly at times of elevated metabolic demand, may contribute to disease risk or severity. Recently, nonlinear

analysis of the blood flux signals has begun to shed new light on the flexibility of the system in response to standard haemodynamic perturbations and in human cohorts at increasing risk and severity of cardiovascular and metabolic disease. Nonlinear complexity methods have been used to quantify the regularity of the blood flux signal by evaluating the presence of repeated patterns, providing complexity variants at single and across multiple spatial and temporal scales. Further, the new approach of attractor reconstruction analysis offers quantitative measures of the microvascular system in phase space and a visual representation in the shape and variability of the signal producing a two-dimensional attractor with features such as density and symmetry. Nonlinear analysis thus provides a better characterisation of the flexibility of the system in a range of pathophysiological conditions.

In conclusion, these mathematical approaches are able to identify changes in microvascular function and have utility in understanding the fundamental mechanistic contributors to microvascular (dys)function. To what extent they can be used to discriminate between (patho)physiological states and in the understanding of the effectiveness of interventions for reversing established vasculopathy and perfusion impairments has yet to be determined. They have yet to be used to inform treatment regimens or to predict clinical outcomes. With machine learning techniques these novel approaches may, in future, support a more effective and mechanism-based classification of tissue perfusion, providing a use in clinical assessment.

References

1. M. Aboy, R. Hornero, D. Abasolo, D. Alvarez, Interpretation of the Lempel-Ziv complexity measure in the context of biomedical signal analysis. IEEE Trans. Biomed. Eng. **53**(11), 2282–2288 (2006)
2. A.M. Albano, X.T. Tigno, P.E. Rapp, Time series analysis, or the quest for qualitative measures of time dependent behavior. Philipp. Sci. Lett. **1**(1), 18–31 (2008)
3. J. Allen, K. Howell, Microvascular imaging: techniques and opportunities for clinical physiological measurements. Physiol. Meas. **35**(7), R91–R141 (2014)
4. P.J. Aston, M. Nandi, M.I. Christie, Y.H. Huang (eds.), Comparison of attractor reconstruction and HRV methods for analysing blood pressure data. Comput. Cardiol. **2014** (2014)
5. P.J. Aston, M.I. Christie, Y.H. Huang, M. Nandi, Beyond HRV: attractor reconstruction using the entire cardiovascular waveform data for novel feature extraction. Physiol. Meas. **39**(2), 024001– (2018)
6. K. Balasubramanian, N. Nagaraj, Aging and cardiovascular complexity: effect of the length of RR tachograms. Peerj **4** (2016)
7. M.A. Basarab, N.S. Konnova, D.A. Basarab, D.D. Matsievskiy (eds.), Digital signal processing of the Doppler blood flow meter using the methods of nonlinear dynamics, in *2017 Progress in Electromagnetics Research Symposium—Spring (PIERS)*, 22–25 May 2017
8. A. Bernjak, A. Stefanovska, Importance of wavelet analysis in laser Doppler flowmetry time series. Conf. Proc. IEEE Eng. Med. Biol. Soc. **1**, 4064–4067 (2007)
9. A. Bernjak, A. Stefanovska, P.V.E. McClintock, P.J. Owen-Lynch, P.B.M. Clarkson, SAMP. Coherence between fluctuations in blood flow and oxygen saturation. Fluct. Noise Lett. **11**(1), 1240013 (2012)

10. A. Bollinger, A. Yanar, I. Hoffman, U.K. Franzeck, Is high frequency fluxmotion due to respiration or to vasomotion activity?, in *Progress in Applied Micrcirculation*, ed. by M. Ke (Karger, Basel, 1993), pp. 52–55
11. J.D. Briers, Laser Doppler, speckle and related techniques for blood perfusion mapping and imaging. Physiol. Meas. **22**(4), R35–R66 (2001)
12. K. Bräuer, M. Hahn, Nonlinear analysis of blood flux in human vessels. Phys. Med. Biol. **44**(7), 1719–1733 (1999)
13. J.T. Butcher, A.G. Goodwill, S.C. Stanley, J.C. Frisbee, Blunted temporal activity of microvascular perfusion heterogeneity in metabolic syndrome: a new attractor for peripheral vascular disease? Am. J. Physiol. Heart Circ. Physiol. **304**(4), H547–H558 (2013)
14. D. Carey, M. Thanaj, T. Davies, E. Gilbert-Kawai, K. Mitchell, D.Z.H. Levett et al., Enhanced flow-motion complexity of skin microvascular perfusion in Sherpas and lowlanders during ascent to high altitude. Sci. Rep. **9** (2019)
15. S. Cerutti, D. Hoyer, A. Voss, Multiscale, multiorgan and multivariate complexity analyses of cardiovascular regulation. Philos. Trans. R. Soc. A **2009**(367), 1337–1358 (1892)
16. P.H. Charlton, L. Camporota, J. Smith, M. Nandi, M. Christie, P.J. Aston et al. (eds.), Measurement of cardiovascular state using attractor reconstruction analysis, in *2015 23rd European Signal Processing Conference (EUSIPCO)*, 31 Aug–4 Sept 2015
17. A. Chipperfield, M. Thanaj, G. Clough, Multi-scale, multi-domain analysis of microvascular flow dynamics. Exp. Physiol. (2019)
18. A.J. Chipperfield, M. Thanaj, E. Scorletti, C.D. Byrne, G.F. Clough, Multi-domain analysis of microvascular flow motion dynamics in NAFLD. Microcirculation **26**(5) (2019)
19. G.F. Clough, K.Z. Kuliga, A.J. Chipperfield, Flow motion dynamics of microvascular blood flow and oxygenation: evidence of adaptive changes in obesity and type 2 diabetes mellitus/insulin resistance. Microcirculation **24**(2) (2017)
20. A. Colantuoni, S. Bertuglia, M. Intaglietta, Quantitation of rhythmic diameter changes in arterial microcirculation. Am. J. Physiol. **246**(4 Pt 2), H508–H517 (1984)
21. A. Colantuoni, S. Bertuglia, M. Intaglietta, Microvascular vasomotion: origin of laser Doppler flux motion. Int. J. Microcirc. Clin. Exp. **14**(3), 151–158 (1994)
22. M. Costa, A.L. Goldberger, C.K. Peng, Multiscale entropy to distinguish physiologic and synthetic RR time series. Comput. Cardiol. **29**, 137–140 (2002)
23. M. Costa, A.L. Goldberger, C.K. Peng, Multiscale entropy analysis of complex physiologic time series. Phys. Rev. Lett. **89**(6) (2002)
24. J.L. Cracowski, M. Roustit, Current methods to assess human cutaneous blood flow: an updated focus on laser-based-techniques. Microcirculation **23**(5), 337–344 (2016)
25. D. De Backer, K. Donadello, D.O. Cortes, Monitoring the microcirculation. J. Clin. Monit. Comput. **26**(5), 361–366 (2012)
26. R. Fatouleh, V.G. Macefield, Cardiorespiratory coupling of sympathetic outflow in humans: a comparison of respiratory and cardiac modulation of sympathetic nerve activity to skin and muscle. Exp. Physiol. **98**(9), 1327–1336 (2013)
27. E. Figueiras, M. Roustit, S. Semedo, L.F. Ferreira, J.L. Crascowski, A. Humeau, Sample entropy of laser Doppler flowmetry signals increases in patients with systemic sclerosis. Microvasc. Res. **82**(2), 152–155 (2011)
28. A.J. Flammer, T. Anderson, D.S. Celermajer, M.A. Creager, J. Deanfield, P. Ganz et al., The assessment of endothelial function: from research into clinical practice. Circulation **126**(6), 753–767 (2012)
29. P. Flandrin, *Time-Frequency/Time-Scale Analysis* (Elsevier Science, 1998)
30. J.C. Frisbee, J.T. Butcher, S.J. Frisbee, I.M. Olfert, P.D. Chantler, L.E. Tabone et al., Increased peripheral vascular disease risk progressively constrains perfusion adaptability in the skeletal muscle microcirculation. Am. J. Physiol. Heart Circ. Physiol. **310**(4), H488–H504 (2016)
31. P.T. Goedhart, M. Khalilzada, R. Bezemer, J. Merza, C. Ince, Sidestream Dark Field (SDF) imaging: a novel stroboscopic LED ring-based imaging modality for clinical assessment of the microcirculation. Opt. Express **15**(23), 15101–15114 (2007)

32. C. González, E.W. Jensen, P.L. Gambús, M. Vallverdú, Poincaré plot analysis of cerebral blood flow signals: feature extraction and classification methods for apnea detection. PLoS ONE **13**(12), e0208642 (2018)
33. A. Grinevich, A. Tankanag, I. Tikhonova, N. Chemeris, A new approach to the analysis of skin blood flow oscillations in human. Microvasc. Res. **126** (2019)
34. B. Gryglewska, M. Necki, M. Zelawski, M. Cwynar, T. Baron, M. Mrozek et al., Fractal dimensions of skin microcirculation flow in subjects with familial predisposition or newly diagnosed hypertension. Cardiol. J. **18**(1), 26–32 (2011)
35. R.J. Gush, T.A. King, M.I. Jayson, Aspects of laser light scattering from skin tissue with application to laser Doppler blood flow measurement. Phys. Med. Biol. **29**(12), 1463–1476 (1984)
36. L.A. Holowatz, C.S. Thompson-Torgerson, W.L. Kenney, The human cutaneous circulation as a model of generalized microvascular function. J. Appl. Physiol. **105**(1):370–372 (2008)
37. H. Hsiu, C.L. Hsu, H.F. Hu, F.C. Hsiao, S.H. Yang, Complexity analysis of beat-to-beat skin-surface laser-Doppler signals in diabetic subjects. Microvasc. Res. **93**, 9–13 (2014)
38. A. Humeau, F. Chapeau-Blondeau, D. Rousseau, P. Abraham, Numerical simulation of laser Doppler flowmetry signals based on a model of nonlinear coupled oscillators. Comparison with real data in the frequency domain. Conf. Proc. IEEE Eng. Med. Biol. Soc. **2007**, 4068–4071 (2007)
39. A. Humeau, F. Chapeau-Blondeau, D. Rousseau, P. Rousseau, W. Trzepizur, P. Abraham, Multifractality, sample entropy, and wavelet analyses for age-related changes in the peripheral cardiovascular system: preliminary results. Med. Phys. **35**(2), 717–723 (2008)
40. A. Humeau, B. Buard, G. Mahe, D. Rousseau, F. Chapeau-Blondeau, P. Abraham, Multiscale entropy of laser Doppler flowmetry signals in healthy human subjects. Med. Phys. **37**(12), 6142–6146 (2010)
41. A. Humeau, G. Mahe, F. Chapeau-Blondeau, D. Rousseau, P. Abraham, Multiscale analysis of microvascular blood flow: a multiscale entropy study of laser Doppler flowmetry time series. IEEE Trans. Biomed. Eng. **58**(10), 2970–2973 (2011)
42. A. Humeau-Heurtier, M. Klonizakis, Processing of laser Doppler flowmetry signals from healthy subjects and patients with varicose veins: information categorisation approach based on intrinsic mode functions and entropy computation. Med. Eng. Phys. **37**(6), 553–559 (2015)
43. K. Kalev, M. Bachmann, L. Orgo, J. Lass, H. Hinrikus, Lempel-Ziv and multiscale Lempel-Ziv complexity in depression. IEEE Eng. Med. Bio. 4158–4161 (2015)
44. H. Kantz, T. Schreiber, *Nonlinear Time Series Analysis*, 2nd edn. (Cambridge University Press, Cambridge, 2003)
45. J. Kastrup, J. Bulow, N.A. Lassen, Vasomotion in human skin before and after local heating recorded with laser Doppler flowmetry. A method for induction of vasomotion. Int. J. Microcirc. Clin. Exp. **8**(2):205–215 (1989)
46. K.Z. Kuliga, R. Gush, G.F. Clough, A.J. Chipperfield, Time-dependent behavior of microvascular blood flow and oxygenation: a predictor of functional outcomes. IEEE Trans. Biomed. Eng. **65**(5), 1049–1056 (2018)
47. P. Kvandal, A. Stefanovska, M. Veber, K.H. Desiree, K.K. Arvid, Regulation of human cutaneous circulation evaluated by laser Doppler flowmetry, iontophoresis, and spectral analysis: importance of nitric oxide and prostaglandines. Microvasc. Res. **65**(3), 160–171 (2003)
48. P. Kvandal, S.A. Landsverk, A. Bernjak, A. Stefanovska, H.D. Kvernmo, K.A. Kirkeboen, Low-frequency oscillations of the laser Doppler perfusion signal in human skin. Microvasc. Res. **72**(3), 120–127 (2006)
49. H.D. Kvernmo, A. Stefanovska, K.A. Kirkeboen, K. Kvernebo, Oscillations in the human cutaneous blood perfusion signal modified by endothelium-dependent and endothelium-independent vasodilators. Microvasc. Res. **57**(3), 298–309 (1999)
50. A. Lempel, J. Ziv, On the complexity of finite sequences. IEEE Trans. Inf. Theory IT **22**(1), 75–81 (1976)
51. F. Liao, Y.K. Jan, Enhanced phase synchronization of blood flow oscillations between heated and adjacent non-heated sacral skin. Med. Biol. Eng. Comput. **50**(10), 1059–1070 (2012)

52. F. Liao, Y.K. Jan, Using modified sample entropy to characterize aging-associated microvascular dysfunction. Front. Physiol. **7**, 126 (2016)
53. F. Liao, D.W. Garrison, Y.K. Jan, Relationship between nonlinear properties of sacral skin blood flow oscillations and vasodilatory function in people at risk for pressure ulcers. Microvasc. Res. **80**(1), 44–53 (2010)
54. D. Low, H. Jones, N. Cable, L. Alexander, W. Kenney, Historical reviews of the assessment of human cardiovascular function: interrogation and understanding of the control of skin blood flow. Eur. J. Appl. Physiol. **120**, 1–16 (2020)
55. R. Martini, A. Bagno, The wavelet analysis for the assessment of microvascular function with the laser Doppler fluximetry over the last 20 years. Looking for hidden informations. Clin. Hemorheol. Micro. **70**(2), 213–229 (2018)
56. J.A. Morlet, E. Fourgeau, D. Glard, Wave propagation and sampling theory. Part 1: Complex signals and scattering in multilayered media. Geophysics **47**, 203–221 (1983)
57. D.M. Muris, A.J. Houben, A.A. Kroon, R.M. Henry, C.J. van der Kallen, S.J. Sep et al., Age, waist circumference, and blood pressure are associated with skin microvascular flow motion: the Maastricht study. J. Hypertens. (2014)
58. N. Nagaraj, K. Balasubramanian, Three perspectives on complexity: entropy, compression, subsymmetry. Eur. Phys. J. Spec. Top. **226**(15), 3251–3272 (2017)
59. N. Nagaraj, K. Balasubramanian, S. Dey, A new complexity measure for time series analysis and classification. Eur. Phys. J. Spec. Top. **222**(3–4), 847–860 (2013)
60. M. Nandi, J. Venton, P. Aston, A novel method to quantify arterial pulse waveform morphology: attractor reconstruction for physiologists and clinicians. **39**, 104008 (2018)
61. D. Narayana Dutt, S.M. Krishnan, Application of phase space technique to the analysis of cardiovascular signals, in *Proceedings of the First Joint BMES/EMBS Conference on Serving Humanity, Advancing Technology*, Atlanta, GA, 16–19 October 1999 (1999), p. 914
62. A.V. Oppenheim, R.W. Schafer, *Discrete-Time Signal Processing* (Pearson, Upper Saddle River, 2010)
63. V.E. Papaioannou, I.G. Chouvarda, N.K. Maglaveras, I.A. Pneumatikos, Temperature variability analysis using wavelets and multiscale entropy in patients with systemic inflammatory response syndrome, sepsis, and septic shock. Crit. Care **16**(2), 15 (2012)
64. D. Parthimos, O. Schmiedel, J.N. Harvey, T.M. Griffith, Deterministic nonlinear features of cutaneous perfusion are lost in diabetic subjects with neuropathy. Microvasc. Res. **82**(1), 42–51 (2011)
65. M. Rossi, A. Carpi, F. Galetta, F. Franzoni, G. Santoro, The investigation of skin blood flowmotion: a new approach to study the microcirculatory impairment in vascular diseases? Biomed. Pharmacother. **60**(8), 437–442 (2006)
66. M. Rossi, A. Cupisti, M.C. Di, F. Galetta, G. Barsotti, G. Santoro, Blunted post-ischemic increase of the endothelial skin blood flowmotion component as early sign of endothelial dysfunction in chronic kidney disease patients. Microvasc. Res. **75**(3), 315–322 (2008)
67. M. Roustit, J.L. Cracowski, Non-invasive assessment of skin microvascular function in humans: an insight into methods. Microcirculation **19**(1), 47–64 (2012)
68. M. Roustit, J.L. Cracowski, Assessment of endothelial and neurovascular function in human skin microcirculation. Trends Pharmacol. Sci. **34**(7), 373–384 (2013)
69. M. Roustit, S. Blaise, C. Millet, J.L. Cracowski, Reproducibility and methodological issues of skin post-occlusive and thermal hyperemia assessed by single-point laser Doppler flowmetry. Microvasc. Res. **79**(2), 102–108 (2010)
70. M. Roustit, C. Millet, S. Blaise, B. Dufournet, J.L. Cracowski, Excellent reproducibility of laser speckle contrast imaging to assess skin microvascular reactivity. Microvasc. Res. **80**(3), 505–511 (2010)
71. E.G. Salerud, T. Tenland, G.E. Nilsson, P.A. Oberg, Rhythmical variations in human skin blood flow. Int. J. Microcirc. Clin. Exp. **2**(2), 91–102 (1983)
72. R. Sassi, S. Cerutti, F. Lombardi, M. Malik, H. Huikuri, C.-K. Peng et al., Advances in heart rate variability signal analysis: joint position statement by the e-Cardiology ESC Working Group and the European Heart Rhythm Association co-endorsed by the Asia Pacific Heart Rhythm Society (2015)

73. G. Schlotthauer, A. Humeau-Heurtier, J. Escudero, H.L. Rufiner, Measuring complexity of biomedical signals. Complexity (2018)
74. S.S. Segal, Regulation of blood flow in the microcirculation. Microcirculation **12**(1), 33–45 (2005)
75. Y. Shiogai, A. Stefanovska, P.V.E. McClintock, Nonlinear dynamics of cardiovascular ageing. Phys. Rep. **488**(2–3), 51–110 (2010)
76. A.E. Simms, J.F.R. Paton, A.M. Allen, A.E. Pickering, Is augmented central respiratory-sympathetic coupling involved in the generation of hypertension? Resp. Physiol. Neurobiol. **174**(1–2), 89–97 (2010)
77. D.W. Slaaf, H.H. Vrielink, G.J. Tangelder, R.S. Reneman, Effective diameter as a determinant of local vascular resistance in presence of vasomotion. Am. J. Physiol. **255**(5 Pt 2), H1240–H1243 (1988)
78. T. Soderstrom, A. Stefanovska, M. Veber, H. Svensson, Involvement of sympathetic nerve activity in skin blood flow oscillations in humans. Am. J. Physiol. Heart Circ. Physiol. **284**(5), H1638–H1646 (2003)
79. A. Stefanovska, M. Bracic, H.D. Kvernmo, Wavelet analysis of oscillations in the peripheral blood circulation measured by laser Doppler technique. IEEE Trans. Biomed. Eng. **46**(10), 1230–1239 (1999)
80. H.A. Struijker-Boudier, A.E. Rosei, P. Bruneval, P.G. Camici, F. Christ, D. Henrion et al., Evaluation of the microcirculation in hypertension and cardiovascular disease. Eur. Heart J. **28**(23), 2834–2840 (2007)
81. F. Takens, Detecting strange attractors in turbulence. Dynamical systems and turbulence, Warwick 1980, in *Lecture Notes in Mathematics* (Springer, Berlin, 1981), pp. 366–381
82. A.V. Tankanag, A.A. Grinevich, T.V. Kirilina, G.V. Krasnikov, G.M. Piskunova, N.K. Chemeris, Wavelet phase coherence analysis of the skin blood flow oscillations in human. Microvasc. Res. **95**, 53–59 (2014)
83. M. Thanaj, A.J. Chipperfield, G.F. Clough, Analysis of microvascular blood flow and oxygenation: discrimination between two haemodynamic steady states using nonlinear measures and multiscale analysis. Comp. Biol. Med. **102**, 157–167 (2018)
84. M. Thanaj, A. Chipperfield, G. Clough, Attractor reconstruction analysis for blood flow signals. Conf. Proc. IEEE Eng. Med. Biol. Soc. **2019**, 2281–2284 (2019)
85. X.T. Tigno, B.C. Hansen, S. Nawang, R. Shamekh, A.M. Albano, Vasomotion becomes less random as diabetes progresses in monkeys. Microcirculation **18**(6), 429–439 (2011)
86. G. Valenza, L. Iozzia, L. Cerina, L. Mainardi, R. Barbieri, Assessment of instantaneous cardiovascular dynamics from video plethysmography, in *2017 39th Annual International Conference of the IEEE Engineering in Medicine and Biology Society (Embc)* (2017), pp. 1776–1779
87. A.H.D. Vélez, H.G. González-Hernández, B.R. Guerra (eds.), Attractor reconstruction for plethysmographic biosignals, in *2014 International Conference on Electronics, Communications and Computers (CONIELECOMP)*, 26–28 Feb 2014
88. X. Wang, J. Meng, G. Tan, L. Zou, Research on the relation of EEG signal chaos characteristics with high-level intelligence activity of human brain. Nonlinear Biomed. Phys. **4**(1), 2 (2010)
89. G.B. Yvonne-Tee, A.H. Rasool, A.S. Halim, A.R. Rahman, Noninvasive assessment of cutaneous vascular function in vivo using capillaroscopy, plethysmography and laser-Doppler instruments: its strengths and weaknesses. Clin. Hemorheol. Microcirc. **34**(4), 457–473 (2006)
90. Y. Zhang, S. Wei, C. Di Maria, C. Liu, Using Lempel-Ziv complexity to assess ECG signal quality. J. Med. Biol. Eng. **36**(5), 625–634 (2016)

Chapter 20
Sleep-Related Modulations of Heart Rate Variability, ECG, and Cardio-Respiratory Coupling

Thomas Penzel, Yaopeng Ma, Jan Krämer, Niels Wessel, Martin Glos, Ingo Fietze, and Ronny P. Bartsch

Abstract *Background*: Integrated physiological systems following regular rhythms are a prime example of biological oscillators. Such systems include the heart with an oscillatory activity on a time scale of 1-second and the circadian pacemaker leading to a close to 24 h sleep-wake rhythm. Other prominent physiological oscillations each characterized by specific time scales are brain waves, respiration, blood pressure and vascular activity, and sleep-stage transitions with non-REM/REM cycles. In the healthy organism, these oscillators interact with each other, and studying those interactions during physiological transitions and in patients with disorders helps to uncover and better understand the underlying mechanisms. *Methods*: In order to investigate the coupling of these oscillators, sleep studies with cardiorespiratory polysomnography are performed on persons with healthy sleep and with sleep disorders. Polysomnography includes the recording of the electrocardiogram (ECG), the sleep-electroencephalogram (EEG), respiration, blood pressure/pulse wave, oxygen saturation, and movement activity by means of electromyogram (EMG). The analysis is performed visually by sleep experts, and computer assisted with time domain, frequency domain, and non-linear methodologies. *Results*: The parameters obtained provide information on the regulation of the autonomic nervous system (ANS) during sleep. The ANS is regulated totally different during slow-wave (non-REM) and REM sleep. Beat-to-beat heart-rate variations allow us to estimate a scoring of sleep stages. To some degree it is possible to track transitions from wakefulness to sleep by solely analyzing heart-rate variations. ECG and heart rate analysis allow assessment of

T. Penzel (✉) · M. Glos · I. Fietze
Interdisziplinäres Schlafmedizinisches Zentrum, Charitecentrum Für Pneumologie CC12, Charité – Universitätsmedizin Berlin, Charitéplatz 1, 10117 Berlin, Germany
e-mail: thomas.penzel@charite.de

T. Penzel
Saratov State University, Saratov, Russia

Y. Ma · R. P. Bartsch
Department of Physics, Bar-Ilan-University, Ramat Gan, Israel

J. Krämer · N. Wessel
Kardiovaskuläre Physik, Arbeitsgruppe Nichtlineare Dynamik, Fachbereich Physik, Humboldt-Universität Berlin, Berlin, Germany

A. Stefanovska and P. V. E. McClintock (eds.), *Physics of Biological Oscillators*, Understanding Complex Systems,
https://doi.org/10.1007/978-3-030-59805-1_20

sleep disorders as well. Cyclical variations of heart rate combined with respiration-modulated changes in ECG morphology (amplitude of R wave and T wave) provides reliable detection of sleep-disordered breathing. *Conclusions*: The assessment of signals being easily accessible like ECG and heart rate can help to assess sleep, sleep stages and sleep disorders with an acceptable accuracy, even if reflecting physiological functions indirectly.

Keywords Sleep stages · Autonomic function · Heart rate variability · ECG · Cardiovascular regulation · Sleep apnea · Cardiorespiratory coupling

20.1 Introduction

Sleep takes about one third of human life and is important for rest and for recovery from daytime activities. Sleep is not a homogenous state but comprises different stages such as light sleep, deep sleep and rapid eye movement (REM) sleep, which serve different physiological functions. For example, deep sleep seems to be most important for physical recovery and for removing waste metabolites from the brain [11]. Growth hormone is secreted during deep sleep, and this sleep stage is most important for immune system build-up. REM sleep is associated with dreaming and memory functions, and thus REM sleep is thought to be important for mental recreation and mood. During the process of sleep, these different sleep stages follow one after the other in a well-defined order and sequence starting with light sleep, followed by deep sleep and then REM sleep. This sequence is called a sleep cycle and has a duration of 80 to 110 min in general. Over the course of the night, there are between 4 and 6 such sleep cycles. In the beginning of the night a sleep cycle contains much more deep sleep and very short REM sleep, while towards the end of the night, a sleep cycle has little, if any deep sleep and much longer REM sleep. As such, the beginning of sleep and the end of sleep are very different. The entire 'sleep cycle program' is sensitive to behavior, external influences (e.g., light, noise, temperature), internal influences (e.g., food, stress, drugs, medications), and is much influenced by disease. Of particular importance in this context are sleep disorders that originate out of the sleep process itself. Sleep medicine has defined 66 distinct sleep disorders, among which insomnia (the inability to fall or stay asleep) and sleep apnea (respiratory cessations during sleep) are the two most prevalent and well-known examples.

In order to investigate sleep, in healthy subjects and in patients with sleep disorders, polysomnography (PSG) is commonly used in a sleep laboratory. PSG recordings include several electroencephalography (EEG) electrodes placed on well-defined locations on the scalp. To recognize REM sleep and to distinguish the different sleep stages, in addition to EEG, the electrooculogram (EOG) and the electromyogram (EMG) of the chin are recorded. A screen shot of these signals is depicted in Fig. 20.1a. In order to detect sleep disorders, such as sleep apnea, additional signals need to be recorded. At first, cardiac and respiratory signals were

added in the 1980's, coining the term cardio-respiratory polysomnography. However, respiration as recorded during sleep needs a longer time window to be evaluated as depicted in Fig. 20.1b. Only with the help of cardio-respiratory polysomnography, sleep apneas could be detected and classified into obstructive sleep apnea (OSA) and central sleep apnea (CSA) (Fig. 20.2). Nowadays, PSGs containing all these raw data are recorded in hundreds of sleep centers worldwide. The matured discipline of sleep medicine trains sleep physicians and sleep scientists to diagnose all the different kinds of sleep disorders based on their PSG characteristics as well as clinical symptoms and consequences.

The cardiac component of cardio-respiratory polysomnography is covered by electrocardiography (ECG) and heart rate recordings. However, cardio-respiratory

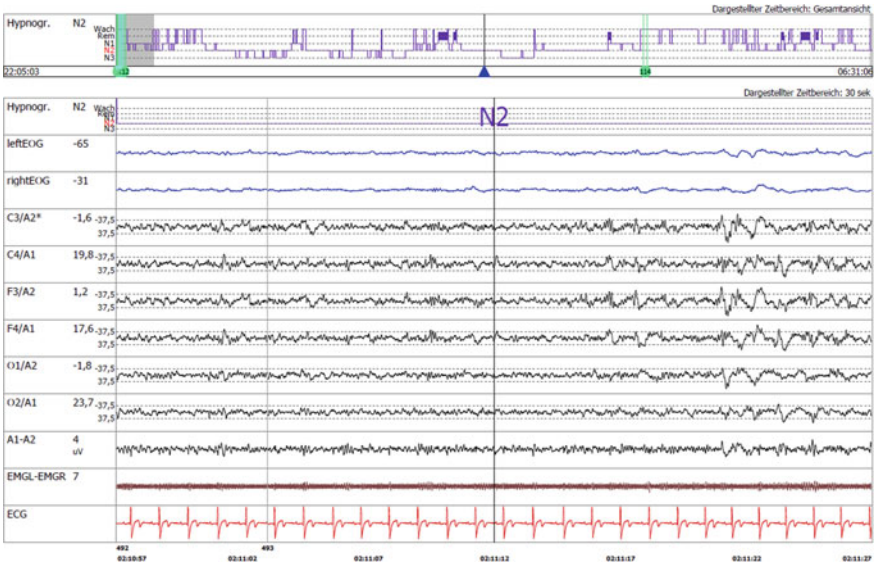

Fig. 20.1 **a** Polysomnography recording in a sleep laboratory. On top the 'Hypnogram', the sequence of sleep stages over the course of the entire night is depicted. The blue arrow marks the time point for which the raw signal traces are presented just below. The time window presented for the raw sleep traces is 30 s. The raw signal traces show from top to bottom, first the sleep stage 'N2' which is 'light sleep'. Then there follows the sleep EOG traces, the sleep EEG traces, the EMG of the chin muscle and the lowest trace is the ECG over the chest wall. The EEG traces do show sleep spindles and K-complexes which are characteristic and required to score sleep stage N2. **b** Polysomnography recording in a sleep laboratory. On top the hypnogram is depicted which shows the time course of sleep stages over the entire sleep recording. The blue arrows (almost at the end of the night) show the time window for which the raw signal traces are depicted below. The time window for the raw signal traces is 5 min. This window length is usually chosen to score respiratory events such as sleep apnea and hypopnea (marked by red bars), and oxygen desaturation events (marked by blue bars). The sleep EEG (shown in the upper raw traces), which was the subject of attention in **a**, are too small to be evaluated here visually. Therefore, the polysomnography is typically analyzed twice using 30 s and 5 min time windows to score sleep stages and respiratory events, respectively

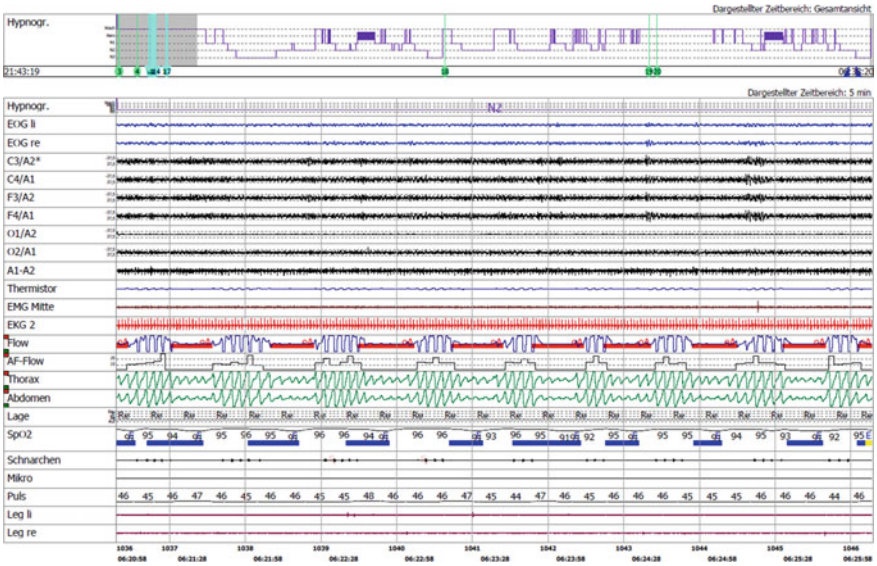

Fig. 20.1 (continued)

evaluation is often underrepresented in clinical sleep reports albeit their important diagnostic information for autonomic nervous system activity during sleep. In this chapter, we present major methodological developments in sleep research regarding ECG, heart rate variability and cardio-respiratory coupling, and we outline physiological and pathophysiological aspects related to sleep medicine obtained by new approaches. We will describe the related technical developments and new possibilities, as well as the present status of limitations of such approaches. At the same time, however, it has been possible to consider only a highly restricted number of studies and, consequently, of approaches and algorithms.

20.2 Nocturnal Electrocardiography (ECG) Recordings to Monitor Changes in Autonomous Nervous System Activity During Sleep

In addition to electrophysiological parameters measured at the head by electroencephalography (EEG), electrooculography (EOG), and electromyography (EMG), investigations of physiological functions in sleep require recordings of respiration, bodily movement, and—as a reflection of the cardiovascular system—the ECG [5]. With respect to its signal amplitude of about 1 millivolt, the ECG represents the strongest electrophysiological signal of the human body. It is recorded with a sampling frequency of at least 100 Hz and, with modern equipment, with 500 Hz

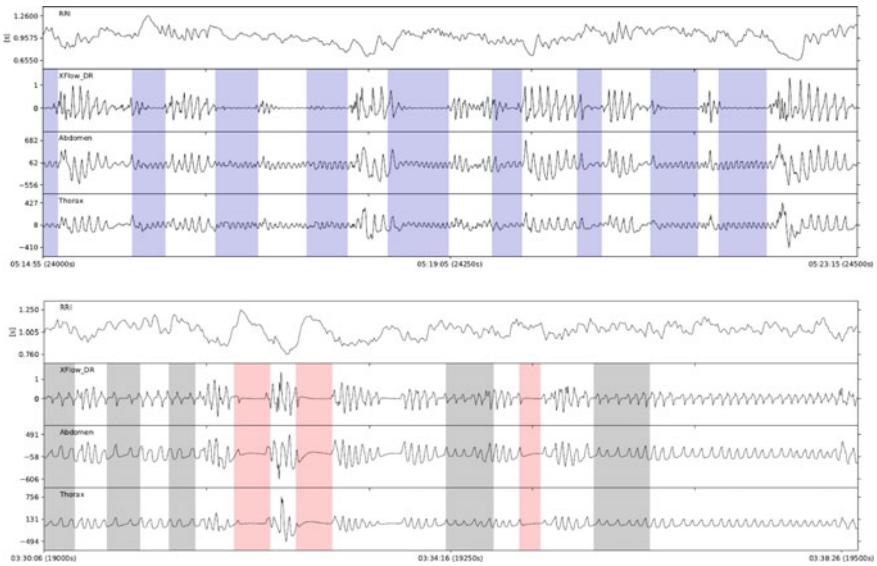

Fig. 20.2 Examples of respiratory events as scored in cardiorespiratory polysomnography. The top panel depicts epochs of obstructive sleep apnea (OSA—marked by purple bars), whereas the bottom panel shows central sleep apnea (CSA—pink bars) and hypopnea (grey bars). OSA and CSA are both characterized by sleep-disordered breathing but have very different physiological origins. While OSA is caused by obstruction of the upper airways, CSA is due to absent respiratory drive from the brain stem. This can be seen in the three simultaneously recorded respiratory signals from airflow, abdomen and thorax. During OSA, thorax and abdominal movements are still detected by respiratory belts, however, no breathing is taking place and the airflow signal stays flat. In contrast, for CSA no activity is detected in all three respiratory signals. The top trace of each panel shows the simultaneously recorded signal of RR interval durations (i.e., inverse heart rate) that significantly changes during apnea events

[5]. ECG recordings below 500 Hz, to be sure, are associated with restrictions involving the detection of minor but important changes in beat-to-beat heart-rate variations ('heart rate variability'—HRV). With respect to amplifier technology, and in comparison to EEGs and EMGs, ECGs are relatively simple to measure owing to their pronounced signal amplitudes. Consequently, and based on knowledge of the fundamental physiology of the autonomic nervous system, interest arose in applying the ECG as a simple diagnostic tool for studying sleep and sleep disorders, in the sense of a surrogate parameter.

During sleep, the autonomic nervous system is subject to pronounced changes and variability [37]. The activity of many physiological systems is greatly reduced during sleep, including the metabolic system, which causes all functions of the autonomic system to adapt accordingly. Indeed, such pronounced alterations are linked to the stages of sleep in a profound way, with the result that sleep itself has been characterized as a serious trial for the autonomic nervous system [45]. Moreover, the particular sleep stages have specific effects on heart rate. As we know from

Snyder's physiological investigations, heart rate continuously falls with sleep depth and reaches lowest values in deep sleep [37]. In parallel, during deep sleep, sympathicotonic nervous activity falls to very low levels, and the parasympathetic nervous system dominates [38]. In contrast, during REM sleep, the brain and other physiological systems show higher levels of activity (comparable to relaxed wakefulness) associated with increased sympathicotonia [38]. Consequently, the mean heart rate and HRV during REM are higher compared to light and deep sleep. In addition to these sleep-stage influences, heart rate and HRV are subject to circadian modulation and are also evidently influenced by prior extensive phases of wakefulness or sleep deprivation leading to increased sleep drive [12].

Variations in heart rate obtained from nocturnal ECG recordings can detect changes in the functions of the sympathetic and parasympathetic nervous systems, and analysis of alterations in this context can be performed by classical techniques such as spectral analysis of HRV [1]. Nowadays, it is common knowledge that the spectral power in the low-frequency range (LF, 0.04–0.15 Hz) mostly relates to sympathetic activity, whereas the high-frequency range (HF, 0.15–0.4 Hz) is associated with respiration and the activity of the parasympathetic nervous system (HRV [40]). Discussion on the significance of very low frequencies (VLF, below 0.04 Hz) is still taking place. Here, in conjunction with sleep-related breathing disorders, these frequencies play a major role as pointed out in a recent systematic review [8].

Based on spectral power and other statistical methods of HRV analysis, sleep stages can be estimated through the differences in autonomic nervous system regulation. Furthermore, up to some degree, it is possible to track transitions from wakefulness to sleep by analysis of heart-rate variations alone. In addition, an ECG during cardiorespiratory polysomnography enables the monitoring of other vital functions during nocturnal sleep studies [27] because it is sensitive enough to detect bradycardia or tachycardia, paroxysmal atrial fibrillation, AV block and in some cases nocturnal coronary ischemia [7]. ECG also enables initial evaluation of nocturnal arrhythmia in the sense of HRV and ectopic beats [7]. As a result, typical procedures involve the recording of only one single-channel ECG, which can provide support for a more comprehensive examination by multi-channel ECG diagnosis or by long-term ECG. ECG and HRV analysis allow the assessment of selected sleep disorders as well. For example, sleep disordered breathing can be detected reliably by studying cyclical variation of heart rate combined with respiration-modulated changes in ECG morphology (amplitude of R wave and T wave).

20.3 Non-linear Analysis of Heart Rate Variability

Attempts to identify sleep stages and sleep apnea on the basis of heart rate and with the help of computer-aided techniques, have encountered problems because of the non-stationary, intermittent characteristics of heart rate interval recordings that violate the preconditions of classical frequency-analysis procedures. This has led to consideration and trial of new techniques taken from statistical physics. These

techniques are otherwise applied in the analysis of weather data, water-level information, and stock-exchange prices, and are widely considered to be methods of fractal analysis and chaos theory. For these approaches, the objectives are to analyze data that appear coincidental and to detect an inner structure and patterns of order that deviate from pure random behavior and that demonstrate phenomena of determinism. One primary attempt here is to analyze the extent to which one value depends on preceding values that happened seconds, minutes or even hours earlier. If there is such non-random dependence among the values of a time series, the data are termed to be auto-correlated.

One of the first applications of non-linear dynamics evaluated the complexity of HRV throughout an entire night by analyzing beat-to-beat variability by means of Wavelet- and Hilbert transform and found differences between healthy subjects and patients with sleep apnea [17]. Subsequent studies on HRV applied detrended fluctuation analysis (DFA) to quantify short and long-term correlations but encountered difficulties due to sudden jumps and fluctuations in the signals' dynamics caused by changes in sleepers' positions at night, and during transition from one sleep stage to the next. Such alterations render it impossible to find uniform patterns of behavior for beat-to-beat variability in the heart rate. To enhance analysis, therefore, the course of nocturnal heart rates was broken down according to the various sleep stages, and the disturbances resulting from stage transitions were disregarded [6]. In other words, sequences of pure sleep stages were prepared for study of heart rate. It was only in the second step that the beat-to-beat sequences of heart rate were once again investigated for variability and sleep apnea. Investigations took place to quantify the extent to which one heartbeat interval is correlated with subsequent heartbeats and revealed distinct and highly pronounced differences between the sleep stages. Specifically, in deep sleep, there is a virtually uncorrelated behavior pattern from heartbeat to heartbeat, whereas extensively correlated heartbeat behavior exists during REM sleep. These differences were greater between the various sleep stages than the differences found for episodes of heart rate with and without sleep apnea [6].

Initially, these results were surprising, since the influence of sleep apnea on heart rate appears to be pronounced and distinct. However, the marked changes in sympathetic tone throughout the sleep stages provide a possible explanation. Changes in sympathetic tone with respect to heart rate are not distinctly visible, since they are smaller in amplitude. Still, they are highly apparent in the beat-to-beat variation in heart frequency. This also explains why differences between the sleep stages as determined by frequency analysis could in fact be determined. Indeed, in frequency analysis, not only the frequencies are taken into account, but precisely also their amplitudes (i.e., spectral power). Furthermore, our investigations of heart rate variability during sleep indicate that influences of autonomic tone on heart-rate regulation are so dominant that they still prevail during sleep apnea, and that they also allow distinction to be drawn between sleep stages among these patients as well [6]. Therefore, with respect to beat-to-beat variability, the cyclical variation in heart rate caused by sleep apnea merely signifies a relatively minor additional disturbance. Accordingly, the results revealed the feasibility of a new procedure for determining, from beat-to-beat regulation of heart rate, differences between sleep stages [28] with

the greatest differences arising between deep sleep on the one hand—with virtually uncorrelated beat-to-beat regulation—and REM sleep on the other, with extensively correlated beat-to-beat regulation of the heart rate.

20.4 Cyclical Variation of Heart Rate with Sleep Apnea

Very shortly after Guilleminault described sleep-related breathing disorders, it became apparent that characteristic alterations in heart rate take place during obstructive apnea events [14]. This phenomenon was described as cyclical variation in heart rate, and the proposal arose to utilize this characteristic pattern for diagnosis of sleep apnea [14]. Many diagnostic devices were developed to detect and diagnose sleep apnea outside the context of a sleep lab utilizing this heart-rate pattern [25].

During each individual apnea phase, relative bradycardia becomes apparent, with relative tachycardia occurring during each subsequent increased respiratory activity. These patterns in heart rate—arising from alterations in sympathetic nervous activity during each apnea event—are, in their temporal course, directly linked to breathing. As a result, it is possible to count the number of apnea events based on heart rate data alone. For example, the MESAM system and its successors, as well as new polygraph devices, employ heart rate for diagnosis of sleep apnea in an outpatient setting [25].

Since the cyclical variation in heart rate presents an impressive periodic pattern, it became obvious to apply methods of frequency and spectral power analysis once again to quantitatively assess cyclical variations in heart rate—and thus, potentially determine the degree of severity of sleep-related breathing disorders. To this end, various teams have employed the method of Fourier analysis, however, limitations arose in the attempt to evaluate the periodic patterns automatically [17]. This is because the cyclical variations are not strictly periodic since apneas and hypopneas show large variation in duration especially when occurring in various sleep stages.

Period analyses in the time domain or by classical spectral methods quickly reach their limits. The cyclical variation in heart rate remains dependent to greater or lesser degree on physical training condition, age, weight, and concomitant diseases (e.g., diabetes). Often, there are individual characteristic patterns of bradycardia and tachycardia that are influenced by several factors such as concomitant cardiologic diseases, arrhythmia, pacemaker ECGs, and heart failure—which make them difficult to be interpreted. For these reasons, a fully automated assessment of sleep-related breathing disorders cannot take place reliably if it is based on cyclical heart-rate variation alone. Determination of oxygen saturation, changes in ECG morphology and more direct recordings of breathing disorders are essential for greater reliability.

20.5 Detection of Sleep Apnea Through Changes in Heart Rate and ECG Morphology

In 2000 at the Computers in Cardiology Conference in Boston, USA, public competition took place as part of a congress held by engineers of biomedical technology who are involved with ECG analysis. This competition involved solving a problem encountered in ECG analysis, i.e., recognition of sleep apnea by study of nocturnal ECGs [29]. ECGs from healthy test subjects, patients with moderate sleep apnea, and patients with severe degree of sleep apnea were made available on a server of PHYSIONET [13]. A total of 35 nocturnal ECG recordings were provided for training purposes, and 35 recordings were provided to competition participants for purposes of analysis. Two teams succeeded in correctly classifying all patients and were even able to correctly identify sleep apnea epochs in 92 and 94% of cases.

In addition to data on the cyclical variation in heart rate, these teams had also analyzed the corresponding ECG plots [29]. This indeed revealed that respiration modulates the amplitudes of the R- and T-waves of the ECG—a phenomenon that was observed earlier but had not been assessed in the context of apnea detection [19]. The so-called electrocardiographically derived respiration signal (EDR)—i.e., data on respiration as derived from an ECG—enables evaluation of the respiration plot and, in turn, detection of apnea and hypopnea events. Although when employed alone, EDR also demonstrates weaknesses in recognition of such events, in combination with data on the cyclical variation in heart rate, it offers an astonishingly high level of certainty in detection of sleep-related breathing disorders from ECGs.

Morphological alterations of the ECG during sleep apnea arise from the fact that the influence of breathing on an ECG is mechanical in nature, and it is therefore independent of factors that affect the eloquence of the cyclical variation in heart rate. As a result, combining the evaluation of autonomic influences on the ECG (i.e., heart rate) and assessment of the mechanical, respiration-mediated influences on the ECG (i.e., EDR) enables good detection of sleep apnea events. If additional physiological measures are included such as oxygen saturation, snoring, and body movement during sleep, a polygraph system can be applied that can achieve a high degree of sensitivity and specificity for detection of sleep-related breathing disorders even without direct registration of respiration [9].

20.6 Cardiopulmonary Coupling and Cardiorespiratory Phase Synchronization

The regulation of breathing and heartbeat is coupled [18], and cardiopulmonary coupling (CPC) is studied mostly in the context of respiratory sinus arrhythmia (RSA), which leads to variations in the heart rate and constitutes a portion of HRV. Respiratory sinus arrhythmia describes the respiratory-gated fluctuation of the heart rate: during inhalation, heart rate increases and during exhalation, it again subsides.

Petr Einbrodt, in 1860, was the first to describe this form of cardiorespiratory coupling [10]. During daytime activity and exercise, RSA is usually not visible, or much attenuated. In contrast, at rest and during sleep, RSA is pronounced and easily recognizable [31]. Early studies were even able to describe correlation between the extent of coupling and the various sleep stages.

An additional coupling phenomenon was found in the synchronization of heart beats and respiratory phases. Phase synchronization as the adjustment of the phases of self-sustained oscillators due to their weak interaction was described for the first time in the seventeenth century in conjunction with pendulum clocks [16, 30]. In the case of cardiorespiratory phase synchronization (CRPS), heartbeats occur in increased numbers during certain phases of the respiratory cycle: e.g., at the beginning of the inhalation phase, at the end of the inhalation phase, and in the middle of the exhalation phase [3, 4, 35, 39, 44].

These two coupling phenomena—respiratory sinus arrhythmia (RSA) and phase synchronization (CRPS)—can occur independently of each other (Fig. 20.3). In addition, the two coupling mechanisms are variously influenced by different physiological parameters. A prominent example is the respiratory frequency that largely impacts the extent of RSA but not CRPS [4].

The physical training condition of the persons examined is thought to influence the extent of CRPS [35]. Athletes have demonstrated pronounced synchronization between respiration and heartbeat, which led to the conclusion that the occurrence of CRPS represents ergonomically effective regulation. The influence of the extent and the effectiveness of this coupling on physical or mental performance have not yet been determined. In this context, such coupling could also represent a good surrogate parameter fore recovery after physical exertion.

Further studies have systematically investigated CRPS during sleep for different age groups of healthy subjects and among sleep-apnea patients [4, 20, 21, 32]. Among healthy persons, the dependence of the extent of synchronization on the various sleep stages becomes evident and CRPS is most distinctly pronounced during deep sleep, and least pronounced in REM sleep [4]. This sleep-stage dependency is many times greater for phase synchronization than for respiratory sinus arrhythmia and is likewise much greater than the variations in mean heart rate, HRV, and respiratory rate. However, as soon as sleep apnea occurs, exertion takes place in the regulation of the breathing and circulatory system. As a result, the phase relationship between these two systems is impaired to the extent that CRPS can no longer be detected.

In order to study cardiorespiratory coupling during sleep apnea, cardiorespiratory coordination was introduced recently [32]. Cardiorespiratory coordination is a time domain measure quantifying chronological interrelations between respiration and heartbeat that is not affected even by epochs of hyperventilation following apnea events [32]. Additionally, cardiorespiratory coordination is less sensitive to cardiorespiratory disturbances in general and therefore may be more suitable for sleep apnea detection than CRPS. This is also because for CRPS, each respiratory cycle is transformed into phase space, which means that during apneas (i.e., prolonged periods of time until the next respiratory onset occurs), many more heartbeats will fall into the ‘apnea’ respiratory cycle than during ‘normal’ respiration. This results in

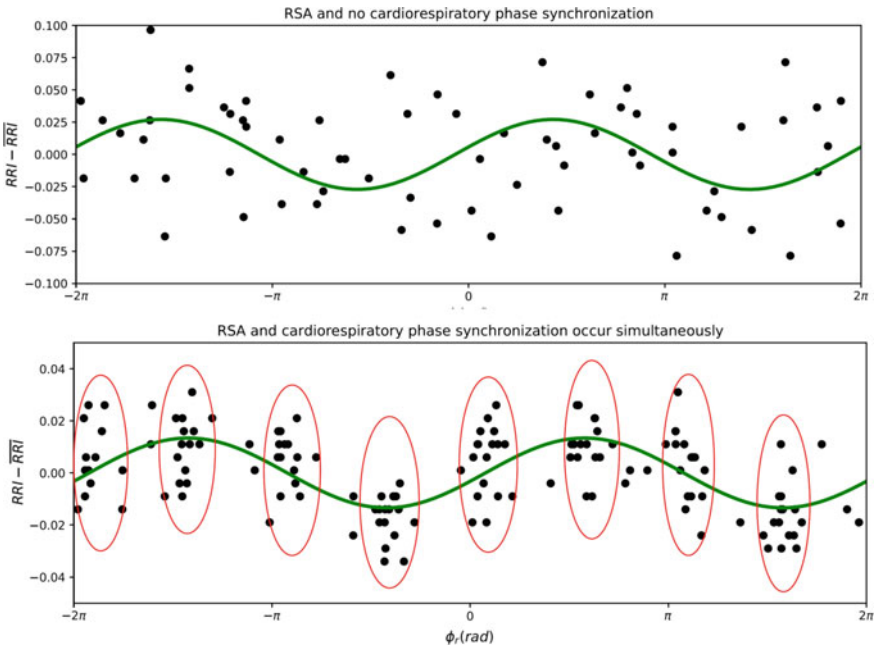

Fig. 20.3 Respiratory sinus arrhythmia (RSA) and cardiorespiratory phase synchronization (CRPS) represent different forms of cardiorespiratory coupling. RSA leads to periodic modulation of the heart rate within each breathing cycle (sinusoid least-squares-fit line through the data points—green color), and CRPS (highlighted by red ovals) is characterized by clustering of heartbeats at particular phases φ_r of the breathing cycle. Shown are consecutive heartbeats over a period of 90 s. The x axis indicates the corresponding respiratory phases φ_r where heartbeats occur; the y axis shows the deviation of each heartbeat interval RRI from the mean RR calculated by averaging all RRI within a given breathing cycle. Heartbeats are plotted over pairs of consecutive breathing cycles, to better visualize rhythmicity. Data are selected from the same subject during deep sleep and show in the top panel a segment with RSA and no CRPS (i.e., heartbeats are homogeneously distributed across all phases of the respiratory cycles) as well as RSA and CRPS occurring simultaneously (lower panel) (adapted from [4] with different data)

diagonal lines in the cardiorespiratory synchrogram as seen in Fig. 20.4 that disrupt any indication of coupling that might be present in phase space. However, in the cardiorespiratory coordigram, prolonged respiratory cycle lengths due to apnea do not disturb the plot itself and the corresponding heartbeats are merely situated farther away from $\Delta t = 0$ (i.e., the respiratory onset) (Fig. 20.4). Overall, cardiorespiratory coordination increases during and after obstructive sleep apnea [32] as well as central sleep apnea. Figure 20.5 shows an example of cardiorespiratory coordination during Cheyne-Stokes respiration with central sleep apnea.

Cardiopulmonary coupling parameters based on RSA, cardiorespiratory phase synchronization and the coordination of respiration and the circulatory system are therefore important additional markers for cardiovascular regulation, similar to HRV [42, 43], blood-pressure variability [23], and baroreceptor sensitivity [22].

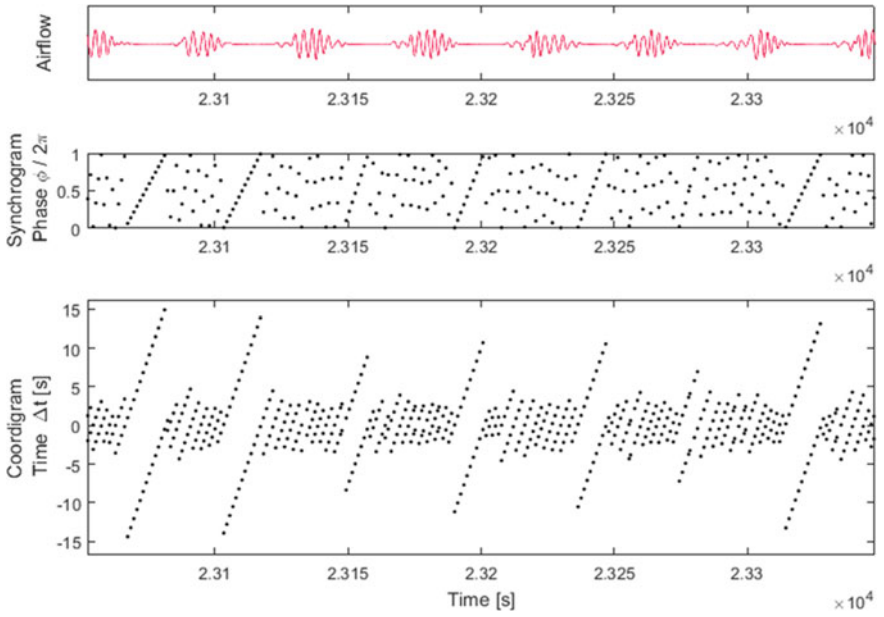

Fig. 20.4 Cardiorespiratory synchronisation versus coordination during central sleep apnea. Breathing frequency and amplitude both influencing the synchrogram as well as the coordigram. Apneas mean prolonged time to the next respiratory onset and thus are represented as disruptive diagonal lines of heartbeats in the cardiorespiratory synchrogram. In the coordigram however, the corresponding heartbeats are plotted farther away from $\Delta t = 0$ and thus do not disrupt the plot (adapted from [4] with different data)

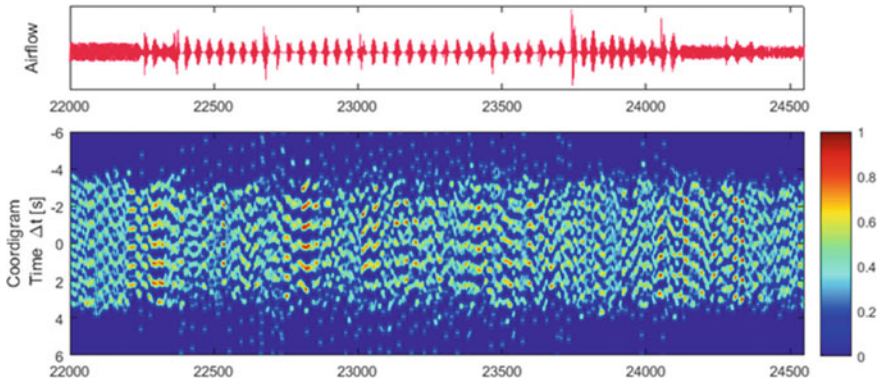

Fig. 20.5 Increase in cardiorespiratory coordination across central sleep apnea. The airflow clearly shows the begin and the end of the apnea and red horizontal lines in the coordigram indicate increased cardiorespiratory coordination

20.7 Discussion

New attempts are being undertaken with procedures involving more cost-effective equipment and with easily accessible devices—such as with smartphones—to record heart and pulse rates. From data gathered in this manner, spectral analysis and procedures from nonlinear dynamics are used to calculate heart rate variability. Attempts are likewise being made to apply findings from the above-described studies to work with the signals involved. Other endeavors with smartphone applications use simply recorded signals to detect not only the respective sleep stages but also the occurrence of sleep apnea.

These often inexpensive applications have found extensive use, since they offer insights into sleep, from analysis conducted simply at home, of nocturnal sleep and sleep apnea. In contrast to cardiorespiratory polysomnography among healthy and sleep-apnea patients, none of these algorithms has until now been validated in clinical studies. Clarification is still required of the extent to which these possibilities offer diagnostic and prognostic potential.

Unfortunately, until now there is no analysis standard for the one-channel ECG that goes beyond simple statistics such as mean heart rate and maximum and minimum heart rate values. Current clinical practice does not apply established or new algorithms for HRV or cardiorespiratory coupling analysis, and therefore lags behind the state-of-the-art techniques and knowledge of basic sleep research. In case of HRV this may be due to the known interference between respiration and heart rate variability parameters and only controlled conditions in terms of paced breathing would allow a comparison of inter and intra individual changes. However, cardiorespiratory coupling does influence both interdependent systems and therefore could be very useful for clinical interpretation of PSG recordings. A necessary step in expediting translational research might be a closer interaction between clinicians and researchers on this topic. This may also help to interpret changes in parameters as observed during autonomous arousals, which are not observed in EEG leads as central nervous activations. Such arousals can be a consequence of brief movements and respiratory irregularities such as sighs or other phenomena observed during sleep that lead to short alterations in ECG and heart rate as well as blood pressure. Currently, these brief events are not further evaluated and may be disregarded as simple perturbations and noise although short transient events may be important for a differential diagnosis and furthermore for a decision in treatment of persons with sleep disorders.

New methods for the evaluation of ECG and blood pressure will allow to better distinguish between subjects being healthy or disturbed sleepers, as already seen in subjects with obstructive snoring, bruxism, or periodic leg movements without cortical arousals. These people do suffer without obvious indications in conventional sleep EEG parameters.

This uncertainty is especially significant in light of the necessary assumption that this form of investigation is being conducted not only with healthy subjects and with patients definitely suffering from sleep apnea, but also with persons who

merely snore and others who represent mixed forms of snoring and sleep apnea. The importance of HRV and cardiorespiratory coupling analyses becomes particularly evident in the context of such borderline cases, which are even more widespread than cases of unequivocal sleep apnea itself. For this reason, reliable validation of such applications must be required before diagnostic employment. Otherwise, they represent merely one more general application intended to measure data from individuals and to expand their personal digital environment, without sustainable background and without the possibility of specific and well-founded intervention.

First attempts in this direction are being made with recordings of single-channel ECGs based on which HRV and EDR are determined, and from these data cardiopulmonary coupling (CPC) is estimated [41]. It is also possible to analyze various frequency bands—i.e., low-frequency coupling (LFC) and high-frequency coupling (HFC)—to evaluate sleep (e.g., stable sleep, instable sleep, and REM sleep/wake) and the occurrence sleep-related breathing disorders (SRBD) that lead to an elevated share of LFC. It is furthermore possible to characterize existing SRBD on the basis of various patterns in LFC. An initial study has revealed greater likelihood of a narrow-band sample in LFC for periodically central apnea events—whereas, in contrast, a more pronounced broad-band pattern is characteristic of predominantly obstructive sleep apnea [36]. However, prospective studies are required to verify the extent to which these indications hold true.

20.8 Summary

Analysis of ECG data and heart rate during sleep provides an appreciable diversity of information on the physiology and the pathophysiology of sleep-wake regulation. Assessment of nocturnal ECGs with respect to cyclical fluctuations of heart rate, combined with studies of respiration-dependent alterations in ECG morphology (e.g., amplitudes of the R waves and T waves), allows reliable recognition of sleep-related breathing disorders. The quality of sleep itself can also be evaluated by analysis of heart-rate variations. Deep sleep and REM sleep, to be sure, demonstrate characteristic properties in heart-rate variability.

Even now, new methods are being applied in practice by presenting sleep findings that already include analysis of healthy sleep and sleep disorders with the aid of long-term ECG systems, data from pacemaker ECGs, multi-night actigraphy data as well as information from innovative, reduced-scale recording systems [2, 15]. To arrive at solid diagnostic and therapeutic conclusions from these results, it will be necessary to conduct prospective validation studies and to perform clinical evaluation with parallel polygraphy and polysomnography. In addition, new algorithms are needed which allow automated processing of heart rate and heart rate variability which results in a conclusive report, similar to the report created from sleep-stage scoring or respiration scoring.

Funding This study was supported by the German-Israeli Foundation (GIF) Grants I-1298-415.13/2015 and I-1372-303.7/2016 and the German National Cohort study (www.nationale-kohorte.de) funded by the Federal Ministry of Education and Research (BMBF) and the Helmholtz Association. TP was partially supported by a Russian Federation Government Grant No. 075-15-2019-1885.

References

1. S. Akselrod, D. Gordon, F.A. Ubel, D.C. Shannon, A.C. Bargerm, R.J. Cohen, Power spectrum analysis of heart rate fluctuations: A quantitative probe of beat-to-beat cardiovascular control. Science **213**, 220–222 (1981)
2. M. Angelova, C. Karmakar, Y. Zhu, S.P.A. Drummond, J. Ellis, Automated method for detecting acute insomnia using multi-night actigraphy data. IEEE Access **8**, 74413–74422 (2020). https://doi.org/10.1109/access.2020.2988722
3. R. Bartsch, J.W. Kantelhardt, T. Penzel, S. Havlin, Experimental evidence for phase synchronization transitions in the human cardiorespiratory system. Phys. Rev. Lett. **98**, 054102 (2007)
4. R.P. Bartsch, A.Y. Schumann, J.W. Kantelhardt, T. Penzel, P.C. Ivanov, Phase transitions in physiologic coupling. Proc. Natl. Acad. Sci. **109**, 10181–10186 (2012)
5. R.B. Berry, R. Brooks, C.E. Gamaldo, S.M. Harding, R.M. Lloyd, C.L. Marcus, B.V. Vaughn, for the American Academy of Sleep Medicine, *The AASM Manual for the Scoring of Sleep and Associated Events: Rules, Terminology and Technical Specifications, Version 2.1* (American Academy of Sleep Medicine, Darien, IL, 2014)
6. A. Bunde, S. Havlin, J.W. Kantelhardt, T. Penzel, J.H. Peter, K. Voigt, Correlated and uncorrelated regions in heart-rate fluctuations during sleep. Phys. Rev. Lett. **85**, 3736–3739 (2000)
7. S.M. Caples, C.L. Rosen, W.K. Shen, A.S. Gami, W. Cotts, M. Adams, P. Dorostkar, K. Shivkumar, V.K. Somers, T.I. Morgenthaler, E.J. Stepanski, C. Iber, The scoring of cardiac events during sleep. J. Clin. Sleep Med. **3**, 147–154 (2007)
8. V.C. Cunha Sequeira, P.M. Bandeira, J.C. Moreno Azevedo, Heart rate variability in adults with obstructive sleep apnea: a systematic review. Sleep Sci. **12**(3), 214–221 (2019). https://doi.org/10.5935/1984-0063.20190082
9. P. De Chazal, C. Heneghan, W.T. McNicholas, Multimodal detection of sleep apnoea using electrocardiogram and oximetry signals. Phil. Trans. R. Soc. A **367**, 369–389 (2009)
10. P.P. Einbrodt, *Über den Einfluss der Athembewegungen auf Herzschlag und Blutdruck. Sitzungsberichte der math.-naturw*. Classe der kaiserlichen Akademie der Wissenschaften. K. K. Hof- und Staatsdruckerei (Wien) (Band XI, 1860), pp. 361–418
11. N.E. Fultz, G. Bonmassar, K. Setsompop, R.A. Stickgold, B.R. Rosen, J.R. Polimeni, L.D. Lewiset, Coupled electrophysiological, hemodynamic, and cerebrospinal fluid oscillations in human sleep. Science **366**(6465), 628–631 (2019). https://doi.org/10.1126/science.aax5440
12. M. Glos, I. Fietze, A. Blau, G. Baumann, T. Penzel, Cardiac autonomic modulation and sleepiness: physiological consequences of sleep deprivation due to 40 h of prolonged wakefulness. Physiol. Behav. **125**, 45–53 (2014)
13. A.L. Goldberger, L.A.N. Amaral, L. Glass, J.M. Hausdorff, P.C. Ivanov, R.G. Mark, J.E. Mietus, G.B. Moody, C.K. Peng, H.E. Stanley, PhysioBank, PhysioToolkit, and PhysioNet components of a new research resource for complex physiologic signals. Circulation **101**, e215–e220 (2000)
14. C. Guilleminault, S. Connolly, R. Winkle et al., Cyclical variation of the heart rate in sleep apnoea syndrome. Mechanisms, and usefulness of 24 h electrocardiography as a screening technique. Lancet **8369**, 126–131 (1984)
15. P.M. Holloway, M. Angelova, S. Lombardo, A. St. Clair Gibson, D. Lee, J. Ellis, Complexity analysis of sleep and alterations with insomnia based on non-invasive techniques. J. R. Soc. Interface **11**(93), 1–8 (2014). https://doi.org/10.1098/rsif.2013.1112

16. C. Huygens, Horologium Oscillatorium: sive de motu pendulorum ad horologia aptato demostrationes geometricae (1673)
17. P.C. Ivanov, M.G. Rosenblum, C.K. Peng, J. Mietus, S. Havlin, H.E. Stanley, A.L. Goldberger, Scaling behaviour of heartbeat intervals obtained by wavelet-based time-series analysis. Nature **383**, 323–327 (1996)
18. H.P. Koepchen, K. Thurau, Über die Entstehungsbedingungen der atemsynchronen Schwankungen des Vagustonus (Respiratorische Arrhythmie). Pflügers Archiv **269**, 10–30 (1959)
19. G.B. Moody, R.G. Mark, A. Zoccola et al., Clinical validation of the ECG-derived respiration (EDR) technique. Comput. Cardiol. **13**, 507–510 (1986)
20. A. Müller, M. Riedl, T. Penzel, J. Kurths, N. Wessel, Ereignisbasierte Charakterisierung kardiovaskulärer Interaktionen während des Schlafs. Somnologie **18**, 243–251 (2014)
21. A. Müller, M. Riedl, N. Wessel, J. Kurths, T. Penzel, Methoden zur Analyse kardiorespiratorischer und kardiovaskulärer Kopplungen. Somnologie **16**, 24–31 (2012)
22. G. Parati, M. Di Rienzo, G. Mancia, How to measure baroreflex sensitivity: from the cardiovascular laboratory to daily life. J. Hypertens. **18**, 7–19 (2000)
23. G. Parati, J.P. Saul, M. Di Rienzo, G. Mancia, Spectral analysis of blood pressure and heart rate variability in evaluating cardiovascular regulation. A critical appraisal. Hypertension **25**, 1276–1286 (1995)
24. T. Penzel, J.W. Kantelhardt, R.P. Bartsch, M. Riedl, J.F. Kraemer, N. Wessel, C. Garcia, M. Glos, I. Fietze, C. Schöbel, Modulations of heart rate, ECG, and cardio-respiratory coupling observed in polysomnography. Front. Physiol. **7**, 460 (2016). https://doi.org/10.3389/fphys.2016.00460
25. T. Penzel, G. Amend, K. Meinzer, J.H. Peter, P. von Wichert, MESAM: a heart rate and snoring recorder for detection of obstructive sleep apnea. Sleep **13**, 175–182 (1990)
26. T. Penzel, C. Garcia, M. Glos, M. Renelt, C. Schöbel, J.W. Kantelhardt, R.P. Bartsch, A. Müller, M. Riedl, N. Wessel, I. Fietze, Herzfrequenz und EKG in der Polysomnographie. Somnologie **19**, 254–262 (2015). https://doi.org/10.1007/s11818-015-0033-5
27. T. Penzel, G. Hajak, R.M. Hoffmann, R. Lund, T. Podszus, T. Pollmächer, T. Schäfer, H. Schulz, W. Sonnenschein, I. Spieweg, Empfehlungen zur Durchführung und Auswertung polygraphischer Ableitungen im diagnostischen Schlaflabor. *Ztschr. EEG - EMG* **24**, 65–70 (1993)
28. T. Penzel, J.W. Kantelhardt, L. Grote, J.H. Peter, A. Bunde, Comparison of detrended fluctuation analysis and spectral analysis for heart rate variability in sleep and sleep apnea. IEEE Trans. Biomed. Eng. **50**, 1143–1151 (2003)
29. T. Penzel, J. McNames, P. de Chazal, B. Raymond, A. Murray, G. Moody, Systematic comparison of different algorithms for apnoea detection based on electrocardiogram recordings. Med. Biol. Eng. Comput. **40**, 402–407 (2002)
30. A.S. Pikovsky, M.G. Rosenblum, J. Kurths, *Synchronization: A Universal Concept in Nonlinear Sciences* (Cambridge Univ Press, UK, 2001)
31. F. Raschke, Coordination in the circulatory and respiratory systems, in *Temporal Disorder in Human Oscillatory Systems* ed. by L. Rensing, U. An der Heiden, M.C. Mackey (Springer, Berlin, Heidelberg, New York, 1987), pp. 152–158
32. M. Riedl, A. Müller, J.F. Kraemer, T. Penzel, J. Kurths, N. Wessel, Cardio-respiratory coordination increases during sleep apnea. PLoS ONE **9**, e93866 (2014)
33. A. Roebuck, V. Monasterio, E. Gederi, M. Osipov, J. Behar, A. Malhotra, T. Penzel, G.D. Clifford, A review of signals used in sleep analysis. Physiol. Meas. **35**, R1–R57 (2014)
34. M. Roos, W. Althaus, C. Rhiel, T. Penzel, J.H. Peter, P. von Wichert, Vergleichender Einsatz von MESAM IV und Polysomnographie bei schlafbezogenen Atmungsstörungen (SBAS). Pneumologie **47**, 112–118 (1993)
35. C. Schäfer, M.G. Rosenblum, J. Kurths, H.H. Abel, Heartbeat synchronized with ventilation. Nature **392**, 239–240 (1998)
36. P. Schramm, S. Magnusdottir, R. Thomas, *Cardiopulmonary Coupling—Clinical Atlas*. Document Number D-4.00026, Revision 3.2 (MyCardio LLC, 2014)

37. F. Snyder, J.A. Hobson, D.F. Morrison, F. Goldfrank, Changes in respiration, heart rate, and systolic blood pressure in human sleep. J. Appl. Physiol. **19**, 417–422 (1964)
38. V.K. Somers, M.E. Dyken, A.L. Mark, F.M. Abboud, Sympathetic-nerve activity during sleep in normal subjects. N. Engl. J. Med. **328**, 303–307 (1993)
39. A. Stefanovska, Coupled oscillators. Complex but not complicated cardiovascular and brain interactions. IEEE Eng. Med Biol. Mag. 25–29 (2007). https://doi.org/10.1109/memb.2007.907088
40. Task force of the European Society of Cardiology and the North American Society of Pacing and Electrophysiology, Heart rate variability. Standards of measurement, physiological interpretation, and clinical use. Circulation **93**, 1043–1065 (1996)
41. R.J. Thomas, J.E. Mietus, C.K. Peng, A.L. Goldberger, An electrocardiogram -based technique to assess cardiopulmonary coupling during sleep. Sleep **28**, 1151–1161 (2005)
42. E. Tobaldini, L. Nobili, S. Strada, K.R. Casali, A. Braghiroli, N. Montano, Heart rate variability in normal and pathological sleep. Front. Physiol. **16**(4), 294 (2013)
43. F. Togo, M. Takahashi, Heart rate variability in occupational health: a systematic review. Ind. Health **47**, 589–602 (2009)
44. E. Toledo, S. Akselrod, I. Pinhas, D. Aravot, Does synchronization reflect a true interaction in the cardiorespiratory system? Med. Eng. Phys. **24**, 45–52 (2002)
45. R.L. Verrier, J.E. Muller, J.A. Hobson, Sleep, dreams, and sudden death: the case for sleep as an autonomic stress test for the heart. Cardiovasc. Res. **31**, 181–211 (1996)

Chapter 21
Brain Morphological and Functional Networks: Implications for Neurodegeneration

Vesna Vuksanović

Abstract The highly complex architecture of brain networks has been characterised by modular structures at different levels of its organisation. Here, the focus is on modular properties of brain networks from in vivo neuroimaging of cortical morphology (e.g., thickness, surface area) and activity (function). In this chapter, I review findings on the mapping of these networks, including the time-varying functional networks, and describe some recent advances in mapping the macro- and micro-scales of brain organisation. The aim is to focus on cross-level and cross-modal organisational units of the brain, with reference to their modular topology. I describe recent approaches in network sciences to form bridges across different scales and properties. These approaches raise great expectations that cross-modal neuroimaging and analysis may provide a tool for understanding brain disorders at the system level.

Keywords Brain networks · Cortical morphology · Functional networks · Neurodegeneration

21.1 Introduction

Traditional approaches to the analysis of experimental recordings of brain activity have focused on the localization of function to specific regions of the brain. While such approaches have enabled progress in understanding neuronal processes in the healthy and diseased human brain, recent work suggests that the description of the brain as a set of independent functional elements is an oversimplification. Each brain region—far from acting in isolation—is functionally connected to other regions

V. Vuksanović (✉)
Health Data Research UK and Swansea University Medical School, Data Science Building, Sketty,SA2 8PP Swansea, Wales, UK
e-mail: vesna.vuksanovic@swansea.ac.uk

Aberdeen Biomedical Imaging Centre, Institute for Medical Sciences University of Aberdeen, Aberdeen, Scotland, UK

A. Stefanovska and P. V. E. McClintock (eds.), *Physics of Biological Oscillators*, Understanding Complex Systems,
https://doi.org/10.1007/978-3-030-59805-1_21

through structural white matter connections and through coherent activity [30, 58], creating complex groups of interconnected functional units. The connectivity architecture of these units exhibits an extraordinary level of complexity, whose properties can be analysed across multiple scales—spatial, temporal or topological. To address these different levels of complexity, significant attention over the past decade has focused on mapping the large-scale networks of the human brain extracted from brain scans using Magnetic Resonance Imaging (MRI) [42, 63, 64]. The aim is to provide a picture of the brain and its connections at the system level.

A common simplified form for brain networks maps is a graph, in which brain regions (nodes) are linked to one another by network connections (edges) [13, 14]. The definition of a node or an edge is of critical importance to the relevance of the resulting brain network models [4, 17, 84]. Inspired by neuroanatomy, the definition of nodes and edges is commonly inferred from diffusion, structural or functional MRIs [17]. For example, nodes are defined by Brodmann areas [37], gross anatomical landmarks [25, 69], or increased functional activation [34]. Likewise, the number of streamlines identified between MRI voxels via diffusion of water along the axons [35], coherent/synchronized activity between voxels time series [55] or correlated morphological characteristics [1] are defined as network edges.

Another level of brain network complexity is the arrangement of nodes and edges, which defines network topology. Evidence has accumulated that large-scale brain networks are characterized by modular topology. This means that they contain communities – groups of nodes that are more densely connected to members of their own group than to members of other groups [65]. Modular architecture, with anatomically segregated and functionally specialised communities, is potentially naturally selected because it reduces metabolic costs [56]. From the graph theory perspective, these networks are preferred since they reduce the wiring cost (the average length and number of connections), which enables more efficient information processing [65]. Moreover, recent findings demonstrate that functional networks are enabled not only by critical modular interactions between brain areas, but also by swiftly reconfiguring patterns of these interactions [16, 43, 68]. Whether the subject is at rest [41], or performing either cognitively demanding or simplistic task, the patterns of functional connections between brain areas change, revealing mutli-layered community structures in time-varying brain activity. Time-varying dynamics of these networks accompany neurological disorders [45], brain injury [47], and psychiatric disease [18, 82].

The estimation of brain structural and functional connections is confounded by experimental limitations of MRI techniques. For example, limitations of diffusion MRIs to accurately reconstruct crossing-fibers within white matter is well documented. More importantly, diffusion MRI, which is predominately used as a surrogate for structural brain connectivity (i.e., physical links between the nodes based on white-matter fiber tracking), lacks tools for reconstruction of axonal connections within gray matter [57]. Given that functional connectivity maps gray matter networks, there is a growing interest in anatomical MRI, (i.e., 3D T1-weighted images) and gross morphological features that can be extracted from both gray and white

matter using these images [2]. Anatomical MRIs are simple to acquire and are not limited by artifacts to the same degree as other MRI-based techniques.

To bridge the above experimental limitations, and provide a new insight into macro-scale brain connectivity and its advantages, my focus in this review is on corticocortical networks extracted from anatomical and functional MRI, namely morphological and functional networks. Corticocortical morphological networks are extracted using T1-weighted anatomical MRI, which is a non-invasive assessment of the brain's structures at a sub-millimeter spatial resolution. Likewise, corticocortical functional networks are extracted using functional MRI (fMRI), which records brain activity via Blood-Oxygen-Level-Dependent (BOLD) signal as a proxy of neural activity at the whole brain level. For the purpose of this article, I will review evidence of (i) the corticocortical connections that are mediated by similarities in the cortical morphology (i.e., cytoarchitecture) (ii) the relationship between functionally relevant regional co-activity and underlying cytoarchitecture that may induce synchronized plastic changes among related brain areas (i.e., activity-dependent plasticity) and (iii) implications of this relationship for neurodegenerative syndromes. From the graph theory perspective, my focus is (i) on the modular organisation of brain functional and anatomical (morphological) networks, (ii) the time-varying modular topology of functional interactions and (iii) on describing the potential of modular interactions to inform theoretical and practical approaches to problems in neurodegenerative syndromes.

21.2 Graph Theory and the Brain

One of the mathematical frameworks for studying the human brain structural (and functional) organisation is graph theory. The brain network (graph) is modeled as a set of nodes and edges. Nodes and edges are elementary building blocks of networks and the definition of a node or an edge is of critical importance to the resulting brain network models [15, 83]. The arrangement of nodes and edges defines the organisation of the network, whose topology is quantified using statistical tools of graph theory. Another major property of brain networks is the discovery that they are modular by their topological organisation—they can be decomposed into groups of nodes that are more densely connected to each other than with the rest of the network. In what follows, I will describe in greater details these critical brain network elements and their topological properties, with reference to the two brain networks in focus.

21.2.1 Brain Network Node

A challenging question in the field of large-scale MRI-based brain network analysis is: how to define meaningful nodes for a brain network? The solutions range from defining nodes using the native resolution of the MRI technique (i.e., voxel-

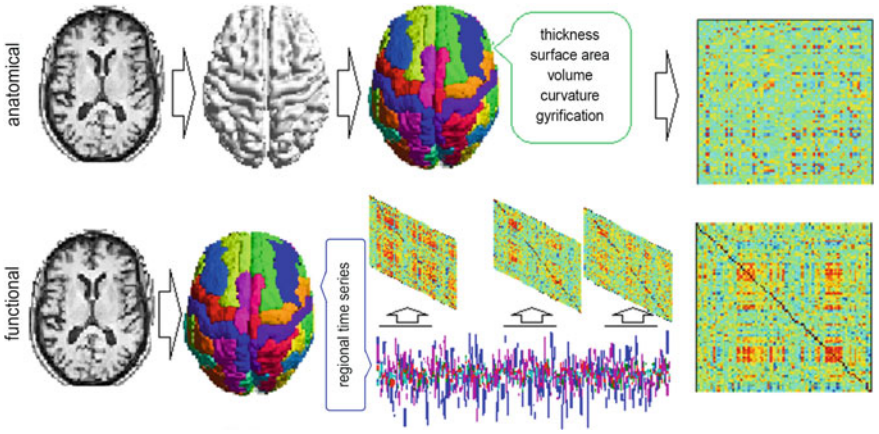

Fig. 21.1 Brain networks from Magnetic Resonance Images (MRI). (Top panel) creating the structural correlation matrix on morphological features measured at different brain regions. From left to right: anatomical MRI, reconstruction of cortical anatomy from images and atlas-based parcellation of the cortex (regions are colour-coded), extraction of the morphological features (thickness, surface area etc.) and creation of the correlation matrix (colour-coded are edge weights). (Bottom panel) creating the functional correlation matrix on regional time series. From left to right: functional MRI, atlas-based parcellation of the cortex (regions are colour-coded), extraction of the regional time series and creation of the correlation matrix from pair-wise correlations between them (color-coded are edge weights). Time-varying functional correlation matrices are shown in the middle of the panel—each matrix is calculated as explained using a sliding window approach

wise resolution) [71], validated parcellations of the cortex based on anatomical or functional landmarks [25, 69] to using random parcellation to ensure equal size for each node [28, 36]. More data-driven approaches include connectivity-defined nodes [34], multivariate decomposition of MRI signal (using statistical techniques such as independent component analysis) [44, 55], or an *a priori* definition of nodes based on meta-analysis [26] (Fig. 21.1).

Most of the studies on anatomical and functional MRI networks use validated parcellations (brain atlases) to define nodes. The advantage of these methods is that they are informed by measures of brain function and anatomy and tailored to test specific hypothesis about brain networks of interest. The limitation is that they are not always transferable across different imaging modalities. Nevertheless, findings show consistency in measures of network topology across different parcellation schemes and MRI modalities. Also, the basic estimates of brain networks organization such as node degree (number of nodal edges), clustering (number of triangles in the network) or path length (average number of edges between two nodes) are consistent across different parcellations with the same number of nodes. Modular organization, which is of interest here, is also consistent across anatomical and functional parcellations and modalities [20, 49, 74]. Future work could corroborate these findings by utilizing available random parcellations of the cortex and multimodal MRI techniques.

21.2.2 Brain Network Edge

In functional and morphological brain networks, edges are defined through an association matrix that captures relations (e.g. cross-correlation, mutual information etc.) between nodal features. The matrix maps all possible pair-wise statistical associations between either regional morphological features or time series of their activity. For the purpose of estimation of network topological organization, these matrices can be binarised—mapping presence (and absence) of associations (edges); or weighted—mapping strengths of association (edge strengths). There are differences in approaches to analyse these networks. Binarised networks are analysed over a range of binarisation thresholds to control for robustness and consistency of topological properties [5] and also for spurious/weak associations or noise [77]. Although arbitrary by its nature, threshold is usually determined by network's deviation from random, null-model topology [60] and the presence of small-world and scale-free topological properties [4]. Network edges can be weighted by the level (i.e., strength) of association between nodal interactions. In functional networks, edges are weighted by pair-wise temporal interactions, which are quantified either by correlation, coherence or synchronicity between time series [55]. In anatomical networks, the edges are weighted by statistical associations (e.g., correlations) between different regional features: thickness, surface area, volume or curvature [3, 62, 79], usually across groups of individuals.

Although neither functional nor morphological correlation networks are constructed on direct neural (axonal) connections between the regions involved, both networks are largely constrained by underlying structural network [38]. For that reason, numerous studies have been focused on functional interactions that mirror the local (segregated) brain anatomy and axonal links between such interactions [38]. However, the two networks organisations and their (within-networks) interactions suggest complex, many-to-one function-structure mapping [32, 54]. Here, the focus is on how the brain cytoarchitecture underpins these patterns of structural-functional network associations. The relation between morphological and functional corticocortical connections, which are mapped by cytoarchitectonic and functional networks is discussed in the Sect. 21.3.

21.2.3 Brain Network Modules

Modular topology is one ubiquitous characteristic of complex networks (including the human brain). Networks can be divided into modules by grouping the densely intra-connected sub-sets of nodes into a single sub-group (i.e., module). Algorithms for the division of a (real-world) network into modules are usually optimized to allow for sparse connections between groups (i.e., detection of overlapping communities) [29, 52]. Furthermore, detecting modules in the network may help to identify those nodes and their connections that may perform different functions with some degree of

independence. At the same time, detecting modular structures that underpin specific function can be identified by characterizing interactions between those nodes that show relatively similar activity/dynamics [29]. Likewise, meta-analysis on more than 1000 fMRI has shown the existence of functional modules specialized for specific cognitive processes [21].

The brain appears to be divided into 'functional modules' whose intra-modular connectivity reflects the underlying structural (axonal) connections [38]. However, although functional modules usually mirror local brain anatomy, they also incorporate long-range interactions (i.e., those between spatially distant brain areas) [31, 75, 78]. More pertinent to this paper, the modular topology of brain functional (MRI) networks is documented across different parcellations of the cortex (i.e., brain atlases) [7, 49, 74]. Modularity as a property of morphology has been widely studied in the context of evolution and development [48]. Recent neuroimaging studies suggest modular organization of cortical morphology across regional thickness [74, 79], surface area [61] or volume [3]. There is consistency in the organisation of these networks whether they are based on correlating these features across individuals within one group [61, 73, 74] or correlating regional features of an individual brain [62]. The brain modular, yet integrated, functional organisation lowers the wiring cost (i.e., the average length and number of connections) of the network [6], thus potentially lowering metabolic costs [8] while providing more efficient information processing [65]. More importantly, modularity, as mapped by large-scale brain fMRI networks, is cognitively and behaviorally relevant; for example, it correlates with variations in working memory [81] (Fig. 21.2).

21.2.4 Dynamical Functional Networks

An additional 'layer' to modular organisation of brain networks is the notion of dynamical functional networks. In this context, the focus is on how likely regions are to change their "module allegiance" and synchronize their activity with a different set of nodes. The analysis of changes in network interactions over time utilises non-stationary, time-varying dynamics of neuro-imaging recordings. Up to this point, I have reviewed some of methods to map functional connections which predominantly utilize static network approaches (in which network edges remain constant throughout time) derived from graph theory [14, 24]. However, such approaches are unable to characterize or identify *changes* in regional interactions over time. Furthermore, the emergence of dynamic functional networks from static structural connections may resolve a fundamental understanding of how structure and function map onto each other.

A promising way to obtain a fundamental understanding of how patterns of functional connectivity change over time is the simulation of brain dynamics using a sophisticated modeling framework that implements nonlinear Kuramoto-like dynamics on a physical network backbone informed by both structural (white matter) and functional (fMRI) connectivity maps [11, 76, 78]. At the same time, the

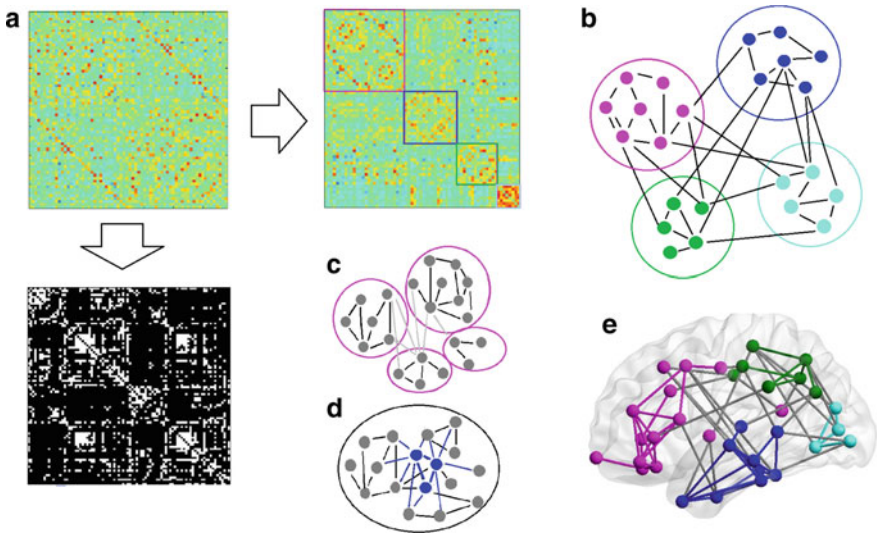

Fig. 21.2 Characterizing the way that different brain regions connect to each other. A brain network can be depicted using association matrix or graphs where the nodes are the brain regions and the edges are statistical associations (connections) between regions. Arrangement of nodes in the network defines its topology. **a** The example of an association matrix with the weighted edges (represented by heat-map colours) between brain regions. This matrix can be binarized at a given threshold (black-white matrix) and/or reordered according to modular connections between the nodes (as in the matrix indicated by the right arrow). In this example network has four modules (colored in magenta, green, blue and cyan). **b** Another way to visualize this same network is in the form of a graph. Nodes within one module are colored with different colours (same as in the matrix). In more general representation, topology of the network can be separated into segregated modules (magenta) (**c** and integrative nodes and interactions (blue) (**d**). **e** Brain view (sagittal) of the network. In this example nodes and edges, that connect nodes within the same module, are visuilised using the same colour, grays are edges that connect nodes across different modules

computational models represent a powerful approach to bridge microscale and macroscale brain organization by simulation of large-scale biophysical models of coupled brain regions. Drawing on the same inspiration as the Virtual Brain Project [59], this approach builds on prior work with nonlinear models of neuronal activity (e.g., of Wilson-Cowan oscillators [23], Kuramoto oscillators [10] or neural mass models [22]) by placing oscillators on an empirically-derived anatomical connection network, thereby directly accounting for heterogeneous connectivity between cortical and subcortical areas. The resulting large-scale circuit models can be used to simulate complex neural dynamics that are transformed into realistic resting-state fMRI (rs-fMRI) signals via an additional biophysical hemodynamic model [33]. Optimization of these models for use in neuroscience, however, requires extensive alterations, additions, and improvements [53] and may benefit from integration of approaches across brain imaging modalities [46] and/or of information on brain interactions other than *functional* connectivity [54].

21.3 Morphology and Function

Corticocortical interactions form a communication system which underpins sensory and higher cognitive and behavioural processes in the brain. It is important to identify specific network properties and how they facilitate this communication; are there general rules that govern organisation of these interactions? In this context, the hierarchical, modular organization is widely documented across neural systems. A well studied example at the micro-level is the modular columnar organisation of the neocortex (i.e., micro-scale of brain organisation related to functionally divided vertical formations of the cortical surface or cortical columns representing the basic functional units of the cortex). Although spatially distant, columns in cytoarchitectural areas usually share some common properties, which are repeated iteratively within each area, and are most commonly grouped into entities by sets of dominating long-range, intracortical connection [50].

While cortical microstructure is mostly used to describe local properties of individual areas, studies investigating cortical connections focus on the relationship between areas (i.e., their structural—morphological—features). Organization of long-range cortical connections across different brain areas can inform our understanding of how the cortical function emerges from structural constraints [40]. MRI studies take a simplified view of cortical morphology by reducing it to a single measure: the mean volume, cortical thickness, surface area, gyrification index or curvature. In contrast to functional networks, computed on correlations of regional fMRI across time within an individual brain, morphological networks are computed on correlations among regional morphological properties across subjects. Only recently, morphometric similarity networks were extracted on an individual brain [62]. The connectivity architecture of these networks is shaped by genetic and environmental factors (that are variable across individuals) [19, 40] and is related to human cognitive performances (e.g, general intelligence) [62].

Mapping a cross-scale organisation at micro- (cytoarchitectonic) and macro- (regional) levels, has shown evidence of a significant association between cytoarchitectonic features of human cortical organization and whole-brain corticocortical connectivity [72, 80]. Findings suggest that aspects of microscale cytoarchitectonics and macroscale connectomics are related and may have the potential to reveal more about the etiology of neuropathological processes in the diseased brain (see Sect. 21.4). There is a number of studies regarding genetic influences upon the coordinated growth of spatially segregated areas during development (see for example [67]) or longitudinal (although) focal changes in morphology following training and learning new skills [9, 27]. With the exceptions of two recent studies [70, 74], comparative studies of whole-brain functional and morphological networks are lacking. Recent findings from fMRI studies, suggest that interindividual variability in functional connectivity is not uniformly distributed across the cortex: the association regions, including language, executive control, and attention networks, are likely more variable than the unimodal regions, such as the visual and sensorimotor cortices [51]. It is known that these cortices share similar morphology and projecting

neural connections, which may pave the way to cross-analysis of these networks. Precisely because they cannot be reduced to spatially close regions, functional modules contain information about non-structural level of neural organisation, which can only be investigated via analysis of time series of neural function. An additional dimension to this investigation are temporal fluctuations in functional networks characterized by striking differences in network organization, in particular nodal affiliations with different modules. Understanding whether these time-varying behaviours of functional networks reflects a discrete cytoarchitecture organisation, may encourage a shift from descriptive correlations to predictive mechanisms. If the later is true, each cytoarchitecture components and switching modules should exhibit similar spatial organisation.

21.4 Implications for Neurodegeneration

MRI studies assessing correlated changes in anatomical or functional regional properties have argued that neurodegeneration targets those networks that are highly correlated in healthy individuals [66], leading to a so called "disconnected network syndrome" hypothesis [12]. Moreover, recent findings on cross-correlated micro- and macro-architectures, in particular the size of layer 3 neurons (known to be affected in Alzheimer's disease) [72], may inform new approaches in studying neurodegenerative syndromes. Similar approaches have been successful in revealing patterns of distinct involvement of the two cortical features (thickness and surface area) in Alzheimer's disease and behavioral variant FrontoTemporal Dementia (bvFTD) [79]. However, more work is needed for these approaches to be validated in clinical settings. I suggest that for the initial application of these methods, in line with [79], the connectome can be sampled at the resolution of anatomical landmarks to examine macro-scale organisational units of the cortex and the role of each unit in the neurodegeneration. By formulating the problem of vulnerability to neurodegeneration as a problem of network topology, one can investigate how different regional morphological features contribute to this vulnerability. When the nature of this vulnerability is clarified, the cross-scale networks could be studied [72] to evaluate micro-scale connectivity. Finally, the roles in network vulnerability can be validated against functional and anatomical networks examined across a range of parcellations schemes, including random parcellation. Thus, the joint properties of functional and morphological brain networks may offer better estimates of vulnerability to neurodegenerative syndromes. The examination of these networks across multiple temporal and spatial scales would represent dynamic network mechanisms underlying not-so-easily differentiated clinical states in these syndromes. These dynamic network interactions and their underpinning morphological properties could inform treatments in these diseases and may mediate treatments outcome.

21.5 Conclusion

Large-scale brain networks provide mathematical tools to assess functional and structural brain organisation upon simple network parcellation schemes and simplified network dynamics. This approach has been successful at providing the different functional and structural topologies of healthy and diseased brain [39, 66]. Here I have provided a support for studies of cross-modal functional and anatomical (morphological) networks, which provide the opportunity to promote a basis for applying a unified network approach that can be extended beyond current approaches. Implementation of the network strategies suggested here will test: (i) how modular architecture of functional network is mediated by structural configuration at the meso- and micro-scales, (ii) that is possible to provide the link of functional network organisation with the cytoarchitecture and (iii) that research in these network properties will inform neurodegenerative models and treatments.

21.6 Glossary

Association Matrix:	A means of displaying the nodes of a network and the edges or relationship between each pair of nodes
Anatomical MRI:	Single 3D volume of the brain, usually acquired as standard in most MRI protocols by utilising so called T1-weighted acquisition sequence
Functional MRI:	Specific 4D sequence sensitive to BOLD contrast reflecting hemodynamic response of neuronal activity. Reasonably high temporal and good spatial resolution
Diffusion MRI:	Specific sequence using gradients to measure free water diffusion as a surrogate measure of white matter tracts. Reconstruction of tracts can be used to imply structural connectivity between brain regions, albeit with some restrictions
Complex Network:	A network with non-trivial features, usually taken to refer to small-world or scale-free topology
Connectome:	A term that describes the structural architecture of the brain that guides the functional connections
Cost:	A measure of the connection density of a network; usually displayed as a percentage of the maximum number of connections in a network; theoretically related to the wiring length cost involved in forming connections between nodes
Degree:	The number of connections a node has with other nodes in the network
Module:	A conglomeration of nodes that are more strongly connected to each other than nodes outside the module, often defined using hierarchical clustering algorithms
Resting-state:	Refers to the brains activity when not engaging in a task

References

1. A. Alexander-Bloch, J.N. Giedd et al., Imaging structural co-variance between human brain regions. Nat. Rev. Neurosci **14**, 322 (2013)
2. J. Ashburner, K.J. Friston, Diffeomorphic registration using geodesic shooting and gauss-newton optimisation. NeuroImage **55**, 954–967 (2011)
3. D.S. Bassett et al., Hierarchical organization of human cortical networks in health and schizophrenia. J. Neurosci. **28**, 9239–9248 (2008)
4. D.S. Bassett, E.T. Bullmore, Small-world brain networks. Neuroscientist **12**, 512–523 (2006)
5. D.S. Bassett, E.T. Bullmore, Human brain networks in health and disease. Curr. Opin. Neurol. **22**, 340–347 (2009)
6. D.S. Bassett, A. Meyer-Lindenberg, D.R. Weinberger, R. Coppola, E. Bullmore, Cognitive fitness of cost-efficient brain functional networks. Proc. Natl. Acad. Sci. U.S.A. **106**, 11747–11752 (2009)
7. M.A. Bertolero, B.T. Yeo, M. Desposito, The modular and integrative functional architecture of the human brain. *Proc. Nat. Acad. Sci.***112**, E6798–E6807 (2015)
8. R.F. Betzel et al., The modular organization of human anatomical brain networks: accounting for the cost of wiring. Netw. Neurosci. **1**, 42–68 (2017)
9. J. Boyke, J. Driemeyer, C. Gaser, C. Büchel, A. May, Training-induced brain structure changes in the elderly. J. Neurosci. **28**, 7031–7035 (2008)
10. M. Breakspear, S. Heitmann, A. Daffertshofer, Generative models of cortical oscillations: neurobiological implications of the kuramoto model. Front. Hum. Neurosci. **4**, (2010)
11. M. Breakspear, S. Heitmann, A. Daffertshofer, Generative models of cortical oscillations: neurobiological implications of the Kuramoto model. Front. Hum. Neurosci. **4**, 1–14 (2010)
12. R.L. Buckner et al., Cortical hubs revealed by intrinsic functional connectivity: mapping, assessment of stability, and relation to alzheimer's disease. J. Neurosci. **29**, 1860–1873 (2009)
13. E.T. Bullmore, D.S. Bassett, Brain graphs: graphical models of the human brain connectome. Annu. Rev. Clin. psychol. **7**, 113–140 (2011)
14. E.T. Bullmore, O. Sporns, Complex brain networks: graph theoretical analysis of structural and functional systems. Nat. Rev. Neurosci. **10**, 186–198 (2009)
15. C.T. Butts, Revisiting the foundations of network analysis. *science* **325**, 414–416 (2009)
16. V.D. Calhoun, R. Miller, G. Pearlson, T. Adalı, The chronnectome: time-varying connectivity networks as the next frontier in fmri data discovery. Neuron **84**, 262–274 (2014)
17. M. Catani, M.T. de Schotten, D. Slater, F. Dell'Acqua, Connectomic approaches before the connectome. Neuroimage **80**, 2–13 (2013)
18. M.S. Cetin et al., Multimodal classification of schizophrenia patients with meg and fmri data using static and dynamic connectivity measures. Fron. Neurosci. **10**, 466 (2016)
19. C.-H. Chen et al., Genetic topography of brain morphology. Proc. Nat. Acad. Sci. **110**, 17089–17094 (2013)
20. Z.J. Chen, Y. He, P. Rosa-Neto, J. Germann, A.C. Evans, Revealing modular architecture of human brain structural networks by using cortical thickness from mri. Cereb. Cortex **18**, 2374–2381 (2008)
21. N.A. Crossley et al., Cognitive relevance of the community structure of the human brain functional coactivation network. Proc. Natl. Acad. Sci. **110**, 11583–11588 (2013)
22. O. David, D. Cosmelli, K.J. Friston, Evaluation of different measures of functional connectivity using a neural mass model. Neuroimage **21**, 659–673 (2004)
23. G. Deco, V.K. Jirsa, A.R. McIntosh, O. Sporns, R. Kötter, Key role of coupling, delay, and noise in resting brain fluctuations. Proc. Natl. Acad. Sci. U.S.A. **106**, 10302–10307 (2009). http://www.pnas.org/content/106/25/10302.full.pdf+html
24. G. Deco, V.K. Jirsa, A.R. McIntosh, Emerging concepts for the dynamical organization of resting-state activity in the brain. Nat. Rev. Neurosci. **12**, 43–56 (2011)
25. R.S. Desikan et al., An automated labeling system for subdividing the human cerebral cortex on mri scans into gyral based regions of interest. Neuroimage **31**, 968–980 (2006)

26. N.U.F. Dosenbach et al., Prediction of individual brain maturity using fmri. Science **329**, 1358–1361 (2010)
27. B. Draganski et al., Neuroplasticity: changes in grey matter induced by training. Nature **427**, 311 (2004)
28. A. Fornito, A. Zalesky, E.T. Bullmore, Network scaling effects in graph analytic studies of human resting-state fMRI data. J. Integr. Neurosci. **4**, (2010)
29. S. Fortunato, D. Hric, Community detection in networks: a user guide. Phys. Rep. **659**, 1–44 (2016)
30. P. Fries, A mechanism for cognitive dynamics: neuronal communication through neuronal coherence. Trends cogn. sci. **9**, 474–480 (2005)
31. P. Fries, A mechanism for cognitive dynamics: neuronal communication through neuronal coherence. Trends Cogn. Sci. **9**, 474–480 (2005)
32. K. Friston, R.J. Dolan, Computational and dynamic models in neuroimaging. Neuroimage **52**, 752–765 (2010)
33. K. Friston, A. Mechelli, R. Turner, C.J. Price, Nonlinear responses in fMRI: the balloon model, Volterra kernels, and other hemodynamics. NeuroImage **12**, 466–477 (2000)
34. M.F. Glasser et al., A multi-modal parcellation of human cerebral cortex. Nature **536**, 171 (2016)
35. P. Hagmann et al., Mapping human whole-brain structural networks with diffusion mri. PLoS One **2**, e597 (2007)
36. P. Hagmann et al., Mapping the structural core of human cerebral cortex. PLoS Biol. **6**, 15 (2008)
37. A.M. Hermundstad, D.S. Bassett, K.S. Brown, E.M. Aminoff, D. Clewett, Structural foundations of resting-state and task-based functional connectivity in the human brain. Proc. Nat. Acad. Sci. **110**, 6169–6174 (2013)
38. C.J. Honey, R. Kötter, M. Breakspear, O. Sporns, Network structure of cerebral cortex shapes functional connectivity on multiple time scales. Proc. Natl. Acad. Sci. U.S.A. **104**, 10240–10245 (2007)
39. P. Hövel, A. Viol, P. Loske, L. Merfort, V. Vuksanović, Synchronization in functional networks of the human brain. J. Nonlin. Sci. **1–24**, (2018)
40. J.M. Huntenburg, P.-L. Bazin, D.S. Margulies, Large-scale gradients in human cortical organization. Trends in Cogn. Sci. **22**, 21–31 (2018)
41. R.M. Hutchison, T. Womelsdorf, E.A. Allen, P.A. Bandettini, V.D. Calhoun, Dynamic functional connectivity: promise, issues, and interpretations. NeuroImage **80**, 360–378 (2013)
42. V.K. Jirsa, A.R. McIntosh, Handbook of brain connectivity. in *Handbook of Brain Connectivity*, vol. 1, ed. by K.J. Viktor, A.R. McIntosh (Springer, Berlin, 2007)
43. S.D. Keilholz, The neural basis of time-varying resting-state functional connectivity. Brain Connectivity **4**, 769–779 (2014)
44. V. Kiviniemi et al., Functional segmentation of the brain cortex using high model order group pica. Hum. Brain Mapp. **30**, 3865–3886 (2009)
45. H. Laufs et al., Altered fmri connectivity dynamics in temporal lobe epilepsy might explain seizure semiology. Front. Neurol. **5**, 175 (2014)
46. K. Lehnertz, C. Geier, T. Rings, K. Stahn, Capturing time-varying brain dynamics. EPJ Nonlin. Biomed. Phys. **5**, 2 (2017)
47. A.R. Mayer et al., Static and dynamic intrinsic connectivity following mild traumatic brain injury. J. Neurotrauma **32**, 1046–1055 (2015)
48. D. Melo, A. Porto, J.M. Cheverud, G. Marroig, Modularity: genes, development, and evolution. Annu. Rev. Ecol. Evol. Syst. **47**, 463–486 (2016)
49. D. Meunier, S. Achard, A. Morcom, E. Bullmore, Age-related changes in modular organization of human brain functional networks. Neuroimage **44**, 715–723 (2009)
50. V.B. Mountcastle, The columnar organization of the neocortex. *Brain J. Neurol.***120**, 701–722 (1997)
51. S. Mueller et al., Individual variability in functional connectivity architecture of the human brain. Neuron **77**, 586–595 (2013)

52. M.E. Newman, Modularity and community structure in networks. Proc. Natl. Acad. Sci. **103**, 8577–8582 (2006)
53. D. Papo, M. Zanin, J.A. Pineda-Pardo, S. Boccaletti, J.M. Buldú, Functional brain networks: great expectations, hard times and the big leap forward. Philos. Trans. R. Soc. B Biol. Sci. **369**, 20130525 (2014)
54. H.-J. Park, K. Friston, Structural and functional brain networks: from connections to cognition. Science **342**, 1238411 (2013)
55. J.D. Power et al., Functional network organization of the human brain. Neuron **72**, 665–78 (2011)
56. M.E. Raichle, D.A. Gusnard, Appraising the brain's energy budget. Proc. Natl. Acad. Sci. **99**, 10237–10239 (2002)
57. C. Reveley et al., Superficial white matter fiber systems impede detection of long-range cortical connections in diffusion mr tractography. Proc. Nat. Acad. Sci. **112**, E2820–E2828 (2015)
58. Y.-A. Rho, R.A. McIntosh, V.K. Jirsa, Synchrony of two brain regions predicts the blood oxygen level dependent activity of a third. Brain connectivity **1**, 73–80 (2011)
59. P. Ritter, M. Schirner, A.R. McIntosh, V.K. Jirsa, The virtual brain integrates computational modeling and multimodal neuroimaging. Brain Connectivity **3**, 121–145 (2013)
60. M. Rubinov, O. Sporns, Complex network measures of brain connectivity: uses and interpretations. NeuroImage **52**, 1059–1069 (2010)
61. G. Sanabria-Diaz et al., Surface area and cortical thickness descriptors reveal different attributes of the structural human brain networks. Neuroimage **50**, 1497–1510 (2010)
62. J. Seidlitz et al., Morphometric similarity networks detect microscale cortical organization and predict inter-individual cognitive variation. Neuron **97**, 231–247 (2018)
63. O. Sporns, Network analysis, complexity, and brain function. Complexity **8**, 56–60 (2002)
64. O. Sporns, Structure and function of complex brain networks. Dialogues clin. Neurosci. **15**, 247 (2013)
65. O. Sporns, R.F. Betzel, Modular brain networks. Annu. Rev. Psychol. **67**, 613–640 (2016)
66. C.J. Stam, Modern network science of neurological disorders. Nat. Rev. Neurosci. **15**, 683–695 (2014)
67. H. Tost, E. Bilek, A. Meyer-Lindenberg, Brain connectivity in psychiatric imaging genetics. Neuroimage **62**, 2250–2260 (2012)
68. N.B. Turk-Browne, Functional interactions as big data in the human brain. Science **342**, 580–584 (2013)
69. B. Tzourio-Mazoyer et al., Automated anatomical labeling of activations in SPM using a macroscopic anatomical parcellation of the MNI MRI single-subject brain. NeuroImage **15**, 273–289 (2002)
70. S.L. Valk et al., Structural plasticity of the social brain: differential change after socio-affective and cognitive mental training. Sci. Adv. **3**, e1700489 (2017)
71. M.P. van den Heuvel, C.J. Stam, M. Boersma, H.H. Pol, Small-world and scale-free organization of voxel-based resting-state functional connectivity in the human brain. Neuroimage **43**, 528–539 (2008)
72. M.P. van den Heuvel, L.H. Scholtens, L.F. Barrett, C.C. Hilgetag, M.A. de Reus, Bridging cytoarchitectonics and connectomics in human cerebral cortex. J. Neurosci. **35**, 13943–13948 (2015)
73. F. Váša et al., Adolescent tuning of association cortex in human structural brain networks. Cereb. Cortex **28**, 281–294 (2017)
74. V. Vuksanović, Cortical thickness and functional networks modules by cortical lobes. *Neuroscience***423**, 172–176 (2019)
75. V. Vuksanović, P. Hövel, Dynamic changes in network synchrony reveal resting-state functional networks. *Chaos***25**, 023116 (2015)
76. V. Vuksanović, P. Hövel, Role of structural inhomogeneities in the resting-state brain dynamics. *submitted*
77. V. Vuksanović, R. Staff, T. Ahearn, A. Murray, W. Claude, Cortical thickness and surface area networks in healthy aging, alzheimer's disease and behavioral variant fronto-temporal dementia. *Int. J. Neur. Sys.* (2019), (in press)

78. V. Vuksanović, P. Hövel, Functional connectivity of distant cortical regions: role of remote synchronization and symmetry in interactions. NeuroImage **97**, 1–8 (2014)
79. V. Vuksanović, R.T. Staff, T. Ahearn, A.D. Murray, C.M. Wischik, Cortical thickness and surface area networks in healthy aging, alzheimers disease and behavioral variant fronto-temporal dementia. Int. J. Neur. Sys. **29**, 1850055 (2019)
80. Y. Wei, L.H. Scholtens, E. Turk, M.P. van den Heuvel, Multiscale examination of cytoarchitectonic similarity and human brain connectivity. Netw. Neurosci. **3**, 124–137 (2018)
81. M. Yamashita, M. Kawato, H. Imamizu, Predicting learning plateau of working memory from whole-brain intrinsic network connectivity patterns. Sci. Rep. **5**, 7622 (2015)
82. Q. Yu et al., Assessing dynamic brain graphs of time-varying connectivity in fmri data: application to healthy controls and patients with schizophrenia. Neuroimage **107**, 345–355 (2015)
83. A. Zalesky et al., Whole-brain anatomical networks: does the choice of nodes matter? NeuroImage **50**, 970–983 (2010)
84. A. Zalesky, M. Breakspear, Towards a statistical test for functional connectivity dynamics. Neuroimage **114**, 466–470 (2015)

Part IV
Applications

Chapter 22
Predicting Epileptic Seizures—An Update

Klaus Lehnertz

Abstract Epilepsy is a malfunction of the brain that affects about 0.8% of the world population. Epileptic seizures are the cardinal symptom of the disease and are usually related to an overly synchronized firing of neurons, as reflected by oscillations on the electroencephalogram (EEG). Seizures often appear as a transformation of otherwise normal brain rhythms, and the exact mechanisms underlying seizure generation are still as uncertain as are mechanisms underlying seizure spreading and termination. Identifying precursors of seizures from brain dynamics could drastically improve therapeutic possibilities and thus, the quality of life of people with epilepsy. Over the last three decades, an improved characterization of the complex spatial-temporal dynamics of the epileptic brain could be achieved with methods from nonlinear dynamics, statistical physics, synchronization and network theory. These methods are capable of identifying seizure precursors from EEG recordings in a large number of subjects and with high sensitivity and specificity. This chapter provides an overview of the progress that has been made in the field: from preliminary descriptions of preseizure phenomena to implantable seizure prediction and prevention systems.

22.1 Introduction

Epilepsy is a group of neurological disorders that is characterized by more than 15 different seizure types and over 30 epilepsy syndromes [20]. It is defined as *a disorder of the brain characterized by an enduring predisposition to generate epileptic seizures and by the neurobiologic, cognitive, psychological, and social consequences of this condition* [43]. An epileptic seizure is defined as *a transient occurrence of signs and/or symptoms due to abnormal excessive or synchronous neuronal activity in the brain* [40, 43]. It may be accompanied by an impairment or loss of consciousness, psychic, autonomic or sensory symptoms, or motor phenomena. Generalized-onset

K. Lehnertz (✉)
Department of Epileptology and Helmholtz Institute for Radiation and Nuclear Physics and Interdisciplinary Centre for Complex Systems, University of Bonn, Bonn, Germany
e-mail: klaus.lehnertz@ukbonn.de

A. Stefanovska and P. V. E. McClintock (eds.), *Physics of Biological Oscillators*, Understanding Complex Systems,
https://doi.org/10.1007/978-3-030-59805-1_22

seizures are believed to instantaneously involve almost the entire brain [40], whereas focal-onset seizures appear to originate from a circumscribed region of the brain (*epileptic focus* [61, 134]).

Epilepsy affects more than 50 million people worldwide [111] and is associated with severe comorbidity, including depression, anxiety and increased mortality [127, 153]. Despite more than 30 licensed epilepsy therapies (anti-epileptic drugs [35, 93], neuromodulation devices [89, 142]), seizures remain poorly controlled in approximately 25% of people with epilepsy. Epilepsy surgery offers the chance of seizure remission for about 50% of these people, though there is still some hesitation because of the associated side effects [41, 58]. For the person with epilepsy, it is the apparent unpredictability of seizures that is central to the burden of an uncontrollable epilepsy. If it were possible to reliably identify seizure precursors, a novel approach to control previously uncontrollable seizures would consist of a precursor-identification-triggered, on-demand delivering a suitable counteracting influence (e.g., neuromodulation, local cooling, local drug perfusion, or behavioral intervention [101, 116, 123]) to prevent the generation of the extreme event [67, 85]. Research over the last three decades provides strong evidence for seizures in many people with epilepsy to be preceded by a measurable changes in brain dynamics, which constitute a precursor of sufficient duration [77]. This review summarizes the advances made in studies on seizure prediction during this time and highlights open issues that would need to be addressed in future studies.

22.2 Seizure Prediction and Time Series Analysis

Seizure prediction is an interdisciplinary research field that targets at predicting (or forecasting or anticipating; these terms are often used interchangeably) the occurrence of epileptic seizures with the aim to enable timely modifications of brain dynamics that prevent seizure generation [77, 91, 106]. Lacking detailed knowledge about the exact mechanisms underlying seizure generation in humans (and the same holds true for seizure spreading and seizure termination, despite many decades of intense research efforts worldwide), there are currently two types of scenarios of how a seizure could occur [92]. The first scenario considers a sudden and abrupt transition between two brain states (normal and seizure) and would be conceivable for the initiation of generalized-onset seizures. The second scenario considers the transition to the seizure state as a gradual change (or a cascade of changes) in dynamics which could in theory be detected. This type of transition could be more common for focal-onset seizures.

Lacking an adequate model of the human brain that is capable of mimicking the immense functionality, and—as in the case of brain pathologies—coexisting normal and abnormal functions [27, 97, 163], seizure prediction mostly relies on time series analysis of accessible observables to identify a preseizure state of sufficient duration, well enough in advance and with high sensitivity and specificity. Most often used are time series of brain dynamics (e.g., invasively and/or non-invasively recorded

electroencephalogram (EEG), single neuron activities and local field potentials, blood oxygenation), followed by/or together with heart activities (e.g., electrocardiogram, heart rate), body movements (e.g., muscle activities) or behavioral symptoms. Given only fragmentary knowledge about why, when and how the human epileptic brain transits from apparently normal dynamical regimes to a preseizure and eventually to a seizure state, time series analysis techniques should be sensitive enough to identify even subtle modifications in the dynamics of observables recorded during normal conditions and similarly account for the large inter- and intraindividual variability. For brain dynamics, a further obstacle arises from its scale-free behavior coexisting with an oscillatory one [87].

The spatial-temporal onset of a seizure is usually defined on the EEG (so called electrographic onset as opposed to the clinical onset, which either coincides with or follows the electrographic onset). One should be aware that a time-series-analysis-based identification of modifications in the dynamics of observables in the order of a few to a few tens of seconds prior to seizure onset merely reflects a seizure-onset detection but not an identification of a preseizure state, taking into account the known uncertainties in reliably and reproducibly defining seizure onset [49, 145, 149, 161].

Time series analysis techniques that are applied to identify a preseizure state using the EEG or other modalities (for an overview, see [26, 32, 45, 77, 106, 123, 156]) can be divided into three main categories: univariate, bivariate and multivariate techniques, depending upon whether data from a single system or a single recording site are analyzed independently or whether data from two or more systems or sites are analyzed for possible interactions. These approaches can further be subdivided into the categories linear and nonlinear.

Univariate linear analysis techniques [115] allow one to draw inferences about preseizure-state-associated alterations of amplitude-, interval-, or period-distributions along with their statistical moments, of properties of the auto-correlation function or of power spectral estimates [14, 19, 44, 60, 117]. Univariate nonlinear analysis techniques allow a more detailed characterization of the dynamics in state space [62], particularly when used in conjunction with surrogate-based tests for nonlinearity [80, 141]. Quantities such as an effective correlation dimension [86], correlation density [98], entropy-related measures [90, 157], Lyapunov exponents [55], or quantities based on recurrence quantification analysis [99, 114] allow one to draw inferences about preseizure-state-associated alterations of the number of degrees of freedom, the amount of order/disorder, or of the degree of chaoticity or predictability in a single time series. Other univariate nonlinear techniques aim at discriminating between deterministic and stochastic dynamics [8] or stationary and non-stationary dynamics [22, 128–130] to identify a preseizure state.

Bivariate analysis techniques allow investigating (linear/nonlinear) relationships between two (linear/nonlinear) systems (e.g., two brain regions or two organs) and aim at characterizing strength and direction of an interaction [24, 118, 119]. Common bivariate linear approaches comprise estimating the linear correlation coefficient, cross-correlation or cross-spectral functions or (linear) partial coherence [33, 166]. These techniques, however, can mostly provide information about the strength of an interaction since correlation does not imply causation. As with univariate linear

techniques, parametric approaches provide an alternative way to estimate (single and joint) properties of the power spectra [95]. Multivariate and/or vector autoregressive models form the basis of techniques such as Granger causality [112, 144, 158] or partial directed coherence [13, 135] that can index the direction of an interaction. Bivariate nonlinear analysis techniques can be subdivided into two main categories depending on the underlying concept for interaction: information-theory-based [52] and synchronization-based techniques [24, 119, 151]. As with univariate nonlinear methods, findings achieved with bivariate techniques need to be interpreted with great care. Although extensions and new development of surrogate techniques can help to avoid misinterpretations about the strength of an interaction [6, 80], causal relationships are notoriously difficult to identify and we are still lacking reliable surrogate techniques for directionality indices. Nevertheless, particularly estimates for the strength of interaction (either using phase-based [110] or state-space-based approaches [11, 36, 121]) were repeatedly shown to reliably identify a preseizure state preceding focal-onset seizures (see, e.g., Refs. [1, 16, 38, 42, 69, 73–75, 83–85, 105, 107, 108, 120, 137, 147, 168, 170]). Interestingly and probably contrary to expectations, decreased levels of the strength of an interactions frequently characterized a preseizure state. Moreover, most of these studies identified interactions between brain regions far off the epileptic focus and even from the opposite brain hemisphere to indicate a preseizure state.

Multivariate analysis techniques (together with graph-theoretical concepts) provide a means to quantify structure and dynamical evolution of complex networks. Network theory has contributed significantly to advance understanding of complex systems, with wide applications in diverse fields, ranging from physics to biology and medicine [3, 10, 23, 25, 30, 113, 124, 152]. In epileptology, the concept of an epileptic network [15, 21, 82, 88, 125, 126, 148] received strong impetus from network-theoretical concepts and multivariate analysis techniques. An epileptic network comprises anatomically, and more importantly, functionally connected cortical and subcortical brain structures and regions. Seizures (and other related pathophysiologic dynamics) may emerge from, may spread via, and may be terminated by network constituents that generate and sustain normal, physiological brain dynamics during the seizure-free interval [148]. So called functional brain networks are supposed to reflect the interaction dynamics between brain regions [30] and such a representation requires identification of vertices and edges. Vertices are usually associated with sensors that are placed to sufficiently capture the dynamics of given brain regions. Interactions between the vertices' dynamics are considered as network edges, and properties of interactions can be characterized with the aforementioned bivariate analysis techniques. Graph theory then provides a large number of concepts and measures to characterize macroscopic (such as clustering, average shortest path length, or assortativity), mesoscopic (such as communities, motifs, or core-periphery structure), and microscopic network properties (such as centrality of single vertices or edges). Studies investigating macroscopic characteristics of time-evolving epileptic networks provided first clues for certain network reconfigurations to promote the formation of a preseizure state [48, 70, 78, 138, 140]. Likewise, this approach allowed to formulate a network mechanism by which most focal epileptic seizures stop spon-

taneously within a few minutes [59, 71, 139, 140]. Recent research into the epileptic network's local characteristics provides increasing evidence that the epileptic focus—widely referred to as the *seizure-generating* or *seizure-initiating* brain area [94]—is not even a distinguished part of the network, neither during the seizure-free interval, nor during the preseizure period, and not even during seizures [31, 46, 47, 132, 159, 165]. Rather, these studies suggest that a rearrangement of the network's path structure—possibly triggered by endogenous and/or exogenous factors—and that results in a formation of bottlenecks [132] which induces the generation of a preseizure state. Earliest indications for such a formation (with lead times up to hours) can be observed in network vertices which generate and sustain normal, physiological brain dynamics during the seizure-free interval.

All the aforementioned characteristics can further be used—either independently or in some combined way—as input to pattern recognition systems, machine learning algorithms or classifiers (such as artificial neural networks) to identify a preseizure state [2, 67, 105, 155].

22.3 Performance Evaluation of Seizure Prediction Algorithms

Predictability of seizures with above-chance performance of prediction algorithms was claimed by many studies published before and around the turn of the millennium. Follow-up studies indicated, however, that these were mostly over-optimistic findings obtained by applying highly optimized algorithms to small, selected data sets and could not be reproduced on unselected, more extended EEG recordings that are more closely related to the real-life challenge of predicting seizures prospectively from the continuous EEG [106, 109]. This key fault of historic literature continues to pervade the field, despite (a) well known minimum requirements to ensure that published prospective and retrospective seizure prediction studies are comprehensible, comparable and assessable (see guidelines in [77, 106]) as well as (b) availability of rigorous frameworks to evaluate the performance of seizure prediction techniques. These frameworks are based on Monte Carlo simulations [5, 7, 72, 109, 146] or on comparison with analytical results derived from naive (random or periodic) prediction schemes [136, 167, 169]. Awareness of the importance of statistical evaluation of seizure prediction algorithms—beyond estimating sensitivity and specificity—as well as adherence to published guidelines is critical for understanding the value of the results of seizure prediction studies and is indispensable to avoid making too strong claims that may raise false hopes in professionals and in people with epilepsy [77].

There are similar concerns about the significance of recent seizure-forecasting contests [28, 76]. Despite availability of large, high-quality databases that provide a pseudo-realistic test bed with continuous, multichannel, multi-day EEG data recorded during sleep, wakefulness and activities of daily life [56, 76, 160], these contests solely investigated preselected, small, discontinuous pieces of data. More-

over, it is to be expected that an approach that inputs a large (>100) number of (mostly correlated) characteristics into various machine-learning algorithms but that does not reasonably control the type-I error (due to multiple testing) will indeed perform better than some random predictor. Even the testing against a random predictor is a debatable point, given that the probability of occurrence of seizures and other epilepsy-related pathophysiologic phenomena is influenced and modulated by various cycles (hormonal, sleeps-wake, circadian, multidien) [17, 50, 51, 63, 66, 72, 78, 81, 137, 143, 154]. Monte-Carlo-based approaches that preserve such periodicities [72] are better suited for such cases.

22.4 Devices for Seizure Prediction

Following studies that demonstrated the feasibility of hardware implementations of seizure prediction algorithms [79, 122], between 2010 and 2012 an Australian group enrolled 15 participants in the first and to date only prospective clinical trial of a fully functioning, ambulatory seizure prediction system [37, 39]. The system consisted of 16 intracranial electrodes that were directly in contact with one brain hemisphere and were connected by subdermal wires to a subdermal telemetry unit implanted in the chest, which wirelessly transmitted the EEG data to a hand-held unit. The system enabled data processing in real time and issued warnings in the form of colored lights indicating an impending seizure, intermediate, or safe states. In a few subjects with epilepsy, recordings were performed over a period of up to three years. For nine subjects above-chance warnings could be issued if subject-specific seizure prediction algorithms were employed that were trained on a great amount of data. Together with many previous studies, this trial demonstrated that not all people with epilepsy have seizures that can be predicted and that not all of a subject's seizures are predictable. Future work will be needed to define epilepsy phenotypes or endophenotypes that are associated with predictability [85]. This study demonstrated that long-term recordings are possible, that people with epilepsy are willing to volunteer for such studies and that research ethics committees see the benefits of these trials. Although this scientifically successful study opened a door for more long-term prospective trials, the device was never commercialized due to a lack of investment.

Currently, other clinical trials explore the feasibility of personalized forecasts from a mobile seizure diary app [64] and of wearables to better understand epilepsy at a large scale [29]. There are also developments towards sub-scalp minimally invasive EEG devices [162] that—if feasible clinically—could represent an interesting alternative to invasive recording techniques that are not without risk [57].

22.5 Open Questions and Outlook

The field of seizure prediction has made remarkable progress over the last three decades. Proceeding from preliminary descriptions of preseizure phenomena, the formulation of guidelines, standardizations, build-up of large databases, prediction contests, and developments of novel analysis concepts together with rigorous statistical tests for performance evaluation resulted in seizure prediction algorithms suitable for clinical applications. These innovations led to the first in-man proof-of-concept study of an implantable seizure prediction system. It can be expected that further miniaturization of electronics, development of connected devices and advances in engineering of neural systems will continue in the coming years; seizure prediction is thus not unthinkable anymore [77, 150]. The field has also impacted on other advances such as single neuron recording techniques in humans [34], brain control techniques based on neuromodulation [4], and the paradigm shift from the concept of an epileptic focus to a network theory of seizure generation [77]. Despite the many achievements, there are important issues that would need to be addressed in the near future.

Most of the time series analysis techniques presented in Sect. 22.2 allow an interpretation of findings in terms of a physiologic and/or pathophysiologic correlate. They are thus important to elucidate mechanisms underlying seizure dynamics and its interactions with normal physiology as well as to derive generic models. Findings achieved so far suggest that physiological understanding of the preseizure state must be improved to determine whether there are universal mechanisms that lead to the variety of observed preseizure states. A better understanding of the underlying mechanisms will also improve understanding of seizure generation, will allow better translation of the information collected into methods for the detection, prediction, and control of seizures, and eventually will allow a better understanding of what a seizure is. Current artificial-intelligence-based approaches, though commendable for their pragmatism, do not readily reveal which physiological aspects underlie the predictive characteristics of EEG or other modalities and have resulted in a limited understanding of the mechanistic underpinnings of the preseizure state. A meaningful combining of data from different modalities requires identification and matching of the relevant though vastly different spatial and temporal scales.

There are similar challenges for computational modeling approaches [97, 163]. The information gained from multi-scale and multi-modal studies of epilepsy results in increasingly sophisticated modeling approaches that are used to gain insights into possible mechanisms of seizure generation and of controlling seizures. Models are important for identifying changes in network or other control parameters or of inputs (environmental and/or endogenous) that might not always be evident or accessible to an observer but are associated with or cause the initiation of seizures. Moreover, models allow to test in silico hypotheses concerning preseizure brain dynamics and their relation to endogenous and exogenous parameters as well as the effectiveness of control strategies [96]. Nevertheless, we are still lacking appropriate tools to bridge

the various temporal and spatial scales assessed with the different computational models in order to finely balance model simplification with biological realism.

Epilepsy is considered a dynamical brain disease [103], and the transition to seizure is often conceptualized as a (critical) phase transition [68, 104]. Such a transition can be heralded by the phenomenon of critical slowing down, and the human brain is among the many natural systems in which critical slowing down has been repeatedly claimed to provide early warning signals for transitions into (and out of) epileptic seizures (see, e.g., [100] and references therein). Recent studies [102, 164], however, could not corroborate these claims when evaluating the predictive performance (cf. Sect. 22.3) of widely used early warning indicators (variance, lag-1 autocorrelation) on large samples. Thus the assumed mechanism behind the critical transition (bifurcation-induced tipping) may be too simplistic for the human epileptic brain which calls for techniques that allow identification of early warning indicators for other transition scenarios [12, 133]. Switching between different states may emerge as a result of multistability of the brain [65] and recent findings indicate that switching might also be induced by changes in the gross connections of the neuronal network [9] and not only by altered properties of neurons or groups of neurons. Notwithstanding the high relevance of improving our understanding of mechanisms underlying the transition to seizure, future studies would also need to address the mechanism underlying the transition to the preseizure state.

The probably most important—but as yet unsolved issue—of prediction and prevention of epileptic seizures centers around the controllability of the human epileptic brain. It is a nonlinear, open, dissipative and adaptive system, innately designed to learn. Learning is not only tightly related to neuronal plasticity [53] but also linked to brain disorders such as epilepsy [18]. One might thus speculate that seizures present an abnormal learned response to recurrent perturbations—such as seizures [54]. If epilepsy is indeed a "earned" disease, it will be a challenging endeavor to identify powerful control strategies to prevent the epileptic brain from generating seizures. Part of this difficulty may be attributed to the brain's stability properties with respect to the aforementioned endogenous and/or exogenous inputs. Indeed, recent findings indicate that in many subjects with epilepsy brain resilience increases rather than decreases prior to seizures and that this preseizure increase clearly exceeds physiologically induced fluctuations of brain resilience [131]. Research along these lines is urgently needed to better understand how, when, and why the epileptic brain efficiently defies control by virtue of its intrinsic plasticity and adaptiveness.

References

1. A. Aarabi, B. He, Seizure prediction in patients with focal hippocampal epilepsy. Clin. Neurophysiol. **128**, 1299–1307 (2017)
2. U.R. Acharya, Y. Hagiwara, H. Adeli, Automated seizure prediction. Epilepsy Behav. **88**, 251–261 (2018)
3. R. Albert, A.L. Barabási, Statistical mechanics of complex networks. Rev. Mod. Phys. **74**, 47–97 (2002). https://doi.org/10.1103/RevModPhys.74.47

4. F.A. Al-Otaibi, C. Hamani, A.M. Lozano, Neuromodulation in epilepsy. Neurosurgery **69**, 957–979 (2011)
5. R.G. Andrzejak, D. Chicharro, C.E. Elger, F. Mormann, Seizure prediction: any better than chance? Clin. Neurophysiol. **120**, 1465–1478 (2009). https://doi.org/10.1016/j.clinph.2009.05.019
6. R.G. Andrzejak, A. Kraskov, H. Stögbauer, F. Mormann, T. Kreuz, Bivariate surrogate techniques: necessity, strengths, and caveats. Phys. Rev. E **68**, 066202 (2003)
7. R.G. Andrzejak, F. Mormann, T. Kreuz, C. Rieke, A. Kraskov, C.E. Elger, K. Lehnertz, Testing the null hypothesis of the nonexistence of a preseizure state. Phys. Rev. E **67**, 010901(R) (2003)
8. R.G. Andrzejak, G. Widman, K. Lehnertz, P. David, C.E. Elger, The epileptic process as nonlinear deterministic dynamics in a stochastic environment: an evaluation on mesial temporal lobe epilepsy. Epilepsy Res. **44**, 129–140 (2001)
9. G. Ansmann, K. Lehnertz, U. Feudel, Self-induced switchings between multiple space-time patterns on complex networks of excitable units. Phys. Rev. X **6**, 011030 (2016). https://doi.org/10.1103/PhysRevX.6.011030
10. A. Arenas, A. Díaz-Guilera, J. Kurths, Y. Moreno, C. Zhou, Synchronization in complex networks. Phys. Rep. **469**, 93–153 (2008). https://doi.org/10.1016/j.physrep.2008.09.002
11. J. Arnhold, P. Grassberger, K. Lehnertz, C.E. Elger, A robust method for detecting interdependences: application to intracranially recorded EEG. Phys. D **134**, 419–430 (1999)
12. P. Ashwin, S. Wieczorek, R. Vitolo, P. Cox, Tipping points in open systems: bifurcation, noise-induced and rate-dependent examples in the climate system. Phil. Trans. Roy. Soc. A **370**, 1166–1184 (2012)
13. L.A. Baccalá, K. Sameshima, Partial directed coherence: a new concept in neural structure determination. Biol. Cybern. **84**, 463–474 (2001)
14. M. Bandarabadi, C.A. Teixeira, J. Rasekhi, A. Dourado, Epileptic seizure prediction using relative spectral power features. Clin. Neurophysiol. **126**, 237–248 (2015)
15. F. Bartolomei, S. Lagarde, F. Wendling, A. McGonigal, V. Jirsa, M. Guye, C. Bénar, Defining epileptogenic networks: contribution of SEEG and signal analysis. Epilepsia **58**, 1131–1147 (2017)
16. F. Bartolomei, F. Wendling, J. Regis, M. Gavaret, M. Guye, P. Chauvel, Pre-ictal synchronicity in limbic networks of mesial temporal lobe epilepsy. Epilepsy Res. **61**, 89–104 (2004). https://doi.org/10.1016/j.eplepsyres.2004.06.006
17. M.O. Baud, J.K. Kleen, E.A. Mirro, J.C. Andrechak, D. King-Stephens, E.F. Chang, V.R. Rao, Multi-day rhythms modulate seizure risk in epilepsy. Nat. Commun. **9**, 88 (2018)
18. H. Beck, Y. Yaari, Plasticity of intrinsic neuronal properties in CNS disorders. Nat. Rev. Neurosci. **9**, 357–369 (2008)
19. S. Behbahani, N.J. Dabanloo, A.M. Nasrabadi, A. Dourado, Prediction of epileptic seizures based on heart rate variability. Technol. Health Care **24**, 795–810 (2016)
20. A.T. Berg, S.F. Berkovic, M.J. Brodie, J. Buchhalter, J.H. Cross, W. van Emde Boas, J. Engel, J. French, T.A. Glauser, G.W. Mathern, S.L. Moshé, D. Nordli, P. Plouin, I.E. Scheffer, Revised terminology and concepts for organization of seizures and epilepsies: report of the ILAE commission on classification and terminology, 2005–2009. Epilepsia **51**, 676–685 (2010). https://doi.org/10.1111/j.1528-1167.2010.02522.x
21. A.T. Berg, I.E. Scheffer, New concepts in classification of the epilepsies: entering the 21st century. Epilepsia **52**, 1058–1062 (2011). https://doi.org/10.1111/j.1528-1167.2011.03101.x
22. S. Blanco, H. Garcia, R. Quian Quiroga, L. Romanelli, O.A. Rosso, Stationarity of the EEG series. IEEE Eng. Med. Biol. **4**, 395–399 (1995). https://doi.org/10.1109/51.395321
23. S. Boccaletti, G. Bianconi, R. Criado, C.I. del Genio, J. Gomez-Gardeñes, M. Romance, I. Sendina-Nadal, Z. Wang, M. Zanin, The structure and dynamics of multilayer networks. Phys. Rep. **544**(1), 1–122 (2014). https://doi.org/10.1016/j.physrep.2014.07.001
24. S. Boccaletti, J. Kurths, G. Osipov, D.L. Valladares, C.S. Zhou, The synchronization of chaotic systems. Phys. Rep. **366**, 1–101 (2002). https://doi.org/10.1016/S0370-1573(02)00137-0

25. S. Boccaletti, V. Latora, Y. Moreno, M. Chavez, D.U. Hwang, Complex networks: structure and dynamics. Phys. Rep. **424**, 175–308 (2006). https://doi.org/10.1016/j.physrep.2005.10.009
26. E. Bou Assi, D.K. Nguyen, S. Rihana, M. Sawan, Towards accurate prediction of epileptic seizures: a review. Biomed. Sig. Proc. Control **34**, 144–157 (2017)
27. M. Breakspear, Dynamic models of large-scale brain activity. Nat. Neurosci. **20**, 340 (2017)
28. B.H. Brinkmann, J. Wagenaar, D. Abbot, P. Adkins, S.C. Bosshard, M. Chen, Q.M. Tieng, J. He, F.J. Muñoz-Almaraz, P. Botella-Rocamora, J. Pardo, F. Zamora-Martinez, M. Hills, W. Wu, I. Korshunova, W. Cukierski, C. Vite, E.E. Patterson, B. Litt, G.A. Worrell, Crowdsourcing reproducible seizure forecasting in human and canine epilepsy. Brain **139**, 1713–1722 (2016). https://doi.org/10.1093/brain/aww045
29. E. Bruno, S. Simblett, A. Lang, A. Biondi, C. Odoi, A. Schulze-Bonhage, T. Wykes, M.P. Richardson, Wearable technology in epilepsy: the views of patients, caregivers, and healthcare professionals. Epilepsy Behav. **85**, 141–149 (2018)
30. E. Bullmore, O. Sporns, Complex brain networks: graph theoretical analysis of structural and functional systems. Nat. Rev. Neurosci. **10**, 186–198 (2009). https://doi.org/10.1038/nrn2575
31. S.P. Burns, S. Santaniello, R.B. Yaffe, C.C. Jouny, N.E. Crone, G.K. Bergey, W.S. Anderson, S.V. Sarma, Network dynamics of the brain and influence of the epileptic seizure onset zone. Proc. Natl. Acad. Sci. U.S.A. **111**, E5321–E5330 (2014). https://doi.org/10.1073/pnas.1401752111
32. P.R. Carney, S. Myers, J.D. Geyer, Seizure prediction: methods. Epilepsy Behav. **22**, S94–S101 (2011)
33. G.C. Carter, Coherence and time delay estimation. Proc. IEEE **75**, 236–255 (1987)
34. S.S. Cash, L.R. Hochberg, The emergence of single neurons in clinical neurology. Neuron **86**, 79–91 (2015). https://doi.org/10.1016/j.neuron.2015.03.058
35. Z. Chen, M.J. Brodie, D. Liew, P. Kwan, Treatment outcomes in patients with newly diagnosed epilepsy treated with established and new antiepileptic drugs: a 30-year longitudinal cohort study. JAMA Neurol. **75**, 279–286 (2018)
36. D. Chicharro, R.G. Andrzejak, Reliable detection of directional couplings using rank statistics. Phys. Rev. E **80**, 026217 (2009). https://doi.org/10.1103/PhysRevE.80.026217
37. M.J. Cook, T.J. O'Brien, S.F. Berkovic, M. Murphy, A. Morokoff, G. Fabinyi, W. D'Souza, R. Yerra, J. Archer, L. Litewka, S. Hosking, P. Lightfoot, V. Ruedebusch, W.D. Sheffield, D. Snyder, K. Leyde, D. Himes, Prediction of seizure likelihood with a long-term, implanted seizure advisory system in patients with drug-resistant epilepsy: a first-in-man study. Lancet Neurol. **12**, 563–571 (2013). https://doi.org/10.1016/S1474-4422(13)70075-9
38. P. Detti, G.Z.M. de Lara, R. Bruni, M. Pranzo, F. Sarnari, G. Vatti, A patient-specific approach for short-term epileptic seizures prediction through the analysis of EEG synchronization. IEEE Trans. Biomed. Eng. **66**, 1494–1504 (2018)
39. D.J. DiLorenzo, K.W. Leyde, D. Kaplan, Neural state monitoring in the treatment of epilepsy: seizure prediction–conceptualization to first-in-man study. Brain Sci. **9**, 156 (2019)
40. J. Engel Jr., Report of the ILAE classification core group. Epilepsia **47**, 1558–1568 (2006). https://doi.org/10.1111/j.1528-1167.2006.00215.x
41. J. Engel Jr., The current place of epilepsy surgery. Curr. Opin. Neurol. **31**, 192–197 (2018)
42. H. Feldwisch-Drentrup, M. Staniek, A. Schulze-Bonhage, J. Timmer, H. Dickten, C.E. Elger, B. Schelter, K. Lehnertz, Identification of preseizure states in epilepsy: a data-driven approach for multichannel EEG recordings. Front. Comput. Neurosci. **5**, 32 (2011). https://doi.org/10.3389/fncom.2011.00032
43. R.S. Fisher, W. van Emde Boas, W. Blume, C.E. Elger, P. Genton, P. Lee, J. Engel Jr., Epileptic seizures and epilepsy: definitions proposed by the International League Against Epilepsy (ILAE) and the International Bureau for Epilepsy (IBE). Epilepsia **46**, 470–472 (2005). https://doi.org/10.1111/j.0013-9580.2005.66104.x
44. K. Gadhoumi, J.M. Lina, J. Gotman, Seizure prediction in patients with mesial temporal lobe epilepsy using EEG measures of state similarity. Clin. Neurophysiol. **124**, 1745–1754 (2013)

45. K. Gadhoumi, J.M. Lina, F. Mormann, J. Gotman, Seizure prediction for therapeutic devices: a review. J. Neurosci. Methods **260**, 270–282 (2016). https://doi.org/10.1016/j.jneumeth.2015.06.010
46. C. Geier, S. Bialonski, C.E. Elger, K. Lehnertz, How important is the seizure onset zone for seizure dynamics? Seizure **25**, 160–166 (2015). https://doi.org/10.1016/j.seizure.2014.10.013
47. C. Geier, K. Lehnertz, Long-term variability of importance of brain regions in evolving epileptic brain networks. Chaos **27**, 043112 (2017). https://doi.org/10.1063/1.4979796
48. C. Geier, K. Lehnertz, S. Bialonski, Time-dependent degree-degree correlations in epileptic brain networks: from assortative to dissortative mixing. Front. Hum. Neurosci. **9**, 462 (2015). https://doi.org/10.3389/fnhum.2015.00462
49. A.C. Grant, S.G. Abdel-Baki, J. Weedon, V. Arnedo, G. Chari, E. Koziorynska, C. Lushbough, D. Maus, T. McSween, K.A. Mortati et al., EEG interpretation reliability and interpreter confidence: a large single-center study. Epilepsy Behav. **32**, 102–107 (2014)
50. G.M. Griffiths, J.T. Fox, Rhythm in epilepsy. Lancet **232**, 409–416 (1938)
51. A.G. Herzog, P. Klein, B.J. Rand, Three patterns of catamenial epilepsy. Epilepsia **38**, 1082–1088 (1997)
52. K. Hlaváčková-Schindler, M. Paluš, M. Vejmelka, J. Bhattacharya, Causality detection based on information-theoretic approaches in time series analysis. Phys. Rep. **441**, 1–46 (2007). https://doi.org/10.1016/j.physrep.2006.12.004
53. A. Holtmaat, P. Caroni, Functional and structural underpinnings of neuronal assembly formation in learning. Nat. Neurosci. **19**, 1553 (2016)
54. D. Hsu, W. Chen, M. Hsu, J.M. Beggs, An open hypothesis: is epilepsy learned, and can it be unlearned? Epilepsy Behav. **13**, 511–522 (2008)
55. L.D. Iasemidis, P. Pardalos, J.C. Sackellares, D.S. Shiau, Quadratic binary programming and dynamical system approach to determine the predictability of epileptic seizures. J. Comb. Optim. **5**, 9 (2001)
56. M. Ihle, H. Feldwisch-Drentrup, C.A. Teixeira, A. Witon, B. Schelter, J. Timmer, A. Schulze-Bonhage, EPILEPSIAE-a European epilepsy database. Comp. Meth. Prog. Biomed. **106**, 127–138 (2012)
57. P. Jayakar, J. Gotman, A.S. Harvey, A. Palmini, L. Tassi, D. Schomer, F. Dubeau, F. Bartolomei, A. Yu, P. Kršek, D. Velis, P. Kahane, Diagnostic utility of invasive EEG for epilepsy surgery: indications, modalities, and techniques. Epilepsia **57**, 1735–1747 (2016)
58. N. Jette, S. Wiebe, Update on the surgical treatment of epilepsy. Curr. Opin. Neurol. **26**, 201–207 (2013)
59. P. Jiruska, M. de Curtis, J.G.R. Jefferys, C.A. Schevon, S.J. Schiff, K. Schindler, Synchronization and desynchronization in epilepsy: controversies and hypotheses. J. Physiol. **591**, 787–797 (2013). https://doi.org/10.1113/jphysiol.2012.239590
60. C.C. Jouny, P.J. Franaszczuk, G.K. Bergey, Signal complexity and synchrony of epileptic seizures: is there an identifiable preictal period? Clin. Neurophysiol. **116**, 552–558 (2005)
61. P. Kahane, E. Landré, L. Minotti, S. Francione, P. Ryvlin, The Bancaud and Talairach view on the epileptogenic zone: a working hypothesis. Epileptic Disord. **8**(Suppl. 2), 16–26 (2006)
62. H. Kantz, T. Schreiber, *Nonlinear Time Series Analysis*, 2nd edn. (Cambridge University Press, Cambridge, UK, 2003). https://doi.org/10.1017/CBO9780511755798
63. P.J. Karoly, D.M. Goldenholz, D.R. Freestone, R.E. Moss, D.B. Grayden, W.H. Theodore, M.J. Cook, Circadian and circaseptan rhythms in human epilepsy: a retrospective cohort study. Lancet Neurol. **17**, 977–985 (2018)
64. P.J. Karoly, M.I. Maturana, M.J. Cook, E.S. Nurse, D. Payne, B. Brinkmann, D.B. Grayden, S.B. Dumanis, M.P. Richardson, G. Worrell, A. Schulze-Bonhage, L. Kuhlmann, D.R. Freestone, medRxiv. Forecasting cycles of seizure likelihood (2019). https://doi.org/10.1101/2019.12.19.19015453
65. J.S. Kelso, Multistability and metastability: understanding dynamic coordination in the brain. Phil. Trans. Roy. Soc. B **367**, 906–918 (2012)

66. S. Khan, L. Nobili, R. Khatami, T. Loddenkemper, C. Cajochen, D.J. Dijk, S.H. Eriksson, Circadian rhythm and epilepsy. Lancet Neurol. **17**, 1098–1108 (2018)
67. I. Kiral-Kornek, S. Roy, E. Nurse, B. Mashford, P. Karoly, T. Carroll, D. Payne, S. Saha, S. Baldassano, T. O'Brien, D. Grayden, M. Cook, D. Freestone, S. Harrer, Epileptic seizure prediction using big data and deep learning: toward a mobile system. EBioMedicine **27**, 103–111 (2018)
68. M.J. Koepp, L. Caciagli, R.M. Pressler, K. Lehnertz, S. Beniczky, Reflex seizures, traits, and epilepsies: from physiology to pathology. Lancet Neurol. **15**, 92–105 (2016)
69. M.A.S. Kolarijani, S. Amirsalari, M.R. Haidari, Analysis of variations of correlation dimension and nonlinear interdependence for the prediction of pediatric myoclonic seizures-a preliminary study. Epilepsy Res. **135**, 102–114 (2017)
70. M.A. Kramer, E.D. Kolaczyk, H.E. Kirsch, Emergent network topology at seizure onset in humans. Epilepsy Res. **79**, 173–186 (2008). https://doi.org/10.1016/j.eplepsyres.2008.02.002
71. M.A. Kramer, W. Truccolo, U.T. Eden, K.Q. Lepage, L.R. Hochberg, E.N. Eskandar, J.R. Madsen, J.W. Lee, A. Maheshwari, E. Halgren, C.J. Chu, S.S. Cash, Human seizures self-terminate across spatial scales via a critical transition. Proc. Natl. Acad. Sci. U.S.A. **109**, 21116–21121 (2012). https://doi.org/10.1073/pnas.1210047110
72. T. Kreuz, R.G. Andrzejak, F. Mormann, A. Kraskov, H. Stögbauer, C.E. Elger, K. Lehnertz, P. Grassberger, Measure profile surrogates: a method to validate the performance of epileptic seizure prediction algorithms. Phys. Rev. E **69**, 061915 (2004)
73. D. Krug, C.E. Elger, K. Lehnertz, A CNN-based synchronization analysis for epileptic seizure prediction: inter- and intraindividual generalization properties, in *11th International Workshop on Cellular Neural Networks and Their Applications*, ed. by D. Vilarino, D. Ferrer, V. Brea Sanchez, (IEEE Press, Piscataway, NJ, 2008), pp. 92–95. https://doi.org/10.1109/CNNA.2008.4588656
74. D. Krug, H. Osterhage, C.E. Elger, K. Lehnertz, Estimating nonlinear interdependences in dynamical systems using cellular nonlinear networks. Phys. Rev. E **76**, 041916 (2007)
75. L. Kuhlmann, D. Freestone, A.L. Lai, A.N. Burkitt, K. Fuller, D. Grayden, L. Seiderer, S. Vogrin, I.M.Y. Mareels, M.J. Cook, Patient-specific bivariate-synchrony-based seizure prediction for short prediction horizons. Epilepsy Res. **91**, 214–231 (2010). https://doi.org/10.1016/j.eplepsyres.2010.07.014
76. L. Kuhlmann, P. Karoly, D.R. Freestone, B.H. Brinkmann, A. Temko, A. Barachant, F. Li, G. Titericz Jr, B.W. Lang, D. Lavery, et al, Epilepsyecosystem.org: crowd-sourcing reproducible seizure prediction with long-term human intracranial EEG. Brain **141**, 2619–2630 (2018)
77. L. Kuhlmann, K. Lehnertz, M.P. Richardson, B. Schelter, H.P. Zaveri, Seizure prediction–ready for a new era. Nat. Rev. Neurol. **14**, 618 (2018)
78. M.T. Kuhnert, C.E. Elger, K. Lehnertz, Long-term variability of global statistical properties of epileptic brain networks. Chaos **20**, 043126 (2010). https://doi.org/10.1063/1.3504998
79. M. Laiho, A. Paasio, A. Kananen, K. Halonen, A mixed-mode polynomial-type CNN for analysing brain electrical activity in epilepsy. Int. J. Circ. Theor. Appl. **2–3**, 165–180 (2002)
80. G. Lancaster, D. Iatsenko, A. Pidde, V. Ticcinelli, A. Stefanovska, Surrogate data for hypothesis testing of physical systems. Phys. Rep. **748**, 1–60 (2018)
81. M. Langdon-Down, W.R. Brain, Time of day in relation to convulsions in epilepsy. Lancet **213**, 1029–1032 (1929)
82. K. Lehnertz, G. Ansmann, S. Bialonski, H. Dickten, C. Geier, S. Porz, Evolving networks in the human epileptic brain. Phys. D **267**, 7–15 (2014). https://doi.org/10.1016/j.physd.2013.06.009
83. K. Lehnertz, S. Bialonski, M.T. Horstmann, D. Krug, A. Rothkegel, M. Staniek, T. Wagner, Synchronization phenomena in human epileptic brain networks. J. Neurosci. Methods **183**, 42–48 (2009). https://doi.org/10.1016/j.jneumeth.2009.05.015
84. K. Lehnertz, H. Dickten, Assessing directionality and strength of coupling through symbolic analysis: an application to epilepsy patients. Phil. Trans. R. Soc. A **373**, 20140094 (2015). https://doi.org/10.1098/rsta.2014.0094

85. K. Lehnertz, H. Dickten, S. Porz, C. Helmstaedter, C.E. Elger, Predictability of uncontrollable multifocal seizures - towards new treatment options. Sci. Rep. **6**, 24584 (2016). https://doi.org/10.1038/srep24584
86. K. Lehnertz, C.E. Elger, Can epileptic seizures be predicted? evidence from nonlinear time series analysis of brain electrical activity. Phys. Rev. Lett. **80**, 5019–5023 (1998)
87. K. Lehnertz, C. Geier, T. Rings, K. Stahn, Capturing time-varying brain dynamics. EPJ Nonlin. Biomed. Phys. **5**, 2 (2017)
88. L. Lemieux, J. Daunizeau, M.C. Walker, Concepts of connectivity and human epileptic activity. Front. Syst. Neurosci. **5**, 12 (2011). https://doi.org/10.3389/fnsys.2011.00012
89. P.M. Lewis, R.H. Thomson, J.V. Rosenfeld, P.B. Fitzgerald, Brain neuromodulation techniques: a review. Neuroscientist **22**, 406–421 (2016)
90. X. Li, G. Ouyang, D.A. Richards, Predictability analysis of absence seizures with permutation entropy. Epilepsy Res. **77**, 70–74 (2007)
91. B. Litt, K. Lehnertz, Seizure prediction and the preseizure period. Curr. Opin. Neurol. **15**, 173–177 (2002)
92. F. Lopes da Silva, W. Blanes, S.N.K.J. Parra, P. Suffczynski, D.N. Velis, Epilepsies as dynamical diseases of brain systems: basic models of the transition between normal and epileptic activity. Epilepsia **44 (Suppl. 12)**, 72–83 (2003)
93. W. Löscher, H. Klitgaard, R.E. Twyman, D. Schmidt, New avenues for anti-epileptic drug discovery and development. Nat. Rev. Drug Discov. **12**, 757–776 (2013)
94. H.O. Lüders, I. Najm, D. Nair, P. Widdess-Walsh, W. Bingman, The epileptogenic zone: general principles. Epileptic Disord. **8**, 1–9 (2006)
95. H. Lütkepohl, New introduction to multiple time series analysis (Springer Science & Business Media, 2005)
96. C.W. Lynn, D.S. Bassett, The physics of brain network structure, function and control. Nat. Rev. Phys. **1**, 318 (2019)
97. W.W. Lytton, Computer modelling of epilepsy. Nat. Rev. Neurosci. **9**, 626–637 (2008). https://doi.org/10.1038/nrn2416
98. J. Martinerie, C. Adam, M.L.V. Quyen, M. Baulac, S. Clemenceau, B. Renault, F.J. Varela, Epileptic seizures can be anticipated by non-linear analysis. Nat. Med. **4**, 1173 (1998)
99. N. Marwan, M.C. Romano, M. Thiel, J. Kurths, Recurrence plots for the analysis of complex systems. Phys. Rep. **438**, 237–329 (2007). https://doi.org/10.1016/j.physrep.2006.11.001
100. C. Meisel, C. Kuehn, Scaling effects and spatio-temporal multilevel dynamics in epileptic seizures. PLoS One **7**, e30371 (2012)
101. R. Michaelis, V. Tang, L.H. Goldstein, M. Reuber, W.C. LaFrance Jr., T. Lundgren, A.C. Modi, J.L. Wagner, Psychological treatments for adults and children with epilepsy: evidence-based recommendations by the International League Against Epilepsy Psychology Task Force. Epilepsia **59**, 1282–1302 (2018)
102. P. Milanowski, P. Suffczynski, Seizures start without common signatures of critical transition. Int. J. Neural Syst. **26**, 1650053 (2016)
103. J.G. Milton, Epilepsy as a dynamic disease: a tutorial of the past with an eye to the future. Epilepsy Behav. **18**, 33–44 (2010)
104. J.G. Milton, Neuronal avalanches, epileptic quakes and other transient forms of neurodynamics. Eur. J. Neurosci. **36**(2), 2156–2163 (2012)
105. P. Mirowski, D. Madhavan, Y. LeCun, R. Kuzniecky, Classification of patterns of EEG synchronization for seizure prediction. Clin. Neurophysiol. **120**, 1927–1940 (2009)
106. F. Mormann, R. Andrzejak, C.E. Elger, K. Lehnertz, Seizure prediction: the long and winding road. Brain **130**, 314–333 (2007). https://doi.org/10.1093/brain/awl241
107. F. Mormann, R. Andrzejak, T. Kreuz, C. Rieke, P. David, C.E. Elger, K. Lehnertz, Automated detection of a preseizure state based on a decrease in synchronization in intracranial electroencephalogram recordings from epilepsy patients. Phys. Rev. E **67**, 021912 (2003). https://doi.org/10.1103/PhysRevE.67.021912
108. F. Mormann, T. Kreuz, R.G. Andrzejak, P. David, K. Lehnertz, C.E. Elger, Epileptic seizures are preceded by a decrease in synchronization. Epilepsy Res. **53**, 173–185 (2003)

109. F. Mormann, T. Kreuz, C. Rieke, R.G. Andrzejak, A. Kraskov, P. David, C.E. Elger, K. Lehnertz, On the predictability of epileptic seizures. Clin. Neurophysiol. **116**, 569–587 (2005). https://doi.org/10.1016/j.clinph.2004.08.025
110. F. Mormann, K. Lehnertz, P. David, C.E. Elger, Mean phase coherence as a measure for phase synchronization and its application to the EEG of epilepsy patients. Phys. D **144**, 358–369 (2000). https://doi.org/10.1016/S0167-2789(00)00087-7
111. S.L. Moshé, E. Perucca, P. Ryvlin, T. Tomson, Epilepsy: new advances. Lancet **385**, 884–898 (2015). https://doi.org/10.1016/S0140-6736(14)60456-6
112. K. Mühlberg, J. Müller, R. Tetzlaff, Seizure prediction by multivariate autoregressive model order optimization. Curr. Dir. Biomed. Eng. **4**, 395–398 (2018)
113. M.E.J. Newman, The structure and function of complex networks. SIAM Rev. **45**, 167–256 (2003). https://doi.org/10.1137/S003614450342480
114. E.J. Ngamga, S. Bialonski, N. Marwan, J. Kurths, C. Geier, K. Lehnertz, Evaluation of selected recurrence measures in discriminating pre-ictal and inter-ictal periods from epileptic eeg data. Phys. Lett. A **380**, 1419–1425 (2016)
115. E. Niedermeyer, F. Lopes da Silva, Electroencephalography: basic principles, clinical applications, and related fields (Lippincott Williams and Williams, Philadelphia, 2005)
116. G. Nune, C. DeGiorgio, C. Heck, Neuromodulation in the treatment of epilepsy. Curr. Treat. Options Neurol. **17**, 43 (2015)
117. Y. Park, L. Luo, K.K. Parhi, T. Netoff, Seizure prediction with spectral power of EEG using cost-sensitive support vector machines. Epilepsia **52**, 1761–1770 (2011)
118. E. Pereda, R. Quian Quiroga, J. Bhattacharya, Nonlinear multivariate analysis of neurophysiological signals. Prog. Neurobiol. **77**, 1–37 (2005). https://doi.org/10.1016/j.pneurobio.2005.10.003
119. A.S. Pikovsky, M.G. Rosenblum, J. Kurths, Synchronization: a universal concept in nonlinear sciences (Cambridge University Press, Cambridge, UK, 2001). https://doi.org/10.1017/CBO9780511755743
120. D. Piper, K. Schiecke, L. Leistritz, B. Pester, F. Benninger, M. Feucht, M. Ungureanu, R. Strungaru, H. Witte, Synchronization analysis between heart rate variability and eeg activity before, during, and after epileptic seizure. Biomed. Eng./Biomed. Technik **59**, 343–355 (2014)
121. R. Quian Quiroga, J. Arnhold, P. Grassberger, Learning driver-response relationships from synchronization patterns. Phys. Rev. E **61**, 5142–5148 (2000)
122. S. Raghunathan, S.K. Gupta, M.P. Ward, R.M. Worth, K. Roy, P.P. Irazoqui, The design and hardware implementation of a low-power real-time seizure detection algorithm. J. Neural Eng. **6**, 056005 (2009)
123. S. Ramgopal, S. Thome-Souza, M. Jackson, N.E. Kadish, I.S. Fernández, J. Klehm, W. Bosl, C. Reinsberger, S. Schachter, T. Loddenkemper, Seizure detection, seizure prediction, and closed-loop warning systems in epilepsy. Epilepsy Behav. **37**, 291–307 (2014)
124. J.C. Reijneveld, S.C. Ponten, H.W. Berendse, C.J. Stam, The application of graph theoretical analysis to complex networks in the brain. Clin. Neurophysiol. **118**, 2317–2331 (2007). https://doi.org/10.1016/j.clinph.2007.08.010
125. M. Richardson, Current themes in neuroimaging of epilepsy: brain networks, dynamic phenomena, and clinical relevance. Clin. Neurophysiol. **121**, 1153–1175 (2010). https://doi.org/10.1016/j.clinph.2010.01.004
126. M.P. Richardson, Large scale brain models of epilepsy: dynamics meets connectomics. J. Neurol. Neurosurg. Psychiatry **83**, 1238–1248 (2012). https://doi.org/10.1136/jnnp-2011-301944
127. L. Ridsdale, J. Charlton, M. Ashworth, M.P. Richardson, M.C. Gulliford, Epilepsy mortality and risk factors for death in epilepsy: a population-based study. Br. J. Gen. Pract. **61**(586), e271–e278 (2011)
128. C. Rieke, R.G. Andrzejak, F. Mormann, K. Lehnertz, Improved statistical test for nonstationarity using recurrence time statistics. Phys. Rev. E **69**, 046111 (2004)
129. C. Rieke, F. Mormann, R.G. Andrzejak, T. Kreuz, P. David, C.E. Elger, K. Lehnertz, Discerning nonstationarity from nonlinearity in seizure-free and preseizure EEG recordings from

epilepsy patients. IEEE Trans. Biomed. Eng. **50**, 634–639 (2003). https://doi.org/10.1109/TBME.2003.810684
130. C. Rieke, K. Sternickel, R.G. Andrzejak, C.E. Elger, P. David, K. Lehnertz, Measuring non-stationarity by analyzing the loss of recurrence in dynamical systems. Phys. Rev. Lett. **88**, 244102 (2002)
131. T. Rings, M. Mazarei, A. Akhshi, C. Geier, M.R.R. Tabar, K. Lehnertz, Traceability and dynamical resistance of precursor of extreme events. Sci. Rep. **9**, 1744 (2019)
132. T. Rings, R. von Wrede, K. Lehnertz, Precursors of seizures due to specific spatial-temporal modifications of evolving large-scale epileptic brain networks. Sci. Rep. **9**, 10623 (2019)
133. P. Ritchie, J. Sieber, Probability of noise-and rate-induced tipping. Phys. Rev. E **95**, 052209 (2017)
134. F. Rosenow, H. Lüders, Presurgical evaluation of epilepsy. Brain **124**, 1683–1700 (2001). https://doi.org/10.1093/brain/124.9.1683
135. B. Schelter, M. Winterhalder, M. Eichler, M. Peifer, B. Hellwig, B. Guschlbauer, C.H. Lücking, R. Dahlhaus, J. Timmer, Testing for directed influences among neural signals using partial directed coherence. J. Neurosci. Methods **152**, 210–219 (2006)
136. B. Schelter, M. Winterhalder, T. Maiwald, A. Brandt, A. Schad, A. Schulze-Bonhage, J. Timmer, Testing statistical significance of multivariate time series analysis techniques for epileptic seizure prediction. Chaos **16**, 013108 (2006)
137. B. Schelter, M. Winterhalder, T. Maiwald, A. Brandt, A. Schad, J. Timmer, A. Schulze-Bonhage, Do false predictions of seizures depend on the state of vigilance? a report from two seizure-prediction methods and proposed remedies. Epilepsia **47**, 2058–2070 (2006)
138. K. Schindler, S. Bialonski, M.T. Horstmann, C.E. Elger, K. Lehnertz, Evolving functional network properties and synchronizability during human epileptic seizures. Chaos **18**, 033119 (2008). https://doi.org/10.1063/1.2966112
139. K. Schindler, C.E. Elger, K. Lehnertz, Increasing synchronization may promote seizure termination: evidence from status epilepticus. Clin. Neurophysiol. **118**, 1955–1968 (2007). https://doi.org/10.1016/j.clinph.2007.06.006
140. K. Schindler, H. Leung, C.E. Elger, K. Lehnertz, Assessing seizure dynamics by analysing the correlation structure of multichannel intracranial EEG. Brain **130**, 65–77 (2007). https://doi.org/10.1093/brain/awl304
141. T. Schreiber, A. Schmitz, Surrogate time series. Phys. D **142**, 346–382 (2000). https://doi.org/10.1016/S0167-2789(00)00043-9
142. A. Schulze-Bonhage, Brain stimulation as a neuromodulatory epilepsy therapy. Seizure **44**, 169–175 (2017)
143. A. Schulze-Bonhage, From moon to earth–ultradian cycles in brain excitability. Lancet Neurol. **17**, 930–932 (2018)
144. A.K. Seth, A.B. Barrett, L. Barnett, Granger causality analysis in neuroscience and neuroimaging. J. Neurosci. **35**, 3293–3297 (2015)
145. S. Singh, S. Sandy, S. Wiebe, Ictal onset on intracranial EEG: do we know it when we see it? state of the evidence. Epilepsia **56**, 1629–1638 (2015)
146. D.E. Snyder, J. Echauz, D.B. Grimes, B. Litt, The statistics of a practical seizure warning system. J. Neural Eng. **5**, 392–401 (2008)
147. R. Sowa, A. Chernihovskyi, F. Mormann, K. Lehnertz, Estimating phase synchronization in dynamical systems using cellular nonlinear networks. Phys. Rev. E **71**, 061926 (2005)
148. S.S. Spencer, Neural networks in human epilepsy: evidence of and implications for treatment. Epilepsia **43**, 219–227 (2002). https://doi.org/10.1046/j.1528-1157.2002.26901.x
149. S.S. Spencer, P.D. Williamson, S.L. Bridgers, R.H. Mattson, D.V. Cicchetti, D.D. Spencer, Reliability and accuracy of localization by scalp ictal EEG. Neurology **35**, 1567 (1985)
150. W.C. Stacey, Seizure prediction is possible-now let's make it practical. EBioMedicine **27**, 3–4 (2018)
151. T. Stankovski, T. Pereira, P.V.E. McClintock, A. Stefanovska, Coupling functions: universal insights into dynamical interaction mechanisms. Rev. Mod. Phys. **89**, 045001 (2017). https://doi.org/10.1103/RevModPhys.89.045001

152. S.H. Strogatz, Exploring complex networks. Nature **410**, 268–276 (2001). https://doi.org/10.1038/35065725
153. R. Surges, J.W. Sander, Sudden unexpected death in epilepsy: mechanisms, prevalence, and prevention. Curr. Opin. Neurol. **25**, 201–207 (2012)
154. E. Taubøll, A. Lundervold, L. Gjerstada, Temporal distribution of seizures in epilepsy. Epilepsy Res. **8**, 153–165 (1991)
155. C.A. Teixeira, B. Direito, M. Bandarabadi, M.L.V. Quyen, M. Valderrama, B. Schelter, A. Schulze-Bonhage, V. Navarro, F. Sales, A. Dourado, Epileptic seizure predictors based on computational intelligence techniques: a comparative study with 278 patients. Comput. Meth. Prog. Biomed. **114**, 324–336 (2014). https://doi.org/10.1016/j.cmpb.2014.02.007
156. S.M. Usman, S. Khalid, R. Akhtar, Z. Bortolotto, Z. Bashir, H. Qiu, Using scalp EEG and intracranial EEG signals for predicting epileptic seizures: review of available methodologies. Seizure **71**, 258–269 (2019)
157. W. Van Drongelen, S. Nayak, D.M. Frim, M.H. Kohrman, V.L. Towle, H.C. Lee, A.B. McGee, M.S. Chico, K.E. Hecox, Seizure anticipation in pediatric epilepsy: use of Kolmogorov entropy. Ped. Neurol. **29**, 207–213 (2003)
158. P. Van Mierlo, M. Papadopoulou, E. Carrette, P. Boon, S. Vandenberghe, K. Vonck, D. Marinazzo, Functional brain connectivity from EEG in epilepsy: seizure prediction and epileptogenic focus localization. Prog. Neurobiol. **121**, 19–35 (2014)
159. G. Varotto, L. Tassi, S. Franceschetti, R. Spreafico, F. Panzica, Epileptogenic networks of type II focal cortical dysplasia: a stereo-EEG study. NeuroImage **61**, 591–598 (2012). https://doi.org/10.1016/j.neuroimage.2012.03.090
160. J.B. Wagenaar, G.A. Worrell, Z. Ives, M. Dümpelmann, B. Litt, A. Schulze-Bonhage, Collaborating and sharing data in epilepsy research. J. Clin. Neurophysiol. **32**, 235 (2015)
161. T.S. Walczak, R.A. Radtke, D.V. Lewis, Accuracy and interobserver reliability of scalp ictal EEG. Neurology **42**(12), 2279-2279 (1992)
162. S. Weisdorf, J. Duun-Henriksen, M.J. Kjeldsen, F.R. Poulsen, S.W. Gangstad, T.W. Kjær, Ultra-long-term subcutaneous home monitoring of epilepsy–490 days of EEG from nine patients. Epilepsia **60**, 2204–2214 (2019)
163. F. Wendling, P. Benquet, F. Bartolomei, V. Jirsa, Computational models of epileptiform activity. J. Neurosci. Methods **260**, 233–251 (2016)
164. T. Wilkat, T. Rings, K. Lehnertz, No evidence for critical slowing down prior to human epileptic seizures. Chaos **29**, 091104 (2019)
165. C. Wilke, G. Worrell, B. He, Graph analysis of epileptogenic networks in human partial epilepsy. Epilepsia **52**, 84–93 (2011). https://doi.org/10.1111/j.1528-1167.2010.02785.x
166. J.R. Williamson, D.W. Bliss, D.W. Browne, J.T. Narayanan, Seizure prediction using EEG spatiotemporal correlation structure. Epilepsy Behav. **25**, 230–238 (2012)
167. M. Winterhalder, T. Maiwald, H.U. Voss, R. Aschenbrenner-Scheibe, J. Timmer, A. Schulze-Bonhage, The seizure prediction characteristic: a general framework to assess and compare seizure prediction methods. Epilepsy Behav. **3**, 318–325 (2003)
168. M. Winterhalder, B. Schelter, T. Maiwald, A. Brandt, A. Schad, A. Schulze-Bonhage, J. Timmer, Spatio-temporal patient-individual assessment of synchronization changes for epileptic seizure prediction. Clin. Neurophysiol. **117**, 2399–2413 (2006)
169. S. Wong, A.B. Gardner, A.M. Krieger, B. Litt, A stochastic framework for evaluating seizure prediction algorithms using hidden Markov models. J. Neurophysiol. **97**, 2525–2532 (2007)
170. Y. Zheng, G. Wang, K. Li, G. Bao, J. Wang, Epileptic seizure prediction using phase synchronization based on bivariate empirical mode decomposition. Clin. Neurophysiol. **125**, 1104–1111 (2014). https://doi.org/10.1016/j.clinph.2013.09.047

Chapter 23
General Anaesthesia and Oscillations in Human Physiology: The BRACCIA Project

Johan Raeder

Abstract General anaesthesia may be induced by a number of different types of drugs, and no clear-cut, single mechanism of action is recognized. Traditional monitoring of general anaesthesia is based on surrogate measures of adequate degree of unconsciousness during painful stimuli; such as heart rate , blood-pressure, respiration, muscle activity and, in recent years, EEG. The dose need of anaesthetic drugs must be adjusted to the individual patient and the surgical invasiveness. The idea of the BRACCIA project was to monitor concomitantly the most relevant physiological changes, to distinguish objectively between awake and general anaesthesia, and between propofol versus sevoflurane anaesthesia in a setup of 27 patients. ECG, respiration, skin temperature, pulse and skin conductivity were recorded. Both raw data, oscillations and interactions between parameters were tested, new hardware and software were developed. A total of 28 different physiological outputs were tested. With a best selection of 11 attributes, 9 from the EEG, 1 from ECG and 1 from respiratory rate we were able with 97% precision to distinguish the state of being awake from the state of general anaesthesia. For the distinction between general anaesthesia caused by either sevoflurane or propofol the precision was 87%.

Until the advent of anaesthesia during the nineteenth century, extensive surgery was almost impossible to do with success; due to intense pain, vigorous movements and muscle spasm, as well as life-threatening cardiovascular responses. The basic requirements for surgery, in this context, is a non-moving patients with relaxed muscles and minor patient discomfort. This may be achieved with local anaesthesia infiltration for minor procedures or regional anaesthetic nerve-blocks, including spinal or epidural anaesthesia, for some more extensive procedures. However, the use of general anaesthesia is a dominating technique for most of the 4–500 million surgical procedures which are performed world-wide every year. Even though general anaesthesia is very

J. Raeder (✉)
Department of Anaesthesia, University of Oslo and Senior Consultant, Oslo University Hospital, Oslo, Norway
e-mail: johan.rader@medisin.uio.no

A. Stefanovska and P. V. E. McClintock (eds.), *Physics of Biological Oscillators*, Understanding Complex Systems,
https://doi.org/10.1007/978-3-030-59805-1_23

widespread and frequent in use, there are still many controversies to this concept, such as: How is general anaesthesia defined? What is the mechanism of general anaesthesia? What drugs are useful for the purpose and which are best? How do we measure and or quantify general anaesthesia?

23.1 Definition and Mechanisms

Definition of anaesthesia and mechanisms of general anaesthesia are linked, as for most biological phenomena there is a relationship between mechanism of action and resultant physiological effects, leading to the physiologic response or state of function which is in question. Not quite so simple with general anaesthesia, even though some distinct receptors and biological actions may be identified for most of the drugs which produce the state of general anaesthesia. Still, general anaesthesia seems to be a fundamental physiologic state of living animals and even plants [7], being the result of a number of very different measures. If we look at immobility and unconsciousness as the two major features, these may be the results of, for instance; diabetic coma, liver coma, a hard blow to the head, overdose of most psychoactive drugs etc. However, the features of clinical general anaesthesia are, in addition to unconsciousness and immobility, rapid reversibility of the condition without any damage of the organism. This may be accomplished by inhalational anaesthetic agents, some iv agents, and hypnotic acting agents in combination with opioids. Still, looking at the molecular structures and their potential actions on human nerve cells, these anaesthetic drugs are quite different from each other. Their actions may be described in terms of cellular targets, but also in terms of altered intercellular interactions, altered neuronal network modes and specific anatomical regions [5].

As to cellular actions we know that most of the hypnotics acts at the GABA receptor, the opioids at the opioid my-receptor [15], ketamine at the NMDA receptor, whereas inhalational agents have a more complex and diversified action. We know that attenuation of neuronal activity in the dorsal spinal horn is a major player in immobility, and attenuation of reflex actions to nociceptive (i.e. painful in the awake) stimuli is important for attenuation of discomfort. Further, downregulation of activity in the cerebral cortex is a major feature of unconsciousness, although in the state of anaesthetic induced unconsciousness there are areas in the deeper brain with increased activities as well. Thus, this brings in the important concept of general anaesthesia and unconsciousness as altered signal patterns within the very complex neuronal network in the central nervous system.

23.2 Monitoring of General Anaesthesia

Monitoring of general anaesthesia is conceptually very difficult, both because of the variety of different drugs and drugs actions involved, as well as the extreme complexity of the target organ: the central nervous system. In the brain and spinal

cord there are a two-digit billion number of neurons, each one of which has hundreds to thousands of contacts with neighbouring cells. Thus, how should these cells and their interactions be monitored in terms of identifying general anaesthetic action, or even more difficult: to determine degree of action in a quantitative way? The answer throughout the soon 175 years of history of general anaesthesia has been to monitor surrogate or secondary signs of unconsciousness and diminished reflex actions. The very simple end logic monitoring will just be to test unconsciousness and immobility when you make a small wound in the skin with the scalpel: Does the patient move? Does the patient moan or show any signs of discomfort? If no—the surgeon may go ahead, if yes—more anaesthetic drug effect is needed. While this may work in some way, there are three problems with this approach: (1) The testing has to be done frequently during a procedure, because different types of surgical activity will require different level of anaesthetic drug effect. (2) Frequent testing will delay and complicate surgery, and there is a risk for discomfort as well as vigorous and dangerous movements if the stimuli is too strong (3) There is no good way to ensure that anaesthesia is not overdosed: a non-moving patient may be a sign of adequate dose level or a profound overdose.

Thus, other signs of low, medium or strong anaesthetic effect without necessarily testing with a knife have to be looked for. Also, the term "effect" becomes problematic, as anaesthetic effect should be determined in a situation with ongoing surgery. This has lead to use of the term "anaesthetic depth" to define quantitatively the total impact of anaesthetic dosing in the individual. The idea is that an adequate depth of anaesthesia should be established without testing before start of surgery, and still ensure close to 100% guarantee of no movement or moaning during subsequent surgery.

During the first decade of ether as a the mono-anaestetic drug, the position and size of the pupils were used as a surrogate sign of anaesthetic effect on the brain, together with signs of respiratory and circulatory depression. With the advent of intravenous agents, i.e. hypnotics and opioids, often used in mixture with inhalational agents; the pupil signs became less specific and the baseline monitoring of anaesthetic effect shifted towards simple general features of unconsciousness: low blood-pressure, low heart rate, attenuation or cessation of spontaneous ventilation, no gross movements upon vigorous surgical stimulation etc. Signs of sympathetic stimulation; such as sweating [4], tear production, together with increased heart rate and blood-pressure were taken as signs of inadequate depth of anaesthesia with the need of either increased anaesthetic drug dosing or reduced surgical stimulation, or both.

Because minor movements or muscle contractions may occur even if the depth of anaesthesia is otherwise adequate (i.e. the patient is unconscious), the use of curare drugs became popular from the mid 20th-century in order to reduce the dose of anaesthetic drugs, resulting in less hemodynamic depression and faster recovery after end of anaesthesia. Curare is also needed when even a slight movement of the patient during surgery may have serious consequences, such as during neurosurgery, eye surgery, middle ear surgery or other areas of microsurgery. However, with the successful advent and use of curare a new problem emerged: some patients got too

low doses of anaesthetic drugs, and were awake during surgery without being able to open eyes or move, thus they could be left in a state of intense anxiety during ongoing surgery without anyone noticing. This phenomenon of so-called "awareness" was reported in about 1 patient per 2000 general anaesthetics with curare, not in any way life-threatening or frequent, but very traumatic for those involved [11]. In most of these cases opioids were used as anti-nociceptive agents, ensuring stable and low readings of BP and HR, but not reliable sleep. Thus, both the awareness cases but also cases of overdosing with subsequent slow recovery called for better monitoring than just looking at BP, HR, minor movements and signs of sympathetic stimulation. It has also been shown in the elderly patients that overdose of general anaesthetic drugs may increase the incidence of postoperative delirium [12] and cognitive decline [2]. As the central nervous system is the target organ of general anaesthetic drugs, ways of monitoring brain function directly, such as the EEG [6], were looked for.

The raw EEG is basically a continuous flow of electrical signals from 20–40 electrodes placed scattered across the full scalp. The spontaneous EEG have some characteristics which allow the expert to define which state the individual patient belongs to along an axis from: excited → quiet awake → asleep → unconscious. However, the complete EEG is very cumbersome to both register and interpret, thus simplified ways of looking at EEG were looked for. One approach was to look at the frontal EEG response (amplitude, frequency and delay) to a standardized stimulus, e.g. sound click, as with the auditory avoked potential (AEP). Another approach was to look for ways to interpret the spontaneous EEG by automatic computer algorithms, basically looking at frequencies, amplitudes and phase positions during different states of depth of anaesthesia. Fortunately, the single and easily accessible frontal EEG lead was useful in this context, as there is a frontal shift of EEG power during general anaesthesia. However, it was soon evident that the EEG changes were complex and not linear with dose, and EEG changes were different with different drugs and drug mixtures, even though they produced the same clinical depth of general anaesthesia [1, 10] Also, there were problems of electrical signals from forehead muscles interfering with the EEG and problems of surgery and nociception interfering with the EEG algorithms. The problems were attempted to be solved by complex signal analyses, such as with the entrophy, narcotrend, cerebral state monitor and other devices [9]. The most successful device proved to be the BIS monitor, launched in the 1990ties, with a single frontal EEG reading, a secret and patented algorithm for EEG interpretation, and a simple output of a score from 0–100. With a score value below 60 the patient was asleep, and with a value of more than 60 for more than 5 min there was a high chance of the patients being awake and aware, while values in the 90–100 range were seen in fully awake individuals. Although the BIS has gained widespread use and proved to reduce the incidence of awareness [3] as well as avoiding cases of inadvertent overdosing, there are problems with this device as well. The signal is delayed with 1–2 min, it may be disturbed by muscle activity, it may be inaccurate with low-power EEG in the elderly, it does not work predictably with nitrous oxide or ketamine and it is inaccurate in monitoring the antinociceptive part of general anaesthesia.

Thus, the search for better tools to monitor anaesthetic depth has gone on, along different conceptual routes. One straightforward and quite successful approach has simply been to monitor the exhaled end-tidal concentration of inhalational agents. If the concentration of e.g. sevoflurane is at 1% or higher (or 3% with desflurane), one can almost with 100% certainty assume that this patient will be asleep. Also, refinements in looking at changes in sympathetic outflow have been promising [9]: looking for subtle variations in the beat-to-beat interval on the EEG, measuring pulse-plethysmography in the finger, looking at sweat-bursts in the palm of the hand [14].

Still, none of these devices has even close to 100% specificity or sensitivity for the state of general anaesthesia, in fact; most of them have not even been tested for these features.

23.3 The Braccia Concept: Anaesthesia Monitoring—Bringing it All Together?

The Braccia concept was developed as a result of physicists looking at the characteristics of numerous bio-rhythms in the body, noting that these change somewhat predictably during sleep and general anaesthesia. Although these changes are not by themselves highly specific or sensitive, the idea came up that bringing a number of different low-specific changes together may increase the sensitivity and specificity. The higher the number of relevant and different changes brought together, the higher the chance of high specificity/sensitivity. The challenge in such a process will be to first determine which changes and bio functions are relevant and non-overlapping. Then build up an algorithm of bringing them together in a unified output for clinical use.

The idea of combining different measures in this way is not new or original, and attempts have been made and are being launched in this direction such as the PSI, NOL index and others; using combinations of pulse-plethysmography signals and/or EEG for a potentially more precise evaluation of anaesthetic depth.

The feature of the Braccia project was to start out very broadly, including most of the documented measures of anaesthetic depth, refine the hardware for each measure, measure simultaneously all measures in the same patients, then developing a complex software program in order to sort out which measures were useful and in which way. The first phase was the development of the hardware and the software for collecting and analysing biorhythmic waves raw signals properly.

The second phase was to apply this prototype devices on a series of patients. The clinical setup was highly standardized: All patents were monitored for about 30 min in the awake state with relaxed and very quiet environment. Then general anaesthesia was induced with either sevoflurane or propofol as a mono anaesthetic. After general anaesthesia was established, the test battery was applied again for about 30 min period of stable general anaesthesia with spontaneous ventilation.

The research questions were fairly simple and straightforward:

(1) What characterises (in the test battery) the awake versus the general anaesthetic state?
(2) What characterises general anaesthesia with propofol versus general anaesthesia with sevoflurane?

For these questions the software development looked for ways to pick out relevant raw signals and signals of biorhythms which were useful for answering the question, and then make an optimal synthetises of the relevant methods in terms of optimal sensitivity and specificity.

The goal was to find a algorithm with 100% sensitivity and specificity in terms of putting each individual patient into the categories above: Awake or asleep? Propofol or sevoflurane?

The measurements were taken from the EEG signal, and also from a number of other oscillating neuronal networks in the body: the heart, the vasculature, the skin, the ventilation. The concept evolved not just on studying how they change, but also on how their interactions and oscillations change during general anaesthesia. For this purpose, soon after the start of this millennium, Aneta Stefanovska and colleagues were able to collect a major European Union research grant, and set up an extensive group of physicists, mathematicians and anaesthesiologists from a number of different European countries, in the BRACCIA Project.

The practical parts of the project were:

(1) To set up and develop a number of tools, including new monitoring devices, for extensive mapping of neuronal functions and networks.
(2) To use this basket of tools in real patients during either inhalational (sevoflurane) or intravenous (propofol) general anaesthesia, and compare with the awake state.
(3) To apply extensive and complicated tools of signal- and wave-analyses to the collected data, in order to develop a targeted, essential algorithm for characterizing general anaesthesia with 100% specificity and sensitivity.

23.4 The Braccia Results, so far

The BRACCIA project has produced new knowledge, published in major journals. In the first publication the use of non-EEG measures was evaluated [8].

We recorded ECG, respiration, skin temperature, pulse and skin conductivity before and during general anaesthesia in 27 subjects in good cardiovascular health, randomly allocated to receive propofol or sevoflurane. Each subject served as their own control for the awake to anaesthetized state, whereas in-group differences was determined for propofol anaesthesia versus sevoflurane anaesthesia. All changes described (below) was statistically significant at < 0.05 level (Fig. 23.1).

For the mean values; respiratory rate, skin conductivity and skin temperature changed with sevoflurane, and skin temperature with propofol. Pulse transit time increased by 17% with sevoflurane and 11% with propofol. Sevoflurane reduced the

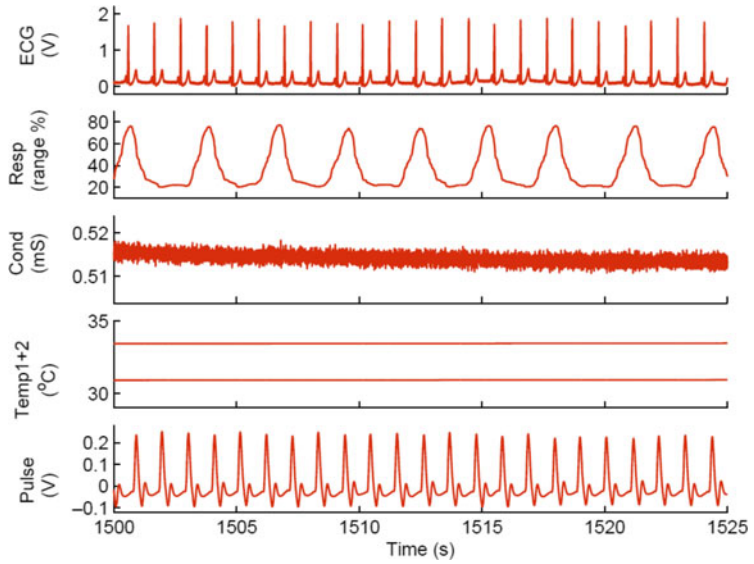

Fig. 23.1 Example of a short segment of signals recorded during anaesthesia (from top to bottom): electrical activity of the heart (ECG); respiration as a percentage of the sensor range; skin conductivity; skin temperature from the wrist (upper) and ankle (lower) and piezoelectric pulse

wavelet energy of heart and respiratory rate variability at all frequencies, whereas propofol decreased the heart rate variability below 0.021 Hz. The phase coherence was reduced by both agents at frequencies below 0.145 Hz, whereas the cardiorespiratory synchronisation time was increased. When putting all awake data together into an optimal set of discriminatory parameters algoritm, we were able to classify 98% of the patients as correctly awake, when awake. When anaesthetized with sevoflurane 93% were classified correctly anaesthetized with sevoflurane, whereas 7% were classified as being awake. Of those being anaesthetized with propofol 100% were classified correctly versus the awake state. In terms of distinguishing between sevoflurane and propofol the classification was less accurate, being correct in 80% of the cases.

However, as the brain is the major target organ of general anaestetic drugs, the second part of the study program involved the frontal raw EEG signal as well a computing of cross-frequency coupling functions between neuronal, cardiac, and respiratory oscillations in order to determine their mutual interactions [13]. The phase domain coupling function reveals the form of the function defining the mechanism of an interaction, as well as its coupling strength. Using a method based on dynamical Bayesian inference, we identified and analyzed the coupling functions for six relationships. By quantitative assessment of the forms and strengths of the couplings, we revealed how these relationships were altered by anaesthesia, also showing that some of them are differently affected by propofol and sevoflurane (Fig. 23.2).

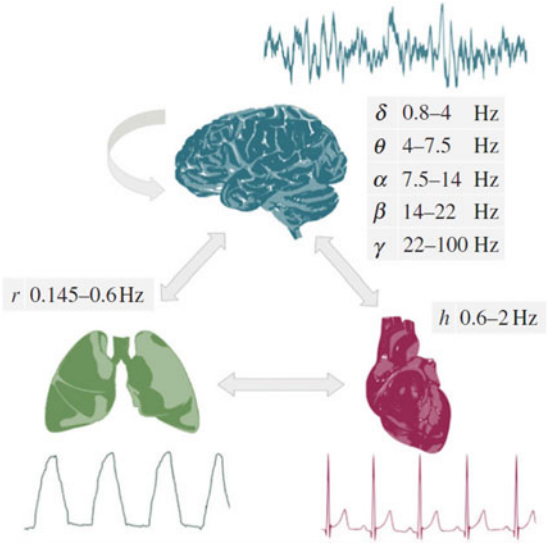

Fig. 23.2 Schematic of the main aims of the study. We seek to investigate the interactions between oscillatory processes in the brain, lungs and heart, and to establish how they are affected by general anaesthesia. The interactions are assessed by reconstruction of the coupling functions. The analyses are performed on non-invasive measurements of the electroencephalogram (EEG), the respiration signal from expansion of the thorax and the electrocardiogram (ECG). Samples of raw measurements are shown adjacent to each of the organs, as are also the relevant cross-frequency intervals

In the final paper (in preparation) we have tried to put everything together, in order to include those measurements and algorithms which are useful for the purpose, excluding those which are not. The signals of EEG, ECG, respiration, temperature, pulse transit time and skin conductivity were analyzed for raw output, frequency distribution and variability, power of oscillations, wavelet phase coherence, wavelet phase synchronization, coupling strength and coupling functions.

A total of 28 different physiological outputs were tested. With a best selection of 11 attributes, 9 from the EEG, 1 from ECG and 1 from respiratory rate we were able with 97% precision to distinguish the state of being awake from the state of general anesthesia. For the distinction between general anesthesia caused by either sevoflurane or propofol the precision was 87%.

In conclusion: The combination of sophisticated analyses on EEG, ECG and respiration rate may thus provide a useful approach in the further strive for increased precision on monitoring depth of anesthesia with objective means.

However, there remain many challenges with the BRACCIA hardware and software. It has to prove its robustness in large and mixed patient materials during a combination of surgery and general anaesthesia, as well as during combinations of different anaesthetic drugs.

Also, there is a challenge in developing the new tools into practical devices that can be embraced and used by busy anaesthesiologists in everyday use.

References

1. O. Akeju, M.B. Westover, K.J. Pavone, A.L. Sampson, K.E. Hartnack, E.N. Brown et al., Effects of sevoflurane and propofol on frontal electroencephalogram power and coherence. Anesthesiology **121**(5), 990–998 (2014)
2. C. Ballard, E. Jones, N. Gauge, D. Aarsland, O.B. Nilsen, B.K. Saxby et al., Optimised anaesthesia to reduce post operative cognitive decline (POCD) in older patients undergoing elective surgery, a randomised controlled trial. PLoS ONE **7**(6), e37410 (2012)
3. A. Ekman, M.L. Lindholm, C. Lennmarken, R. Sandin, Reduction in the incidence of awareness using BIS monitoring. Acta Anaesthesiol. Scand. **48**(1), 20–26 (2004)
4. A.C. Gjerstad, H. Storm, R. Hagen, M. Huiku, E. Qvigstad, J. Raeder, Comparison of skin conductance with entropy during intubation, tetanic stimulation and emergence from general anaesthesia. Acta Anaesthesiol. Scand. **51**(1), 8–15 (2007)
5. H.C. Hemmings Jr., P.M. Riegelhaupt, M.B. Kelz, K. Solt, R.G. Eckenhoff, B.A. Orser et al., Towards a comprehensive understanding of anesthetic mechanisms of action: a decade of discovery. Trends Pharmacol. Sci. **40**(7), 464–481 (2019)
6. L.C. Jameson, T.B. Sloan, Using EEG to monitor anesthesia drug effects during surgery. J. Clin. Monit. Comput. **20**(6), 445–472 (2006)
7. M.B. Kelz, G.A. Mashour, The biology of general anesthesia from paramecium to primate. Curr. Biol. **29**(22), R1199–R1210 (2019)
8. D.A. Kenwright, A. Bernjak, T. Draegni, S. Dzeroski, M. Entwistle, M. Horvat et al., The discriminatory value of cardiorespiratory interactions in distinguishing awake from anaesthetised states: a randomised observational study. Anaesthesia **70**(12), 1356–1368 (2015)
9. F.A. Lobo, A. Shander, Modern anesthetic noninvasive monitoring: a deep look into perioperative care. J. Cardiothorac. Vasc. Anesth. **33**(1), S1–S2 (2019)
10. P.L. Purdon, E.T. Pierce, E.A. Mukamel, M.J. Prerau, J.L. Walsh, K.F. Wong et al., Electroencephalogram signatures of loss and recovery of consciousness from propofol. Proc. Natl. Acad. Sci. USA. **110**(12), E1142–E1151 (2013)
11. R.H. Sandin, Awareness 1960–2002, explicit recall of events during general anaesthesia. Adv. Exp. Med. Biol. **523**, 135–147 (2003)
12. M. Soehle, A. Dittmann, R.K. Ellerkmann, G. Baumgarten, C. Putensen, U. Guenther, Intraoperative burst suppression is associated with postoperative delirium following cardiac surgery: a prospective, observational study. BMC Anesthesiol. **15**, 61 (2015)
13. T. Stankovski, S. Petkoski, J. Raeder, A.F. Smith, P.V. McClintock, A. Stefanovska, Alterations in the coupling functions between cortical and cardio-respiratory oscillations due to anaesthesia with propofol and sevoflurane. Philos. Trans. A Math. Phys. Eng. Sci. **374**(2067) (2016)
14. H. Storm, M. Shafiei, K. Myre, J. Raeder, Palmar skin conductance compared to a developed stress score and to noxious and awakening stimuli on patients in anaesthesia. Acta Anaesthesiol. Scand. **49**(6), 798–803 (2005)
15. G.M. Yip, Z.W. Chen, C.J. Edge, E.H. Smith, R. Dickinson, E. Hohenester et al., A propofol binding site on mammalian GABAA receptors identified by photolabeling. Nat. Chem. Biol. **9**(11), 715–720 (2013)

Chapter 24
Processed EEG as a Measure of Brain Activity During Anaesthesia

EEG Oscillations Under Anaesthesia

Pablo Martínez-Vázquez, Pedro L. Gambús, and Erik Weber Jensen

Abstract Introduction to depth of anaesthesia monitoring, a crucial tool to guide anaesthesiologist for safer surgical procedures. Description of the main EEG activity changes induced by hypnotic anaesthetic agents and the distinct analysis perspectives in their characterizations. Design principles, minimal validation requirements, limitations and current challenges.

24.1 Introduction. The Need of Anaesthesia Monitoring

Despite the widespread clinical use of general anesthetics from their evident benefit for the patients undergoing surgery, since the beginning of its modern history, their use has been recognized as a hazardous endeavour with potential adverse effects to the patients [32]. Unconsciousness, analgesia and immobility (muscle relaxation) are the fundamental components of General Anaesthesia (GA). For safe surgical procedures it is crucial for the anaesthesiologist to possess objective methods to estimate the level of each GA component continuously along the different phases of the surgical procedure, in particular, the unconsciousness or hypnosis and the analgesia or nociception. With around 250 million worldwide surgeries per year, any enhancement in the perioperative care preventing anaesthesia adverse effects is a major public health issue. Traditional parameters such as tachycardia, hypertension, sweating or movements between others have shown low sensitivity and specificity in estimating

P. Martínez-Vázquez (✉)
Deutsches Primaten Zentrum (DPZ), 37077 Goettingen, Germany
e-mail: pmvazquez@dpz.eu

P. L. Gambús
Department of Anesthesia, Hospital Clinic de Barcelona, Barcelona, Spain

Biomedical Engineering, Universidad de Barcelona, Barcelona, Spain

E. Weber Jensen
R&D of Quantium Medical/Fresenius Kabi. Barcelona & Automatic Control and Informaic (ESAII) Department, Centre for Biomedical Research (CREB) UPC-Barcelonatech, Barcelona, Spain

A. Stefanovska and P. V. E. McClintock (eds.), *Physics of Biological Oscillators*, Understanding Complex Systems,
https://doi.org/10.1007/978-3-030-59805-1_24

sedation levels and detecting nociceptive stimuli. This limitation becomes crucial under potential unintentional Awareness with Recall (AWR) not predicted by pharmacological models. In the last decades, there has been a significant increase in the research and development of non-invasive neuromonitoring technologies based on the Electroencephalogram (EEG), guiding anaesthesiologists during surgical procedures where the traditional hemodynamic and clinical signs may not be reliable. This research and development followed a Depth of Anaesthesia-Effect site concentration (DoA-Ce) approach, which links the Depth of Anaesthesia (DoA) to the drug effect site concentration (Ce), the concentration at the biophase (the place where the drug actuates), and where the EEG has the binding role. This approach allows tailoring drug administration to each patient and surgical context, to prevent AWR events due to underdoses [11, 36, 57] and excessive concentrations (overdoses), optimizing the anaesthesia drug consumption [46, 50, 56], and improving patients' outcomes. [8, 25, 28, 44, 55].

24.2 Main EEG Patterns During Anaesthesia

The general anaesthetics, inhaled or intravenous, mediate at the neuronal level by inhibiting or blocking excitatory neurotransmissions, acting on specific neutrotransmitters and voltage-gated ion channels. Roughly, the general anaesthetics produce a widespread neurodepression in the central nervous system (CNS), causing multiple behavioural responses such as unconsciousness (hypnosis), analgesia and immobility depending on which specific neurotransmitters, synaptic receptors and neuronal pathways the drugs target to. Since the EEG reflects the activity of hundreds of thousands of synchronized cortical pyramidal cells [23], the net inhibitory induced changes in neural neurotransmission by GA drugs, affect the synchronization of the pyramidal neurons, inhibiting their communication with other neurons and other brain areas such as thalamus and hippocampus. The drug-induced changes of the EEG wave patterns depend on multiple factors such as the intrinsic mechanism of action of each drug, the Ce, potential drug interactions with other drugs, patients variability and many other factors that might take place during the surgical procedure. Understanding the main qualitative changes of the EEG wave patterns is complex, but current depth of anaesthesia monitoring technologies track quantitatively the EEG pattern changes summarizing them into useful indexes describing the patient's hypnosis or sedation state.

The most widely used drugs to induce and maintain the hypnotic component of GA are broadly divided as intravenous and inhalation agents according to their route of administration. While intravenous agents such as propofol or barbiturates act mainly at the GABA receptor complex systems, the mechanisms of action of inhalation agents such as sevoflurane, desflurane or isoflurane are, additionally to a GABA agonist mechanism, different and probably related to transient alterations of lipid membrane of neurons. Even though, for the mentioned drugs, their surrogate effects at the cortical level, and thus, on the EEG, are very similar.

This chapter focuses exclusively on this widely used hypnotic drugs that elicit common well-known patterns on the EEG. Other drugs such as opioids operate under very different mechanisms, and agents such as nitrous oxide, dexmedethomidine and ketamine among others, possess an ambivalent effect, both hypnotic and analgesic, all inducing distinct effects on EEG outside the scope of this chapter, see [29, 32] for more details.

The two main EEG induced effects observed under propofol, similarly for sevoflurane, desflurane and isoflurane, are shown from an example case under a Total Intravenous Anaesthesia (TIVA) procedure with propofol and remifentanil (opiod). Figure 24.1 shows segments of EEG collected at different propofol Ce concentrations. Clearly, the changes in the EEG activity regarded to the hypnotic drug concentrations are not following a continuous transitional pattern [30, 32], but two major changes regarded to the preservation of the statistical stationary properties of the signal,[1] which will require consequently two different major signal processing approaches. The two main type changes are:

EEG changes preserving signal stationary. In these circumstances, there is a continuous wise modification of the EEG signal spectral components related to the drug concentration. For lower and moderate propofol concentrations the EEG induced changes vary continuously without affecting signal stationary properties (strict sense) in mean and variance. See some EEG example segments in Fig. 24.1a, for several propofol Ce levels (Ce = 2.2 μg/ml and Ce = 3 μg/ml) respect to the awake state, Ce = 0 μg/ml. As drug concentration increases the EEG becomes "smoother" in time, with its corresponding translation in the frequency representation, shifting the spectrum content to lower frequencies, diminishing the beta and gamma components, see Fig. 24.1b. Additionally, at some concentrations, propofol induces strong periodic oscillations around 10 Hz (α-band) and low frequencies, δ-band.[2] Similar effects occur under other agents such as sevoflurane, desflurane and isoflurane.

Non-stationary time preservation induced patterns. At higher concentrations of propofol, a strong disruption from the previous "smoothing" transition pattern takes place, see Fig. 24.1c for Ce = 5.8 μg/ml. High doses induce major temporal changes in the EEG waveform, losing the time stationary properties since the signal variance changes abruptly along time. The EEG activity alternates with periods of no activity, low signal amplitude periods consistently less than 5 μV for more than 500 ms (clinical definition), a pattern known as Burst Suppression (BS). Traditionally, the BS is quantified coarsely with the Burst Suppression Rate (BSR), defined as the percentage of periods with no activity, isoelectric EEG, respect to the total time, a measurement proportional to the drugs Ce [13]. As before, the BS takes place at high concentrations under other GABA agents such as sevoflurane and isoflurane.

[1] A stationary process (strict sense), is a stochastic process preserving the unconditional joint probability distribution across shifts in time. Under second-order statistics, this implies that mean and variance do not change over time [41].

[2] Despite, GA agents (such propofol) provoke a broad neurodepression, the activity in some frequency bands may increase due to the networks deviation from their natural dynamics, altering (thalamocortical) loops and leading to synchronous (α and δ) activities [9].

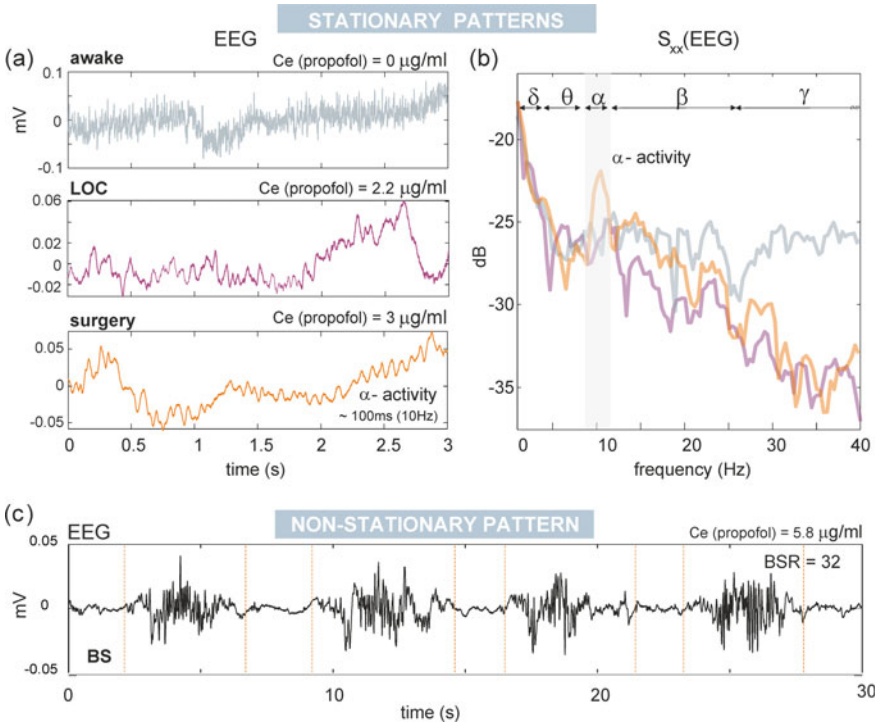

Fig. 24.1 Example of the two coarse changes induced by propofol: stationary and non-stationary changes. EEG signals under different concentration levels of propofol. Induced changes preserving signal stationary properties. **a** Three raw EEG activities of 3 s at different propofol concentrations, from awake to the loss of consciousness (LOC) and a surgical level. **b** Their three power spectral density, in decibels (dB), with the conventional EEG frequency bands. As the drug concentration increases the EEG spectra shift to lower frequencies and a narrow band frequency component rises around α-band. Induced non-stationary changes in the signal. Temporal changes in the signal variance. **c** EEG activity (30 s) under high concentrations of propofol, with BS periods and a BSR = 32. These EEG segments were extracted from a patient case under GA shown in Fig. 24.2b

These two EEG induced patterns under different drug concentration levels usually require different, signal processing approaches for feature extractions. While there are well-known effects of the anaesthetics agents on the EEG power spectral density such as the spectral shift to lower components or alpha power increase, other effects were described regarded to the synchronization activities [10, 38, 45]. Significant frequency widespread changes in synchronization appear under propofol administration, in particular, synchrony increments in α (8–10 Hz) and β_2 (18.5–21 Hz).

The models based on the mechanism of action of propofol acting GABA receptors [4, 5] showed that an increasing in the GABA conductance and decay time [9, 54] resulting in coherent α activity, which facilitates the involvement of the thalamus in a highly coherent thalamocortical α oscillation loop. Thus, at the cortical level,

Table 24.1 Qualitative summary of the main EEG changes by propofol. Similar to sevoflurane, desflurane and isoflurane

EEG frequency bands						
	LF	δ	α	β_1	β_2	γ
f(Hz)	(0.1–1)	(1–4)	(8–12)	(18.5–21)	(21–30)	$\geq$32
Amplitude	$\uparrow$	$\uparrow$	$\uparrow$	$\downarrow$	$\downarrow$	$\downarrow$
Coherence	–	$\uparrow$	$\uparrow$	$\downarrow$	$\uparrow$	$\downarrow$

unconsciousness under propofol is characterized by α oscillations which are strongly coherent across the frontal cortex, in addition to a substantial coherence in the δ (1–4 Hz) waves. On the other hand, propofol attenuates the coherence at other frequencies, especially at γ and β_1, in parallel with their power attenuation. Despite propofol induces high slow (0.1–1 Hz) oscillations, these are incoherent [10, 45]. Table 24.1 summarizes qualitatively the main EEG changes for propofol. Similar oscillatory coherence patterns were described for sevoflurane [3], desflurane and isoflurane, but the frequency band behaviour and range might differ slightly.

24.3 Algorithms and Monitoring Design Approaches

In the last decades, there has been intensive research and development of systems to monitor DoA. Multiple distinct approaches were followed to quantify the previously described changes of the EEG activity induced by the anaesthetic drugs. The different approaches covered a wide range of quantification methods of stochastic processes, from linear techniques in the spectral domain to non-linear techniques such as entropy measurements. In Table 24.2 are shown a list of different methods applied to the EEG signals under anaesthesia.

Despite several studies have indicated that the EEG exhibit some non-linear or chaotic behaviour under anaesthesia and physiological sleep stages [1, 12, 43, 58], still, non-linear analysis method applied to the DoA such as entropy, Hurst exponent, fractal analysis among others, have shown significant enhancement in performance respect the linear based methods. Similarly, to the research approaches, the dominant techniques implemented in the current commercial systems in clinical daily use [3] and with more extensive validation studies, are based on linear theory. In that respect, while BIS, qCON and PSI indices are based on linear methods (Bispectrum and Fourier Transform, respectively) the unique non-linear method commercially applied is the spectral entropy in the SE module, with comparable results [35], and with small differences attributable mostly to the systems artefact management [2, 42].

[3]Main commercial DoA indices: The Bispectral index **(BIS)**^{TM} (Medtronic, USA), the index of hypnosis/sedation **(qCON)** © (Fresenius Kabi, GmbH, Germany), **(PSI)** SEDLine^{TM} (Masimo, Irvine CA, USA), and State Entropy index **(SE)**® (Datex-Ohmeda, GE).

Table 24.2 EEG feature extraction algorithms under GA. Commercial DoA monitors main approach (see Footnote 3)

Methods	Commercial monitors
Spectral domains analysis	
Bispectrum [22]	**BIS**
Fourier transform [16, 18]	**qCON**, **PSI**
Time domain-algorithms	
Entropy measurements	
Approximate entropy [7, 24]	
Lempel-Ziv entropy [14, 58]	
Shannon entropy [15, 20]	
Spectral entropy [51, 53, 56]	**SE**
Chaos and long term correlation analysis	
Hurst [26]	
DFA [21]	
Fractal analysis [40]	
Time-frequency analysis	
Wavelets [34, 37]	

Independently of the methodology applied, any method, in general, summarizes the complexity of the EEG information into a continuous single value ranging in an accessible scale easy and fast to interpret. Typically, the depth of hypnosis indexes provided by different manufacturers such as BIS, qCON, PSI, are dimensionless indexes ranging continuously from 100 to 0, with values near 100 representing the "awake" state while 0 denoting isoelectric EEG. In between, different ranges correlate with important clinical endpoints. While BIS and qCON define the ranges as: [99–80]—awake state, [80–60]—light hypnotic state, [60–40]—GA, [40–20]—deep hypnotic state and [20–0]—EEG with Burst Suppression. The definition of other manufactures might differ slightly. In that respect, the SE is defined from 91 (awake) to 0 (isoelectric), and the PSI establishes the recommended GA range from 50 to 25.

The basic design scheme, shown in Fig. 24.2a, consists of an acquisition stage followed by a preprocessing and artefact rejection stage. This stage is crucial since these monitors operate in a hostile environment under very distinct types of interferences. Thus, to the common artefacts present in any EEG recording [39] such as Electromyography (EMG), eye movements and blinking, ECG, mains interference, among others, in the surgical environment a wide variety of strong interferences coming from distinct electrical medical devices and apparatus must be detected and filtered out: electrocautery, ventilators, infusion pumps, pacemakers, orthopaedic surgery drills, etc. Due to the hostility of the surgical environment and how critical is the information that a DoA monitor provides to the practitioner any depth of anaesthesia monitor must provide continuously a Signal Quality Index (SQI). The SQI measures the quality of the acquired EEG signal and usually is provided as a percentage of the number of artefacts during a fix period of time. Additionally, the

electrode-to-skin impedance is measured and included in the SQI calculation. The EMG, which also acts on the SQI, is also provided as a monitor parameter since per se since it is an indicator of potential significant biases on the DoA estimation as well as a continuous indicator of the patient muscular relaxation under neuromuscular blocking agents (NMBAs). It is worth mentioning that EMG activity measured from the EEG recording refers to the facial muscular activity which is not entirely linked to the body muscular relaxation. Following the artifact rejection and the preprocessing stage, feature extraction is performed to characterize the EEG activity. At this point any algorithm such as the ones in Table 24.2 extracts the necessary features to be integrated into an index. The BS is also quantified at this step, commonly as the percentage of time where the EEG is isoelectric, BSR. Despite the simplicity of this measure, it works nicely with the anaesthetic agents under deep anaesthesia [6, 52], and it is easy to interpret and visually inspect by the anaesthesiologists. Anaesthesiologists generally try to avoid deep anaesthesia levels, where the BSR is high, since lighter monitor-guided depth of anaesthesia level conducted to improved postoperative outcomes [8, 25, 28, 55]. Finally, the latest step integrates the extracted features into an easy and fast to interpret scale correlated with: (1) the clinical assessment, e.g. scores like the Observer Assessment of Alertness/Sedation scale (OAA/S) or Ramsay scale [32], and (2) the pharmacological information obtained from the pharmacokinetic/pharmacodynamic models (PK/PD) models.

Figure 24.2b shows the time evolution of the propofol Ce under the Schnider PK/PD model [48, 49] on a patient during GA and under remifentanil (analgesic). The panel below shows the Density Spectral Array (DSA) for the whole intraoperative procedure where it is possible to observe the characteristic effects of propofol on the EEG. A strong elicited α-band activity with a decrease of β and γ activities respect to the awake state. In lower panel, it is shown two simultaneously recorded Processed EEG (pEEG) neuromonitoring indices, BIS and qCON, lower panel. Clearly, both EEG indexes follow relatively well the Ce. The anaesthesia induction, in intravenous and volatile anaesthesia, usually is performed inducing high concentrations in a short time; a fast induction is generally more pleasant and less problematic in the hemodynamic stability. Independently of the anaesthesiologist procedure any monitor index must be fast enough to track fast changes in the patient hypnotic state. Fast inductions induce periods of BS, as it is shown in this example, with BSR reaching 32. After the induction, the common practice is to keep the patient into a stable adequate balanced anaesthesia level, until the end of the surgery.

Current example shows a novel index, qNOX® (Fresenius Kabi, GmbH, Germany) [18], linking the EEG to the patient probability of response to noxious stimulation. This index was formulated, similarly to the qCON hypnotic index with those spectral features of the EEG which integrated into a model produced the best correlation with the remifentanil Ce (analgesic) given by the Mintos' PK/PD model [33] and the response of the patients to noxious stimuli, in this case, different types of airway intubation: laryngoscopy, LMA insertion and tracheal intubation. See [18, 19] for more details.

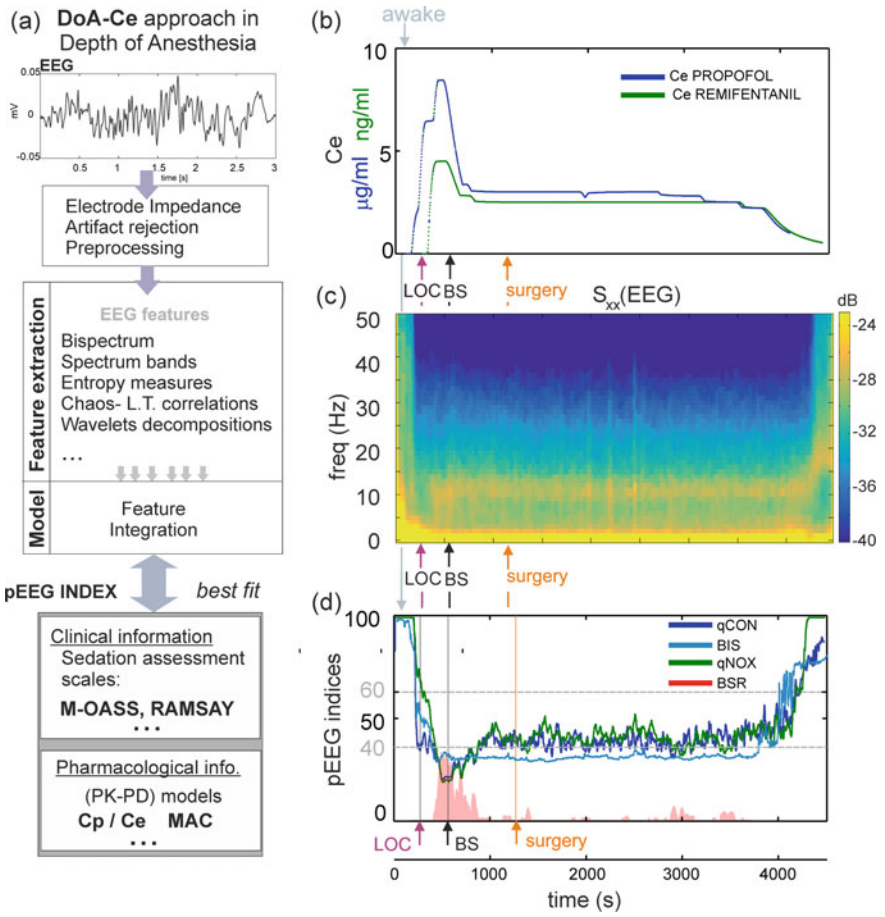

Fig. 24.2 **a** Flow diagram procedure of DoA monitors. General scheme approach to estimate the patient's depth of anaesthesia level. **b** Example of the time evolution of anaesthetic drugs Ce for a patient during an intraoperative procedure with propofol and remifentanil. **c** Density Spectral Array (DSA) for the whole intraoperative procedure, representing the power spectral density every second. **d** Time evolution of two pEEG derived indices for sedation, BIS and qCON, the BSR and a probability of response to noxious stimulation index qNOX. LOC—Loss of consciousness

24.4 Depth of Anaesthesia Monitoring Validation

There are several methodologies to validate any DoA index. Without considering technical aspects between different definitions and implementations, one of the validations rely on the correlation between the index and the hypnotic drug Ce. Figure 24.3a, shows the relation between the qCON index and the propofol Ce concentration for n = 660 patients in gynecologic surgery who underwent intravenous anesthesia with remifentanil, giving a high Prediction probability (Pk) value of 0.825

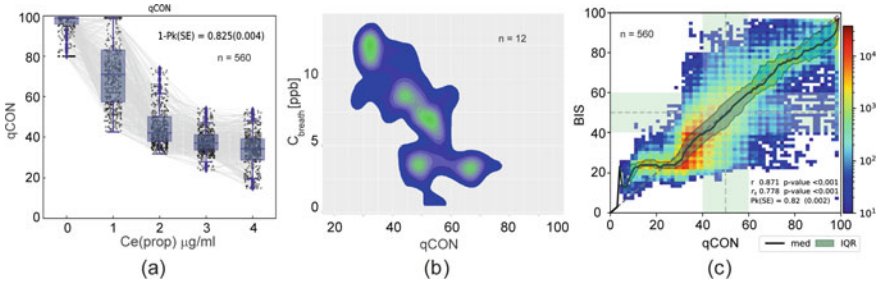

Fig. 24.3 **a** Correlation of the qCON index with the propofol Ce concentration provided by the PK/PD model (n = 560 patients). **b** qCON index vs. the expired propofol (ppb-parts per billion) (n = 12 patients) (unpublished data). **c** Scatter plot between two DoA indices, BIS and qCON.

(0.004, $p < 0.001$). A novel complementary evaluation of the Ce concentration can be obtained by measuring the expired concentration of propofol (Cbreath), measured in parts per billion (ppb). Preliminary results for n = 12 patients showed also a high correlation between this index, Fig. 24.3b, Spearman corr. Rs = −0.69 ($p < 0.001$). The latter data was collected during a TIVA with propofol and remifentanil in elective routine surgery. Accordingly, other studies have confirmed a good agreement between other indexes such as BIS with the propofol Ce [13, 47]. Despite some differences among the monitors [2, 42], in general, the available processed EEG monitors show strong similarities [35] in the assessment of the hypnotic patient's state. The fact that different approaches have similar performances can be thought as another indicator that these methods are approaching to the desired estimation with all limitations of this statement, since, unfortunately, there is no gold standard. Considerable differences in the performances, without a gold standard, would put directly under doubt any approach. The agreement across different indices, such as BIS and qCON can be evaluated under a correlation measurement. Figure 24.3c shows a scatter plot between the two indexes for a large dataset of patients (n = 560). Both exhibit high correlations values measured with the prediction probability (Pk) and the Spearman correlation (r_s). Other similar analysis with different datasets and surgeries showed comparable results between BIS and qCON, for instance, $r_s = 0.89$ [35] or Pk = 0.92 [18].

Especially for the commercial systems, which are used constantly in the daily practice, there is an extensive evaluation of their performance at different surgical conditions and different anaesthesiology procedures and drug combinations. However, despite the good performances, there are other situations where these technologies need to be enhanced with new knowledge of the brain behaviour under GA.

24.5 Advantages and Challenges in Depth of Anaesthesia Monitoring

The DoA monitoring is a relatively recent technology in constant development, updating to the newer research findings in neuroscience, pharmacology and anaesthesiology. The main advantages of these technologies are: (1) Reduction the incidence of AWR [11, 31, 36, 57]. (2) Tailoring the anaesthetic agents to the present patient's condition and surgical context, optimizing drug consumption [46, 50], attenuating potential adverse effects from overdose and facilitating faster recovery [17, 27]. (3) Potential reduction of anaesthetic exposure decreasing the risk of postoperative delirium and cognitive declines [8]. Yet, the limitations of processed EEG monitoring come basically from the lack of complete knowledge of all the complex mechanisms involved during the anaesthesia procedure, and the lack of a gold standard. Some of the current challenges in the depth of anaesthesia monitoring are: (1) Attenuation of the electromyographic (EMG) interference activity present in all EEG recordings. (2) Enhancement of the discrimination between the different components of the balanced anaesthesia: the hypnosis, the analgesia and the areflexia as well as the interaction between their different associated drugs. (3) Currently, there is no reliable solution to deal with ketamine , and some volatile agents as the nitrous oxide and halothane among others. (4) Development of robust closed-loop control system to titrate the anaesthetics, to continuously optimize automatically the drug-delivering according to the patient's context.

24.6 Conclusions

In this chapter, we introduced the basic changes and patterns of the EEG oscillations induced by anaesthetics. Due to the complexity of the EEG oscillations, their characterization followed multiple distinct perspectives, from linear system theory to non-linear methods. Despite there is no gold standard on the estimation of the patient state, the different perspectives point to similar estimations. Independently of the taken approach any EEG based DoA index must agree with the pharmacological and clinical assessment information. Processed EEG, for DoA monitoring, is a multidisciplinary field in constant research and development for newer methods to support for preventing AWR episodes and reduce other adverse effects such as postoperative cognitive declines in elderly and new-borns.

References

1. U.R. Acharya et al., Non-linear analysis of EEG signals at various sleep stages. Comput. Methods Programs Biomed. **80**(1) (2005)
2. A.J. Aho et al., Comparison of Bispectral Index and Entropy values with electroencephalogram during surgical anaesthesia with sevoflurane. BJA **115**(2) (2015)
3. O. Akeju et al., Effects of sevoflurane and propofol on frontal electroencephalogram power and coherence. Anesthesiology **121**(5) (2014)
4. M.T. Alkire, A.G. Hudetz, G. Tononi., Consciousness and anesthesia. Science **322**(5903) (2008)
5. E.N. Brown, R. Lydic, N.D. Schiff., General anesthesia, sleep, and coma. N Engl. J. Med. **363**(27) (2010)
6. J. Bruhn et al., Electroencephalogram approximate entropy correctly classifies the occurrence of burst suppression pattern as increasing anesthetic drug effect. Anesthesiology **93**(4) (2000)
7. J. Bruhn et al., Shannon entropy applied to the measurement of the electroencephalographic effects of desflurane. Anesthesiology **95**(1) (2001)
8. M.T. Chan et al., BIS-guided anesthesia decreases postoperative delirium and cognitive decline. J. Neurosurg. Anesthesiol. **25**(1) (2013)
9. S. Ching et al., Thalamocortical model for a propofol-induced alpha-rhythm associated with loss of consciousness. PNAS **107**(52) (2010)
10. A. Cimenser et al., Tracking brain states under general anesthesia by using global coherence analysis. PNAS **108**(21) (2011)
11. A. Ekman et al., Reduction in the incidence of awareness using BIS monitoring. Acta Anaesthesiol. Scand. **48**(1) (2004)
12. T. Elbert et al., Chaos and physiology: deterministic chaos in excitable cell assemblies. Physiol. Rev. **74**(1) (1994)
13. R.K. Ellerkmann et al., The correlation of the bispectral index with propofol effect site concentrations is not altered by epochs indicated as artefact-loaded by narcotrend. J. Clin. Monit. Comput. **18**(4) (2004)
14. J. Fell et al., Discrimination of sleep stages: a comparison between spectral and nonlinear EEG measures. Electroencephalogr. Clin. Neurophysiol. **98**(5) (1996)
15. R. Ferenets et al., Comparison of entropy and complexity measures for the assessment of depth of sedation. IEEE Trans. Biomed. Eng. **53**(6) (2006)
16. P.L. Gambús et al., Modeling the effect of propofol and remifentanil combinations for sedation-analgesia in endoscopic procedures using an Adaptive Neuro Fuzzy Inference System (ANFIS). Anesthesia & Analgesia **112**(2) (2011)
17. T.J. Gan et al., Bispectral index monitoring allows faster emergence and improved recovery from propofol, alfentanil, and nitrous oxide anesthesia. BIS Utility Study Group. Anesthesiology **87**(4) (1997)
18. E.W. Jensen et al., Monitoring hypnotic effect and nociception with two EEG-derived indices, qCON and qNOX, during general anaesthesia. Acta Anaesthesiol. Scand. **58**(8) (2014)
19. E.W. Jensen et al., Validation of the qNOX Pain/Nociception Index for monitoring loss of response to tetanic stimulation during general anaesthesia. Anesthesiology **119** (2013)
20. D. Jordan et al., EEG parameters and their combination as indicators of depth of anaesthesia. Biomed. Tech. (Berl) **51**(2) (2006)
21. M. Jospin et al., Detrended fluctuation analysis of EEG as a measure of depth of anesthesia. IEEE Trans. Biomed. Eng. **54**(5) (2007)
22. L.A. Kearse et al., Bispectral analysis of the electroencephalogram during induction of anesthesia may predict hemodynamic responses to laryngoscopy and intubation. Electroencephalogr. Clin. Neurophysiol. **90**(3) (1994)
23. T. Kirschstein, R. Kohling, What is the source of the EEG? Clin. EEG Neurosci. **40**(3) (2009)
24. M. Koskinen et al., Monotonicity of approximate entropy during transition from awareness to unresponsiveness due to propofol anesthetic induction. IEEE Trans. Biomed. Eng. **53**(4) (2006)

25. S.R. Lewis et al., Bispectral index for improving intraoperative awareness and early postoperative recovery in adults. Cochrane Database Syst. Rev. **9** (Sept. 2019)
26. Z. Liang et al., Multiscale rescaled range analysis of EEG recordings in sevoflurane anesthesia. Clin. Neurophysiol. **123**(4) (2012)
27. M. Luginbuhl et al., Different benefit of bispectal index (BIS) in desflurane and propofol anesthesia. Acta Anaesthesiol. Scand. **47**(2) (2003)
28. C. Luo, W. Zou, Cerebral monitoring of anaesthesia on reducing cognitive dysfunction and postoperative delirium: a systematic review. J. Int. Med. Res. **46**(10) (2018)
29. L.P. Malver et al., Electroencephalography and analgesics. Br. J. Clin. Pharmacol. **77** (1 Jan 2014)
30. P. Martinez-Vazquez et al., *Taking on TIVA: Debunking Myths and Dispelling Misunderstandings* (Cambridge University press, 2020) (Chapter 9). ISBN: 1316609367
31. G.A. Mashour et al., Prevention of intraoperative awareness with explicit recall in an unselected surgical population: a randomized comparative effectiveness trial. Anesthesiology **117**(4) (2012)
32. R.D. Miller, *Miller's Anesthesia*, 7th edn. (Churchill Livingstone: Elsevier, Philadelphia, PA, 2015)
33. C.F. Minto et al., Influence of age and gender on the pharmacokinetics and pharmacodynamics of remifentanil. I. Model development. Anesthesiology **86**(1) (1997)
34. S.M. Mousavi et al., A wavelet transform based method to determine depth of anesthesia to prevent awareness during general anesthesia. Comput. Math Methods Med. (2014)
35. J.N. Muller et al., Monitoring depth of sedation: evaluating the agreement between the Bispectral Index, qCON and the Entropy Module's State Entropy during flexible bronchoscopy. Minerva. Anestesiol. **83**(6) (2017)
36. P.S. Myles et al., Bispectral index monitoring to prevent awareness during anaesthesia: the B-Aware randomised controlled trial. Lancet **363**(9423) (2004)
37. T. Nguyen-Ky et al., Measuring and reflecting depth of anesthesia using wavelet and power spectral density. IEEE Trans. Inf. Technol. Biomed. **15**(4) (2011)
38. N. Nicolaou et al., EEG-based automatic classification of 'awake' versus 'anesthetized' state in general anesthesia using Granger causality. PLoS One **7**(3) (2012)
39. E. Niedermeyer, F.L. da Silva, *Electroencephalography: Basic Principles, Clinical Applications, and Related Fields*, 5th edn (LippincottWilliams & Wilkins, 2005). ISBN: 0781751268
40. E. Olejarczyk, R. Stepien, P. Jalowiecki, W. Klonowski, R. Rudner, Monitoring the depth of anaesthesia using fractal complexity method. Complex. Mundi. Emerg. Pattern. Nat. **116** (2006)
41. A. Papoulis, S.U. Pillai, *Probability, Random Variables, and Stochastic Processes*, 4th edn. (McGraw Hill, Boston, 2002). ISBN: 0-07-366011-6
42. S. Pilge et al., Differences between state entropy and bispectral index during analysis of identical electroencephalogram signals: a comparison with two randomised anaesthetic techniques. Eur. J. Anaesthesiol. **32** (2015)
43. W.S. Pritchard, D.W. Duke, K.K. Krieble., Dimensional analysis of resting human EEG. II: Surrogate-data testing indicates nonlinearity but not low-dimensional chaos. Psychophysiology **32**(5) (1995)
44. Y. Punjasawadwong, A. Phongchiewboon, N. Bunchungmongkol, Bispectral index for improving anaesthetic delivery and postoperative recovery. Cochrane Database Syst. Rev. **6** (2014)
45. P.L. Purdon et al., Electroencephalogram signatures of loss and recovery of consciousness from propofol. PNAS **110**(12) (2013)
46. W. Riad, M. Schreiber, A.B. Saeed., Monitoring with EEG entropy decreases propofol requirement and maintains cardiovascular stability during induction of anaesthesia in elderly patients. Eur. J. Anaesthesiol. **24**(8) (2007)
47. A. Rigouzzo et al., The relationship between bispectral index and propofol during target-controlled infusion anesthesia: a comparative study between children and young adults. Anesth. Analg. **106**(4) (2008)

48. T.W. Schnider et al., The influence of age on propofol pharmacodynamics. Anesthesiology **90**(6) (1999)
49. T.W. Schnider et al., The influence of method of administration and covariates on the pharmacokinetics of propofol in adult volunteers. Anesthesiology **88**(5) (1998)
50. A. Vakkuri et al., Spectral entropy monitoring is associated with reduced propofol use and faster emergence in propofol-nitrous oxide-alfentanil anesthesia. Anesthesiology **103**(2) (2005)
51. A. Vakkuri et al., Time-frequency balanced spectral entropy as a measure of anesthetic drug effect in central nervous system during sevoflurane, propofol, and thiopental anesthesia. Acta Anaesthesiol. Scand. **48**(2) (2004)
52. P.L. van den Broek et al., An effective correlation dimension and burst suppression ratio of the EEG in rat. Correlation with sevoflurane induced anaesthetic depth. Eur. J. Anaesthesiol. **23**(5) (2006)
53. H. Viertio-Oja et al., Description of the Entropy algorithm as applied in the Datex-Ohmeda S/5 Entropy Module. Acta Anaesthesiol. Scand. **48**(2) (2004)
54. S. Vijayan et al., Thalamocortical mechanisms for the anteriorization of alpha rhythms during propofol-induced unconsciousness. J. Neurosci. **33**(27) (2013)
55. E.L. Whitlock et al., Postoperative delirium in a substudy of cardiothoracic surgical patients in the BAG-RECALL clinical trial. Anesth. Analg. **118**(4) (2014)
56. A. Yli-Hankala et al., EEG bispectral index monitoring in sevoflurane or propofol anaesthesia: analysis of direct costs and immediate recovery. Acta Anaesthesiol. Scand. **43**(5) (1999)
57. C. Zhang et al., Bispectral index monitoring prevent awareness during total intravenous anesthesia: a prospective, randomized, double-blinded, multicenter controlled trial. Chin. Med. J. Engl. **124**(22) (2011)
58. X.S. Zhang, R.J. Roy, E.W. Jensen., EEG complexity as a measure of depth of anesthesia for patients. IEEE Trans. Biomed. Eng. **48**(12) (2001)

Chapter 25
Medical Products Inspired by Biological Oscillators: Intermittent Pneumatic Compression and the Microcirculation

Clare Thorn and Angela Shore

Abstract To sustain life oxygen must be transported from the lungs to the heart and then out to the trillions of cells that make up the human body. This process is dependent upon many oscillatory systems that exquisitely respond to the fluctuating needs of each cell. The interplay between these systems that oscillate between an active and passive state provides the unique balance of a healthy life. To circulate blood to each cell in the body there is an intricate network of vessels. Blood leaves the heart through a ~2 cm diameter aorta and branches down to <10 μm capillaries at a cellular level before returning to the heart through the venae cavae. In these non-rigid vessels haemodynamic regulation is controlled by complex oscillatory systems that determine the resistance of vessels and therefore the local blood flow. These mechanisms are also supported by the presence of valves that ensure venous return and cyclical muscle pumps such as in the foot and calf that aid the circulation whilst walking. However, inadequate circulation can arise from the narrowing of vessels such as atherosclerosis, diseases such diabetes, incompetent valves and lack of mobility. This chapter reviews how medical products have been developed to enhance circulation including microcirculation, through the external application of intermittent pneumatic compression.

25.1 The Microcirculation

25.1.1 Overview

Many medical products have been developed to support the cardiovascular system when our innate biological oscillatory system fails. When the heart is incapable of sustaining these oscillations a pacemaker can be fitted. When these systems are

C. Thorn (✉) · A. Shore
Institute of Biomedical and Clinical Science, University of Exeter Medical School, Exeter, UK
e-mail: c.e.thorn@exeter.ac.uk

A. Stefanovska and P. V. E. McClintock (eds.), *Physics of Biological Oscillators*, Understanding Complex Systems,
https://doi.org/10.1007/978-3-030-59805-1_25

temporarily suppressed such as under anaesthesia then a ventilator can be implemented. These medical products are systems that can substitute or support these innate fluctuations of life. Here we look at the effects of a particular medical product, intermittent pneumatic compression and its effect on microcirculation.

The viability of all biological tissue is dependent upon dynamic changes in the delivery of nutrients and removal of metabolic waste products through the microcirculation, both to maintain homeostasis and meet fluctuating needs. Albert Szent-Györgyi (Nobel Prize, Physiology or Medicine, 1937) succinctly states "Life is nothing but an electron looking for a place to rest". To sustain life in any aerobic systems undergoing respiration such as in man, electrons pass through an electron transport chain and the final electron acceptor is oxygen. Therefore to sustain life at a cellular level, the transport of oxygenated blood from the heart to trillions of cells in the body is achieved through an exquisite complex system of microscopic blood vessels known as the microcirculation.

A resin cast of horse skin microcirculation in Fig. 25.1 demonstrates vessels of sizes less than 50 μm in diameter, less than the size of a human hair. In theory, blood needs to be transported to within 100 μm of every living cell in the body as this is the limit of diffusional transport of oxygen in tissue, beyond which necrosis can occur (Franko and Sutherland 1979). Convective transport of blood is therefore required for distances greater than 100 μm and this is provided by this microcirculation of arterioles, capillaries and venules. These microscopic vessels are not only conduit vessels but also play an integral role in the control systems that ensures adequate delivery of oxygen to tissue to match fluctuating oxygen demands. This is achieved through spontaneous local oscillations in the smooth muscle tone of blood vessels known as vasomotion [50] and readers are referred to Part 3 Biological Oscillators for a more detailed description.

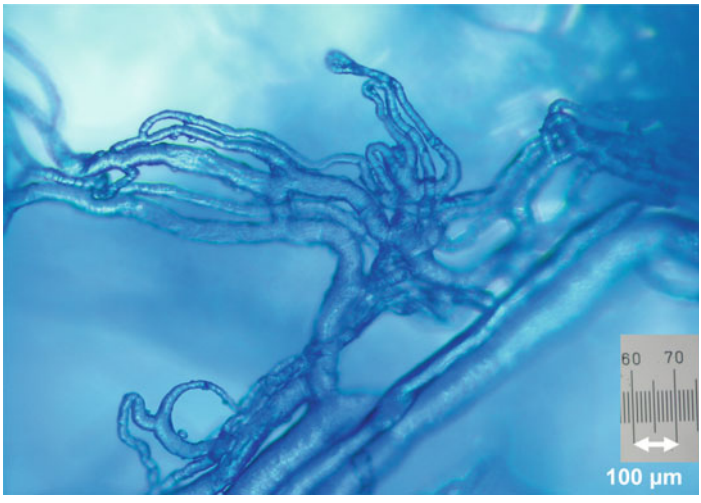

Fig. 25.1 Resin cast of the microcirculation of horse skin

25.1.2 Structure and Function of the Microcirculation

An understanding of in vivo microcirculation in man has predominantly been derived using non-invasive optical techniques to study both the structure and function of these vessels [25]. Skin is surprising transparent to visible light and provides access to ~1.7 m^2 of microcirculation that lies just below an avascular surface of stratum corneum and epidermis. Unfortunately light attenuation in Caucasian skin is dominated by scattering rather than absorption (transport scattering coefficient $\mu_s^{'} = 2.73 \pm 0.54$ mm^{-1} versus absorption coefficient $\mu_a = 0.033 \pm 0.009$ mm^{-1} at 633 nm) thus hindering the direct visualisation of all vessels in the microcirculation. The skin microcirculation consists of a mesh of vessels <300 μm predominantly laid out as two parallel horizontal plexi. Due to the high scattering of light in skin these plexi cannot be visualised directly. However, there are capillary loops rising perpendicular to the surface from the superficial plexus that can be observed simply using a microscope and a camera or video recorder. These capillary loops supply oxygen and nutrients to the avascular epidermis. As can be seen in Fig. 25.2a only the tips of the capillary loops are visualised in the majority of skin and quantitative measures are predominantly confined to capillary density, this being the number of capillary tips in one square millimetre. An exceptional site is at the nailfold on fingers and toes where these capillaries run parallel to the skin surface Fig. 25.2b. In visualising these nailfold capillaries over time it is possible to study the haemodynamics of red blood cells as they travel through these smallest vessels, demonstrating the continuous fluctuations in blood flow induced by vasomotion. Similarly, there are a few uniquely accessible sites in the body such as sublingual tissue in the mouth (Fig. 25.2c) and the retina of the eye where there is a thin epithelial layer covering the microcirculation and images of arterioles and venules can be obtained directly by light microscopy [68]. A measure of capillary density changes in chronic venous insufficiency has also been made by imaging the "*visual*" capillaries that come into focus in supra-malleolar skin 5 cm proximal to the medial malleolus [33].

Access to the microcirculation of deeper tissues including muscle can be achieved using longer wavelengths of light such a near infrared. With a reduced transport scattering coefficient $\mu_s^{'} = 1.63$ mm^{-1} at 900 nm compared to $\mu_s^{'} = 2.73$ mm^{-1} at 633 nm [66] it is possible for near infrared light to penetrate up to ~6 cm of tissue. Techniques such as laser Doppler fluximetry (LDF) and near infrared spectroscopy at these longer wavelengths cannot produce images but can interrogate the haemodynamics of microcirculation in deeper tissues even with high melanin concentrations [2] and can derive a measure of the oxygen content of the blood in the microcirculation [3].

25.2 Endogenous Vascular Oscillators

With advances in optical techniques and digital imaging it is now possible to undertake non-invasive, in vivo research in man to study both the dynamic changes in the

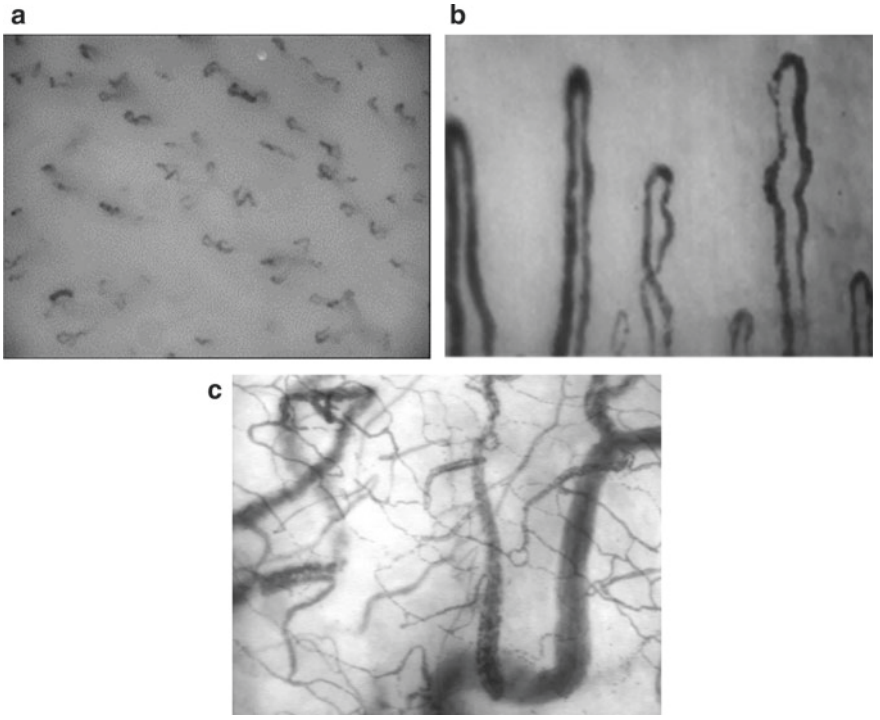

Fig. 25.2 **a** Video image of dorsal finger skin showing capillary tips (Microscan, MicroVision Medical, Amsterdam). **b** Video image of skin nailfold capillaries that run parallel to skin surface (CapiScope HVCS, KKTechnology, UK). **c** Video image of the sublingual microcirculation in mouth where thin epithelial layer enables the visualisation of arterioles, capillaries and venules (Microscan, MicroVision Medical, Amsterdam)

diameters of blood vessels and the effects, in the microcirculation. Oscillations in intrinsic vascular tone are observed as a change in vessel diameter and is known as vasomotion whilst oscillations in blood flow (flowmotion) result from many mechanisms including vasomotion. For a current overview of the specific mechanisms involved in vasomotion readers are directed to review articles [15, 1] and Part 3 Biological Oscillators. Historically, vasomotion has been studied in vitro with techniques such as myography but with the development of new optical techniques it is now possible to monitor both the anatomy and physiology of the microcirculation in situ.

The regulation of blood flow to organs is primarily driven by a need to maintain a rapid transport of nutrients to the tissues and washout of metabolic waste products. In a living system, the regulation of a variable is maintained through a dynamic balance between activation and deactivation—a basic principle of an oscillator [71]. This is predominantly achieved by the dilation and constriction of blood vessels thus altering their resistance. From the structure of the vascular walls it can be seen that this can be mediated through either a neurogenic, myogenic or

endothelial response. The local control of vascular resistance is primarily achieved through vascular smooth muscle activity changing the arteriolar diameter to regulate local blood flow, arterial pressure and capillary filtration. However, vascular resistance may also be altered through vascular smooth muscle activity in venules and the potential dilate of capillaries by actively relaxing pericytes [31]. The dynamic interaction of pressure-dependent vasoconstriction, flow-dependent endothelium-mediated vasodilation, metabolic vasodilation and spontaneous myogenic activity acting on basal vascular tone produces local changes in blood volume and blood flow. Oscillations can be observed as fluctuations in blood volume, blood flux (flowmotion) and oxygenation in microcirculation when studied with optical techniques such as laser Doppler fluximetry and reflectance spectroscopy. It is hypothesised that these oscillations are generated at different frequencies depending upon the regulatory control mechanism. In quantifying the amplitude and proportion of these oscillations by Fourier and wavelet analysis it is believed that it is possible to monitor the changes in myogenic, neurogenic and endothelial activity regulating blood flow and oxygen delivery. Pioneering work by Stefanovska using LDF in forearm skin has revealed five characteristic frequencies of oscillation in blood flux in microcirculation at around 1 Hz (heart rate), 0.3 Hz (respiration), 0.1 Hz (myogenic activity), 0.04 Hz (sympathetic activity) and 0.01 Hz (endothelial activity) [12–39].

Why vasomotion occurs is still very much a matter of debate but it has been suggested that vasomotion is beneficial for tissue oxygenation [50, 15–73]. Tissue oxygenation can be improved by increasing the surface area available for exchange i.e. capillary recruitment or by optimising oxygen delivery. How vasomotion might ensure adequate oxygen delivery to all tissues has come primarily from theoretical modelling [75, 30, 37]. These models suggest that pO_2 transients caused by vasomotion can oxygenate tissue domains which under steady-state conditions would remain anoxic [75]. Therefore vasomotion appears to play a role in improving oxygen perfusion especially to hypoxic tissue. It has been shown that ischaemia elicits an amplification of skin blood flow oscillations besides an increment of skin perfusion [57, 58].

25.3 Medical Products Inducing Oscillations Through Intermittent Impulse Compression

For over two hundred years external applied pressure systems have been wrapped around limbs with the aim of improving the circulation of blood. A historical review of these methods designed to improve peripheral blood flow can be found in *The Venous System in Health and Disease* by A.M.N. Gardner and R.H. Fox (IOS Press, The Netherlands, 2001). In the past, compression bandages and hosiery have been the most effective tool to treat impaired blood flow due to venous insufficiency. These techniques continue to provide clinical benefits in conditions such as venous hypertension and chronic venous insufficiency [24] and have been found to improve ulcer

healing rates [9, 43]. There is good evidence that compression bandages and hosiery heal more ulcers compared with no compression [44, 51] and evidence from one trial that compression hosiery reduces rates of re-ulceration of venous ulcers compared with no compression [45]. The first pneumatic devices appeared around the end of the 19th century automating the uniform, sequential or graded sequential compression to the limbs provided by compression bandaging. Intermittent pneumatic compression has found clinical application in the management of advanced chronic venous disease, specifically venous ulceration [46], lymphedema [63], and the prevention of deep vein thrombosis [62]. IPC devices consist of an electrical pneumatic pump that inflates a cuff around the foot/hand or calf/thigh, compressing the deep veins and improving venous return to the heart. Upon cuff deflation the veins refill with arterial blood assuming that the venous valves are competent. External compression to the peripheral circulation displaces blood proximally increasing arteriovenous pressure gradient [22], however *intermittent* pneumatic compression also augments vascular homeostasis [7] through the perturbation of blood flow, which stimulates the release of endothelium-derived vasoregulatory signals [35]. A schematic diagram of the setup for intermittent impulse compression to the hand can be seen in Fig. 25.3 including methods to measure its effect on skin microcirculation. Interestingly in a clinical study, IPC has been shown to restore vasomotion in skin [54].

The benefits of an oscillatory compression system in the peripheral circulation was first highlighted by Gardner and Fox who identified a venous foot pump that enhanced venous return from the plantar venous plexus by the rhythmic motion of walking [27, 28]. IPC mimics these physiological fluctuations through cyclical pneumatic mechanical compression, to the limb or venous plexus of the hand or foot, from a fast inflating cuff at frequencies around 0.03–0.05 Hz (2–3 cycles per

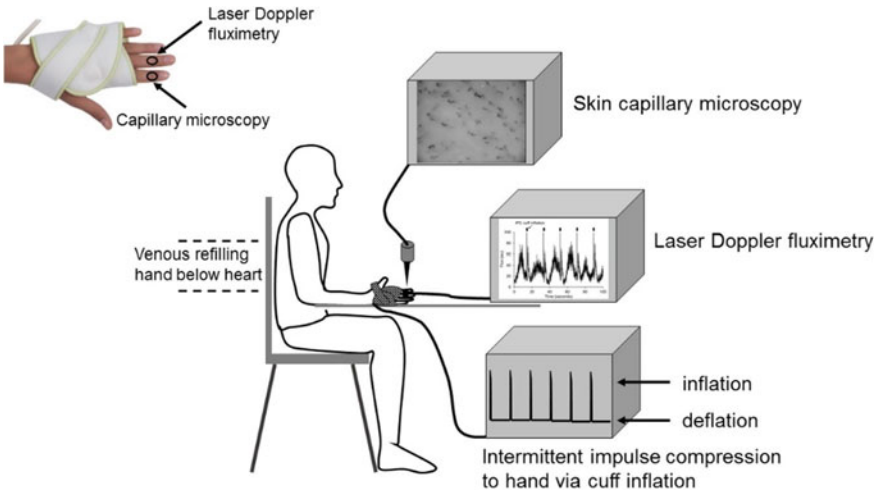

Fig. 25.3 Setup for intermittent impulse compression to the hand via fast intermittent cuff inflation to the palm with methods to measure its effect on finger skin microcirculation

minute). Although blood is indeed displaced proximally it is the oscillatory nature of IPC inducing intermittent fluctuations in shear stress to the endothelium that is now thought to induce further clinical benefits [48].

Human studies on the physiological effects of IPC on circulation have predominantly focused on large vessels such as the popliteal artery [22, 39–40] and vein [23] in the leg and brachial artery in the arm [56]. Scanning and Doppler ultrasound are non-invasive techniques that are frequently used to provide measures of large vessel diameter, blood flow, velocity and also to provide an indirect measure of shear rate on the vascular endothelium [64, 5], a useful approximation of shear stress that does not account for blood viscosity. In these large vessels it has been shown that IPC induces periods of increased arterial inflow [64, 40] and enhanced venous outflow [23] that have been attributed to both mechanical effects and enhanced shear stress [64, 10]. In summary, IPC intermittently compresses deep compliant veins facilitating venous emptying by accelerating blood forward, distending that section of the vessel. As the vessel wall stretches strain occurs in the vascular endothelium with the change in diameter [10]. Using haemodynamic modelling of flow in a flexible tube, Dai concluded that an external pressure of 50 mmHg would induce strains at the vessel lumen border of approximately 20% [19]. In turn, the increase in arterial-venous pressure gradient significantly increases arterial inflow and hence shear stress to the vascular endothelium [8]. It is the consequences of these *changes* in strain and shear stress to the vascular endothelium induced by IPC that are thought to provide many of the observed clinical benefits. It is now recognised that the cyclical compression of IPC increases the shear and compressive strain on the vascular endothelial cells resulting in the release of biochemical vasoactive mediators [10]. For many decades compression strain to vessels in the limbs has been associated with a reduction in the incidence of deep vein thrombosis (DVT) and pulmonary embolism indicative of the release of anti-thrombotic, pro-fibrinolytic agents [45–17]. The induction of vasodilation by shear stress on vascular endothelial cells has been well documented. In vitro cell culture systems have demonstrated a rapid release of nitric oxide in response to shear stress induced by both compression and pulsatile flow [20]. In animal studies IPC increased the expression of endothelial nitric oxide synthase (eNOS), inhibiting smooth muscle cells contraction and inducing vasodilation [50–11]. In a rat model IPC has also been shown to upregulate VEGF mRNA in skeletal muscle but only at a higher frequency of compressions (2 s on/2 s off) and seemingly independent of compression pressure [55]. It can therefore be seen that to optimise the clinical benefits of IPC it is important to consider the parameters that influence venous emptying, arterial inflow and the shear and strain induced in the vascular endothelium. Although the mechanistic effects of IPC have been studied and clinical benefits reported widely, single sessions of IPC have not be shown to impact vascular function [64].

Commercial IPC devices have been developed using a wide range of not only compression pressures but also varying compression cycles (Table 25.1). Readers are directed to literature reviews on the comparative effectiveness of these devices [53, 79].

The number of pneumatic compressions per minute has predominantly been determined by the need for adequate venous refilling time following compression [29]

Table 25.1 Commercial Intermittent Impulse Compression devices and compression parameters

Intermittent pneumatic compression device	Inflation type and pressure (mmHg)	Inflation time (s)	Compression duration (s)	Cycles per minute
VADOplex Oped	130 foot constant 60–200	<0.4	1	3
VenaFlow® Aircast DJO Global	52/45 calf distal/proximal	<0.5	6	1
A-V Impulse™ Foot Compression **Cardinal**Health™	60–200 constant	rapid	1–3	3
Kendell SCD 700 Covidien **Cardinal**Health™	130 foot constant 30-45 leg sequential	–	5 11	1–3 Vascular refill detection
Flowtron® Huntleigh	130 foot constant 30-60 calf/thigh constant	– –	3 12	2 1
VasoPress® Zimmer Biomet	80 foot constant 40 calf constant	–	12	1

and is most often set at 1–3 cycles per minute or every 20–60 s. These frequencies occur in vasomotion and encompass vascular oscillations considered to be induced by endothelial and neurogenic activity. Sheldon compared IPC cycles of 3 and 12 per minute and during the first 5 minutes of IPC for both protocols there was a twofold increase in mean popliteal artery blood flow. However after 45 minutes of IPC blood flow fell significant during the deflation period at the higher inflation frequency of 12 cycles per minute [64]. This would suggest inadequate time for venous refilling. However, it is noteworthy that refilling of coronary vessels during the cardiac cycle occurs in less than a second and in a similar timeframe deep veins in the leg refill during walking. The rate of cuff inflation with IPC devices also affects the enhanced blood flow and subsequent shear stress and strain on the vascular endothelium. This has led to the term intermittent *impulse* compression instead of intermittent pneumatic compression. IPC systems can be adapted to change both the rate and amplitude of cuff inflation pressure. It has been shown that optimal venous emptying by IPC from the lower limb occurs with a higher applied pressure (120–140 vs 60–100 mmHg) and a higher frequency (3–4 vs 2 impulses per minute) [21]. Intermittent pneumatic compression with a cuff inflation of 0.5 s has been shown to heal more venous leg ulcers in 6 months of IPC then with a cuff inflation over 60 s [49]. This is consistent with findings that during IPC of rat cremaster muscle, vasodilation is only induced with inflation rates of 0.5 s but not 10 s, independent of peak pressure [41]. However there has been no systematic review of the many complex physiological mechanism activated by IPC that contribute to these known clinical benefits. Although IPC devices differ in practical features and in effects on physiology, current evidence does not show a clear difference in effects on clinically important outcomes [52].

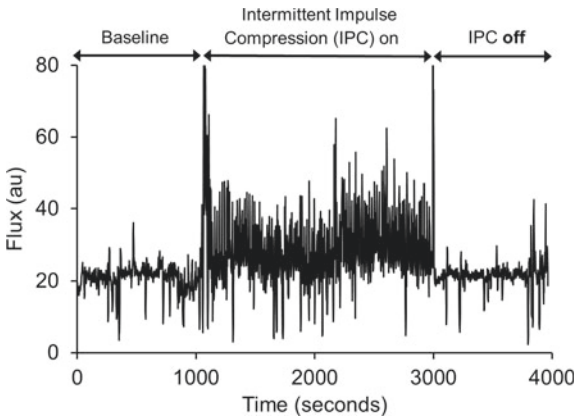

Fig. 25.4 Effect of 30 minutes of intermittent impulse compression applied to the palm of the hand on the blood flux in dorsal finger skin as measured by laser Doppler fluximetry (data collected at 0.5 Hz)

Research on the effects of IPC at a microcirculatory level has been limited by available technology. In skin, laser Doppler fluximetry is an excellent non-invasive tool for studying the microvascular haemodynamic changes that arise from IPC and significant increases in skin flux at the microcirculatory level have been observed [40, 74, 4]. Examples of the effect of 30 minutes of IPC to the palm of the hand on blood flux in dorsal finger skin are shown in Figs. 25.4 and 25.5 (authors' unpublished data).

The combination of LDF along with spectroscopic techniques has identified an increase in the oxygenation status of the enhanced microcirculatory blood flow induced by IPC indicating enhanced arterial inflow in the microcirculation [74]. This

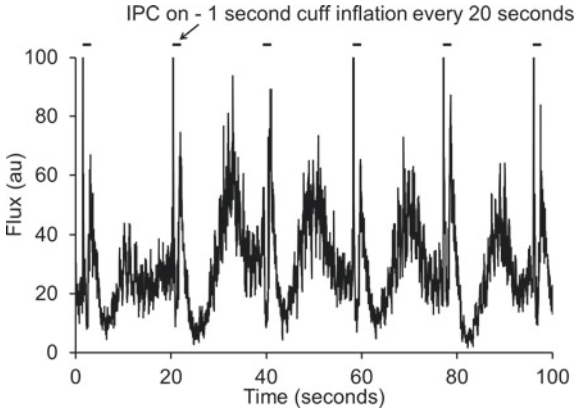

Fig. 25.5 Cyclical changes in flux induced in dorsal finger skin microcirculation during intermittent impulse compression with a cuff inflation of 3 cycles per minute (data collected at 40 Hz). Cuff was inflated to 130 mmHg in <0.5 s and held for 1 s before deflation. A temporary surge in flux can be seen upon each cuff inflation due to mechanical compression followed by a steady increase of flux indicative of vasodilation in response to shear stress [74]

is in agreement with the findings of a study where transcutaneous oxygen tension was monitored at the skin surface during IPC and the partial pressure of oxygen in the skin was shown to significantly increase [4]. Furthermore the enhanced blood flow induced by IPC has also been observed by capillaroscopy to increase the capillary density in the skin [74]. Research on the effects of IPC on skeletal muscle perfusion shows some similarities with the well-known exercise induced hyperaemia observed following a single muscle contraction [42, 14]. Contract-induced rapid onset vasodilation results from a rapid increase in blood flow within the first second attributed to an acute mechanical effect of muscle contraction (muscle pump) followed by an additional active dilatation of resistance vessels [65, 76] induced by vasoactive metabolites released from contracting fibres [67–18] and the vascular endothelium [18]. Endothelial signalling pathways induce upstream vasodilation in feed arteries known as conducted vasodilation [67]. The relative contribution of the muscle pump versus interstitial or endothelial vasodilators to this contract-induced vasodilation is still a matter of debate. In studies in rat muscle IPC has been shown to increase the production of endothelial vasodilator nitric oxide [72, 11]. The upregulation of eNOS mRNA not only occurred in compressed muscle but also in adjacent uncompressed muscle and it is suggested that this is induced by IPC-mediated shear stress. The upregulation of VEGF mRNA in rat skeletal muscle by IPC suggests it may also encourage new vessel growth and improved perfusion. Single impulse cuff inflation to 200 mmHg to the forearm muscle has also been shown to evoke vasodilation in the muscle bed increasing the forearm vascular compliance [36].

Intermittent pneumatic compression has therefore found a range of clinical applications both from the improved venous return and the effects of changing shear stress and strain on the vascular endothelium. These mechanisms not only induce vasodilation but also induce a cascade of biochemical responses which downregulate the expression of adhesion molecules, inflammatory and chemokine genes; and promote the inhibition of white blood cell adhesion and platelet aggregation [7, 13, 16]. It can therefore be seen that IPC devices can activate physiological mechanisms that have a wide range of clinical applications. Intermittent pneumatic compression is a well-established technique in the management of advanced chronic venous disease, specifically venous ulceration [46, 16, 6]. The IPC devices can enhance venous return and prevent stasis, especially where valves are not compromised. Exploiting the many biochemical response induced by IPC has led to it also being widely used for the prevention of deep venous thrombosis (DVT) and pulmonary embolism [47, 34, 12] both during surgery [47, 79, 34, 26] and whilst on bed rest. In 11 non-orthopaedic surgical randomised controlled trials, IPC reduced the incidence of asymptomatic DVT from 25% in the control group to 7.9% in the IPC group [47]. In 11 multimodality studies, combining IPC with anticoagulant medication further decreased the incidence of DVT from 4.1% with IPC alone to 2.19% with IPC and pharmacological prophylaxis [34].

IPC systems have also been shown to reduce oedema [10] and are therefore used in the treatment of lymphedema [78, 61]. This reduction in oedema through IPC has further been shown to increase dermal oxygen tension [38], possibly through

increased perfusion pressure and hence the potential for improved wound healing [45, 16, 6].

In terms of IPC use in venous leg ulcers a Cochrane review of nine randomised controlled trials looked at the effects of IPC compared to no IPC, and between IPC with and without other treatment regimens in venous ulcer management. In 4 out of 9 studies IPC was shown to enhance the healing of venous leg ulcers suggesting that IPC may increase the healing of venous leg ulcers compared with no compression. However it was unclear whether IPC can be used instead of compression bandages [46].

Despite these observed clinical benefits of IPC and the exceedingly large clinical usage of the device, there is a lack of evidence from randomised controlled trials to establish exactly which of the impulse pressure sequences provide the greatest therapeutic effects [79]. Whilst the mechanistic effects of IPC have predominantly been studied locally in large vessels it is also the systemic changes in shear stress that are likely to enhance these clinical benefits. For IPC to improve perfusion to tissue for complications such as venous leg ulcers; to promote angiogenesis and to mitigate the risk of DVT and pulmonary embolism it is essential that we also fully understand the effects of IPC at a microcirculatory level, this requires further research.

In health many oscillatory mechanisms alter their periodicity to accommodate the changing demands of life such as heart rate variability, respiratory sinus arrhythmia, vasomotion, muscle contraction and muscle pumps. A greater understanding of the integration of these oscillators in health along with the mechanisms induced by IPC that generate clinical benefits in DVT, venous disease and oedema may enable us to optimise the application of externally applied oscillatory devices to support and enhance these mechanisms when they are compromised.

References

1. C. Aalkjaer, D. Boedtkjer, V. Matchkov, Vasomotion: what is currently thought? Acta Physiol. **202**(3), 253–269 (2011)
2. Y.A. Abdulhameed, G. Lancaster, P.V.E. McClintock, A. Stefanovska, On the suitability of laser-Doppler flowmetry for capturing microvascular blood flow dynamics from darkly pigmented skin. Physiol. Meas. **40**(7), 074005 (2019)
3. Y.A. Abdulhameed, P.V.E. McClintock, A. Stefanovska, Race-specific differences in the phase coherence between blood flow and oxygenation: A simultaneous NIRS, white light spectroscopy and LDF study. J. Biophotonics **13**(4), e201960131 (2020)
4. A. Abu-Own, T. Cheatle, J.H. Scurr, P.D. Coleridge Smith, Effects of intermittent pneumatic compression of the foot on the microcirculatory function in arterial disease. Eur J Vasc Surg. **7**(5), 488–492 (1993)
5. K. Aizawa, S. Sbragi, A. Ramalli, P. Tortoli, F. Casanova, C. Morizzo, et al., Brachial artery vasodilatory response and wall shear rate determined by multigate Doppler in a healthy young cohort. J. Appl. Physiol. (1985) **124**(1), 150–159 (2018)
6. U. Alpagut, E. Dayioglu, Importance and advantages of intermittent external pneumatic compression therapy in venous stasis ulceration. Angiology **56**(1), 19–23 (2005)
7. S. Baratchi, K. Khoshmanesh, O.L. Woodman, S. Potocnik, K. Peter, P. McIntyre, Molecular sensors of blood flow in endothelial cells. Trends Mol Med. **23**(9), 850–868 (2017)

8. P.S. van Bemmelen, M.A. Mattos, W.E. Faught, M.A. Mansour, L.D. Barkmeier, K.J. Hodgson et al., Augmentation of blood flow in limbs with occlusive arterial disease by intermittent calf compression. J. Vasc. Surg. **19**(6), 1052–1058 (1994)
9. M.R. De Carvalho, B.U. Peixoto, I.A. Silveira, B. Oliveria, A meta-analysis to compare four-layer to short-stretch compression bandaging for venous leg ulcer healing. Ostomy Wound Manage. **64**(5), 30–37 (2018)
10. A.H. Chen, S.G. Frangos, S. Kilaru, B.E. Sumpio, Intermittent pneumatic compression devices: physiological mechanisms of action. Eur. J. Vasc. Endovasc. Surg. **21**(5), 383–392 (2001)
11. L.E. Chen, K. Liu, W.N. Qi, E. Joneschild, X. Tan, A.V. Seaber, et al., Role of nitric oxide in vasodilation in upstream muscle during intermittent pneumatic compression. J. Appl. Physiol. (1985). **92**(2), 559–566 (2002)
12. S. Chibbaro, H. Cebula, J. Todeschi, M. Fricia, D. Vigouroux, H. Abid et al., Evolution of prophylaxis protocols for venous thromboembolism in neurosurgery: results from a prospective comparative study on low-molecular-weight heparin, elastic stockings, and intermittent pneumatic compression devices. World Neurosurg. **109**, e510–e516 (2018)
13. J.J. Chiu, S. Chien, Effects of disturbed flow on vascular endothelium: pathophysiological basis and clinical perspectives. Physiol. Rev. **91**(1), 327–387 (2011)
14. P.S. Clifford, Skeletal muscle vasodilatation at the onset of exercise. J. Physiol. **583**(Pt 3), 825–833 (2007)
15. W.C. Cole, G.R. Gordon, A.P. Braun, Cellular and ionic mechanisms of arterial vasomotion. Adv. Exp. Med. Biol. **1124**, 297–312 (2019)
16. A.J. Comerota, Intermittent pneumatic compression: physiologic and clinical basis to improve management of venous leg ulcers. J. Vasc. Surg. **53**(4), 1121–1129 (2011)
17. A.J. Comerota, V. Chouhan, R.N. Harada, L. Sun, J. Hosking, R. Veermansunemi, et al., The fibrinolytic effects of intermittent pneumatic compression: mechanism of enhanced fibrinolysis. Ann Surg. **226**(3), 306–313 (1997); discussion 13–14
18. A.R. Crecelius, B.S. Kirby, G.J. Luckasen, D.G. Larson, F.A. Dinenno, Mechanisms of rapid vasodilation after a brief contraction in human skeletal muscle. Am. J. Physiol. Heart Circ. Physiol. **305**(1), H29–H40 (2013)
19. G. Dai, J.P. Gertler, R.D. Kamm, The effects of external compression on venous blood flow and tissue deformation in the lower leg. J. Biomech. Eng. **121**(6), 557–564 (1999)
20. G. Dai, O. Tsukurov, M. Chen, J.P. Gertler, R.D. Kamm, Endothelial nitric oxide production during in vitro simulation of external limb compression. Am. J. Physiol. Heart Circ. Physiol. **282**(6), H2066–H2075 (2002)
21. K.T. Delis, Z.A. Azizi, R.J. Stevens, J.H. Wolfe, A.N. Nicolaides, Optimum intermittent pneumatic compression stimulus for lower-limb venous emptying. Eur. J. Vasc. Endovasc. Surg. **19**(3), 261–269 (2000)
22. K.T. Delis, N. Labropoulos, A.N. Nicolaides, B. Glenville, G. Stansby, Effect of intermittent pneumatic foot compression on popliteal artery haemodynamics. Eur. J. Vasc. Endovasc. Surg. **19**(3), 270–277 (2000)
23. K.T. Delis, G. Slimani, H.M. Hafez, A.N. Nicolaides, Enhancing venous outflow in the lower limb with intermittent pneumatic compression. A comparative haemodynamic analysis on the effect of foot vs. calf vs. foot and calf compression. Eur. J. Vasc. Endovasc. Surg. **19**(3), 250–260 (2000)
24. R.T. Eberhardt, J.D. Raffetto, Chronic venous insufficiency. Circulation **130**(4), 333–346 (2014)
25. S. Eriksson, J. Nilsson, C. Sturesson, Non-invasive imaging of microcirculation: a technology review. Med Dev. (Auckl). **7**, 445–452 (2014)
26. M. Fujisawa, M. Naito, I. Asayama, T. Kambe, K. Koga, Effect of calf-thigh intermittent pneumatic compression device after total hip arthroplasty: comparative analysis with plantar compression on the effectiveness of reducing thrombogenesis and leg swelling. J Orthop Sci. **8**(6), 807–811 (2003)
27. A.M. Gardner, R.H. Fox, The venous footpump: influence on tissue perfusion and prevention of venous thrombosis. Ann. Rheum. Dis. **51**(10), 1173–1178 (1992)

28. A.M. Gardner, R.H. Fox, C. Lawrence, T.D. Bunker, R.S. Ling, A.G. MacEachern, Reduction of post-traumatic swelling and compartment pressure by impulse compression of the foot. J. Bone Joint Surg. Br. **72**(5), 810–815 (1990)
29. A.M.N. Gardner, R.H. Fox, *The Venous System in Health and Disease* (IOS Press, 2001)
30. D. Goldman, A.S. Popel, A computational study of the effect of vasomotion on oxygen transport from capillary networks. J. Theor. Biol. **209**(2), 189–199 (2001)
31. C.N. Hall, C. Reynell, B. Gesslein, N.B. Hamilton, A. Mishra, B.A. Sutherland et al., Capillary pericytes regulate cerebral blood flow in health and disease. Nature **508**(7494), 55–60 (2014)
32. N. Hori, R. Wiest, R.J. Groszmann, Enhanced release of nitric oxide in response to changes in flow and shear stress in the superior mesenteric arteries of portal hypertensive rats. Hepatology **28**(6), 1467–1473 (1998)
33. M.H. Howlader, P.D. Smith, Microangiopathy in chronic venous insufficiency: quantitative assessment by capillary microscopy. Eur. J. Vasc. Endovasc. Surg. **26**(3), 325–331 (2003)
34. S.K. Kakkos, J.A. Caprini, G. Geroulakos, A.N. Nicolaides, G. Stansby, D.J. Reddy, et al., Combined intermittent pneumatic leg compression and pharmacological prophylaxis for prevention of venous thromboembolism. Cochrane Database Systematic Rev. **9**, CD005258 (2016)
35. R.F. Kelly, H.M. Snow, Characteristics of the response of the iliac artery to wall shear stress in the anaesthetized pig. J. Physiol. **582**(Pt 2), 731–743 (2007)
36. B.S. Kirby, R.E. Carlson, R.R. Markwald, W.F. Voyles, F.A. Dinenno, Mechanical influences on skeletal muscle vascular tone in humans: insight into contraction-induced rapid vasodilatation. J. Physiol. **583**(Pt 3), 861–874 (2007)
37. V.V. Kislukhin, Regulation of oxygen consumption by vasomotion. Math. Biosci. **191**(1), 101–108 (2004)
38. P.J. Kolari, K. Pekanmaki, R.T. Pohjola, Transcutaneous oxygen tension in patients with post-thrombotic leg ulcers: treatment with intermittent pneumatic compression. Cardiovasc. Res. **22**(2), 138–141 (1988)
39. H.D. Kvernmo, A. Stefanovska, K.A. Kirkeboen, K. Kvernebo, Oscillations in the human cutaneous blood perfusion signal modified by endothelium-dependent and endothelium-independent vasodilators. Microvasc. Res. **57**(3), 298–309 (1999)
40. N. Labropoulos, L.R. Leon Jr., A. Bhatti, S. Melton, S.S. Kang, A.M. Mansour et al., Hemodynamic effects of intermittent pneumatic compression in patients with critical limb ischemia. J. Vasc. Surg. **42**(4), 710–716 (2005)
41. K. Liu, L.E. Chen, A.V. Seaber, J.R. Urbaniak, Influences of inflation rate and duration on vasodilatory effect by intermittent pneumatic compression in distant skeletal muscle. J. Orthop. Res. **17**(3), 415–420 (1999)
42. M.L. Mihok, C.L. Murrant, Rapid biphasic arteriolar dilations induced by skeletal muscle contraction are dependent on stimulation characteristics. Can. J. Physiol. Pharmacol. **82**(4), 282–287 (2004)
43. P. Moscicka, M.T. Szewczyk, J. Cwajda-Bialasik, A. Jawien, The role of compression therapy in the treatment of venous leg ulcers. Adv Clin Exp Med. (2018)
44. E.A. Nelson, U. Adderley, Venous leg ulcers. BMJ Clin Evid. (2016)
45. E.A. Nelson, S.E. Bell-Syer, Compression for preventing recurrence of venous ulcers. Cochrane Database Systematic Rev. **9**, CD002303 (2014)
46. E.A. Nelson, A. Hillman, K. Thomas, Intermittent pneumatic compression for treating venous leg ulcers. Cochrane Database Systematic Rev. **5**, CD001899 (2014)
47. A.N. Nicolaides, J. Fareed, A.K. Kakkar, A.J. Comerota, S.Z. Goldhaber, R. Hull et al., Prevention and treatment of venous thromboembolism–international consensus statement. Int. Angiol. **32**(2), 111–260 (2013)
48. S. Nikolovska, L. Pavlova, A. Ancevski, A. Petrov, A. Arsovski, E. Dejanova, The role of nitric oxide in the pathogenesis of venous ulcers. Acta Dermatovenerol. Croat. **13**(4), 242–246 (2005)
49. S. Nikolovska, A. Arsovski, K. Damevska, G. Gocev, L. Pavlova, Evaluation of two different intermittent pneumatic compression cycle settings in the healing of venous ulcers: a randomized trial. Med. Sci. Monitor **11**(7), CR337–CR343 (2005)

50. H. Nilsson, C. Aalkjaer, Vasomotion: mechanisms and physiological importance. Mol Interv. **3**(2), 79–89, 51 (2003)
51. S. O'Meara, N. Cullum, E.A. Nelson, J.C. Dumville, Compression for venous leg ulcers. Cochrane Database Systematic Rev. **11**, CD000265 (2012)
52. J.M. Pavon, S.S. Adam, Z.A. Razouki, J.R. McDuffie, P.F. Lachiewicz, A.S. Kosinski et al., Effectiveness of intermittent pneumatic compression devices for venous thromboembolism prophylaxis in high-risk surgical patients: a systematic review. J. Arthroplasty **31**(2), 524–532 (2016)
53. J.M. Pavon, J.W. Williams, Jr., S.S. Adam, Z.A. Razouki, J.R. McDuffie, P.F. Lachiewicz, et al., *Effectiveness of Intermittent Pneumatic Compression Devices for Venous Thromboembolism Prophylaxis in High-risk Surgical and Medical Patients* (Washington (DC), 2015)
54. K. Pekanmaki, P.J. Kolari, U. Kiistala, Laser Doppler vasomotion among patients with post-thrombotic venous insufficiency: effect of intermittent pneumatic compression. Vasa **20**(4), 394–397 (1991)
55. B.T. Roseguini, S. Mehmet Soylu, J.J. Whyte, H.T. Yang, S. Newcomer, M.H. Laughlin, Intermittent pneumatic leg compressions acutely upregulate VEGF and MCP-1 expression in skeletal muscle. Am. J. Physiol. Heart Circ. Physiol. **298**(6), H1991–H2000 (2010)
56. B.T. Roseguini, R. Sheldon, A. Stroup, J.W. Bell, D. Maurer, B.D. Crist et al., Impact of chronic intermittent external compressions on forearm blood flow capacity in humans. Eur. J. Appl. Physiol. **111**(3), 509–519 (2011)
57. M. Rossi, S. Bertuglia, M. Varanini, A. Giusti, G. Santoro, A. Carpi, Generalised wavelet analysis of cutaneous flowmotion during post-occlusive reactive hyperaemia in patients with peripheral arterial obstructive disease. Biomed. Pharmacother. **59**(5), 233–239 (2005)
58. M. Rossi, A. Carpi, C. Di Maria, F. Franzoni, F. Galetta, G. Santoro, Post-ischaemic peak flow and myogenic flowmotion component are independent variables for skin post-ischaemic reactive hyperaemia in healthy subjects. Microvasc Res. (2007)
59. M. Rucker, O. Strobel, B. Vollmar, W.J. Spitzer, M.D. Menger, Protective skeletal muscle arteriolar vasomotion during critical perfusion conditions of osteomyocutaneous flaps is not mediated by nitric oxide and endothelins. Langenbecks Arch Surg. **388**(5), 339–343 (2003)
60. T. Sakurai, N. Terui, Effects of sympathetically induced vasomotion on tissue-capillary fluid exchange. Am. J. Physiol. Heart Circ. Physiol. **291**(4), H1761–H1767 (2006)
61. C. Sanal-Toprak, T. Ozsoy-Unubolo, Y. Bahar-Ozdemir, G. Akyuz, The efficacy of intermittent pneumatic compression as a substitute for manual lymphatic drainage in complete decongestive therapy in the treatment of breast cancer related lymphedema. Lymphology. **52**(2), 82–91 (2019)
62. R. Saunders, A.J. Comerota, A. Ozols, R. Torrejon Torres, K.M. Ho, Intermittent pneumatic compression is a cost-effective method of orthopedic postsurgical venous thromboembolism prophylaxis. Clinicoecon Outcomes Res. **10**, 231–241 (2018)
63. M.V. Schaverien, J.A. Moeller, S.D. Cleveland, Nonoperative treatment of lymphedema. Semin Plast Surg. **32**(1), 17–21 (2018)
64. R.D. Sheldon, B.T. Roseguini, J.P. Thyfault, B.D. Crist, M.H. Laughlin, S.C. Newcomer, Acute impact of intermittent pneumatic leg compression frequency on limb hemodynamics, vascular function, and skeletal muscle gene expression in humans. J. Appl. Physiol (1985). **112**(12), 2099–2109 (2012)
65. J.K. Shoemaker, M.E. Tschakovsky, R.L. Hughson, Vasodilation contributes to the rapid hyperemia with rhythmic contractions in humans. Can. J. Physiol. Pharmacol. **76**(4), 418–427 (1998)
66. C.R. Simpson, M. Kohl, M. Essenpreis, M. Cope, Near-infrared optical properties of ex vivo human skin and subcutaneous tissues measured using the Monte Carlo inversion technique. Phys. Med. Biol. **43**(9), 2465–2478 (1998)
67. S.Y. Sinkler, S.S. Segal, Rapid versus slow ascending vasodilatation: intercellular conduction versus flow-mediated signalling with tetanic versus rhythmic muscle contractions. J. Physiol. **595**(23), 7149–7165 (2017)
68. B.M. Sorensen, A. Houben, T. Berendschot, J. Schouten, A.A. Kroon, C.J.H. van der Kallen et al., Cardiovascular risk factors as determinants of retinal and skin microvascular function: The Maastricht Study. PLoS ONE **12**(10), e0187324 (2017)

69. A. Stefanovska, M. Bracic, Reconstructing cardiovascular dynamics. Control Eng Pract. **7**(2), 161–172 (1999)
70. A. Stefanovska, M.B. Lotric, S. Strle, H. Haken, The cardiovascular system as coupled oscillators? Physiol. Meas. **22**(3), 535–550 (2001)
71. A. Stefanovska, Cardiorespiratory interactions, Nonlinear Phenom. Complex Sys. 462–469 (2002)
72. X. Tan, W.N. Qi, X. Gu, J.R. Urbaniak, L.E. Chen, Intermittent pneumatic compression regulates expression of nitric oxide synthases in skeletal muscles. J. Biomech. **39**(13), 2430–2437 (2006)
73. C.E. Thorn, H. Kyte, D.W. Slaff, A.C. Shore, An association between vasomotion and oxygen extraction. Am J Physiol-Heart C. **301**(2), H442–H449 (2011)
74. C.E. Thorn, A.O. Adio, C.P. Winlove, A.C. Shore, Effects of intermittent impulse compression on microvascular perfusion and capillary density. Microcirculation **27**(2) (2020)
75. A.G. Tsai, M. Intaglietta, Evidence of flowmotion induced changes in local tissue oxygenation. Int. J. Microcirc. Clin. Exp. **12**(1), 75–88 (1993)
76. M.E. Tschakovsky, A.M. Rogers, K.E. Pyke, N.R. Saunders, N. Glenn, S.J. Lee, et al., Immediate exercise hyperemia in humans is contraction intensity dependent: evidence for rapid vasodilation. J. Appl. Physiol. (1985). **96**(2), 639–644 (2004)
77. J.W. VanTeeffelen, S.S. Segal, Rapid dilation of arterioles with single contraction of hamster skeletal muscle. Am. J. Physiol. Heart Circ. Physiol. **290**(1), H119–H127 (2006)
78. M.T. Zaleska, W.L. Olszewski, The effectiveness of intermittent pneumatic compression in therapy of lymphedema of lower limbs: methods of evaluation and results. Lymphat Res Biol. **17**(1), 60–69 (2019)
79. J.M. Zhao, M.L. He, Z.M. Xiao, T.S. Li, H. Wu, H. Jiang, Different types of intermittent pneumatic compression devices for preventing venous thromboembolism in patients after total hip replacement. Cochrane Database Systematic Rev. **12**, CD009543 (2014)

Chapter 26
Phase Coherence Between Cardiovascular Oscillations in Malaria: The Basis for a Possible Diagnostic Test

Yunus A. Abdulhameed, Abdulrazaq G. Habib, Peter V. E. McClintock, and Aneta Stefanovska

Abstract We show how a non-autonomous dynamics approach using time-resolved analyses of power spectra and phase coherence can help in the noninvasive diagnosis of malaria. The work is based on studying oscillations in blood flow and the variability of the heart and respiratory frequencies. The model used assumes that the heart and respiration are two oscillatory pumps with variable frequencies and that the vascular resistance also changes in an oscillatory manner. Red blood cells circulating through the system deliver oxygen to each cell. Malaria changes the red blood cells so that this delivery is compromised. The oscillatory properties of both pumps are also affected. We quantify the latter and compare three groups of subjects: febrile malaria patients (37); non-febrile malaria patients (10); and healthy controls (51). For each subject, time series of skin blood flow, respiratory effort, cardiac activity (ECG) and skin temperature were recorded simultaneously over an interval of 30 minutes. The oscillatory components within the range 0.005–2 Hz were analysed and their degree of coordination throughout the cardiovascular system was assessed by wavelet phase coherence analysis. It is shown that malaria, either febrile or non-febrile, substantially reduces the coordination.

Y. A. Abdulhameed · P. V. E. McClintock · A. Stefanovska (✉)
Department of Physics, Lancaster University, Lancaster LA1 4YB, UK
e-mail: aneta@lancaster.ac.uk

P. V. E. McClintock
e-mail: p.v.e.mcclintock@lancaster.ac.uk

Y. A. Abdulhameed
Now at Department of Mathematics, University of Texas at San Antonio, San Antonio, TX 78249, USA
e-mail: yunusabhamid@yahoo.com

A. G. Habib
Department of Medicine, Bayero University, Kano, Nigeria
e-mail: abdulrazaq_habib@yahoo.co.uk

A. Stefanovska and P. V. E. McClintock (eds.), *Physics of Biological Oscillators*, Understanding Complex Systems,
https://doi.org/10.1007/978-3-030-59805-1_26

26.1 Introduction

Malaria is a life-threatening mosquito-borne disease [41], involving changes in the dynamical properties of blood flow. There are still more than 200 million cases of malaria annually, resulting in about 600,000 deaths. The disease is treatable when arrested soon enough, so early diagnosis is highly desirable. Despite the development of non-invasive alternatives [22], the current gold standards in malaria diagnosis are still antigen-based rapid diagnostic tests (RDTs) and the microscopic examination of blood films by a trained microscopist. Results vary widely in diagnostic sensitivity and specificity.

To our knowledge, malaria-related impairment of cardiovascular oscillation has not been investigated. To try to understand such effects, and to assess their potential for detecting malaria, the present study involves simultaneous monitoring of blood flow, skin temperature, respiration and electrocardiography. The time series are analysed using wavelet-based methods to establish, not only the intensity of oscillatory processes involved in cardiovascular regulation, but also their degree of coordination which, as we will see, is adversely affected by malaria.

Physiological oscillations and their potential for characterising cardiovascular dynamics in malaria. Measurements of blood flow and oxygenation in human subjects reveal several co-existing oscillatory processes, covering a very wide range of frequencies. Use of the continuous wavelet transform reveals at least six such processes [34, 36]; with the same oscillations being seen at different sites and for different measured quantities, not only in blood flow and oxygenation. Their physiological attribution has been established. Briefly: hemodynamic oscillations near 1 Hz (frequency interval FI-I) and 0.25 Hz (FI-II) are due to cardiac and respiratory activity respectively; the oscillation near 0.1 Hz (FI-III) is attributable to the natural properties of smooth muscle which oscillates at about 0.1 Hz even *in vitro*; that near 0.03 Hz (FI-IV) is neurogenic, associated with autonomic nervous activity; and those near 0.01 Hz (FI-V) and 0.007 Hz (FI-VI) arise [23] from NO-related and NO-independent endothelial activities respectively. The underlying physiological oscillatory processes suggested the introduction of a coupled-oscillator model of the cardiovascular system [36, 37, 39]. Understanding the nature of these oscillations in healthy subjects allows their sometimes distinctive differences in pathological states to be identified. This approach has not yet been applied to malaria, however, even though the disease may be expected to cause significant changes in microvascular dynamics.

Possible effects of malaria on the oscillations in blood flow. The increased stiffness of the membrane of an infected erythrocyte (red blood cell, or RBC) [19], and its tendency to stick to the endothelial cells lining all the blood vessels, cause infected cells to pass less easily through the capillaries. The cell also changes shape, and its ability to transport/release oxygen is compromised. Consequently, the viscosity, flow properties, and oxygenation of blood are all changed by malaria in ways that do not occur in other diseases. Hemodynamics is altered [18] on account of the spatial distribution of erythrocytes [33] and merozoites, and it is reasonable to infer

that endothelial reactivity is affected too. Erythrocytes are an important factor determining the hemorheological properties of blood, its corresponding shear-thinning and increased shear stress at walls [46]. We therefore hypothesise that the oscillatory properties and their degree of coherence between different parts of the system will be altered in malaria. Blood flow takes place in a thermodynamically open system, and therefore the oscillations are time-varying. Time series analysis methods for non-autonomous dynamics [8, 9] must therefore be employed.

26.2 Materials and Methods

Here we summarise salient features of the measurements and data analysis, which are described in fuller detail by Abdulhameed [1]. The anthropomorphic data for the subjects used in the study are listed in Table 26.1.

Table 26.1 Anthropometric data for the subjects, presenting their: ages; body mass index (BMI); skin temperature (ST); core temperature (CT); instantaneous heart rate (IHR); instantaneous respiration rate (IRR); systolic blood pressure (SBP); diastolic blood pressure (DBP); and blood packed cell volume (PCV). Median values and their ranges (25th and 75th percentiles) are shown, with significant differences ($p < 0.05$) highlighted in grey. $p1$, $p2$ and $p3$ are values obtained from the sign rank test for FM–NFM, FM–NM and NFM–NM comparisons respectively

	FM ($n = 37$)	NFM ($n = 10$)	NM ($n = 51$)	$p1$	$p2$	$p3$
Age (years)	20(18–25)	23(20–27)	22(20–24)	0.08	0.169	0.382
BMI (kg/m^2)	19.8 18.1–21.8	20 19.5–21.5	21.1 19.1–22	0.53	0.058	0.6
ST (^{o}C)	38.2 37.6–38.9	35.5 35.1–36.4	35.9 35.7–36.1	2×10^{-6}	10^{-9}	0.514
CT (^{o}C)	38.9 38.2–39.2	37.80 37.6–38.0	36.15 35.9–36.5	10^{-9}	2×10^{-5}	7×10^{-5}
IHR (Hz)	1.72 1.53–1.85	1.36 1.28–1.55	1.14 1.02–1.26	0.002	0.00009	0.00009
IRR (Hz)	0.44 0.37–0.49	0.35 0.32–0.45	0.33 0.30–0.37	0.02	3×10^{-7}	0.325
SBP (mm Hg)	112 106–125	113 106–118	124 110–128	0.79	0.039	0.07
DBP (mm Hg)	63 57–70	73 68–80	77 69–82	0.03	0.00014	0.45
PCV (%)	42 40–43	44 41–45	44 42–47	1	0.02	0.17

26.2.1 Subjects and Plan of the Study

Consecutive adult male patients presenting to Murtala Mohammed Specialist Hospital, Kano, Nigeria with acute ailments and fever during August–November 2017 were evaluated by taking clinical history and examination. Blood samples for tests were collected from patients considered likely to have malaria for subsequent malarial smear microscopy, rapid diagnostic tests (RDT), haematocrit level and for haemoglobin genotype. These tests were conducted later, but the physical data acquisition was conducted immediately in a cool and quiet place as detailed in Sect. 26.2.2 on patients considered likely to have malaria. Where the results of the medical tests subsequently confirmed presence of malaria, absence of anaemia (low haematocrit) and AA genotype, patients were retained in the study and categorized as febrile malaria (FM) (37) or non-febrile malaria (NFM) (10). The results of 20 patients who did not fit the criteria were discarded, regardless of malarial status, because anaemia and/or abnormal haemoglobin genotype are known to affect blood flow dynamics and RBC morphology, and consequently the physical parameters being studied. A control group of 51 healthy non-malaria (NM) male subjects was also recruited.

For all subjects, the inclusion criteria included: (i) informed consent for participation in the study, under a protocol approved by the Ethical Committees of both the Kano State Ministry of Health, Nigeria and Bayero University Kano, Nigeria; (ii) absence of overt alternative/superadded cause of febrile illness; (iii) absence of significant co-morbidity/complications known to affect the test, e.g. hypertension or peripheral vascular disease; (iv) absence of sickle cell anaemia in a blood group genotype test; and (v) having the AA genotype blood group.

For the FM and NFM groups, additional inclusion criteria were: (vi) presence of malarial parasites in blood film microscopy; and (vii) a positive malarial Rapid Diagnostic Test (RDT). The difference in the inclusion criteria for febrile malaria and non-febrile malaria group was body temperature. Malaria patients presenting with a core temperature above 38.0 °C were defined as FM, while those with lower temperatures were defined as NFM.

For the NM group, the additional inclusion criteria were: (vi) no acute febrile illness (temperature $< 37.0°C$); (vii) absence of malarial parasites in blood film microscopy; and (viii) a negative malarial RDT.

In the FM group, 30% of the patients had taken antimalarial and antipyretic drugs before presenting; 40% had taken antipyretic drugs only, and 30% had not taken any drugs. In the NFM group, all patients had taken antimalarial and/or antipyretic drugs for at most 3 days.

26.2.2 Data Acquisition

The measurements were all made between 09:00 and 18:00 in a quiet air-conditioned room, with a controlled ambient temperature and constant low illumination.

Microvascular blood flow was recorded by laser-Doppler flowmetry (LDF), which provided a continuous measurement of the microcirculation in the skin, thus reflecting the perfusion in the capillaries, arterioles, venules and dermal vascular plexus. The instrument (moorLAB, Moor Instruments Ltd, UK) used in the present study transmits a near-IR laser light from a temperature-stabilized laser diode operating at a wavelength of 780 nm and with a maximum power of 2.5 mW into the skin through an MP1-V2 probe (Moor Instruments Ltd, UK), which has two optical fibres. A time constant of 0.1 s was selected and the LDF processor bandwidth was between 18 Hz and 22.5 KHz. A flexible probe holder (PH1-V2, Moor Instruments Ltd., UK) was attached to the skin surface on the outer side of each ankle (lateral malleolus) using double-sided adhesive discs. One fibre delivers light to the site under observation, while the backscattered (reflected) light is collected by the other fibre. The light reflected back from moving RBCs is Doppler-shifted in frequency by an amount related to the blood flow in the illuminated volume of tissue, the frequency shift being proportional to red cell speed, while the frequency of the light reflected from stationary cells and tissue remains unchanged [29]. The difference between incident light and the Doppler-shifted back-scattered light yields the LDF signal, known as the blood perfusion signal. The LDF output is semi-quantitative and is expressed in perfusion units (PU) of output voltage (typically 1 PU = 10 mV) [29]. The sampling frequency was 40 Hz.

An electrocardiogram (ECG) was used to record the electrical activity of the heart with a sampling frequency of 1 kHz. The ECG was measured using a bipolar precordial lead. The electrodes were attached on both shoulders and the lowest left rib, as this maximizes the sharpness of the R-peak.

The respiration was measured using an elasticated belt fastened across the chest and fitted with a Biopac TSD201 Respiratory Effort Transducer (Biopac Systems Inc., CA, USA).

Skin temperature was monitored using two high-sensitivity, low-heat-capacity thermistors—YSI 709B Thermilinear sensors (YSI Inc, Yellow Springs, OH, USA) of 8.5 mm diameter, which were taped onto the skin. The thermistors were positioned outside the left ankles, over the lateral malleolus, close to the LDF probes.

The individual time series were recorded simultaneously using a signal conditioning system (Cardiosignals, Institute Jožef Stefan, Slovenia) over an interval of 30 min.

Blood pressure was measured prior to the initiation of signal acquisition. A Digital Automatic Blood Pressure Monitor (Omron, M10-IT) was used, with a cuff wrapped on the subjects' upper right arm while they were seated. The subject then moved to a supine position on a comfortable bed, where the necessary sensors were installed. In this way, subjects relaxed in a supine position for 15–20 min of acclimatisation, prior to the recordings. The equipment was either battery supplied or connected to the electrical supply via a mains filter.

26.3 Analysis of Cardiovascular Time Series

Prior to analysis, time-series were inspected in order to detect any apparent anomalies, e.g. movement artefacts or rhythmic patterns clearly different from the blood flow oscillations of interest. Such effects might be expected to stem from methodological or physiological factors including poor electrode placement or poor electrical contact due e.g. to dry skin. The intention was that time series that were demonstrably defective would be discarded. In practice, this occurred only once: data from one febrile malaria patient were removed from the data set on account of a defective respiratory signal, seemingly because the respiratory belt had not been properly fastened around the patient's thorax.

26.3.1 Spectral Analysis

Traditionally, representations of time series in the frequency domain are obtained with the fast Fourier transform, which constitutes a periodic function in terms of sines and cosines. This makes it suitable for analysing time series whose components are strictly periodic in nature, but it is unsuitable for LDF blood flow signals whose spectral content is inherently non-periodic. Although the limitations of the Fourier transform can partially be addressed by dividing the time series into shorter time-windows within which there is not much time variation, a better way forward is by the use of wavelet analysis [38] which, by using an adaptive window length that simultaneously analyses time series at each moment in time, provides both optimal frequency resolution and time localisation [8, 14].

Wavelet analysis is a scale-independent method comprising an adaptive window length allowing low frequencies to be analysed using longer wavelets, and higher frequencies with shorter wavelets. The continuous wavelet transform $W_s(s,t)$ of a signal $f(t)$ is defined as

$$W_s(s,t) = |s|^{-1/2} \int_{-\infty}^{\infty} \psi\Big(\frac{u-t}{s}\Big) f(u) du, \tag{26.1}$$

where s is the scaling factor, t is the temporal position on the signal, and the wavelet function is built by scaling and translating a chosen mother wavelet ψ which, in this study, was chosen to be the complex Morlet wavelet, Eq. (26.2), because it maximizes joint time-localisation and frequency-resolution [38]

$$\psi(u) = \frac{1}{\sqrt{\pi}} \big(e^{-i\omega_0 u} - e^{-{\omega_0}^2/2}\big) e^{-u^2/2}. \tag{26.2}$$

26.3.2 Extracting the Instantaneous Heart Frequency

The instantaneous heart rate (IHR) was extracted from the data using both time-frequency and time domain analysis techniques [16]. The methods used included nonlinear mode decomposition (NMD) [17], a technique that decomposes a signal into a set of components, or modes. Using NMD, the instantaneous frequency of the heart beat was extracted from the wavelet transform of the ECG, thus yielding the IHR. The IHR was also derived from the LDF signals using the same technique. Note that in the literature [15, 26] IHR is often referred to as HRV and, occasionally, as IHF.

26.3.3 Wavelet Phase Coherence

While waves can be coherent in space, oscillations can be coherent in time. Quite generally, correlation properties between physical quantities, whether at a single or several oscillation frequencies, can be studied by investigating their coherence in time. If we observe oscillations at the same frequency in two different time series and find that the difference between their instantaneous phases $\phi_{1k,n}$ and $\phi_{2k,n}$ is constant, then the oscillations are said to be coherent at that frequency [3, 5, 32]. A phenomenon closely related to phase coherence is that of phase synchronization [13, 20, 28, 30]. While oscillations can be coherent without necessarily being directly coupled, the existence of coupling is fundamental for synchronization [8]. For example, if we have an n:m relationship between the frequencies of two signals, this implies that there are n oscillation cycles in one time series per m cycles of the other time series: 1:1 phase synchronization may equally be considered as phase coherent oscillations. Thus phase coherence can be used directly to investigate 1:1 synchronization between two signals, such as the two blood flow signals used in the present study. The wavelet phase coherence (WPC) $\gamma(f)$ between the two signals $f_1(t)$ and $f_2(t)$ is estimated from their respective wavelet transforms as obtained in Eq. (26.1), i.e. $W_{s_{1,2}}(t, f)$ [38] as

$$\gamma(f) = \left| \frac{1}{T} \int_0^T e^{i \arg[W_{s_1}(s,t) W^*_{s_2}(s,t)]} dt \right|, \tag{26.3}$$

where T is the duration of the signal. This equation reflects the extent to which the phases $\phi_{1k,n}$ and $\phi_{2k,n}$ of both signals at each time t_n and frequency f are entirely correlated. Unlike the usual coherence measures, wavelet phase coherence takes no account of the amplitude dynamics of the signals. This is appropriate because (i) the amplitudes of most physiological signals are subject to artefacts and noise, and (ii) the amplitudes of common physiological oscillations can often be mixed. In all cases, however, the relationship between their phases remains the same (up to a constant phase shift). Their relative phase difference is thus calculated as

$$\Delta\phi_{kn} = \phi_{2k,n} - \phi_{1k,n}\,. \tag{26.4}$$

The phase coherence function $C_\phi(f_k)$ is obtained by calculating and averaging in time the components of the sine and cosine of the phase differences for the whole signal, effectively defining the time-averaged WPC as

$$C_\phi(f_k) = \sqrt{\langle \cos \Delta\phi_{kn}\rangle^2 + \langle \sin \Delta\phi_{kn}\rangle^2}. \tag{26.5}$$

The idea behind Eq. (26.5) is that, while we are considering individual times and frequencies, these come from a discrete set (since all the signals in the present study are discrete and finite-time), and so the subscripts k and n just reflect this discreteness. The phase coherence function $C_\phi(f_k)$ as defined in Eq. (26.5) is exactly the discrete version of the phase coherence formula Eq. (26.3), where ϕ is the phase difference between the signals in question.

The function $C_\phi(f_k)$ characterises the tendency of $\Delta\phi_{kn}$ to remain constant, or not, at a certain frequency. Its value lies between 1 implying perfect coherence, and 0 implying total incoherence.

26.3.3.1 Effective (or Significant) Coherence

Note that the coherence computed in the first instance does not necessarily reflect a genuine phase relationship and requires careful evaluation. The problem arises because some of the coherence values obtained can be less than zero (although formally coherence values range between 0 and 1). These negative coherence values are then subtracted. Following this procedure, the very low frequency oscillations may appear to have a coherence values close to 1, because of bias resulting from the use of recordings that are too short to encompass the content at low frequencies.

Even in the case of two noisy signals, there is a tendency for there to be some apparent coherence in the sense that $C_\phi(f_k)$ rarely approaches 0 at very low frequencies. The degree of apparent phase coherence depends on frequency. So the coherence baseline will not be the same for all scales. The low-frequency components, particularly for signals of finite length (like those recorded in this study) are evaluated using fewer periods than for the higher frequency components [5]. The result can be an artificially increased coherence $\simeq$1 even where, in reality, the dynamics of the signals are completely unrelated.

To minimise random effects giving rise to apparent (but spurious) coherence, whether at low or high frequency, we checked/tested the significance of the computed coherence using the method of surrogates [24, 31]—by setting as a null hypothesis that, for all frequencies, the phases in the signals are independent. We used iterative amplitude-adjusted Fourier transform (IAAFT) surrogates to estimate the significance level of the apparent coherence, thereby avoiding the bias associated with the power spectrum of the more commonly used amplitude-adjusted Fourier transform (AAFT) surrogates. First, the IAAFT surrogates are constructed by randomizing all the properties of the signals in question, whilst keeping only the phases unshuffled.

Subsequently, this is accomplished in an iterative fashion, simply by using the appropriate value and re-scaling the distribution to substitute Fourier amplitudes, which allows us to obtain resemblance between the distributions and power spectra of the surrogates and the original signals. At each frequency we took the coherence threshold to be 95% of the highest value of 100 random realisations of IAAFT surrogates.

Finally, the effective/significant coherence was estimated by subtracting the 95th percentile of the 100 surrogate values, thus yielding the extent to which the phases of the two signals at each frequency are correlated.

26.3.4 Statistical analysis

Non-parametric statistical tests were used, implying that no assumptions were being made about any underlying distributions, thus allowing robust conclusions to be drawn. The Wilcoxon rank sum test [43] was used to test for possibly significant differences between blood flow and other signals measured from malarial and control subjects, respectively, as the corresponding time-series do not match. The Wilcoxon rank sum test is used to determine whether two unmatched samples come from similar distributions, whilst the sign rank test requires that the samples are matched. In all cases, $p < 0.05$ was considered as being statistically significant.

26.4 Results

26.4.1 Effect of Malaria on Blood Pressure, Respiration Frequency, and Skin Temperature

As summarised in Table 26.1, the FM group differed from the NM group in all parameters, including skin and core temperatures, heart and respiratory rates, systolic and diastolic blood pressures, and blood packed cell volume. The NFM group, on the other hand, differed in some parameters but not in all. FM differed from NFM in all parameters except SBP and PCV. NFM differed from NM only in core temperature and IHR.

26.4.2 Detecting Oscillations Using Time-Frequency Analysis

The signals were transformed to the time-frequency domain by wavelet analysis with a Morlet wavelet of $f_0 = 1.5$ Hz, using custom Matlab codes. The time-averaged power was then calculated and normalised in each case. Note that, even where the time-averaged values of two signals are the same, computation of their time-evolving

properties using wavelet transforms can often reveal statistically significant differences. A similar scenario was observed in the subsequent analysis of cardiovascular dynamics in malaria and non-malarial states in some of the characteristic frequency intervals.

The power spectra within individual frequency intervals are usually normalized by dividing by their total powers. In the present case, this was done for the frequency rage 0.005–2 Hz.

The differences observed in power spectra between malaria states and non-malaria were further investigated in order to ascertain whether they could be used to distinguish between groups. Machine learning algorithms were then applied to parameters extracted by spectral and coherence analysis to classify the FM, NFM and NM states.

26.4.2.1 Spectral Power in Blood Perfusion Fluctuations

The normalized time-averaged wavelet powers of left (BF1) and right (BF2) blood flow oscillations for the three groups are shown in Fig. 26.1.

For the left ankle and right ankle blood flows, the febrile malaria group had significantly lower normalized power than NM in the 0.07–0.1 and 0.8–1.4 Hz frequencies associated with the myogenic and cardiac activities respectively, and a significantly higher normalized power than NM in 0.13–0.16 Hz, the neurogenic and NO-dependent endothelial frequency intervals. A major shift was seen in the cardiac oscillatory peak between the febrile malaria and non-malaria groups, with that of the febrile malaria and non-malaria groups found at ∼1.83, ∼1.02 Hz in the left ankle blood flow and at ∼1.8, ∼1.04 in the right ankle blood flow respectively (Fig. 26.1a, b). As was the case for the febrile malaria group, the cardiac peak frequency was slightly higher in non-febrile malaria (found at ∼1.44 Hz, ∼1.45 Hz in left ankle and right ankle blood flow respectively) than non-malaria. In a similar pattern to that of febrile malaria, non-febrile malaria exhibits a lower normalized power in the 0.07–0.1 Hz but was not statistically significant, and a higher normalized power around the neurogenic and NO-dependent endothelial frequency intervals all of which are statistically significant except at ∼0.02 Hz in left ankle blood flow and 0.14–0.16 Hz in right ankle blood flow, when compared to non-malaria (Fig. 26.1c, d).

Comparisons of the normalized power between FM and NFM revealed differences in the cardiac interval, with the difference being significant only in right ankle blood flow—noting that the frequencies of their cardiac peaks also differ. At frequencies 0.04–0.05 Hz within the neurogenic interval, NFM was found to exhibit a higher normalized power although this was only statistically significant in the right ankle blood flow (Fig. 26.1e, f).

The box-plots in Fig. 26.1 compare the normalised power spectral component of the LDF blood flows within the intervals investigated for different groups. The FM group was found to have cardiac oscillations of lower power than either the NFM or NM groups in blood flow recorded from the right ankle, and a similar significant difference in the febrile malaria group was observed in the left ankle blood flow

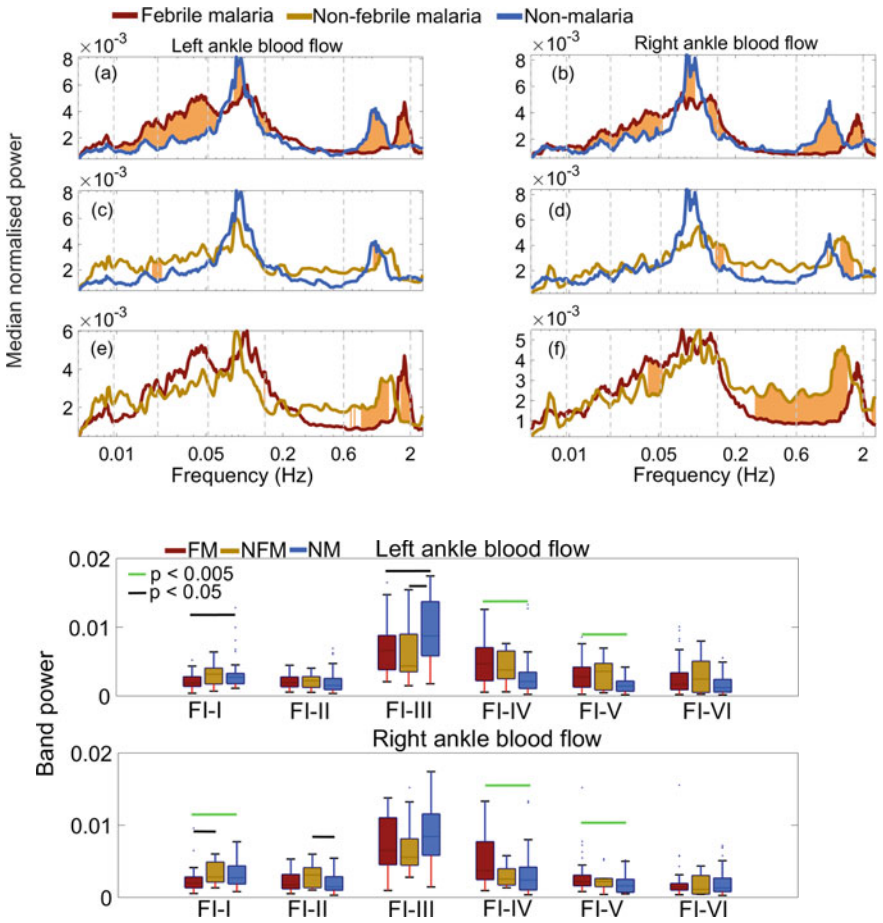

Fig. 26.1 Normalised wavelet power: **a–f** Normalised time-averaged wavelet power of left (first column) and right (second column) ankle blood flow for each group. Significant differences ($p < 0.05$) in pair comparisons are highlighted in brown. The frequency intervals FI–I... FI–VI on the abscissae of the lower panel are specified in Sect. 26.1. The upper and lower limits of each box represent the 75th and 25th percentiles, respectively; the line between these is the median value. The FM group is represented in red, NFM in gold, and NM in blue

cardiac band power only for the FM–NM comparison. For the respiratory interval, no significant difference was found between groups in left ankle blood flow, but respiratory normalized power in the right ankle blood flow significantly increased in non-febrile malaria only when compared with non-malaria. In contrast, values of the myogenic band power in the left ankle blood flow are less widely separated; yet they are significantly lower in the febrile and non-febrile malaria groups for the FM–NM and NFM–NM comparisons, although no such significant differences were found in the right ankle blood flow. Comparisons between FM and NM revealed striking

differences in the neurogenic and NO-dependent endothelial intervals, with their band powers being markedly increased in FM patients. No significant differences were found during the same comparisons for normalized band power within the NO-independent endothelial interval.

26.4.2.2 Spectral Power in Instantaneous Heart Frequency Fluctuations

The IHF analysis results are summarised in Fig. 26.2 (lower panel). Fluctuations in the IHF signal (derived from the ECG) in the frequency intervals associated with myogenic (FI-III), nitric oxide-dependent endothelial activity (FI-V) and nitric oxide-independent endothelial activity (FI-VI) ($p = 0.000006$, $p = 0.003$ and $p = 0.003$), respectively decreased significantly in febrile malaria compared to NM (Fig. 26.2), although the spectral power around 0.021 Hz tended to be lower for FM (Fig. 26.2a). But in the FI-II frequency interval associated with respiratory activity, FM exhibited a significantly higher normalised spectral power ($p = 0.0001$) compared to NM (Fig. 26.2), a similar finding being evident in the IHF absolute power (although not shown here). In a similar manner, the power of the IHF oscillations of the NFM group was significantly higher ($p = 0.004$) within the FI-II respiratory frequency interval when compared to NM, but markedly lower in the frequency intervals associated with myogenic (FI-III), neurogenic (FI-IV) and NO-related endothelial activity (FI-V) ($p = 0.017$ and $p = 0.018$ respectively). No significant difference was observed in any of the frequency intervals of IHF normalised spectral power in the FM and NFM comparison.

26.4.2.3 Coherence Between Fluctuations in IHF in Left and Right Ankles

Figure 26.3 presents the averaged coherence between IHF1 and IHF2, showing that there is significant coherence in the oscillations reflecting respiratory (II), myogenic (III), neurogenic (IV) and NO-independent endothelial activity (VI), but most pronounced in the NM group, whilst within the high frequencies (> 0.1 Hz) the coherence is diminished in NFM and extremely small in FM (Fig. 26.3a). The coherence in frequency intervals II, III, IV, V and VI is significantly smaller in FM ($p = 0.000000$, $p = 0.00000$, $p = 0.0000000$, $p = 0.000000$ and $p = 0.00000004$, respectively) and NFM ($p = 0.0008$, $p = 0.0005$, $p = 0.0038$, $p = 0.0021$ and $p = 0.0068$, respectively) when compared to the NM group. In the FM–NFM comparison, however, the coherence did not differ significantly in any frequency interval.

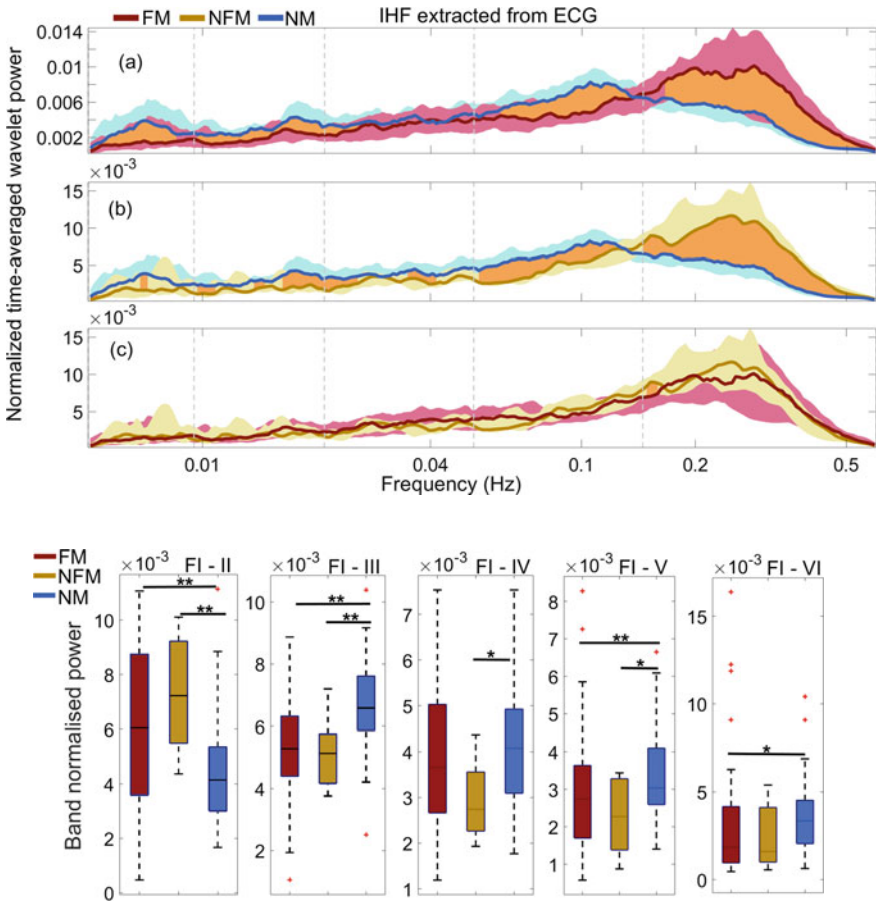

Fig. 26.2 Comparisons of normalised time-averaged wavelet power of the IHF extracted from ECG recordings. Each curve is obtained as a median over all subjects. **a** Febrile malaria (FM) compared with non-malaria (NM). **b** Non-febrile malaria (NFM) compared with non-malaria (NM). **c** FM compared with NFM. Red shading indicates the range between 25th and 75th percentiles in FM, blue shading indicates the range between 25th, and 75th percentiles in NM, gold shading indicates the range between 25th, and 75th percentiles in NFM, and brown shading indicates significant ($p<0.05$) differences between the FM–NM and NFM–NM comparisons. The lower panel divides the results into the six characteristic frequency intervals. The upper and lower limits of each box represent the 75th and 25th percentiles, respectively; the line between these is the median value. *$p < 0.05$, **$p < 0.001$. The FM group is represented in red, NFM in gold, and NM in blue. The FI-II to FI-VI frequency intervals are specified in Sect. 26.1

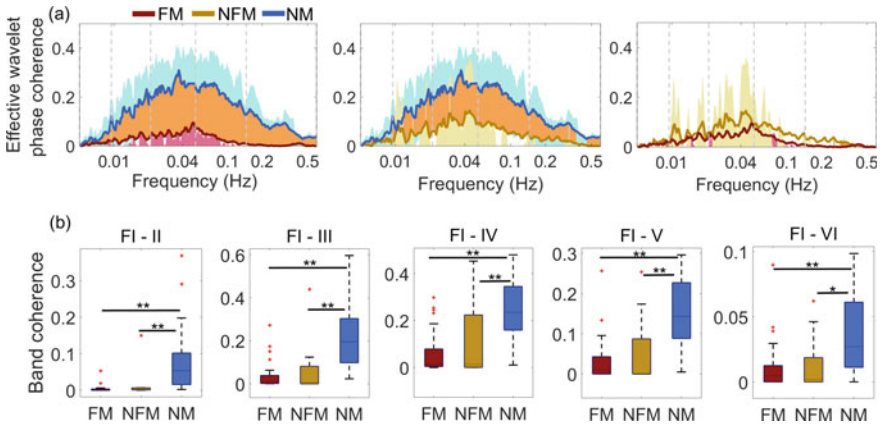

Fig. 26.3 Effective phase coherence: Wavelet phase coherence (minus surrogate thresholds) between IHF derived from left ankle blood flow and IHF extracted from right ankle blood flow, mean over groups, where **a** indicates comparisons between groups: the first column is the FM–NM, with NFM–NM (second column) and FM–NFM (third column). Red, blue and gold shading indicates respectively the ranges between the 25th and 75th percentiles for the FM, NM, and NFM groups; brown shading indicates significant ($p < 0.05$) differences between groups. **b** Box-plots showing coherence between the IHF signals within the frequency intervals FI-II to FI-VI (see Sect. 26.1). $^{*}p < 0.05$, $^{**}p < 0.005$

26.5 Non-invasive Diagnosis of Malaria

Detection and classification between malaria and non-malaria. We have found that there is a set of attributes that identifies malaria efficiently, arguably providing the basis of a dynamical biomarker for malaria:

- The area under the curve showing phase coherence between the instantaneous heart frequencies (extracted from the left/right ankle LDF blood flow signals, i.e. IHF1–IHF2) in the 0.005–1 Hz frequency interval <0.0254.
- The area under the curve showing phase coherence between the blood flow signals in the 0.6–1.6 Hz frequency interval <0.2013.
- The area under the curve showing phase coherence between respiration and the instantaneous heart frequency in 0.145–1 Hz frequency interval extracted from the ECG <0.0245.

Combining these characteristic attributes and using five classification algorithms from Waikato Environment for Knowledge Analysis (WEKA): J48, LMT, Random forest, Bagging and boosting-AdaBoos results in a high predictive performance with a classification accuracy (i.e. instances correctly classified) of 83%, 82%, 84%, 85% and 89% respectively in discriminating between FM, NFM and NM, based on the

Table 26.2 Confusion matrix, giving both the numbers and likelihoods of correct and incorrect classifications, using a Boosting algorithm

Classified state			
Febrile malaria (%)	Non-febrile malaria (%)	Non-malaria (%)	
92	3	5	Febrile malaria
50	40	10	Non-febrile malaria
4	0	96	Non-malaria
Correctly classified instances		87	88.7755%
Incorrectly classified instances		11	11.2245%
Total number of instances		98	

available training data (with the corresponding confusion matrix expressed in percentages in Table 26.2). The determining step of the diagnostic test involves detecting whether the markers are below the normal values of 0.0254, 0.2013, 0.0245 respectively for each of the markers.

26.6 Discussion

Uncomplicated malaria presents with acute periodic episodes of fever, chills, rigors, sweating and headache. These episodes reflect infection of the RBCs by the malarial organism, its subsequent multiplication within RBCs and later bursting of RBCs to release more organisms into blood. This cyclical process coincides with the episodes of fever. In addition the blood platelets are often affected and reduced, and abnormal adhesion of RBCs to the microvasculature results. Combined with changes in plasma, these changes lead to clogging of the microvasculature, with resulting low oxygen tension in surrounding tissues. The underlying mechanisms and pathologic processes described are unique and highly characteristic of malaria. It is probable that the physical findings observed from the study are equally specific to malaria, thereby providing an avenue for non-invasive diagnosis of malaria in the future.

Based on the hypotheses proposed above, clear distinctions have been demonstrated in the cardiovascular dynamics of subjects with febrile malaria, non-febrile malaria and healthy non-malaria, contributing to an understanding of the physiological processes occurring within the microvasculature in malaria. Furthermore, a diagnostic test has been developed based on recordings of LDF, respiration and ECG. Analyses by wavelet phase coherence and nonlinear mode decomposition enable malaria and non-malaria to be differentiated with 88 % accuracy, as classified by machine learning algorithms, based on the training data presented. Note that, we use “malaria” to describe both the febrile and non-febrile malaria patients, while “controls” or “non-malaria” are healthy subjects without malaria.

As demonstrated in earlier studies on malarial microvascular function [18, 19, 45], it was observed that febrile malaria resulted in a significantly increased respiratory rate and instantaneous heart frequency, compared to healthy subjects. Skin temperature was significantly higher in malaria. Skin temperature is believed to be a determining factor of respiratory rate, and of heart rate [10]. This increase in instantaneous heart frequency alongside skin temperature in malarial subjects may perhaps result in a mixture of vasodilation, resulting in hypovolaemia, and high metabolic rate due to pyrexia. It is worth noting that a significant increase in skin temperature also leads to more vasodilation, and lowers diastolic and systolic blood pressure as observed in the malaria patients. This decrease in blood pressures of malarial patients demonstrates significant effects of the disease on both the heart's pumping function and the systemic resistance. The striking reduction in the diastolic pressure may perhaps be associated with the tachycardia observed in malaria.

Hematological examination showed a decrease of PCV in malaria. This is probably due to the compromised red blood cell deformation, and ineffective erythropoiesis within malarial vasculature [2, 42]. In terms of cardiovascular dynamics, malaria resulted in significantly reduced blood flow spectral power in the frequency interval associated with cardiac and myogenic activity. This effect is probably associated with the compromised delivery of oxygen and nutrients observed in malaria [4, 7]. Furthermore, the lactic acidosis in the malarial state is exacerbated by inadequate removal of metabolic waste products, resulting from increased production of lactic acid by the parasites as well as reduced clearance by the liver [11].

It has also been reported that many treatments fail due to the reduced oxygen delivery in malaria, resulting in metabolic acidosis (through stimulation by cytokines), leading in turn to respiratory distress [40]. Significantly higher normalised spectral power was observed in the blood flow frequency intervals related to neurogenic (IV) and NO-dependent endothelial (V) activity in febrile malaria, compared to healthy non-malaria (Fig. 26.1a, b). However, no such effects were found in the same frequency intervals for non-febrile malaria. This might imply that these physiological processes are not markedly affected in non-febrile malaria due the absence of fever.

Coherence provides additional insight into the changes that occur with malaria in the modulation of the heart rate by the respiratory frequency. The significant attenuation of cardiac interval coherence between IHF (derived from the ECG) and breathing in malaria implies an impairment in respiratory sinus arrhythmia (RSA), given that the high frequency component in IHF reflects the influence of breathing on the heart rate [12, 21, 44], an inference that is supported by an additional finding: significantly decreased blood flow coherence in the frequency interval associated with cardiac activity. In addition, the results may also signify destruction of both the sympathetic and parasympathetic modulations that critically influence the oscillations in heart beat intervals. These modulations are widely known to contribute to the oscillatory components manifesting in IHF [6, 25, 27, 35]. Hence this finding may perhaps explain the alteration we observed in the power spectra of skin blood flow cardiac oscillations.

As mentioned above in the introduction, there are drawbacks associated with existing methods for assessing and diagnosing malaria. These have made the quest

for real-time techniques for noninvasive malaria diagnosis an active area of research. Based on our findings, a cut-off was established in line with differences in cardiovascular dynamics between malarias and healthy non-malaria, with a classification accuracy of 88% (Table 26.2). Early cases of non-febrile malaria, where subjects had started taking antimalarial or antipyretic drugs, were also considered as malaria in this study, due to its similarity to febrile malaria in terms of blood properties: the cytoadherence and microvasculature characteristics, including the increased stiffness of the membrane of an infected erythrocytes and their abnormal tendency to stick to endothelial cells lining the blood vessels. Consistent with this similarity, no significant differences were found in mean blood flow recorded from the extremities of the body, or in respiratory rate, between febrile malaria and non-febrile malaria. In addition, there was no significant difference in the blood flow or IHF dynamics in any of the six frequency intervals between febrile and non-febrile malaria. On the contrary, febrile malaria and non-febrile malaria differed mainly in terms of their mean skin temperature and IHF.

In summary, this study demonstrated changes in both the average values and oscillatory components of cardiovascular dynamics in malaria, in comparison with healthy non-malaria subjects, providing a better understanding of the cardiovascular physiology of malaria. A diagnostic cut-off for the early distinction between malaria and non-malaria is presented, based on differences observed in both IHF, blood flow and IHF dynamics, extracted through wavelet based analysis and nonlinear mode decomposition. Whilst this approach looks promising, as it has potential for identifying malaria noninvasively within a short period of time, future studies are needed to compare the physical findings in malaria with those in other febrile infections.

Acknowledgements We are grateful to the participants who generously volunteered to be measured in this project. The work was supported by the Engineering and Physical Sciences Research Council (UK) Grant No. EP/M006298/1, the Tertiary Education Trust Fund (Nigeria), the Petroleum Technology Development Fund (Nigeria) under Grant No. PTDF/ED/OSS/PHD/1120/17, and the Joy Welch Educational Charitable Trust (UK).

References

1. Y.A. Abdulhameed, Nonlinear cardiovascular oscillatory dynamics in malaria. Ph.D. thesis, Lancaster University (2020)
2. O.O. Aina, C.O. Agomo, Y.A. Olukosi, H.I. Okoh, B.A. Iwalokun, K.N. Egbuna, A.B. Orok, O. Ajibaye, V.N. Enya, S.K. Akindele et al., Malariometric survey of Ibeshe community in Ikorodu, Lagos state: dry season. Malar. Res. Treat. **2013** (2013)
3. A. Bandrivskyy, A. Bernjak, P.V.E. McClintock, A. Stefanovska, Wavelet phase coherence analysis: Application to skin temperature and blood flow. Cardiovasc. Engin. **4**(1), 89–93 (2004)
4. S.C. Beards, G.M. Joynt, J. Lipman, Hæmodynamic and oxygen transport response during exchange transfusion for severe falciparum malaria. Postgrad. Med. J. **70**(829), 801–804 (1994)
5. A. Bernjak, J. Cui, S. Iwase, T. Mano, A. Stefanovska, D.L. Eckberg, Human sympathetic outflows to skin and muscle target organs fluctuate concordantly over a wide range of time-varying frequencies. J. Physiol. (London) **590**(2), 363–375 (2012)

6. P.F. Binkley, E. Nunziata, G.J. Haas, S.D. Nelson, R.J. Cody, Parasympathetic withdrawal is an integral component of autonomic imbalance in congestive heart failure: demonstration in human subjects and verification in a paced canine model of ventricular failure. J. Am. Coll. Cardiol. **18**(2), 464–472 (1991)
7. D. Bruce-Hickman, Oxygen therapy for cerebral malaria. Travel Med. Infect. Dis. **9**(5), 223–230 (2011)
8. P.T. Clemson, G. Lancaster, A. Stefanovska, Reconstructing time-dependent dynamics. Proc. IEEE **104**(2), 223–241 (2016)
9. P.T. Clemson, A. Stefanovska, Discerning non-autonomous dynamics. Phys. Rep. **542**(4), 297–368 (2014)
10. P. Davies, I. Maconochie, The relationship between body temperature, heart rate and respiratory rate in children. Emerg. Med. J. **26**(9), 641–643 (2009)
11. M. English, R. Sauerwein, C. Waruiru, M. Mosobo, J. Obiero, B. Lowe, K. Marsh, Acidosis in severe childhood malaria. QJM: Int. J. Med. **90**(4), 263–270 (1997)
12. J.B. Hinnant, L. Elmore-Staton, M. El-Sheikh, Developmental trajectories of respiratory sinus arrhythmia and preejection period in middle childhood. Dev. Psychobiol. **53**(1), 59–68 (2011)
13. A.E. Hramov, A.A. Koronovskii, V.I. Ponomarenko, M.D. Prokhorov, Detection of synchronization from univariate data using wavelet transform. Phys. Rev. E **75**(5), 056,207 (2007)
14. D. Iatsenko, *Nonlinear Mode Decomposition* (Springer, Berlin, 2015)
15. D. Iatsenko, A. Bernjak, T. Stankovski, Y. Shiogai, P.J. Owen-Lynch, P.B.M. Clarkson, P.V.E. McClintock, A. Stefanovska, Evolution of cardio-respiratory interactions with age. Phil. Trans. R. Soc. Lond. A **371**(1997), 20110,622 (2013)
16. D. Iatsenko, P.V.E. McClintock, A. Stefanovska, On the extraction of instantaneous frequencies from ridges in time-frequency representations of signals. Signal Proc. **125**, 290–303 (2016)
17. D. Iatsenko, A. Stefanovska, P.V.E. McClintock, Nonlinear mode decomposition: a noise-robust, adaptive, decomposition method. Phys. Rev. E. **92**, 032,916 (2015)
18. Y. Imai, H. Kondo, T. Ishikawa, C.T. Lim, T. Yamaguchi, Modeling of hemodynamics arising from malaria infection. J. Biomech. **43**, 1386–1393 (2010)
19. P.G. Jayathilake, G. Liu, Z. Tan, B.C. Khoo, Numerical study on the dynamics and oxygen uptake of healthy and malaria-infected red blood cells. Adv. Appl. Math. Mech. **7**(5), 549–568 (2015)
20. A.S. Karavaev, M.D. Prokhorov, V.I. Ponomarenko, A.R. Kiselev, V.I. Gridnev, E.I. Ruban, B.P. Bezruchko, Synchronization of low-frequency oscillations in the human cardiovascular system. Chaos **19**(3), 033,112 (2009)
21. P.G. Katona, J. Felix, Respiratory sinus arrhythmia: noninvasive measure of parasympathetic cardiac control. J. Appl. Physiol. **39**(5), 801–805 (1975)
22. F. Krampa, Y. Aniweh, G. Awandare, P. Kanyong, Recent progress in the development of diagnostic tests for malaria. Diagnostics **7**(3), 54 (2017)
23. P. Kvandal, S.A. Landsverk, A. Bernjak, A. Stefanovska, H.D. Kvernmo, K.A. Kirkebøen, Low frequency oscillations of the laser Doppler perfusion signal in human skin. Microvasc. Res. **72**(3), 120–127 (2006)
24. G. Lancaster, D. Iatsenko, A. Pidde, V. Ticcinelli, A. Stefanovska, Surrogate data for hypothesis testing of physical systems. Phys. Rep. (2018)
25. S. Lehtipalo, O. Winsö, L.O.D. Koskinen, G. Johansson, B. Biber, Cutaneous sympathetic vasoconstrictor reflexes for the evaluation of interscalene brachial plexus block. Acta Anaesthsiol. Scand. **44**(8), 946–952 (2000)
26. M. Malik, Heart rate variability. Ann. Noninvas. Electro. **1**(2), 151–181 (1996)
27. M.F. Meyer, C.J. Rose, J.O. Hülsmann, H. Schatz, M. Pfohl, M, Impaired 0.1-Hz vasomotion assessed by laser Doppler anemometry as an early index of peripheral sympathetic neuropathy in diabetes. Microvasc. Res. **65**, 88–95 (2003)
28. F. Mormann, K. Lehnertz, P. David, C.E. Elger, Mean phase coherence as a measure for phase synchronization and its application to the EEG of epilepsy patients. Phys. D **144**(3–4), 358–369 (2000)

29. G.E. Nilsson, T. Tenland, P.L. Öberg, Evaluation of a laser Doppler flowmeter for measurement of tissue blood flow. IEEE Trans. Biomed. Eng. **27**, 597–604 (1980)
30. A. Pikovsky, M. Rosenblum, J. Kurths, *Synchronization—A Universal Concept in Nonlinear Sciences* (Cambridge University Press, Cambridge, 2001)
31. T. Schreiber, A. Schmitz, Surrogate time series. Phys. D **142**(3–4), 346–382 (2000)
32. L.W. Sheppard, A. Stefanovska, P.V.E. McClintock, Testing for time-localised coherence in bivariate data. Phys. Rev. E **85**, 046,205 (2012)
33. J.M. Sherwood, D. Holmes, E. Kaliviotis, S. Balabani, Spatial distributions of red blood cells significantly alter local haemodynamics. PLOS ONE **9**, e100,473 (2014)
34. Y. Shiogai, A. Stefanovska, P.V.E. McClintock, Nonlinear dynamics of cardiovascular ageing. Phys. Rep. **488**, 51–110 (2010)
35. T. Söderström, A. Stefanovska, M. Veber, H. Svenson, Involvement of sympathetic nerve activity in skin blood flow oscillations in humans. Am. J. Physiol.: Heart. Circ. Physiol. **284**(5), H1638–H1646 (2003)
36. A. Stefanovska, Coupled oscillators: complex but not complicated cardiovascular and brain interactions. IEEE Eng. Med. Bio. Mag. **26**(6), 25–29 (2007)
37. A. Stefanovska, M. Bračič, Physics of the human cardiovascular system. Contemp. Phys. **40**(1), 31–55 (1999)
38. A. Stefanovska, M. Bračič, H.D. Kvernmo, Wavelet analysis of oscillations in the peripheral blood circulation measured by laser Doppler technique. IEEE Trans. Bio. Med. Eng. **46**(10), 1230–1239 (1999)
39. A. Stefanovska, M. Bračič Lotrič, S. Strle, H. Haken, The cardiovascular system as coupled oscillators? Physiol. Meas. **22**(3), 535–550 (2001)
40. T.E. Taylor, A. Borgstein, M.E. Molyneux, Acid-base status in paediatric Plasmodium falciparum malaria. QJM **86**(2), 99–109 (1993)
41. D.A. Warrell, H.M. Gilles, *Essential Malariology*, 4th edn. (CRC Press, London, 2019)
42. D. Weatherall, L. Miller, D. Baruch, K. Marsh, O. Doumbo, C. Casals-Pascual, D. Roberts, Malaria and the red cell. Hematology **2002**, 35–57 (2002)
43. F. Wilcoxon, Individual comparisons by ranking methods. Biom. Bull. **1**(6), 80–83 (1945)
44. F. Yasuma, J. Hayano, Respiratory sinus arrhythmia—why does the heartbeat synchronize with respiratory rhythm? Chest **125**(2), 683–690 (2004)
45. T.W. Yeo, D.A. Lampah, E. Kenangalem, E. Tjitra, J.B. Weinberg, D.L. Granger, R.N. Price, N.M. Anstey, Decreased endothelial nitric oxide bioavailability, impaired microvascular function, and increased tissue oxygen consumption in children with falciparum malaria. J. Infect. Dis. **210**(10), 1627–1632 (2014)
46. E. Yeom, Y.J. Kang, S.J. Lee, Changes in velocity profile according to blood viscosity in a microchannel. Biomicrofluidics **8**, 034,110 (2014)

Part V
Outlook

Chapter 27
Physics of Biological Oscillators: Outlook

Robert S. MacKay, Aneta Stefanovska, and Constantino Tsallis

Abstract The volume closes with a brief summary of highlights and pointers to further directions for the physics of biological oscillators.

To understand living systems requires more than just traditional dynamical systems theory.

Living systems are subject to a time-varying environment, so a key first step is to use and further develop the theory of non-autonomous dynamical systems. Also, they do not last forever, so practical versions of dynamical systems concepts like limit cycles are required that make sense for long but finite time-intervals.

Secondly, a lot of the environment may not be known explicitly, so it is appropriate to model the residual effects by a stochastic process. There are many candidates, however, and it is unlikely to be enough to consider only Weiner processes. Many processes in Nature that serve as perturbations of living systems are in fact oscillatory.

Thirdly, for systems where discreteness plays a role, for example at the level of biomolecules or at the level of individuals in a population, the dynamics of the system itself may require a stochastic formulation. Alternatively, individuals in a population can be treated as oscillatory systems and analysed as networks of coupled non-autonomous oscillators.

Finally, living systems operate far from thermodynamic equilibrium. Principles are required to treat this realm of physics. The minimum entropy production rate principle of Glansdorff and Prigogine is valid only near equilibrium. Maes and Netocny

R. S. MacKay (✉)
Mathematics Institute and Centre for Complexity Science, University of Warwick, Coventry, UK
e-mail: R.S.MacKay@warwick.ac.uk

A. Stefanovska
Department of Physics, Lancaster University, Lancaster L1 4YB, UK
e-mail: aneta@lancaster.ac.uk

C. Tsallis
Centro Brasileiro de Pesquisas Fisicas and National Institute of Science and Technology for Complex Systems, Rua Xavier Sigaud 150, 22290-180 Rio de Janeiro - RJ, Brazil
e-mail: tsallis@santafe.edu

A. Stefanovska and P. V. E. McClintock (eds.), *Physics of Biological Oscillators*, Understanding Complex Systems,
https://doi.org/10.1007/978-3-030-59805-1_27

[4] have come up with an extension that is valid for all Markov processes, namely that the stationary distribution maximises the Donsker-Varadhan large deviation rate function for fluctuations in the occupation probabilities, but more work is required to make this physically meaningful. See [3] for a recent survey.

Another principle, that goes back to Helmholtz, then Ashby in the days of cybernetics, and has been extended by Friston [2], is the free energy principle. It states that systems act to minimise "surprise": the discrepancy between observations and beliefs. See the Wikipedia page for more. On the other hand, a totally opposite principle has been promoted, the future state maximisation principle, that individuals act to keep their options open as much as possible (for an application, see [1]).

Although various of the above phenomena in living organisms are describable within the realm of statistical mechanics and thermodynamics, they cannot be described in terms of the Boltzmann–Gibbs theory. This is because, in one way or another, the latter requires the microscopic dynamics to be strongly chaotic, i.e., basically mixing and ergodic, being consistently based on the usual additive entropic functional. Living and living-like organisms and systems (economics, linguistics, geophysics, astrophysics), with their subtle nature, usually evolve within weak chaos, at the edge of chaos, between strong chaos and order (typically with vanishing Lyapunov exponents). This feature usually mandates nonadditive entropic functionals, and, consequently, an entire reformulation and mesoscopic interpretation of thermodynamics itself (see, for instance, [5]).

This volume has concentrated on the physics of biological oscillations. The pervasiveness of oscillations in living systems suggest that none of the above principles will really get to the heart of how living systems function. Their dynamical nature must be taken into account. So also must the continuous exchange of energy and matter, which is the key characteristic of living systems. It occurs on all scales ranging from exchange across the cell membrane to exchanges at organ and system levels. So, conservation of matter (mass) is not an appropriate principle. It is the exchange of matter that results in the continuous sustained oscillations that are observed, with frequencies that are non-constant. Perhaps one can focus on the interactions between different parts of the system to develop new principles based on the phase differences between non-autonomous oscillatory systems, or networks of such systems. This scenario seems realistic in view of the studies that have already pointed to the stabilising effect of non-autonomicity.

References

1. H.J. Charlesworth, M.S. Turner, Intrinsically motivated collective motion. PNAS **116**, 15362–15367 (2019)
2. K. Friston, The free-energy principle: a unified brain theory? Nat. Rev. Neurosci. **11**, 127–138 (2010)
3. C. Maes, Frenesy. https://arxiv.org/abs/1904.10485
4. C. Maes, K. Netocny, Minimum entropy production principle from a dynamical fluctuation law. J. Math. Phys. **48**, 053306 (2007)
5. C. Tsallis, Beyond Boltzmann-Gibbs-Shannon in physics and elsewhere. Entropy **21**, 696 (2019)

Index

A. Stefanovska and P. V. E. McClintock (eds.), *Physics of Biological Oscillators*, Understanding Complex Systems,
https://doi.org/10.1007/978-3-030-59805-1

S

T

U

V